Hondata R&D





Technical Review







October 2003



Comment on the Cover

As time goes on, more and more sweets and snacks come with some kind of free gift. More and more customers buy the sweets and snacks for the free gift and take some small pleasure in it.
The cover shows scenes that stir emotions, encounters with people, and the discovery of the unknown. These are the free gifts that we obtain when we buy a Honda product.
I look for Honda products because I want this kind of free gift. I also want to go on providing customers with products that will give them pleasure, too.



Asaka R&D Center
Sanae Shimizu

Research on Electric Power System for Honda FCX Fuel Cell Vehicle

Hidekazu TAKENAKA*

ABSTRACT

An ultra capacitor has been utilized as a back up power source to give the Honda fuel cell vehicle acceleration performance rivaling that of a conventional vehicle. To control the difference in voltage between the two power sources at system start-up or takeoff from idle stop, a VCU (Voltage and current Control Unit) has been set between the fuel cell and the high-voltage device for the traction motor. The VCU charges the ultra capacitor gradually by chopping control of the current from the fuel cell, equalizing the voltage of the fuel cell and the ultra capacitor. This prevents the occurrence of over-current at system start-up or takeoff from idle stop. When the ultra capacitor is being charged with regenerated braking energy, chopping control of the current from the fuel cell by the VCU electrically separates the fuel cell and the ultra capacitor, and the current from the fuel cell is restricted. This enables the energy provided by regeneration to be utilized for charging the ultra capacitor.

1. Introduction

In December 2002 the Honda FCX fuel cell vehicle became the world's first fuel cell vehicle to be marketed in Japan and the U.S. The vehicle is fueled by pure hydrogen, and represents an attempt to exploit an alternative energy source in consideration of the future exhaustion of the world's oil reserves. By utilizing pure hydrogen as a fuel, the vehicle produces no CO_2 and achieves a zero level of emissions. Vehicles employing a fuel cell, which produces no pollutants, are being focused on as the way of the future in the automotive field, and the FCX is designed as one ideal form in which a zero-emission vehicle should be realized[1].

Development of the FCX did not focus solely on the environmental performance of the vehicle. The aim of the development was to produce a vehicle that matched the performance of conventional vehicles, for example, acceleration performance, high responsiveness, and smooth drivability, which tend to be sacrificed when environmental performance is a development focus.

The transient power performance of a fuel cell is not as rapid as that of a gasoline internal combustion engine. A level of acceleration performance equivalent to that of a vehicle employing a gasoline engine cannot currently be obtained in a vehicle which relies only on a fuel cell as its power source. Therefore, a Honda ultra capacitor has been used in combination with the fuel cell in the

* Tochigi R&D Center

FCX as the electric power system to improve acceleration performance.

When the fuel cell and the ultra capacitor are used in combination, the difference in voltage between the two power sources becomes an issue. To eliminate this voltage difference, a voltage and current control unit (VCU) that regulates the output of the fuel cell has been set between the fuel cell and the high-voltage device for the traction motor.

This paper will discuss the principle of operation of the VCU and the actual performance of electric power control.

2. Study of the Power Train System

Table 1 shows the results of a comparison of power supply systems[2]. The simplest of these systems is that in which the motor is driven directly by the output of the fuel cell. In addition to this type of system, there are also systems providing power assist and braking energy regeneration mechanisms, in which a battery or an ultra capacitor is used in combination with the fuel cell.

When only the output of the fuel cell provides the driving force, driving performance depends entirely on the output characteristics of the fuel cell. The transient power performance of the fuel cell is inferior to that of a gasoline engine. In particular, it is difficult to ensure equivalent driving force during acceleration to that provided by a conventional gasoline engine vehicle when using this type of system. In addition, this type of system requires a startup device for starting the generation of power in the fuel cell from system shutdown status.

The types of systems that utilize a battery or an ultra capacitor as an energy storage unit in combination with the fuel cell were studied next. Here, the use of a nickel metal-hydride (Ni-MH) battery was taken as the base case, because this battery is at present conventionally employed in high-voltage applications. A comparison of the output characteristics of the Ni-MH battery and the ultra capacitor is shown in Fig. 1. It is clear from Fig. 1 that the ultra capacitor has a very high power density in comparison with the Ni-MH battery[3]. This output characteristic is particularly desirable for automotive dynamic performance, which requires high acceleration performance over a short period of time.

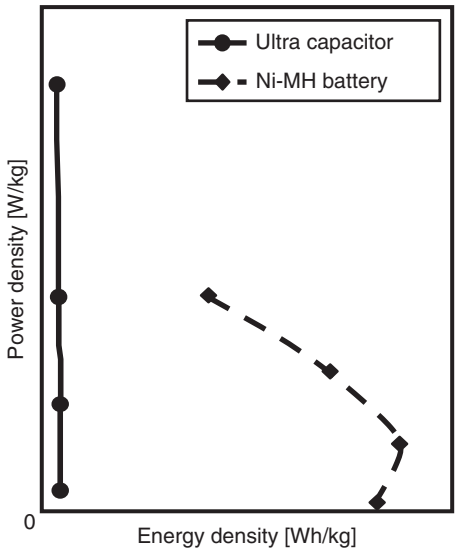


Fig. 1 Comparison of power density of Ni-MH battery and ultra capacitor

Table 1 Comparison of system configurations

	Basic configuration	High-voltage distribution system	Transmission efficiency	Braking regeneration	Power performance
Capacitor-assisted system	Traction motor, Fuel cell stack, Ultra capacitor	Not required	High	Yes	Instantaneous high-power assist
Battery-assisted system	Traction motor, High-voltage control device, Fuel cell stack, Battery	Required	Medium (Losses of high-voltage controllers)	Yes	Power assist
Fuel cell direct-supply system	Traction motor, Fuel cell stack	Not required (Startup device required)	High	No	Power and responsiveness depend on fuel cell stack

Voltage differences between the power sources become an issue when the fuel cell and the Ni-MH battery are used in combination. The fuel cell and the Ni-MH battery have specific current-voltage characteristics which are different from each other. It is therefore necessary to employ a high-voltage control mechanism which enables the voltage of the Ni-MH battery to be constantly maintained at the same voltage as the fuel cell in order to provide power assist and charge the battery with regenerative braking energy in accordance with the current-voltage characteristic of the fuel cell. On the other hand, the voltage of the ultra capacitor can be varied according to the current-voltage characteristic of the fuel cell, and the output current characteristic is very stable. Therefore, when electrically connected to the fuel cell, the ultra capacitor is capable of constantly maintaining the same voltage as the fuel cell. This makes the use of the high-voltage control mechanism unnecessary when the ultra capacitor is employed.

The comparison discussed above led to the selection of the ultra capacitor as the backup power source for the FCX, given its superiority to the Ni-MH battery in (1) enabling instantaneous high-power assist, and (2) eliminating the requirement for a high-voltage control mechanism.

3. Principle of Electrical Control Using VCU

When the system is shut down, and the fuel cell and the ultra capacitor remain connected with the high-voltage device, electricity gradually leaks away as dark current from the vehicle. At this time, as the hydrogen storage tank valve has closed, electric power is generated by the fuel cell from the hydrogen remaining in the hydrogen supply pipes. This may cause negative pressure in the pipes and have a bad influence on the fuel cell stack. In addition, the ultra capacitor continues to discharge, and if its voltage falls below the threshold level, the system will not start-up.

To prevent this situation, relay units are set between the fuel cell and the high voltage devices, and the ultra capacitor and the high voltage devices. When the fuel cell and the ultra capacitor are electrically disconnected by the relay units, their voltages have a difference. If these relay units are connected while there is a difference in voltage between the two power sources, it is possible that an over-current could occur in the circuit connecting the fuel cell and the ultra capacitor. A VCU, which regulates the output current of the fuel cell by chopping to gradually reduce the difference in voltage with the ultra capacitor, is therefore required. In this system, the VCU is set between the fuel cell and the high-voltage devices for the traction motor. Figure 2 shows a system diagram of the VCU and the high-voltage devices.

The operation of the VCU and a diagram of the current-voltage control waveforms are shown in Fig. 3. IGBT is switched on or off by a control signal, which enables chopping of the output current from the fuel cell. In other words, IGBT functions as a switch. When IGBT is on, the current from the fuel cell, I_{FC}, becomes the current to the high-voltage devices, I_{OUT}. The current I_{OUT} becomes the current flowing into IGBT, I_{sw}, and finally returns to the negative side of the fuel cell. Therefore, $I_{FC} = I_{OUT} = I_{sw}$.

When IGBT is off, the current path from the fuel cell is closed and the current I_{FC} does not flow. Instead, the inductor placed in the current path charges electromagnetic energy by its inductance, and the discharge of this energy supplies the current when IGBT is off. This discharged current becomes the current flowing to diode 2, I_D, and flows into the high-voltage devices. In other words, $I_D = I_{OUT}$. The inductance of the inductor is designed to charge an amount of electromagnetic energy corresponding to the amount required for the current when IGBT is off. The total current flowing to the high-voltage devices becomes $I_{OUT} = I_{SW} + I_D$. The ability to vary the ratio of on to off in IGBT enables the output current of the fuel cell to be continuously varied.

At the same time, the current from the fuel cell is used to charge the ultra capacitor. The voltage of the ultra capacitor, V_{CAP}, increases as charging proceeds, until it becomes the same level with V_{FC}, the voltage of the fuel cell. V_{FC} becomes smaller as I_{FC} becomes greater. When $V_{FC} = V_{CAP}$, the VCU stops chopping and remains constantly on.

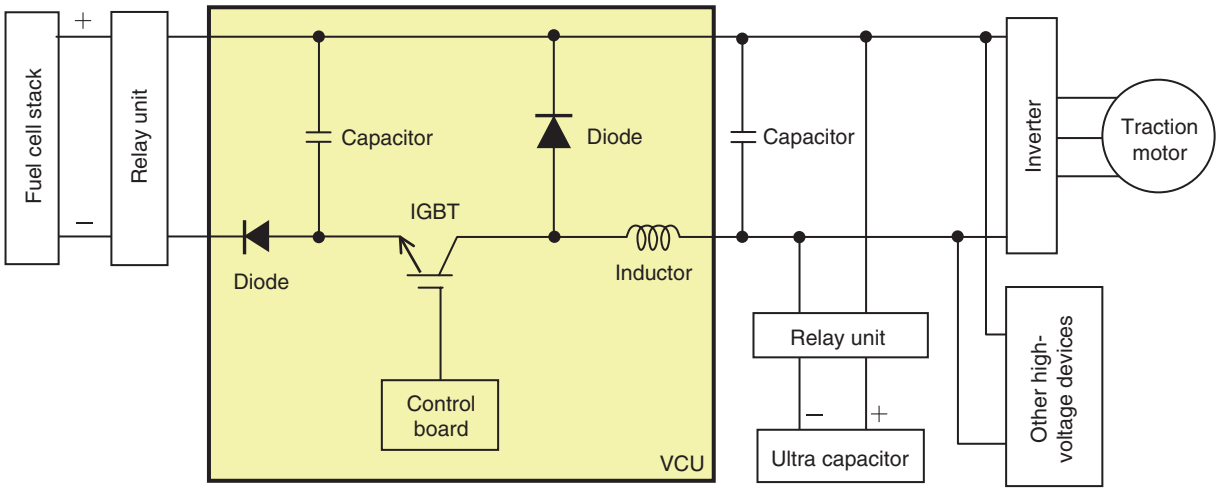


Fig. 2 System diagram of VCU and high-voltage devices

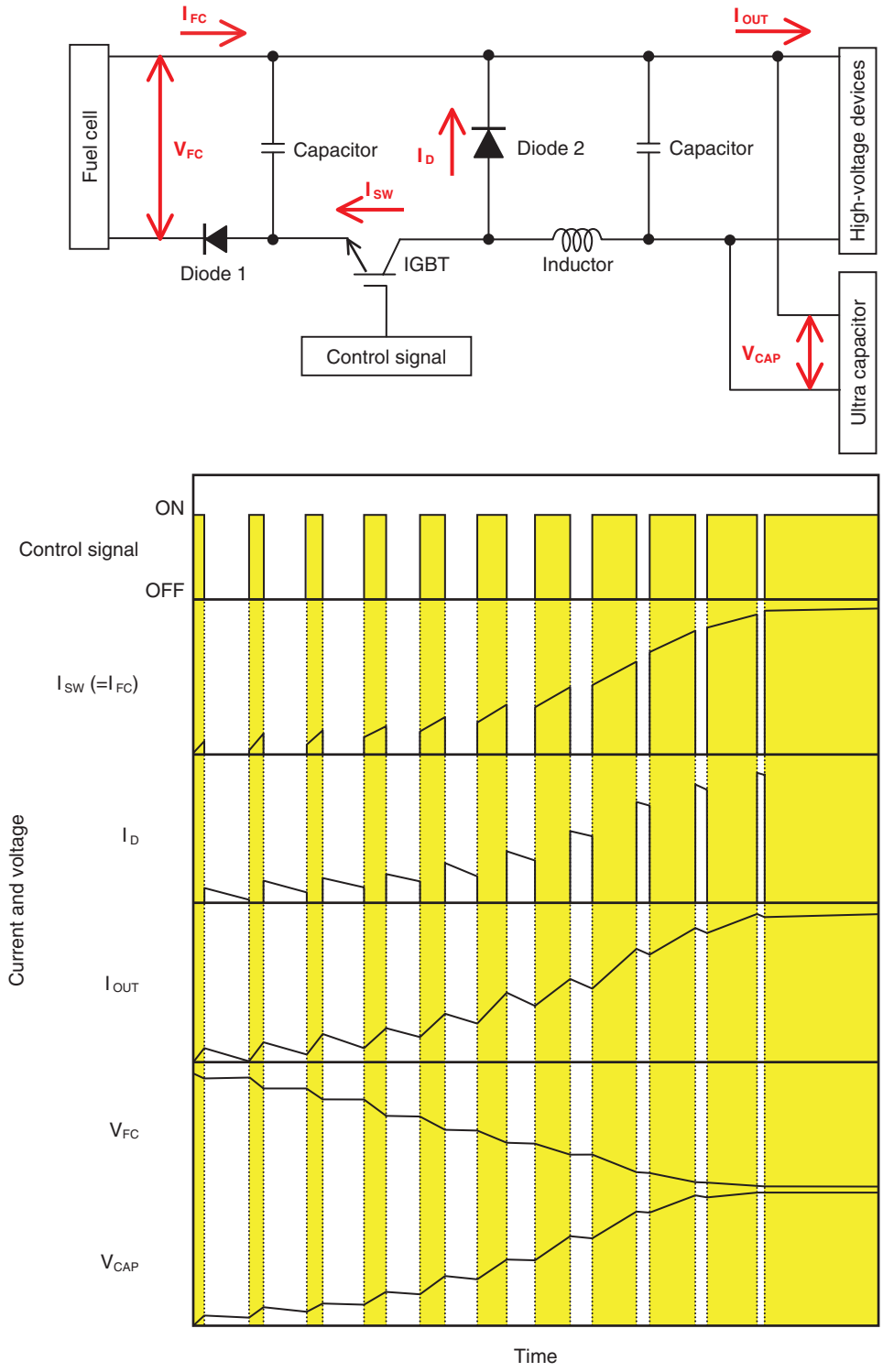


Fig. 3 Diagram of VCU current control mode

4. Verification of the VCU Operation in a Vehicle

4.1. Operation at System Start-up

Figure 4 shows fuel cell voltage, V_{FC}, and current, I_{FC}, ultra capacitor voltage, V_{CAP}, and current, I_{CAP}, when the system is started up and the fuel cell begins generating power from system shutdown status. When the system is started up, first the relay unit for the ultra capacitor starts to operate, and then the relay unit for the fuel cell operates. The voltage of the fuel cell is different from that of the ultra capacitor. Chopping by the VCU charges the ultra capacitor with current from the fuel cell, causing the voltage of the ultra capacitor to approach that of the fuel cell gradually. When the voltages are equal, the VCU stops chopping and constantly remains on.

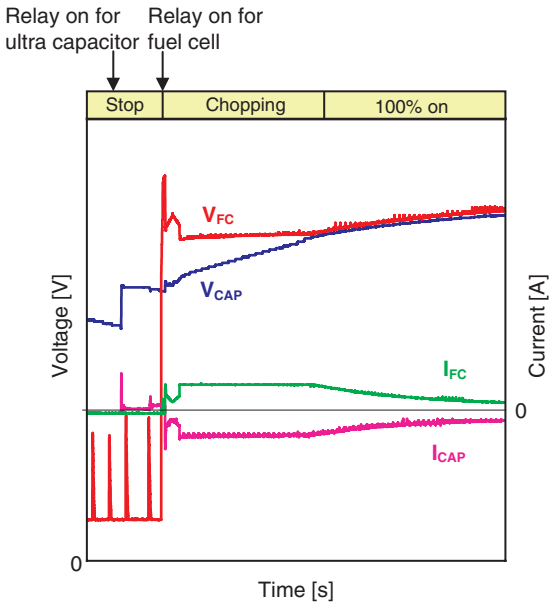


Fig. 4 Voltage and current profiles of fuel cell and ultra capacitor at start-up

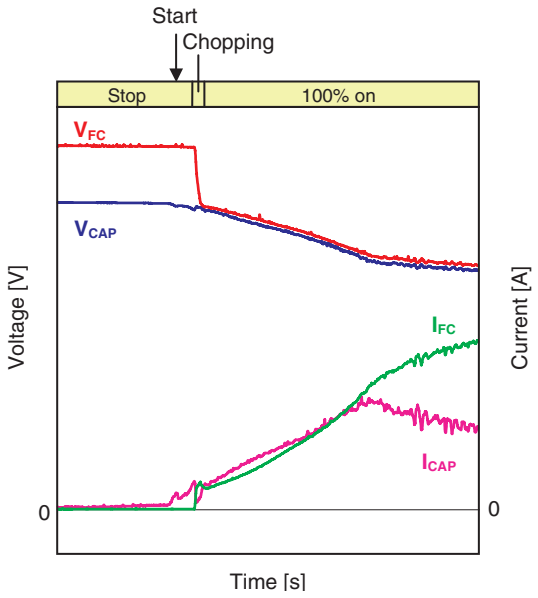


Fig. 5 Voltage and current profiles of fuel cell and ultra capacitor when driving from idle stop mode

4.2. Operation at Takeoff from Idle Stop

To control the consumption of electric power, the fuel cell in the FCX is provided with an idle stop function which goes into operation when a traction command for the motor has not been received for a certain period of time. Because the VCU is 100% off during idle stop, a difference in voltage occurs between the fuel cell and ultra capacitor. Figure 5 shows the voltage and current profiles of the fuel cell and the ultra capacitor when the vehicle takes off from the idle stop mode. When a traction command goes to the motor while the vehicle is in the idle stop mode, the VCU starts chopping. Continuous chopping equalizes the voltages of the fuel cell and the ultra capacitor, after which the VCU stops chopping and constantly remains on.

Power assist mode by the ultra capacitor at acceleration from a standstill can also be seen in Fig. 5. The fuel cell attempts to provide current to the motor when the traction command is received, but there is a slight time lag between the idle stop mode and restarting power generation. Current is output from the ultra capacitor to compensate for this output delay. Current continues to be provided from the ultra capacitor even after the fuel cell begins to generate electricity, because it has not generated the level of power required for acceleration. The amount of current from the ultra capacitor gradually diminishes as the amount generated by the fuel cell increases, and power assist stops when the amount of power generated in the fuel cell reaches the required level.

4.3. Operation of Regeneration during Braking

The FCX is able to charge the ultra capacitor with energy regenerated during braking. The voltage and current profiles of the fuel cell and the ultra capacitor in the regeneration mode are shown in Fig. 6. When the vehicle begins to decelerate, the power generated by the

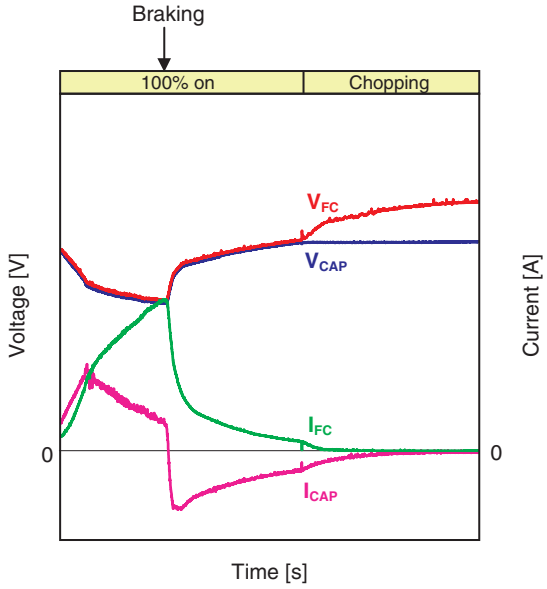


Fig. 6 Voltage and current profiles of fuel cell and ultra capacitor in regeneration mode

fuel cell is controlled to the minimum, and the motor starts regenerating braking energy. As a result, the current from the ultra capacitor becomes negative, and the ultra capacitor begins to charge with regenerated energy. However, because the VCU is constantly on when braking starts, the ultra capacitor is charged with energy from the fuel cell in addition to energy from braking regeneration. To reduce charging from the fuel cell, and to maximize the amount of charging from braking regeneration, the VCU starts chopping to electrically disconnect the fuel cell and the ultra capacitor. This enables output power from the fuel cell to be restricted, and the energy provided by regeneration to be increased.

5. Conclusion

A voltage and current control unit (VCU) has been utilized to control the power provided by the fuel cell in a fuel cell vehicle that also uses an ultra capacitor as a power source. The following results have been obtained:

(1) Chopping by the VCU when the system is started up and when taking off from the idle stop mode controls the current from the fuel cell, enabling the difference in voltage between the fuel cell and the ultra capacitor to be eliminated.
(2) In the regeneration mode, chopping by the VCU electrically disconnects the fuel cell and the ultra capacitor, enabling the energy from the fuel cell to be restricted. This enables the energy provided by regeneration to be utilized for charging the ultra capacitor.

References

(1) Kawasaki, S., Ogura, M., Ono, T., Kami, Y.: Development of the Honda FCX Fuel Cell Vehicle, Honda R&D Technical Review, Vol. 15, No. 1, p. 1-6 (2003)
(2) Ogawa, T., Kimura, K., Uchibori, K., Fujimoto, S., Shimizu, K.: Development of New Power Train for Honda FCX Fuel Cell Vehicle, Honda R&D Technical Review, Vol. 15, No. 1, p. 7-12 (2003)
(3) Tamenori, K., Yamamoto, K., Anekawa, A., Taguchi, T., Kubota, S., Kawahara, M.: Development of Electric Double-layer Capacitor System for Fuel Cell Vehicle, Honda R&D Technical Review, Vol.15, No.1, p. 25-30 (2003)

■ Author ■



Hidekazu TAKENAKA

Research of Micro-gasturbine Generator

Koichi SHINMURA* Koji YAMAGUCHI* Sadachika TSUZUKI*
Hidemi KIMURA* Takeshi KATO*

ABSTRACT

Research has been conducted on a micro-gasturbine generator as a compact distributed energy resource in order to improve energy usage efficiency. While aiming at a low emission level by introducing a premixed, lean-burning combustor, the engine has achieved a generation efficiency of 30.8 percent and the system achieved 26.7 percent by also adopting a recuperator and by reducing the heat and mechanical loss within its compact structure. Electricity output from the high-speed generator is converted into commercial power and supplied to the power grid. The engine, inverter and other auxiliary devices have been arranged into one compact package, achieving the highest performance and lowest noise level in the 40 kW class. Further modifications of the engine have improved the efficiency to 32.9 percent at the engine end.

1. Introduction

Most electrical power demand thus far has been supplied by large-scale thermoelectric, hydroelectric, and nuclear power plants. Higher efficiency has been pursued by increasing the scale of these facilities, but this has in turn created the issues of long construction periods, mounting equipment costs, and transmission loss over the long distances to the demand sites. Factors, such as global trends toward electric power deregulation and the increased environmental load of nuclear power plants and other facilities, have raised interest in distributed generation. Of these, micro-gasturbine generators are gathering attention due to expectations for lower costs from mass production and for reduced environmental load as a result of improvements both in generation efficiency, by adoption of a recuperator, and in low emission combustor performance[(1), (2)].

2. Research Aims and Themes

Honda is tackling the practical application of advanced environmental technologies. As a part of these efforts, the company has promoted research on distributed energy to improve energy usage efficiency and to meet a part of the electrical power demand.

This research's aim is to realize a micro-gasturbine as a distributed generation (grid connect) system based on the concepts of 1) superior cost performance through high efficiency generation and long life, 2) environmentally friendlier with low emissions, and 3) a quiet and compact package. The research themes were as follows.

Themes

Engine

- A high efficiency, compact recuperator
- A compact, high-speed generator for a simple shaft configuration
- A premixed, lean-burning combustor for a low exhaust gas emission level

Electric power conversion system

- A compact and long-life inverter
- Optimum control for improving the electricity quality

Package

* Wako Research Center

- A compact package with a small installation space
- Easy maintenance
- Quiet

3. Major Specifications and Overview

Table 1 gives the major specifications of the newly developed generator system, and Fig. 1, Fig. 2 and Fig. 3 show internal and external views and the system configuration. The gasturbine engine of this system uses a recuperator to recover the energy of the exhaust gas, and has a simple, single spool structure with a high-speed generator directly coupled to the centrifugal compressor and radial inflow turbine.

The fuel used is ordinary town gas 13A which is pressurized to approximately 560 kPa by a fuel gas booster and then supplied to the gasturbine engine through a metering valve. The 1.3 kHz high frequency AC generated by the high-speed generator is converted to DC by the converter unit of the electric power control system, and then converted to commercial 3-phase AC by the inverter unit and connected to the grid.

Table 1 Major specifications of micro-gasturbine generator

Items		Specifications
Type of output		3 phase 200VAC, 50/60Hz
Rated output	(kW)	42 (ISO conditions)
Thermal efficiency (engine end)	(%)	30.8 (ISO conditions)
Thermal efficiency (system end)	(%)	26.7 (ISO conditions)
Emissions (CO, HC, NOx)	(ppm)	< 3
Fuel type		Town gas 13A
Dimensions (W × D × H)	(mm)	1 506 × 942 × 1 501
Weight	(kg)	950
Life	(hr)	60 000
Noise level	(dB(A))	65 (at 1m)

The auxiliary oil system lubricates the engine shaft bearings and cools the generator stator, and the oil cooler fan also ventilates the package interior. In addition, an air pump is used to ensure the differential pressure at the bearing oil seal.

The package design was divided into upper and lower

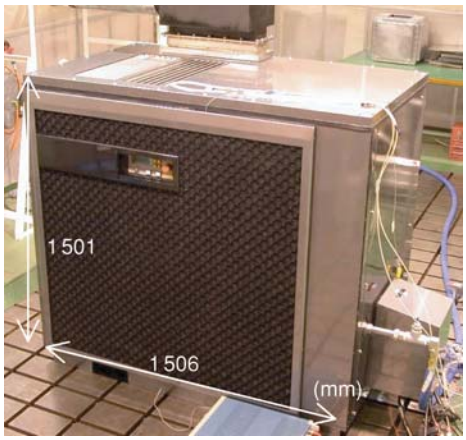


Fig. 1 External view of micro-gasturbine generator

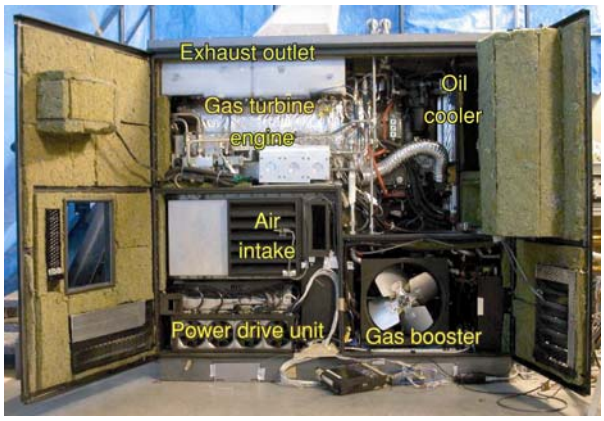


Fig. 2 Internal view of micro-gasturbine generator

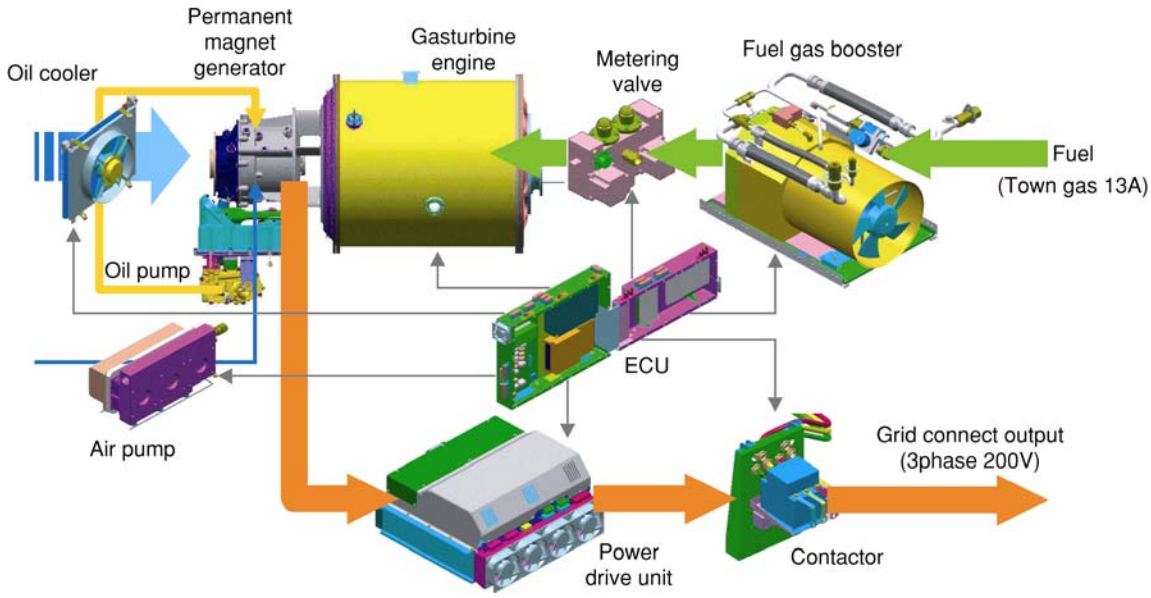


Fig. 3 System diagram of micro-gasturbine generator

sections as shown in Fig. 2 to allow efficient ventilation of the package interior. The engine and other heat sources are located in the upper section, and the engine air intake duct, electric power conversion system, electrical fittings and other components with low heat tolerance are located in the lower section. The required maintenance space was also reduced by adopting a layout that allows all components to be inspected and replaced from the front during periodic maintenance. The size is the smallest in the 40 kW generator class.

The dominant noise is the noise leak from the ducts. To reduce this noise, a 3-vent structure with sound absorbing material was adopted for each duct. This reduced the noise level to 65 dB (A)/l m (a level that allows daytime operation in a commercial district).

Figure 4 shows the engine and system performance. A generation efficiency of 30.8% at the engine end and 26.7% at the system end was achieved under standard atmospheric conditions. This is the highest performance level in the 40 kW class (Fig. 5). In addition, gasturbine performance generally drops as the air temperature rises, but these effects were suppressed by varying the engine speed.

The engine combustor adopted the premixed, lean-burning method[3] using a multi-venturi mixer that generates a homogenous air-fuel mixture. This method allows stable combustion while suppressing the flame

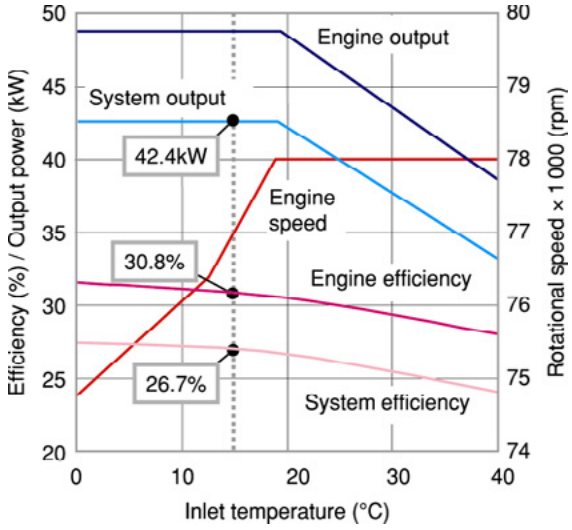


Fig. 4 System and engine performance characteristics

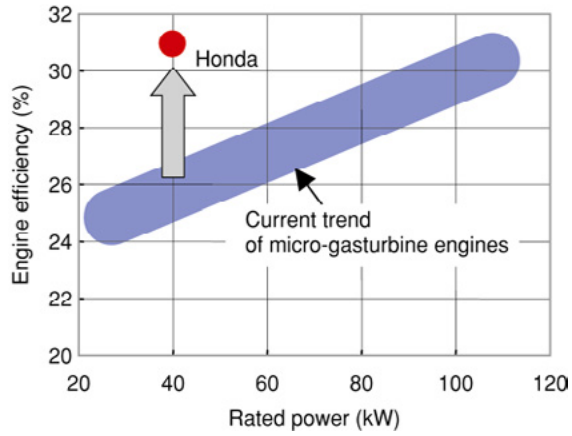


Fig. 5 Honda engine compared with current trend

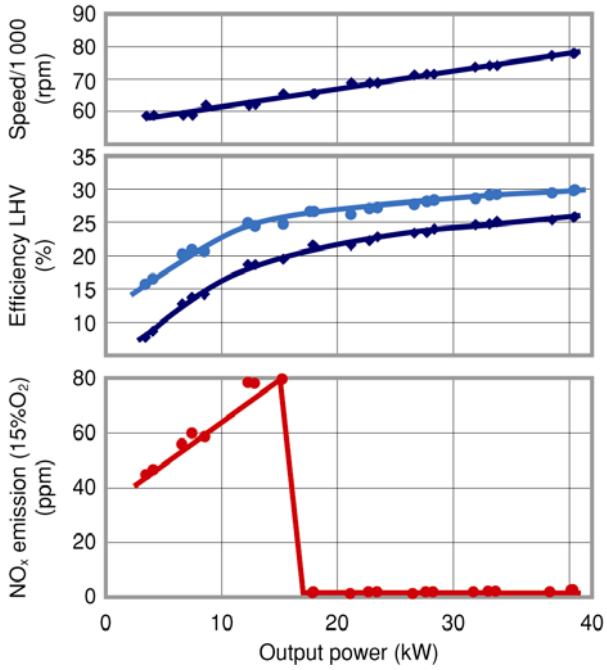


Fig. 6 System emissions and efficiency (at inlet temp. 24 °C)

temperature, and achieved an emission level of 3 ppm or less (NOx, CO, HC at 15% O_2) over the wide operating range from 50% to 100% engine load (Fig. 6). This is lower than the average value for all power plants including nuclear power plants[4].

4. Engine

The gasturbine engine efficiency generally tends to drop together with the size. This is caused by 1) increased loss due to a relative increase in the rotor tip clearance, 2) limitations on raising the turbine inlet temperature (difficulty in incorporating a complex cooling structure), and 3) a relative increase in the bearing and other mechanical losses.

The efficiency of the newly developed engine was improved by adopting a regenerative cycle using a recuperator which recovers the heat of the exhaust gas (Fig. 7). In addition, the recuperator has a multi-tube structure with an annular shape. This made it possible to locate high temperature parts on the inside and to cover the outer circumference of the engine with low temperature air from the compressor, thus greatly reducing the radiation loss to the outside from the turbine exit passage, the recuperator,

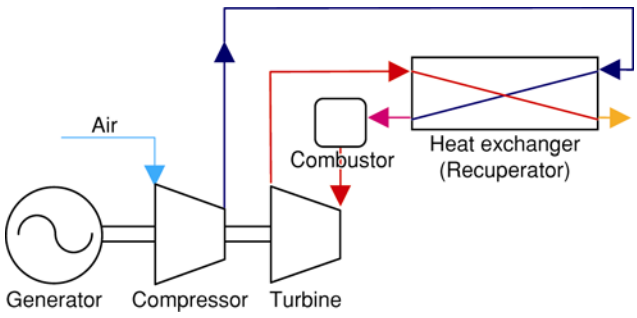


Fig. 7 Flow chart of recuperated gasturbine cycle

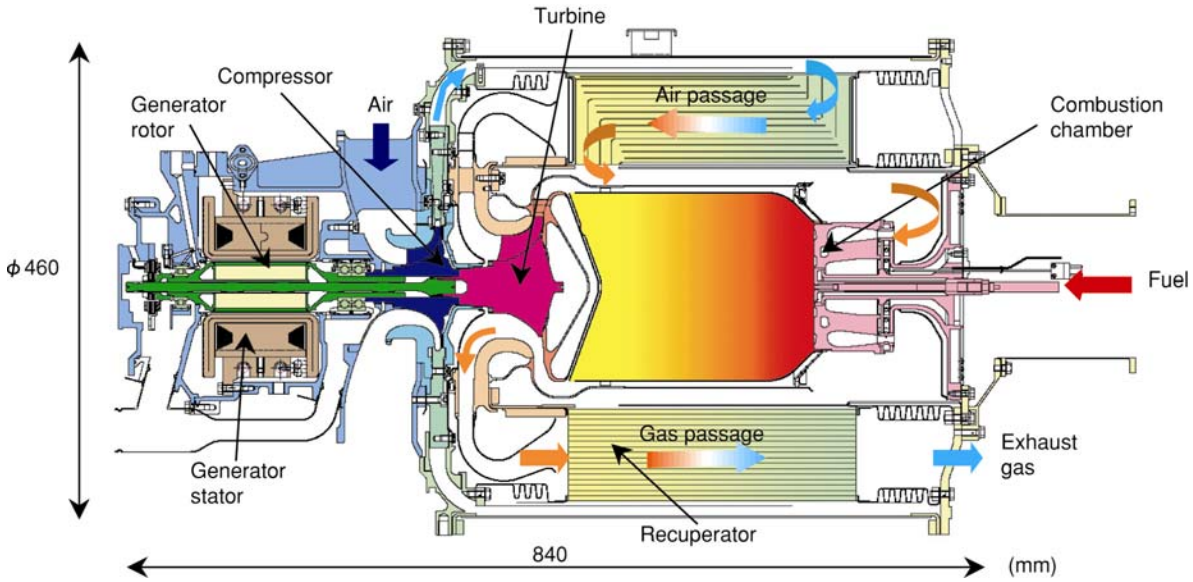


Fig. 8 Cross-sectional view of micro-gasturbine engine

etc. Mechanical loss was reduced by adopting a single spool structure with the high-speed generator directly coupled to the centrifugal compressor and radial inflow turbine, thus eliminating the need for reduction gears. Figure 8 shows the engine structural drawing. This structure is axially symmetric, which reduces the stress on high temperature parts with a large temperature gradient.

Table 2 gives the engine specifications, and Fig. 9 shows a comparison of estimated and experimental results of the

Table 2 Engine specifications at ISO conditions

Items		Specifications	
		Version 1	Version 2
Engine speed	(rpm)	77 000	
Turbine inlet temperature	(°C)	900	
Max. electrical output	(kW)	47.8	51.7
Engine efficiency	(%LHV)	30.8	32.9
Recuperator temperature efficiency	(%)	87.6	90.6
Dimensions	(mm)	ϕ460 × L840	
Weight	(kg)	145	

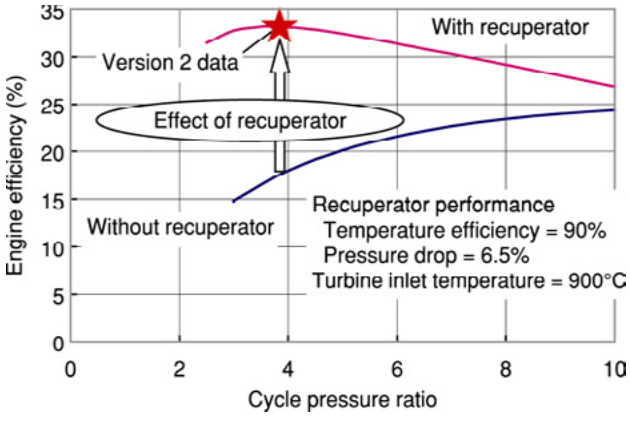


Fig. 9 Relationship between cycle pressure ratio and engine efficiency

improved engine efficiency through exhaust heat recovery by the recuperator. The Version 1 engine mounted in the system had a recuperator temperature efficiency of 87.6% and a generation efficiency at the engine end of 30.8%. In contrast, the Version 2 engine was further modified to reduce friction and improve the recuperator temperature efficiency to 90.6%, thus achieving a generation efficiency of 32.9% at the engine end[5].

The gasturbine engine efficiency can be improved by increasing the turbine inlet temperature (TIT), but this has a large effect on the life span of high temperature parts. The newly developed engine set the TIT at 900 °C in consideration of this life, and the results of FEM analysis with the accuracy confirmed by high temperature spin tests and measurements of turbine component temperatures during operation provided prospects for a turbine life span of 60 000 hours.

In addition, engine overspeed burst tests were conducted to verify that fragments did not fly out of the engine even in the event of rotor burst, and the safety was confirmed.

The recuperator and the high-speed generator, which are the major components, are described below.

4.1. Recuperator

Table 3 and Fig. 10 show the major specifications and the external view, respectively. The annular shaped recuperator has compact and highly efficient counterflow passages.

Table 3 Recuperator specifications

Items		Specifications
Core size	(mm)	ϕ430 × L289
Core weight	(kg)	45
Material		SUS304
Plate thickness	(mm)	0.1
Flow rate	(kg/s)	0.4
Temperature efficiency	(%)	90.6
Pressure drop	(%)	6.4

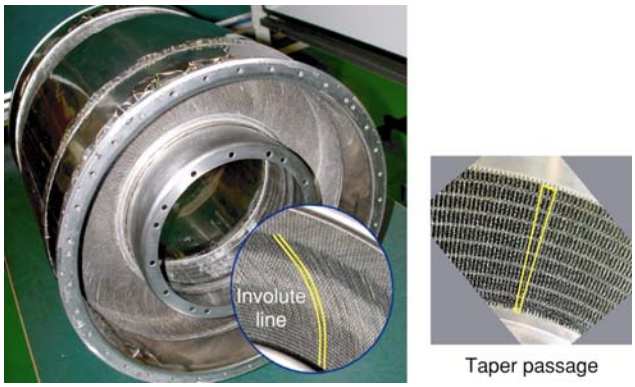


Fig. 10 Front view of recuperator with two different passage types

The main factor lowering the recuperator temperature efficiency is generally an uneven air and exhaust gas flow profile. Figure 11 shows the results of estimating the drop in temperature efficiency due to the flow profile. Line A shows the case when the exhaust gas and air flow profiles match, and line B shows the case when these do not match. According to these estimation results, the target flow profile value needed to achieve the target efficiency of 90% has a standard deviation of 0.07 or less (area Q in Fig. 11).

When the heat exchange plates are arranged radially in an annular shaped recuperator, the passages become tapered with a narrower passage width on the inside and a wider passage width on the outside (Fig. 10). This produces a distorted flow which causes the efficiency to drop (point P in Fig. 11). To prevent this distorted flow, an involute shape was adopted which has a constant passage width at any cross section. In addition, the air passage turns the flow, so the flow profile easily becomes slanted towards the inside. Therefore, the flow profile was equalized by placing ribs in the turn sections to control the flow (Fig. 12). Temperatures inside the recuperator were measured to confirm the effect. The results are shown in Fig. 15. The temperature drops at a constant gradient from the inlet to the outlet, indicating that heat transfer is performed evenly throughout the entire recuperator.

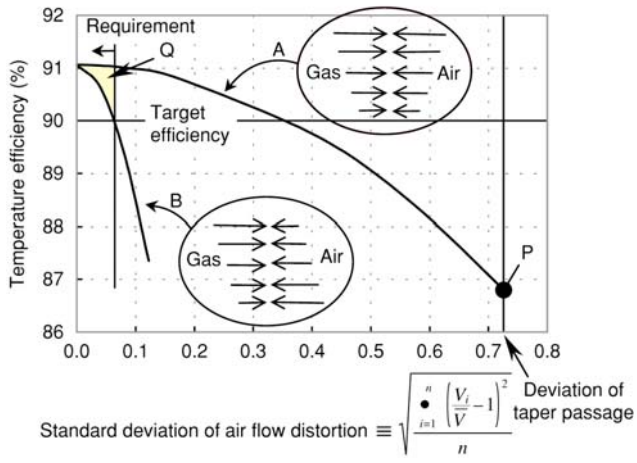


Fig. 11 Calculated effect of flow distortion

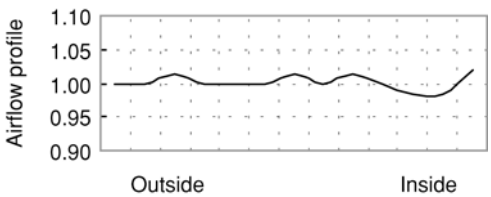


Fig. 12 Air flow profile at 100%N

The heat exchange plates have a primary surface structure that does not use fins or other separate parts. The stainless steel plates that form the exhaust gas passages are corrugated plates shaped into fins. These are matched with rib-pressed stainless steel plates that form the air passages, and both are laser welded along the sides to form a pair (Fig. 13, Fig. 14). 510 of these plates are then brazed into an integrated annular shape to create air and exhaust gas seals. The size and weight

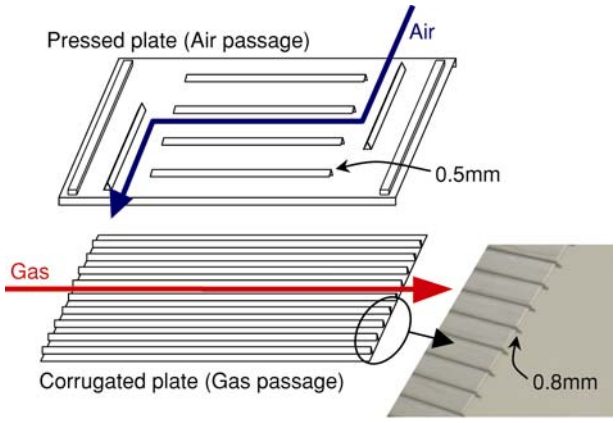


Fig. 13 Plate model of passage

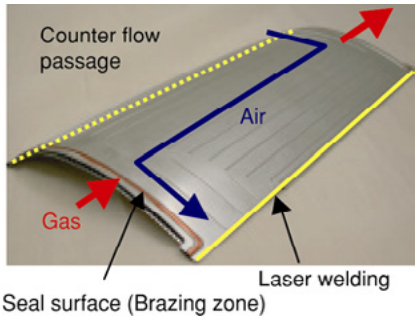


Fig. 14 Laser welded cell (Involute shaped)

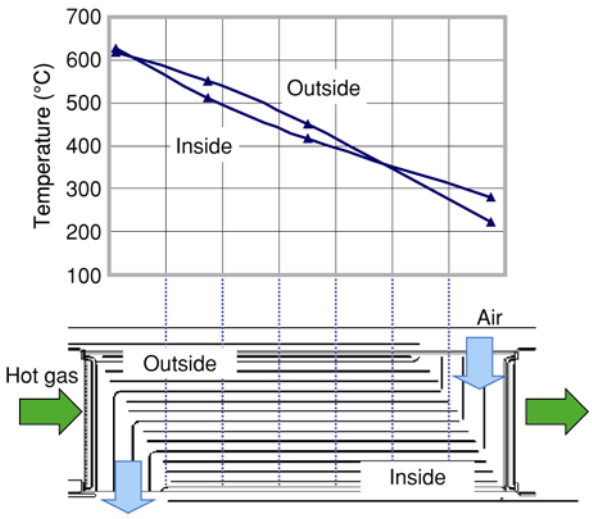


Fig. 15 Measured temperature of recuperator

were reduced by using small air and exhaust gas passage heights of 0.5 and 0.8 mm, respectively, and raising the coefficient of heat transfer. The total seal length for all 510 heat exchange plates is 306 m for the laser welded portions and 122 m for the brazed portions, but the leak amount was kept to 1% or less (equivalent to a non-sealed area of ϕ2.7 mm).

Preventing flow distortion and developing a brazing method for a leakless recuperator fulfilled the recuperator efficiency target of 90% or more.

4.2. High-Speed Generator

The high-speed generator is a permanent magnet type and is directly coupled to the engine. Table 4 gives the major specifications, and Fig. 16 shows a structural drawing of the rotor. Using an integrated shaft reduces the number of bearings which in turn reduces mechanical loss; however, the shaft length must be shortened to avoid shaft bending resonance, and the structure must be capable of supporting a low strength magnet at high revolutions. In addition, a sufficient amount of magnetic flux must be ensured with this limited size, and rotor eddy current loss and stator loss must also be reduced.

To ensure the amount of magnetic flux needed for the required output, the generator rotor uses a permanent magnet (Nd Fe B) with a high magnetic flux density. This magnet was shrink fitted onto a high strength nickel-chrome alloy tube to create a structure with a compressive load even at high revolutions.

Rotor eddy current loss not only lowers the efficiency, but also heats the ring, resulting in demagnetization of the magnet due to the temperature rise and a lower magnet compressive load due to thermal expansion of the ring, ultimately impairing basic functions. The teeth in a slot type stator have low reluctance so magnetic flux passes easily through the teeth, causing fluctuation of the magnetic flux which can easily produce eddy currents on the rotor surface. As a countermeasure for preventing this eddy current loss, a slotless type stator was adopted in which the coil is arranged in a cylindrical shape on the inside of a toothless core (Fig. 17). The coil is formed by heat pressing self-bonding wires (Fig. 18).

Table 4 Generator specifications

Items		Specifications
Generator type		Permanent magnet
Rotor size	(mm)	ϕ48.8 × L90
Magnet material		Nd Fe B
Stator type		Slotless
Electromagnetic conversion efficiency	(%)	97

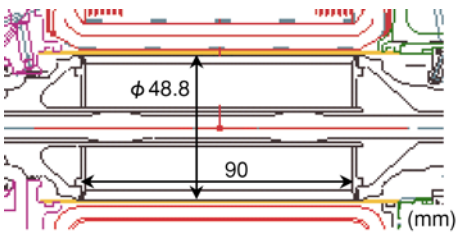


Fig. 16 Cross-sectional view of generator rotor

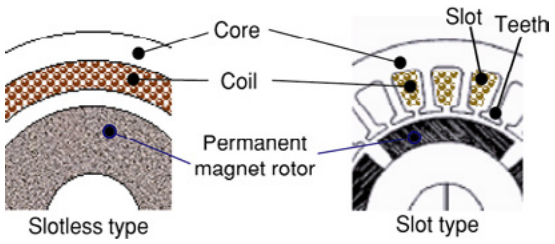


Fig. 17 Structures for slotless and slot stator

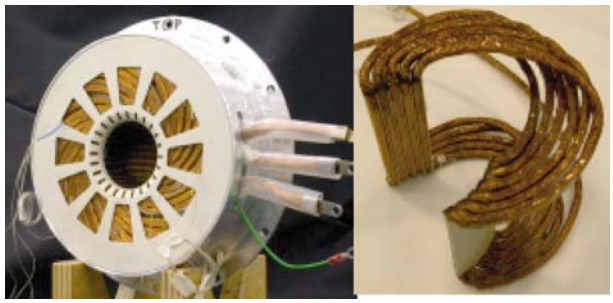


Fig. 18 External view of stator coil

In addition to copper loss caused by the resistance inside the coil, stator loss also includes eddy current loss which occurs inside the strands due to magnetic flux fluctuations and circulating current loss which is caused by the phase difference between each strand in an in-phase bundle. Both of these losses can be reduced by using fine strands (ϕ0.3), and by adopting Litz wire twisted together with strand bundles.

Ensuring a sufficient amount of magnetic flux and reducing both rotor eddy current loss and stator loss in this manner resulted in a generator efficiency of 97%.

5. Electric Power Conversion System

The electric power conversion system must ensure an output electric power quality that conforms to the grid connect guidelines and other regulations[6), 7), 8)], and must also be highly efficient and compact.

Table 5 gives the achieved values and the major specifications. The electricity quality as measured on an actual grid shows a power factor of 0.99 and a total harmonic distortion (THD) of 3.5%, both of which easily clear the respective standard values of 0.95 or more and 5% or less as prescribed by the grid connect guidelines and other regulations. With this high power factor and measures, such as reducing the DC filter loss, the efficiency achieved was 95.1% at rated power.

Table 5 Electric power control unit specifications

Items		Specifications
Type of control		3 phase PWM control
Output power	(kW)	42
Efficiency	(%)	95.1
Total harmonic distortion	(%)	3.5
Power factor		0.99
Volume	(litter)	87
Weight	(kg)	98

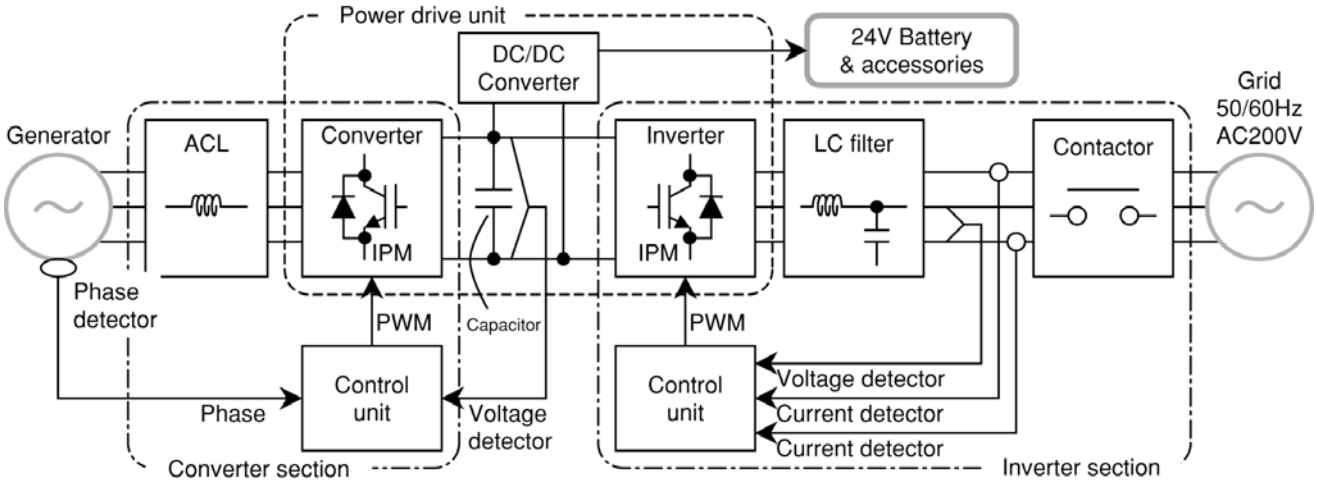


Fig. 19 Block diagram of electric power control system

Figure 19 shows the block diagram. This electric power control system is comprised of a converter unit that commutates the high frequency AC from the high-speed generator into DC, a DC filter capacitor group, an inverter unit that converts the DC into commercial 3-phase AC and connects it to the grid, and a DC/DC converter for the auxiliary power supply.

Figure 20 shows the power drive unit (PDU) which is the major portion of the electric power conversion system. The hot switching devices (converter and inverter) and the DC/DC converter are concentrated in a single area over a heat sink to increase the cooling efficiency and reduce the size. In addition, the converter and inverter have been combined into an integrated structure and the output control responsiveness has also been improved. This made it possible to reduce the DC filter capacitor charge/discharge loss, and achieved high efficiency with a small volume while ensuring the required long life span of 60 000 hours.

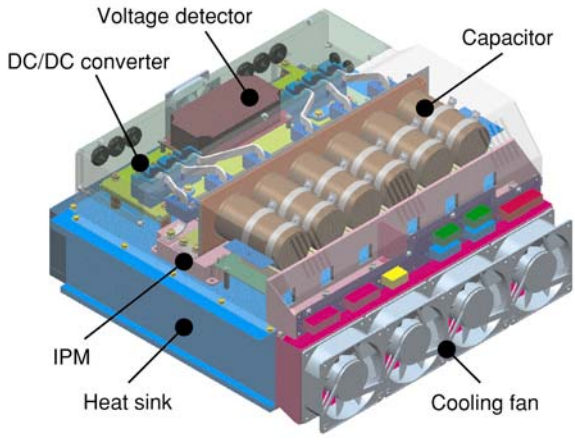


Fig. 20 Detail of power drive unit

5.1. Converter Unit

When converting the AC voltage of the high-speed generator to DC, systems that use ordinary diode commutation only can provide a low DC voltage at low engine speeds and cannot supply electric power to the grid. In addition, there is also the disadvantage that an inverter must be installed separately to power the generator as a motor during engine startup.

On the other hand, the pulse width modulation (PWM) system can generate the desired DC voltage at any engine speed, making it possible to supply electric power to the grid over a wide range from low speed to high speed. Furthermore, starter functions can be obtained by simulating inverter action with the PWM, which helps to reduce the size. For these reasons, the PWM system was adopted for the converter unit, and by performing vector control for each phase current enabled high efficiency and stable operation over a wide operating range.

5.2. Inverter Unit

The inverter must ensure an electricity quality (power factor, harmonic distortion, etc.) that conforms to the above-mentioned grid connect guidelines and other regulations, and must also possess functions to protect the grid when trouble occurs, such as when isolated operation is detected. In order to satisfy the required electricity quality, high accuracy grid voltage phase detection and high-speed current waveform shaping control were adopted. As a result, the low-order harmonics were reduced and the LC filter in the output stage only needed to eliminate the switching harmonics, which helped to reduce the size. In addition, the various processing needed for the grid connect protection functions was performed by software, making it possible to satisfy the required functions without adding new dedicated circuits or other components.

6. Engine Control

The generator must not only provide the rated power, but must also be capable of continuous generation at partial power (rated or less). There are two methods for controlling the output with a single spool gasturbine engine such as this system. The first is to fix the engine speed and lower the turbine inlet temperature (TIT) and the turbine exhaust temperature (TET) as shown in Fig. 21, and the second is to lower the engine speed and operate near the temperature upper limit. In consideration of the engine characteristics, the latter method which has less of a drop in engine thermal efficiency was adopted.

On the other hand, the gasturbine engine speed changes

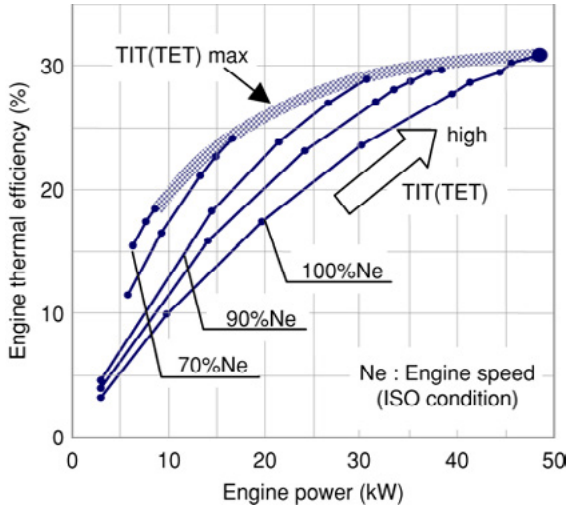


Fig. 21 Engine performance

when TIT or TET reaches the upper limit depending on the air temperature (T1) and air pressure (P1), so control that allows operation which traces an efficient line under any atmospheric conditions is required. When a method that directly feeds back the TET and other temperatures is used, the transient characteristics prevent the control period from being shortened, which means that stable control and a fast transient response cannot be obtained. For these reasons, the stability was improved by adopting an engine speed control method that uses engine performance map data.

Figure 22 shows this engine control block diagram. The TIT and TET characteristics relative to the engine speed and output are converted to map data, and the appropriate operation line at that time is derived from that map and the sensed T1 and P1 (upper block). The target engine speed is then obtained and engine control is performed based on this operation line and the required output value (lower block). T1 and P1 are not subject to sudden changes, so the operation line update interval can be made sufficiently longer than the engine speed control period, thus reducing the processing load. This control method succeeded in reducing the engine speed fluctuation at rated power to ±100 rpm or less.

In addition, the engine characteristics may change gradually when operated for long periods, but these time-based changes are supported by sensing the TET and periodically correcting the initially set map based on the difference from the TET assumed from the map.

7. Conclusions

Research on a micro-gasturbine generator as a compact distributed energy resource was conducted in order to improve the energy use efficiency, and the following results were obtained.

(1) A generator system equipped with a high efficiency regenerative cycle engine was developed which satisfied the life span and safety requirements. This system achieved a generation efficiency of 30.8% and 26.7% at the engine and system ends, respectively. These are currently the highest reported values in the world for the 40 kW class. In addition, further improvements to the engine unit resulted in a generation efficiency of 32.9% at the engine end.

(2) An emission level of 3 ppm or less was achieved over the wide output range from 50% to 100% by a premixed lean burning combustor that uses a multi venturi mixer. This is lower than the average value for all types of power plants including nuclear power plants.

(3) The engine, inverter and other components were arranged into a compact package in consideration of heat and ease of maintenance, and the low noise level of 65 dB (A)/1 m was achieved.

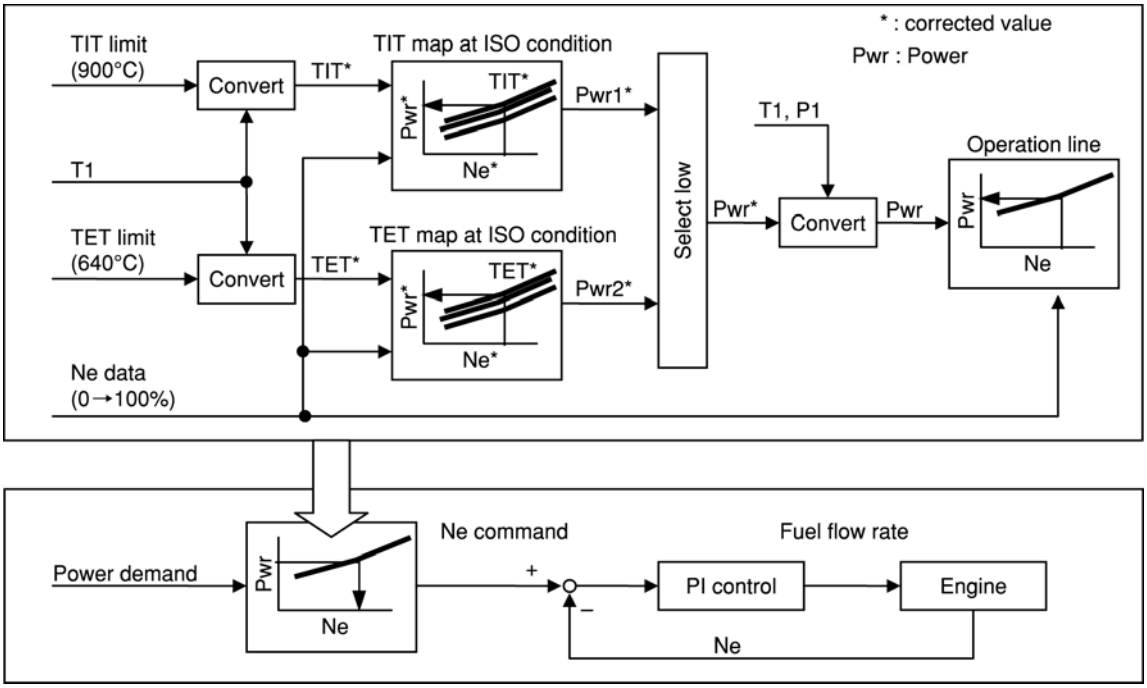


Fig. 22 Engine control block diagram

References

(1) Yoshiki, H.: Development and Problems of Micro Gas Turbines, Journal of the Gas Turbine Society of Japan, Vol. 29, No. 3, p. 123-128 (2001)

(2) Miura, S.: Development Status of Small Distributed Power Generation Technologies Micro Gas Turbine Technologies, Journal of the Gas Turbine Society of Japan, Vol. 29, No. 3, p. 134-140 (2001)

(3) Yamazaki, A., Kurokawa, M., Inoue, T., Murakami, H.: Research of Natural Gas Low Emission Combustor, HONDA R&D Technical Review, Vol. 15, No. 2, p. 85-92 (2003)

(4) The Tokyo Electric Power Company, Inc.: TEPCO Environmental Action Report 2002, p. 113 (2002)

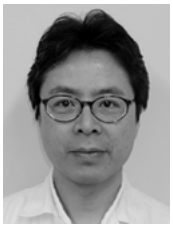
(5) Shinmura, K.: Microturbine Research at Honda, Presented in 2003 ASME TURBO EXPO Panel session (2003)

(6) Agency for Natural Resources and Energy: Guideline for islanding protection technique of dispersed generator ’98 (1998)

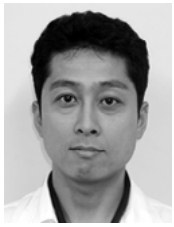
(7) Japan Electric Association: Technical Guidelines for the Grid Connection of Dispersed Energy Sources, JEAG9701 (2001)

(8) Japan Electrical Safety & Environment Technology Laboratories: Test Methods for Compact Solar Cell Generation System Grid Connect Protection Devices (1993)

■ Authors ■


Koichi SHINMURA


Koji YAMAGUCHI


Sadachika TSUZUKI


Hidemi KIMURA


Takeshi KATO

Presentation of RC211V Equipped with 4-stroke Engine

Hisashi KADOMASU*

ABSTRACT

The 4-stroke engine road racer, RC211V, has been developed with the concept “Launching Honda’s own advanced technology in pursuit of speed and functionality.” Employing a lightweight, compact 4-stroke V-type 5-cylinder engine for the first time in the world, the aim was to realize linear torque characteristics, easy operational traction characteristics, highly controllable handling and improved turning ability when compared to 2-stroke road racers. A semi dry sump crankcase utilizing the transmission room for the oil tank, and a pressure controllable fuel injection system were adopted to achieve the engine performance targets. In addition, the specified minimum weight of 145 kgs for 5-cylinder engine motorcycles was satisfied by employing a new type of aluminum twin spar frame, a low gravity fuel tank, and a Unit Pro-link suspension, as well as through weight reductions for each of the parts.

1. Introduction

The WGP500, the pinnacle of motorcycle road racing world championships, became known as the Moto-GP in 2002. In meeting the new regulation standards that allow 4-stroke engine configurations with a maximum displacement of 990 cm^3, Honda has developed a road racer configured with a new type 4-stroke engine instead of the conventional 2-stroke type.

2. Development Concept

On the WGP road racing circuit, even on models configured with an exceptionally powerful engine, motorcycles tend to suffer from fast tire wear if they are not provided with linear torque and easy operational traction characteristics. Since tire wear is directly related to a reduction in lap time performance, it is imperative that the load exerted on the tires be reduced. Moreover, motorcycles need to be easy to control in progressive tire wear conditions in order to maintain a stable fast speed through to the final stages of the race. Taking these points into consideration, a design featuring an engine offering maximum power and operational ease, a body frame offering highly controllable handling, and a suspension system offering favorable traction characteristics were targeted to enable a fast pace ride over the entire race circuit.

* Asaka R&D Center

3. Overview of RC211V

Figure 1 shows an external view of the RC211V and Table 1 lists the major specifications. The size of the RC211V frame is similar to the lightweight compact 2-stroke engine configured NSR500, which has won both individual and manufacturer's titles at the WGP500 seven times over the last eight years. A study of vehicle weight and maximum power output was conducted by comparing engine sizes with different cylinder configurations and types, and by the positioning of power/weight ratios standardized in accordance with new regulation guidelines. Under the new regulation standards, a multi cylinder engine configuration, which is advantageous in terms of its power output, becomes disadvantageous in terms of vehicle weight. Conversely, an engine configuration with fewer cylinders offers an advantageous vehicle weight but suffers from insufficient engine power output. As the vehicle weight and engine power are increased, there is a greater tendency toward tire wear as previously described. After considerable deliberation, the most compact V-type 5-cylinder engine was selected for its superior balance of engine output and complete vehicle weight. Table 2 lists the regulation specifics and Fig. 2 shows a comparison of the power-weight ratio for the respective engine configurations.



Fig. 1 External view of RC211V

Table 1 Major specifications

Items		Specifications
Overall length	(mm)	2 050
Overall width	(mm)	600
Overall height	(mm)	1 130
Wheelbase	(mm)	1 440
Ground clearance	(mm)	130
Vehicle dry mass	(kg)	145
Engine type		Liquid cooled 4-stroke DOHC five cylinder
Engine displacement	(cm^3)	Under 990
Valve train		DOHC 4 valve
Max power		Over 160kW
Throttle body type		GQ type
Fuel capacity	(Liter)	24
Clutch type		Dry multi-plate type
Transmission		6 speed constant mesh
Tire size	Front	12/60-17
	Rear	19/67-16.5
Brake system	Front	Double, Carbon disk
	Rear	Single, SUS disk
Suspension	Front	Telescopic
	Rear	Unit Pro-link
Frame type		Aluminum twin-spar

4. Engine

In approaching engine design, the three component motion characteristics, the inertia momentum of roll, pitch and yaw were targeted for reduction while improving maneuverability. Toward this end, the vehicle's structural assembly was taken into consideration and a design closely approximating a sphere form was finally decided upon. Conclusively, the V-type 5 cylinder configuration, taking up the smallest sphere layout, was adopted. Figure 3 shows the comparison results of the different engine sizes and Fig. 4 shows a cutaway drawing of the engine. Figure 5 shows the analysis model of the crankshaft. This engine is designed to cancel out the primary and coupling vibrations without a balancer mechanism. The engine is configured with a counter weight that weighs 50% of the reciprocating parts on each cylinder. Imbalances are cancelled out in cylinders 1 and 2 and 4 and 5 by 25% each and the remaining 50% imbalance (25% + 25%) was cancelled on cylinder 3. This has effectively cancelled out the primary vibration. Figure 6 shows a schematic diagram of the crank balances. As cylinders are positioned symmetrically centered around cylinder 3, the coupling oscillation is logically zero. Eliminating the balancer from the engine and reducing relentless concerns with a lack of strength in frame body parts caused by engine vibration have contributed to a reduction of the overall vehicle weight. Computer analysis was applied and optimal settings for valve timing and the various intake and exhaust system specifications were obtained in order to achieve a greater level of power output without losing the flat torque characteristics associated with the 4-stroke engine configuration. As a result, the targeted output level has been achieved. The output and torque values have been increased significantly over those for conventional 2-stroke engines and the amount of fuel flow has been considerably reduced. Figure 7 shows a comparison of the performance curves for the NSR500 and RC211V.

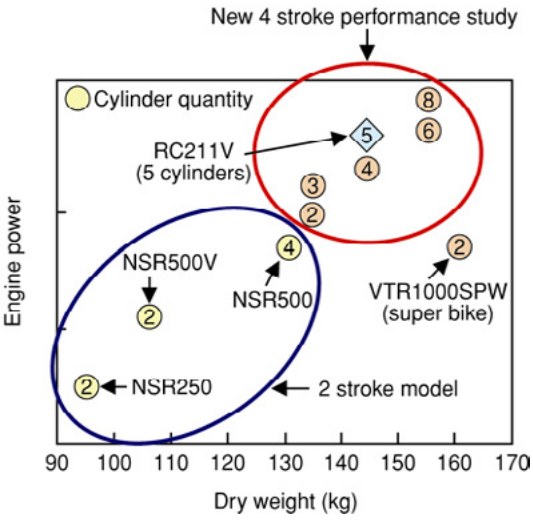
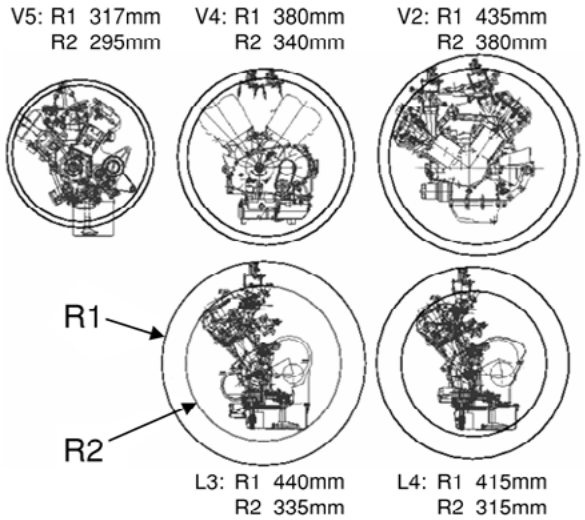


Fig. 2 Comparison of power-weight ratio

Table 2 Regulation of Moto-GP (from 2002)

Engine type		4-stroke			2-stroke		
Engine displacement	(cm^3)	Maximum 990			350 ~ 500		
Cylinder quantity		Free			Maximum 4		
Supercharging		Prohibition			Prohibition		
Vehicle dry mass	(kg)	Over 6 cylinder	4 ~ 5 cylinder	Under 3 cylinder	4 cylinder	3 cylinder	2 cylinder
		155	145	135	131	116	101
(Oval piston)		155	155	145			
Fuel capacity	(Liter)	Maximum 24			Maximum 32		
Noise	(dB)	Maximum 125			Maximum 113		



R1: Circumscribed circle from center of gravity to air intake
R2: Circumscribed circle from center of gravity to cylinder head

Fig. 3 Comparison of engine size

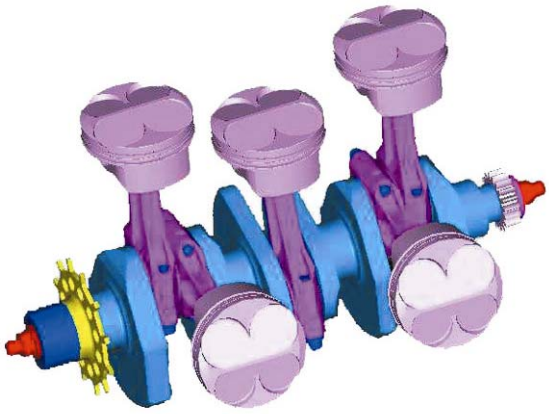


Fig. 5 FEM analysis model of crankshaft

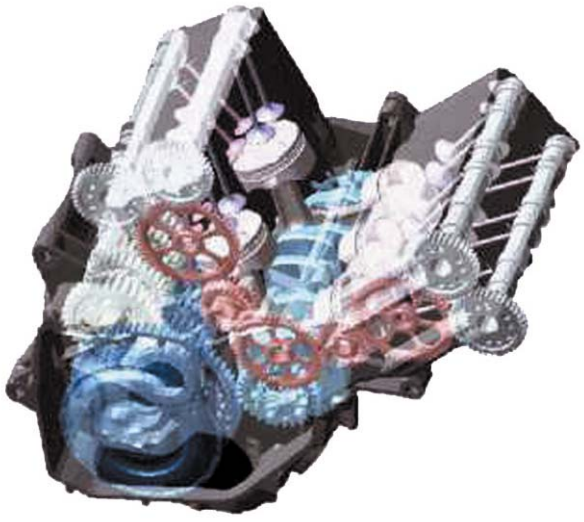


Fig. 4 Cutaway drawing of RC211V engine

The crankcase is constructed of aluminum casting and a semi dry sump crankcase has been configured to use the transmission room for the oil tank. Each crank chamber throw is sealed. Three scavenging oil pumps have been placed to each of the throws. These pumps have fortified the discharge of the oil and blow-by gas from the oil feed fitted beneath the oil separator plate to the transmission case. The discharged oil is directed into the oil pan from the transmission room. A constant negative pressure of about 70 kPa is generated in the crankcase while the engine is being driven. Figure 8 shows the structure of the crankcase and lubricating mechanism. Adopting this mechanism has reduced the pumping loss that occurs behind the pistons and the oil agitation loss in the crank system compared with the conventional wet sump configuration. Also, the maximum output has been improved by 4% and friction has been reduced by 19%. Figure 9 shows a correlation between the output and friction. A complete dry sump configuration requires a separate oil tank and oil piping which increases the overall weight of the vehicle. On the other hand, the semi dry sump configuration incorporates a layout design that is integrated with the engine, making it approximately 1 kg less than the complete dry sump configuration.

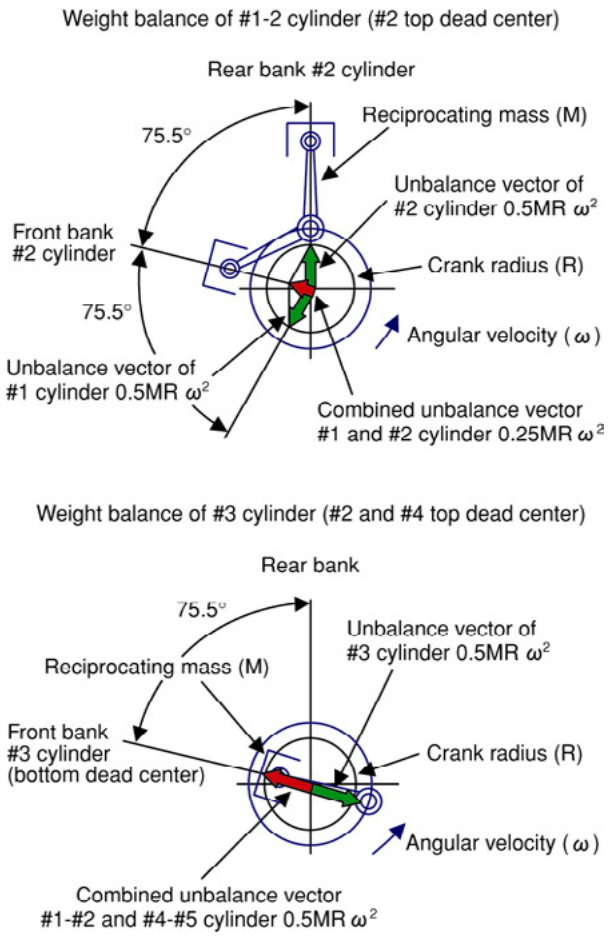


Fig. 6 Weight balance of cylinder

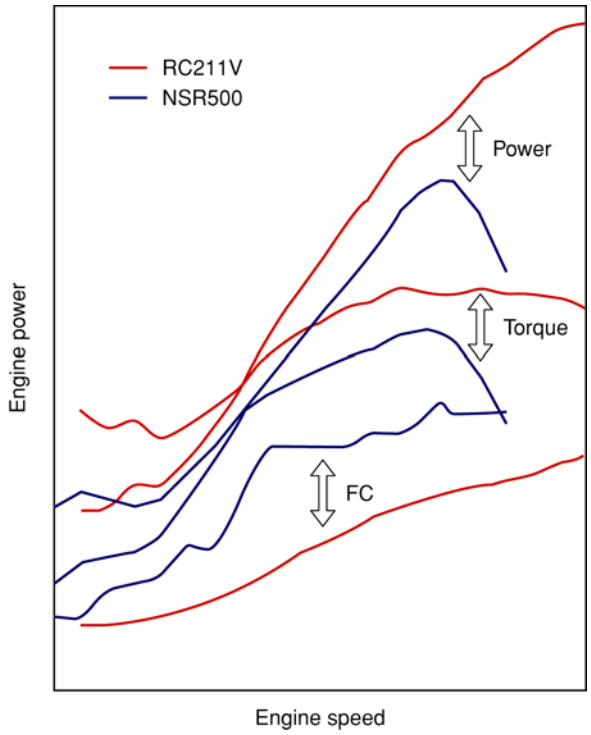


Fig. 7 Engine performance curve

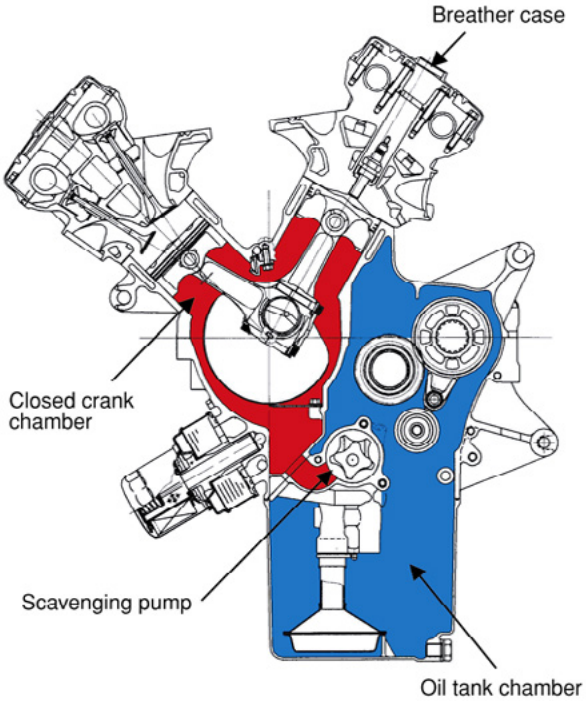


Fig. 8 Structure of crankcase

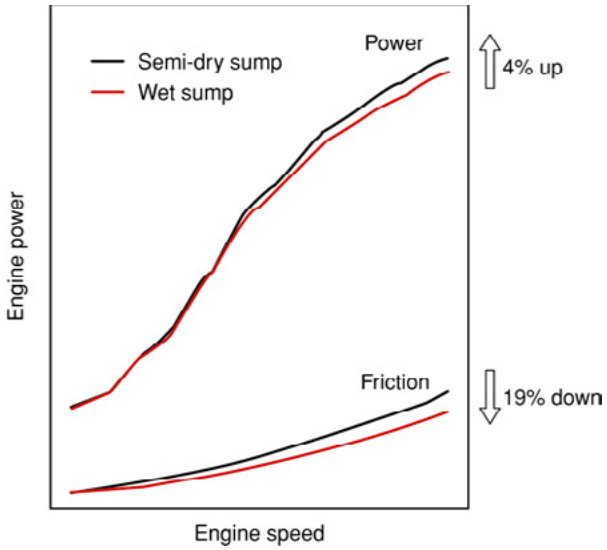


Fig. 9 Effect of new crankcase

5. Fuel System

The throttle body is configured with a deflective multi-hole twin injector. An injector is fitted to the upper and lower sides of each cylinder. Sharing the fuel injector for both the low load and high load areas has been instrumental in achieving driveability and greater output. Figure 10 shows the structural overview of the twin fuel injectors.

Employing a fuel pressure regulator that enables the injector pressure to change continuously has improved the output transient characteristic. Figure 11 shows a structure view of the pressure regulator and Fig. 12 shows examples of fuel pressure programs.

As the throttle opens and closes, there is inevitably some fuel remaining in the inlet port. Estimation control of this adherent fuel amount that flows in the next combustion cycle was employed to optimize the air fuel ratio mix and has improved drivability and fuel consumption.

6. Frame Body

In conventional 2-stroke engine road racers, the fuel tank is fitted above the engine and in front of the rider. A full tank of gasoline in the early stages of a race provides a high center of gravity, which causes sluggish handling and makes it difficult to travel the race circuit from the start at a fast pace. Furthermore, as the remaining gasoline is consumed dramatic shifts in handling and stability occur which creates a handicap in terms of balanced lap times. On the RC211V, part of the fuel tank is positioned beneath the sheet cowl which lowers the positioning of the stored gasoline to concentrate the vehicle's mass. This also serves to provide ease of handling in full tank conditions and provides a minimal level of gravitational fluctuation as the fuel level decreases during the race. This configuration has enabled a dash start in the early stage of the race and also promotes a stable lap time over the duration of the race. To lower the positioning of the stored gasoline while preserving the capacity of the air box located above the throttle body and the 24 liter tank capacity, there is a need to keep as much space as possible beneath the sheet for the fuel tank. Adopting a unit pro-link suspension system on the RC211V has removed the need for a suspension mount on the top side of the body frame. This has created a large space for the fuel tank beneath the sheet. Figure 13 shows the structural layout of the motorcycle. In designing the basic body frame structure, CAE analysis was conducted based on a new theoretical approach to fabricating a suitable level of structural stiffness. The analysis has yielded a completely new set of measurements. The resultant design incorporates a 17% lateral flexure increase and 23% improved resistance to twisting in comparison to the NSR500. This has served to attain a frame body stability that is able to support high engine output exceeding 160 kW, and to improve the turning

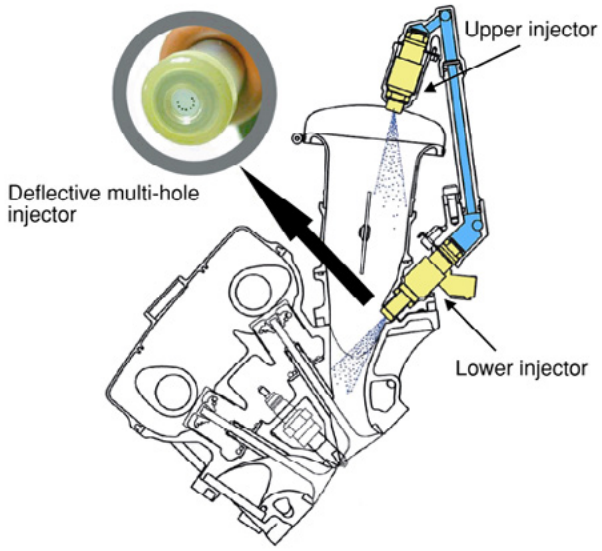


Fig. 10 Twin injector

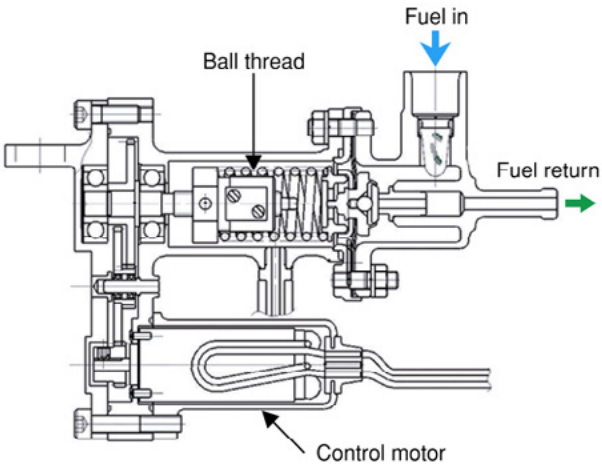


Fig. 11 Structure of fuel pressure regulator

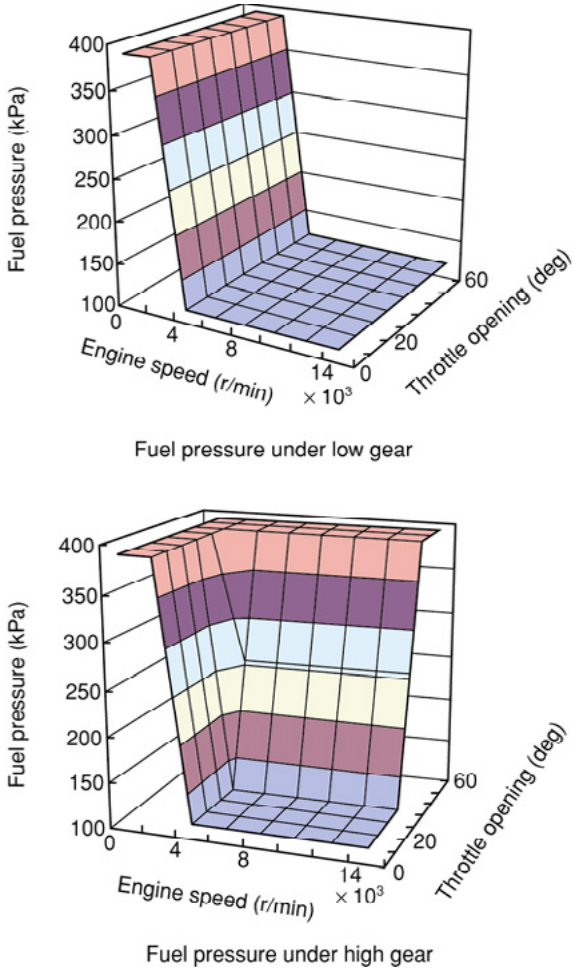


Fig. 12 Program of fuel pressure control

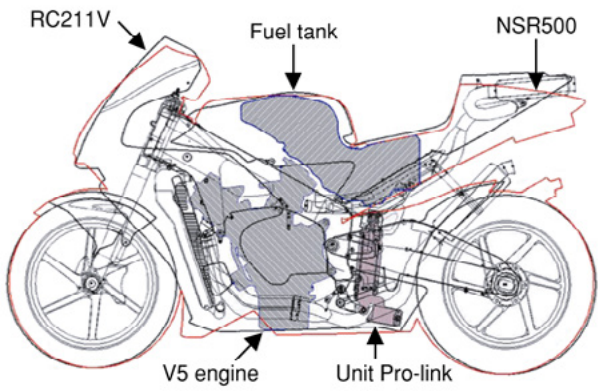


Fig. 13 Comparison of motorcycle size

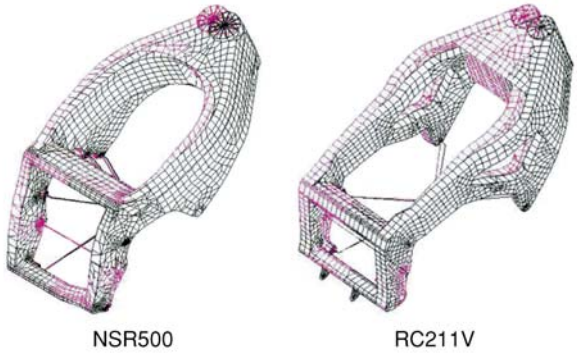


Fig. 14 Frame body stiffness model with FEM

ability. To achieve better deceleration performance than the conventional lightweight 2-stroke engine road racer, the frame stiffness in the direction of pitching has been preserved and the vehicle stability during braking has been improved. Figure 14 shows a CAE analysis model of the mainframe body stiffness.

7. Suspension

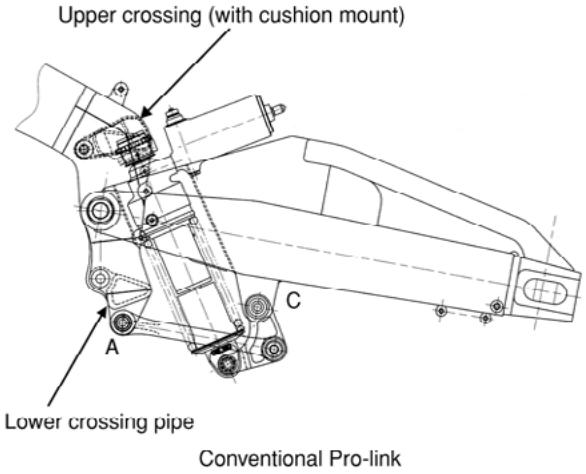
The unit pro-link suspension stabilizes the turning behavior of the motorcycle at the exit of a corner and displays superior rear traction. Also, the unit connector is attached to the topside of the swing arm instead of connecting the rear cushion unit to the topside of the frame body. This has removed the necessity for reinforcing the frame body unit connector as typically applied in conventional designs. This offers the advantage of greater flexibility in setting frame stiffness values. Figure 15 shows a comparison of rear suspension systems.

8. Fairing

Contemporary motorcycle road racers emphasize improved wind protection for the rider and lower air resistance values. While the fairing tends to envelop the entire motorcycle, it is contrary to the motorcycle's handling. The fairing on the RC211V has been designed to reduce the surface area air contact and was implemented to provide ease of handling and stability against cross winds, while achieving a balance between air resistance and wind protection. A total projection surface area and air resistance values lower than the NSR500 were achieved to provide an improved level of handling performance. Figure 16 shows an external view of the 2002 RC211V model and the NSR500 model released in 1998.

9. Electrical System

The new type ECU incorporated on the RC211V is assembled in a single unit that provides ignition timing



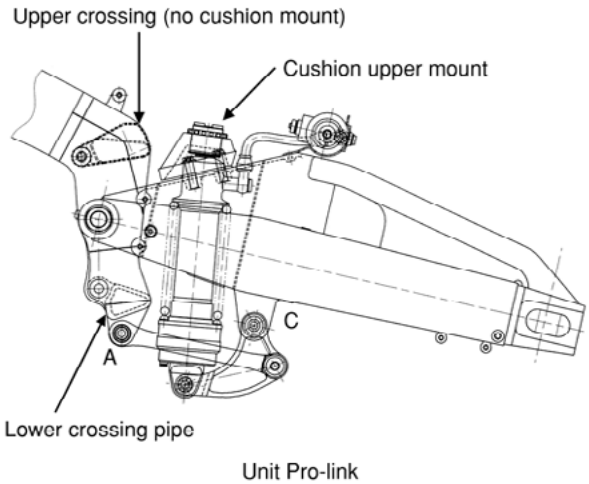


Fig. 15 Structure of unit Pro-link





Fig. 16 Comparison of external view



Fig. 17 ECU unit and CAN meter

control, FI setting control and actuators control in addition to data logger functionality. The ECU and meter offer CAN (Controller Area Network) capability developed by Robert Bosch GmbH in 1989 and transmit data according to standard serial ISO communication protocols. The meter provides multiple displays including water temperature and lap time as well as failure information and sensor condition. Display modes are controlled with the selector switch on the left side of the meter. Employing CAN capability has enabled a simple signal line design to achieve a lightweight harness. Figure 17 shows an external view of the ECU unit and meter. Bluetooth protocols have been adopted to provide condition adjustments such as fuel injection settings and mode (Map) changes. In accordance with race regulations, real time interactive communication is prohibited while the motorcycle is traveling, and allowed to operate only after the engine has stopped. Data logging settings and data uploads can be performed immediately after the engine is stopped. A quantitative analysis of any mechanical problem perceived by the rider can be performed by conducting full-time measurements of a range of engine and body related conditions including vehicular speed, engine speed, throttle opening, gear positioning, suspension stroke, etc. This enables the most accurate machine settings.

Figure 18 shows an external view of the Bluetooth unit and a sample of measured logging data.

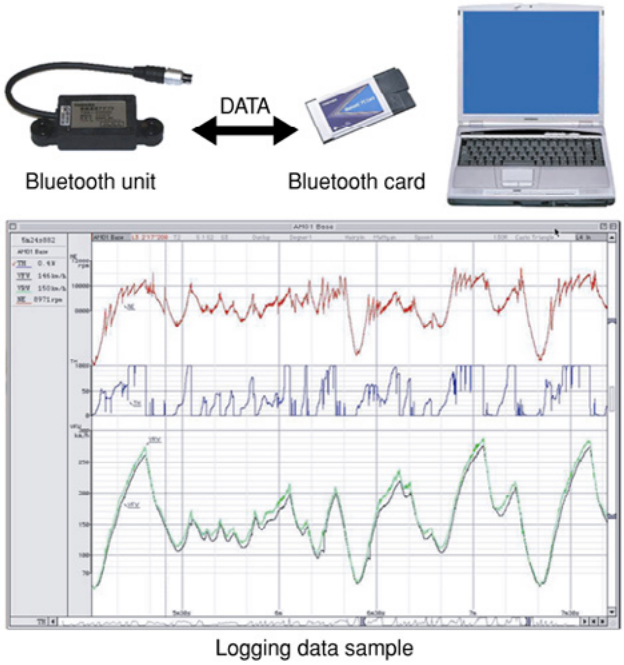


Fig. 18 Bluetooth unit and logging data sample

10. Conclusion

The RC211V is configured with a V-type 5 cylinder 4-stroke engine which provides output characteristics that are easy to handle, and has achieved the target performance including a compact configuration and superior traction performance from the Unit pro-link suspension. The machine won both individual and manufacturer titles in the 2002 Moto-GP class. We will continue to explore technologies using the RC211V, which is a leader among Honda super sport motorcycles.

■ Author ■



Hisashi KADOMASU

Development of Variable Mowing System (VMS)

Christopher OSBORNE* Dean HARTLEY* Vincent PRINZO*

ABSTRACT

The HRX217 lawnmower was developed for general consumer use based on the key concept of maximizing performance in both the bagging and mulching modes of operation. Performance has been increased by the development of a variable mowing system (VMS). The variable mowing system allows the customer to select either the bagging or mulching configuration for their lawnmower by easily rotating a lever. This gives the customer a never before achieved control on the performance of his/her lawnmower. Notably, this is done without the customer having to remove or replace any parts, or use any tools. The VMS technology was also achieved without an increase in cost to the customer over existing mulch plug technology. Lastly, the VMS significantly reduced the overall quantity of grass clippings collected in the bagging mode, therefore reducing the environmental impact of grass clipping disposal.

1. Introduction

Approximately 5 million lawnmowers are purchased in the USA each year. As part of our lawnmower developments, we strive to provide new and innovative features to improve the lawn mowing experience for our customers. It was during interviews with customers that we noticed an increasing number of lawnmower users that want to be able to bag a portion of their lawn and mulch the remaining (Fig. 1). The existing models can accommodate this situation, but the customer is required to remove parts from the mower and store them. Many times these parts are lost or inconvenient when the customer is ready to change modes[(1), (2)]. From this customer demand, the variable mowing system (VMS) (Fig. 2) was developed, and this report will detail the background of this development.

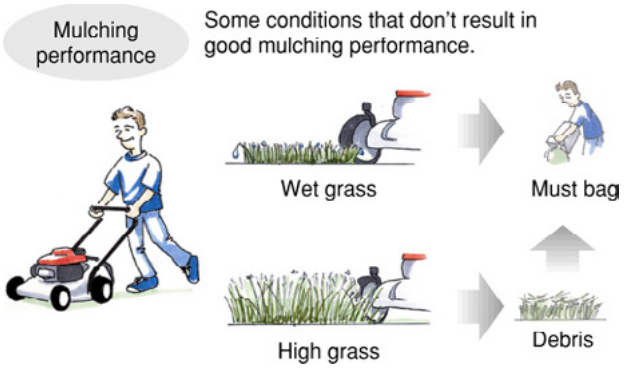


Fig. 1 Mulching performance

* Honda R&D Americas, Inc.

2. Development Goals

The development concept for this product was defined as a high-performance lawnmower that anyone can easily operate. In specific terms, the goals were as follows:

(1) Attain best in class performance in both mulching and bagging modes (this normally requires two separate models each designed for their respective purpose)
(2) Increase the convenience for the customer to convert between mulching and bagging modes. Achieving this ability without the use of any tools was also a goal of the development.
(3) Provide new functionality by allowing a partial mulch/bag operation that allows the customer to choose what percentage of grass clippings were mulched or bagged.
(4) Improve bagging performance by increasing the distance that the customer can mow between bag clearings, while maintaining the high appearance standards expected by the bagging customer.

3. Basic Configuration

Table 1 lists the major specifications of the HRX217 lawnmower shown in Fig. 3.

The HRX217 distinguishes itself from other lawnmowers by its main new technology, the VMS. The VMS is exclusive to the Honda HRX, and this is the first machine in the world to use such a technology. The VMS itself consists of several components that replace the conventional mower mulch plug (Fig. 4).

Table 1 Major specifications of HRX217

Item	Specification
Model name	HRX217
Engine model name	GCV190
Engine type	Air cooled single cylinder OHC 4-stroke
Engine displacement	187 cm^3
Maximum power	6.5 HP
Dry weight	43 kg (95lbs)
Blade diameter	530mm / 21”
T/M speeds	3
Maximum speed	1.75m/s (4mph)
Height adjust range	19 – 100 mm (3/4” - 4”)
Wheel diameter	228mm (9”)



Fig. 3 HRX217 PP1 Machine

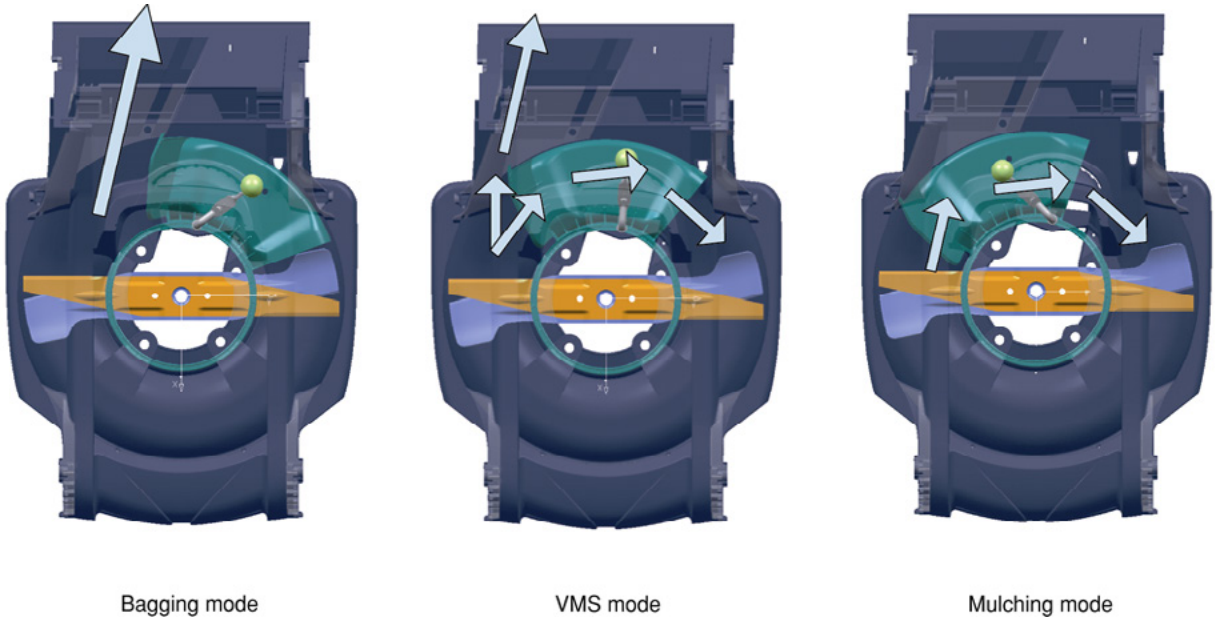


Fig. 2 Clipping path in various modes of VMS



Fig. 4 Mulch plug part from previous model

The grass flow with the VMS can be controlled by merely rotating a lever behind the engine to place the mower in either mulch mode, bag mode, or someplace in between. This allows the customer to select their lawnmower's mode by simply rotating the clip director knob, without the need for additional parts or the use of hand tools. The direction of the grass clippings is controlled by means of a rotating shutter scroll located under the housing and hidden from operator view. As the customer rotates the convenient lever on the top of the mower (Fig. 5), the shutter is placed to either allow clippings to escape through the back of the mower into the bag, or when the lever is placed in the mulch position, the shutter scroll closes off the bag chute and diverts grass clippings to the ground for mulching (Fig. 6).

This actuation is achieved by means of a lever that rotates on a boss molded into the polymer cutter housing of the lawnmower. This lever is held in its various positions by means of notches molded into the opening in the cutter housing in which the lever is installed. These notches provide not only the full mulch and full bag positions, but also 8 positions between. These additional settings allow the customer to choose the amount of grass clippings that are bagged or mulched, depending on their own preference and lawn conditions.

Several different constructions were considered before arriving at the final shape seen in Fig. 7. Some ideas that the team evaluated included a shutter that closed across the bag chute in a linear path. This proved to be difficult to support in the outermost position and was abandoned in favor of the rotating type of shutter. Once the final shape and configuration was chosen as the rotary type (Fig. 7), the



Fig. 5 Clip director (VMS) control area model

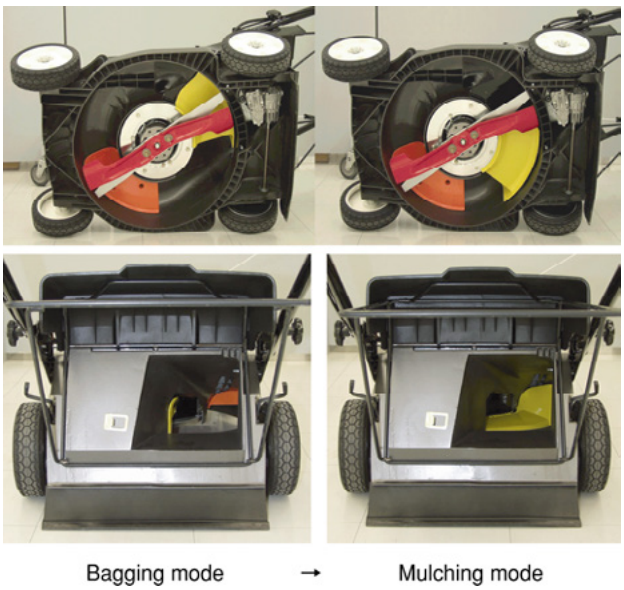


Fig. 6 Prototype in both positions



Fig. 7 VMS mechanism and components

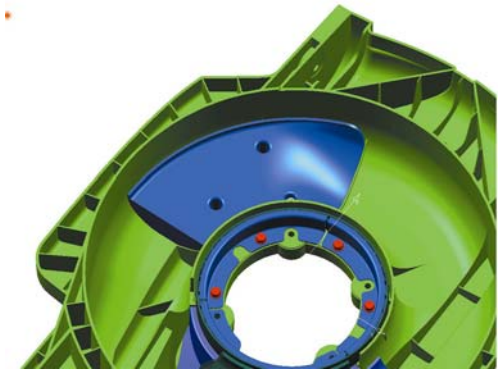


Fig. 8 Ramp scroll

shape was modified numerous times in order to maximize the flow of grass clippings and minimize clogging of the opening to the bag chute. After showing this concept to customers in focus groups, the sales division decided to name this feature the “Clip Director” (Fig. 5). This name conveys the ability of the customer to direct the grass clippings as they want for their own conditions. It is also important to note that the Honda HRX217 is the first Honda mower to achieve the specification of “4 in 1” in the box. In other words, without purchasing any additional parts, the customer can mulch, bag, discharge, or leaf shred (four functions by one machine, also known as 4 in 1). This is a milestone achieved only by the introduction of this model.

The improved performance of the HRX217 lawnmower in the bagging mode was achieved by the use of ramp scroll (Fig. 8).

This scroll is added to the underside of the cutter housing slightly forward of the rotating shutter scroll. The ramp scroll provides a downward airflow just before the beginning of the bag chute. The airflow helps reduce the number of clippings directed into the bag, and forces some clippings into the blade to be cut into smaller sizes before being stored in the bag. The ramp scroll also decreases the cross sectional area of the cutter housing at the entry to the bag chute. This decreased area causes an increase in air velocity, which helps prevent grass clogging during mulching and VMS operation, and helps fill the bag more efficiently during bagging. The ramp scroll is an integral part of the VMS system and helps improve its overall performance significantly.

The improved performance in the mulching mode was achieved by several changes. New blade shapes were introduced with the primary design change being an increased offset between the upper and lower blades cutting edges (Fig. 9). This allows for a more efficient cutting of the grass with less clogging of the cutter housing under severe conditions. The most significant effect on the mulching performance was achieved by optimizing the cutter housing shape itself (Fig. 10).

Allowing enough volume for the amount of grass clippings cut, while maintaining enough vacuum lift to pull the clippings up into the housing, is the key to a good housing shape. Also, the clearance between the tip of the blade and the cutter housing was reduced in order to improve the ability of the cutter housing to circulate clippings until they are cut to smaller size. Lastly, the scroll ramp (Fig. 8) improves mulching by diverting clippings from the upper portion of the housing back into the blade, resulting in smaller clippings as well.

4. Performance

The bagging performance of a lawnmower is based on two fundamental aspects. First is filling the grass catcher as full as possible between bag clearings. Second is traveling as far between bag clearings as possible to save time. The VMS system accomplishes both extended distance and fully filling the bag.

The VMS system’s performance envelope is best illustrated in Fig. 11. The illustration is divided up into 3 zones: bagging, mulching and VMS. The performance zones are predominately defined by grass conditions (height, thickness, dampness) and distance to completely fill the grass bag. The bagging zones are divided up in four vertical zones. Each zone expands out as distance increases and grass condition

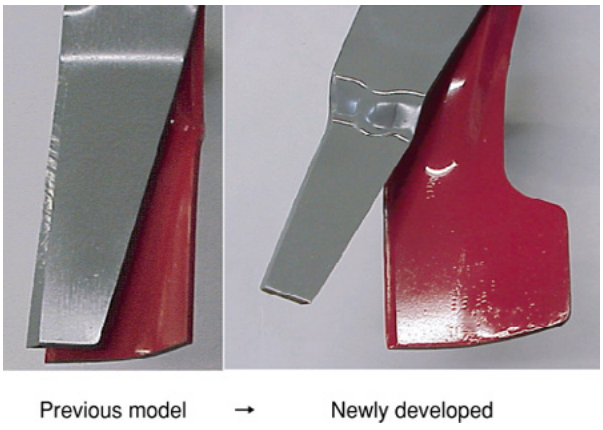


Fig. 9 Blade offset change

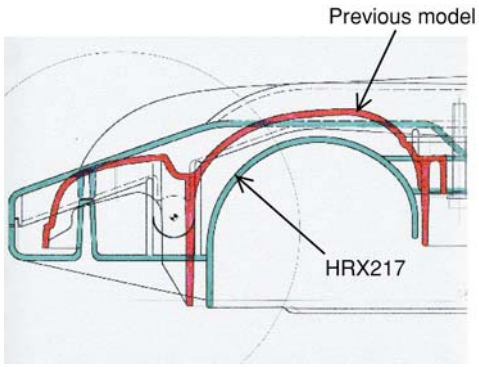


Fig. 10 Cutter housing shape change

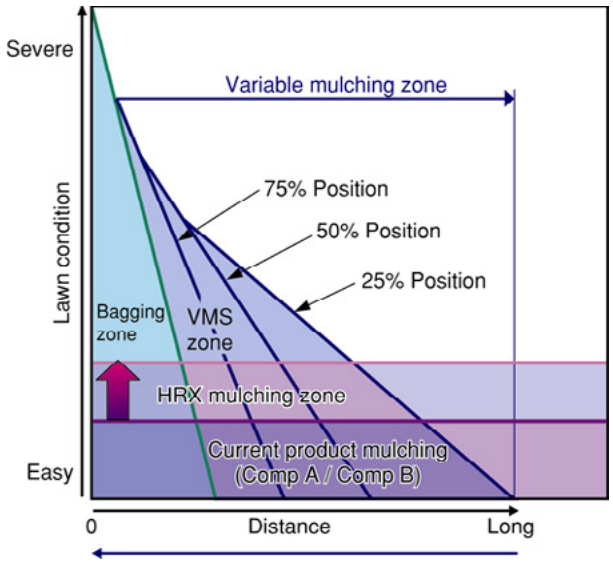


Fig. 11 VMS performance envelope

severity decreases. Fundamentally, closing the VMS shutter cuts the grass into smaller pieces and places the smaller grass particles back into the lawn, which ultimately increases the distance. As the condition becomes more severe, the VMS must be opened to achieve the same performance as in a dry condition. The horizontal zones are to define the traditional lawnmower's limitations when grass conditions become severe. The limitation of traditional lawnmowers occurs due to dedicated modes; either 100% mulching, or 100% bagging. When the grass condition becomes more severe, the ability to use both modes (VMS mode) is instrumental in achieving the improved performance. As for the HRX217, the VMS expands the performance into a more severe condition because of the combination bagging / mulching of grass clippings.

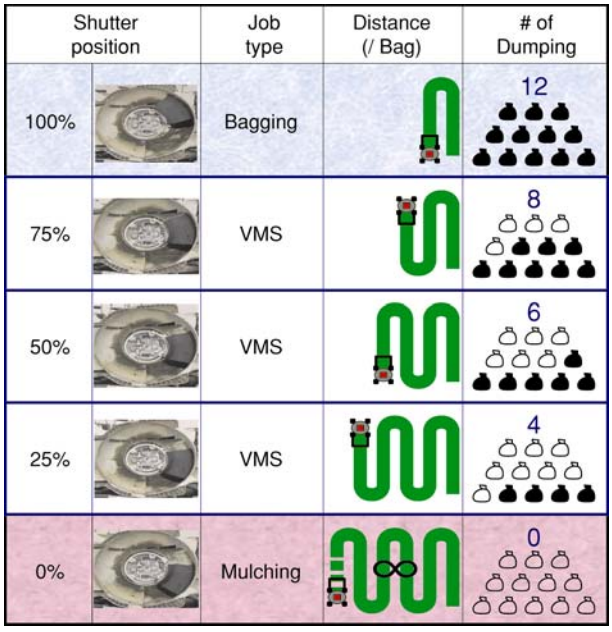


Fig. 12 VMS bag performance at different settings

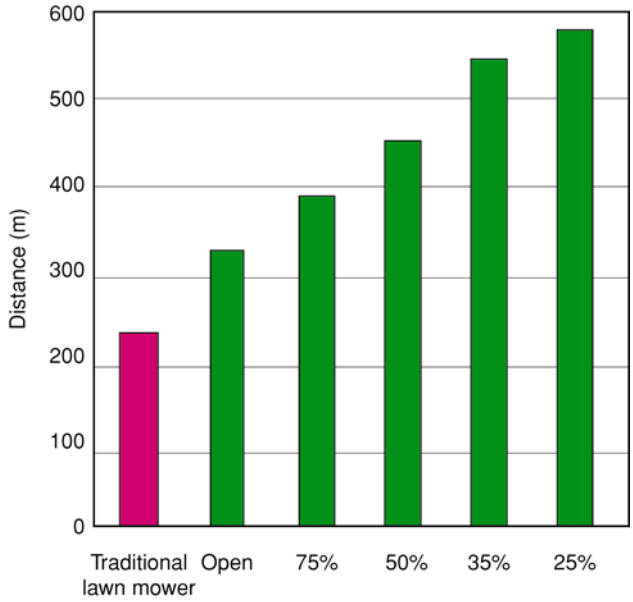


Fig. 13 VMS bagging distance at different settings

Another way to illustrate mowing performance is by showing how it affects the customer's time and convenience. Many municipalities are restricting grass clippings to be placed in the landfills. This has caused an increase in the desire for mowers that produce less yard waste. The VMS system is the answer to this environmental trend. The chart shown in Fig. 12, illustrates how opening the VMS shutter (35%, 50%, 75%, etc) decreases the number of times the grass catcher fills up. In optimum conditions, bag emptying decreases by up to 66% when compared to a traditional lawn mower that has fixed operation modes. The shutter position (in column one) helps illustrate this function.

The third column, distance, is the distance required to fill one typical grass bag. The added distance to fill the grass bag translates into fewer bags to dispose of. The fourth column, bag clearings, is the expected number of bags you might have over a typical 1/4 acre lawn.

The mowing distance is shown in Fig. 13. The actual data shows how the mowing distance varies between grass bag clearings. The grass is held within the housing for a longer period of time before passing through a narrower opening in the discharge chute. The added time in the deck will cause the particles of grass to become smaller, and in doing so, the mower is able to pack clippings tightly into the grass bag. This effect increases the distance between grass bag clearings.

5. Summary

The following achievements were made in the development of the variable mowing system for the HRX217 walk-behind lawnmower:

(1) Along with normal mulching and bagging modes, the VMS system also provides new functionality allowing the customer to find an optimal mowing position in between mulching and bagging that recycles some of the grass to the ground, while still giving the clean look of bagging.

(2) The customer's optimal VMS setting leads to fewer bags of grass collected over the entire lawn than the bagging mode by increasing the distance to fill the bag by partially mulching. This equals fewer bags of clippings at the curb, which will cost most customers less money for services to collect, and will be better for the environment.

(3) Customer convenience was increased by allowing them to convert from bagging, to mulching, to anywhere in between with the ease of turning a lever. No extra mulch plugs or tools are required to do so as in conventional lawnmowers.

(4) The shape and configuration of the cutter deck, blades, rotating scroll, and the deflection scroll developed for the VMS system resulted in the best pure mulching and pure bagging cut quality of any single Honda lawnmower.

(5) A rotating shutter scroll was developed for the VMS system, which rotates just above the blade in the path of the cut grass. Developing the shape and durability of this part was the key to the performance of the VMS system.

(6) The VMS system, while adding convenience and excellent performance, does not add any extra cost to the customer over a conventional system.

6. Conclusion

The variable mowing system on the HRX217 has achieved a new level of performance, convenience, and versatility for a walk-behind lawnmower. The concept for the variable mowing system came about from listening to customer's needs for cutting performance and convenience, and from trying to add more value to our products by adding new features for the same price.

The variable mowing system will build new excitement around the HRX217 and the entire Honda lawnmower lineup. The development of the variable mowing system was made possible by the cooperation and dedication of Honda R&D Americas, Inc., Honda R&D Co., Ltd. and American Honda Motor Co., Inc. The authors would like to thank all the members of those departments that worked to make the HRX217 a reality.

References

(1) Christians, N.: Lawns, Your Guide to a Beautiful Yard, Des Moines IA, Meredith Books, 192 p. (2002)

(2) Hartin, J.: Reusing Turfgrass Clippings to Improve Turfgrass Health, Sacramento CA, University of California, June 2001

■ Authors ■



Christopher OSBORNE



Dean HARTLEY



Vincent PRINZO

Introduction of Hydrogen Refueling Station with Photovoltaic Modules

Masaki UEYAMA* Masato KITA* Satoshi TAGUCHI*
Koji NAKAZAWA* Hisashi NAGAOKA* Shinichi ARAKAWA*

ABSTRACT

An experimental hydrogen refueling station has been built in order to propose a solution for energy and global environmental issues, using solar radiation as its energy source. An improvement in system total efficiency was achieved by using an electrolyzer with a newly composed catalyst. As a result, it is predicted that this system is capable of producing enough hydrogen to drive a fuel cell vehicle for 10 000 miles per year with electricity from only the photovoltaic modules. A drastic reduction of CO_2 emissions per unit of hydrogen produced is possible by employing a CIGS thin film compound photovoltaic module in place of a single-crystalline Si photovoltaic module. The hydrogen refueling station has demonstrated a form in which future hydrogen production may cleanly, efficiently, and renewably be achieved from solar energy, with a design that enables the everyday user to feel comfortable.

1. Introduction

To find a substitute for fossil fuels, reduce exhaust gas emissions, and help alleviate global warming, Honda has been developing fuel cell vehicles with the belief that hydrogen fuel cells will be the ultimate next-generation power plant.

As for the energy source for producing the hydrogen, it would be desirable to use sunlight that is readily available anywhere, as opposed to the case of petroleum, supplies of which are overly concentrated in a few areas. However, while there are sufficient quantities of sunlight on a global scale, the energy to be derived per unit area is still small and fluctuates depending on the time of day, the climate and the season. Because of this, it is essential to increase the energy density and to stabilize the energy supply.

As research and development into fuel cell vehicles has advanced in recent years, so has research and development into the large-scale production of hydrogen led by the infrastructure industry and government agencies. This has included research into hydrogen production using sunlight[(1)]. However, there has been no research into what capacity of photovoltaic modules would be required to produce the hydrogen needed to power a single fuel cell vehicle, or into how much CO_2 would be emitted by the manufacture of these systems. For these reasons, in 1998, Honda assembled commercially available equipment into a prototype hydrogen producing system using photovoltaic modules, and measured the energy inputs and outputs in tests of hydrogen production. The results indicated that because the auxiliaries consumed so much energy, the amount of hydrogen that could actually be derived was rather small and therefore it was necessary to research ways to make the system more efficient.

To conduct this efficiency research, Honda set up a first-generation hydrogen production and refueling station in Los Angeles, California, in 2001, and began testing. A Honda FCX, which was already being used in public road tests in

* Wako Research Center



Fig. 1 External view of Hydrogen Refueling Station

the area, was selected to serve as the fuel cell vehicle. This type of experiment was the first of its kind anywhere by an automobile manufacturer, and was announced in July 2001.

This paper discusses a second-generation refueling station (Fig. 1) that began operating in July 2002, using knowledge gained through the first-generation station and designing the new one to be more efficient and compact.

2. Outline of Hydrogen Refueling Station

2.1. Appearance

Figure 1 shows the appearance of the hydrogen refueling station discussed in this report. Thorough safety measures were taken, and the station was designed differently from existing plant equipment to impart a sense that the hydrogen society is coming closer, and not an image that such equipment is inaccessible to the average person.

As a symbol of the project, a design was chosen that features the image of a sailboat carrying society into the future with the help of natural energy. This image emphasizes the clean and advanced aspects of hydrogen produced from light and water (Fig. 2).

2.2. Specifications

The design goal for the amount of hydrogen production was calculated as the amount which would enable driving of 10 000 miles per year. This figure was based on historical solar radiation data[2] and the average annual driving distance per household automobile throughout the US[3]. A goal was set to derive all the energy needed for this only from sunlight. To accommodate unpredictable climate conditions and variations in driving distances, it was decided to also allow production of hydrogen from grid power. Table 1 lists the major specifications.

2.3. Overall Configuration

The hydrogen refueling station consists of photovoltaic modules, an electrolysis unit for making hydrogen, a high pressure hydrogen storage tank unit and a dispenser unit for



Fig. 2 Design image sketch

Table 1 Major specifications

Item	Specification
Hydrogen generation	2Nm³/h (Max.) over 2 000Nm³/year
Unit size (L × W × H)	600 × 600 × 1 200 (Electrolysis unit & Dispenser unit)
Storage volume	110 Nm³
Charge pressure	35 MPa (Max.)
Charge system	Pressure gap
Energy source	Photovoltaic modules Grid power (aux.)
Type of electrolysis	Solid polymer electrolysis membrane
Input material	Tap water
Purity of hydrogen	99.9999% (without water)

filling the fuel cell vehicle with hydrogen (Fig. 3).

In order to keep each unit from being overwhelmingly large, even up close, the design standard called for each unit to be as wide across as a person's shoulder breadth and as high as breast height. The basic unit was a box measuring two feet on each side, and the station was constructed by combining multiple units (Fig. 4). The component equipment was made compact and configured into individual units for each function. As a result, all of the equipment other than the photovoltaic modules could be placed under a canopy evoking the image of a sail, making the station resemble the project image.

The user interface has a touch panel screen and uses a dialogue system for easy operation (Fig. 5). Figure 6 illustrates the overall layout of equipment.

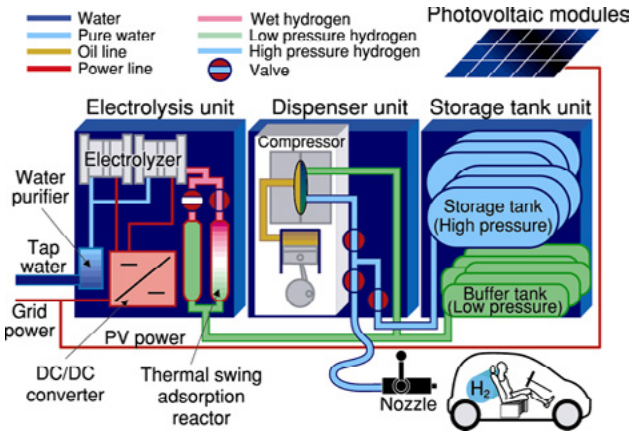


Fig. 3 Schematic illustration of Hydrogen Refueling Station

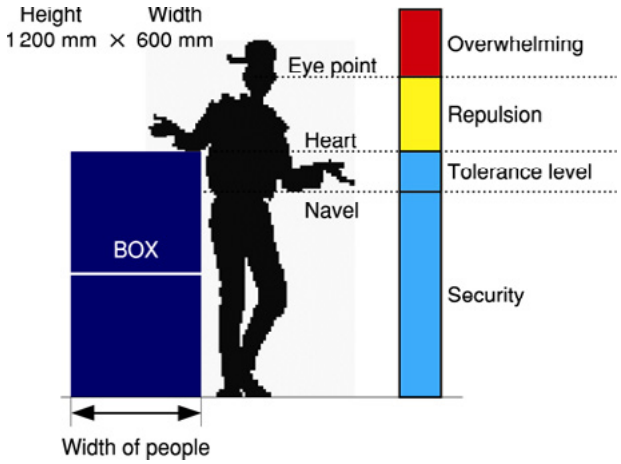


Fig. 4 Concept of unit size



Fig. 5 Scene of refueling for FCX

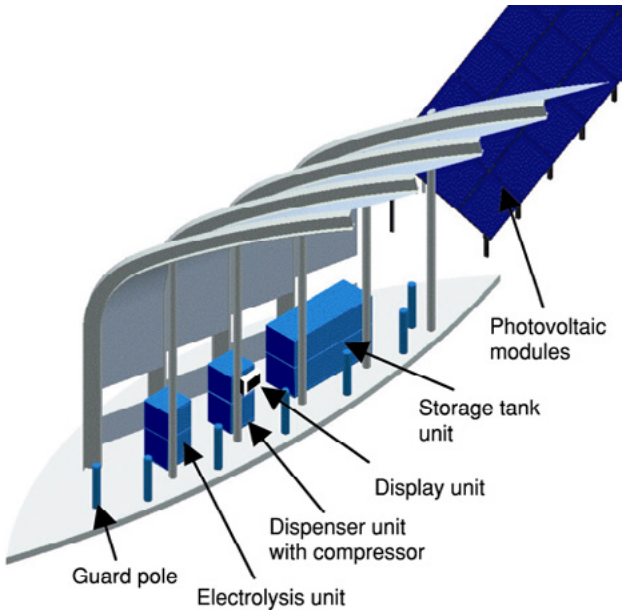


Fig. 6 Station layout

3. Photovoltaic Modules

The photovoltaic modules used are the single-crystalline Si type, which are the most efficient among those used in ordinary households; they are used in a quantity sufficient for about two households. To maximize annual power generation, it is desirable to place the photovoltaic modules at an angle to the planet surface that is about the same as the latitude. In this case, therefore, the modules were placed at about 35°, the approximate latitude of Los Angeles (Fig. 7).



Fig. 7 External view of photovoltaic modules

4. Hydrogen Production Unit

4.1. Configuration

The hydrogen production unit consists of a water purifier for turning tap water into pure water, an electrolyzer for producing hydrogen through the electrolysis of pure water, an H_2 gas-liquid separator for separating the water from the

hydrogen still mixed with pure water derived by the electrolyzer, and a hydrogen purifier that removes water vapor and a trace amount of O_2 gas contained in the separated hydrogen gas (Fig. 8).

The hydrogen production unit was designed to minimize energy consumption. This was achieved by using a pure water circulation system (to reduce the amount of pure water produced) and a hydrogen circulation and recycle system (to reuse hydrogen when the hydrogen purifier is restored and thereby reduce the amount of hydrogen produced). Figure 9 illustrates the water and hydrogen recycle systems.

The pure water circulation system for reducing the amount of pure water produced sends pure water made by the water purifier to the electrolyzer via an O_2 gas-liquid separator and an ion exchanger. Pure water that has not been electrolyzed still contains O_2 gas, so the O_2 gas is separated using the previously mentioned O_2 gas-liquid separator and reused. On the other hand, the hydrogen produced still contains some pure water, so the pure water is separated using the H_2 gas-liquid separator and returned to the circulation system. Reusing pure water this way makes it possible to reduce the amount of energy consumed to produce pure water.

The hydrogen produced contains a trace amount of O_2 gas and water vapor so these are removed with the hydrogen purifier. This device has two molecular sieves consisting of oxidation catalysts and thermal swing adsorption reactors; O_2 gas is turned into water using the oxidation catalysts and the water is removed by adsorption using one of the molecular sieves. After a certain amount of water is adsorbed, the system switches to the other sieve. The sieve that has finished adsorbing water is heated and supplied with hydrogen so that the adsorption reactor is restored. The hydrogen used for restoration is reused after it is cooled and dehumidified.

4.2. Electrolyzer

Figure 10 illustrates the basic principle of the electrolyzer. Pure water is supplied to the anode electrode, a voltage is applied between that and the cathode electrode, the pure water separates into hydrogen ions and O_2 gas, and the O_2 gas and unused pure water are released together. Hydrogen ions pass through a proton exchange membrane and at the cathode electrode are turned into gaseous hydrogen. As the hydrogen ions move, some of the pure water also moves to the cathode electrode side. When water is electrolyzed, there are two electrons transferred for every hydrogen molecule produced, and the theoretical amount of hydrogen that can be produced is determined by the amount of current. The electrolyzer's current-voltage (IV) properties indicate the relationship between current density and the voltage required to produce that current (Fig. 11).

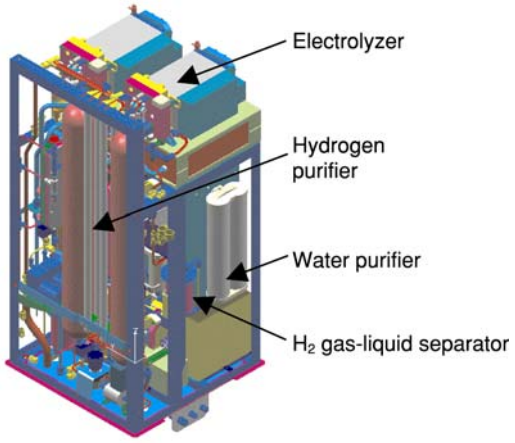


Fig. 8 Assembly of electrolysis unit

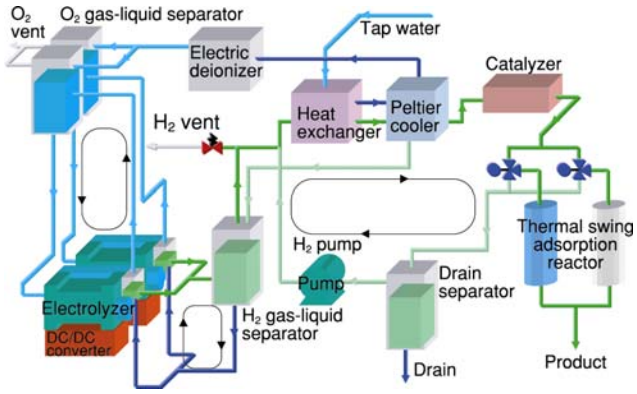


Fig. 9 Water and hydrogen recycle system

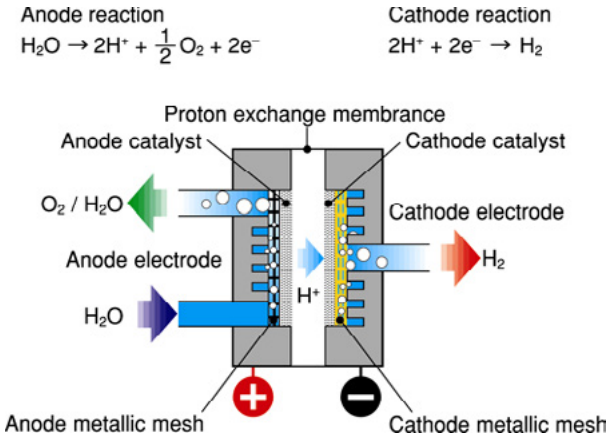


Fig. 10 Schematic illustration of electrolyzer

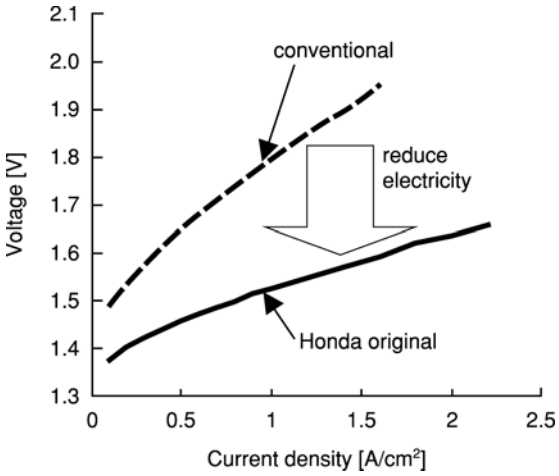


Fig. 11 Characteristics of electrolysis cell

Achieving high efficiency, which is to say, producing hydrogen with minimal power consumption, requires minimizing the voltage needed for electrolysis. Three primary factors affect voltage: catalyst, membrane and ion supply. The voltage constituent determined by the catalyst is that required to break the water's state of equilibrium with the electrodes and promote the electrolysis reaction. This depends principally on the type of catalyst on the anode electrode side; in terms of IV properties, the voltage where the current density approaches zero in the graph corresponds to this. The voltage constituent determined by the membrane is affected by the resistance when the current is passing through the component materials and when the hydrogen is moving through the proton exchange membrane. It is expressed as the slope of the IV curve. The voltage constituent determined by the ion supply does not appear in Fig. 11, but it is what occurs as a result of insufficient ion supply. It occurs as a sudden increase in voltage in the region of the graph where current density is high. The grand total of these voltages determines the electrolysis voltage. For the purpose of lowering the electrolytic voltage, we have adopted a thinner proton-exchange membrane to reduce resistance, and developed a new Ru-Ir-Fe oxide catalyst to enable electrolytic reaction at a voltage lower than with a conventional platinum catalyst. Figure 11 shows the electrolysis voltage reduction effect of incorporating these improvements.

Figure 12 shows the layout of the electrolyzer. While the operating voltage is low in a single electrolysis cell, the high current makes it difficult to control the reaction to be stable and efficient. To deal with this characteristic, cells consisting of a combination of anode electrodes, proton exchange membranes and cathode electrodes are stacked. This is called an electrolysis stack. The endplate fastening each cell of the stack requires sufficient rigidity to assure uniform and appropriate surface pressure, so it becomes thick and heavy. To make the electrolyzer more compact and lighter, the endplate was not made solid, but rather the pure water circulation pumps and O_2 gas-liquid separators were all built integrated with the channels in the electrolysis stack's endplates so that there are no pipes on the exterior. Setting the pure water channels within the electrolysis stack significantly shortened the pipes of the pieces of auxiliaries such as ion exchangers. Shorter pipes in turn reduced ion elution, so fewer ion exchangers were necessary. In addition, making the pipes shorter and the ion exchangers more compact resulted in reduced pressure loss in the pure water circulation system and reduced the work of the water circulation pump, thus achieving both compactness and efficiency.

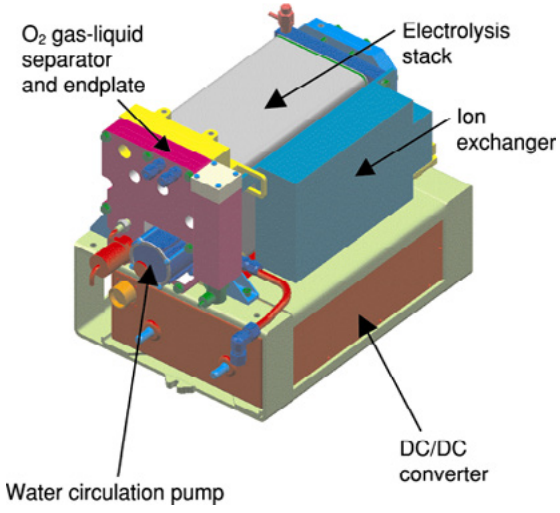


Fig. 12 Assembly of electrolyzer

4.3. Power Converter

Commonly marketed hydrogen production systems are designed to operate on a fixed amount of grid power. A feature of the system described in this report is that it does not depend on grid power but is able to produce and supply hydrogen efficiently even on the variable power supply from photovoltaic modules.

Because the refueling station was to be located outdoors, it had to be impenetrable by sand and rain and resist condensation caused by changes in humidity. The 5 kW-class power equipment used in this station is not commonly sold in a form suitable for outdoor use. To make it usable in this station, a sealed power system was developed using the electronic system technology of electric and hybrid vehicles to prevent the penetration of sand and rain and not allow condensation to occur. Heat dispersion is an issue with power devices used in sealed conditions, but the design assured reliability with a water cooling system using water emitted from the pure water production process; this also enabled the equipment itself to be more compact. As a result, it was possible to place the power source system directly beneath the electrolysis stack and greatly reduce the length of high-current (close to the 100 A) wiring peculiar to the electrolyzer, thus minimizing transmission loss.

As Fig. 13 shows, the photovoltaic modules can operate at any point on the voltage-current curve, but the power output will vary depending on the operating point. Moreover, the voltage at which peak power is produced (V_{Pmax}) will vary depending on fluctuations in amount of solar radiation and temperature of the photovoltaic modules, so a peak power tracker, or PPT, a system that keeps the photovoltaic modules constantly operating in their most efficient state, is typically used. This system, however, omits this device because it is possible to achieve the same function by controlling the load on the DC/DC converter used for electrolysis.

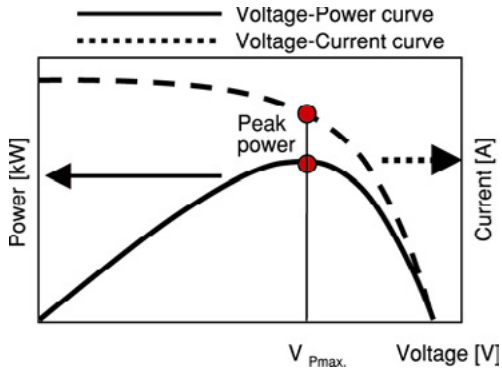


Fig. 13 Characteristic of photovoltaic modules

Moreover, this system was built to use a rectifier with an active filter when using grid power and to bypass the rectifier when the photovoltaic modules are used, thus supplying DC power to the respective power equipment. Using this system greatly simplifies the configuration of the power conversion equipment.

5. Tank Unit

The tank unit consists of six high pressure tanks for storing high pressure hydrogen and of six buffer tanks that temporarily store low pressure hydrogen prior to pressurization and protect the electrolysis unit from pressure fluctuations occurring during compressor operation. As Fig. 14 demonstrates, the high pressure tanks are set horizontally with the buffer tanks lying in the gaps, an arrangement that minimizes empty space and makes the tank unit smaller.

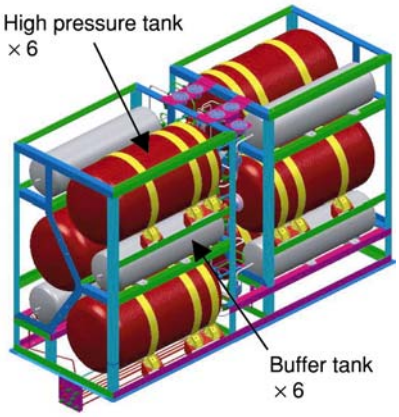


Fig. 14 Assembly of storage tank unit

6. Dispenser Unit

The dispenser unit has a diaphragm compressor capable of discharging 35 MPa hydrogen at a rate of 2 Nm^3/h, a hose, a nozzle and a breakaway (Fig. 15). In case the vehicle starts moving before the nozzle is released from the vehicle, the breakaway has a mechanical device that causes the hose to break away if pulled and a valve to cut off the flow of hydrogen so that the hose will not break and let hydrogen gas escape.

The refueling station uses two different filling systems: fast fill, which uses the difference in pressure between the vehicle's tank and the station's high-pressure tank, and slow fill, which uses a compressor to fill the hydrogen directly without storing the hydrogen produced.

Fast fill employs a cascading, continuous supply system in which hydrogen is supplied in succession from those of the six high pressure tanks with relatively low pressure, and maximizes the supply of hydrogen to the automobile (Fig. 16). Fast filling takes under five minutes to complete, but it does not allow the on-board tank to fill completely as the temperature of the tank rises because of the sudden adiabatic compression. This phenomenon occurs not just with hydrogen but with any gaseous fuel under high pressure that is filled in a short length of time.

Slow filling takes more time so the heat can be sufficiently dissipated from the on-board tank. Therefore, the tank can be completely filled.

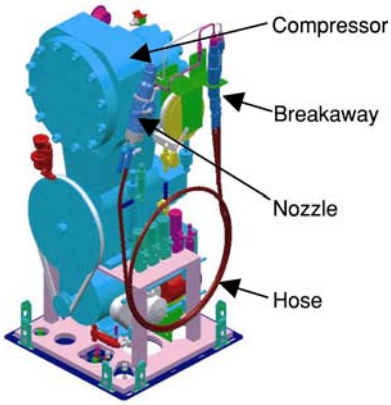


Fig. 15 Assembly of dispenser unit

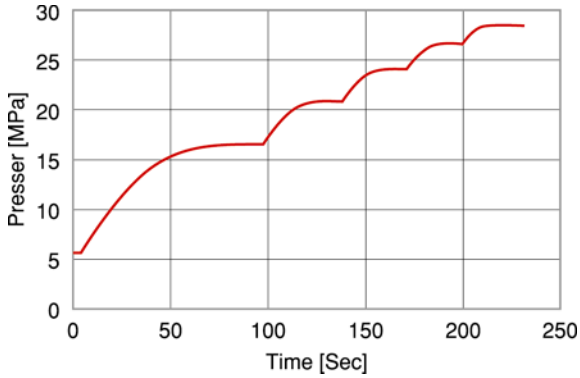


Fig. 16 Example of hydrogen refueling for on-board tank

7. Amount of Hydrogen Produced, Efficiency and Amount of CO_2 Emissions

Figure 17 gives an example of the measured amount of solar radiation, generated power and hydrogen production in one day during operation of the system, while Fig. 18 gives the energy flow. The efficiency of the station (the percentage of solar radiation energy hitting the photovoltaic modules that is ultimately supplied to the vehicle as hydrogen) was approximately three times better than that of the prototype.

Electrolysis loss, in particular, has been reduced to as small as 1.4% of the total power generated by the photovoltaic modules. This was made possible by the development of a new electrolytic catalyst, the optimization of the operating temperature and the electrolytic current density, the reuse of hydrogen for purifier regeneration, and other design improvements.

Because of the great improvements in the efficiency of various pieces of equipment as described above, the overall system efficiency has risen dramatically, to approximately three times the corresponding percentage of the prototype station assembled from commonly available equipment.

Based on these results and records of the amount of solar

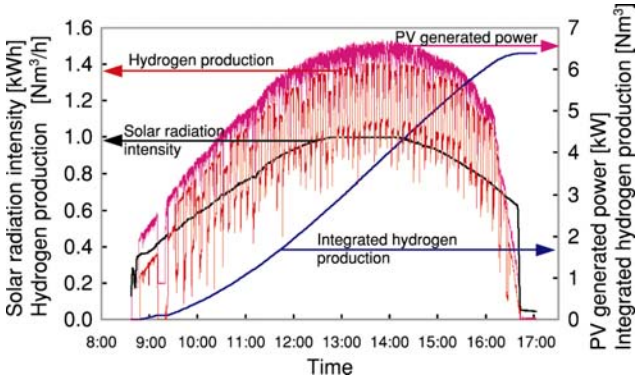


Fig. 17 Example of hydrogen generation

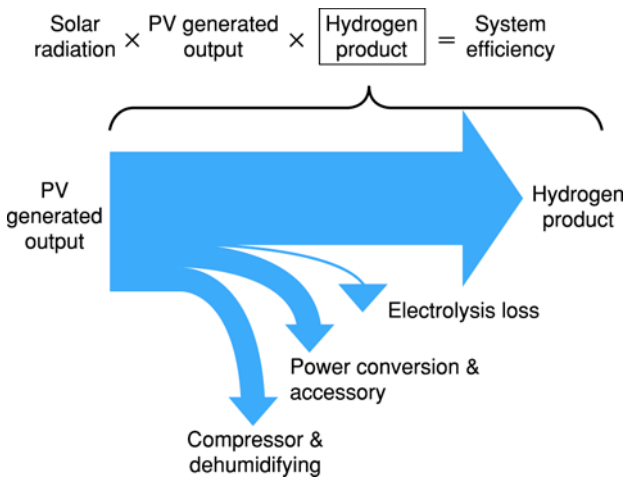


Fig. 18 Energy flow

radiation in Los Angeles from 1961 to 1990, it was estimated that this system could produce over 2 000 Nm^3 of hydrogen annually. Performing calculations based on the fuel efficiency label values[4] for city driving mode of the Honda FCX, sold since December 2002, as determined by the Environmental Protection Agency and the California Air Resources Board, this corresponds to about 10 000 miles (16 000 km), showing that the experimental station achieved its goal of providing enough hydrogen for driving 10 000 miles annually only with sunlight as the energy source.

The social significance of fuel cell vehicles includes the fact that not only do they provide an alternative to the use of fossil fuels and reduce exhaust gas emissions. but that they reduce CO_2 emissions. Therefore hydrogen production systems will not only have to be more efficient but also cause lower CO_2 emissions when the component equipment of the systems is manufactured.

In the case of fuel cell vehicles running on hydrogen, no CO_2 is emitted while driving, but CO_2 may be released from the energy source used, depending on the way in which the hydrogen is produced. This is because CO_2 is emitted as a result of burning fossil fuels in thermal power generation. Consequently when electrolysis depends on grid power, more CO_2 is emitted especially when thermal power is used to generate a greater proportion of the total energy used.

On the other hand, when photovoltaic modules are used to produce hydrogen, no CO_2 is emitted during hydrogen production itself, but it is still necessary to consider that CO_2 is released form the portion of thermal power generated electricity used to manufacture the photovoltaic modules. Because single-crystalline Si photovoltaic modules require a great deal of energy to produce[5], the photovoltaic modules account for the majority of CO_2 emitted during the manufacture of the equipment used in the hydrogen refueling station. Improving system efficiency and reducing energy consumption during the manufacture of photovoltaic modules are crucial to reducing emissions of CO_2 per unit of hydrogen produced.

For the above reasons, this study tested the CO_2 emissions reduction effect of adopting CIGS (copper-indium-galium-selenide) thin film photovoltaic modules developed by Honda, which consume considerably less energy during manufacture. This assessment used the Well to Wheels CO_2 emissions, that is, the amount of CO_2 emissions including all emissions from fuel production to fuel consumption while driving. Using the conditions listed below, CO_2 emissions to produce hydrogen of 1 Nm^3 by electrolysis were compared for three scenarios: using grid power, using single-crystalline Si photovoltaic modules and using CIGS compound thin film photovoltaic modules.

- CO_2 emissions from grid power: 0.40 [kg-CO_2/kWh] Because there will be great differences according to time and region, this figure was set based on values from the US and Japan[6]
- Depreciation period for photovoltaic modules: 10 [years]
- Driving distance: 10 000 [miles/year]

The results show that, compared to the use of grid power, using single-crystalline Si photovoltaic modules will make no great difference in CO_2 emissions, but the use of CIGS thin film compound photovoltaic modules will reduce CO_2 emissions per unit of hydrogen significantly. This suggests that producing hydrogen with natural energy can be very effective for the objective of reducing CO_2 emissions.

8. Conclusion

The research described herein was conducted to improve the performance of hydrogen refueling stations using photovoltaic modules and to make the stations more compact with the ultimate objective of helping to solve energy and global environmental issues. Findings of the research were as follows.

(1) Equipment efficiency was improved and total system efficiency approximately three times greater than that of the station assembled from commonly available equipment was achieved through such means as developing an electrolyzer with a newly composed catalyst.
(2) It is predicted that the power generated from photovoltaic modules sized for approximately two households would supply enough hydrogen to fuel a Honda FCX for 10 000 miles or more in one year.
(3) It is predicted that CO_2 emissions would be reduced significantly by employing CIGS compound thin film photovoltaic modules, as compared with single-crystalline Si photovoltaic modules.
(4) By making the equipment smaller, it was possible to project an image of the future hydrogen society as clean and advanced.

Acknowledgements

Many individuals helped to make possible the unprecedented, personal-sized hydrogen refueling station described in this report. This was the first such station in Torrance, California, and city and fire department officials cooperated generously. The authors would like to take this opportunity to thank the many individuals at Honda and beyond who helped in this research.

References

(1) http://www.enaa.or.jp/WE-NET/database/kaigai.html

(2) http://rredc.nrel.gov/solar/Typical Meteorological Year 2 (TMY2)

(3) Energy Information Administration U. S. Department of Energy: Household Vehicles Energy Consumption 1991, U.S.DOE Reports, p. 50 (1993)

(4) Ogawa, T., Kimura, K., Uchibori, K., Fujimoto S., Shimizu, K.: Development of New Power Train for Honda FCX Fuel Cell Vehicle, Honda R&D Technical Review, Vol. 15, No. 1, p. 11 (2003)

(5) The Institute of Electrical Engineers of Japan, Special Committee for the Study of Photovoltaic Modules, ed.: Photovoltaic Module Handbook, Chapter 9: Examining Economy, Corona, Tokyo, p. 302-305 (1985)

(6) http://www.tepco.co.jp/env/environment/siryou/kankyou/2002/index-j.html, Report Part 1: Environment; Environmental Protection, Global Environment

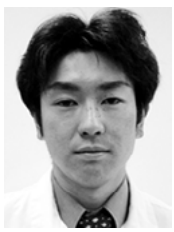
■ Authors ■


Masaki UEYAMA


Masato KITA


Satoshi TAGUCHI


Koji NAKAZAWA


Hisashi NAGAOKA


Shinichi ARAKAWA

Establishment of a New Research Center for the Study of Extremely Low Emission Vehicles (SELEV)

Jeff JETTER* Ben KNIGHT* Tatsuya OKAYAMA**
Seiji HATCHO** Nicole DAVIS*** John COLLINS***

ABSTRACT

Vehicles such as the new Honda Accord PZEV (Partial Zero Emission Vehicle) can help California and other regions achieve their air quality objectives. However, the potential impact of this technology upon air quality is not fully understood by regulators or by the general public, and it has not been accurately quantified. For this reason, Honda has initiated a research center at the University of California, Riverside, for the "Study of Extremely Low Emission Vehicles" (SELEV). There are three interrelated objectives for this center: (1) Measure the emissions of advanced-technology vehicles under real-world conditions; (2) Build a database of vehicle population and activity; and (3) Use these data to develop air quality models that can accurately assess the impact of near-zero-emission vehicles.

This paper will detail the development and validation of an on-board system capable of determining mass-based emissions, and the use of this system to prove that advanced-technology vehicles maintain their emission performance under real-world driving conditions. It will also be shown that data collected during this program can be used to improve the accuracy of emission inventory predictions. The preliminary, encouraging results of this program have been recognized by the California Air Resources Board (CARB), and some of the recent changes in the ZEV regulation reflect the real-world near-zero emission vehicle performance being confirmed in this research program. This program has also received the attention of the national media.

1. Introduction

1.1. Background

In the 1980's, it became clear in the US that vehicle emission standards would require additional tightening. As a result, the Clean Air Act was amended in 1990, thereby producing the federal "Tier 1" standards. In the same year, the California Air Resources Board initiated the Low Emission Vehicle (LEV) program, a key component of which was the Zero Emission Vehicle (ZEV) regulation. Several additional states subsequently adopted the California program. The concept behind the ZEV regulation was that Battery EV technology looked promising, and in 1990,

* Honda R&D Americas, Inc.
** Tochigi R&D Center
***University of California Riverside, College of Engineering - Center for Environmental Research and Technology

CARB considered gasoline-powered vehicles to have limited emissions reduction potential such that air quality goals could not be achieved.

However, at the dawn of the 21st century, a technological breakthrough occurred that could not have been foreseen a decade earlier. Gasoline-powered vehicles began entering the market with emissions at near-zero levels. For example, most Honda Accords sold in California in 2003 had emissions essentially equivalent to that of an electric vehicle, when the powerplant emissions associated with the latter are considered. Current air quality predictions do not account for the impact of this technology, because it has not been quantified. Therefore, the government agencies could not accurately account for these "Extremely Low Emission Vehicles" (ELEV) vehicles in their regulatory framework. Environmentalists and the general public remained skeptical that a vehicle powered by gasoline could be so clean.

It was against this backdrop that the CARB, US EPA, and Honda initiated the SELEV Center at the University of California, Riverside. The purpose for establishing this center was to establish an independent, credible entity with the ability to objectively measure and assess the effect of ELEV technology upon air quality. The University's College of Engineering Center for Emission Research and Technology (CE-CERT) group was uniquely suited for this role, due to their extensive experience with emission measurement and air quality modeling.

1.2. SELEV Strategy

The key components of the SELEV Center are shown in Fig. 1. A cornerstone of the program is the collection of real-world data. It was known that ELEVs perform well under laboratory conditions, but laboratory measurements alone cannot confirm the performance of these vehicles under actual-use situations. Therefore, tailpipe emissions were measured while the vehicles were being driven on the road, using an on-board analyzer. Another group of CE-CERT researchers collected data regarding the current vehicle activity and fleet distribution in Los Angeles; i.e., driving patterns and a breakdown of the various vehicle classes. These data were then used to improve California's existing emission inventory, using modeling tools such as CMEM (Comprehensive Modal Emissions Model) and modifications to current inventory models. CMEM is described later in this paper. Traditional laboratory measurements were used to provide some of the data used to calibrate CMEM, and also to validate the accuracy of the on-board measurement system. For the final step, the inventory data were prepared for use in air quality models, thereby permitting the assessment of ELEV impact upon the air basin of an entire city.

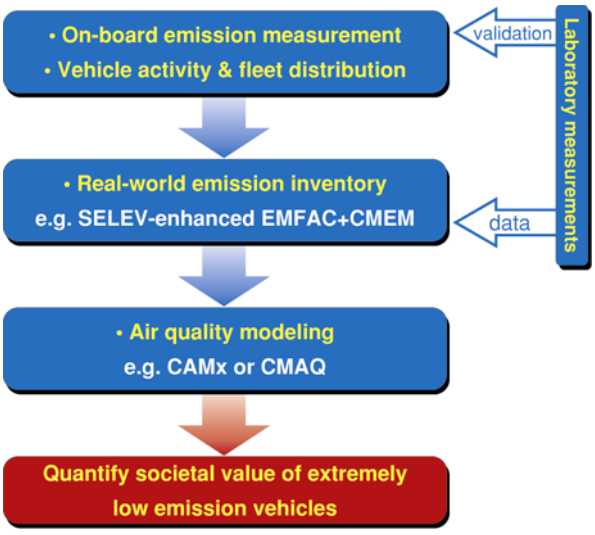


Fig. 1 Overview of SELEV Center strategy

2. Experimental

2.1. On-board Emission Measurement

2.1.1. Background

The importance of measuring the emissions on board a vehicle under real-world conditions is well understood. For example, the US EPA is seriously considering the implementation of "on-vehicle" compliance standards, and perhaps even on-vehicle certification. The reason for this is that the EPA has discovered that some low-emission technology emits two to three times the standard under real-world conditions, despite the fact that the standards were met in the laboratory. The National Academy of Sciences is also pushing the EPA to use on-board measurement to assess the effect of federal emission regulations[1), 2)].

Within the SELEV Center, the measurement of on-road emissions serves two purposes: (1) It determines the real-world performance of ELEV technology, and confirms that the near-zero emission levels measured under laboratory conditions are realized in actual on-road driving; (2) It provides emission calibration data for modeling tools such as CMEM.

2.1.2. Hardware

The on-board analyzer assembled by CE-CERT was based upon technology developed by Honda R&D, Los Angeles[3),4)]. The accuracy of Honda's FTIR-based system compared favorably to traditional laboratory techniques, based upon an independent assessment performed by CE-CERT[5)]. The Honda system was dedicated to a single vehicle, and was designed to simultaneously measure ambient air quality and tailpipe emissions. In contrast, the CE-CERT system was designed to be easily transferred between vehicles in less than two hours, and required only a single FTIR (Fourier Transform Infrared Spectroscopy) analyzer. Most of the system hardware was contained within two modular components: a sample conditioning module and an analytic module; Fig. 2. The conditioning system consisted of two Nafion (Nafion is registered trademark of E.I. du Pont de Nemours and Company.) driers, one fitted with a piezoelectric cooler to increase efficiency. Sample water content was maintained at a constant low level through the use of dewpoint feedback control. The analytic module consisted of a modified FTIR with an 8.3 meter cell. The CE-CERT system also included instrumentation to record vehicle speed, location, and various engine operating parameters. This permitted an accurate measurement of tailpipe emission on a mass basis. Also, emission

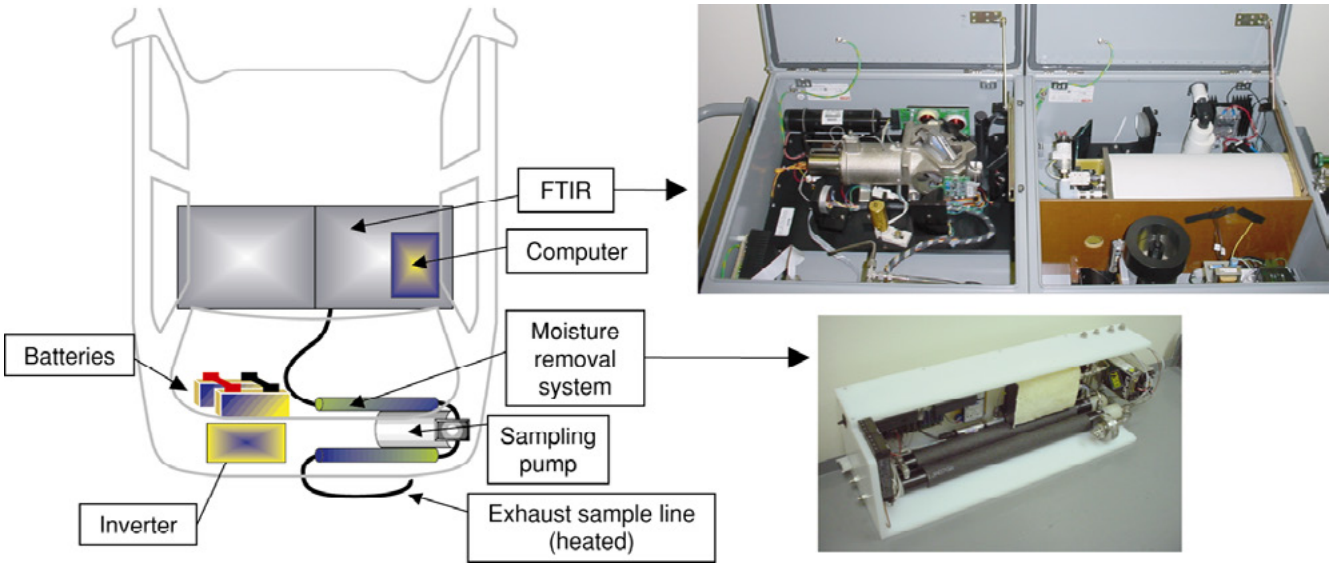


Fig. 2 Modular on-board analyzer system developed by CE-CERT

performance could be correlated to specific events, such as acceleration on a freeway on-ramp.

2.1.3. System validation

The validation of this system was a two-step process. The first step was to confirm that the on-board analyzer could match the accuracy and precision of a traditional dynamometer system; i.e., a CVS (Constant Volume Sampler) and bench analyzers. A variety of low-emission vehicles were tested in a dynamometer laboratory, while the on-board system measured emissions concurrently with the dyno bench analyzers. No information was shared between the two analytic systems; i.e., the mass-based emissions were calculated for the on-board analyzer using only the data acquired from the vehicle's ECU. The second validation step involved driving the vehicles over a test cycle (e.g. FTP-75) on the road, while the on-board analyzer collected data. Because this procedure was very challenging for the driver, it was conducted at the Honda Proving Center in California (HPCC). These tests were critical, because the analyzer system must retain its accuracy and precision in on-road conditions to produce credible real-world data.

The on-board analyzer passed both validation steps, as can be seen in Fig. 3. In this example, the first two columns in each set represent the laboratory testing with results collected concurrently from the dyno bench and on-board analyzer, and the third column represents the separate on-road testing.

2.2. Laboratory Testing

In addition to validating the on-board analyzer, laboratory testing fulfilled other requirements of the SELEV Center research. For example, data collected during laboratory testing, such as catalyst efficiency, was used to calibrate the CMEM emissions inventory model.

All testing of SULEV-technology vehicles was performed at the California Air Resources Board laboratory

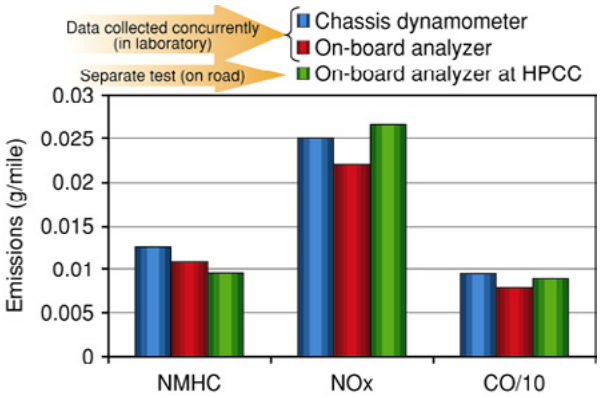


Fig. 3 Validation of CE-CERT on-board analyzer. Test vehicle = 2001 Honda ULEV Accord.

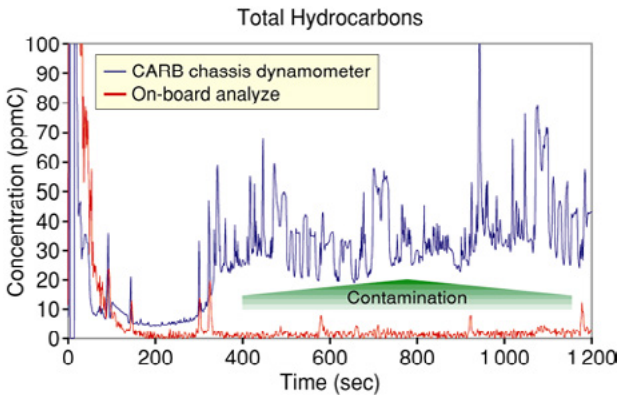


Fig. 4 Contamination of CARB laboratory system discovered by on-board analyzer

in El Monte, because the CE-CERT laboratory was not certified to test SULEVs. In one interesting example of this work, the on-board analyzer identified a contamination problem in the CARB's laboratory system during US06-cycle testing; see Fig. 4. Similar contamination was discovered at the CE-CERT laboratory. In both cases, it was due to the out-gassing of emission sampling hardware during periods of high temperatures. These problems were subsequently corrected.

2.3. Vehicle Activity Patterns and Fleet Distribution

In order to determine mobile source emission inventories using models such as CMEM, it is necessary to have a good understanding of vehicle activity patterns and fleet distributions for the target area. In the SELEV program, vehicle activity was measured in three cities within the South Coast Air Basin. Within each city, three types of roadways were studied: Freeway, arterial (major non-freeway highways), and residential. Equipment used for this study:

A. Digital video camera, with automated data analysis; "Autoscope". This equipment provided data such as average speed, vehicle type, and traffic volume.
B. High-resolution digital video camera. This camera captured the license plates of passing vehicles. The Vehicle Identification Number (VIN) could be determined by cross-reference with the license data, thereby providing information such as vehicle make, model, catalyst type, etc.
C. Instrumented vehicle. This vehicle was driven along the targeted roadways during monitoring periods, providing speed, acceleration, road grade, and position data on a second-by-second basis.

Equipment configuration "A" is shown in Fig. 5, together was an example of the data. This figure demonstrates how the Autoscope placed "virtual detectors" on the video image during post-processing. Vehicles passing through these detection areas were automatically counted and classified as to speed and vehicle class. This data example indicates average speed over the various roadways monitored in the city of Yorba Linda.

2.4. Emission Inventory Models

An accurate inventory of emissions is a prerequisite to the understanding the factors that affect air quality. The on-road mobile source emissions models used today for inventory and regulatory purposes are MOBILE, which was developed by the USEPA[6], and EMFAC, which was developed specifically for California[7]. These two models are structured similarly and they calculate mass emissions by multiplying the vehicle activity data by the emissions factors. Both models have built-in assumptions for emission rates, deterioration rates, and other factors. Unfortunately, these assumptions are generally not appropriate for ELEV technology, and can lead to an over-prediction of the emissions for these vehicles. The data being collected in the SELEV program will allow appropriate adjustments to be made to these default assumptions.

CE-CERT has developed CMEM, which takes a different approach to vehicle emissions modeling. The CMEM framework computes a vehicle's emissions based upon operating mode. For example, the number of stops, acceleration events, the traffic conditions, and other factors

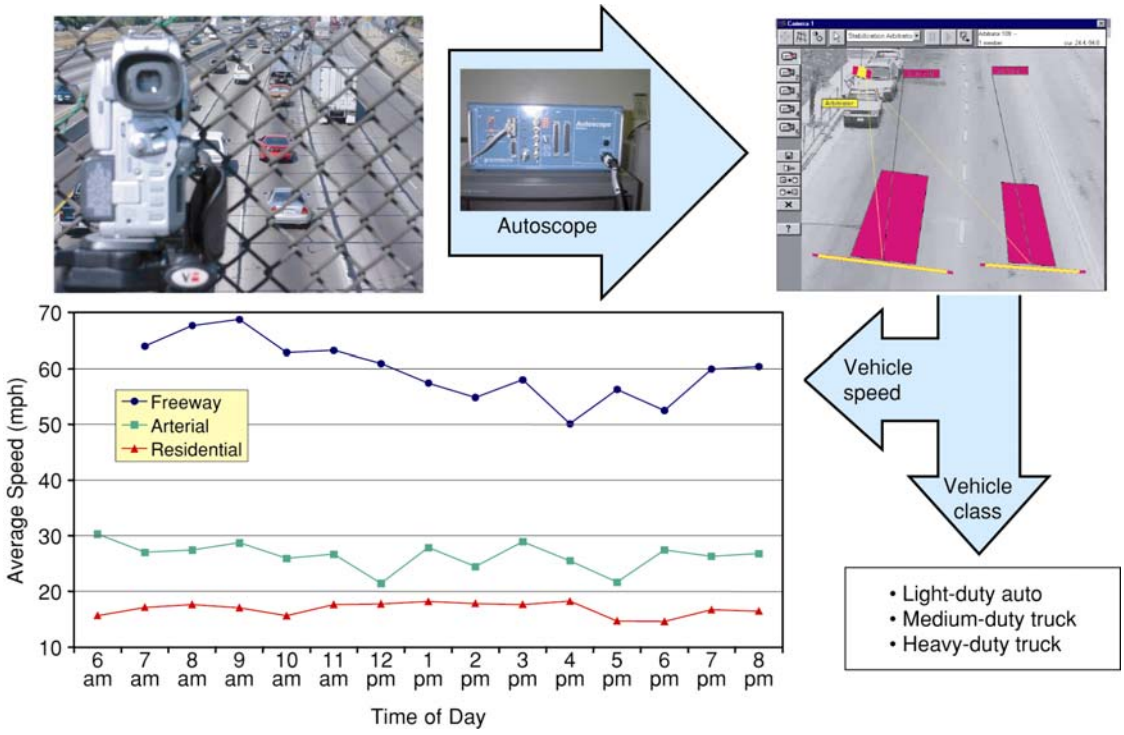


Fig. 5 Measurement of vehicle activity patterns and fleet distribution. Equipment configuration "A". Data from city of Yorba Linda.

are accounted for in the CMEM framework. Specifically, CMEM uses a power-demand modal modeling approach based on a parameterized analytical representation of emissions production. In such a model, the entire emissions process is broken down into different components that correspond to physical phenomena associated with vehicle operation and emission production[8]. Each component is then modeled as an analytic representation consisting of various parameters. The architecture of the model is shown in Fig. 6. Over 400 extensive dynamometer tests were used in the development of the CMEM model. Laboratory and on-road data collection during the SELEV program have enabled the development of CMEM modules for vehicles with emission categories of ULEV and below. This aspect of the program is still in progress; the elements currently being modified to accommodate ELEV technology are highlighted in Fig. 6. This enhanced version of CMEM can then be used as a supplement to the SELEV-modified EMFAC, resulting in an emission inventory that will reflect the introduction of ELEV technology.

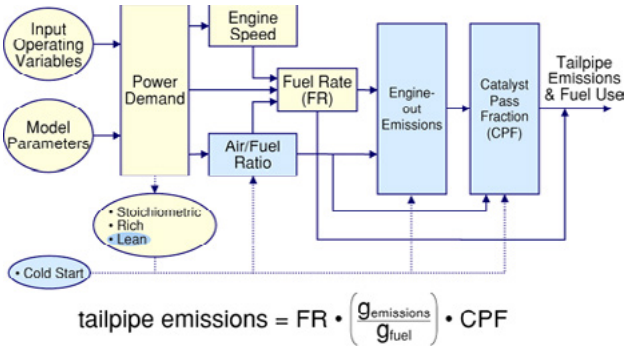


Fig. 6 Basic architecture of CMEM modal emission model. Blue areas are being modified to accommodate ELEV technology.

2.5. Air Quality Modeling

Emission inventories are the major component of air quality models. Other key components are meteorological data and photochemical reaction mechanisms. These sophisticated air quality models can predict the concentration of ambient air pollutants. An example of the output of one such model, CAMx (Comprehensive Air Quality Model with extensions), is shown in Fig. 7.

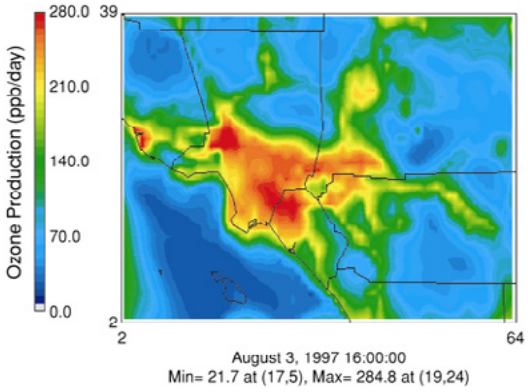


Fig. 7 Example of CAMx air quality model prediction of ozone production for Southern California. (August 3, 1997)

This figure represents the CAMx "prediction" of ozone production for Southern California over a specific timeframe in 1997. In the SELEV program, the 1997 air quality scenario will be compared to a predicted scenario for the year 2010. In this prediction, a high percentage of ELEVs will be assumed. Other emission sources, such as stationary and biomass, will be held constant. In this manner, the impact of ELEV technology upon air quality can be quantified. This work is currently in progress. Thus far, substantial progress has been made on the integration of emission models and atmospheric models. This has been accomplished through the use of the SMOKE (Sparse Matrix Operator Kernel) emission processing system.

3. Results and Discussion

3.1. Real-world Emission Measurement

Data from on-road, real-world driving are shown in Fig. 8 for a 2000 SULEV Accord. Emissions are plotted versus time. Vehicle speed is also shown. Three types of roadways are represented, as indicated in the figure. The GPS system that was used to collect the speed data also recorded elevation data, which is not shown. The latter data are important for the understanding and subsequent modeling of vehicle emission behavior, because the grade of the roadway is an important parameter that affects the vehicle's power demand.

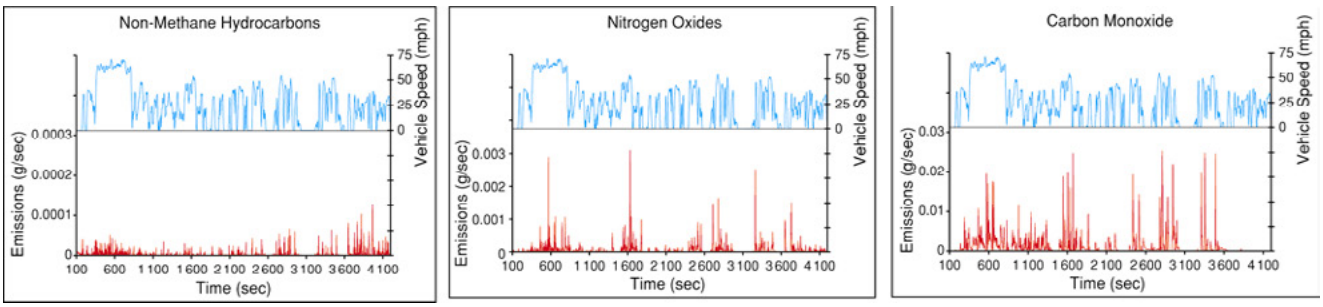


Fig. 8 Emission and speed measurements acquired on road under real-world conditions. 2000 Honda SULEV Accord.

The speed data itself can be used to help validate the CMEM emission inventory model. For example, the cycle's speed data can be used as an input for CMEM, and the emission results calculated by CMEM can be compared to the actual results measured on-road during that cycle. Of course, any on-road data used for the calibration of CMEM cannot be used for this purpose, or the validation would be invalid.

Throughout the various driving conditions encountered during the approximate one-hour period of data collection, tailpipe emissions remained extremely low. Based on previous research performed by Honda[3],[4], the exhaust species concentrations depicted in Fig. 8 are often below those of ambient air in the Los Angles area. It's important to note that exhaust emissions remained low even during periods of rapid acceleration that are not encountered during laboratory FTP-75 testing.

3.2. Real-world Data Compared to EMFAC Model

Data acquired from on-board measurements can also be used to check EMFAC model predictions. A comparison of EMFAC-predicted emissions for SULEV technology with actual on-road emissions from a Honda SULEV Accord is shown in Fig. 9. In both cases, data from arterial driving are shown. For further comparison, the second phase of an "on-road" FTP result acquired at HPCC is also shown. Only the second phase was used here in order to produce a valid comparison with an arterial driving situation in which no starts are observed. It can be seen that the emissions predicted by the EMFAC model are significantly higher than the actual emissions produced by the SULEV vehicle. The latest version of EMFAC available at the time of this writing was used for this comparison; (EMFAC 2002 version 2.2).

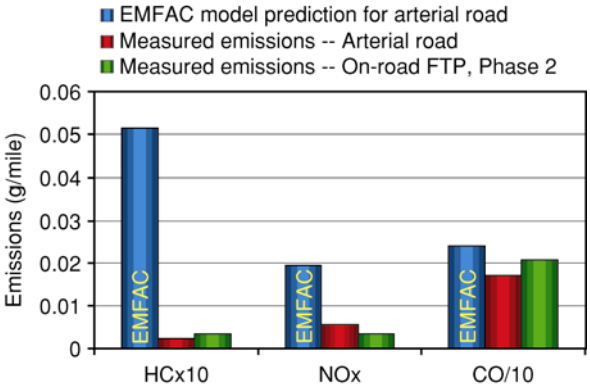


Fig. 9 EMFAC-predicted emissions for SULEV technology compared to actual measurements.
2000 Honda SULEV Accord, warmed-up conditions.

3.3. Observed Vehicle Fleet and Impact on Emission Models

The accuracy of emission model estimates is dependent upon the accuracy of the input data. The composition of the on-road fleet is one of the key parameters. The fleet composition data collected during the SELEV program were used as inputs for both the EMFAC and CMEM models. The purpose of this was not to compare the models themselves, but rather to determine the effect of using actual SELEV fleet composition data as inputs compared to using default parameters. In the case of EMFAC, the default settings used for this comparison were those for calendar year 2001, for the counties indicated in Fig.10. The model was then re-run using the SELEV fleet data collected during the summer of 2001. The SELEV data were prorated to keep the total vehicle population constant between the two cases. As can be seen in Fig. 10a, running the EMFAC model with the SELEV data produced emissions that were 22% to 45% lower than those calculated using the default values.

A similar exercise was performed using the CMEM model. In this case, the default input values consisted of a random sampling of vehicles registered with the DMV (Department of Motor Vehicles) within each target city. Running the CMEM model with the SELEV data produced emissions that were 8% to 70% lower than those calculated using the default values; see Fig. 10b.

These two comparisons demonstrate the importance of using actual, observed fleet characterizations as inputs to emission models. The default data used in many such models

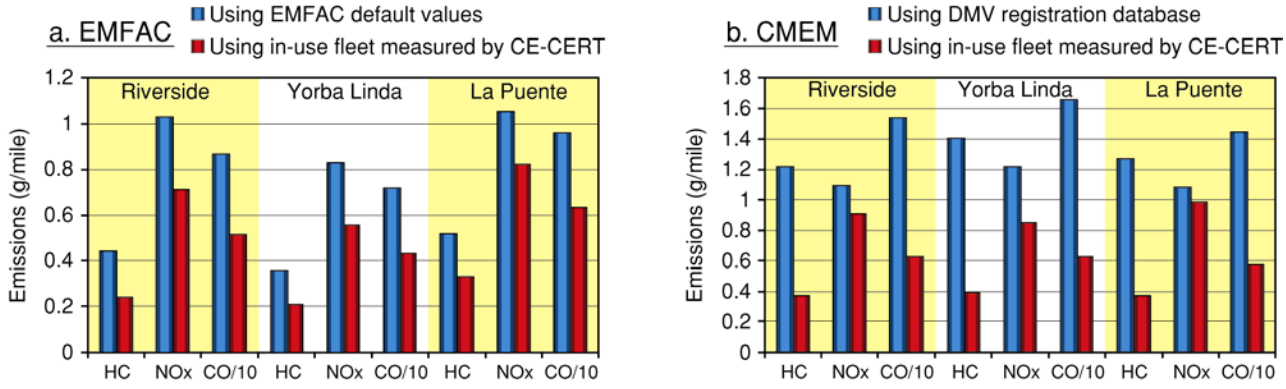


Fig. 10a and 10b Effect of using CE-CERT-measured in-use fleet composition data as inputs to emission models, compared to using default values.

are based upon vehicle registration data, which has been shown to be a poor predictor of the actual on-road vehicle composition[9].

3.4. SELEV Public Symposium and Response

In September of 2002, the University of California, Riverside, held a symposium at which interim results of the SELEV Center research program were presented. The response to this event greatly exceeded expectations. Regarding regulatory policy, a number of publications cited the SELEV Center results as being a factor in the CARB's recent changes to the ZEV regulation; one article called it a "primary catalyst for the change of heart from CARB[10] - [12]". The SELEV results also reached the general public, thereby helping to foster interest in and promote understanding of low-emission vehicle technology, such as that developed by Honda. The SELEV story reached a nationwide audience; it has been estimated that 32 million people heard about the SULEV results in some way[13]. The largest audiences were reached with a front-page article in "USA Today[14]", and a prime-time story featured on the "CBS Evening News with Dan Rather".

4. Conclusion

A new research center has been established to determine the impact of extremely low emission vehicles (ELEVs) upon the environment. The SELEV Center has applied a methodical and technically sound approach to achieve this objective, beginning with the measurement of vehicle emissions under real-world, on-road conditions. Extensive measurements have also been made of vehicle activity and class distributions. Supplemented by laboratory measurements, this collection of unique data is being used to produce inventory models that can accurately predict the emissions of advanced technology vehicles.

The significance of the SELEV Center findings has been recognized by the regulatory agencies and has been reported in the national media. The California Air Resources Board now has a better understanding of the positive impact ELEV technology can have towards their goal of improving California's air quality.

Research at the SELEV Center continues, with a focus on the assessment of the long-term, full-cycle air quality impact of extremely low emission vehicles.

References

(1) US EPA: Cooperative Research Proposal Regarding the development of a Commercially Viable On-Vehicle Emissions Measurement Product, June 12, 2001

(2) Spears, M., US EPA: Portable Emission Measurement Strategy, CRC On-road Vehicle Emissions Workshop, April, 2002

(3) Jetter, J. et al.: Development of an On-Board Analyzer for use on Advanced Low Emission Vehicles, SAE Technical Paper 2000-01-1140

(4) Jetter, J. et al.: Development of an On-Board System for the Simultaneous Analysis of Tailpipe Exhaust and Ambient Air, Honda Technical Review, Vol. 13, No.1, 49-58 p. (April, 2001)

(5) Truex, T. et al.: Measurement of Ambient Roadway and Vehicle Exhaust Emissions- An Assessment of Instrument Capability and Initial On-Road test Results with an Advanced Low Emission Vehicle, SAE Technical Paper 2000-01-1142

(6) US EPA: User's Guide to MOBILE6.1 and MOBILE6.2; Mobile Source Emission Factor Model, EPA420-R-02-028, October, 2002

(7) CARB: EMFAC2001/EMFAC2002; Calculating Emissions Inventories for Vehicles in California: User's Guide (2002)

(8) Barth, M.: Comprehensive Modal Emissions Model Users Guide, January 3, 2000

(9) Younglove, T. et al.: Observed On-Road Vehicle Fleet Differences and their Effect on Emissions, CRC On-Road Vehicle Emissions Workshop, April, 2002

(10) Bohanan, F.: The Winds of Change - CARB Acknowledges the Technical and Economic Realities of ZEVs, SEMA News, November, 2002

(11) Polakovic, G.: State Takes a Sharp Turn on Emissions, Los Angeles Times, September 15, 2002

(12) Bridges, A.: Study; California Should drop bid to Eliminate Tailpipe Emissions, Associated Press, September 18, 2002

(13) Data compiled by FM Strategic Communications, Washington, DC

(14) Healey, J.: New Gas Engines Rated Nearly Pollution Free, USA Today, September 5, 2002

■ Authors ■


Jeff JETTER


Ben KNIGHT


Tatsuya OKAYAMA


Seiji HATCHO


Nicole DAVIS


John COLLINS

Development of Light Weight and Lower Cost Aluminum VTEC Rocker Arm

Chikara TANAKA* Noriyuki YAMADA*

ABSTRACT

A VTEC rocker arm has been produced from aluminum die-cast materials to reduce weight and lower cost. The new arm, like the majority of rocker arms in use, employs a roller follower to reduce drive friction loss in the valve system. The VTEC connecting holes, in which strength must be guaranteed, were a primary focus to enable the shift to aluminum for the new VTEC system. A coaxial roller structure with a hollow roller bearing shaft was adopted, allowing the roller shaft to be press-fit into place and ensuring sufficient strength and accuracy in the new rocker arm. As a result, both the weight and the cost of the new rocker arm were reduced by more than 20% compared to the forged steel arm. The new arm was first mass-produced for use in the Fit.

1. Introduction

The use of VTEC engines has grown in recent years because of the improved output and fuel economy of these engines[(1)]. They occupy a 60% share of the entire range of engines in use today.

The rocker arm of the conventional VTEC engine has been made of forged steel with the target of providing high strength. However, as a large number of rocker arms were used in the engines, lighter weight and cost reduction became serious issues.

In view of this background, the need arose to strike a balance between weight reduction and the use of existing facilities, as well as curtailing the processing time and reducing costs by cutting down the number of processes. Aluminum was proposed as the material to resolve these issues, but its use in the VTEC rocker arm did not allow the proper balance between strength and precision.

An aluminum VTEC rocker arm has been developed. The methods used for resolving issues related to the structural development of the rocker arm and their effects are reported here.

2. Development Objectives

Figure 1 shows the structure of the newly developed aluminum VTEC rocker arm and the conventional VTEC rocker arm.

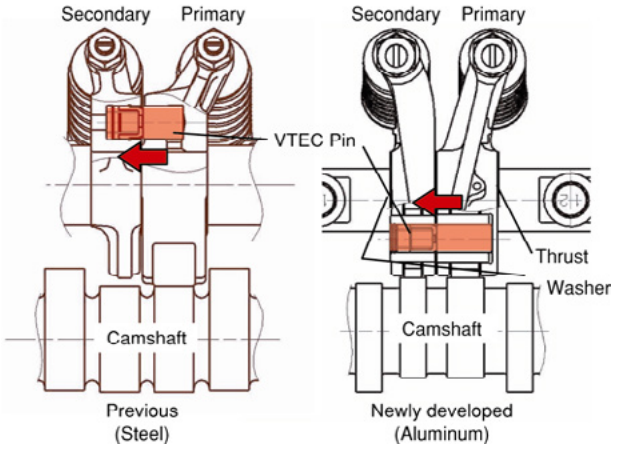


Fig.1 Comparison of VTEC rocker arms structure

The basic rocker arm structure consists of the rocker shaft hole, the rocker bearing hole and the VTEC connecting hole. The connecting hole in particular requires extremely high positioning accuracy because not only high strength but proper function and accuracy should be maintained during VTEC changeover. Furthermore, the connecting hole needs to possess high strength and wear resistance since durability for the synchronizing piston pin has to be ensured[(2)]. The conventional VTEC rocker arm was made of steel, and was then carburized or nitrided to satisfy the required

* Tochigi R&D Center

performance, however a large number of machining processes were required for the materials used in the rocker arm as shown in Fig. 2, and thus cost became a challenge.

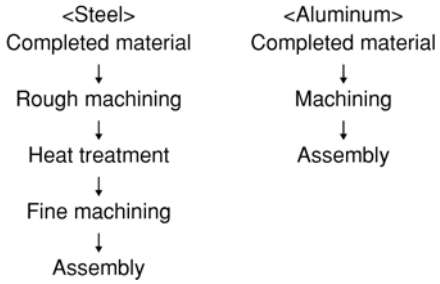


Fig.2 Comparison of machining process

The objectives of the present investigation were to develop a rocker arm that satisfies the requirements of the VTEC system mentioned above, based on conventionally used aluminum die-cast material in order to achieve weight and cost improvements, and to ensure valve system motion and reliability in the same space as forged steel VTEC rocker arms so that only the rocker arm can be replaced without making any changes to the valve system layout for engines in which existing forged steel rocker arms are being used.

3. Basic Structure and Technical Concerns

The issues that relate to the manufacture of aluminum VTEC rocker arms include strength of each part of the rocker arm; rigidity affecting the valve system motion; and strength, wear resistance, and accuracy of the components around the connecting hole. The newly developed rocker arm (Fig. 1) was designed with a shape that satisfies the required rigidity and strength using FEM analysis.

The thickness of the roller bearing arm, which is the weakest part in the rocker arm structure, was increased to enhance the strength. As a result, the width of the roller had to be reduced. Since high stresses also occur between the roller hole and the shaft hole, the thickness between these holes was optimized. Stresses also occur on the inside diameter of the VTEC oil supply hole because of deformation on the internal diameter of the rocker shaft hole. Consequently, the oil supply hole was moved in the upward direction away from the center of the rocker shaft hole and positioned at a location where compressive strain occurs on the inside diameter of the rocker shaft, thereby reducing the internal stress in the oil supply hole (Fig. 3).

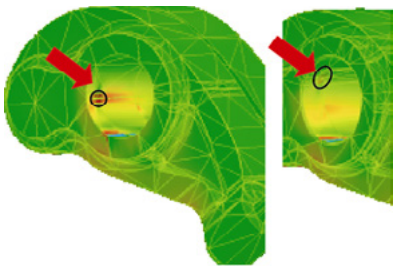


Fig.3 FEM analysis (oil supply hole location)

A rigidity greater than that of steel was obtained by adopting a structure in which the roller shaft and connecting shaft were made coaxial. The results of adopting such a structure are shown in Fig. 4.

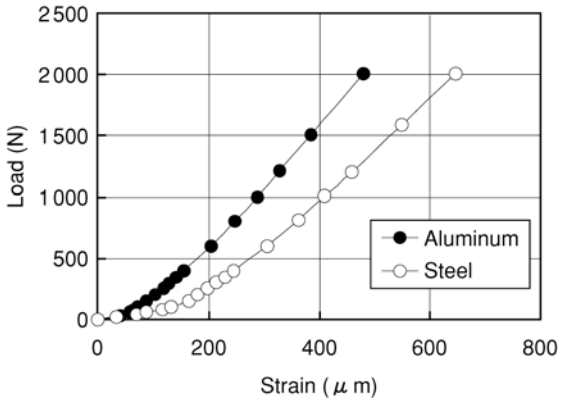


Fig.4 Rigidity comparison

By adopting a coaxial structure, the connecting hole does not engage the synchronizing piston with aluminum but with the roller shaft material, thus ensuring a good balance between strength and wear resistance.

The method of attaching the roller shaft by press fitting rather than by staking was selected because of the accuracy requirement of the connecting hole diameter. Consequently, the deformation of the inside diameter could be restrained and adequate accuracy of the connecting hole could be maintained.

There were also some concerns about wear on the end faces of the aluminum rocker arm caused by rubbing with adjacent rocker arms in the VTEC structure so steel washers were inserted as a measure to resolve this issue.

4. Fixing of Press Fit Assembly Method and Setting of Interference Fit

Since the method of attaching the roller shaft by press fitting was uniquely adopted at this time, the loads occurring during actual engine operation, the attachment method, the fatigue strength of the press-fit hole in the roller arm, the method of selecting the amount of interference for the press fit, and other factors affecting the part strength due to the press-fitting process were clarified, and important control items were set.

4.1. Drive Torque Generated in the Engine

Drive torque and thrust load are stress inducing inputs to the roller shaft. Figure 5 shows the method to measure those inputs.

The roller shaft was allowed to rotate freely and a load cell that could measure forces in the rotational and thrust directions was connected. Under this condition, the engine was operated and measurements were made. Figure 6 shows the measured results at various engine rpms.

The results show that a maximum drive torque of 1.11 Nm and a thrust load of about 3.31 kN were acting on the roller shaft.

It was observed that the load increased in the high-speed region where the valve motion became unstable. Load also increased during mis-engagement when the rocker arm

dropped onto the low lift cam because of an error when the VTEC was switched over. To account for the differences in the behavior during actual measurements, such as use of a rocker arm with load cell, variations in the spring load and so on, the requirements for target strength were taken as a drive torque greater than 2.94 Nm and a thrust load greater than 6.87 kN.

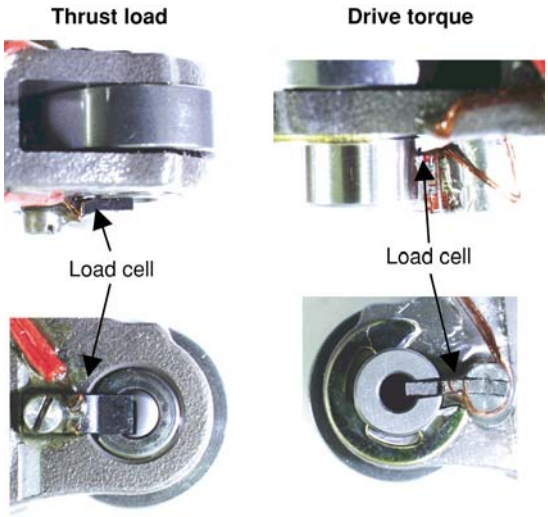


Fig.5 Load cells for measuring thrust load and drive torque

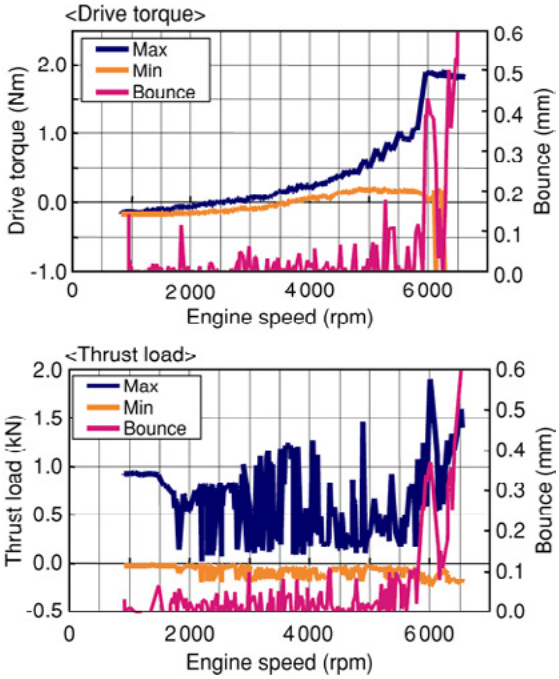


Fig.6 Drive torque and thrust load measurement results

4.2. Press Fit Tolerance and Part Strength

Figure 7 shows the part strength (drive torque and thrust load) for a variety of press fit tolerances, while Fig. 8 shows the remaining press fit. The remaining press fit is reduced as temperature is increased. The oil temperature during operation was taken as 150 °C, and the part strength was measured.

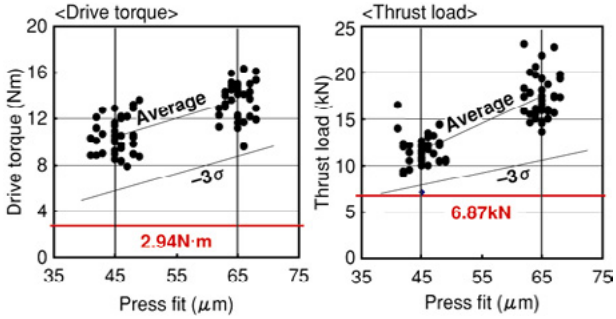


Fig.7 Drive torque and thrust load

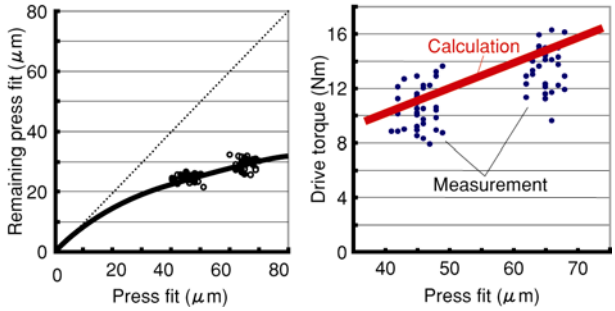


Fig.8 Remaining press fit and comparison between calculated and measured drive torque

The measured values were compared with the calculated values using the measurement of the remaining press fit and the coefficient of friction between the roller shaft and the aluminum die cast rocker arm. The double pipe equation shown below was used in the calculations.

A : Contact area between rocker arm and roller shaft
r_1 : Inner diameter of roller shaft
r_2 : Outer diameter of roller shaft
r_3 : Outer diameter of rocker arm
E_A : Young's modules of rocker shaft
ν_A : Poisson's ratio of rocker arm
E_B : Young's modules of rocker shaft
ν_B : Poisson's ratio of rocker arm
δ : Strain
P : Surface pressure
μ : Coefficient of friction between rocker arm and roller shaft

· Press fit force $F = \mu \cdot P \cdot A$ (1)

$$P = \frac{\delta}{r_2} \frac{1}{\frac{1}{E_B}\left(\frac{r_3^2 + r_2^2}{r_3^2 - r_2^2} + \nu_B\right) + \frac{1}{E_A}\left(\frac{r_2^2 + r_1^2}{r_2^2 - r_1^2} - \nu_A\right)} \quad (2)$$

· Stress at each location on rocker arm

$$\text{Outer diameter } (\sigma)_{r3} = P \cdot \frac{2 \cdot r_2^2}{r_3^2 - r_2^2} \quad (3)$$

$$\text{Inner diameter } (\sigma)_{r2} = P \cdot \frac{r_3^2 + r_2^2}{r_3^2 - r_2^2} \quad (4)$$

The remaining press fit is only about 50% of the initial press fit because of plastic deformation during the press fitting process. Under such conditions, it was observed that the calculated values agreed well with the test results, and the part strength can be expressed by a relationship between the press fit and the coefficient of friction.

In view of the above, it can be said that the press fit tolerance is an important item for controlling the strength of the roller shaft. Furthermore, it can be concluded from the results above that a press fit greater than 45 µm is necessary for the rocker arm to satisfy the part strength during actual operation.

4.3. Strain and Fatigue Strength of the Rocker Arm

The fatigue strength of the aluminum parts that underwent plastic deformation after press fitting is described here. Figure 9 shows the press-fit amount and the resulting fatigue strength for the rocker arm.

With an increase in the press fit amount, the fatigue strength is observed to improve. By preparing test specimens of the same material and measuring the relationship between plastic deformation and fatigue strength, it was confirmed that the fatigue strength increase was due to the increase in plastic deformation of the aluminum as a result of the increase in the press fit.

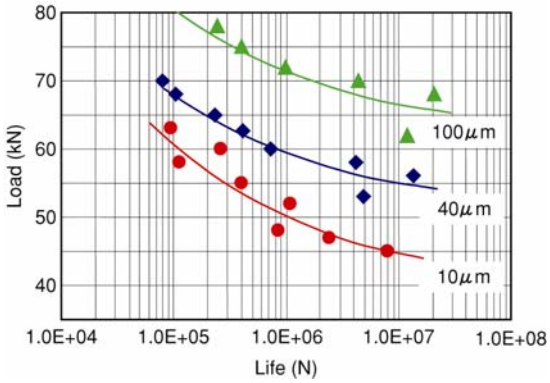


Fig.9 Fatigue strength

These results were evaluated using the fatigue limit curves. It was found that the residual stress increases on account of the increase in the press fit, and the fatigue strength improves. Therefore, evaluation can be performed using the fatigue limit as is done conventionally (Fig.10).

It was also observed that confirmation of the toughness of the rocker arm by unit and durability tests of actual engines at the lower limit of part strength may be accomplished using components with the lower limit of press fit.

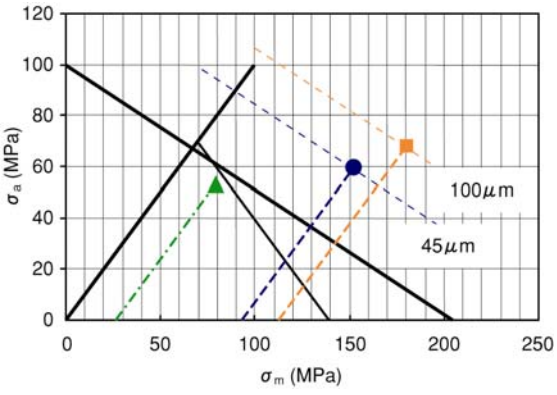


Fig.10 Fatigue strength limit

4.4. Summary of Press Fit Settings

Press fitting causes deformation in various parts and leads to dimensional changes. Accordingly, the upper limit of the press fit needs to be set in order to ensure dimensional accuracy.

Figure 11 shows scoring of the aluminum material of the rocker arm by the shaft during press fitting and the limit of occurrence of peeling. When peeling occurs, not only does the problem of grinding of the roller by dust particles occur, but the part strength is also affected. The upper limit of the press fit is also determined by the peeling limit.

Consequently, the procedure for determining the press fit is decided by setting the lower limit to ensure adequate part strength against engine load and by setting the upper limit based on dimensional accuracy and peeling limit.

The lower limit of the press fit for the newly developed rocker arm was set at 45 µm considering part strength. Considering dimensional accuracy, the upper limit was set at 65 µm since a 20 µm tolerance is considered to be necessary for good manufacturability.

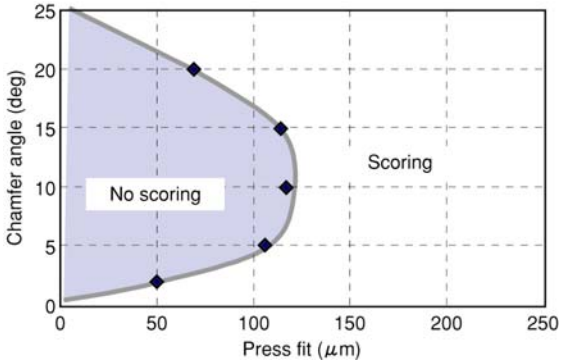


Fig. 11 Scoring limit

5. Reduced Roller Width

With the use of aluminum as the material for the rocker arm, the thickness of the roller support arm had to be increased to ensure its strength and rigidity. As a result, the width of the roller had to be reduced. The size of the roller is determined from the roller life according to the rated capacity and the stress that occurs in the outer race. The rated load of the roller can be lowered by reducing the weight of the rocker arm, and consequently, the roller width can also be reduced. However, the lower limit is considered to be two times the needle bearing diameter considering the shape and function of the needle bearing.

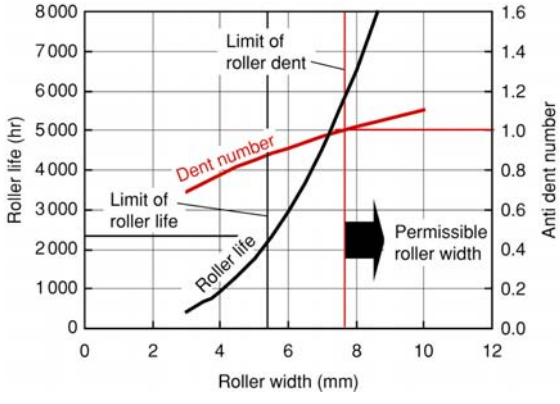


Fig.12 Optimization of roller width

If used in the VTEC rocker arm, dents from the needle bearing occur in the inner race of the roller on account of impact loads when VTEC mis-engagement occurs. It was concluded that the lower limit size of the roller had to be set so that this phenomenon could be avoided. Figure 12 shows the roller dimensions determined from the necessary rated loads, the weight reduction of the rocker arm, and from the number of dents allowed.

6. Confirmation of Durability

6.1. Valve System Motion

Factors that impact valve motion include rigidity and inertial weight. The comparison between the steel rocker arm and the aluminum rocker arm mentioned earlier showed that the rigidity of the aluminum rocker arm was greater than that of the steel rocker arm. Additionally, the inertial weight was reduced by 30%.

Figure 13 shows the measurement results of valve bounce relative to engine speed for each rocker arm design.

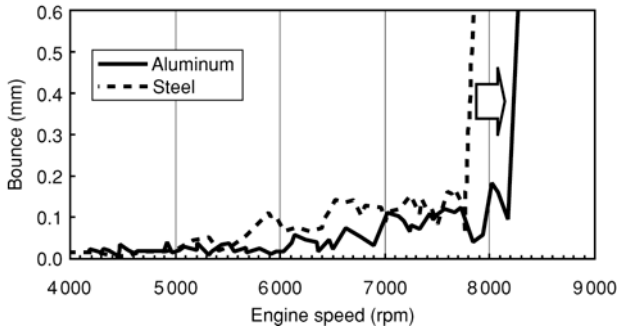


Fig.13 Valve bounce comparison between steel and aluminum rocker arm

An improvement in the engine speed by 500 rpm was confirmed due to the weight reduction. When this impact is translated to valve spring load, the effect is a 12% reduction. This caused a reduction of about 1% in friction in the roller rocker arm system, thus reducing fuel consumption.

6.2. Rocker Arm Stresses

The stresses that occurred in various parts of the rocker arm during operation were measured. The measurement points were the high stress locations according to FEM analysis. Figure 14 shows the measurement results at typical points.

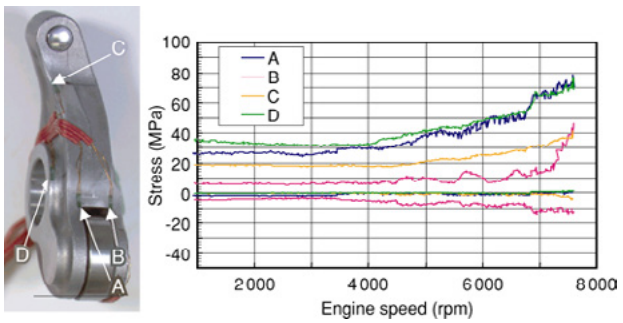


Fig. 14 Rocker arm stress under VTEC-engaged condition

It was confirmed that the locations of maximum stress were on the end faces of the rocker shaft hole and the outer surface of the roller support arm, but the stresses were within the fatigue strength limits of the material confirming sufficient durability.

6.3. Change in the Tappet Clearance

Figure 15 shows the change in the tappet clearance during the running of endurance tests.

The results of the mass-produced steel rocker arm and the newly developed aluminum rocker arm were compared. The performance of the newly developed rocker arm was confirmed as equivalent to that of the steel rocker arm. From the results above, it was concluded that the valve lift curve of the camshaft can be made the same as that of the steel rocker arm, and when used in the engine, only the rocker arms need to be replaced.

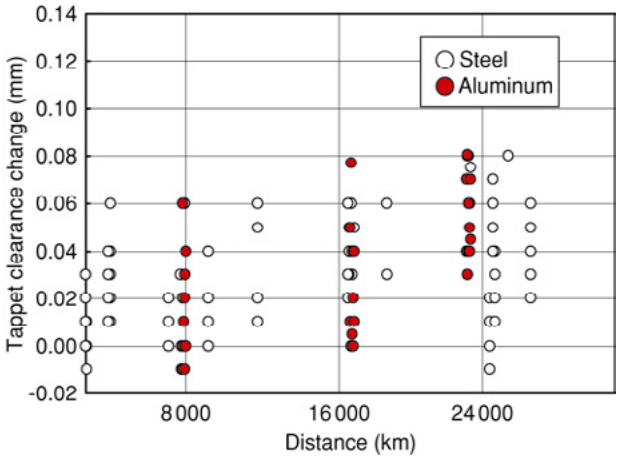


Fig.15 Tappet clearance change variation

6.4. Confirmation of Reduction in Fixing Strength of Roller Shaft after Durability Test

The durability test was conducted in the specified evaluation mode. It was confirmed that no damage, wear or excessive changes in tappet clearance occurred. Figure 16 shows the part strength confirmation results after the durability test.

It was observed that the initial part strength had been retained. Moreover, there was no shift of the roller shaft in the radial or the thrust direction, and adequate reliability of the part strength was confirmed.

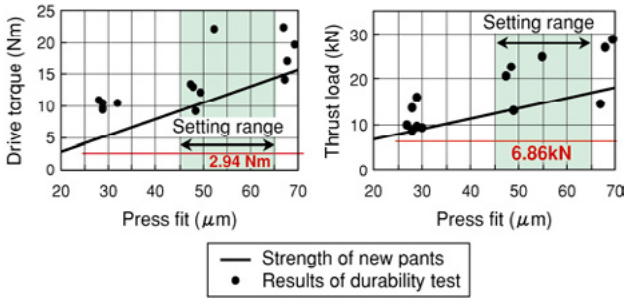


Fig.16 Fixing strength after durability test

6.5. End Face Wear of the Rocker Shaft

Wear of the end faces due to rubbing between adjacent aluminum rocker arms is a problem in the structure of the

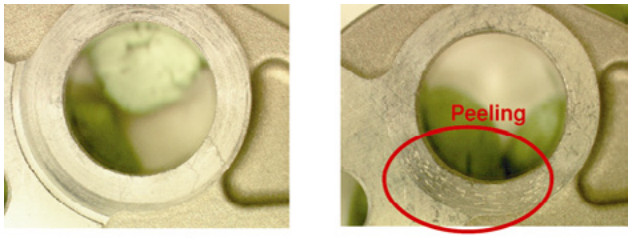


Fig.17 Effect of thrust washer against peeling of rocker arm end face

VTEC system. Figure 17 shows the status of wear in the end faces.

Excessive wear occurs if no washer is used. There was concern that the switching response would deteriorate due to the increase in the clearance between the VTEC switching holes. As a countermeasure, steel washers were inserted between the rocker arms, the rubbing between the aluminum members was avoided, and a reduction in wear was confirmed.

7. Productivity and Costs

7.1. Concept of Cost Reduction using Aluminum

Figure 18 shows a typical example of cost breakdown of the VTEC rocker arm. With the improvement in machinability due to the use of aluminum, both labor and equipment costs of machining could be reduced. Theoretically, this cost reduction amounted to about 50%. This means that a 20% reduction in the total cost can be achieved while maintaining the level of performance.

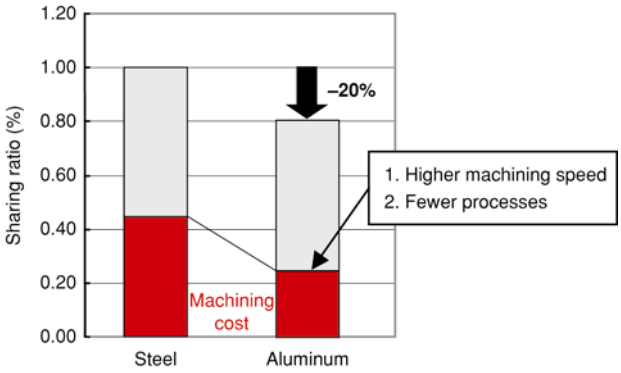


Fig.18 Impact of cost reduction

8. Conclusion

An aluminum die-cast VTEC rocker arm was developed achieving a proper balance between weight and cost reduction relative to conventional VTEC rocker arms made of steel.

(1) The load occurring in the roller shaft was successfully measured, and the required part strength for the roller shaft was clarified.

(2) Reliable durability around the shaft of the rocker arm with the press-fitted roller shaft structure was established by obtaining a good balance between the part strength and the fatigue strength.

(3) The dimensional limits that affect the layout of the roller VTEC rocker arm were established.

Acknowledgment

We are deeply grateful to the staff of Tanaka Seimitsu Kogyo Co., Ltd., Nissin Manufacturing Co., Ltd. and NTN Corporation for the cooperation they gave us in our research.

References

(1) Miura, et al.: Development of High-Efficiency Gasoline Engine With Variable Valve Lift and Timing System, Journal of Society of Automotive Engineers of Japan, Vol. 45, No. 8, p. 93 (1991)

(2) Inoue, et al.: Efficient engine with a new variable-valve-timing and -lift mechanism, Part 1 Development of variable valving system, JSAE Annual Congress Proceedings (891004)

■ Authors ■


Chikara TANAKA


Noriyuki YAMADA

Development of Engine Oil Deterioration Monitoring System

Nobuaki TAKAOKA* Hiroshi HASHIMOTO* Akihisa SAITO*
Hiroshi KUBO* Shouji KAWAUCHI* Tsuyoshi EGUCHI*

ABSTRACT

An oil deterioration monitoring system has been developed to more accurately judge oil change intervals. The system calculates oil life using an oil deterioration algorithm. When the oil deterioration variable reaches a predetermined value, the oil change meter recommends an oil change. The algorithm first estimates oil temperature, which is a parameter of the oil deterioration factor. Then the factor and engine speed are used to calculate how much of the oil's service life has been used. The oil deterioration factor is dependent on oil temperature. It was calculated from oil life test results gathered from endurance tests where oil temperature was varied. A market survey was conducted to verify the applicability of the measures to a variety of driving modes. These results were correlated in calculations of oil life. It has been demonstrated that this system is successful in enabling U.S. users to change their oil at more appropriate intervals.

1. Introduction

Engine oil serves to protect the engine by lubricating, cleaning, sealing, and cooling, and helps prevent rusting and corrosion. The efficacy of these oil functions is reduced as the vehicle is driven, eventually requiring that the oil be replaced. Changing the oil sooner rather than later helps prevent engine damage. On the other hand, longer intervals between oil changes are desired to preserve the environment by conserving oil resources, and lowering vehicle maintenance work.

The deterioration of engine oil and the oil change interval vary according to the engine driving conditions. For example, if the engine is repeatedly driven over short distances and shut off, the oil temperature will not reach a sufficient level to allow the water content to evaporate. This will lead to NOx, nitric, and nitrous acid contamination in the oil from blow-by. This ultimately produces low temperature sludge. Driving at high oil temperatures causes the oil to oxidize, which increases the oil's viscosity and breaks down the component additives. The level of oil deterioration varies according to the history of driving conditions. This makes it difficult for the user to determine the optimal period for changing the oil.

This paper introduces an oil deterioration monitoring system that has been developed to address these issues. The monitoring system displays the oil change recommendation on a monitor after calculating the oil change interval that is dependent on the vehicle's driving conditions.

2. Development Goals

The oil deterioration monitoring system was developed to address the following two goals.

(1) Optimize the distance for which oil replacement is required
(2) Provide a simple monitoring system that does not require a sensor

Figure 1 shows the surveyed results of the number of miles at which drivers in the U.S. change their engine oil and the number of miles that could be traveled if the oil had reached its usable life.

The figure shows survey results gathered by Honda in America during 1999 and the results of a questionnaire

* Tochigi R&D Center

(n = 7414) conducted over the Internet in 2002 between April 18 and June 27 by USA TODAY. The results from the survey conducted by USA TODAY demonstrate a greater distribution of longer oil change maintenance periods.

Oil replaced by drivers in North America was collected and analyzed. The blue line shows the estimated results of the oil service life distances based on the degree of oil deterioration.

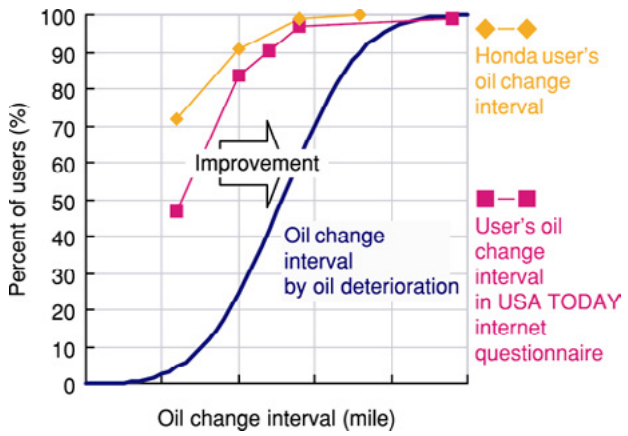


Fig. 1 Oil change interval

It was discovered that the drivers in North America actually changed their oil earlier than required. The oil deterioration monitoring system is required to have a level of effectiveness that could improve the distribution of the user's oil change interval to the maximum potential oil life interval.

Various testing has been conducted to directly detect oil deterioration. Optical sensors evaluate oil deterioration by measuring the degree of pollution in the oil while capacitor type sensors evaluate the degree of oil deterioration by measuring the changes in the oil's dielectric constant. However, neither of these methods is able to distinguish the correlation between these deterioration levels[1]. Although changes in the oil's viscosity are an important indicator of its condition, it is difficult to determine the change of oil viscosity associated with the different types of oils[2]. Measurement of the neutralization number is an effective means of evaluating the deterioration of the oil additives, consumption, and oxidation of the base oil. At Dayton University, they have developed an in-vehicle technology for measuring these conditions[3]. An additional technology was developed that measures nitric ester concentration through infrared spectroscopic analysis[1]. However, these methodologies have not been successfully adapted for actual use.

The system introduced in this paper is a simple and practical system that does not use such sensors and encourages drivers to change their oil at optimal periods.

Table 1 lists the oil maintenance systems employed by other car manufacturers.

Table 1 Oil maintenance indication system

Maker	System name	Oil change interval	Method	Model/Year	Note
BENZ	Active service system	Max 30000km	Algorithm	97M	With oil level sensor
BMW	BMW maintenance system	Max 30000km	Algorithm	98M	With oil level sensor
AUDI	AUDI variable service	Max 30000km	Algorithm	00M	With oil level sensor
GM	Oil life system	4800 ~ 16000km	Algorithm	98M	

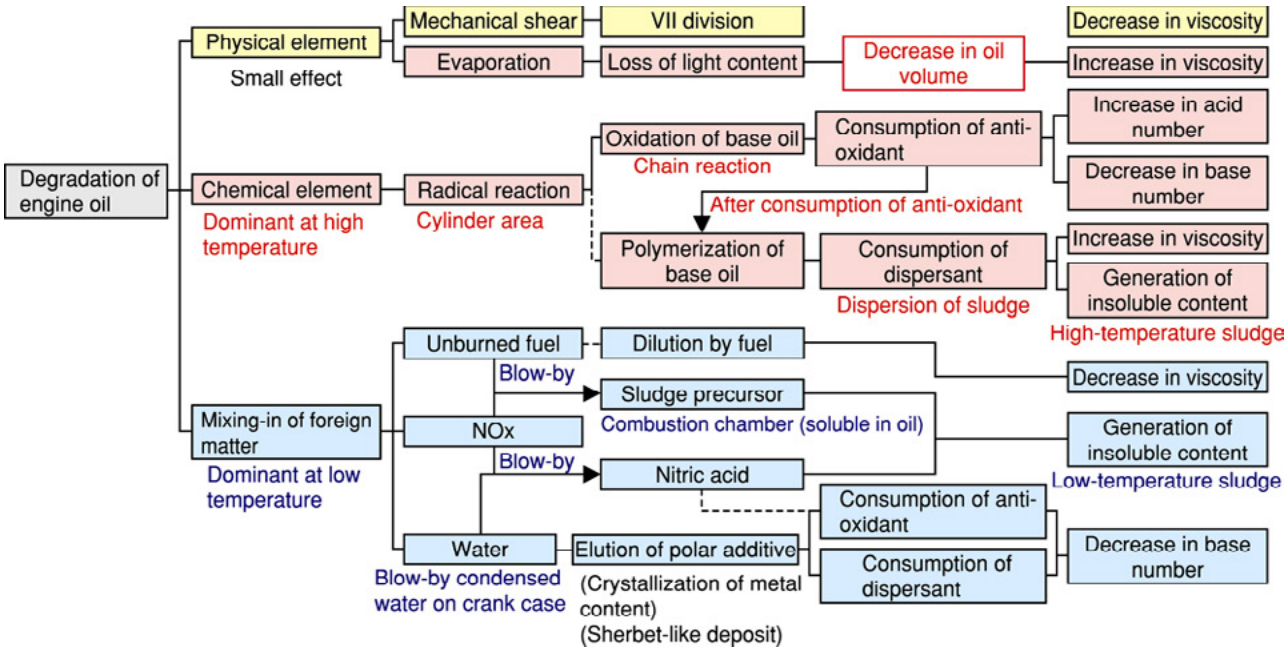


Fig. 2 Mechanism of deterioration of engine oil

3. Causes of Oil Deterioration and Oil Life Estimating Methods

3.1. Causes of Oil Deterioration

Figure 2 shows the causes of engine oil deterioration. Engine oil is made up of base oil and additive components. The following conditions have been identified as causes of engine oil deterioration.

(a) Oxidation, deterioration and evaporation of the base oil component
(b) Functional reduction due to deterioration and consumption of the additive components
(c) Foreign matter contamination

Condition (a) is dominant at high oil temperatures. As the base oil component in the cylinder area oxidizes, the antioxidants are consumed. This is linked to the increase of the acid value and the reduction of the base number. Furthermore, as the antioxidants are consumed, the base oil polymerizes and the dispersant agent is consumed. This leads to increased viscosity and the production of insoluble content. Condition (c) is influenced by contamination from blow-by gas components at low temperatures. The blow-by gas consists of non-combustible fuel, water and NOx. This produces a sludge precursor, nitric acid, and promotes the production of insoluble content and the consumption of the additive components.

A reduction in oil viscosity leads to concerns such as wear in the valve train. An increase in viscosity increases friction and leads to deterioration in fuel consumption and engine startability at low temperatures. Decreases in the base oil number and increases in acid value cause corrosive wear in the bearings from acid ions. The insoluble content then restricts the oil flow, causing various issues due to the lack of oil. The base number, acid value, viscosity level and insoluble component volume are all critical in determining oil life.

3.2. Perspectives on Estimating Oil Deterioration

The deterioration of oil as described in Section 3.1 can be largely explained by fluctuations in the oil temperature. As shown in Fig. 3, deterioration of the engine oil is accelerated as temperatures increase or decrease from the medium temperature of 80 °C[4]. As the oil temperatures increase beyond 80 °C deterioration through oxidation increased. This promotes oxidization of the base oil, deterioration, and consumption of the additive components. As the oil temperatures fall below the 80 °C mark, the oil additives deteriorate from blow-by gas contamination. The oil life curve can be calculated from running durability tests that vary load, trip distance and running temperatures. Using oil temperature measurements as an independent variable and applying it to the oil life curve yields the oil deterioration factor. Oil life is then calculated from the oil deterioration factor. The oil life calculated value has been verified by in vehicle testing.

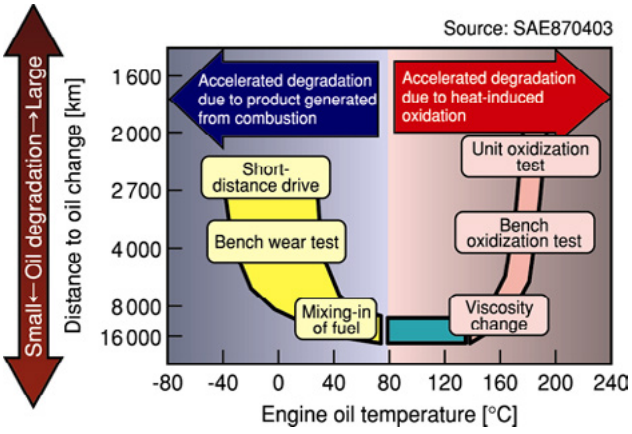


Fig. 3 Effect of oil temperature on engine oil deterioration

4. Engine Oil Deterioration Monitoring System

4.1. Engine Oil Deterioration Monitoring System Configuration Overview

Figure 4 provides a configuration overview of the engine oil deterioration monitoring system.

To estimate the oil temperature, sensors are used to measure the water coolant temperature, engine speed, vehicle speed, intake air temperature, and the intake air pressure. The deterioration factor is then determined according to the estimated oil temperature. The amount of oil deterioration is calculated from the deterioration factor and the engine speed. By resetting the oil deterioration monitoring system each time the oil is changed reinitializes the oil life calculation process. When the oil life falls below the predetermined value setting, the indicator for replacing the oil is displayed on a monitor. The driver is able to verify the oil life all the time through the monitor.

4.2. Engine Oil Deterioration Factor (DF) that is Dependent on Oil Temperature

Based on the perspective described in Section 3.2, the engine oil life curve was obtained according to the oil

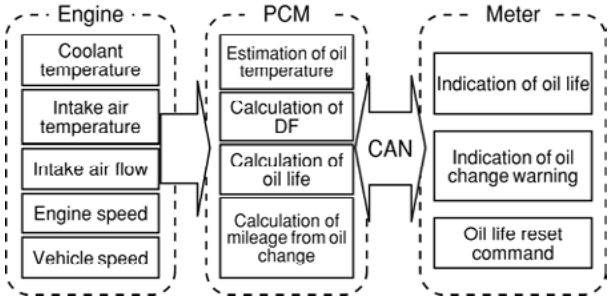


Fig. 4 Oil deterioration monitoring system

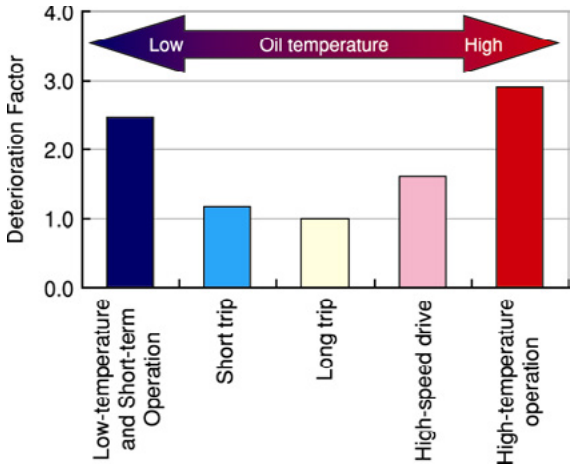


Fig. 5 Deterioration factors for driving conditions

temperature. This was done through endurance testing at different oil temperatures. Figure 5 shows the results of calculations for the deterioration factor, which represents the difference between the current oil life and the longest oil life value obtained from the endurance tests. As described in Section 4.3, the oil life is calculated by the estimated cumulative engine speed and the oil deterioration factor. The factor indicated in Fig. 5 is a ratio of the cumulative engine speed until oil life runs out for each endurance condition. This value is called the DF (deterioration factor) and is represented by using the oil temperature as the working parameter. The results of each of the respective endurance tests shown in Fig. 5 are arranged according to average temperatures thereby creating DF characteristics. To verify DF characteristics the endurance test results were calculated according to the method described in Section 4.3. It has been verified that the calculated values become constant when oil life is at 0.

4.3. Calculating Method of Oil Life

Oil life is calculated by integrating the values attained by multiplying the engine speed and DF values. That value represents the oil life consumption and is calculated by formula (1).

$$REVOLF = \Sigma (REVSEC \times DF) \quad (1)$$

REVOLF : Oil life consumption (times)
REVSEC : Engine speed (times/sec)
DF : Oil deterioration factor that is dependent on oil temperature

After the engine is started and the oil temperature increases, the calculation is conducted by using the DF value, which is dependent on the oil temperature. After the oil is replaced, the calculation is reset with the oil life consumption set to zero. After that, the oil life consumption increases as the engine is driven. The calculation is conducted so that the ratio of remaining oil life becomes zero when the oil life consumption reaches a predetermined value.

Oil deterioration endurance tests were revaluated to confirm when the ratio of remaining oil life becomes zero. The test methods were different from that used in determining the DF characteristic. The testing was conducted under the following conditions.

(1) When the DF characteristic test was conducted, oil was flushed and all deteriorated oil was completely removed. In the confirmation testing, a typical oil change was assumed and new oil was added to the remaining quantity of deteriorated oil.

(2) Oil life of commercially available oil

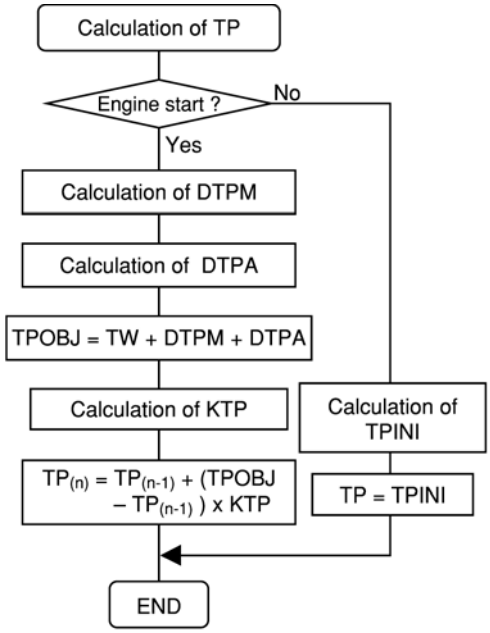
Since there is a range of oil available on the market, unit tests were applied for selecting oils that deteriorate faster. Of those, the oils that hold a relatively high North American market share were used to verify oil life consumption in actual vehicle testing.

The results of the verification mentioned above, errors in estimated oil temperature and other errors were considered to establish oil life consumption so that the ratio of remaining oil life becomes zero.

4.4. Estimating Method of Oil Temperature

Figure 6 outlines the oil temperature estimation algorithm.

The temperature of the oil immediately following IG ON is equal to the water temperature. However, during a hot start, a value approximating the oil temperature when the engine



DTPM : TPOBJ correction value against engine condition
DTPA : TPOBJ correction value against ambient temperature
TPOBJ : Target value of TOILP
TW : Water temperature
KTP : Coefficient for estimation
TP : Estimated oil temperature
TPINI : Initial value of TOILP

Fig. 6 Oil temperature estimation algorithm

was stopped is used as the initial value in the calculation.

DTPM, the correction term of target value for the estimated oil temperature is set so that the X axis is the parameter calculated from amount of fuel injection and the engine speed, and the Y axis is the map data of vehicle speed. This map is assembled from the measured oil temperatures in the conditions from fully open throttle to fully closed throttle.

The estimated oil temperature is corrected in relation to the outside air temperature. The outside air temperature is estimated from the intake air temperature and the vehicle speed. The oil temperature immediately after the vehicle has been started from cold is equal to the water temperature. Since the estimated oil temperature increases from the water temperature, correction with the outside air temperature is not required immediately after the engine is started. Instead the

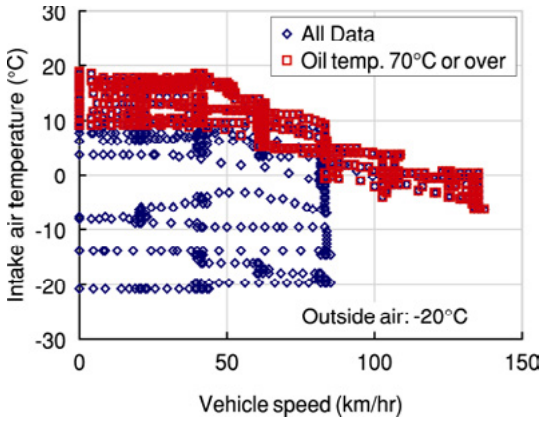


Fig. 7 Vehicle speed and intake air temperature

steady state oil temperature is corrected with the outside air temperature. Restricting the correction with the outside temperature only to steady state oil temperatures improves the accuracy of estimating the outside air temperature. Figure 7 shows the relationship between the vehicle speed and the intake air temperature when the outside air temperature is –20 °C. For example, when the oil temperature for estimating the outside air temperature is greater than 70 °C, the correlation between the vehicle speed and the intake air temperature is recognized. However, there is no correlation in all the data plotted for conditions after the engine started.

Formula (2) shows how the oil temperature is estimated.

$$TP_{(n)} = TP_{(n-1)} + (TPOBJ - TP_{(n-1)}) \times KTP \qquad (2)$$

TP : Estimated oil temperature (°C)
TPOBJ : Target value for estimated oil temperature (°C)
KIP : Estimated coefficient

The estimated coefficient corrects the values so that they reflect actual oil temperature variations. It is calculated through reverse calculation of the actual measured oil temperature as follows.

$$KTP = (Toil_{(n)} - Toil_{(n-1)})/(TPOBJ - Toil_{(n-1)}) \qquad (3)$$

Toil : Actual oil temperature (°C)

4.5. Other

The calculated results of the oil life are not erased even when the battery terminals are disconnected while the vehicle is being serviced or repaired. Also, the calculated oil life results are retained even when the PCM is replaced with a new part.

5. Accuracy of Oil Deterioration Monitor

5.1. Accuracy of Oil Temperature Estimation

The accuracy of the oil temperature estimation was verified on actual vehicles fitted with the oil deterioration monitoring system. During the verification process the actual oil temperature was measured with a temperature sensor. Errors in the calculated value for the oil life determined by the actual oil temperature, and estimated oil temperature are treated as oil temperature estimation errors. Figure 8 shows the oil temperature estimation error. The difference in the calculated results of the estimated oil temperature is –6.6% ~ +3.6% within 3σ in respect to the calculated results from the actual oil temperature ranges.

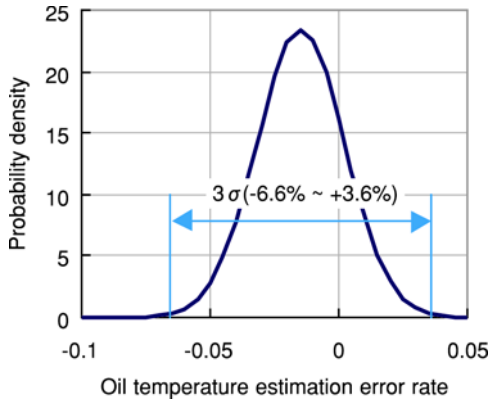


Fig.8 Data comparison for oil life calculations

5.2. Accuracy of Oil Life Estimation

The accuracy of the oil life calculated value was verified in vehicles configured as described in Section 5.1. In the verification method employed, a few samples of oil taken from vehicles fitted with the monitoring system were analyzed. The error arising from the difference between the calculated value and the set value for oil life at the remaining oil life service was then verified. The maximum degree of error measured as the calculated value for the oil life compared to the actual level of deterioration was 15%. The error values including estimated oil temperatures can reach 20%.

The calculated oil life data was set with consideration to the above error rates.

6. Effect of System Introduction

The travel distance at which the calculated oil life would reach zero was estimated for American drivers. The means for estimating the oil life is based on a distribution of the average vehicular speed in America and the oil life distance corresponding to the average vehicular speed.

Since oil life is calculated over the cumulative engine speed, it is possible to travel a longer distance at the same engine speed when a high gear is used. The higher the average speed, more frequent use of high gear also increases the oil life distance.

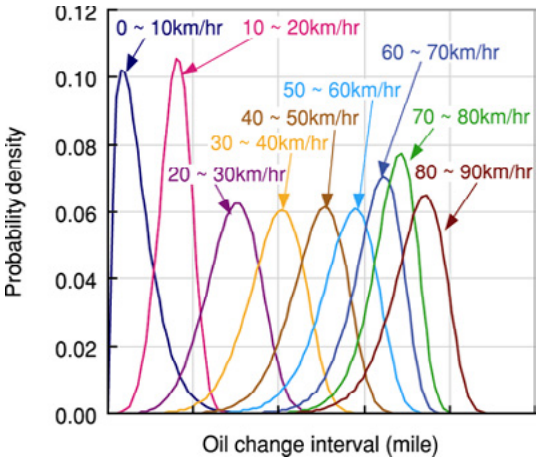


Fig. 9 Vehicle speed and oil life

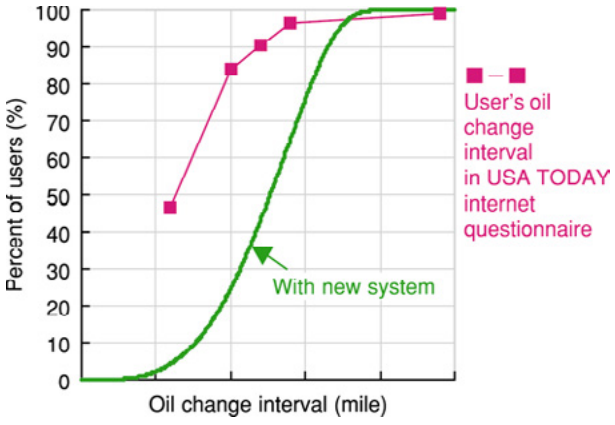


Fig. 10 Oil change interval with new system

Data from each driving cycle taken from vehicles fitted with the monitoring system in America and Japan were used in the calculation and processing illustrated in Fig. 9. The life distance at which the oil life reaches zero was calculated with the oil life consumption and travel distance from one driving cycle. Then a statistical measure was conducted at average vehicular speeds. The average vehicular speed distribution in America was overlapped and the cumulative ranges were attained as shown in Fig. 10. This showed that the oil change intervals are larger in comparison to actual oil change intervals. This new system has enabled the average driver to reduce their number of oil changes by 30%.

7. Conclusion

The oil deterioration monitoring system conducts calculations from the oil deterioration factor that is dependent on the oil temperature and the cumulative engine speed. The accuracy of this system has been verified and the calculations were conducted to avoid the calculation error from the actual oil deterioration. The distribution of the oil change interval based on the set data has enabled optimal oil change intervals for the drivers in America.

References

(1) Murakami, Y., Matsumoto, E., Nogami, Y.: Research and Development of an Oil Deterioration Sensor, Nissan Gihou, No. 30, P. 92-98 (1991)

(2) Greenberg, A.: Cost Puts Direct Oil Condition Sensing in Back Seat, Automotive Electronics Journal, January 15th, p. 9, 12 (1990)

(3) Kauffman, R. E.: Development of a Remaining Lubricant Evaluation Technique. Part: Cyclic Voltammetric Methods, Lub. Eng., 45-11, p. 709 (1988)

(4) Schwartz, S., Smolenski, D. J.: Development of an Automatic Engine Oil-Change Indicator System, SAE Paper, No. 870403

■ Authors ■


Nobuaki TAKAOKA


Hiroshi HASHIMOTO


Akihisa SAITO


Hiroshi KUBO


Shouji KAWAUCHI


Tsuyoshi EGUCHI

Development of Image Inspection System for CVT Steel Belt Element

Junji EGUCHI* Kenji HAGIWARA*
Ryuhei KATAOKA* Takao ITOH*

ABSTRACT

An image inspection system has been developed to reduce the time expended on product inspection. This system has been designed for inspection of the elements utilized in CVT steel belts. Images from a CCD camera are automatically inspected on the basis of a quantified grading standard. In addition, a new element transport system, which automatically sorts and arranges the elements according to the results of inspection of the images, has been developed to specific elements to be sorted out. The use of this system for inspection of CVT elements has reduced the time required for inspection by more than half against the visual product inspection method.

1. Introduction

Honda has developed a steel belt as a structural element of CVT systems, which are designed to contribute to driving comfort and increased fuel economy. The unit has been in mass production since 2001[(1)]. As shown in Fig. 1, the steel belt is composed of 400 elements and two rows of layered metal rings. The quality of the elements and metal rings affects the ability of the belt to transmit traction. Therefore high reliability is demanded [(2)].

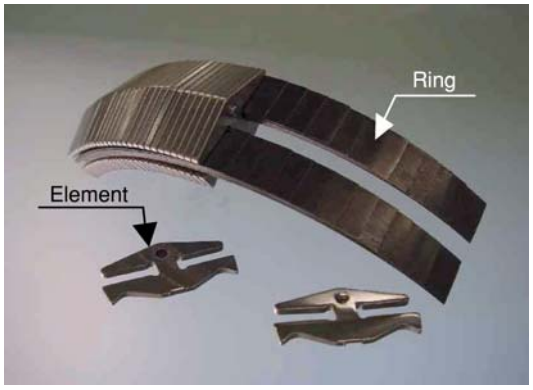


Fig. 1 CVT steel belt

Figure 2 shows a chip-off on an element saddle surface that will make contact with the metal rings. Inspection of the saddle surfaces and detection of these chip-offs takes time. The authors developed an inspection system that employs image processing technology that enables inspection time to be reduced.

This paper discusses the application of the new image inspection system to CVT elements.

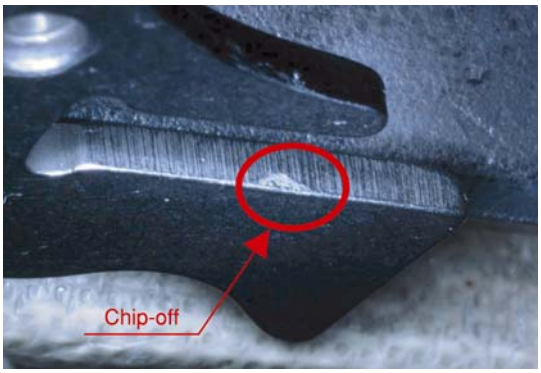


Fig. 2 Chip-off on saddle surface

* Tochigi R&D Center

2. Development Goals

Figure 3 shows the configuration of an element, and Fig. 4 shows an example of a chip-off on a saddle surface. The aim of the project discussed here was to develop an image inspection system that would detect such chip-offs on the saddle surface and quantify their size.

The following were required in the course of development of this system:

(1) Imaging of the entire saddle surface including the R section of the neck
(2) Establishment of an inspection standard for image processing
(3) Development of a system that enables automatic transport of the elements, and sorting and separation on the basis of the results of the image inspection

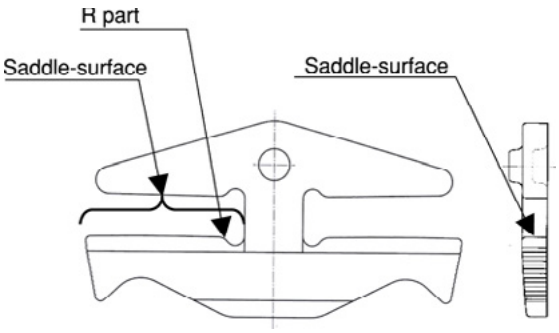


Fig. 3 Configuration of element

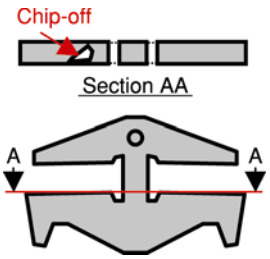


Fig. 4 Sample of chip-off on element

3. CVT Element Image Inspection System

3.1. System Overview

Figure 5 shows the image inspection system. As Fig. 6 shows, the system is composed of three sections: A carrier section that transports individual elements to the imaging processing section and sets them in position, the image processing section that takes and processes images of the saddle surfaces to detect chip-offs, and the selector section that sorts and separates the elements on the basis of the results of image inspection. Each section is controlled by a system control unit and the PC in the image processing section.



Fig. 5 Image inspection system for CVT element

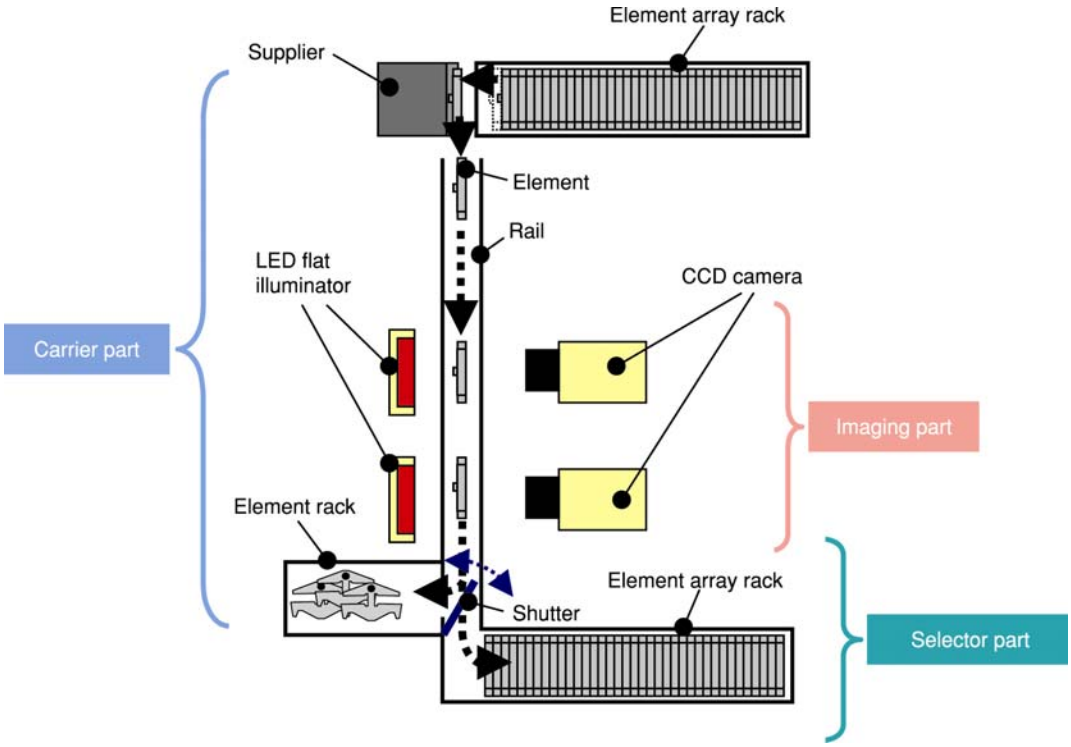


Fig. 6 System configuration

3.2. Carrier Section

The carrier section is made up of a supply unit that provides the elements to the carrier unit and the carrier unit that transports the elements to the imaging position and sets them in place.

As shown in Fig. 7, the supply unit is composed of an element array rack, which arranges the elements in a row and stores them until required, and a supplier mechanism that enables the elements to be individually sent to the carrier unit. If there are no elements in the carrier unit, a command is output from the system control unit, and the supplier mechanism, which is positioned coaxially with the element array rack, moves towards the front element in the element array rack. The selection mechanism is provided with a suction function, and can draw in the front element. After this element has been sent to the carrier unit, the supplier mechanism returns to its original coaxial position with the element array rack.

Figure 8 shows an external view of the carrier unit, Fig. 9 shows one of the imaging positions, and Fig. 10 shows the configuration of the imaging positions. The carrier unit consists of a rail to transport the elements, an optical sensor to detect the presence of elements on the rail, an air blower to assist in sliding the elements along the rail, a piston and a stopper to set the elements in the imaging position, and an optical sensor to determine that elements are in the imaging position.

Elements sent from the supply unit are slid along the rail until they are set in the imaging position. The elements are sent down the transport rail at an oblique angle. The air from the air blower assists the elements in moving down the rail.

When the element reaches the first imaging position, it hits a stopper. The optical sensor detects the position of the element. On the basis of that information, a piston receives a command from the system control unit to press down from above the element and hold it in place in the imaging position. When imaging is completed, the piston is removed and the stopper is simultaneously retracted to the underside of the transport rail, enabling the element to move to the second imaging position. After the identical procedure is carried out in the second imaging position, the element is transported to the selector section.

3.3. Image Processing Section

The image processing section is made up of an imaging unit, which takes images of the element saddle surfaces, and an image processing unit.

To enable the CCD cameras and LED flat illuminators to be set up with an adequate degree of freedom, the image processing section in this system enables right and left images of the element saddle surfaces to be processed

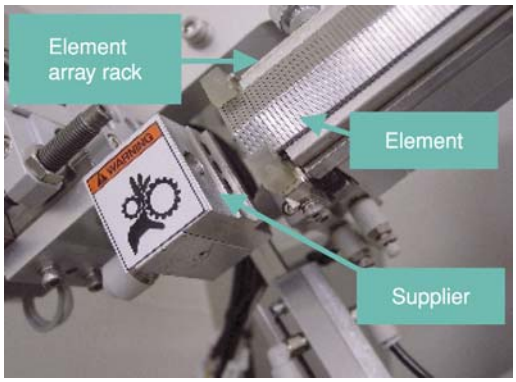


Fig. 7 Supply unit

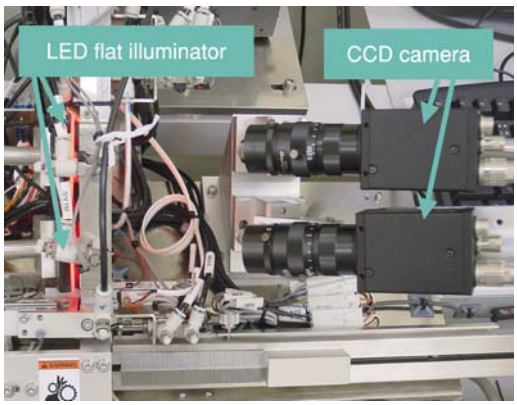


Fig. 9 Imaging position

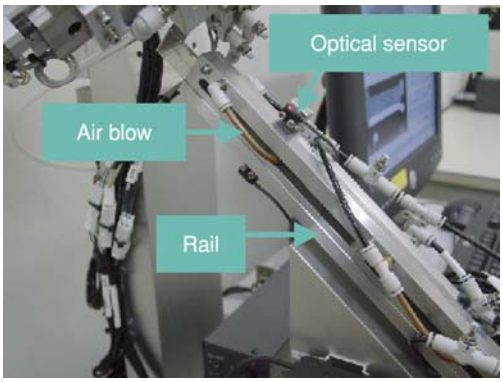


Fig. 8 Carrier unit

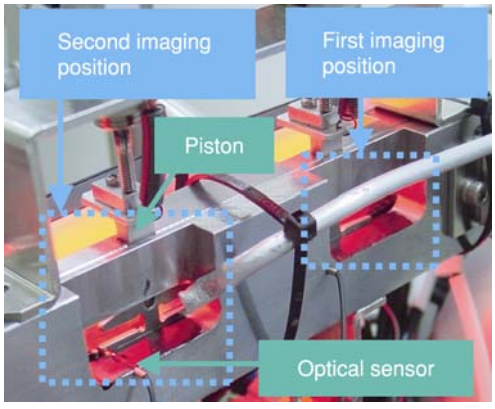


Fig. 10 Configuration of imaging positions

independently. This allows an image of the saddle surface on the left side of the element (as seen from the front; refer to Fig. 3) to be processed in the first imaging position, and permits an image of the saddle surface on the right side to be processed in the second imaging position.

The imaging unit is comprised of red LED flat illuminators and CCD cameras. The illuminators were chosen with the ability to project a uniform illumination over the entire saddle surface with no shadow at the R section of the neck. This criterion led to the adoption of red LED flat illuminators with numerous parallel optical elements. When normal halogen illuminators are utilized, the numerous scattered optical elements cause shadows to occur on target objects with surface irregularities, making it difficult to detect chip-offs over the entire saddle surface, including the R section of the neck. Figure 11 shows a comparison of images produced using red LED and halogen flat illuminators. The image taken using the LED flat illuminator shows uniform brightness with no shadow across the entire saddle surface including the R section of the neck.

Figure 12 shows the relative positions of the red LED flat illuminator, the CCD camera and the element being imaged. The light from the illuminator is reflected off of the element saddle surface, and retrieved by the CCD camera. The illuminator and the camera are set in position so that the optic angle θc of the camera to the front of the element, and the vertical angle θl of the illuminator to the front of the element are symmetrical.

As Fig. 13 shows, the image processing unit is made up of an image processing PC, an image capture board, a digital I/O board, and image processing software. The images taken by the CCD camera are input to the image processing computer RAM by the image capture board. The image processing software quantifies the quality of the element saddle surface using the input images. The results are transmitted to the system control unit via the digital I/O board.

The program employed in the image processing software to quantify the quality of the saddle surface was designed as a multi-thread application capable of simultaneously monitoring the control signals from the system control unit, operating programs, and processing images.

Image inspection is carried out with cooperation between the system control unit and the image processing unit. The system control unit ensures that the element reaches the imaging position; the image processing unit takes an image of the element in position and conducts image processing.

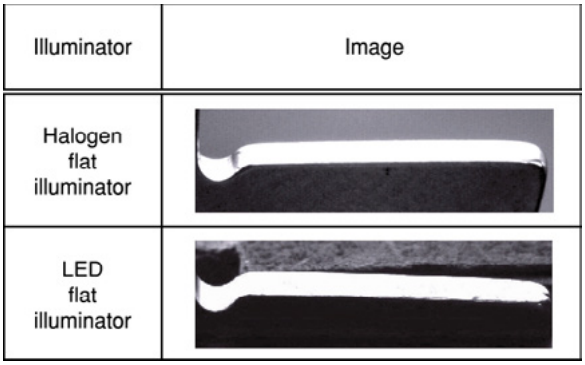


Fig. 11 Images using each illuminator

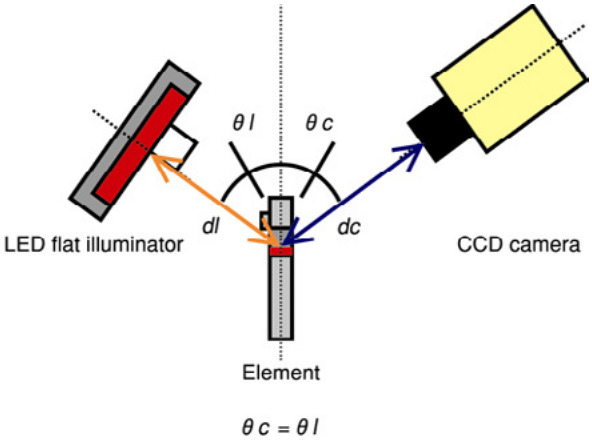


Fig. 12 Layout of CCD camera and LED flat illuminator

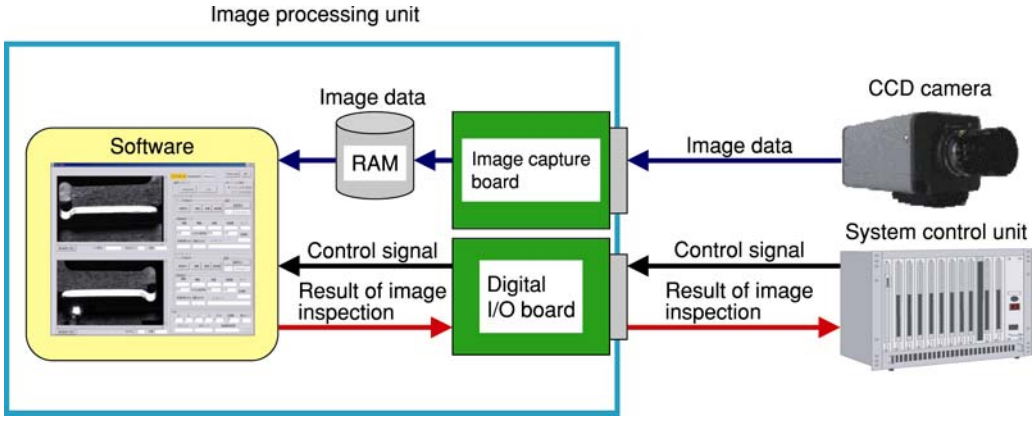


Fig. 13 Configuration of image processing unit

Figure 14 shows a flow chart of the operation of the system control unit and image processing unit in image inspection. When the element reaches the first imaging position, an imaging trigger is sent from the system control unit to the image processing unit. Immediately after receiving the imaging trigger, the image processing unit takes an image of the saddle surface and subjects it to image processing. The results are sent to the system control unit. When image processing at the first imaging position is completed, the element is transported to the second imaging position, where the identical image processing procedures are conducted.

3.4. Selector Section

The selector section is made up of an inspected element selector unit located at the lower end of the transport rail, and a specific element selector unit.

The inspected element selector unit shown in Fig. 15 comprises a pushing mechanism, an optic sensor to detect elements sent to the unit by the rail, an element array rack, and a stopper. The optic sensor detects the presence of an inspected element sliding along the rail. After this, a command is sent to the pushing mechanism from the system control unit, which pushes the elements onto the element

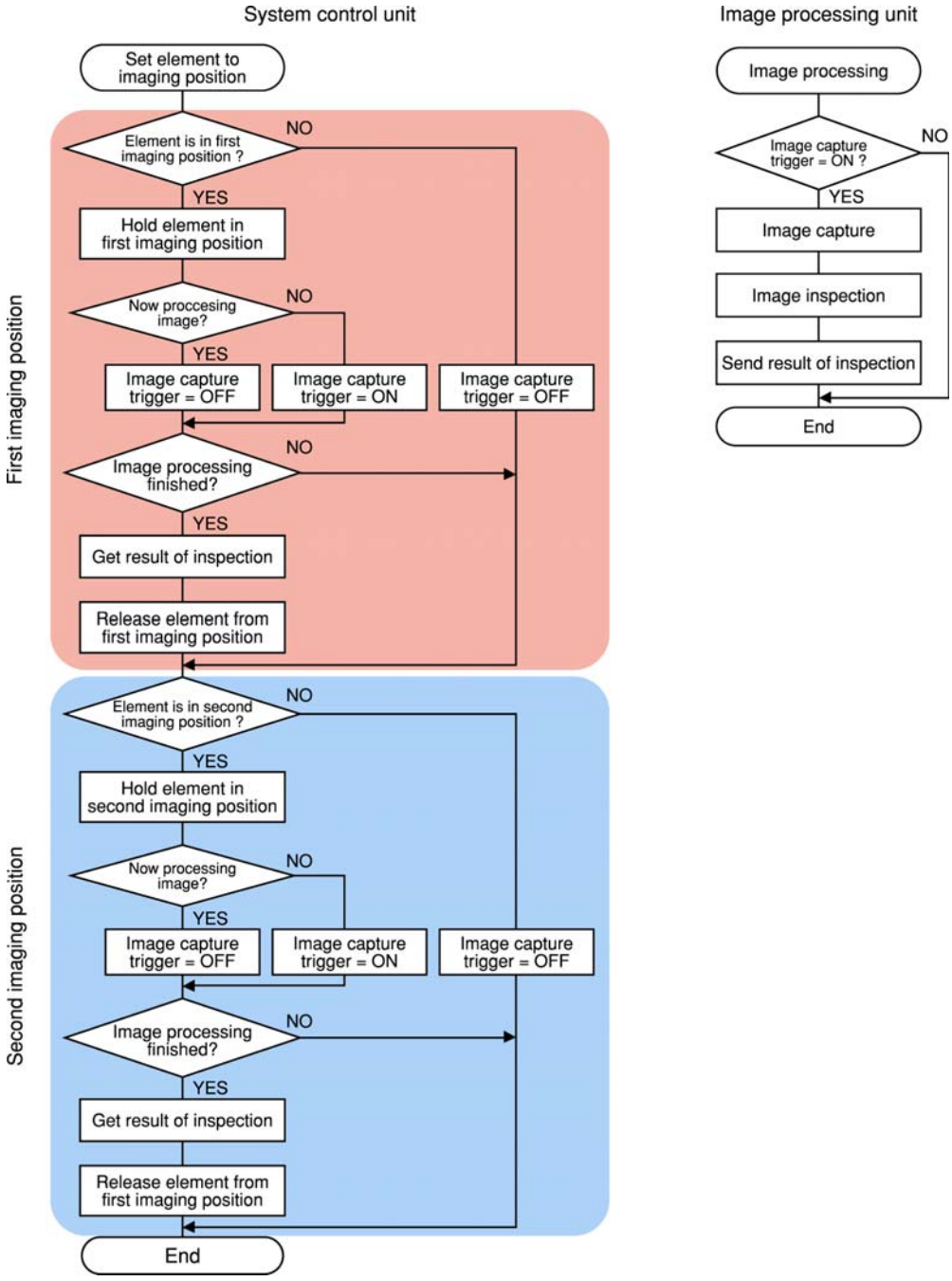


Fig. 14 Flow chart of image inspection

array rack set at right angles to the rail. Movable stoppers on the element array rack enable the elements to be consecutively aligned.

The specific element selector unit shown in Fig. 16 is made up of a discharge shutter, a sensor to detect discharged elements, and a specific element array rack. The shutter is positioned on the underside of the lower end of the transport rail, and opens and closes in response to commands from the system control unit. When specific elements are judged, the inspected elements are sent down the transport rail, the shutter opens and they drop into a specific element array rack. The optical sensor detects the element dropping into the rack, and as a result the system control unit closes the shutter.

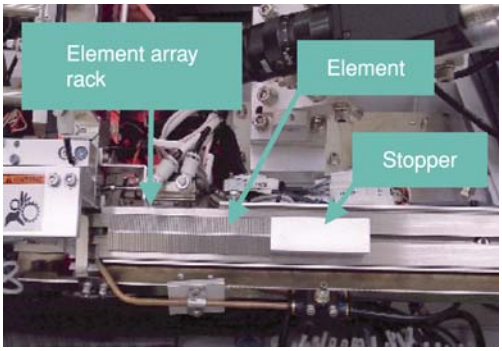


Fig. 15 Inspected element selector unit

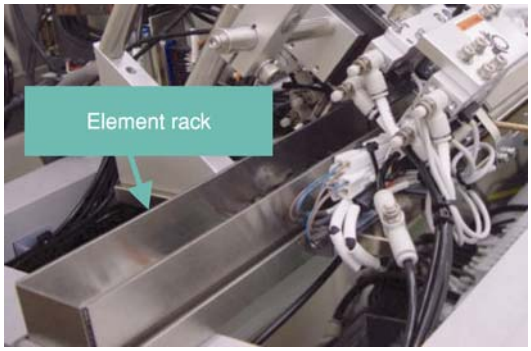


Fig. 16 Specific element selector unit

4. Establishing a Standard for Element Inspection

To inspect elements using the image inspection system, it was essential to establish a standard for the judgment of deviations. The area of the chip-off, the total area of multiple chip-offs, and the length of chip-offs in the direction of the thickness of the element were therefore established as criteria for specific elements. The following sections discuss the method by which chip-offs are detected from the images and the standard used in judgment.

4.1. Method of Detecting Chip-offs from Images

Figure 17 shows the procedure for detecting chip-offs on the element saddle surface by image processing. The different levels of brightness in the outline of the section with the chip-off and the other sections (i.e. the sections with no chip-offs) were focused on to enable the detection of chip-offs. Figure 18 shows the original image of an element with a chip-off on the saddle surface taken by a CCD camera, and Fig. 19 shows the results of an analysis of the distribution of brightness using that image. This figure demonstrates that the brightness drops significantly in the outline area of the chip-off in comparison with areas with no chip-offs.

The procedure for detection of chip-offs shown in Fig. 17 is discussed below.

The original image shown in Fig. 18 contains more information than an image of the saddle surface, which will be the focus of image processing. The image is therefore first binarized on the basis of brightness values to enable the saddle surface to be extracted. The saddle surface is highly reflective of light from the illuminators and its brightness is therefore high in the image. The largest area of high brightness in the original image can therefore be extracted as the saddle surface. Figure 20 shows an example of an extracted saddle surface after binarization. Next, the edge section, which shows the greatest modulation in brightness, is extracted from the area previously extracted by binarization. The edge area is extracted using a Kirsch operator [3]. This enables an image of the edge of the saddle surface to be obtained, as shown in Fig. 21. The saddle surface edge area can be extracted from this image of the edge. This image of the edge area is subjected to a closing operation, enabling the chip-off section, the outline area, and the edge of the saddle surface to be extracted. Figure 22 shows the result of this extraction superimposed on the extraction of the saddle surface shown in Fig. 20. Next, the image resulting from the

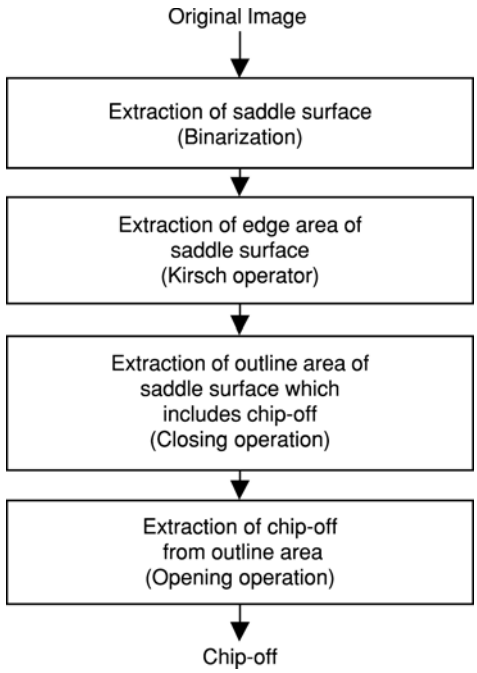


Fig. 17 Image processing for extraction of chip-off

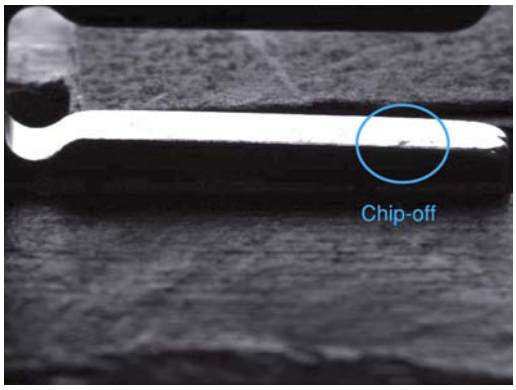


Fig. 18 Original image

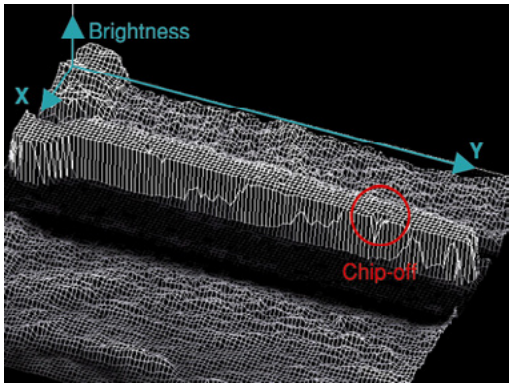


Fig. 19 Distribution map of brightness



Fig. 20 Result of extraction of saddle surface

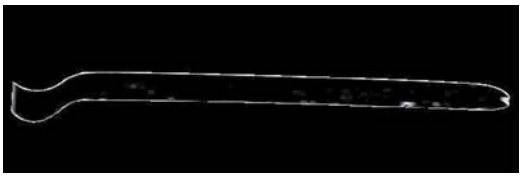


Fig. 21 Edge image



Fig. 22 Result of closing operation



Fig. 23 Result of opening operation

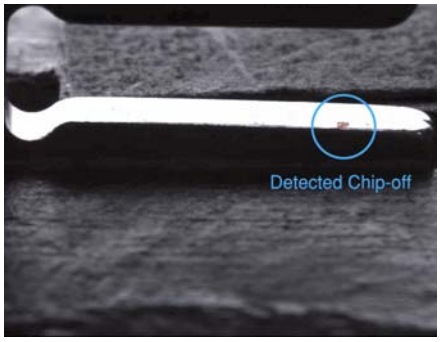


Fig.24 Result of image processing

closing operation shown in Fig. 22 is subjected to an opening operation to eliminate the outline area. The result is shown in Fig. 23. The edge shown here will not make contact with the rings, and is therefore not judged as a deviation.

The processing described above enables detection of chip-offs on the element saddle surface. Figure 24 shows the image at the completion of processing superimposed on the original image. The area in which the chip-off was detected is shown as red in Fig. 24. This image demonstrates that the method described here was able to correctly detect a chip-off in the element saddle surface.

4.2. Inspection Standard

The image processing described in 4.1 has made it possible to detect chip-offs on the element saddle surface. Values for the size of chip-offs have been quantified for use in the image processing system.

These quantified values were correlated with the standards utilized in visual inspections, and the three quantified standards for inspection shown in Fig. 25 were developed.

(1) The area of a single chip-off
(2) The total area of multiple chip-offs
(3) The length of a chip-off in the direction of element thickness

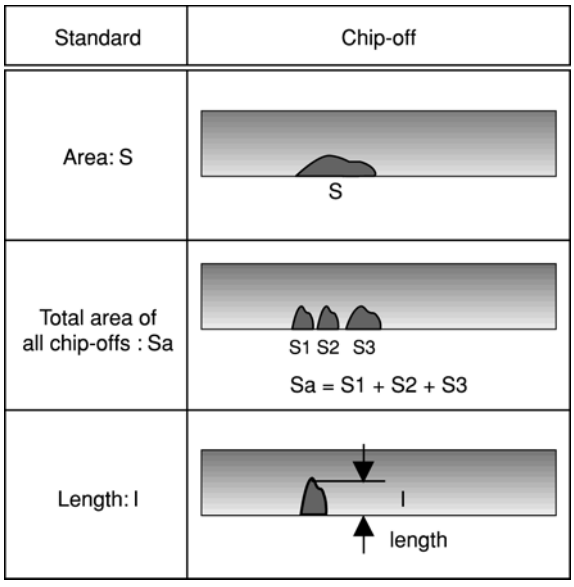


Fig. 25 Standard for inspection

Multiple samples of each type of chip-off were utilized in deciding on these standards, and the minimum values for the standards utilized in visual inspections were set as the standard values for image inspection. Because the depth of the chip-off is a factor in establishing the standard value for the area of chip-offs, the edge extraction parameters were optimized at the stage of generation of the image of the edge, to make the area of the chip-offs detected by image processing match the area detected by visual inspection.

5. Employment of Image Inspection System

This section compares the time required for inspection using the image inspection system described here and for visual inspection. Figure 26 shows the results of inspection of the length of chip-offs in the direction of element thickness of the 400 elements used in a vehicle with a CVT employing the image inspection system. This figure shows the ratio of the time required for inspection by the system to the time required for visual inspection considered as 100%. The image inspection system required less than half the time required for visual inspection.

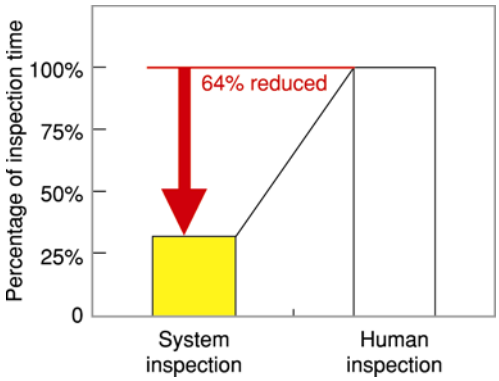


Fig. 26 Inspection time

6. Conclusion

A system that employs image inspection has been developed for the inspection of the saddle surfaces of CVT elements. The following three technological considerations were basic in the development of this system:

(1) Red LED flat illuminators are employed to illuminate the element saddle surface. Light is reflected from the mirror surface. An image of the elements is captured by CCD cameras, enabling the entire saddle surface, including the R section of the neck, to be imaged. Chip-offs on the saddle surface can then be detected using image processing.
(2) The size of chip-offs is quantified by image processing, and three inspection standards have been established.
(3) The system automatically transports the elements and sorts and separates them on the basis of the results of the image inspection.

These features of the system have enabled it to reduce the time required for inspection by more than half against visual inspection.

References

(1) Yagasaki, T., Aoyama, H., Saito, T., Ishii, K., Okada, Y., Arikawa, M.: Development of Metal Pushing V-Belt for Continuously Variable Transmission, Honda R&D Technical Review, Vol. 14, No. 1, p. 181-190 (2002)

(2) Arikawa, M., Shima, H.: A Configuration Evaluation Technique for CVT Metal Belt Rings, Honda R&D Technical Review, Vol. 14, No. 2, p. 57-62 (2002)

(3) The Institute of Image Electronics Engineers of Japan: Image Electronics Handbook, Tokyo, Corona Publishing, p. 37 (1993)

■ Authors ■


Junji EGUCHI


Kenji HAGIWARA


Ryuhei KATAOKA


Takao ITO

Newly-developed Cost Management System for Motorcycles

Seiji TSUCHIYA* Katsunobu YAMAMOTO*
Masako WATANABE* Takashi ARAMAKI*

ABSTRACT

A system, which efficiently totals the cost of the parts of a motorcycle throughout the model development process, from the concept stage through the prototype stage, to mass production, has been developed. This is characterized by the capability of introducing cost and supplier information into mass production parts and newly developed parts of the Development division, linking Manufacturing BOM (Bill of Material) managed by the Manufacturing division and the Development BOM managed by the Development division. This system has been developed with Java, one of the fundamental technologies of webification. Furthermore, such method has been introduced as lowering the maintenance cost and load on the network and PC clients, which reduces the concerns when considering overseas use. Consequently, this system makes it easier to see the cost changes of a new model being developed, and helps to improve operation efficiency in calculating model costs in overseas offices as well as offices in Japan.

1. Introduction

Cost management for motorcycle development was conducted largely using spreadsheet software and a host computer in the Purchasing Division. The number of models being developed has been increasing in recent years, which along with an increase in overseas production, has made it extremely time-consuming to collect the necessary information needed for such a cost management method, and also has made it difficult to contribute to shortening development time. It is also necessary to have the capability to manage locally-procured parts cost and supplier information together with the cost for Japan-supplied parts in order to manage total cost per unit for models produced overseas. Therefore, a cost management system that could link the engineering bill of material (BOM)[1] and the factory BOM became necessary. Consequently, a cost management system was developed that could be used efficiently by development, purchasing, and production divisions.

* Asaka R&D Center

2. Development Concept

2.1. Issues in Model Cost Management

Management was previously conducted independently by the divisions concerned, so that the engineering BOM would manage technical information relating to the development of a model, and the factory BOM would manage parts costs and suppliers involved in production. Cost management of a new model therefore necessitated obtaining the two separate BOMs from the development and production divisions, then expending a large number of person-hours in order to combine the two by hand. Obtaining the cost for locally-procured parts managed by production divisions overseas also required a great deal of time. Many hours and much manpower were required to calculate the model cost for these reasons. Furthermore, the same issues were faced at overseas offices as well as in Japan. These issues are summarized below:

- Engineering BOM and factory BOM are not managed in an integrated manner
- No tools are available for efficiently calculating new model costs
- A long time is required to obtain information on locally-procured parts from overseas offices

The new system was developed in order to overcome the above issues, and the objectives were set accordingly, as follows:

Provide information-sharing tools that can be used efficiently to share the interactive information required for model development both in Japanese and overseas offices as a cost management system for motorcycle parts aimed to establish common tooling.

2.2. System Requirements

The requirements for a system to deal with these issues are as follows:

(1) Centralize engineering BOM and factory BOM
(2) Provide function to calculate the single unit cost for a model
(3) Share information on locally-procured parts at overseas offices
(4) Implement global utilization (highly responsive, 24-hour operation, local-language support)

The new system was developed using a Web-based system architecture in order to meet the extremely large number of needs for overseas use.

3. Development Method

3.1. System Development Method

3.1.1. Change of development style

With the dizzying pace of change in recent years, there is demand for systems that are capable of handling multiple user needs. There are also increasingly complex architecture-related concerns, which arise repeatedly, such as distributed systems, parallel systems, replication, security, load balancing, and fault tolerance. The design of the system model (program structure and database structure) that forms its foundation has become a crucial element in system construction and maintenance. The reason for modeling a complex system is that it has become difficult to completely grasp the system as a whole. Just as the focus in computers has shifted from mainframes to personal computers and the Internet, the conceptual approach of system development methods is also undergoing change. It has become necessary to carry out system development with engineering drawings like these, which could not be represented using conventional system development methods by uniting incompatible system development methodologies, such as the Object Oriented Approach (hereafter OOA) and the Data Oriented Approach (hereafter DOA), in order to produce.

3.1.2. Development process and objectives

The aim with the new system was to unite the strengths of OOA and DOA to realize flexibility and reusability. The specific objectives of each phase in the development process are as follows:

(1) User requirement definition phase
- User requirement documentation (use case scenario)
- Business flow (business flow diagram)
- Prototype screen

(2) Analysis & design phase
- Class relationship diagram based on use cases (program structure)
- Database model
- Skeleton source code (Program template)
- Test specifications
- Manual of operating procedure

(3) Program development & testing phase
- Program source code
- Test report

The above summarizes the output yielded by each phase.

3.2. System Design Methods

3.2.1. User Requirement Definition

The business flow of the system (Fig. 1) was laid out in the initial phase of development in order to express the specific objectives below with regard to user requirement definitions.

Based on the business flow created here, prototype screens were created and the final image of the system was confirmed with users. This work was performed at the initial stage of development in order to prevent any deviation from occurring in the direction of system development.

(1) Understand the organizational structure and its fluidity
(2) Users and developers share a common understanding aimed at an efficient operational structure
(3) Elicit system requirements
(4) Reach agreement with users and concerned parties regarding necessary system requirements
(5) Have program developers gain a firm understanding of system requirements
(6) Clearly define the scope of system application

3.2.2. Database design by DOA

Data modeling[(2) – (4)] was carried out with the intention of focusing on the forms used in the workplace, the spreadsheet data itself, and performing logical analysis and modeling in time series with the business flow. Commercially available tools were employed for the new system in order to ease the task of system modification while maintaining the logic of the database structure with respect to future changes in the business model.

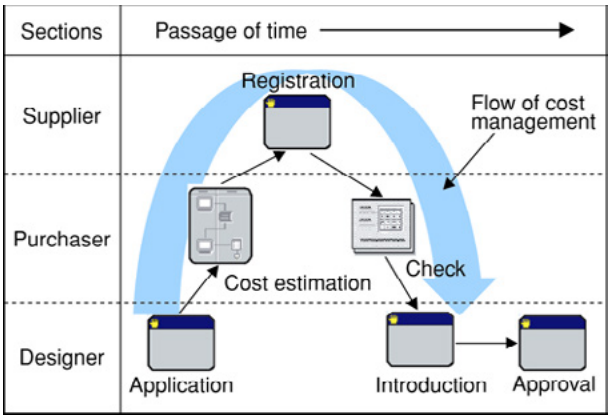


Fig. 1 Business flow diagram

3.2.3. Program design by OOA

During the design phase, it was calculated that this system included approximately 700 programs. In consideration of the relatedness, reusability, quality, and so on of the program as a whole, an object-oriented language was utilized for program development. This does not mean that measures to address the immediate issues were all developed from the ground up. Rather, programs used to address issues in the past were reused and such programs were accumulated within the system as whole. This method linked such programs together much in the way that a structure is built out of building blocks. Repeated trials of this kind of program reuse were carried out during the design phase with the building blocks further revised each time until the design was finally complete. It is also necessary to model the programs by a process similar to modeling data, as explained in section 3.2.2. In this process the structure of the program itself is defined and the roles of the business logic layer (Model), the screen display layer (View), and the control layer (Control) are clearly assigned. The group of programs used in common is extracted, and then the building blocks are made into parts[5] so they can be reused. The system was designed in this way to give it the flexibility to deal with future changes.

4. System Construction

4.1. System Architecture

The new system utilized a system architecture as shown in Fig. 2. All processing demanded by clients is controlled and executed on an application server. Periodically demanded processing is managed by a job controller and executed at fixed times on the application server. Processing was concentrated in the application server to reduce the load on the clients and improve system maintainability. Processes executed on the application server can access databases on the database management server to conduct queries and updates. The server is divided into an application server and database management server in order to distribute system load on the server.

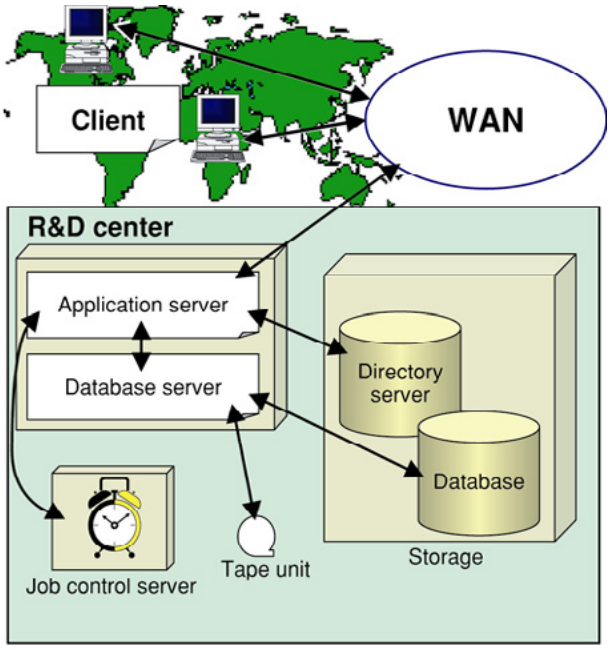


Fig. 2 System architecture

4.2. System Construction Techniques

4.2.1. Centralized management of engineering BOM and Factory BOM

As shown in Fig. 3, the new system defines the engineering BOM and factory BOM, which have different management configurations, on the database. This associates the two BOMs and represents them as though they were a single BOM.

When a new drawing is issued, the drawing issue information is transferred from the engineering BOM system to this system. Cost information is also acquired from the factory BOM system. A setup was also developed for the new system whereby a single cost bill of material (cost BOM) can be generated by matching the information in the engineering BOM with the costs in the factory BOM.

This had made it possible to grasp both the centrally managed engineering BOM and factory BOM at the same time. Users can now automatically compute costs on the new system without having to read the two BOMs and then re-input that information into spreadsheet software as they did before. This has significantly improved work efficiency. Costs of production parts can also be registered and updated without having any effect on information in the engineering BOM. This has made it possible to conduct cost variation control that tracks changes in engineering specifications in development divisions.

4.2.2. Security management

The security-related logic for the new system is set up as shown in Fig. 4. It was designed in this way to enable user security to be restricted by specific product models.

The user management server (referred to below as the directory server) is set up in advance with information on staff members, and the database with information on model

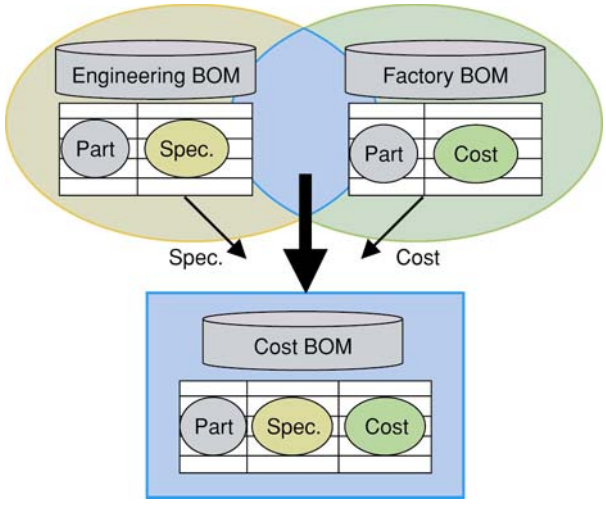


Fig. 3 Structure of cost BOM

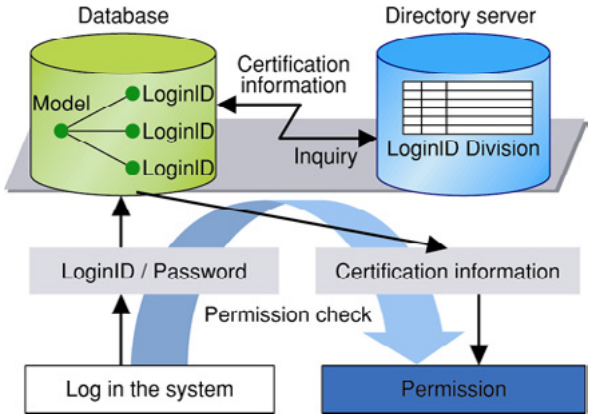


Fig. 4 Setting of authorization information

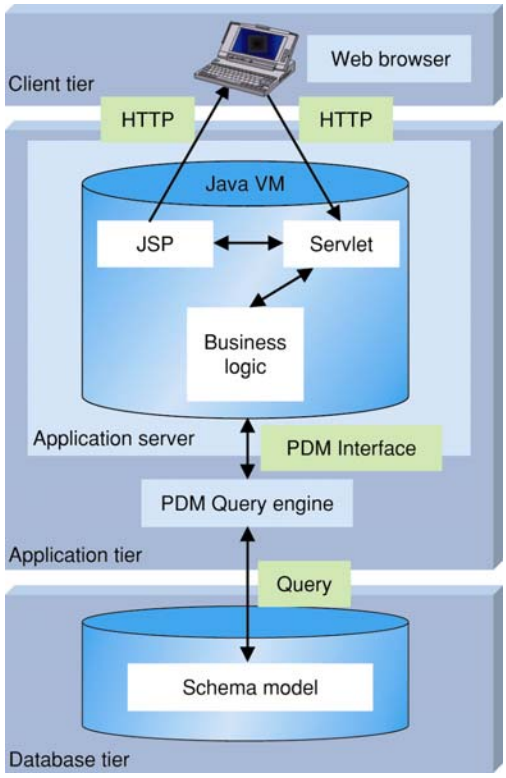


Fig. 5 Logical architecture

restrictions.

When users log into the systems, the directory server authenticates their log-in IDs and passwords. It then uses a model authentication program to query the database regarding model restrictions for the particular user logging in, after which it makes a final determination. This has made it possible to conduct authority control that differs for each individual user. This authorization set-up was designed not only to restrict updates of model data but also to restrict queries according to authorization. As a result, the new system has realized a high degree of security against leakage of cost information for offices or other models.

4.2.3. Summarizing the single unit cost for a model

The cost BOM in the new system is subject to transition history management for each part. This allows users to summarize the registered cost-related information for a single model unit at any point in time, and it also makes it very simple for them to find the costs at that point in the transition history.

The cost calculation method is to multiply the unit cost of a part by the share rate (the proportion ordered from each supplier), the fitting rate (a rate of use of that part), and the number applied. That quantity is then multiplied by the share rate, fitting rate, and number applied of all parts. By summarizing the costs for each part, this method yields the single unit cost for a model.

4.2.4. Dealing with globalization

The new system was designed with a view to deployment to overseas offices. It is a characteristic of motorcycle operations that most of the overseas offices tend to be small in size. It is necessary to assure a minimum level of network response for offices located in fragile network environments. It is also necessary to provide a user interface that allows simple operation by users in all offices when sharing information on locally-procured parts. The new system was designed to meet these objectives by running on Web browsers that have intuitive operating methods and that users at any office have experience using (Fig. 5).

The issues faced in deploying the new system to overseas offices include the following:

(1) Operational maintenance

Some small-scale offices do not have maintenance personnel to provide support during times the system is down or being upgraded. This causes a time lag in trouble shooting, program maintenance, and updates.

(2) Networks

There are many communication control units (hereafter referred to as routers) interposed on the networks between Japan and remote locations such as overseas offices. They are required in order to carry on communication, but when communication data is congested in the routers, delays are caused in proportion to the number of routers and their processing capacity.

A server-side processing approach (JSP/Servlet type)[6), (7)] was adopted for the new system in order to overcome the above issues. Compared to processing on the client (applet type), this limits consumption of both loads on the client and the network while assuring good response.

Elements of network load under the new system include not only transmission volume (traffic volume) but also the number of transmission times (number of packets). System development took these factors into account. Fig. 6 shows the number of transmission times (number of packets) per second for the same process performed on the client and performed on server side.

4.2.5. Program structure

An MVC model was adopted that divides the programs among a business logic layer (Model), screen display layer (View), and control layer (Controller).

The database access, data processing, and other such business logic processes of the system are written into the Model. This is the main body of the system. Screen display and data I/O components are handled by the View. The

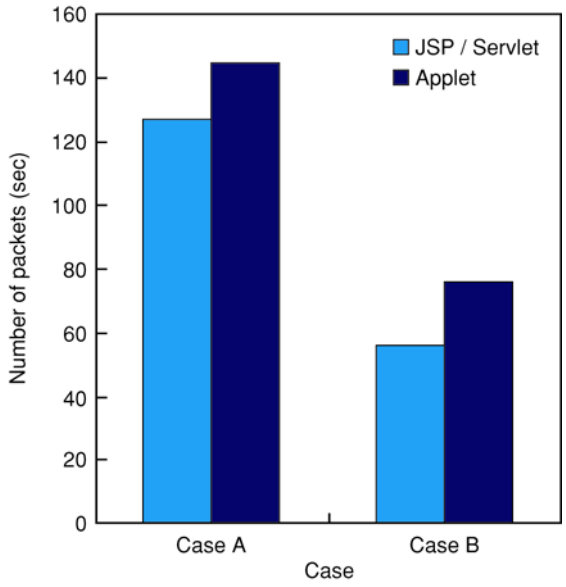


Fig. 6 Difference of the volume of packet transferred in retrieving BOM

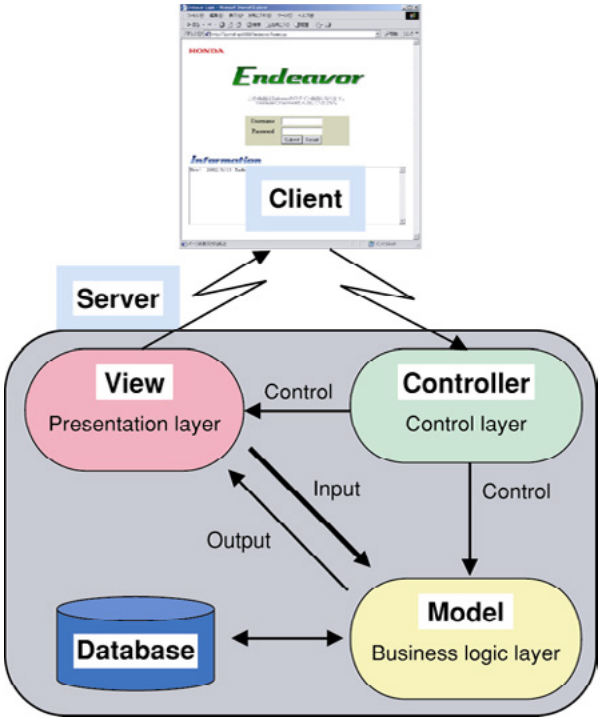


Fig. 7 MVC architecture

Controller controls the View and Model. The controller itself does not execute screen display or logic, but instructs the Model to execute the necessary logic according to the input, then passes the result to the View and causes it to display the result on the screen (Fig. 7).

Designing the system in accordance with this model clarifies the separation of individual functions, and assures their autonomy. Having the functions clearly separated during development makes it possible to apportion the development work for each function. At the same time, this makes it possible to limit the sharing between layers to a minimum, so that the program structure can be made less susceptible to the influence of changes in other components. This enables a flexible development, so that when the database design is going to be changed, only the business logic needs to be altered and the database can be redesigned repeatedly in order to create further programs.

4.2.6. Support for multiple languages

When conventional methods were used to provide support for multiple languages, screens and systems were created in each of the languages. This reduced system maintenance efficiency because every screen required maintenance whenever the system was modified.

The new system avoids such issues by introducing program component groups that can support multiple languages. These program component groups can be used in combination, thus enabling programming with uniform quality and without dependency on the level of the developers. In the course of plotting out a number of program component groups, it was determined that superior system maintainability was afforded by Struts (a program component group for Web application development that was developed by Jakarta Project, a standardization organization)[8), (9)], which was capable of display control and integration with the MVC model. This Struts framework manages display messages for each language, and it provides a method for switching between languages as necessary.

The use of Struts yielded the following four advantages:

- Messages are centrally managed in definition files, so that the text styles for every screen can be made uniform. It is not necessary to alter programs even when the display messages are changed.
- New languages can be supported by simply adding definition files for the messages translated into those languages.
- Conventional JSP tended to grow complex because HTML files included Java language. However, this could be organized by using the tags (screen program components) provided by Struts, thus enabling reduction of development person-hours.
- Screen transition information is managed centrally in XML files. This eliminated the need to create screen transition control processes in the business logic layer, thus improving program productivity and quality.

4.2.7. Load balancing and fault tolerance

The new system was given load balancing and fault tolerance (cluster configuration) capabilities by utilizing application servers (Fig. 8).

The system handles processing requests from multiple clients by tracking the load conditions and distributing the processing requests among application servers where the load is lower. This load balancing function realizes a uniform response to clients even when processing requests are concentrated together (Fig. 9).

The system was given fault tolerance by connecting multiple application servers together so that when a fault occurs in an application server, the system could switch to another application server that is connected. This enables system operation that does not need to shut down service to users even when faults occur in the application servers.

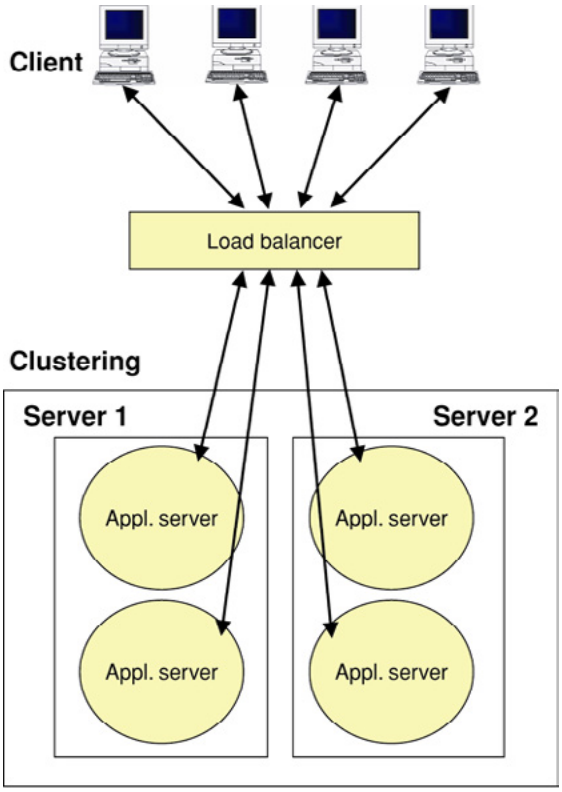


Fig. 8 Load balancing and clustering

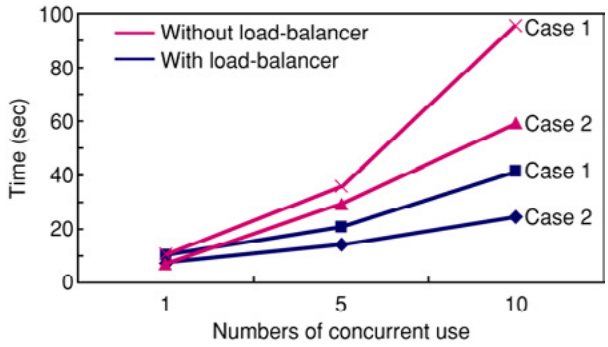


Fig. 9 Load balanced performance

5. Conclusions

The new system was developed as an effective system for the cost management of new models, and it has the features and yields the effects described below:

(1) Features

- Flexibility to handle the future addition of management items and increases in data
- Scalability to ease deployment overseas, support multiple language environments, and reduce network load

(2) Effects

- Enabled sharing of supplier information and management of the single unit cost of a model for individual development events, including models produced overseas
- Enabled clearly understandable look-up of costs and supply patterns for individual locally-procured parts used in models produced overseas
- Reduced the time required to calculate the single unit cost for a new model to two-thirds of the conventional method

Due to the above, the new system is expected to be utilized at offices not only in Japan but also overseas.

6. Future Developments

A dedicated user screen (portal screen) is going to be offered in the future. This will offer the information required by each division in an organized form, so that users can more efficiently track transitions in technical specifications and cost information. As deployment at overseas offices proceeds, overseas requirements will be incorporated into the system in order to enhance the system.

References

(1) Yamamoto, M.: Development of Engineering BOM Data Management System, HONDA R&D Technical Review, Vol. 14, No. 1, p. 77-84 (2002)

(2) Martin, J.: Information Engineering, Book I-III, TOPPAN (1991-1994)

(3) Client/Server Database Design Techniques, Soft Research Center Inc. (1993)

(4) T-Form ER-Diagram Database Design Techniques, Soft Research Center Inc. (1998)

(5) Pree, W.: Design Patterns for Object-Oriented Software, TOPPAN PRINTING CO., LTD., p. 75-78 (1996)

(6) Singh, I.: Designing Enterprise Applications with Java 2 Platform, Enterprise Edition, Second Edition, Sun Microsystems, p. 79-180 (2002)

(7) Harada, Y.: Java Server-Side Programming, Gijutsu-Hyohron Co., Ltd., p.164-269 (2000)

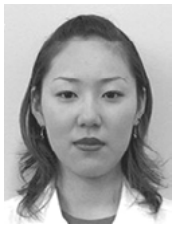
(8) Goodwill, J.: Mastering Jakarta Struts, SHOEISHA, p. 87-156 (2003)

(9) Cavaness, C.: Programming Jakarta Struts, O'Reilly, p. 104-193 (2002)

■ Authors ■


Seiji TSUCHIYA


Katsunobu YAMAMOTO


Masako WATANABE


Takashi ARAMAKI

Development of Traction Motor for Fuel Cell Vehicle

Shigemitsu AKUTSU* Hiroyuki SATOH*
Tomoya MIYAMURA* Hiroaki SHINOKI*

ABSTRACT

A DC brushless motor has been developed as the traction motor for the FCX, the world's first commercially marketed fuel cell vehicle.

This motor employs a salient pole type surface permanent magnet (SPM) rotor, which enables it both to produce reluctance torque and to minimize the use of magnets, improving dynamic performance. The inductance value is set at the limit value to ensure output at the maximum rotor speed, which suppresses field-weakening current. The motor, therefore, achieves both high output and high efficiency. Continuous operation at the maximum rotor speed was enabled by suppressing eddy current loss through surface insulation, segmentation of the magnet, and by raising the limit of irreversible demagnetization through the use of magnet materials displaying high coercive force. Strength reliability at high rotor speed was ensured by applying the Weibull theory as a method of evaluating the strength of magnets formed from brittle materials, and by considering the degradation of the magnet as a factor in evaluations.

The employment of the methods described above has resulted in the achievement of a maximum output of 60 kW, a maximum torque of 272 Nm, a maximum speed of 11 000 rpm, and a continuous rated torque of 200 Nm. In addition, an average combined efficiency of 93% in LA4 mode was achieved in the motor and inverter.

1. Introduction

Heightened worldwide awareness of environmental issues has increased the demand for the production of low emission vehicles and the reduction of the level of CO_2 in automotive exhausts to help combat global warming. The development of fuel cell vehicles as one fundamental response to these demands has therefore become an urgent issue.

In December 2002, Honda led the world by marketing a fuel cell vehicle. The use of fuel cells enables a significant increase in power over conventional batteries. Therefore, the development of the Honda fuel cell vehicle aimed at a high level of dynamic performance to give the vehicle a higher level of commercial viability than an electric vehicle. The power and rotational speed of the traction motor used in the EV PLUS electric vehicle (MCF11 below)[1] marketed in 1997 were significantly increased in the traction motor for the fuel cell vehicle.

Development of the motor proceeded using an already existing prototype small, high-efficiency traction motor[2] as a base, for which performance and specification targets were established to enable installation in a vehicle framework of more than 1.6 tons.

This paper will discuss the technologies employed in the

* Tochigi R&D Center

development of the traction motor for the Honda FCX fuel cell vehicle (MCF21 below) and the level of performance that they have enabled.

2. Development Goals and Target Performance

Balancing the following two factors was a major goal of the development of the MCF21:

(1) Increased efficiency

(2) Increased power and larger range of continuous power

Target drive efficiency was established as more than 90% of the average efficiency displayed by the MCF11 in LA4 mode; this level of efficiency would be balanced with the target power performance. The target for the power of the motor was set as described below from the required dynamic performance and various other factors.

The relationship between maximum driving force F_{max}, maximum velocity V_{max}, maximum motor torque $T_{max,}$ and maximum number of motor revolutions N_{max}, is shown by Eq. (1).

$$F_{max}\, V_{max} = 2\pi * T_{max}\, N_{max} \qquad (1)$$

Given the target maximum velocity of 150 km/h and the maximum driving force required for acceleration, the maximum number of motor revolutions, N_{max}, was set at 11 000 rpm on the basis of various considerations, including the available range of reduction ratio in the twin-shaft parallel gearbox and increases in friction. This figure led to a figure of 272 Nm being established as the value for maximum motor torque, T_{max}.

A lowest motor torque (bottom torque) value of 262 Nm or more at 0 rpm was established as generating the minimum driving force required to enable the vehicle to start on a climbing slope. At the same time, the torque constant was set high to ensure that the maximum phase current at 0 rpm did not exceed the allowed current for the inverter, while achieving the above value for bottom torque.

The target for the maximum power of the motor was set at 60 kW, established from the target acceleration performance and the power of the fuel cells. The requirement for continuous running at maximum speed and the necessary torque conditions to maintain the vehicle stationary on a climbing slope using only the accelerator led to a target of possible continuous power output in all power ranges at a torque of less than 180 Nm. Reduction of loss and improvement of cooling performance were further development goals.

Considerations of decline in voltage with degradation of the fuel cells led to the establishment of a minimum source voltage of 260 V to ensure maximum motor power. It is a goal of this development that a balance between the contradictory characteristics of a high torque coefficient and the required power at maximum rotational speed be achieved under this voltage condition.

3. Technologies Employed in the Motor

Table 1 shows the main specifications of the MCF21, and Fig. 1 shows a schematic of the motor, including the reduction box.

To make the drive shafts of equivalent length to produce no torque steering against the high drive torque, the right shaft has been made a half-shaft, and a support has been fitted to the right side of the motor housing. This structure has made it possible to move the large diameter drive shaft inboard section from the rear of the motor to outside the motor, which has in turn enabled the distance between the shafts of the one-speed fixed reduction gear to be reduced. In combination with a 5% reduction in the external diameter of the motor, a 52 mm reduction of the length from the center of the differential shaft to the front of the motor in comparison to the MCF11 has enabled the space required to house the motor to be reduced.

Table 1 Comparison of motor specifications

		MCF11 (EV PLUS)	MCF21 (FCX)
Type		PM synchronous motor	PM synchronous motor
Phase		3	3
Pole		18	12
Rotor	Type	SPM	Salient SPM
	Cover	GFRP	None
Magnet	Material	Nd-Fe-B	Nd-Fe-B
	iHc	> 2 388kA/m	> 2 785kA/m
Cooling system		Water cooled	Water cooled

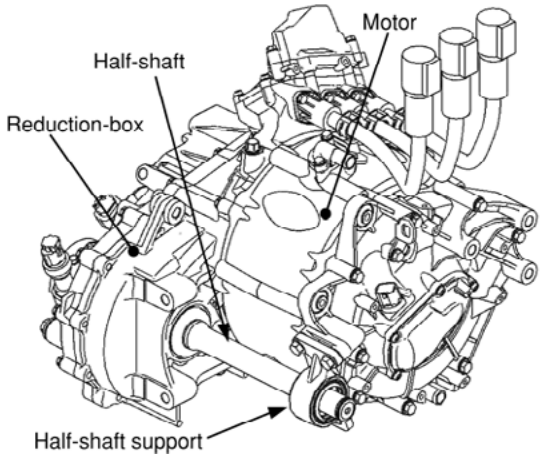


Fig. 1 Appearance of MCF21

3.1. Basic Motor Configuration

To achieve high efficiency in all driving modes, a reluctance torque permanent magnet (PM) motor, the benefits of which had been demonstrated from previous research[(2)], was selected as the basic type of motor to be employed. To limit the use of high-cost magnets, a salient pole surface permanent magnet (SPM) type was utilized for the rotor[(2)]. Figure 2 shows a cross-section view of the basic structure of the salient pole SPM rotor.

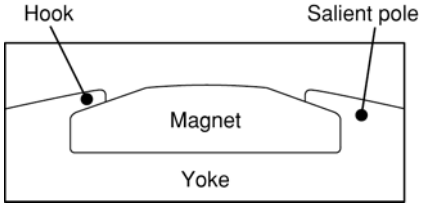


Fig. 2 Rotor structure of salient SPM

3.2. Reluctance Torque PM Motor

The torque generated by a reluctance torque DC brushless

motor, T_q, can be shown by Eq, (2), where ϕ_a is the flux linkage due to the magnet, P_n is the number of pole pairs, i_d and i_q are the d- and q-axis currents respectively, and L_d and L_q are the d- and q-axis inductances respectively[3].

$$T_q = P_n \phi_a i_q + P_n (L_d - L_q) i_d i_q \quad (2)$$

A difference between L_d and L_q is a condition of generation of reluctance torque; as the difference between the two increases, a greater amount of reluctance torque is produced.

The current i_d required for field weakening can be found from Eq. (3), where ω is electrical angular velocity, and V_b is source voltage.

$$i_d = -\frac{\phi_a}{L_d} + \frac{1}{L_d}\sqrt{\frac{V_b^2}{\omega^2} - (L_q i_q)^2} \quad (3)$$

Utilizing high inductance to increase L_d has the effect of reducing the current required for field weakening[2].

However, achieving high inductance reduces the maximum power at the voltage limit. The maximum power when magnetic saliency is taken into consideration can be expressed by Eq. (4) when approximated on the d-axis in Fig. 3.

$$P = V_{b\,max}\frac{\phi_a}{L_d} \quad (4)$$

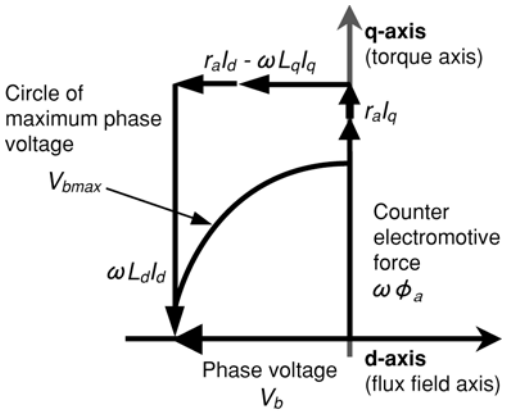


Fig. 3 Vector diagram of operating point at maximum power

The power at maximum rotational speed in particular makes a direct contribution to ensuring maximum vehicle velocity. For these contradictive requirements in the MCF21, inductance L_d was set as the limit value (maximum value) at which the target power at maximum rotational speed could be ensured, while the current required for field weakening was minimized. In addition, magnetic circuit simulations were utilized to enable the design of a form ensuring a maximum difference between L_d and L_q under the above conditions. As the measurement results in Fig. 4 show, it has been possible to ensure that the reluctance torque component increases by up to 38% against magnet torque.

To make maximum use of both types of torque, it is necessary to provide an accurate and appropriate current phase degree at all rotational speeds, including 0 rpm, and full digital vector control was therefore adopted. In addition, a Variable Reluctance (VR)-type resolver, which enables position detection even when rotation has stopped, has been utilized to detect the magnetic pole.

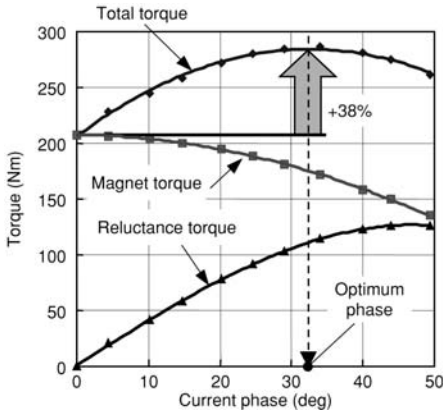


Fig. 4 Torque characteristic and current phase

3.3. Technologies Utilized to Achieve High Rotational Speed

Equation (4) shows that power at the maximum rotational speed of 11 000 rpm, at the same time as being limited by the size of inductance L_d, is proportional to the flux linkage due to the magnet, ϕ_a. The flux linkage due to the magnet varies during driving because of changes in the flux density caused by changes in the temperature of the magnet. In Nd-Fe-B magnets the flux density decreases as temperature increases. Because of this characteristic, flux linkage ϕ_a decreases as temperature rises due to the increase in eddy currents generated by making the motor high-revolution, causing a consequent decrease in maximum power in Eq. (4).

In the MCF21, stable generation of the target power at the maximum rotational speed established for the voltage limit under conditions of high inductance has been guaranteed by controlling the temperature of the magnet and increasing the limit of irreversible demagnetization. In addition, the employment of a method enabling strength to be ensured in magnets formed from brittle materials has ensured strength reliability in the high-speed rotor.

3.3.1. Ensuring power at the limit voltage by control of magnet temperature

The maximum power at the rated voltage is determined by the value of inductance, and drops, as the calculated values in Fig. 5 show, with the reduction in flux linkage that occurs as the temperature of the magnet rises. From Fig. 5, it is also possible to obtain the upper limit for allowable magnet temperature determined from the value for motor power required to ensure maximum speed and the thermal characteristics of the magnet.

In the new motor it was possible to achieve the target power by maintaining the temperature of the magnet below the upper limit. Figure 5 also shows test measurements of the change in power with rising magnet temperature. It was confirmed that magnet temperature reaches a point of equilibrium below the upper limit for temperature, and as a result the output power comes to equilibrium at the target power level. The differences between the results of calculations and measurements are believed to occur because the temperature of the magnet differs with measurement position and overall distribution.

Applying an insulating surface treatment to the magnet to reduce the amount of heat generated in the salient pole section of the yoke by eddy currents is known as a method of controlling the temperature of magnets[2]. Because eddy currents in the interior of the magnet also caused its temperature to noticeably rise in the MCF21, in addition to

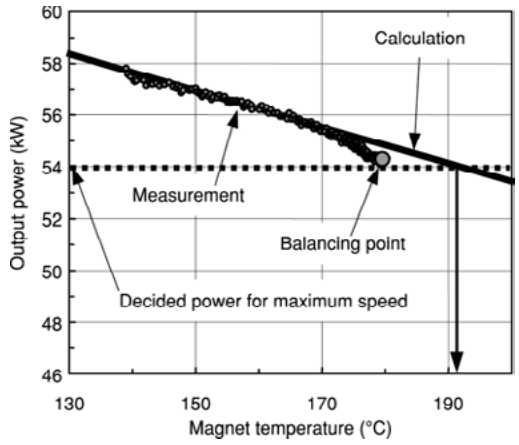


Fig. 5 Output at maximum speed

application of the surface treatment, the magnet was divided in the axial direction to control the production of eddy currents.

In addition, the resistivity of the metal plating used to prevent corrosion in the magnet is approximately 1/20 – 1/80 that of the magnet materials. It was therefore judged that the level of heat generated by eddy currents in the metal plating layer could not be ignored, and would contribute to increasing the temperature of the magnet. As Fig. 6 shows, increasing the divisions of magnet by 30% or more is required to maintain the temperature of a magnet with a metal plating at the same level as that of a magnet without a metal plating. The metal plating was therefore eliminated and the insulating surface treatment was relied on to prevent corrosion, requiring no increase in the number of divisions.

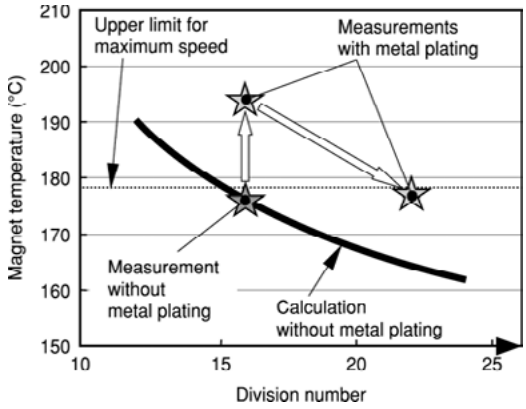


Fig. 6 Magnet temperature by division number

3.3.2. Ensuring toughness against irreversible demagnetization

Studies have already demonstrated that high-inductance surface-mounted permanent magnet rotor-type motors increase the demagnetizing fields acting on the magnet, and that the employment of a hook structure to hold the magnet is effective in increasing its toughness against irreversible demagnetization[2].

In combination with the magnet temperature control discussed above, in the MCF21, the employment of a high coercive force Nd-Fe-B magnet, able to maintain coercive force of 756 kA/m or more at 200 °C, means that no irreversible demagnetization occurs at the temperatures or currents generated during driving, as shown in Fig. 7. Results of calculation and measurement points are shown in the figure.

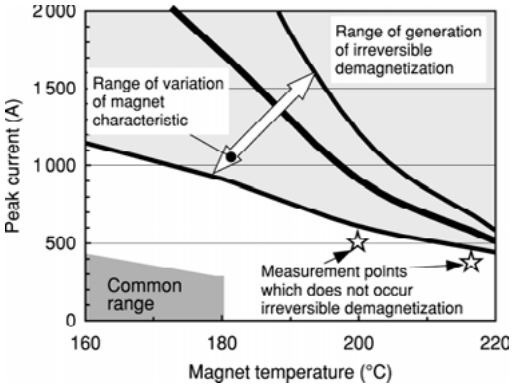


Fig. 7 Results of simulation of resistance to irreversible demagnetization

3.3.3. Ensuring rotor strength

As shown in Fig. 2, the salient pole SPM rotor utilized in the MCF21 is provided with hook sections extending from the salient pole section of the yoke to hold the magnet. This structure takes the burden of the centrifugal force exerted on the magnet with the hook sections and the strength of the magnet itself. Figure 8 shows the results of calculations conducted for a nonlinear structural analysis of the distribution of stress on the magnet and the yoke section.

In tests, the hook structures of the yoke designed on the basis of this analysis have demonstrated a fracture strength of more than 17 500 rpm.

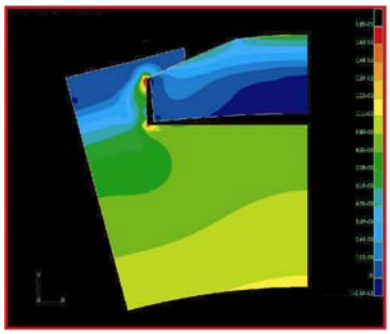


Fig. 8 Nonlinear analysis of salient SPM Rotor

However, because Nd-Fe-B magnets are constructed of brittle materials, conventional design methods used to ensure strength do not guarantee reliability. It has been shown that the fracture behavior of these magnets can be explained by weakest link theory. The probability of fracture of the magnets obeys a Weibull distribution, and it is possible to apply the Weibull theory to their strength characteristics[4].

In the MCF21, this method was used to design a form which guaranteed a sufficient ratio of safety against the maximum stress to enable the reliability targets (probability of fracture) to be achieved. Consideration was also given to the drop in strength caused by degradation of magnetic strength demonstrated by fracture tests on magnets in the forms in which they will be used. Figure 9 shows a Weibull plot illustrating these concepts. The utilization of this method to develop technologies applicable to actual vehicles has made it possible to ensure strength in a surface-mounted permanent magnet without an anti-scattering cover, has increased the rate of utilization of the magnetic flux, and has contributed to a reduction in the amount of use of the magnet, thereby ensuring strength reliability in the high-speed rotor.

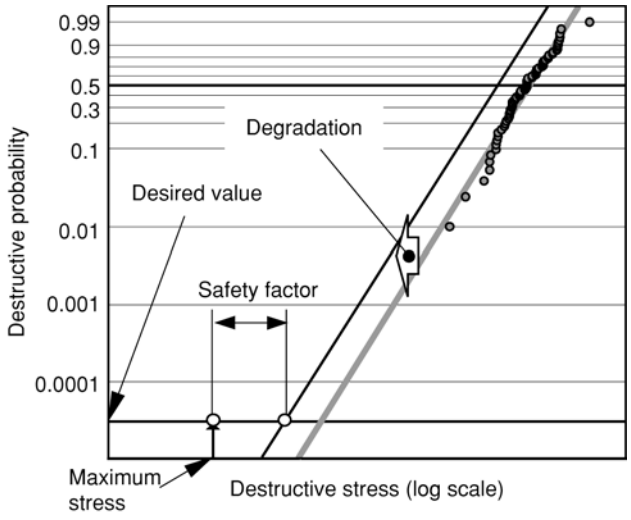


Fig. 9 Weibull plot for magnet strength

3.4. Setting Rotor Skew

Skewing the rotor magnet was one of various methods, including shaping the waveform of the magnetic flux, utilized to control the maximum phase current while increasing the bottom torque at 0 rpm. Skewing was achieved by dividing the entire rotor into two in the axial direction and setting the two pieces at different angles forward and backward in the direction of rotation. This structure is no more difficult to assemble in production than a structure with no skew.

As Fig. 10 shows, an area of skew angle was determined in which the combination of base torque ripple and skew angle produces the maximum results in terms of minimizing the drop in average torque with the lowest angle of skew. At identical conditions of bottom torque, the maximum phase current can ultimately be reduced by 14%.

At the same time, the electromotive force (maximum voltage) at maximum rotational speed has been reduced to contribute to the preservation of the high-voltage system. The average drop in the voltage of electromotive force caused by the skew is 2%, while a drop in peak voltage of 9% has been achieved.

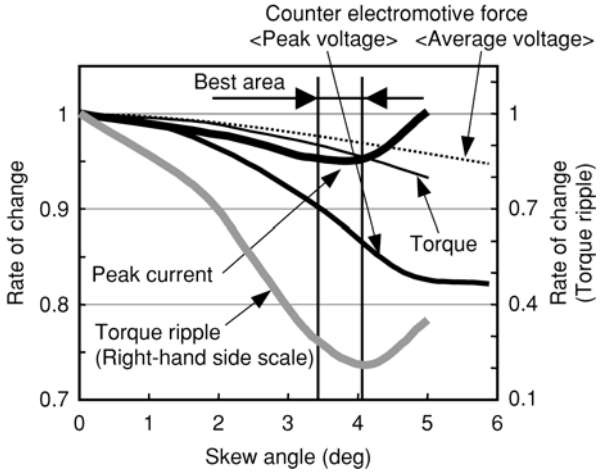


Fig. 10 Characteristic of torque, current and electromotive force by rotor skew angle (calculation)

3.5. Stator Cooling Technologies

To maintain high power over the continuous power range, copper loss has been reduced and the heat resistance of the stator has been lowered. Measurements taken in the heat paths from the winding to the water jacket on the exterior of the stator demonstrate that heat resistance is largely dependent on the area of the sections connecting the winding and the stator. The results of these measurements are shown in Fig. 11. On the basis of these results a balance was achieved between the amount of winding and the number and form of the slots required to reduce phase resistance (loss) and increase the area of the sections connecting the winding and the stator, thereby enabling target cooling performance to be achieved.

By this means, winding temperature is maintained within the allowable limits even when continuous current is flowing at the levels attained when torque reaches 200 Nm or when the motor is running at the maximum rotational speed, at which the current for field weakening is at its peak.

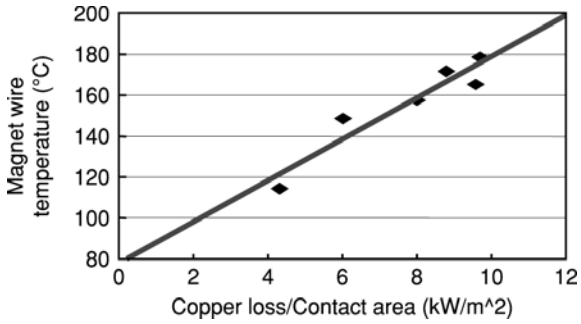


Fig. 11 Heat resistance

3.6. Motor Control

As mentioned above, full digital vector control has been adopted to provide motor control. To increase effective voltage at high rotational speed, the system switches to one-pulse control and does not perform pulse width modulation (PWM) switching, thus ensuring maximum power.

Control parameters are expressed in the form of a map. The use of an instantaneous analysis system for motor performance[5] to determine the parameters reduced the time formerly required to formulate detailed map data by one-half, contributing to a reduction in the length of the development period.

4. Motor Performance

Table 2 shows the achieved performance of the MCF21. Maximum torque multiplied by maximum rotational speed is used as an indicator of the breadth of the power range of a motor. This measure is increased by 24% in the MCF21 over the MCF11.

Table 2 Motor performance

Type	MCF11 (EV PLUS)	MCF21 (FCX)
Maximum power (kW)	49	60
Maximum torque (Nm)	275	272
Maximum speed (rpm)	8750	11000
Max. torque x Max. speed (kNm rpm)	2406	2992
LA4 ave. efficiency (%)	90	93
Maximum efficiency (%)	96	97

4.1. Power

Test results show that the new motor has achieved a power outline following the targets set in development, with measurements of 60 kW for maximum power, 272 Nm for maximum torque and 11 000 rpm for maximum rotational speed. Continuous rated power was ensured below a torque of 200 Nm. Test results are shown in Fig. 12. Figure 13 shows a driving force curve for the fuel cell vehicle plotted on the basis of these results.

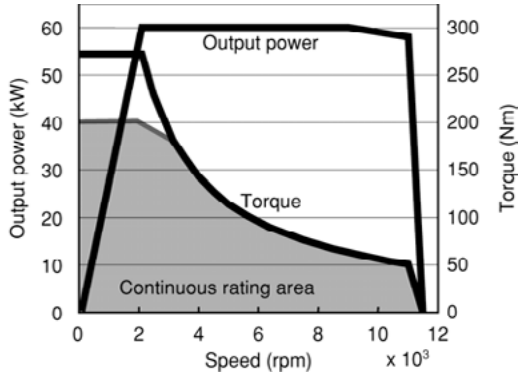


Fig. 12 Motor output performance

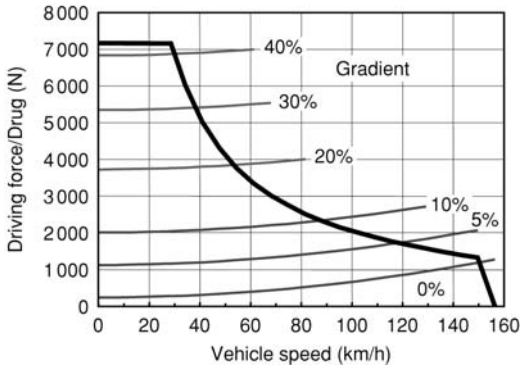


Fig. 13 Driving force curve

4.2. Efficiency

Figure 14 shows the results of measurements of the combined efficiency of the motor and the inverter used for traction, and the driving force locus in LA4 mode.

An average efficiency of 93% was measured when providing driving force in LA4 mode. This figure is a 3% improvement over the 90% efficiency of the MCF11 in the same mode, and this 3% increase in efficiency corresponds to a 30% reduction in loss.

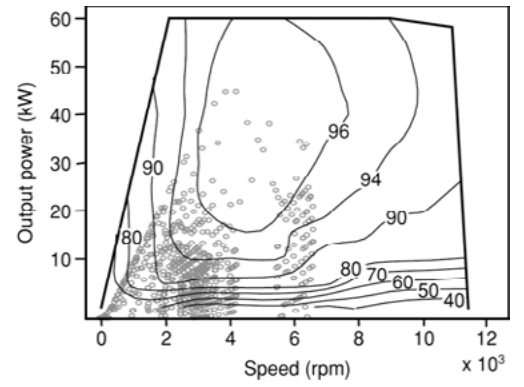


Fig. 14 Motor efficiency (including inverter efficiency) and driving force locus of LA4 mode

5. Conclusion

A new motor was developed and installed as a traction motor for a fuel cell vehicle.

(1) By using power up to the voltage limit, high rotational speed was balanced with a high torque constant.
(2) The high torque constant has centralized the efficiency of the motor in the low speed range, increasing efficiency in LA4 mode.
(3) Skewing the rotors has controlled the maximum phase current when the motor is stalled, enabling the size of the inverter to be reduced.
(4) The Weibull theory was applied to the strength of Nd-Fe-B magnets, enabling strength reliability to be ensured in a surface-mounted permanent magnet rotor.

References

(1) Yamamoto, K., Akutsu, S., Takizawa, K., Saito, Y.: Development of a Propulsion Motor the Honda EV PLUS, HONDA R&D Technical Review, Vol. 10, p. 24-31 (1998)

(2) Takizawa, K., Itoh, T., Satoh, H.: Development of a Compact, Highly Efficient Traction Motor for Fuel Cell and Electric Vehicles, HONDA R&D Technical Review, Vol. 12, No. 2, p. 105-112 (2000)

(3) Morimoto, S., Ueno, T., Takeda, Y.: Wide Speed Control of Interior Permanent Magnet Synchronous Motor, Trans. of IEE Japan, Vol. 114-D, No. 6, p. 668-673 (1994)

(4) Nagi, T., Kita, T.: Strength Evaluation Method for Nd-Fe-B Rare Earth Sintered Magnets, Honda R&D Technical Review, Vol. 13, No. 2, p. 225-230 (2001)

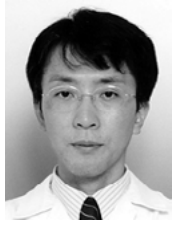
(5) Murayama, Y., Atarashi, H., Kishida, M., Asami, K.: Development of a Real-time Analytical System for Motor Performance Measurement, Honda R&D Technical Review, Vol. 13, No. 2, p. 107-112 (2001)

■ Authors ■


Shigemitsu AKUTSU


Hiroyuki SATOH


Tomoya MIYAMURA


Hiroaki SHINOKI

Development of Stator for Thin Electric Motor

Hirofumi ATARASHI* Mitsuyoshi TAKAO*
Takeo FUKUDA* Toshinori TSUKAMOTO*

ABSTRACT

Lap winding was adopted as the winding method for the stator in order to increase the efficiency and reduce the size of an electric motor to be fitted into a hybrid electric vehicle. This has enabled the motor to be made thinner and loss of the motor to be reduced. Three nozzles are utilized to wind from the outer circumference around I-shaped split cores, enabling the length of the braided winding overhang to be minimized, and reducing the length of the winding. The use of multi-hole alignment nozzles and a jig for fixing the winding has increased the space factor. In addition, employing a two-step stamping process in which the first load is applied to increase the internal diameter and the second is applied in the axial direction has enabled the height of the winding overhang to be limited to 10 mm. As a result, operation efficiency has been improved by 7%.

1. Introduction

Deepening concern towards global environmental issues has increased the expectations being placed on low-pollution vehicles, such as hybrid cars, fuel cell vehicles, and the like. The motors which provide the traction sources for these vehicles are required to display high torque and power density, achieved by increasing efficiency and reducing size and weight. The effectiveness of changing the winding of the coil from the conventionally employed lap winding to concentrated winding is well known as a method of improving performance for the purpose of reducing loss and decreasing the size of the motor, as described in a number of recent papers[(1) - (3)]. However, little research has been directed towards finding methods of improving performance employing the lap winding structure, which has a high effective rate of use of magnetic flux. The characteristics of lap winding and concentrated winding are compared in Table 1. Lap winding has a winding factor of 1.0, while that of concentrated winding is 0.866. In identical rotors, it is therefore possible to reduce the current in a lap-wound coil, which leads to decreasing copper loss. In addition, unlike concentrated winding, the distribution of magnetomotive force in lap windings is a sine wave, meaning that there are fewer harmonic waves in the stator flux, and therefore less iron loss and noise than in concentrated windings. The superiority of lap winding from the perspectives of winding factor and harmonic waves in the stator flux demonstrated by these considerations led to it being selected as the winding method for the motor, despite the fact that the size of the winding overhang increases when this method is used. This research project also focused on improving the core structure and winding method to achieve the goals of reducing the size of the motor and minimizing loss.

Table 1 Comparison of winding types

Factor	Effect	Winding type	
		Lap winding	Concentrated winding
Winding overhang	Thickness	–	good
	Copper loss	–	good
Winding factor	Copper loss	good	–
Harmonic wave of stator flux	Iron loss	good	–
	Necessity of high voltage parts in inverter	good	–
	Torque ripple	good	–
	Noise	good	–

* Tochigi R&D Center

2. Development Goals

The loss occurring in stators can be broadly divided into copper loss and iron loss (hysteresis loss and eddy current loss). Copper loss is determined by the square of the current multiplied by wiring resistance. It is therefore possible to reduce it by reducing either winding resistance or the current in the winding. The use of lap winding increases the winding factor, enabling the current in the wires to be reduced. Winding resistance increases in proportion to the length of the wire and decreases in inverse proportion to cross-sectional area. Reducing the length of the wire and increasing the space factor inside the slots are both effective methods of reducing winding resistance. Higher diameter wire cannot be employed for lap winding. Comparatively lower diameter wire is employed to increase the number of parallel wires, thus increasing the total cross-sectional area. A further benefit of lap winding is that it produces less iron loss than concentrated winding. The aim of this research project was therefore to achieve a balance between an overhang height equivalent to that produced by concentrated winding, which was conventionally considered difficult using this method, and a space factor equivalent to that of inserted winding, by exploiting these benefits described above and decreasing the bulge of the winding overhang in order to reduce the size of motor and copper loss. Figure 1 shows the development targets established for this project.

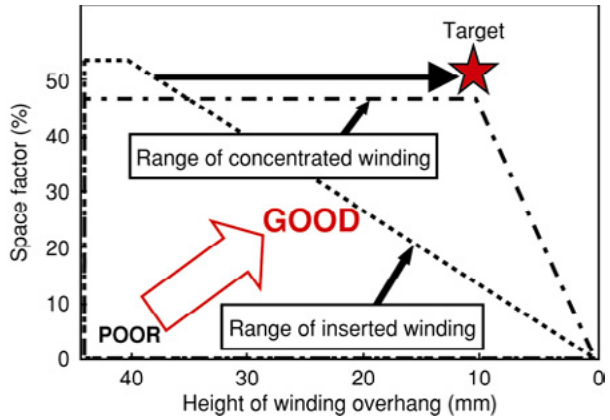


Fig. 1 Relation between space factor and height of winding overhang

3. Methods Employed

3.1. Balancing Smaller Winding Overhang with Reduction of Copper Loss

The formation of the winding overhang into the braided structure shown in Fig. 2 was considered as a method of balancing a reduction in the size of the overhang with an increased space factor. Lap winding produced by a conventional inserter winding machine overlaps the ends of each phase of wire with the ends of other phases in the same slot, thereby increasing the height of the overhang, as shown in Fig. 3. If the curvature of the bundles of wires is increased to lower the overhang, spaces are produced in the slots, reducing the space factor. Figure 4 shows a schematic of this phenomenon. To prevent this, in the new method the section of each phase of bundled wire which has been wound is braided with the sections of other phases which are beginning to be wound to form the winding overhang, enabling the achievement of a high space factor while lowering the overhang. In addition, adjustment of the positioning of the braided sections has enabled flexibility in the choice of the number of crossings in the braid, making it possible to freely adjust the height of the overhang and the space factor. The following six factors were considered in the development of the new method:

(1) Minimizing the length of the braided overhang by winding the coil from the outer circumference using three nozzles.
(2) Splitting the core into I-shaped sections to enable winding from the outer circumference.
(3) Increasing the curvature of bundles by employing split winding using groups of multiple wires.
(4) Using a multi-hole alignment nozzle to align the wires in the slots.
(5) Employing a jig for fixing winding to improve the space factor in the slots.
(6) Reducing the height of the winding overhang by employing low-tension lacing and a two-step stamping process for formation in which loads are applied first to increase the internal diameter and then in the axial direction.

As a result, the winding overhang was reduced in size and copper loss was reduced, enabling the motor to be made thinner and loss to be reduced.

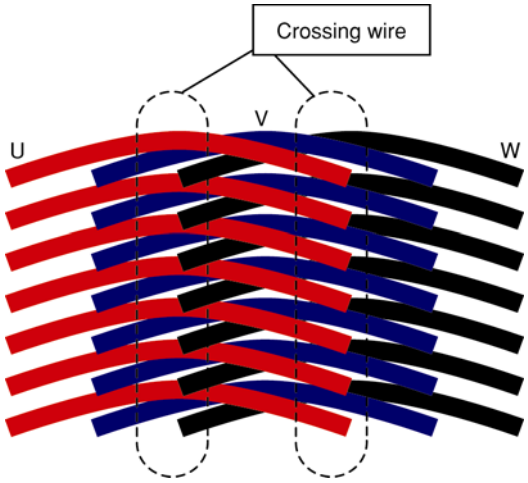


Fig. 2 Method of crossing wire



Fig. 3 Winding overhang produced by insert coil Machine

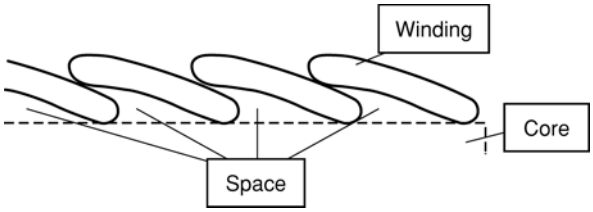


Fig. 4 Reduction of space factor

3.2. Reducing the Length of the Wiring

Table 2 shows the specifications of the prototype open-slot stator for use in an inner rotor motor. The reduction of the length of the wiring was prioritized to make the unit thinner and reduce copper loss, and nozzle winding enabling winding directly to the core was employed. Winding multiple wires simultaneously increases the size of the winding machine and the number of wire bobbins, leading to an increase in production costs, therefore, the wires to be wound in parallel have been separated into groups for winding in the slots. To further reduce the length of the wire used for the overhang, three nozzles (U phase, V phase and W phase) are operated simultaneously, to enable the overhang to be formed into braids. Figure 5 shows the position of the nozzles used to wind each phase. To enable accurate adjustment of the wiring overlap, a multi-hole adjustment nozzle is adopted, in which only one wire is utilized in each nozzle hole and the nozzle holes are aligned. A jig is employed to fix the winding, enabling the positions at which the wires cross to be controlled. The use of these methods has enabled the length of the winding to be reduced by 29%. The multi-hole alignment nozzle is shown in Fig. 6, the jig for fixing the winding is shown in Fig. 7, and the resulting reduction in the length of the winding is shown in Fig. 8.

Table 2 Stator specifications

Outer diameter (mm)	260.0
Inner diameter (mm)	200.9
Core length (mm)	40.0
Number of slots	48
Wire diameter (mm)	Φ0.5
Number of turns	5
Winding type	Lap winding
Number of poles	4

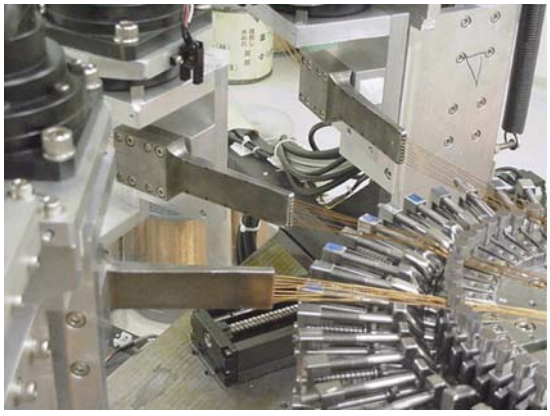


Fig. 5 Nozzles for winding of three phases

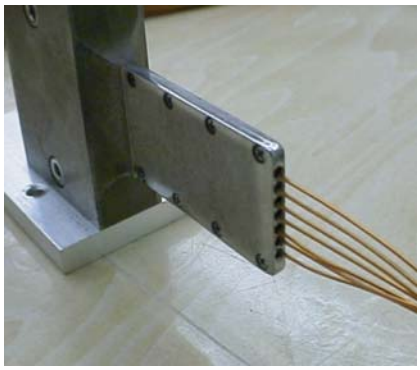


Fig. 6 Multi-hole alignment nozzle



Fig. 7 Jig for fixing winding

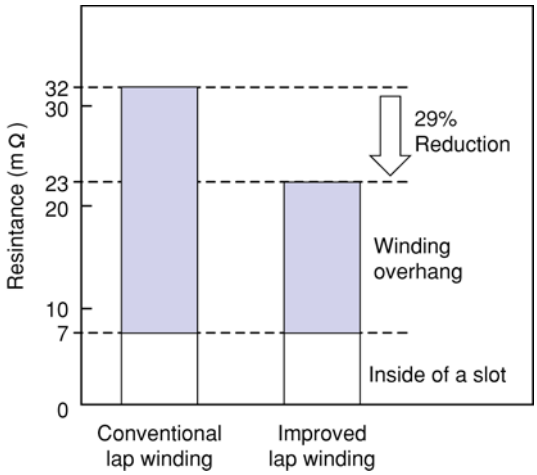


Fig. 8 Effect of reduction of length of winding

3.3. Increasing the Space Factor Inside the Slots

When winding from the inner circumference of an integrated stator using nozzles, the space factor inside the slot is reduced to ensure the paths of movement of the nozzle. The research discussed in this paper made a high space factor a priority, and therefore ensured the paths of movement of the nozzle on the external circumference. A split core structure, divided into I-shaped teeth and back yokes, was adopted and the opening was positioned on the external circumference. Figure 9 shows the split core structure, and Fig. 10 shows a flow chart of the winding process. The I-shaped teeth are fitted on a jig for fixing the teeth of the winding machine, and the nozzles wind the wiring from the outer circumference. The jig for fixing winding shown in Fig. 7 is also used to prevent the inserted wiring from moving in the slot. When the winding of each group of wires is completed, the jig moves towards the outer diameter of the coil. The alignment of the wires inserted in the slot by the multi-hole alignment nozzle (Fig. 6) is shown in Fig. 11. The nozzle does not rotate during winding, and the wires therefore cross at $n \times (n-1)$ places for n wires in each turn. This enables each wire to be made a uniform length, which produces the same effect of equalization of impedance as that obtained in the standard process of dislocating the bundles of wires by twisting. After the completion of winding, the insulating paper is folded and the back yokes are inserted. At this time, the spaces between the wires in the slots are compressed. The combination of the methods described above has increased the space factor in the

slots. Each back yoke has two semi-circular projections, as shown in Fig. 9. The projection on the inner side functions to prevent the I-shaped teeth from moving, while the projection on the outer circumference functions to increase the cylindricality of the core. The space factor in the slots has increased to 48.3% from a figure of 40.3% measured before the improvements described above. Figure 12 shows the space factor before and after the improvements.

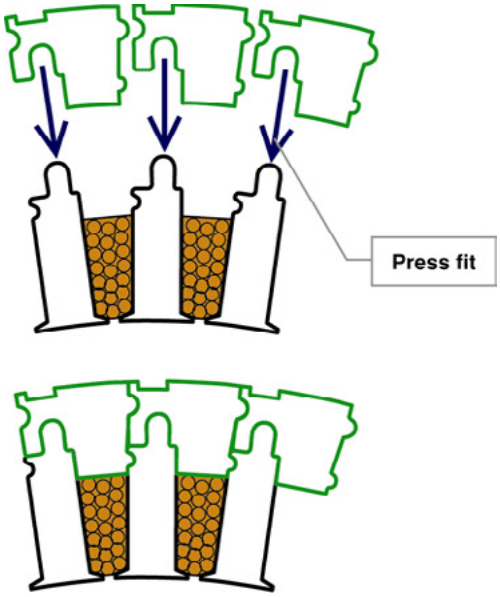


Fig. 9 Structure of split core

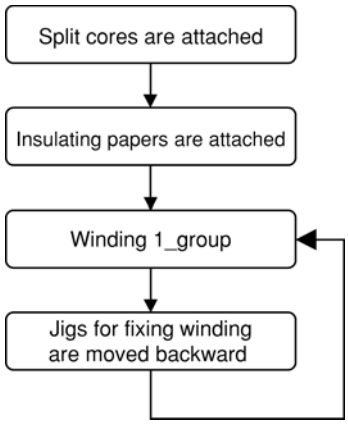


Fig. 10 Winding process



Fig. 11 Winding aligned inside a slot

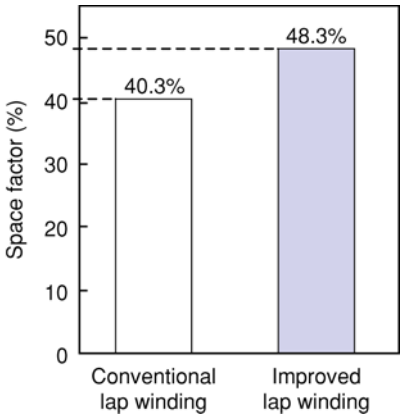


Fig. 12 Space factor of winding

3.4. Making the Motor Thinner

The winding overhang is stamped to decrease its volume, to enable the motor to be made thinner. In conventional lacing, force is applied to the lacing materials to bind the wires in the winding overhang in the process of winding the lacing. Slight stamping is applied when the coil is in its final form, and there is comparatively little deformation of the wires. In the new process, the winding overhang is stamped after lacing, and there is therefore considerable deformation of the wires. For this reason, the lacing is applied at a lower tension than in the conventional method. This method exploits the fact that when the winding overhang is stamped, the peripheral length of its cross-section increases, in order to achieve an equivalent binding force on the wires to that achieved by the standard process. Figure 13 shows a conceptual diagram of this method. The wires used in the lacing do not stretch, which has increased both the binding force on the winding and the space factor of the winding overhang. Because it was found that the wiring bends when it is stamped once in the axial direction, the stamping process has been divided into two steps. The winding overhang is first stamped to increase the internal diameter and then stamped in the axial direction. This has reduced mechanical stress on the wiring to a minimum, and enabled the wiring in the winding overhang to maintain its mesh shape during stamping. Figure 14 shows the two-step stamping process, and Fig. 15 shows the thinness of the winding overhang after stamping.

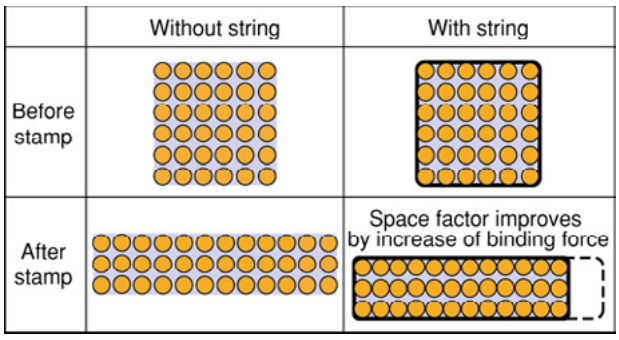


Fig. 13 Method of increasing force which binds winding overhang

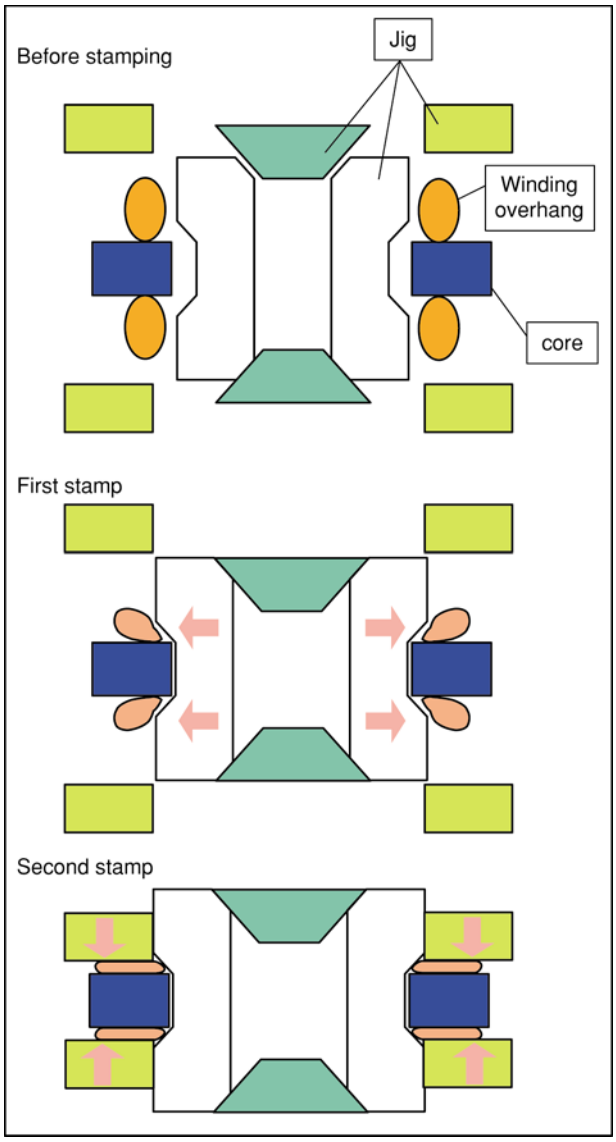


Fig. 14 Stamping process of two steps

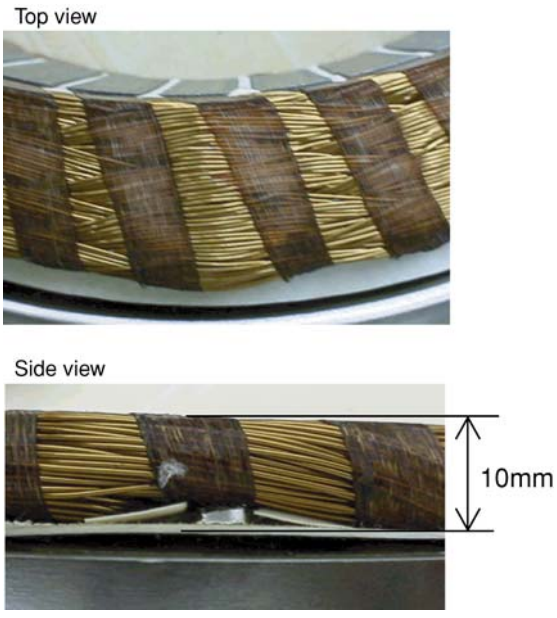


Fig. 15 Winding overhang after stamping process

4. Verifying Motor Performance

Operation efficiency and axial output were evaluated in the hybrid vehicle induction motor shown in Fig. 16. A 41% reduction in primary copper loss in comparison to the conventional method was confirmed. A breakdown of contribution shows 29% resulted from the reduction of the length of the wiring and 12% from the increase in the space factor.

The height of the winding overhang was verified as having been reduced to 10 mm. The reduction of primary copper loss increased operation efficiency by 7%. Reduction of the drop in voltage due to wiring resistance has increased axial output by 16%. These improvements in operation efficiency and axial output are shown in Fig. 17.



Fig. 16 Induction motor for hybrid vehicle

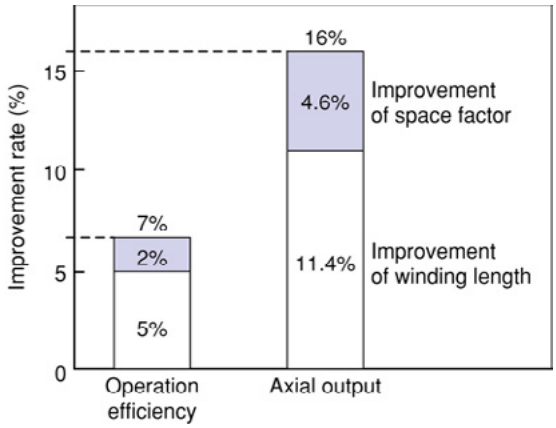


Fig. 17 Improvement of operation efficiency and axial output

5. Confirmation of Ease of Production

Figure 18 shows the stator assembly process. The automation of the new winding process with the development of a winding machine enables a stator to be wound in 45% less time than required to wind a Honda stator of equivalent size with concentrated winding using bobbin winding. The comparison in winding time is shown in Fig. 19.

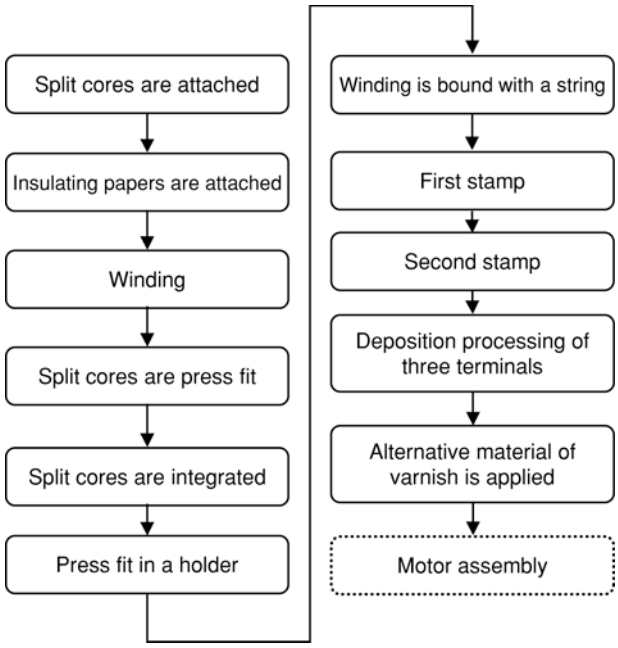


Fig. 18 Assembly process of stator

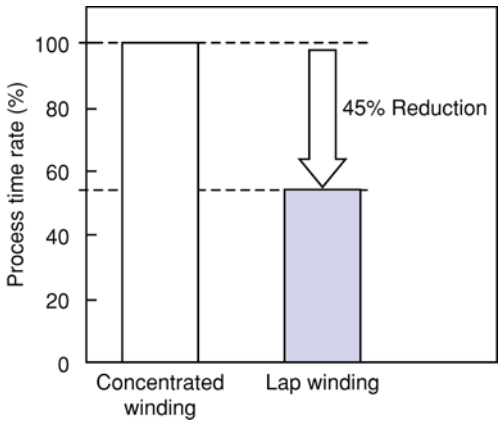


Fig. 19 Comparison of winding time

6. Conclusion

The issue of increased wiring length and winding volume of the winding overhang when the lap winding method is employed were focused on in order to make motors thinner and reduce loss of the motor. The following results were achieved by improvements to the core structure and the winding method:

(1) The height of the winding overhang has been reduced to 10 mm, equivalent to that achieved in concentrated winding, and a space factor of 48.3% in the slots has been achieved, equivalent to the space factor of inserted winding.

(2) The increase of the space factor in the slots and the reduction of the length of the wiring have reduced coil resistance and increased operation efficiency by 7% and power by 16%.

(3) The development of an automatic winding machine has enabled the stators to be wound using the new process in 45% less time than required to wind a Honda stator of equivalent size using bobbin winding.

Acknowledgments

The authors wish to thank all those at Nittoku Engineering Co., Ltd., who offered their assistance in developing the automatic winding machine described in this paper.

References

(1) Baba, K., Oikawa, T., Akita, H., Kometani, H., Kawaguchi, H.: Examination of Performance Improvement Brushless DC Motors, IEE Japan, RM-00-141 (2000)

(2) Ikkai, Y., Nishiyama, N., Kishibe, T., Kondo, Y., Kadoya, N.: A Split-core Concentrated Winding IPM Motor for an EV, JEVA EV Forum, p. 199-206 (2000)

(3) Akita, H., Hirai, Y., Kawaguchi, S., Kawaguchi, H.: Conserving Energy and Achieving High Efficiency in an Air-conditioner Compressor Motor, Mitsubishi Electric Technical Review, Vol. 75, No. 10, p. 25-28 (2001)

■ Authors ■


Hirofumi ATARASHI


Mitsuyoshi TAKAO


Takeo FUKUDA


Toshinori TSUKAMOTO

Research of Natural Gas Ultra Low Emission Combustor

Atsushi YAMAZAKI* Masatoshi KUROKAWA*
Tsutomu INOUE* Hisashi MURAKAMI*

ABSTRACT

A lean burn combustor, which provides homogeneous mixing of air and natural gas and prevents autoignition, was developed by adopting a dispersely arranged multi-venturi design. By taking advantage of the characteristics of the venturi mixers, a highly accurate determination of the state of combustion was enabled and an expansion of the premixed combustion range was achieved. The combustor system above was installed on a micro-gasturbine, achieving an ultra low emission level of 3 ppm (at 15 percent oxygen equivalent) NOx, CO and THC at a 50 to 100 percent load.

1. Introduction

Micro-gasturbines are receiving attention as a distributed energy source, but low emissions performance equivalent to a large capacity power plant is still demanded, for environmental reasons. The lean premix combustion method, which combusts a homogenous mixture at relatively low temperatures, is an effective method for reducing gas turbine emissions. However, it is difficult to generate a homogenous mixture and at the same time prevent autoignition during the mixing process. Also, a lean mixture can easily lower the combustion efficiency and produce unstable combustion, such as combustion oscillation.

Furthermore, to prevent flameout and to ensure a wide, low-emissions operating range when applying this method, especially to a micro-gasturbine, it is necessary to establish a simple method for accurately acquiring the combustion state, which changes according to the operating conditions, and for switching between diffusion combustion and premix combustion as appropriate[(2), (3)].This research was intended to develop an environmentally-friendlier micro-gasturbine with low emissions. The goal was to produce a practical lean premix combustor, which was previously considered to be difficult[(1), (2), (3), (4)].

2. Premix Combustor

2.1. Emission Targets

This combustor is intended for application on a micro-gasturbine, so the NOx emission target was set at 3 ppm or less (at 15% oxygen equivalent), which is below the average of all electric power plants including nuclear energy as shown in Fig. 1. In addition, the CO and THC emissions targets were set at the same level as NOx.

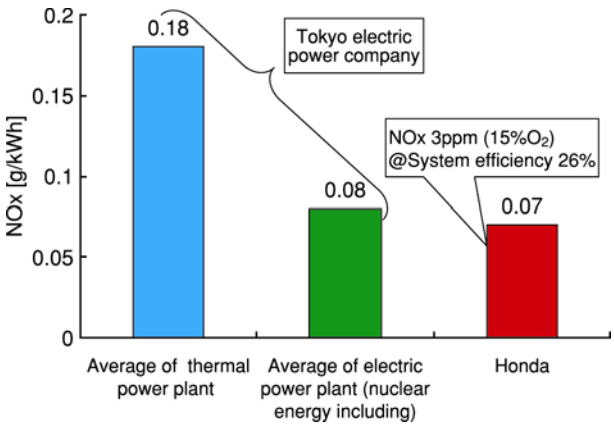


Fig. 1 NOx emission of electric power plant [(5)]

* Wako Research Center

An additional target was set to verify the above emission values over the 50% to 100% load range which is the normal operating range for a micro-gasturbine[6].

It is generally known that in a lean premix combustor, the range of the adiabatic flame temperature where low emission combustion occurs can be expanded by homogenizing the concentration distribution of the air-fuel mixture. The combustor targets were set as follows based on the results of preceding basic combustion tests (Fig. 2).

(1) Degree of mixing for the premixed air-fuel
Nonuniformity ratio: ±10% or less
(Low-emission combustion Tad bandwidth: 200 °C)

(2) Combustion state estimation accuracy
Tad calculated estimation error: ±25 °C or less
(Combustion air mass flow estimation error: equivalent to ±5% or less)

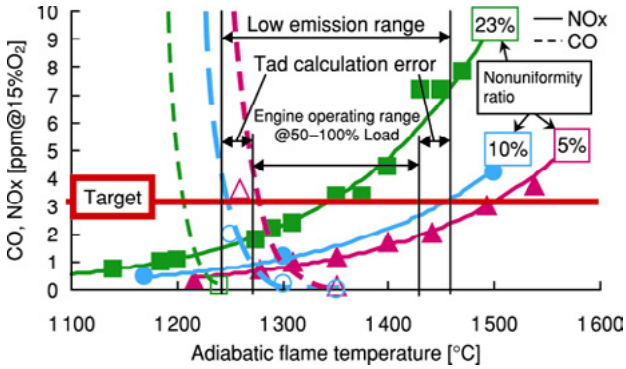


Fig. 2 Effect of adiabatic flame temperature on NOx, CO emissions

2.2. Premix Mixer

A venturi mixer was adopted as the premix mixer. Venturi mixers have high mixing performance and allow for the estimation of air mass. In addition, a multi-venturi mixer composed of a number of dispersely arranged compact venturi mixers as shown in Fig. 3 was used to prevent autoignition during the mixing process and to reduce the size. Pipe swirlers were also used to ensure flame stability by turning the mixture into a spiral flow.

3. Venturi Mixer

3.1. Analysis of the Mixed State inside a Venturi Mixer

Figure 4 shows the CFD calculation results of the distribution of air and CH_4 concentrations at the diffuser of a venturi mixer. Table 1 shows the boundary conditions for calculation (equivalent to micro-gasturbine rated operation). The concentration calculation results in Fig. 4 show that the mixing length becomes shorter as the diffuser expansion angle (deceleration rate) increases. However, separation occurs when the diffuser expansion angle is too wide, leading to mixture retention which can cause autoignition. Therefore, the expansion angle was set at 12° which is the widest angle at which separation does not occur.

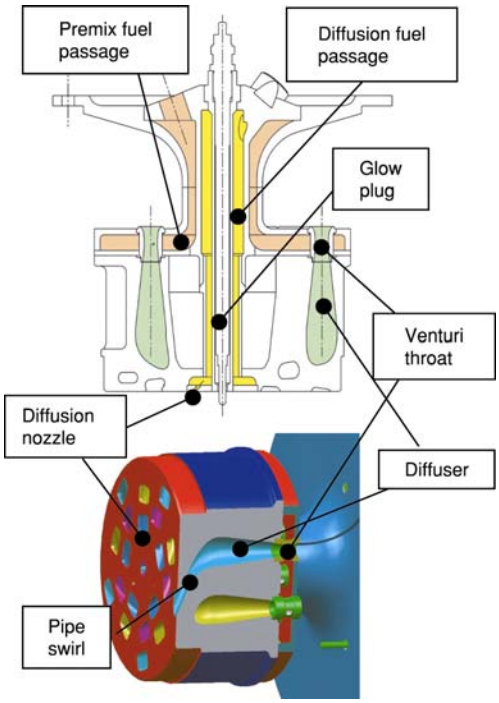


Fig. 3 Layout of multi venturi mixer

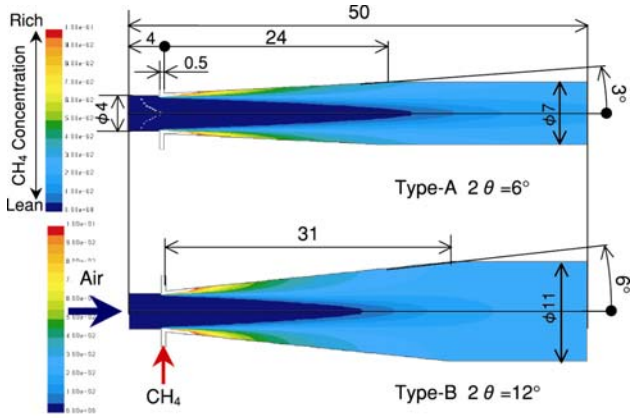


Fig. 4 Calculation results of CH_4 concentration

Table 1 Boundary conditions for calculation of CH_4 concentration

	Velocity [m/s]	Temperature [K]	Pressure [kPaA]
Air in	100	873	–
CH_4 in	2.2	473	–
Outlet	–	873	400

3.2. Single Venturi Mixer Unit Test

A single venturi mixer was fabricated based on the CFD calculation results, to analyze the mixing state and optimize the fuel injection method.

3.2.1. Unit test rig

Figure 5 shows the single venturi mixer unit test rig. The mass flow of the air and fuel is arbitrarily adjusted and then supplied to the test rig. The mixture is sampled and the CH_4 concentration is measured using a sampling probe installed downstream from the diffuser.

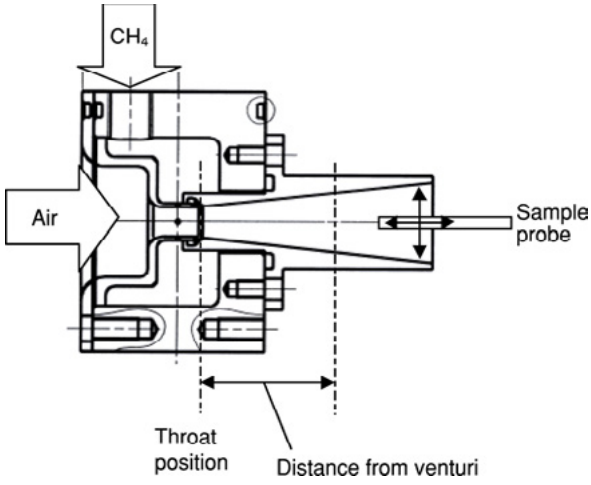


Fig. 5 Cross-sectional view of single venturi mixer

3.2.2. Effect of diffuser expansion angle and flow velocity through the throat on nonuniformity ratio

Figure 6 shows results of the measured nonuniformity ratio of a cross section at an arbitrary distance from the throat. The nonuniformity ratio is defined as the value obtained by dividing the standard deviation of the local concentration by the average concentration. In accordance with the CFD results, the mixing length becomes shorter as the diffuser expansion angle (deceleration rate) increases, and the target nonuniformity ratio at an expansion angle of 12° (TYPE-B) was obtained at the distance of 28 mm from the venturi throat (mixing length/throat diameter: L/D = 7).

In addition, Fig. 7 shows the nonuniformity ratio for different air flow velocities through the venturi mixer, and shows that the difference in the flow velocity has little effect on the mixing length.

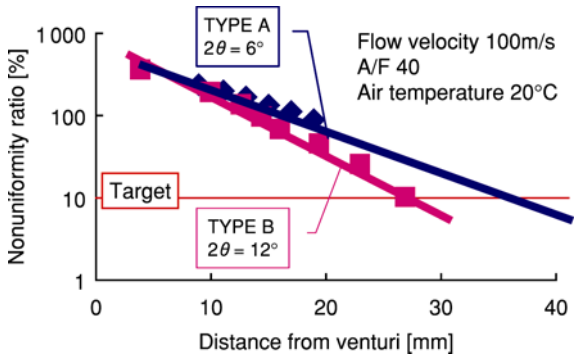


Fig. 6 Effect of diffuser angle on nonuniformity ratio

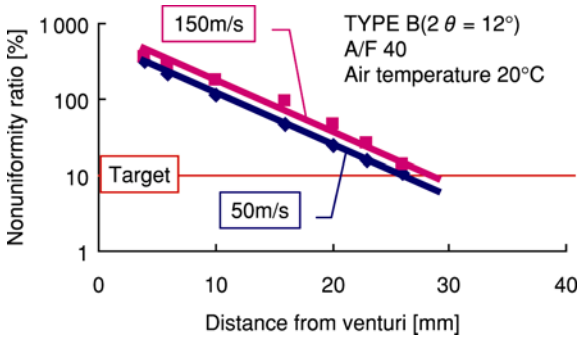


Fig. 7 Effect of velocity on nonuniformity ratio

3.2.3. Effect of fuel injection method on nonuniformity ratio

In order to investigate the effect of the fuel injection method on the nonuniformity ratio, the mixing state downstream from the throat was visualized and the nonuniformity ratio was measured and optimized for the three fuel injection methods shown in Fig. 8. Figure 9 shows the mixing states immediately after the venturi throat and 20 mm downstream from the throat. The mixing state was visualized by supplying oil smoke as a seeding to the fuel side and filming with a laser sheet beam as a light source. In the case of the base type which injects the swirling fuel to the air flow from slits in the throat, the fuel does not disperse over the entire diffuser. This is thought to be because the fuel sticks to the outer walls due to centrifugal force. For the two holes type which injects the fuel toward the center of the throat, the fuel penetrates the air flow appropriately without sticking to the walls, and mixing is promoted.

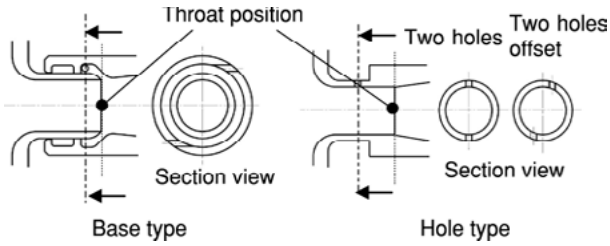


Fig. 8 Cross-sectional view of fuel supply shape

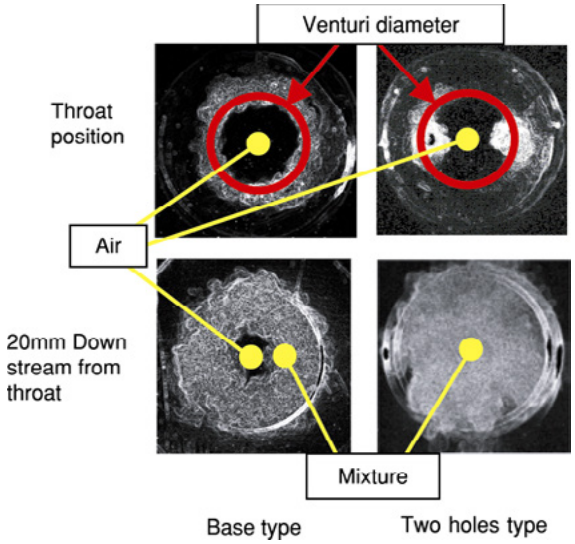


Fig. 9 Comparison of mixture distribution for two different fuel supply shapes

Figure 10 shows the nonuniformity ratio at the diffuser outlet. Homogeneous mixing can be improved by offsetting the injection holes. This is thought to be because the offset causes the fuel to disperse in the perpendicular direction near the throat walls. Therefore, the two holes + offset type is effective for mixing with in a shorter length.

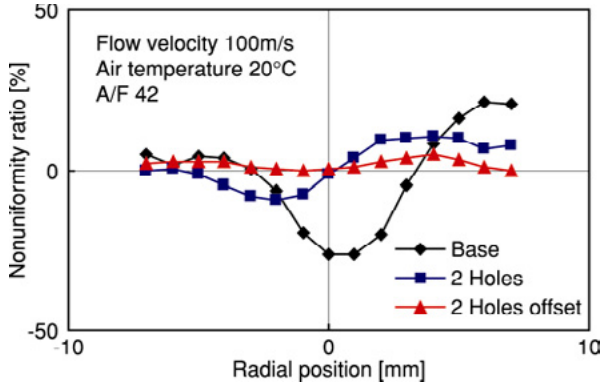


Fig. 10 Effect of fuel supply shape on nonuniformity ratio

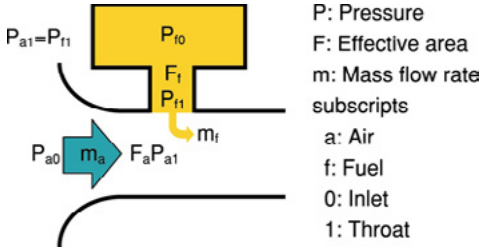


Fig. 11 Model of venturi mixer

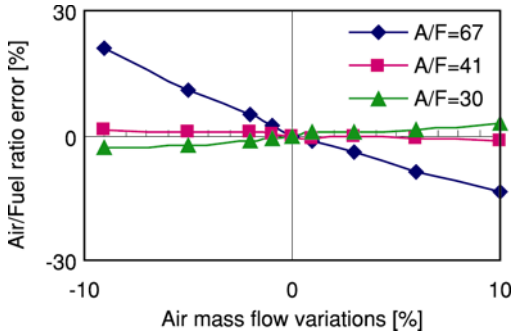


Fig. 12 Effect of air mass flow variations on air/fuel ratio error

3.3. Multi Venturi Mixer

3.3.1. Synchronization of mixture ratio between venturi mixers

The multi-venturi mixer for use in an actual combustor shown in Fig. 3 may experience variation in the air mass flow passing through each venturi mixer due to the pressure distribution inside the combustion cylinder during combustion, diffuser shape error, etc. This causes variation in the mixture ratio of each venturi mixer, and consequently variation in the distribution of the mixture concentration within the combustion cylinder. Therefore, the following method was used to synchronize the mixture ratio of each venturi mixer.

Assuming the fuel inlet total pressure, P_{f0}, and the air inlet total pressure,P_{a0}, in Fig. 11 to be equal (fuel throat static pressure, P_{f1}, equals air throat static pressure, P_{a1}), the flow velocities through the fuel effective area, F_f, and the air effective area, F_a, are equal, so the effective area ratio, F_a/F_f, equals the mass flow ratio, m_a/m_f.

Since the physical properties (density, specific heat ratio) of fuel and air are similar under actual operating conditions, it can be said that when P_{f0} and P_{a0} are equal, F_a/F_f and m_a/m_f are approximately equal. This indicates that even if the air mass flow changes due to the effects of the venturi downstream, m_a/m_f can be kept constant by maintaining a constant P_{f0} and P_{a0}. Application of this principle made it possible to reduce the air/fuel ratio variation between each mixer by setting the F_a/F_f of the multi-venturi mixer near the required air/fuel ratio.

Figure 12 shows the error relative to the set air/fuel ratio when the fuel and air inlet pressures are kept constant and the air mass flow passing through the venturi mixer is varied by changing the outlet pressure on a venturi mixer with the effective area ratio set to 40. This shows that the air/fuel ratio error relative to changes in the air mass flow becomes smaller at an air/fuel ratio near the set effective area. This indicates that the air/fuel ratio variation between each venturi mixer can be reduced even when the air mass flow passing through each venturi mixer in a multi-venturi mixer changes.

3.3.2. Nonuniformity ratio of the multi-venturi mixer

Figure 13 shows results of the measured nonuniformity ratio at the mixer outlet cross section (combustion cylinder inlet cross section) of a multi-venturi mixer for use in an actual combustor in order to confirm the nonuniformity ratio of the mixture. The nonuniformity ratio was within ±5% for over 95% of the mixer outlet cross section, which sufficiently achieved the target of ±10% or less. This confirmed that a homogenous mixture could be formed within the combustion cylinder even with a multi-venturi mixer arrangement by synchronizing the mixture ratio between each venturi mixer.

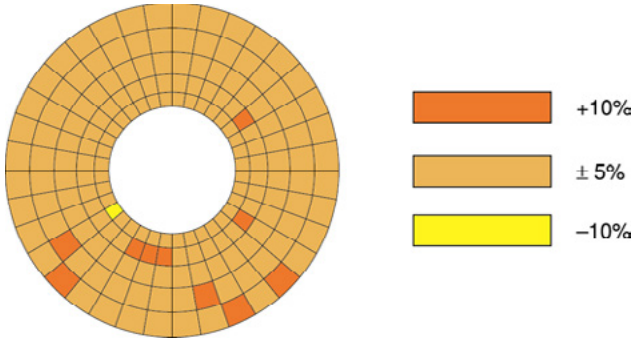


Fig. 13 Nonuniformity ratio at the outlet of multi venturi mixer

4. State Detection

4.1. Combustion State Detection Method

In order to ensure the low emission performance of 3 ppm or less at a micro-gasturbine load of 50% to 100% and to realize combustion switching without flameout, the Tad inside the combustor must be acquired in real time. Figure 14 shows the parameters needed to estimate Tad.

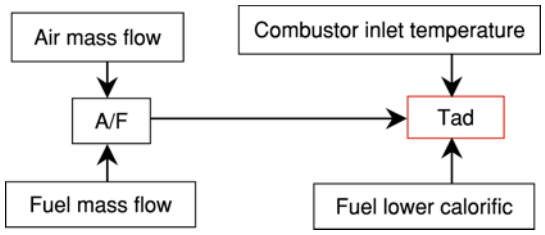


Fig. 14 Parameters for estimation of Tad

The air passing through this multi-venturi mixer becomes the combustion air, so the air mass flow was estimated using the venturi characteristics of the venturi mixers. When the venturi equation is transformed as shown in equation (1), it can be broadly divided into two parts, the inlet and throat pressure term and a flow characteristic term containing the effective area, which expresses the venturi mass flow characteristics. The mass flow characteristics (effective area) change due to the effects of the flow velocity and the viscosity, thus investigations were conducted to obtain the air mass flow from the measured venturi inlet conditions, fuel mass flow and fuel pressure from a map expressing the air mass flow with the fuel mass flow and pressure provided to the venturi mixer.

$$Ga^{*}=F\sqrt{\frac{2\kappa}{\kappa-1}}\frac{1}{\sqrt{R}}\sqrt{\left(\frac{P_s}{P_{in}}\right)^{2/\kappa}-\left(\frac{P_s}{P_{in}}\right)^{\kappa+1/\kappa}} \quad (1)$$

Flow characteristic term Pressure term

Ga*: Corrected Air mass flow, F: Effective area,
P: Pressure
κ: Specific heat ratio, T: Temperature, R: gas constant
Subscripts in: Inlet, s: Throat

Based on the corrected test results of the venturi mixer, when the mass flow that includes varying mass flow characteristics is converted to the standard conditions (15 °C at standard atmospheric pressure) and expressed as the corrected air mass flow, Ga* corrected, the mass flow characteristics remain fairly constant and do not change relative to the pressure term value even when the inlet conditions differ as shown in Fig. 15. This means that it is possible to obtain the air mass flow based on the inlet pressure and the throat pressure. However, measuring the throat pressure is difficult in an actual combustor, so the fuel mass flow and the fuel pressure were corrected to the standard state and expressed as the corrected fuel mass flow, Gf*, and the corrected fuel pressure, Pf*. In this case as well, the Ga* at different inlet conditions exhibited approximately the same gradient (Fig. 16).

The air mass flow at different inlet conditions can be obtained by compiling the Gf*, Pf* and Ga* obtained from the above corrected tests into a three-dimensional map (Fig. 17). The feature of this map is that when the air mass flow is reduced at a constant fuel mass flow, the venturi characteristics cause the throat static pressure to rise, which causes the fuel supply pressure to also rise. Thus, the map takes the general form of a graph sloping downward to the right.

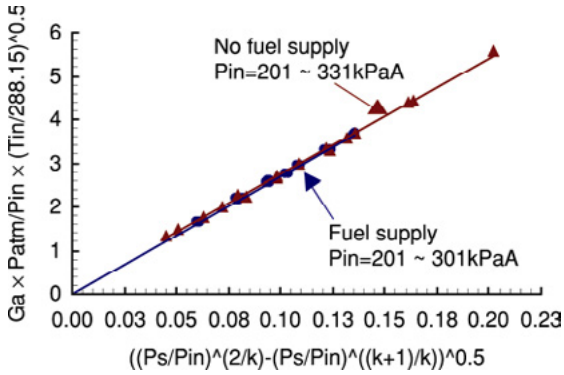


Fig. 15 Venturi flow characteristic

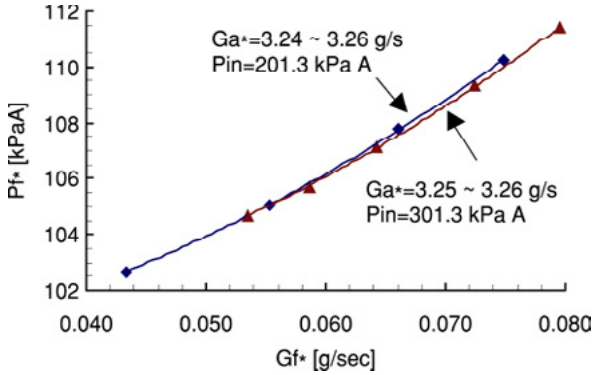


Fig. 16 Venturi flow characteristic

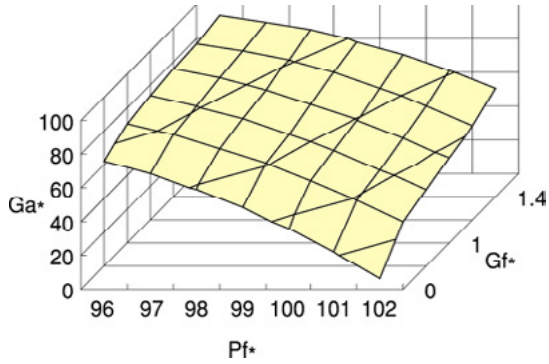


Fig. 17 Air mass flow map

4.2. State Detection Accuracy

4.2.1. Combustion air mass flow calculation accuracy

Figure 18 shows the results of combustion tests conducted in the condition where the entire mass of the supplied air was used as combustion air in order to confirm the accuracy of the air mass flow calculations. The calculation error was approximately ±5% or less in all regions except for the low mass flow region of diffusion combustion, which confirmed that there are no problems for practical application. The factor lowering the measurement accuracy in the low mass flow region is thought to be the accuracy of the pressure and temperature sensors.

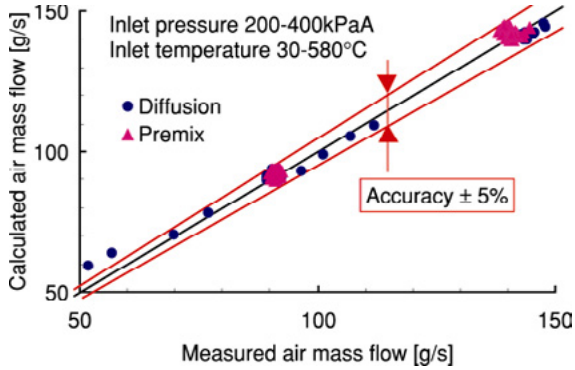


Fig. 18 Accuracy of calculated air mass flow

4.2.2 Adiabatic flame temperature calculation accuracy

The adiabatic flame temperature (Tad) is calculated using the air/fuel ratio, combustor inlet air temperature, fuel temperature, fuel lower calorific value, and the gas enthalpy before and after combustion. However, regressive calculation should be avoided in actual combustor control calculations. In addition, calculation was performed using a map in order to simplify the calculations. Figure 19 shows the Tad calculation results based on tests to confirm the fuel and air mass flow calculation accuracy. This confirmed that the calculation error does not worsen when using a map, and that the error was within the target range of ±25 °C.

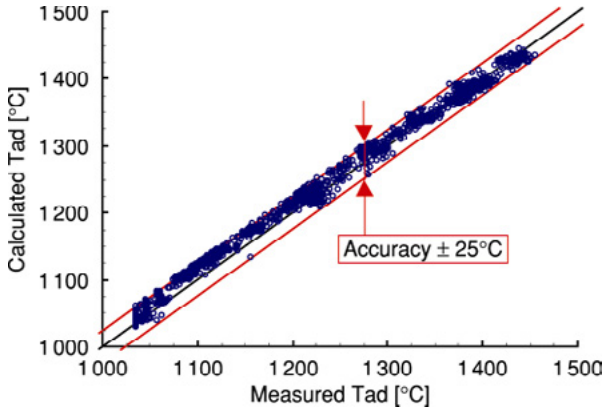


Fig. 19 Accuracy of calculated Tad

5. Combustion Tests

Methods for generating a homogenous mixture using a multi-venturi mixer and for detecting the combustion state by Tad estimation were established, so the combustion and practical performance were evaluated using a combustion test rig.

5.1. Combustion Test Rig

Figure 20 shows the test rig used for the combustor combustion tests. The air is pressurized by a compressor, adjusted to the prescribed mass flow and temperature by a flow adjusting valve and a heater, and then supplied to the combustion test rig. In addition, the pressure is adjusted by a pressure regulation valve located downstream from the combustion test rig. The fuel (natural gas, equivalent to 13A: CH_4 = 88.5%, C_2H_6 = 4.6%, C_3H_8 = 5.4%, C_4H_{10} = 1.5%) is pressurized by a fuel compressor, then the mass flow is

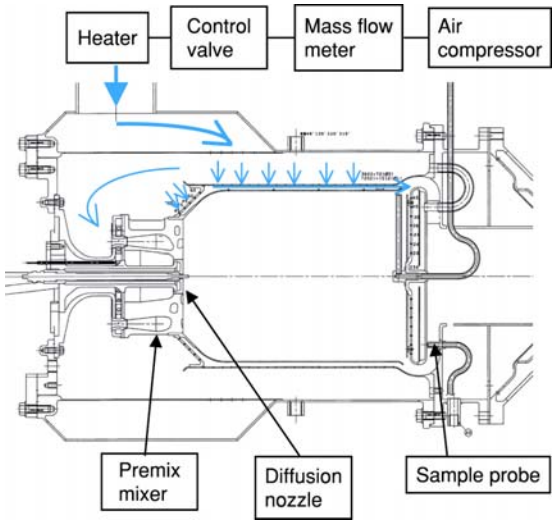


Fig. 20 Cross-sectional view of combustor rig

controlled by independent diffusion and premix fuel control valves, and the fuel is supplied to the combustion test rig. The combustion gas mixes with the diluted air that has cooled the combustion cylinder, and the mixture is then sampled by a sampling probe installed in the exhaust passage. Note that analysis was performed using two analysis meters with different resolutions in accordance with the concentration of the combustion gas components.

5.2. Premix Combustion Performance

Figure 21 shows the results of combustion tests performed at air mass flow and pressure conditions equivalent to the micro-gasturbine load conditions of 50% and 100% with the combustor inlet air temperature, Tin and Tad, as parameters. Note that the tests were performed with Tin set from 420 °C to 600 °C which corresponds to actual combustor conditions. The results showed that the low-emission combustion Tad range during premix combustion was 250 °C, which satisfied the target of 200 °C. This is thought to be because the nonuniformity ratio was ±5% or less for over 95% of the cross section area at the mixer outlet as shown in Fig. 13. Thus, an even temperature distribution was achieved over the entire combustion flame. In addition, there was no combustion oscillation or autoignition which had been a concern for premix combustion. Stable combustion was obtained.

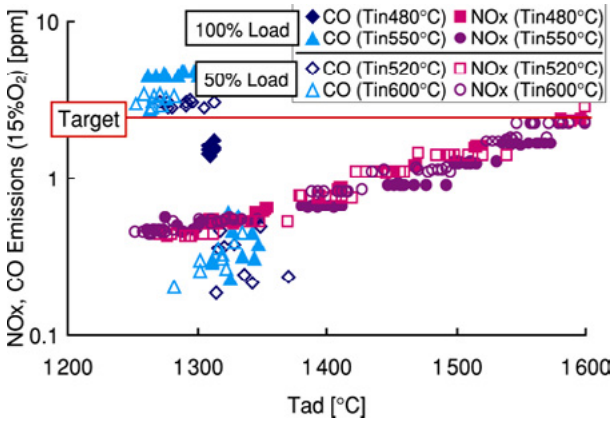


Fig. 21 Effect of Tad and inlet temperature on NOx, CO emissions

5.3. Switching between Diffusion Combustion and Premix Combustion

The results in Fig. 21 show that the point at which the CO concentration exceeds 3 ppm is around Tad = 1 300 °C, although this varies slightly according to Tin. Therefore, the switching test conditions were set as shown in Table 2. The diffusion → premix and premix → diffusion conditions differ for the following two reasons.

- There is a Tad calculation error of ±25 °C
- To prevent unnecessary switching due to temperature variation

The combustion state is switched when the Tad calculation value and Tin exceed the threshold values given in Table 2. However, the fuel passage differs for diffusion combustion and premix combustion, so a time lag occurs until the fuel pressure and temperature reach a static state depending on the piping and fuel passage volume, etc. This causes combustion to become unstable, and under some conditions can result in flameout. To prevent this, a time interval was established during which the fuel is supplied to both fuel passages, and switching was performed in steps. That is, diffusion combustion is possible even at 0.3 g/sec fuel mass flow (equivalent to an air/fuel ratio of 400), so when switching, the total fuel supply was maintained and a distribution ratio was used whereby the diffusion fuel mass flow was set to 0.3 g/sec and the remainder was provided as premix fuel. Figure 22 shows the switching test results. In both cases (diffusion → premix, premix → diffusion), stable combustion switching was confirmed with no flameout. These results provided prospects for stable operation of an actual micro-gasturbine.

Table 2 Set value for switching conditions

	Diffusion → Premix	Premix → Diffusion
Tin [°C]	520	480
Tad [°C]	1 350	1 300

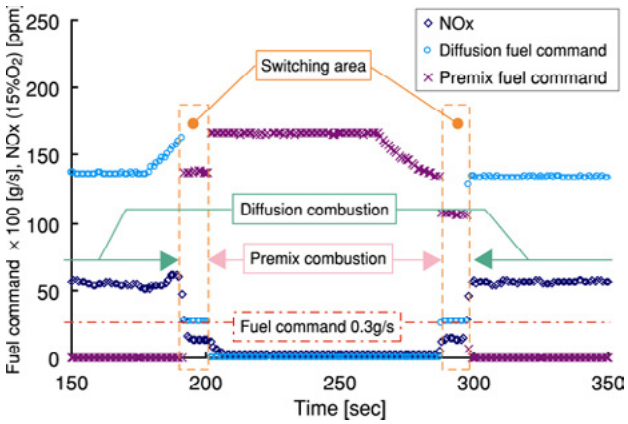


Fig. 22 Switching test results

5.4. Observation of the Combustion Flame

Figure 23 shows photographs of the combustion flame before and after diffusion and premix combustion switching as observed downstream from the combustion test rig. The flames (luminous flame, blue flame, etc.) evident during normal combustion cannot be observed at all during premix combustion, indicating that an ideal lean premix combustion was realized.

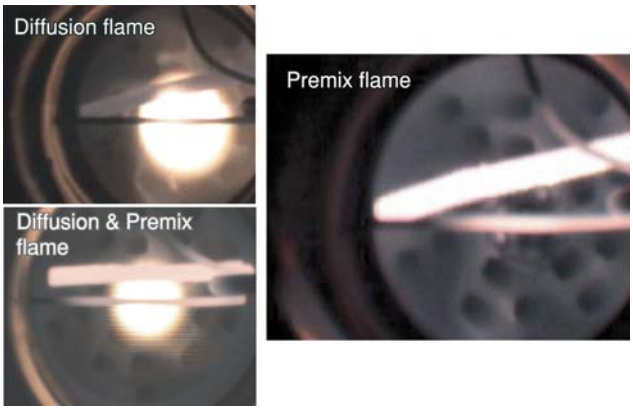


Fig. 23 Combustion flame pictures

6. Actual Micro-gasturbine Tests

Figure 24 shows the operation results for the combustor installed in a micro-gasturbine when the load is varied incrementally from ignition to a 100% load. This shows that operation switches from diffusion combustion to premix combustion and the NOx level drops sharply when the engine load rises to around a 50% load (22.5 kW) which is the combustion switching condition. At this time the engine revolution speed fluctuation was 1% or less, and operation was stable. In addition, operation at the emission (NOx, CO, THC) level target of 3 ppm or less (at 15% oxygen equivalent) was confirmed within the operation range of a 50% to 100% engine load as shown in Fig. 25[6), (7)].

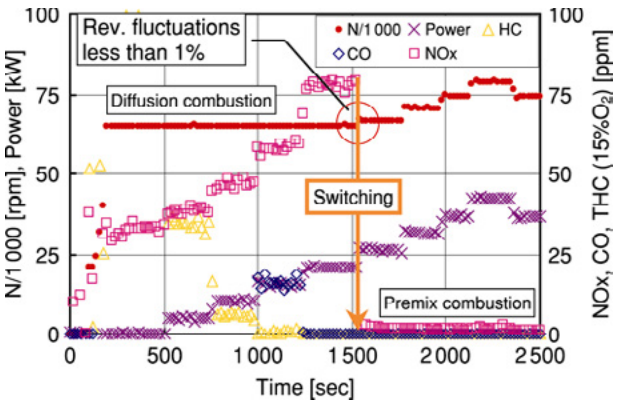


Fig. 24 Engine operation chart

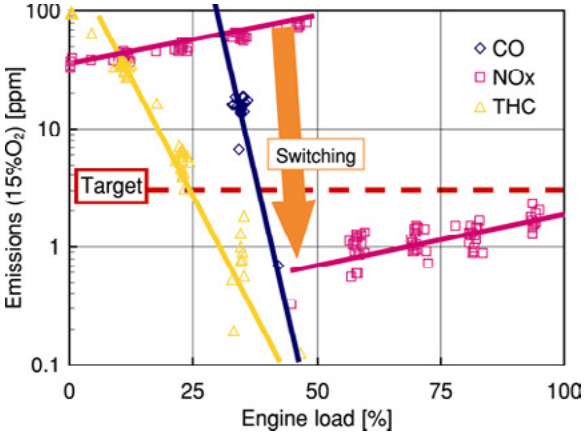


Fig. 25 Emissions characteristics of engine test at engine inlet temperature 10 °C

7. Conclusions

A multi-venturi mixer was adopted as a natural gas lean premix low emission combustor for micro-gasturbine, and the following knowledge was gained as a result of unit tests and actual engine tests.

(1) Venturi mixers were applied as the premix mixer, and the mixer shape and fuel injection method were optimized to create a compact premix mixer that can generate a homogenous mixture. This resulted in a natural gas lean premix low emission combustor that simultaneously achieves wide low emission combustion range and autoignition immunity.
(2) An accurate fuel control method that does not require complex devices was constructed by utilizing the venturi characteristics of the premix mixer.
(3) This combustor was mounted in a micro-gasturbine, and an emission value of 3 ppm or less (NOx, CO, THC at 15% oxygen equivalent) was verified within the normal operating range of a 50% to 100% load.
(4) These research results provide prospects for the practical application of a low emission micro-gasturbine.

References

(1) Tou, H., Watanabe, T., Hosoi, J.: Research and Development of Gas Turbine Combustors, IHI ENGINEERING REVIEW, Vol. 34, No. 3, p. 181-185 (1994)

(2) Kajita, S., Ohga, S., Ogata, M., Itaka, S., Kitajima, J., Kimura, T., Okuto, A.: Development of a Dry, low-NOx Combustor for 1 500-Class Gas Turbine, Kawasaki Technical Review, No. 128, p. 25-30 (1996)

(3) Fujimori, T., Saito, T., Mizutani, T., Tou, H.: Research on Low NOx Combustor Using Lean Premixed Pre-Vaporized Combustion in High Temperature and High Pressure Gas Turbine, IHI Engineering Review 2000, Vol. 40, No. 3, p. 83-87 (2000)

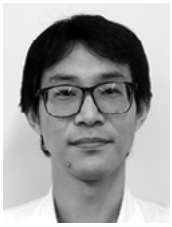
(4) Manda, S., Inada, M., Fukue, I., Tanimura, S.: Research on Low NOx Combustor for High-Temperature Gas Turbine, Mitsubishi Heavy Industries Technical Review, Vol. 31, No. 4, p. 243-246 (1994)

(5) Tokyo Electric Power Company: TEPCO Environmental Action Report 2002, p. 113 (2002)

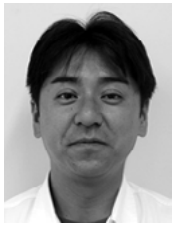
(6) Shinmura, K., Yamaguchi, K., Tsuzuki, S., Kimura, H., Kato, T.: Research of Micro-Gasturbine Generator, HONDA R&D Technical Review, Vol. 15, No. 2, p. 7-16 (2003)

(7) Shinmura, K.: Microturbine Research at HONDA, Presented in 2003 ASME TURBO EXPO Panel session (2003)

■ Authors ■



Atsushi YAMAZAKI



Masatoshi KUROKAWA



Tsutomu INOUE



Hisashi MURAKAMI

Research of High Speed Shaft System Using Air Foil Bearing

Norio SHIMIZU* Mitsuo MATSUSHIMA* Ichiro ISHII*
Hitoshi IWADATE* Hidehiko NAKATA*

ABSTRACT

The demand for a reliable, low maintenance, oil-free micro-gasturbine imposes significant demands on the bearing system. The air foil bearing provides low power loss, adequate damping for supercritical operation and long life with oil-free lubrication. In this application, foil bearings support a 9.2 kg, multi-component rotor operating at 77 000 rpm with a bending critical speed of approximately 42 500 rpm. Stable and reliable operation over full speed range on a shaft system rig and a micro-gasturbine has been demonstrated.

1. Introduction

While the small sized distributed generation is increasingly drawing attention, the micro-gasturbine has some superiority for its economical operation as the generator engine. Because its drive element is restricted to the main shaft, and it has few structural parts. To further increase this functional superiority requires an increased product life span and low level of maintenance. The air foil bearing has been targeted in meeting this demand.

The air foil bearing uses air flow to suspend the shaft thereby enabling rotation without additional mechanical contact support. Consequentially, eliminating the need for a lubrication system and achieving low maintenance due to a longer life are possible. Configuring an air foil bearing to a micro-gasturbine has become a key technology. Although this technology is currently applied to APUs on aircraft, the details of these applications are not made public. The aim of this research is to establish an air foil bearing structure that is capable of achieving a high damping performance, and to configure this to an actual engine to verify its application on a micro-gasturbine.

2. Overview and Targeted Settings

2.1. Micro-gasturbine

Table 1 lists the specifications of a micro-gasturbine for which an air foil bearing is configured. Figure 1 shows the layout of a micro-gasturbine [(1), (2)].

The engine shown in the figure adopts a symmetrical shaft layout in which high temperature components are positioned toward the center of the engine. This serves to suppress heat dissipation and prevent thermal stress. This layout has resulted in a shaft configuration that supports a high pressure compressor and turbine with extreme overhang thereby creating the severest bearing load conditions.

* Wako Research Center

Table 1 Specifications of micro-gasturbine

Items	Specifications
Rated engine speed	77 000 rpm (ISO conditions)
Allowable Max. speed	84 000 rpm
Life	60 000 hrs
Max. generator output	47.8 kW (ISO conditions)
Emissions (CO, HC, NOx)	< 3 ppm
Dimensions (D × L)	ϕ460 mm × 840 mm
Weight	145 kg

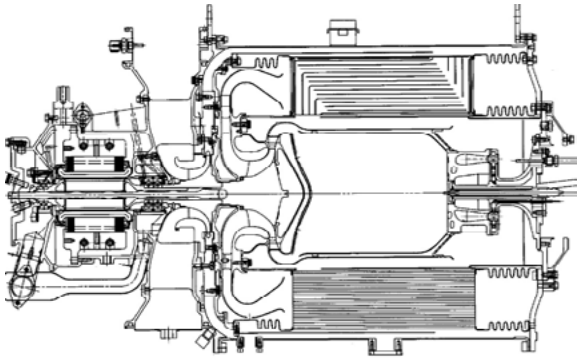


Fig. 1 Layout of micro-gasturbine

2.2. Targeted Settings

The greatest difficulty in applying the air foil bearing is the existence of the 1st bending critical speed on the shaft within the operating range which is caused by the low level of air foil bearing stiffness. Generally, when a low level of shaft stiffness is employed, critical speeds are avoided in low speed ranges. However, this requires a complex shaft structure and does not facilitate smooth substitution with rolling bearing. Consequentially, significant engine layout modifications are required.

In this research, the 1st bending critical speed has been allowed to set within the operating range, and passing through this critical speed at a low vibration level would make it possible to realize an air foil bearing capable of engine operation without making significant changes to the engine layout. Table 2 lists the targeted shaft system values for this engine. The 2nd bending critical speed was set above the maximum permissible engine speed of 84 000 rpm while the permissible amplitude for the bearing when the 1st bending critical speed is exceeded was set to 30 μm according to the cyclic fatigue strength of bump foil (refer to section 2.3.2). The bearing inside diameter was set to 48.8 mm in line with the magnetic rotor outside diameter on the applied engine.

Table 2 Shaft system performance target

Items	Performance target
Rated engine speed	77 000 rpm (ISO conditions)
1st bending critical speed	Above lift up speed & As low as possible
2nd bending critical speed	Above 84 000 rpm
Life	60 000 hrs
Bearing inner diameter	ϕ 48.8 mm

2.3. Air Foil Bearing

2.3.1. Operating principle

Figure 2 shows the operating principle of a typical air bearing with a cylindrical air bearing mechanism. As shown in the figure, the shaft's eccentric edging on the bearing produces tapered gaps. As the shaft rotates, dynamic pressure is generated by the air flow which is pulled in as working fluid to the tapered gaps and causes the shaft to be suspended. However, as dynamic pressure increases due to higher engine speed, the taper position in the bearing moves in the rotating direction. This creates a misalignment between the direction of the shaft weight and the direction of the load generated by dynamic pressure. As the misalignment increases, it becomes impossible to maintain the shaft's suspension. The resultant self-induced vibration, referred to as Whirl Instability, limits the operating range. In order to maintain the tapered gaps, the inner bearing ring must have compliance.

2.3.2. Layout and function

To achieve the required level of compliance, this research has adopted a layout design based on bump foil as shown in Fig. 3. This layout adopts waveform bump foil made of a thin plate of high-strength Ni-Cr alloy (AMS5542) and a cylindrically shaped top foil that is laminated to the bearing surface. The bearing stiffness was set in accordance to the

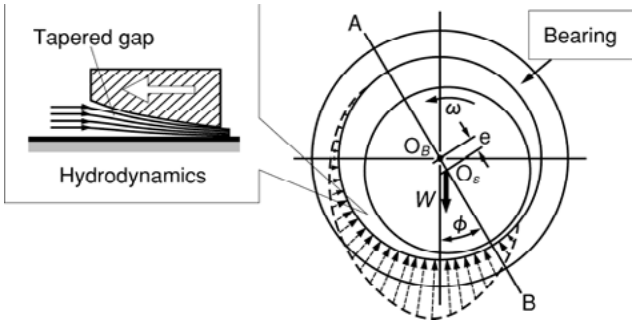
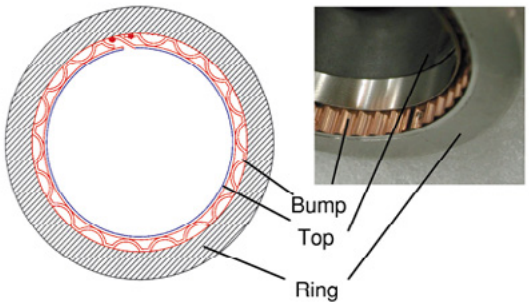


Fig. 2 Mechanism of air bearing[3]



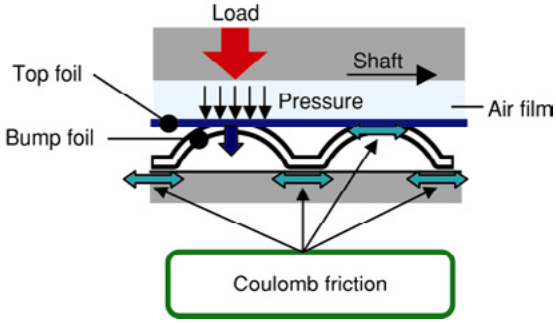


Fig. 3 Compliant foil bearing

bump foil and air film stiffness. The damping performance was set in accordance to the sliding friction (coulomb friction)[4] between the foils. The compliance standard was determined by the foil deformation according to the operating conditions.

2.3.3. Technical issues

As previously stated, the air foil bearing structure has a remarkably low level of shaft support rigidity compared to conventional rolling bearing configurations. Thus, the 1st bending critical speed exists within the operating range. To pass beyond this critical speed, the bearing must be able to accommodate an extremely high level of damping performance, which is also needed to avoid self-induced vibrations that occur at high speed ranges (refer to section 2.3.1). Additionally, in shaft speed ranges from zero to low speed levels (start-up or shutdown), measures must be employed to reduce friction and wear where contact with the shaft cannot be avoided since the formation of air film does not occur.

To suppress the shaft excitation force as the critical speed is being passed, the 1st bending critical speed was set to as low speed as possible within the operating range. This required that the 2nd bending critical speed should be set to levels that exceed the operating range.

3. Air Foil Bearing Structure

3.1. Damping Performance

Damping for the air foil bearing occurs because of the relative sliding friction between foils as shown in Fig. 3. A vibration test was conducted to verify specific areas where damping occurs, to evaluate the effect of the coating on the damping performance and the influence of the overall bearing structure. An excitation apparatus was used to excite a semicircle bearing sample and the damping performance was estimated from the resultant response. Figure 4 shows an overview of the vibration test rig.

3.1.1. Coating effect and identification of damping occurrence area

A coating was applied to the foils to increase the sliding friction and to improve the damping performance between the foils. A Cu coating was selected for its high friction coefficient characteristic, low cost and durability. Figure 5 shows the effects of the coating and the results of identifying the areas where damping occurred.

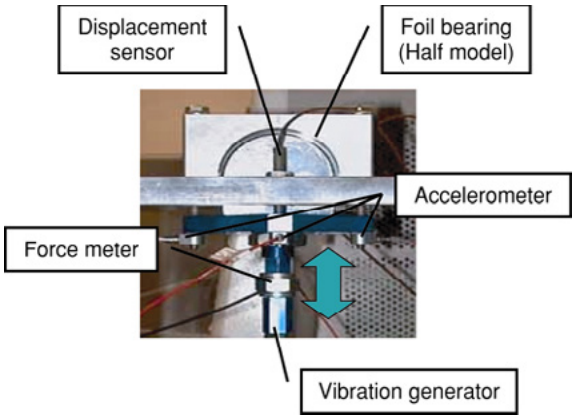


Fig. 4 Vibration test rig

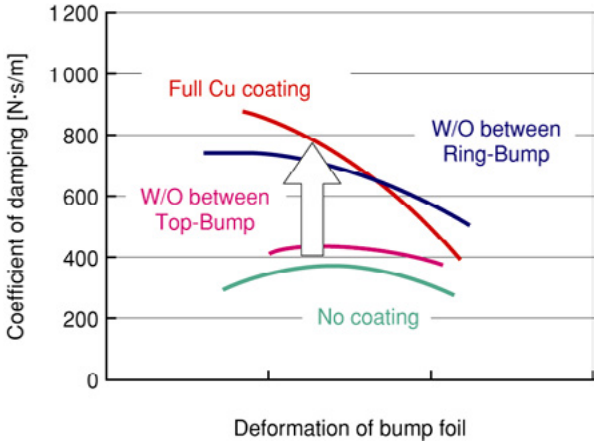


Fig. 5 Effect of Cu coating on damping coefficient

It is clear from this figure that the application of the Cu coating increased the sliding friction, thereby improving damping performance. It was found that when the Cu coating was removed between the bump foil and top foil as compared to the application of Cu coating to all contact surfaces of the foil, damping performance deteriorated to a level with no coating at all. On the contrary, when the coating was removed between the ring and bump foil, no difference in damping performance was observed. This indicates that damping is caused largely from the friction between the top foil and bump foil as the top foil moves. These results were used in support of applying Cu coating to the top and bump foils.

3.1.2. Effects of bearing structure to damping performance

3.1.2.1. Bump foil shape, thickness and separation

Figures 6, 7 and 8 show respectively the effects of the bump foil shape, thickness and separation on damping performance.

Figure 6 shows a comparison of two different bump foil shapes in which almost no significant difference in the damping coefficient was observed. Here, Shape A bump foil was selected because its high damping performance and surface contacts would restrain the top foil from falling between the bump foils when pressurized. This is thought to be effective in forming the tapered shape.

From Fig. 7, a bump foil that is the thickness of 4 mils was selected. Although there was almost no variation in the maximum damping coefficient, the bump foil thickness of 4 mils tended to alleviate the reduction in damping performance in areas where significant bump foil deformations appeared. On the other hand, a bump foil that is the thickness of 3 mils with its reduced level of foil strength had a low load limit.

Figure 8 shows the effect of bump foil separation on damping. A bump foil separation of 13 mm over 2 layers worked best in terms of the maximum damping coefficient. Separating the bump foil reduced the load level to facilitate functional performance. However, there was a remarkable drop in performance in areas with large foil deformation, which caused vibration as critical speed level was being passed. Narrowing the foil width reduced the allowable load limit and caused plastic deformation to the foil, which was of concern. For these reasons it was decided not to employ foils without separation.

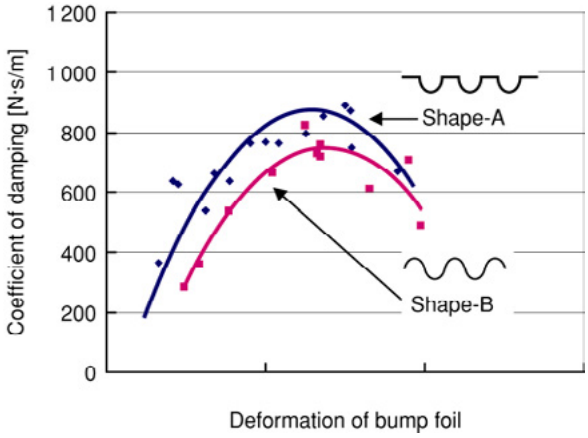


Fig. 6 Effect of bump foil shape on damping coefficient

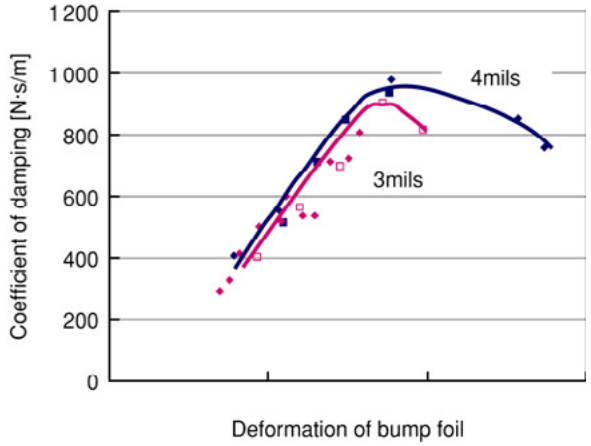


Fig. 7 Effect of bump foil thickness on damping coefficient

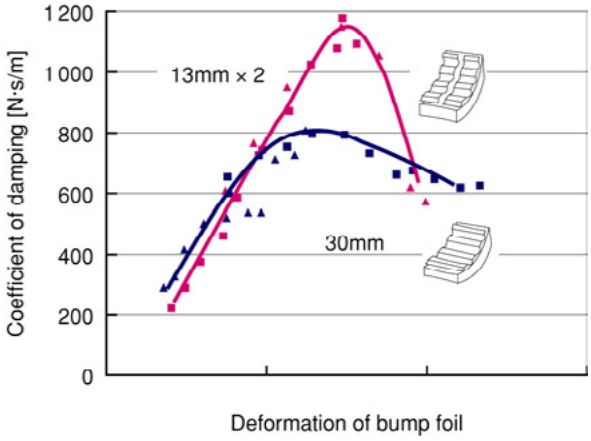


Fig. 8 Effect of bump foil separation on damping coefficient

3.1.2.2. Adding a middle foil

Damping between the top foil and bump foil is a result of movement of the top foil. By adding a middle foil between the foils, an improvement in the damping performance was achieved. Figure 9 shows the changes in the damping performance according to the number of middle foils applied. Increasing the number of foils created a shift of the peak damping coefficient points to the areas where the large foil deformation appeared. Where three middle foils were applied, the damping performance tended to moderately improve along with the foil deformation. In other cases, the damping performance peak was exceeded which led to a drastic reduction in performance. This has shown that the application of three middle foils promotes high damping performance where the greatest vibration occurs as the critical speed level is being passed. Therefore, the three middle foils specification was adopted.

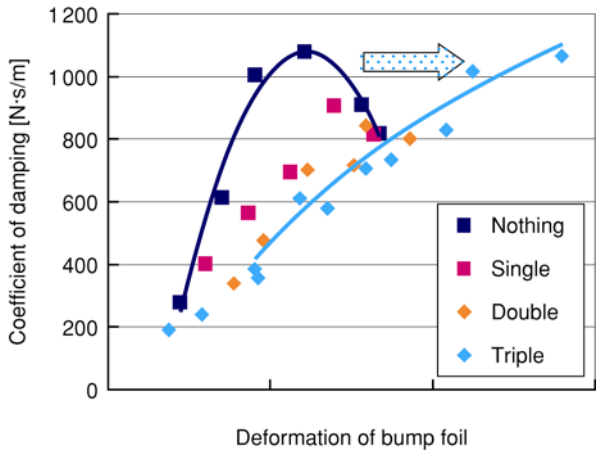


Fig. 9 Effect of multiplex middle foil on damping coefficient

3.2. Selecting a Top Foil Rubbing Coating

In selecting a top foil coating to resist rubbing, low friction and wear resistance were focused on.

Figure 10 shows the results of the rubbing test conducted on coatings. In the test, a rotating shaft was rubbed up against the foil on which a load was exerted and changes to the wear coefficient were measured. The instances where fluctuation was recorded were then used in determining the wear limit. A period of 20 000 seconds (10 seconds × 2 000 cycles) was set as the standard period of wear resistance for the allowable period of continuous rubbing action. A hard coating of DLC (Diamond like carbon) was applied to the shaft and PTFE (fluorocarbon resin) was applied to the foil since this combination satisfied the standard and demonstrated the lowest wear coefficient.

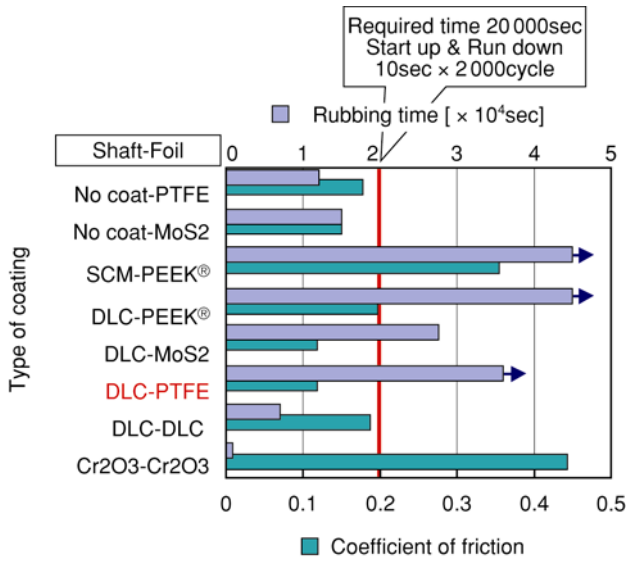


Fig. 10 Results of coating rubbing test

3.3. Air Foil Bearing Specifications

Table 3 and Figs. 11 and 12 provide the air foil bearing specifications and layout design determined from the above test results. The positioning of the shaft support for the air foil bearing provides an extremely efficient level of damping and achieves maximum sliding between the foils. More specifically, the air foil bearings were positioned at the edge of the shaft and the section corresponding to the loop of the 1st shaft bending mode where maximum amplitude is observed (See Fig. 13 for details).

Table 3 Specifications of air foil bearing

Items	Specifications
Bearing inner diameter	ϕ 48.8
Bearing width	30 mm
Top foil	Thickness 4 mils PTFE & Cu coating
Middle foil	Thickness 3 mils 3 pieces
Bump foil	Thickness 4 mils Cu coating 7 pieces
Foil material	AMS 5542

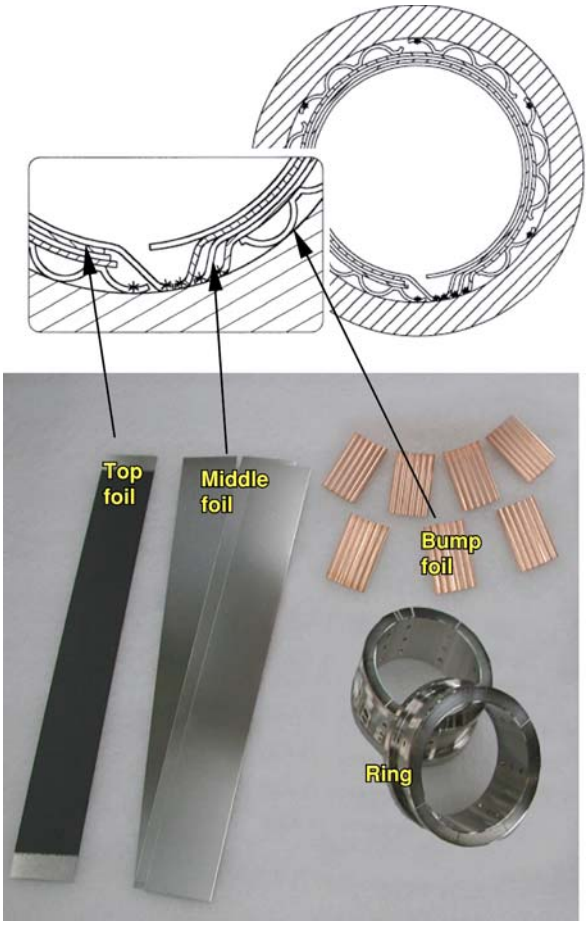


Fig. 11 Air foil bearing (Component)



Fig. 12 Air foil bearing (Cut model)

4. Shaft Structure

4.1. Shaft Structure Applied to Air Foil Bearing

Figure 13 shows the layout of the shaft to which the air foil bearing has been applied. In accordance with the conducted FEM analysis, the engine shaft with air foil bearings was configured with a uniform shaft diameter and an extended shaft length, in contrast to the engine shaft employing rolling bearings. The shaft weight was set to a weighty 9.2 kg. This configuration succeeded in reducing the critical speed to a minimum. Also, since the engine shaft was constructed so that multiple components, including permanent magnet, compressor rotor, and turbine rotor, were firmly tightened by tie shaft tension, a reduction in the stiffness of contact sections between shaft components and the effects of bending caused when the 1st bending critical speed is exceeded had to be taken into consideration. In addressing these issues, an experimental modal analysis was used to determine the optimal shaft layout. Figure 14 shows the critical speed map and the results of this analysis from which a design capable of accommodating the targeted values for each of the critical speeds was achieved.

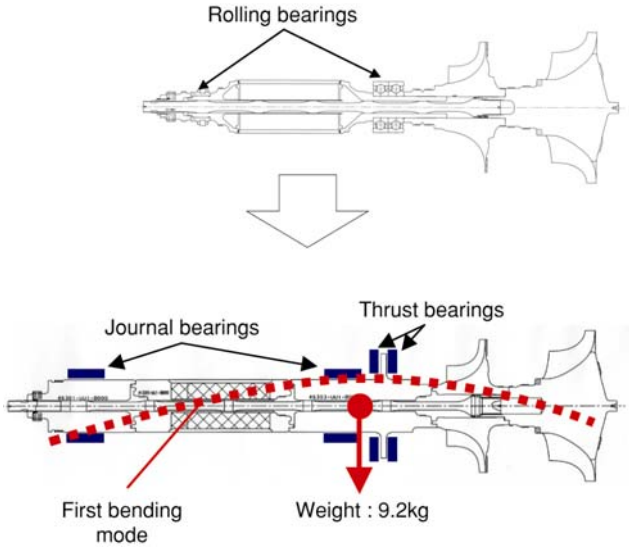


Fig. 13 Multi-component shaft for air foil bearing

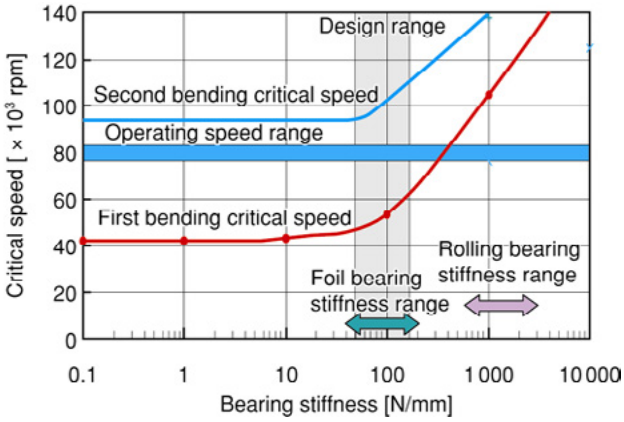


Fig. 14 Critical speed map

5. Unit Testing of Shaft System

5.1. Shaft System Unit Test Stand

A shaft system unit test was conducted to evaluate the air foil bearing performance and the configuration of the shaft itself. Figure 15 shows the shaft system test stand. The shaft is driven by the air turbine mounted on the right end of the shaft. The thrust bearing in the center of the shaft restricts the shaft movement to the shaft direction. During operation, displacement sensors mounted to the shaft components detect shaft displacement, and a thermocouple measures the air foil bearing outer ring temperature, foil temperature and thrust bearing temperature. The load cell mounted on the bearing stand was used to measure the friction torque of the air foil bearing.

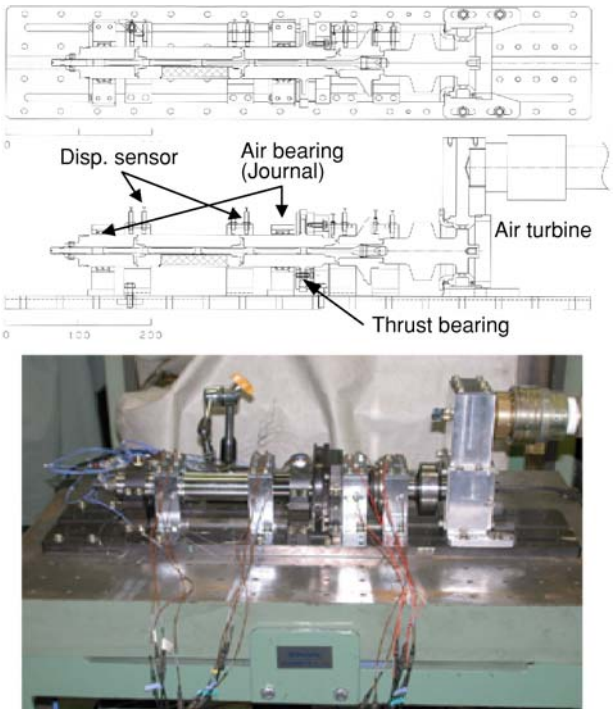


Fig. 15 Shaft system test stand

5.2. Unit Test Results

5.2.1. Speed test results

Figure 16 shows the results of the shaft system test. The graph in the upper part of Fig. 16 shows tracking data which indicates that by improving the damping performance on the air foil bearing, the 1st bending critical speed of the shaft was passed at around 42 500 rpm with a low amplitude level, and a rated speed of 77 000 rpm was attained. The contour diagram shown in the bottom of Fig. 16 indicates that the level of whirl instability induced by the frequency of the shaft's rigid body mode at rated speed was low, and a stable shaft rotation was achieved. The test results shown in Fig. 17 provide the damping ratio required for surpassing the 1st bending critical speed (the damping coefficient being represented by a dimensionless value). Verifying the dynamic characteristics of shaft (including shaft 1st bending critical speed and damping ratio) at speeds lower than the 1st bending critical speed level enabled estimation of the tested bearing performance and amplitude for surpassing the 1st bending critical speed.

Figure 18 shows the effect of the air bearing ring cylindricality and the fitting clearance with the shaft in respect to whirl instability. In order to reduce the level of whirl instability (indicated in the figure by W. I. Amplitude) to less than 4 μm, a cylindricality of less than 65 μm was set as the targeted bearing dimensions (indicated in the blue dots). The fitting clearance was set to −25 ~ 0 μm after taking the startup torque into consideration.

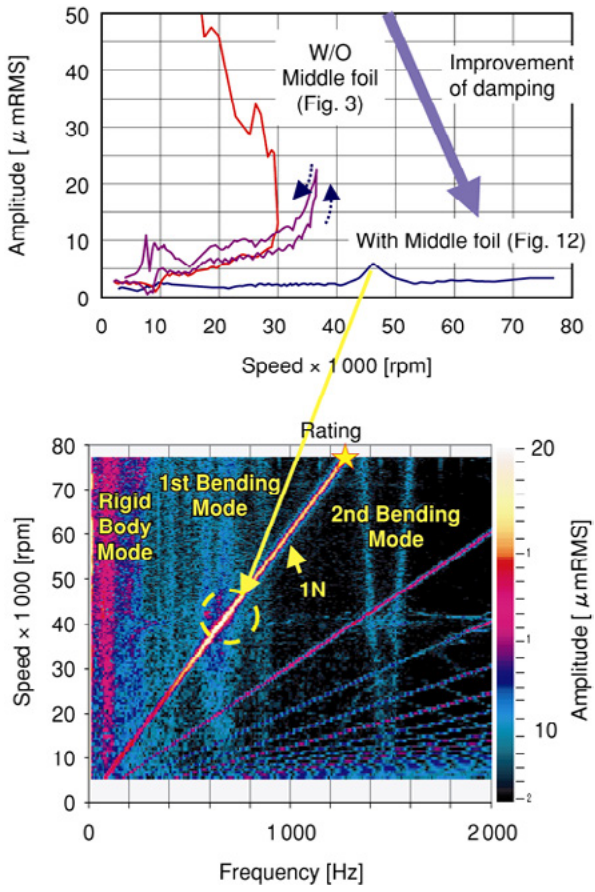


Fig. 16 Shaft system test results

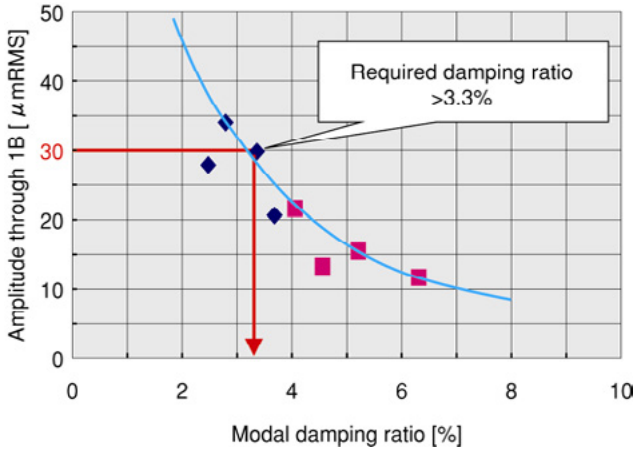


Fig. 17 Required damping ratio

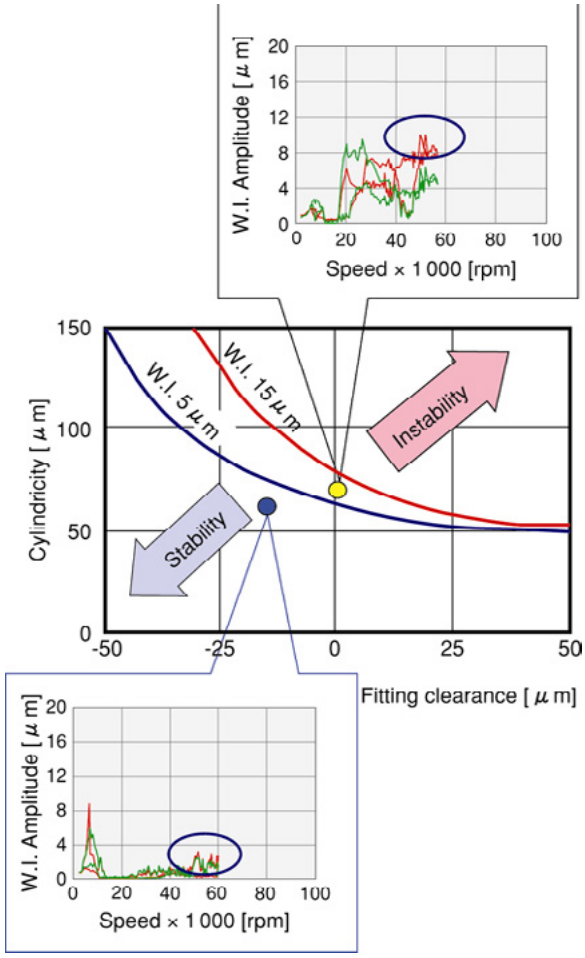


Fig. 18 Whirl Instability toughness

5.2.2. Friction measurement results

Figure 19 shows the friction measurement test results where the bearing loss on the air foil bearings is 0.7 kW at a rated speed of 77 000 rpm. Correlating this loss to a loss of one roller bearing of the rolling bearing specifications has shown that friction can be reduced by employing an air foil bearing. Friction increases when the 1st bending critical speed is passed because the shaft shakes and the air film diminishes. However, since the 1st bending critical speed is passed in an instant and is out of the normal speed range, it has been judged not to present any concern.

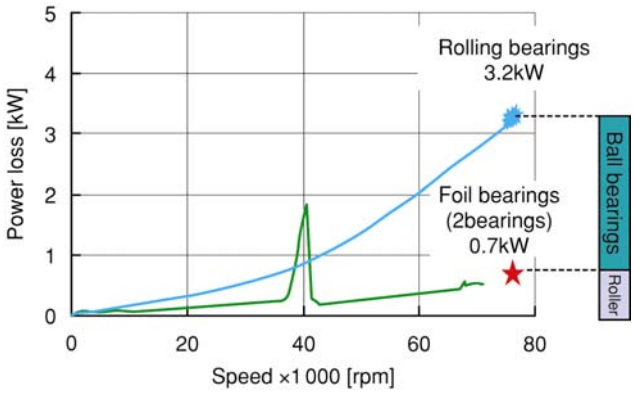


Fig. 19 Comparison of friction for foil and rolling bearings

6. Application to Micro-Gasturbines

6.1. Application to Micro-Gasturbines

In the shaft system test, it has been verified that the shaft's 1st bending critical speed was passed and a stable performance was achieved at high speeds. This has allowed the air foil bearing to be applied to a micro-gasturbine. Figure 20 shows an example of the micro-gasturbine layout.

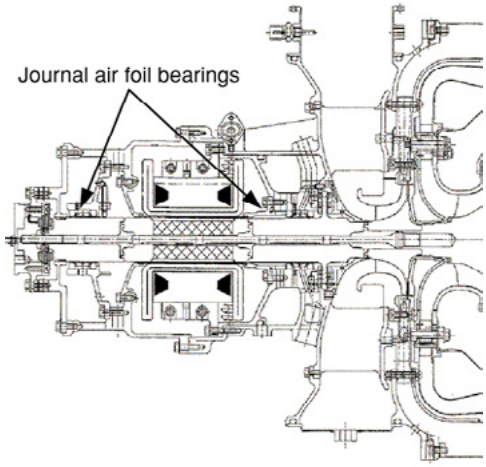


Fig. 20 Micro-gasturbine layout with air foil bearing

6.2. Operating Results of Micro-Gasturbine

Figure 21 shows the measurement results of shaft vibration on the micro-gasturbine. The amplitude where the 1st bending critical speed is surpassed is less than 15 μm and the amplitude at the rated speed is less than 5 μm, indicating that the targeted values have been achieved. In applying an air foil bearing to a micro-gasturbine, there were concerns with the effects to the air bearing performance because of the exciting force brought on by load fluctuation when the permanent magnetic generator is in operation, the exciting force by the aerodynamic element and the overriding effects of heat from high temperature engine parts. Although the test results have shown that the effects of the magnetic force during magnetic generator operation created differences in the surpassing amplitude at speed increases and decreases, this was shown not to be a significant concern.

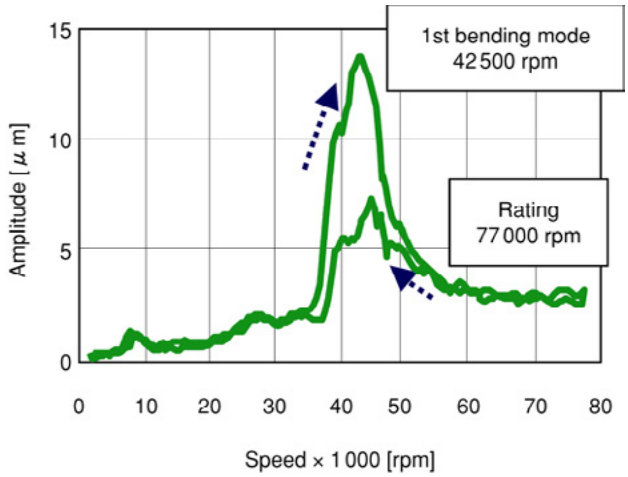


Fig. 21 Shaft vibration of micro-gasturbine

7. Conclusion

In improving the level of maintenance required for the micro-gasturbine, testing was conducted on the shaft system and the air foil bearing from which the following results were achieved.

(1) In the testing of the shaft system in which an air foil bearing of unique configuration was used, it was verified that the 1st bending critical speed that occurs within the operating range of a 9.2 kg shaft with supported overhang was surpassed at a low amplitude with a moderate μm measurement, and stable driving performance was possible at high speeds.

(2) An air foil bearing was fitted to a micro gasturbine engine and a similar performance level to the results of the test was reproduced. This configuration has been successfully verified for adoption in an actual engine.

Acknowledgements

In carrying out this research, the authors would like to extend their deepest appreciation to the individuals, both internal and external, for their invaluable support. Particular acknowledgement is extended to those in the technical testing section for their overwhelming assistance and support in fabricating air bearings.

References

(1) Shinmura, K., Yamaguchi, K., Kimura, H., Tsuzuki, S., Kato, T.: Research of Micro-gasturbine Generator, Honda R&D Technical Review, Vol. 15, No. 2, p. 7-16 (2003)

(2) Shinmura, K.: Micro-gasturbine Research at HONDA, Presented in 2003 ASME TURBO EXPO panel session (2003)

(3) Togo, S.: Gas Bearings design and manufacture, Kyoritsu Shuppan Co., Ltd., P. 195 (1984)

(4) Yamamoto, T., Ishida, Y.: Linear and Nonlinear Rotordynamics, Modern Treatment and Application, Koronasha (2001)

■ Authors ■


Norio SHIMIZU


Mitsuo MATSUSHIMA


Ichiro ISHII


Hitoshi IWADATE


Hidehiko NAKATA

Efficiency and Noise Evaluation of AC Link Soft-switching Inverter

Katsuhiko FURUKAWA* Sadao SHINOHARA*

ABSTRACT

Soft switching inverter technology was examined as a means of increasing the efficiency and reducing the noise of the inverters used to drive motors in hybrid electric vehicles and fuel cell vehicles. From the various soft switching circuit topologies available, AC link inverters were selected as the research focus, because they can be used in high-power applications and require few additional circuit components. Specifically, the single inductor auxiliary resonant AC link inverter was worked out to further reduce the number of inductors. Comparisons with hard switching inverters showed a 0.5% improvement in efficiency. In addition, conduction noise was reduced at almost all frequency bands and radiation noise was reduced at all frequency bands, and demonstrated maximum reductions of 10 dB and 20 dB respectively.

1. Introduction

The demand for reductions in automotive fuel consumption and emissions continues in light of the issue of global warming. Honda has consistently beaten the competition in these areas, with our introduction of the electric vehicle EV PLUS in 1997, with the hybrid vehicles Insight and Civic Hybrid, which combine a gasoline engine and electric motor and were introduced in 1999 and 2001, respectively, and with the FCX, a fuel cell vehicle which rolled out at the end of 2002. The electric motors in these vehicles provide part or all of the driving force. Motor output power is controlled in an inverter, which converts electricity from DC to AC using semiconductor switching devices such as insulated gate bipolar transistors (IGBT). Conversion in the inverter is accomplished by cycling the switching devices between the on and off conditions (switching), but during the transition, the elements are exposed to large currents and voltages; this causes large losses. Other undesirable results of the simultaneous, rapid changes in currents and voltage are surge voltages and electromagnetic noise.

Soft-switching inverter technology is expected to allow reductions in both the losses which occur during switching in semiconductor switching devices (switching losses) and electromagnetic noise. This paper shows the circuit operation of an AC link soft-switching inverter, a new soft-switching inverter topology proposed here, and the results of efficiency and noise compared with those parameters in a hard-switching inverter.

2. Conventional Technology

Inverters are devices which convert DC input into 3-phase AC by continual switching with semiconductor switching devices according to magnetic pole position

* Tochigi R&D Center

(Fig. 1). They are placed between batteries or other DC sources and their loads, the motors. The output power can be controlled by pulse width modulation (PWM) which varies the ratio of on time to off time. The waveforms for voltage V_{ce}, current I_c, and loss, expressed by $V_{ce} \times I_c$, in the semiconductor switching devices in the circuit in Fig. 1, are shown in Fig. 2. This conventional method of switching is called 'hard-switching', in contrast with 'soft-switching'.

Two kinds of losses occur in semiconductor switching devices during switching, conduction loss and switching losses.

Conduction loss is calculated from the product of 2V saturation voltage across the two leads of the switching device, and current, during on condition in which current runs through the semiconductor switching device. Another term for it is 'ON loss'. This loss depends on the materials and structure of the semiconductor switching device and has been reduced with advances in semiconductor technology.

Switching losses occur during the transient conditions while the semiconductor switching device is being changed from on condition to off condition (turn-off), and from off condition to on condition (turn-on).

Both conduction loss and switching losses must be reduced in order to minimize losses in semiconductor switching devices. Reduction of conduction loss is a matter of advances in semiconductor technology. In contrast, switching losses can be decreased by two methods: By reducing the incidence of switching between conductive and off conditions by reducing the switching frequency, and by shortening the time necessary for changing between conditions, so that there is less time of overlap between current and voltage. However, decreasing the switching frequency raises the issue of motor noise when it enters audio frequencies. Also, shortening the switching time increases the rate of change of the current (dI/dt) flowing through the semiconductor switching device; this causes a surge voltage due to wiring inductance, which, in turn, causes a high rate of change of the voltage applied across the semiconductor switching device (dV/dt). This raises the issues of increased conduction noise and radiation noise. If the surge voltage is particularly large and exceeds the withstand voltage, the semiconductor switching device can be destroyed. When semiconductor switching devices with high withstand voltages are used in order to guard against this, the conduction loss is actually augmented, the opposite of the desired solution. A snubber circuit can be used to absorb the surge voltage, but there are losses associated with the consumption of the energy absorbed by the snubber circuit. Thus, there are limits to the reductions attainable in hard-switching.

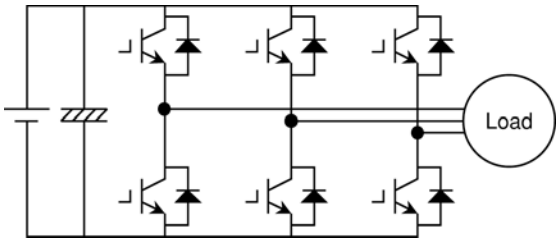


Fig. 1 Inverter circuit

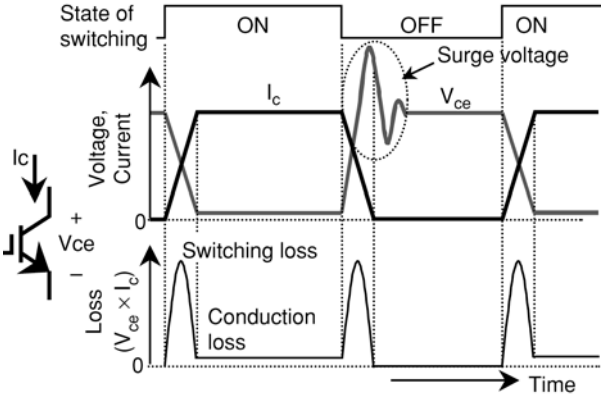


Fig. 2 Voltage, current and loss under hard-switching condition

3. Soft-Switching Technology

3.1. Concepts

Soft-switching technologies have been proposed as a solution for the issues attendant upon reducing the losses in hard-switching. Resonant switches (see Fig. 3) in which inductors (L) and condensors (C) are connected to the semiconductor switching devices moderate the speed of changes of current and voltage at the semiconductor switching devices, for the purpose of switching between the conductive and off conditions while the actual current or voltage is at low or even zero values. As shown in Fig. 4, the current and voltage at the semiconductor switching devices under resonant switches change at lower rates than during hard-switching. This enables reductions in switching losses, since overlap of voltage and current has been reduced. During turn-on, switching is performed while current from the added inductor is flowing into the free wheeling diode connected to the semiconductor switching device. The current and voltage at the semiconductor switching device

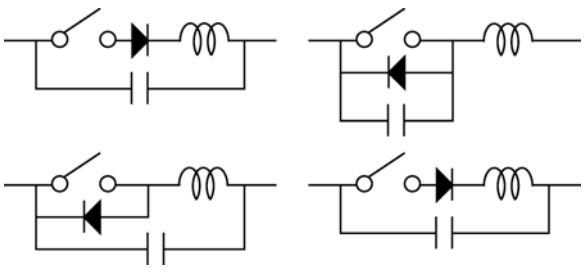


Fig. 3 Resonant switches

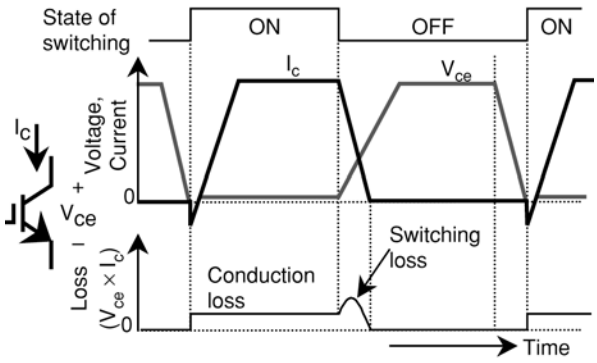


Fig. 4 Voltage, current and loss under soft-switching condition

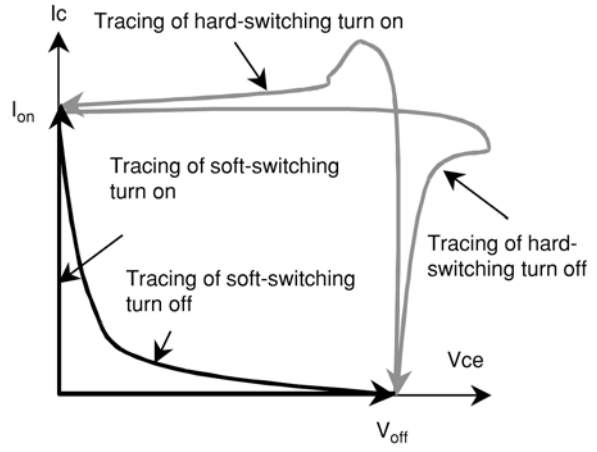


Fig. 5 Lissajous waveform of Ic and Vce

reach zero together, allowing the loss to be eliminated. During turn-off, losses are lessened by the reduction in voltage and current overlap, as the changes in voltage are moderated by the condensor at both ends of the switch. As shown in Fig. 5, the Lissajous waveforms of current and voltage during turn-on and turn-off have come closer to the axes than during hard-switching. It is not possible to completely eliminate losses during turn-off, but it is clear that they are much smaller than during hard-switching.

3.2. Circuit Topology

There are many circuit topologies for reducing losses[1] [2] besides the soft-switching method shown in Fig. 4. One performs switching when the current has been brought to zero at both turn-on and turn-off; another does so when the voltage across not only the semiconductor switching device but also the entire inverter has been brought to zero. Representative examples will be described in this section.

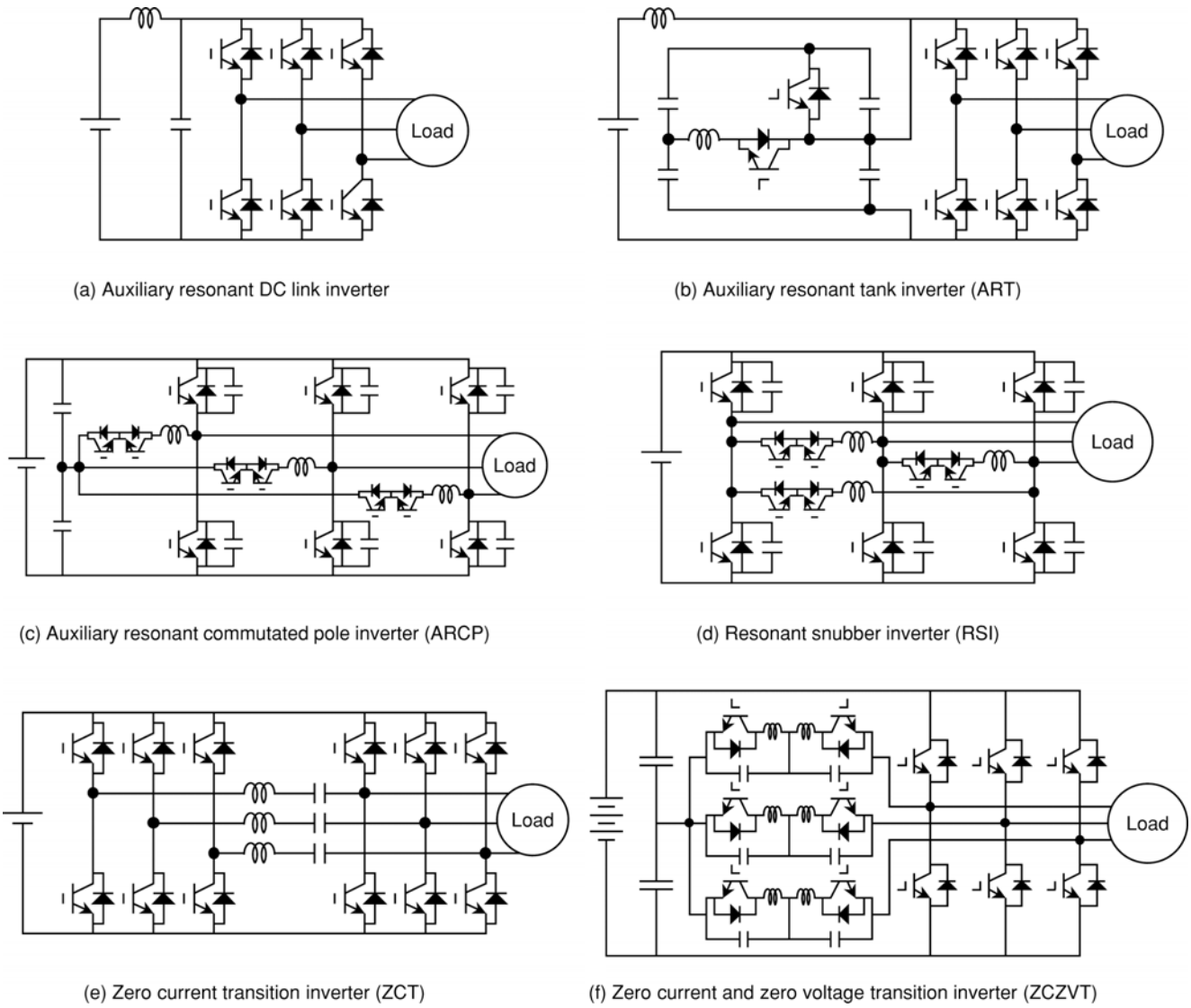
The resonant DC link inverter shown in Fig. 6(a) uses the method of an LC resonant circuit inserted between the power supply and the inverter. The resonant circuit changes the input voltage to the inverter to a sinusoidal shape using the resonant circuit, and switching is done when the voltage across the inverter reaches zero. Switching losses are reduced; however, this circuit is still vulnerable to some issues. The voltage in the resonant circuit depends on the load current and cannot be assumed always to reach zero, and the resonance can increase the voltage to several times that of the power supply. At present, improved versions of this circuit have been proposed. The auxiliary resonant tank (ART) inverter shown in Fig. 6(b) is one of these. The auxiliary resonant circuit is inserted in the DC side of the inverter, and does not produce voltages exceeding that of the power supply. It can reduce the voltage to zero at switching time. A 100 kW class version of this circuit is already being used in the field, as the inverter for the motor drive circuit of an electric bus in the United States[3]. There are many DC link inverters besides the above, including those with a clamp switch inserted between the power supply and the inverter to isolate the inverter and power supply during switching[1] [2], but they are considered better for low-power applications because clamp switches have conduction losses.

In the auxiliary resonant commutated pole (ARCP) inverter, shown in Fig. 6(c), the auxiliary resonant circuits are inserted between the DC and the AC side, in contrast to the DC link inverter described above. Turn-off in this circuit is performed at zero voltage, maintained by condensors on both sides of the semiconductor switching device; during turn-on, current is passed from auxiliary resonant circuits to free wheeling diodes, allowing switching at zero voltage and zero current. The waveforms of voltage and current from this semiconductor switching device are those presented in Fig. 4. Since there are no components between the power supply and the inverter in this circuit, in contrast to the DC link circuit, it is suited to handling high power applications, and it allows separate PWM control of each phase. However, a condensor is necessary to maintain the neutral DC voltage point, and under high power applications, a very large condensor is needed.

The resonant snubber inverter[4] (RSI), shown in Fig. 6(d), has an auxiliary resonant circuit on the AC side. This type does not need the condensor to hold the neutral point required by the previous circuit, and since it has no components on the DC side, it suffers no losses there. It is considered to be suited for high power applications. As in the ARCP inverter, switching is through zero voltage at turn-off, due to condensors, and at turn-on, auxiliary resonant circuits containing free wheeling diodes enable switching through zero current and voltage. However, this circuit does not have the ARCP circuit's capacity for isolated switching of each phase. At least two phases must be switched simultaneously, complicating PWM output during three phase control.

The circuits shown in Figs. 6(a)-(d) all fit into the classification of zero-voltage switching, as they all feature zero voltage potential at both ends of the switching device during switching. In contrast, the zero current transition (ZCT) inverter[5] [6] shown in Fig. 6(e) fits into the classification of zero-current switching. Since no current flows through the semiconductor switching devices during switching in this circuit, switching losses are completely eliminated during both turn-on and turn-off.

Figure 6(f) shows the newest version, soft-switching circuit with the zero current and zero voltage transition (ZCZVT) inverter. This circuit allows switch current and voltage of zero at both turn-on and turn-off[7].



(a) Auxiliary resonant DC link inverter
(b) Auxiliary resonant tank inverter (ART)
(c) Auxiliary resonant commutated pole inverter (ARCP)
(d) Resonant snubber inverter (RSI)
(e) Zero current transition inverter (ZCT)
(f) Zero current and zero voltage transition inverter (ZCZVT)

Fig. 6 Soft-switching inverter circuits

4. Single Inductor Auxiliary Resonant AC Link Inverter

The single inductor auxiliary resonant AC link inverter proposed in this paper is pictured in Fig. 7. This circuit is superior to the RSI in both suitability for high power applications and its small number of auxiliary resonant circuit components. It has just a single inductor. It has the smallest number of components of any AC link inverter.

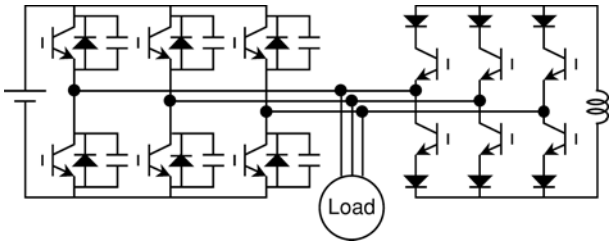


Fig. 7 Single inductor auxiliary resonant AC link inverter

4.1. Principle of Operation

The operation of the single inductor auxiliary resonant AC link inverter will be described using a single-phase circuit. Figure 8 provides the circuit diagram, the designations of the elements, and symbols. The explanation will begin with the circuit as shown in Fig. 10(a), where S_2 and S_3 are on and current is being supplied to the load. Those switches are turned off, transforming the condition to that shown in Fig. 10(e), with continuity through D_1 and D_4; subsequently, the circuit is returned to the condition of Fig. 10(a), completing the cycle. Since the load current flowing through the inductor is nearly constant, it functions as a current source. The on/off signals of the switches and the waveforms at each part are shown in Fig. 9.

Mode 1. Stationary mode 1

In Fig. 10(a), S_2 and S_3 are on and the currents are flowing as indicated at the power supply, S_2, the load, and S_3.

Mode 2. Inductor charging mode 1

As shown in Fig. 10(b), before turning S_2 and S_3 off, auxiliary resonant switches S_{r1} and S_{r4} are turned on and current flow is initiated through resonance inductor L_r. Since the inductance of L_r is set lower than that of the load, the current (I_{Lr}) through L_r increases quickly. S_{r1} and S_{r4} are turned on while the current is zero, so this corresponds to zero-current switching.

Mode 3. Resonant mode 1

Once I_{Lr} reaches a value sufficient to enable charge and discharge of the condensor, S_2 and S_3 are turned off. C_{r2} and C_{r3} are charged by the resonant current, as shown in Fig. 10(c), their voltage rises, and C_{r1} and C_{r4} are discharged, lowering their voltage. Then, S_2 and S_3 are turned off while the voltage is kept at zero; thus, this corresponds to zero-voltage switching.

Mode 4. Inductor discharging mode 1

When the voltages across C_{r1} and C_{r4} reach zero, diodes D_1 and D_4 become conductive, as shown in Fig. 10(d). When semiconductor switching devices S_1 and S_4 are turned on under this condition, the current passing through them is zero and the forward drop voltage is equal to those across D_1 and D_4 ($\fallingdotseq 0$); thus, switching is accomplished at zero current and zero voltage. Since the power supply voltage V_i is applied to L_r in the opposite sense, I_{Lr} falls steadily, and when it reaches zero, the flow of current is stopped by the reverse-current blocking diodes connected to S_{r1} and S_{r2} in series. This establishes stationary mode 2. Also, switches S_{r1} and S_{r4} are turned off after I_{Lr} has reached zero, so that zero-current switching is performed.

Mode 5. Stationary mode 2

Under this condition, the load current runs through the diodes D_1 and D_4, as shown in Fig. 10(e), and S_1 and S_4 are on.

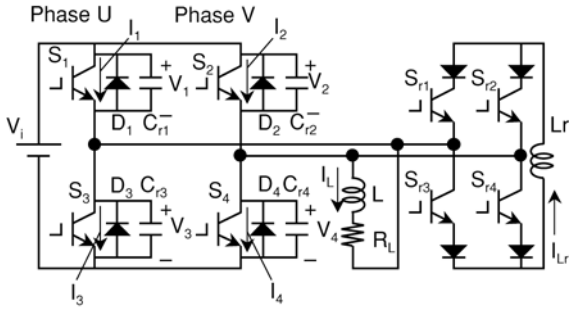


Fig. 8 Single inductor auxiliary resonant AC link inverter two phase circuit

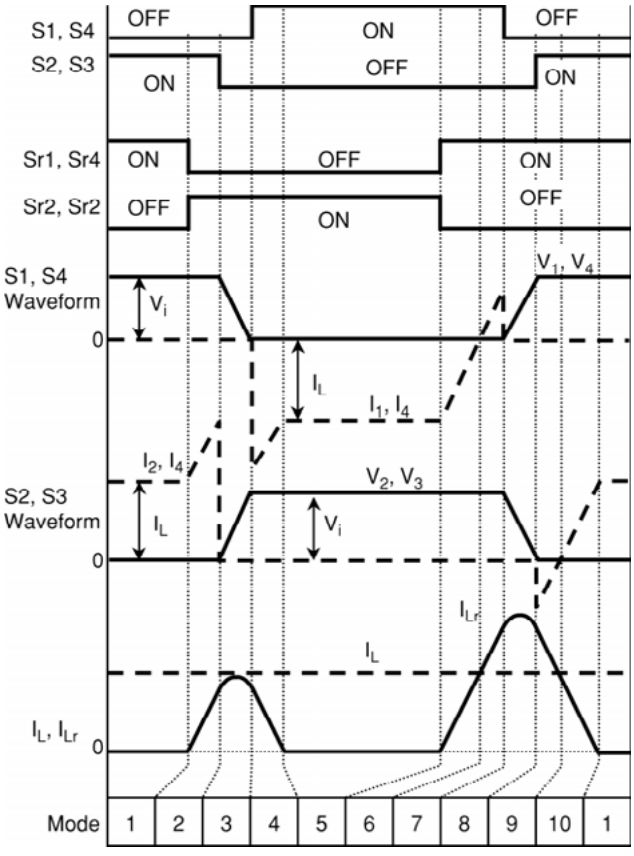


Fig. 9 Single inductor auxiliary resonant AC link inverter waveforms

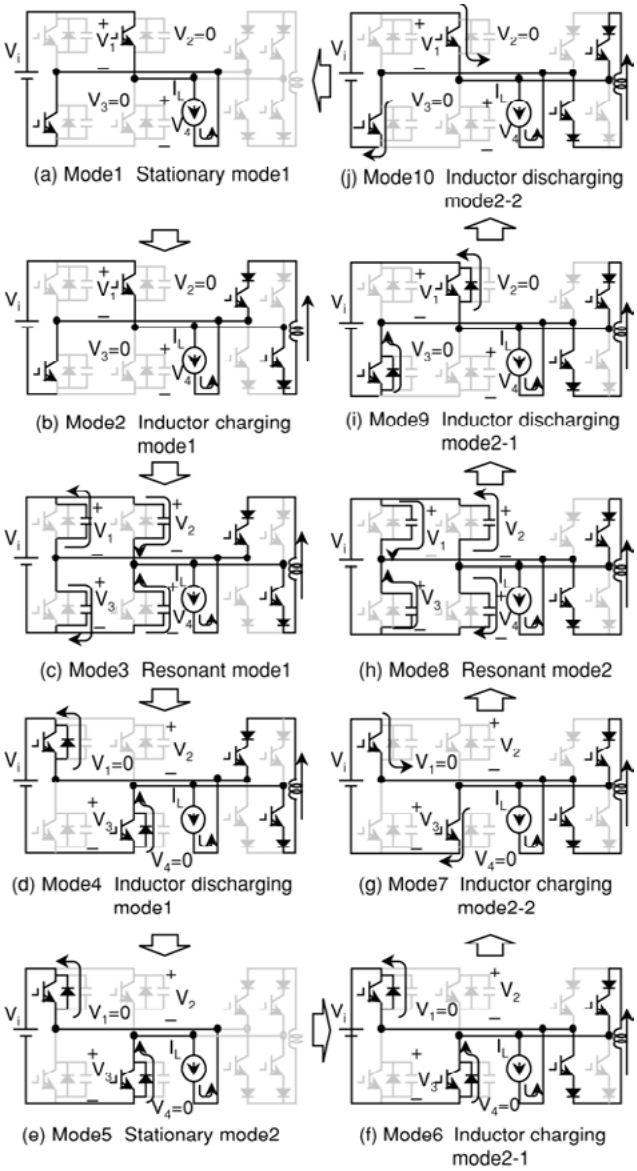


Fig. 10 Single inductor auxiliary resonant AC link inverter switching modes

Mode 6. Inductor charging mode 2-1

When the auxiliary switches S_{r2} and S_{r3} are turned on, the collector potential of S_{r3} is V_i and the emitter potential of S_{r2} is zero, so the current I_{Lr} begins to run in the resonance inductor L_r, as shown in Fig. 10(f). As with S_{r1} and S_{r4} in Mode 2, S_{r2} and S_{r3} can be switched at zero current.

Mode 7. Inductor charging mode 2-2

I_{Lr} increases, and when it exceeds the load current, the current through diodes D_1 and D_4 shown in Fig. 10(g) fall to zero, and a resonance current begins to flow in S_1 and S_4. When I_{Lr} reaches the value sufficient for charge and discharge of the resonance condensors, S_1 and S_4 are turned off and the next mode is reached.

Mode 8. Resonant mode 2

When S_1 and S_4 are turned off, condensors C_{r1} and C_{r4} are charged, as shown in Fig. 10(h), increasing their voltages; meanwhile, the condensors C_{r2} and C_{r3}, connected across S_2 and S_3, are discharged, reducing their voltages. Since S_1 and S_4 are switched while their voltages are held at zero by the condensors across them, this corresponds to zero-voltage switching.

Mode 9. Inductor discharging mode 2-1

As shown in Fig. 10(i), the voltage across C_{r2} and C_{r3} falls, and when it reaches zero, D_2 and D_3 become conductive. S_2 and S_3 can be turned on at this time under conditions of zero current and zero voltage. The resonance inductor is exposed to the reverse of the supply voltage V_i, so the current I_{Lr} begins to decrease.

Mode 10. Inductor discharging mode 2-2

When the currents entering D_2 and D_3 fall to zero due to the decrease of I_{Lr}, current begins to flow through the semiconductor switching devices S_2 and S_3, as shown in Fig. 10(j). Once I_{Lr} drops to zero, it is blocked by the reverse-current blocking diodes and stops flowing, and the circuit reverts to Mode 1. S_{r2} and S_{r3} can be switched on after I_{Lr} is zero, under zero-current conditions.

The above shows the process of soft-switching. From Mode 2, when the load current and resonant current flow in the same direction, through Mode 3, if the current from charging and discharging the condensor is flowing into the load, switching at zero voltage can be performed without activity in the auxiliary resonant circuit. In the following, this control method will be called 'soft-switching with non-resonant operation'.

4.2. Explanation of 3-Phase Operation

In contrast to the ARCP circuit shown in Fig. 6(c), the DC link inverters and some other circuits which allow isolated switching of each phase, soft-switching inverters with auxiliary resonant circuits on the load side such as the RSI shown in Fig. 6(d) and the single inductor auxiliary resonant AC link inverter shown in Fig. 7, cannot supply current to auxiliary resonant circuits unless at least two phases are switched simultaneously. This was shown in Fig. 10. Soft-switching is not possible if only a single phase is switched; the process is then equivalent to hard-switching. Also, when switching is done while all three phases are conductive on either the high side or the low side, it is impossible to supply current to the auxiliary resonant circuit. This places limits on how the conductive and off conditions can be changed. It is easier to consider the method of switching under AC link PWM control if the vector diagram in Fig. 11 is used.

Consider the condition for each phase as 1 when the high side is on and the low side is off, and 0 when the low side is on and the high side is off; the phases are expressed in the order U, V, W from left to right. Then, the complete conduction pattern is as shown by the vectors in Fig. 11. The limitations on the conduction pattern of the AC link inverter are that (1) soft-switching cannot be done when the output conditions are 111 or 000, and (2) because soft-switching requires switching on the high and low sides on at least 2 phases, it is not possible to move directly from one phase on the vector space to a neighboring phase. For example, when the motor is set to the rotor position between vector 100 and vector 110 in Fig. 11, this can be obtained under hard-switching by voltage commands of 100 → 110 → 000. With the AC link inverter, the following conduction pattern is followed: Since it is not possible to reset to a neighboring phase after outputting 100, first, the vector opposite in sense to the desired vector, 001, is output; then, vector 110 is output. As shown in Fig. 12, the same result as with the vector 000 in hard-switching is obtained in soft-switching by outputting 110 and 001 for the same time to cancel each other out.

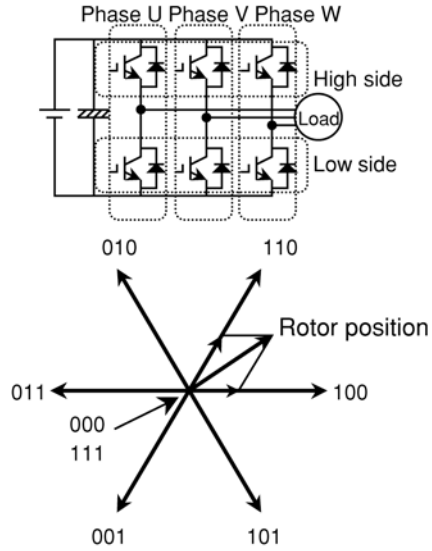


Fig. 11 Command voltage vector diagram

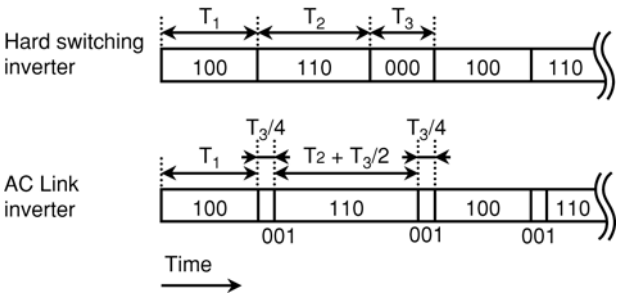


Fig. 12 Comparison of command voltage control

4.3. Experimental Results

4.3.1. Waveforms in each operation

Figure 13 shows the current waveform at the load for the three phases output by the single inductor auxiliary resonant AC link inverter. It is possible to obtain a sine wave of output current using the conduction pattern shown in the lower part of Fig. 12. Also, Fig. 14 shows the waveforms of voltage and current at the semiconductor device during turn-off under hard and soft-switching. Changes in voltage are moderated under soft-switching and surge voltage is suppressed. However, oscillation occurred in the voltage waveform because resonance condensors were attached. It was confirmed that this oscillation could be reduced by attaching the resonance condensors to the semiconductor switching devices with the shortest possible leads. By creating semiconductor modules for soft-switching which include resonance condensors in the semiconductor switching device package, it is expected to be possible to reduce the oscillations. However, since the resonance condensors in this configuration are physically close to the semiconductor switching devices, which emit heat, they must be of a heat-resistant type.

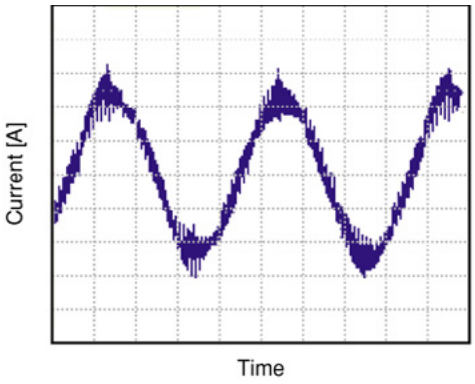


Fig. 13 Load current of 3 phase AC link soft-switching inverter

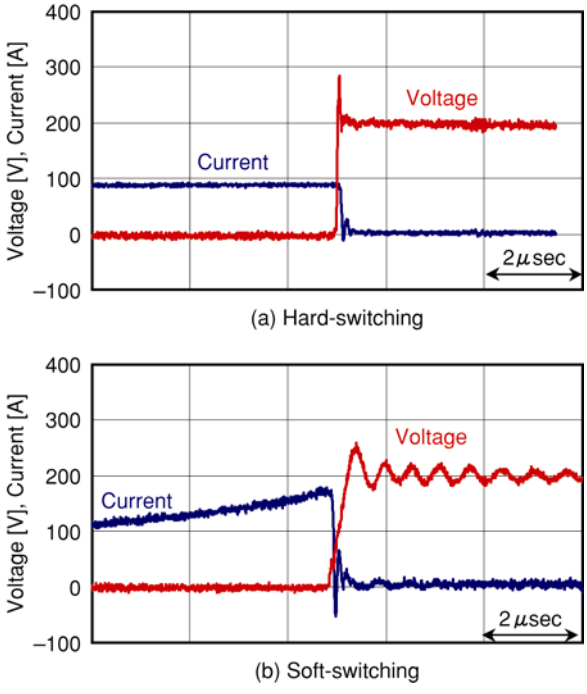


Fig. 14 Voltage and current at turn off

4.3.2. Efficiency

Figure 15 shows the results of measurements of efficiency under hard-switching and the single inductor auxiliary resonant AC link inverter. As in the noise measurements, described below, the hard-switching measurements were taken by removing the resonant circuits from the single inductor auxiliary resonant AC link inverter. First, it was found that soft-switching yielded a higher efficiency than hard-switching in the high load region above 3.2 kW; on the other hand, efficiency was lower than in hard-switching in the low load region. One of the causes of the inferior efficiency is that resonance current is superimposed on the load current, so it appears that conduction losses are higher than in hard-switching. Because of this, the previously described non-resonant operation can be used to expand the range over which efficiency can be improved. Nevertheless, at very low load levels, the load current is too small to charge and discharge the condensors, necessitating operation of auxiliary resonant circuit, so efficiency cannot be improved here.

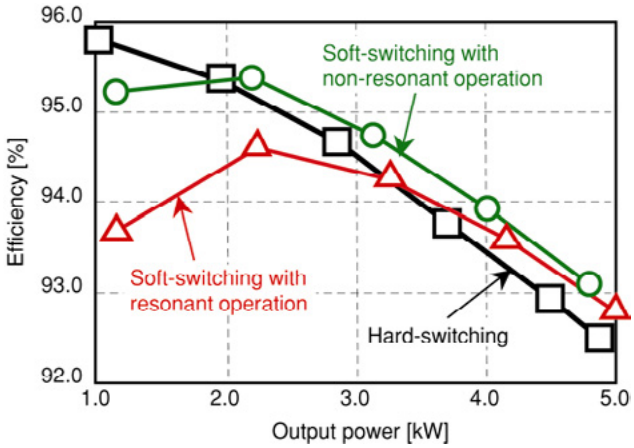


Fig. 15 Comparison of inverter efficiency

4.3.3. Noise

Conduction noise (common mode) was measured using a line impedance stabilization network and radiation noise was measured using an electric field probe. Figure 16 provides the results for measurements of conduction noise. The conduction noise levels under soft-switching with resonant operation was several dB worse than under hard-switching in the several hundred kHz and several MHz bands, but otherwise, noise levels were lower at frequencies up to 30 MHz. The reason for the higher noise was the superimposition of the resonance current on the load current mentioned above, causing higher currents than under hard-switching. This was successfully countered at all frequencies but a small band at several MHz with non-resonant operation. The reason for the persistent noise in this band was oscillation by the resonance condensors attached at both sides of the semiconductor switching

devices, as shown in Fig. 14(b).

Figure 17 shows the results of measurements of radiation noise. As a result of suppression of the rate of change of voltage and current in all the circuit components, the noise levels under soft-switching were lower at all frequency bands under 30 MHz than those under hard-switching. Noise reduction was effective, with a maximum decrease of about 20 dB.

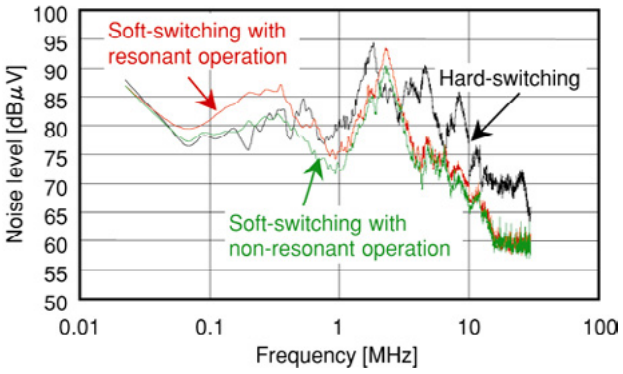


Fig. 16 Conduction noise

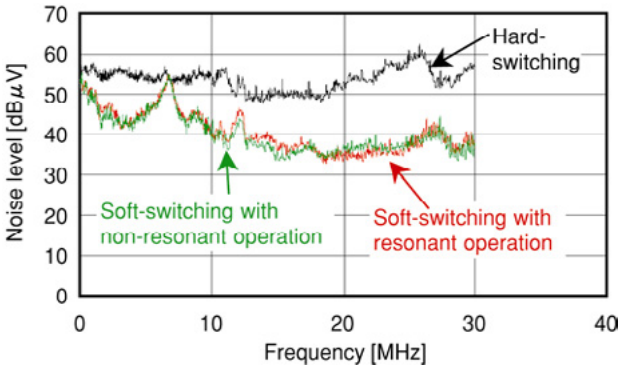


Fig. 17 Radiation noise

5. Conclusion

Efficiency and noise were compared under the single inductor auxiliary resonant AC link inverter and hard-switching and the following results were obtained.

(1) The efficiency under soft-switching was enhanced in the high load region over that under hard-switching, but in the low load region, the efficiency was degraded. Using non-resonant operation allowed improved efficiency throughout the load range when the load current and resonance current flowed in the same direction. An improvement in efficiency of 0.5% over hard-switching was found in the high load range.

(2) Conduction noise was reduced to lower levels under soft-switching than under hard-switching, except for the frequency bands of several hundred kHz and several MHz. Noise was also reduced to levels lower than under hard-switching in the several hundred kHz band by using non-resonant operation.

(3) Radiation noise under soft-switching was reduced at all frequencies below 30 MHz than under hard-switching. The maximum reduction was approx. 20 dB.

Acknowledgments

We would like to extend our deepest appreciation to Prof. Mutsuo Nakaoka, Teaching assistant Eiji Hiraki and Mr. Masanobu Yoshida of the Engineering Dept., Yamaguchi University, for their great assistance in this research.

References

(1) Pickert, V., Johnson, C.M.: Three Phase soft-switching voltage source converters for motor drives. Part1: Overview and Analysis, IEE Proc.-Electr. Power Appl., Vol.146, No.2, March (1999)

(2) Johnson, C.M., Pickert, V.: Three Phase soft-switching voltage source converters for motor drives. Part2: Fundamental limitations and critical assessment, IEE Proc.-Electr. Power Appl., Vol.146, No.2, March (1999)

(3) Fang Z. Peng, Adams, D.J.: An Auxiliary Quasi-Resonant Tank Soft-Switching Inverter, IAS (2000)

(4) Jih-Sheng Lai: Practical Design Methodology of Auxiliary Resonant Snubber Inverters, PESC96, Vol.1, p.432-437 (1996)

(5) Yong Li, Lee, F.C.: Design Considerations for a 50-kW Soft-Transition Inverter with Zero-Current and Near-Zero-Voltage Switching, APEC2001, Vol.2, p.931-937 (2001)

(6) Yong Li, Lee, F.C.: Comparative Study of a Family of Zero-Current-Transition Schemes for Three-Phase Inverter Applications, APEC2001, Vol.2, p.1158-1164 (2001)

(7) Stein, C.M.O., Grundling, H.A., Pinheiro, H., Pinheiro, J.R., Hey, H.L.: Zero-Current and Zero-Voltage Soft-Transition Commutation Cell for PWM Inverters, APEC2002, Vol.1, p.525-531

■ Authors ■





Katsuhiko FURUKAWA Sadao SHINOHARA

Research on Flywheel Batteries

Yoshihiro SUNAGA* Shoei ABE* Yukihiko ITAI**

ABSTRACT

A 100 Wh flywheel battery was fabricated and demonstrated. Research was conducted on the element technologies of the battery, a carbon fiber reinforced plastic (CFRP) rotor and magnetic bearing control, with the following outcomes. Burst tests conducted on the rotor showed that its achieved strength was more than 80% of the theoretical strength. In addition, 25 000 – 50 000 rpm (operating speed range) cyclic stress tests carried out at ordinary temperatures demonstrated that the rotor is durable to 30 000 cycles without fiber breaking or delamination. The digital processing technique of a speed tracking type band-stop filter for automatic balancing control of magnetic bearing was proposed. It was clarified that the stability of conical forward mode decreases by a gyroscopic effect as speed increases. The control method of magnetic bearing providing low-vibration and stable suspension up to the maximum operating speed of 50 000 rpm was established.

The results described above confirm the feasibility of high specific energy and low loss flywheel battery systems.

1. Introduction

Flywheel batteries are also called mechanical (electro mechanical) batteries, and have superior life, environmental temperature characteristics and other features compared to chemical batteries. The principle of storing energy in flywheel batteries is kinetic energy of the spinning rotor, and the stored energy is proportional to the product of the moment of inertia of the flywheel rotor and the square of the rotor speed. This means that given the same mass and volume, more energy can be stored at higher rotor speeds. Increasing the rotor speed is an effective means of increasing the specific energy; therefore, high speed technology is the key to realizing high specific energy flywheel batteries. Most technical themes for flywheel batteries concern increasing speeds such as high strength rotors that can withstand high speeds, and bearings that can suspend high speed rotors with high stability and low friction loss. Except for low speed systems that use steel rotors, high speed flywheel batteries are currently in the development stage. Establishing practical technology, understanding performance, and ensuring durability and reliability are currently the central themes. This paper describes the results of research on high speed rotor and bearing technologies that are vital for realizing a high speed flywheel battery system, and reports the results of system tests using a 100 Wh flywheel battery model fabricated with the aim of realizing a flywheel battery system.

* Tochigi R&D Center
** Wako Research Center

2. Outline of the Flywheel Battery

2.1. System Outline

Figure 1 shows a concept drawing of the flywheel battery system.

The flywheel battery is a mechanical battery that stores kinetic energy in the form of a spinning flywheel rotor, and inputs/outputs electrical energy via an internal motor/generator.

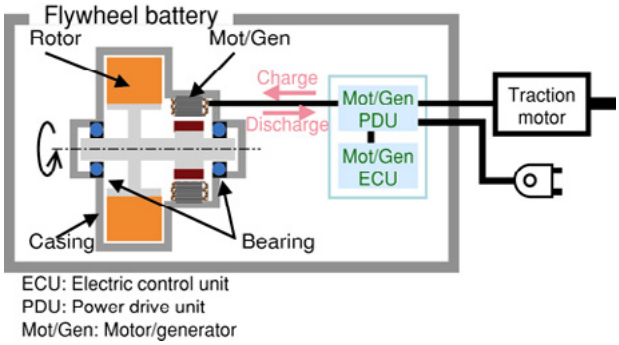


Fig. 1 Outline of flywheel battery system

2.2. Performance Targets

The flywheel battery performance targets were set with the basic concept of the battery for series hybrid vehicles. Table 1 shows the performance targets of the flywheel battery.

Table 1 Performance target of flywheel battery

Max. power (kW)	15 (@25 000 ~ 50 000 rpm)
Max. stored energy (Wh)	333
Max. operating speed (rpm)	50 000
Usable energy (Wh)	250
Operating speed range (rpm)	25 000 ~ 50 000
Total weight (kg)	50

This research aimed to achieve a flywheel battery system that satisfied the performance targets noted above. The primary goal was to realize a flywheel battery system with a usable energy of 100 Wh by shortening the rotor thickness in the axial direction while maintaining the same rotor diameter and rotor speed.

3. Element Technologies of the Flywheel Battery

As shown in Fig. 1, the flywheel battery is composed of the following four main technical elements.

- Rotor which performs the energy storage function
- Motor/generator that performs the charging and discharging (mutual conversion of electrical and kinetic energy) function
- Vacuum housing for reducing windage loss
- Bearings which suspend the high speed flywheel rotor within the vacuum

Research on a high strength rotor and magnetic bearings which are particularly important for realizing a compact and lightweight flywheel battery system is described below.

3.1. Rotor

The specific energy of the rotor is determined by the specific strength which is the value obtained by dividing the tensile strength of the material by the density. Various high specific strength materials were compared, and carbon fiber reinforced plastic (CFRP) was selected as the rotor material. Filament winding was selected as the rotor forming method, and in order to prevent delamination, a press fit multi-ring construction shown in Fig. 2 was adopted. This “high elastic modulus CFRP ring + medium elastic modulus CFRP ring + aluminum ring” construction has different ring densities and elastic moduli in the radial direction[1]. Considering ease of fabrication and testability, a CFRP rotor with a usable energy

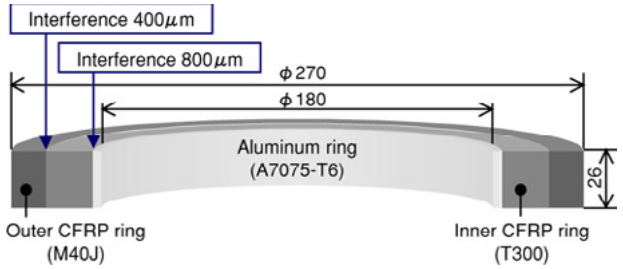


Fig. 2 Press fit multi-ring rotor

of 250 Wh was comprised of five CFRP rings. The 100 Wh flywheel battery model used two CFRP rings.

3.1.1. CFRP rotor stress limit and durability

An important theme for rotor research is ensuring strength and durability. This research set the targets for ensuring performance of the flywheel battery system as follows.

- Designing a CFRP rotor with an initial guaranteed rotor speed of 70 000 rpm (a stress safety factor of 2.0 with respect to the system maximum operating speed of 50 000 rpm)
- Designing the system to prevent overspeed of 50 000 rpm or more

Thus, the rotor research goals were to guarantee the rotor initial performance and durability. In consideration of the fiber strength dispersion, the stress limit of the CFRP rings used for rotor design was assumed to be 70% of the theoretical strength calculated from the fiber tensile strength and the fiber volume fraction (V_f). The rotor was designed so that the hoop stress of the rotor at 70 000 rpm did not exceed this stress limit. In research thus far, rotational tests using the designed and fabricated rotor have verified this speed of 70 000 rpm, and confirmed the following points:

- Stress measurements match the design values.
- The stress limit exceeds 66% of the theoretical strength.

This means that the remaining theme for ensuring performance of the CFRP rotor is to confirm durability. In addition, confirming the stress limit is also important for improving the accuracy of future rotor design. This paper describes the stress limit and durability of the designed and fabricated CFRP rotor.

(1) CFRP rotor stress limit and evaluation method

The theoretical strength of the CFRP rotor (V_f = 60%) is 2.64 GPa for the outer ring which uses the high elastic modulus fiber M40J, and 2.12 GPa for the inner ring which uses the general-purpose fiber T300. Figure 3 shows the relationship between the hoop stress of each CFRP rotor and the rotor speed. The stress reaches the theoretical strength at the rotor speed of 88 600 rpm for the outer ring (M40J fiber) and 92 900 rpm for the inner ring (T300 fiber). The stress limit of an actual CFRP rotor is thought to be lower than the

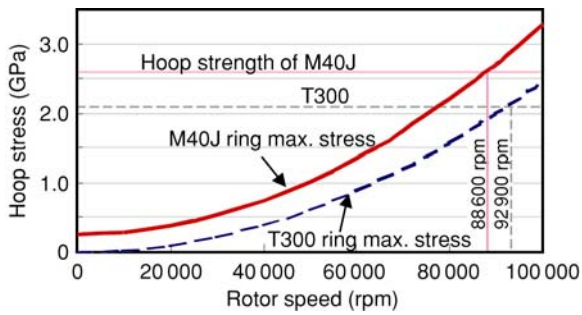


Fig. 3 Hoop stress of CFRP rotor

theoretical strength due to factors such as fiber breaking caused by applying tension during shaping and the contact with the guide rollers, and fiber cutting due to machining.

While there are cases of burst tests having been performed by creating deviations in portions of rotors in order to understand the burst phenomenon of composite material rotors, there are no reports on the evaluation of composite material rotor strength. Strength evaluation of CFRP rotors is important for achieving the optimum rotor design, and understanding the burst phenomenon is also important for ensuring performance with regards to burst. This research entailed conducting CFRP rotor burst tests with the aim of confirming the CFRP rotor stress limit and understanding the burst phenomenon. The stress limit of the CFRP rotor is evaluated from the results of analyzing the burst phenomenon, and the burst speed.

Table 2 Mechanisms and inspections of fatigue

Mechanism	Phenomenon	Nondestructive inspection	Destructive inspection
Breaking of fiber	Deterioration of · Young's modulus · Strength	· Dimension check · Evaluation of diameter during rotation	Burst test
Degradation of resin	Deterioration of strength	· Ultrasonic inspection · Color check · X-ray analysis	
Delamination of layer	Deterioration of strength	———	

(2) CFRP rotor endurance deterioration and inspection method

Like general deterioration, the deterioration of composite materials can be broadly divided into the following two causes.

- Chemical action (corrosion, chemical changes produced by ultraviolet rays or other factors)
- Physical action (fatigue, creep)

The CFRP rotor exists in a vacuum environment, so deterioration due to chemical action can be ignored. Carbon fibers are said to experience almost no fatigue and creep, and numerous test data supporting this have been published[(2)]. However, there are no cases which clearly describe the fatigue mechanisms of the CFRP rotor, and also no reports of research on deterioration due to the centrifugal force of the rotor. Therefore, this research focused on changes in the physical properties of each constituent element of the CFRP rotor, and investigated deterioration phenomena and methods for inspecting deterioration. Table 2 shows the deterioration phenomena and inspection methods. This research employed non-destructive inspection for measurements during the endurance tests, and performed evaluation by measuring the dimensions before and after the endurance test and by ultrasonic inspection after the test.

3.1.2. Evaluation of CFRP rotor stress limit

(1) Rotor for burst test

Figure 4 shows an external view of the rotor used for the burst test.

An aluminum hub (A7075-T6) with spokes was prepared for the burst test, and the CFRP rings were colored white in order to film the burst phenomena. The hub spokes had a tapered shape which became thicker toward the center to alleviate the stress concentration at the spoke joint on the shaft center side. The stress on the spoke joint reached the stress limit for A7075-T6 at a rotor speed of approximately 82 000 rpm, which means that the CFRP rotor strength that

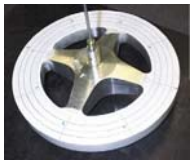


Fig. 4 Rotor for burst test

can be verified at this rotor speed is 85% of the theoretical strength. The burst test was conducted with the test target set as the rotor speed at which hub destruction occurs.

(2) Burst test

Figure 5 shows the transition in test rotor speeds. The test was performed twice, and instantaneous burst occurred at 79 766 rpm (81.1% of CFRP rotor theoretical strength) and 78 507 rpm (78.5% of same). Figure 6 shows a fragment of the burst CFRP rotor. The CFRP rotor shattered into fiber bundles with a maximum length of 80 mm and a maximum width of 3 mm. Based on filmed images of the burst instant and analysis of the destroyed hub, the conclusion was reached that in both cases, hub spoke destruction (originating in the balancing portion of the spoke joint) occurred first, and resulted in bursting of the CFRP rotor.

The fact that burst originated from hub destruction confirmed that the stress limit of the CFRP rings is 80% or more of the theoretical strength. In addition, the burst phenomenon is an instantaneous release of energy, which confirmed the importance of preventing burst.

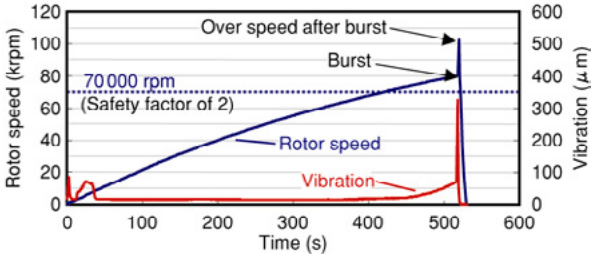


Fig. 5 Burst test of CFRP rotor



Fig. 6 Broken CFRP

3.1.3. Evaluation of CFRP rotor durability

(1) Setting the endurance test conditions

As shown in Fig. 3, the centrifugal force at 50 000 rpm generates stress of approximately 1 GPa on the CFRP rotor. Endurance fatigue was evaluated by repeating this stress. The test pattern was set at a repeated cycle between 25 000 and 50 000 rpm (1 cycle: 25 000 → 50 000 → 25 000 rpm) which produces the maximum stress amplitude in the operation speed range. Cyclic fatigue was assumed to be dependent on the stress amplitude and the number of cycles, and the number of test cycles was calculated based on the charge/discharge pattern of the flywheel battery during cruising modes. The cruising modes used were the 10-15 mode (Japan) and the city mode (US). The number of cycles

when cruising for 100 000 km was approximately 21 500 cycles in 10-15 mode, and approximately 20 500 cycles in city mode. This research set the number of test cycles at 30 000 cycles, and conducted the endurance test at ordinary temperature as the first step in evaluating durability. The test conditions are shown in Table 3.

Table 3 Conditions of cyclic stress test

Speed range (rpm)	25 000 ~ 50 000
Number of cycles	30 000
Spin up/down time (sec/cycle)	60
Vacuum level (Pa)	< 10

(2) Endurance test

Figure 7 shows an external view of the rotor used for the endurance test. The endurance test was conducted for 30 000 cycles under the conditions given in Table 3. The rotor dimensions were measured and ultrasonic inspection was performed every 10 000 cycles, and expansion of the diameter during rotation was also measured before and after the endurance test. Figure 8 shows the dimension measurement results, and Fig. 9 shows the measurement results for expansion of the diameter during rotation. These results can be summarized as follows.

- Measurement of the dimensions of each part showed that the diameter changed by approximately 10 µm after 10 000 cycles but did not change thereafter, and that the change in thickness was 10 µm or less.



Fig. 7 Rotor for cyclic stress test

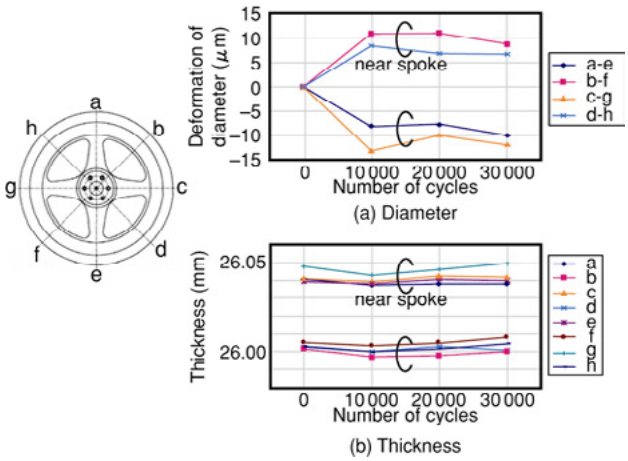


Fig. 8 Inspection of dimensions

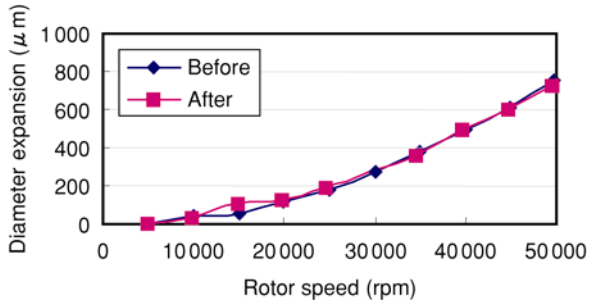


Fig. 9 Evaluation of diameter during rotation

- Ultrasonic inspection did not confirm any delamination around the entire circumference of the rotor.
- Expansion of the diameter during rotation was the same both before and after the endurance test.

The CFRP rotor did not burst during the endurance test. While minute changes occurred in the shape, ultrasonic inspection of the CFRP rotor and measurement of expansion of the diameter during rotation after the endurance test showed that there was no delamination which might indicate deterioration of resin, and no drop in Young's modulus which might indicate fiber cutting. This confirmed that the CFRP rotor has a durability of 30 000 cycles at ordinary temperature.

3.2. Bearings

Requirements for flywheel battery bearings include high speed, low loss, use in a vacuum, and so on. Magnetic bearings that can satisfy these requirements were selected.

3.2.1. Magnetic bearings

Magnetic bearings are non-contact bearings that suspend the rotor by magnetic force. Objects (rigid bodies) have three translational and three rotational degrees of freedom (DOF) for a total of six DOF. The five DOF excluding the rotor spinning motion should be suspended by magnetic bearings. In this system, five DOF active magnetic bearings were adopted. Figure 10 shows a schematic drawing of a general magnetic bearing. Radial magnetic bearings are located in two places in the axial direction, and thrust magnetic bearings are located at the end of the shaft. In addition, non-contact displacement sensors for sensing the rotor motion are located near each electro magnet.

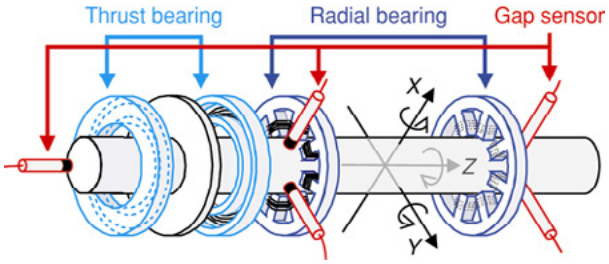


Fig. 10 Schematic of 5 DOF active magnetic bearing

3.2.2. Modeling

The coordinates are as defined in Fig. 11.

This system is a multi-input multi-output (MIMO) (multivariable) system. Here, the state equation for radial magnetic bearings is derived assuming the application of modern control theory which can easily handle a MIMO system and allows systematic design of the control system.

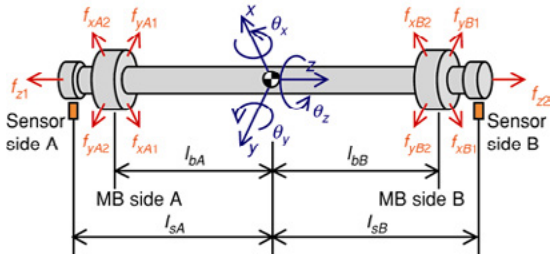


Fig. 11 Definition of Axes

The equation of motion for flywheel rotor in the radial direction is expressed as follows.

$$\begin{cases} m\ddot{x} = (f_{xA2} - f_{xA1}) + (f_{xB2} - f_{xB1}) \\ m\ddot{y} = (f_{yA2} - f_{yA1}) + (f_{yB2} - f_{yB1}) \\ J_d \ddot{\theta}_x = -J_p \omega \dot{\theta}_y + (f_{yA2} - f_{yA1})\, l_{bA} - (f_{yB2} - f_{yB1}) l_{bB} \\ J_d \ddot{\theta}_y = J_p \omega \dot{\theta}_x - (f_{xA2} - f_{xA1})\, l_{bA} + (f_{xB2} - f_{xB1}) l_{bB} \end{cases} \quad (1)$$

Where m is the rotor weight, and J_p, J_d are the moments of inertia around the z axis and the x (y) axis, respectively. Equation (1) is converted to state space form as follows.

$$\frac{d}{dt}\begin{bmatrix} \boldsymbol{x}_g \\ \dot{\boldsymbol{x}}_g \end{bmatrix} = \begin{bmatrix} \boldsymbol{O}_{4\times4} & \boldsymbol{I}_{4\times4} \\ \boldsymbol{O}_{4\times4} & \boldsymbol{A}_{r1} \end{bmatrix}\begin{bmatrix} \boldsymbol{x}_g \\ \dot{\boldsymbol{x}}_g \end{bmatrix} + \begin{bmatrix} \boldsymbol{O}_{4\times4} \\ \boldsymbol{B}_{r1} \end{bmatrix} \boldsymbol{f}_r \quad (2)$$

$$\boldsymbol{x}_g = [x \;\; y \;\; \theta_x \;\; \theta_y]^T$$

$$\boldsymbol{f}_r = [f_{xA2} - f_{xA1} \;\; f_{yA2} - f_{yA1} \;\; f_{xB2} - f_{xB1} \;\; f_{yB2} - f_{yB1}]^T$$

$$\boldsymbol{A}_{r1} = \left[\begin{array}{c:c} \boldsymbol{O}_{2\times2} & \boldsymbol{O}_{2\times2} \\ \hdashline \boldsymbol{O}_{2\times2} & \boldsymbol{A}_{r2} \end{array}\right], \quad \boldsymbol{A}_{r2} = \frac{J_p}{J_d}\omega\begin{bmatrix} 0 & -1 \\ 1 & 0 \end{bmatrix}$$

$$\boldsymbol{B}_{r1} = \begin{bmatrix} \frac{1}{m} & 0 & \frac{1}{m} & 0 \\ 0 & \frac{1}{m} & 0 & \frac{1}{m} \\ 0 & \frac{l_{bA}}{J_d} & 0 & -\frac{l_{bB}}{J_d} \\ -\frac{l_{bA}}{J_d} & 0 & \frac{l_{bB}}{J_d} & 0 \end{bmatrix}$$

The electro magnetic force can be expressed by the following equation.

$$f = \frac{\mu_0 N^2 S}{4}\left(\frac{i}{g}\right)^2 = k\left(\frac{i}{g}\right)^2 \quad (3)$$

Where g is the magnetic bearing clearance, i is the electro magnet coil current, N is the number of electro magnet coil turns, S is the sectional area of the magnet core, and μ_0 is the permeability of free space (= $4\pi \times 10^{-7}$).

Based on equation (2), the linearized force vector $\boldsymbol{f}_r$ can be expressed as follows.

$$\boldsymbol{f}_r = \boldsymbol{C}_{r1}\boldsymbol{x}_{rb} + \boldsymbol{C}_{r2}\boldsymbol{i}_r$$

$$\boldsymbol{i}_r = [i_{xA} \;\; i_{yA} \;\; i_{xB} \;\; i_{yB}]^T \quad (4)$$

$$\boldsymbol{C}_{r1} = diag\left(\left[4k_{rA}\frac{I_{rA}^2}{G_{rbA}^3} \; 4k_{rA}\frac{I_{rA}^2}{G_{rbA}^3} \; 4k_{rB}\frac{I_{rB}^2}{G_{rbB}^3} \; 4k_{rB}\frac{I_{rB}^2}{G_{rbB}^3}\right]\right)$$

$$\boldsymbol{C}_{r2} = -diag\left(\left[4k_{rA}\frac{I_{rA}}{G_{rbA}^2} \; 4k_{rA}\frac{I_{rA}}{G_{rbA}^2} \; 4k_{rB}\frac{I_{rB}}{G_{rbB}^2} \; 4k_{rB}\frac{I_{rB}}{G_{rbB}^2}\right]\right)$$

Where $\boldsymbol{x}_{rb}$ represents the rotor displacement vector, $\boldsymbol{i}_r$ represents the control current vector, G_{rbA} and G_{rbB} are the normal clearance of each magnetic bearing, and I_{rA} and I_{rB} are the bias current of each electro magnet. Using the following relational equation of the control voltage and current,

$$\boldsymbol{e}_r = \boldsymbol{L}_r\frac{d\boldsymbol{i}_r}{dt} + \boldsymbol{R}_r\boldsymbol{i}_r \quad (5)$$

$$\boldsymbol{e}_r = [e_{xA} \;\; e_{yA} \;\; e_{xB} \;\; e_{yB}]^T$$

$$\boldsymbol{L}_r = diag(L_{rA} \;\; L_{rA} \;\; L_{rB} \;\; L_{rB})$$

$$\boldsymbol{R}_r = diag(R_{rA} \;\; R_{rA} \;\; R_{rB} \;\; R_{rB})$$

and the following relational equations,

$$\boldsymbol{x}_{rb} = \begin{bmatrix} x_{bA} \\ y_{bA} \\ x_{bB} \\ y_{bB} \end{bmatrix} = \begin{bmatrix} 1 & 0 & 0 & -l_{bA} \\ 0 & 1 & l_{bA} & 0 \\ 1 & 0 & 0 & l_{bB} \\ 0 & 1 & -l_{bB} & 0 \end{bmatrix}\boldsymbol{x}_g = \boldsymbol{T}_{gb}\,\boldsymbol{x}_g$$

$$\boldsymbol{x}_{rs} = \begin{bmatrix} x_{sA} \\ y_{sA} \\ x_{sB} \\ y_{sB} \end{bmatrix} = \begin{bmatrix} 1 & 0 & 0 & -l_{sA} \\ 0 & 1 & l_{sA} & 0 \\ 1 & 0 & 0 & l_{sB} \\ 0 & 1 & -l_{sB} & 0 \end{bmatrix}\boldsymbol{x}_g = \boldsymbol{T}_{gs}\,\boldsymbol{x}_g \quad (6)$$

where vector $\boldsymbol{x}_{rs}$ represents rotor displacement of each sensor portion, combining equations (2) and (4) results in the following state equation.

$$\frac{d}{dt}\begin{bmatrix} \boldsymbol{x}_{rs} \\ \dot{\boldsymbol{x}}_{rs} \\ \boldsymbol{i}_r \end{bmatrix} = \begin{bmatrix} \boldsymbol{O}_{4\times4} & \boldsymbol{I}_{4\times4} & \boldsymbol{O}_{4\times4} \\ \boldsymbol{T}_{gs}\boldsymbol{B}_{r1}\boldsymbol{C}_{r1}\boldsymbol{T}_{gb}\boldsymbol{T}_{gs}^{-1} & \boldsymbol{T}_{gs}\boldsymbol{A}_{r1}\boldsymbol{T}_{gs}^{-1} & \boldsymbol{T}_{gs}\boldsymbol{B}_{r1}\boldsymbol{C}_{r2} \\ \boldsymbol{O}_{4\times4} & \boldsymbol{O}_{4\times4} & -\boldsymbol{L}_r^{-1}\boldsymbol{R}_r \end{bmatrix}\begin{bmatrix} \boldsymbol{x}_{rs} \\ \dot{\boldsymbol{x}}_{rs} \\ \boldsymbol{i}_r \end{bmatrix} + \begin{bmatrix} \boldsymbol{O}_{4\times4} \\ \boldsymbol{O}_{4\times4} \\ \boldsymbol{L}_r^{-1} \end{bmatrix}\boldsymbol{e}_r \quad (7)$$

3.2.3. Magnetic bearing control

Rotational vibration is an issue for suspending a high speed rotor, and the causes of this vibration can be broadly divided into the following two factors:

- Rotor unbalance
- Resonance

Countermeasures for these factors are described below.

(1) Reduction of unbalanced vibration

A residual unbalance exists in the rotor, and this unbalance produces rotational vibration. Various methods using observers and filters have been proposed to suppress unbalanced vibration[3], and these methods can be broadly divided into the following two types. The first is methods that suspend the rotor around the axis of rotation (geometrical axis) by control force that negates the centrifugal force produced by the unbalance, and the second is methods that suspend the rotor around the principal axis of inertia without generating control force for unbalanced vibration. The latter type is also called automatic balancing (rotation on principal axis of inertia) control.

This research selected automatic balancing control using a band stop filter. The filter eliminates the rotational frequency vibration (unbalanced vibration) from signals and the filtered signals are fed back, so the control forces (stiffness) with respect to the whirling vibration are set to zero. In particular, this research devised a method of digital filter processing so that the center frequency (band stop frequency) tracks the rotor speed. Figure 12 shows the block diagram for this processing. The filter characteristics are varied based on the rotor speed signal. Figure 13 shows the rotational vibration reduction effects due to automatic balancing control using this filter.

(2) Avoiding resonance

Resonance of a rotor suspended by magnetic bearings can be broadly divided into rigid body mode and bending mode. Rigid body mode is produced by the stiffness of the magnetic bearings (spring and damper suspension), and has the two modes of parallel and conical. Bending mode is the so-called bending resonance of the rotor. The issues in rotating are the excitation and instability of these resonance modes, and these factors are the critical speed and gyroscopic effect. The

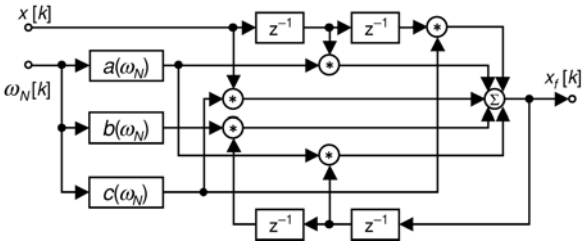


Fig. 12 Block diagram of a speed tracking band stop filter

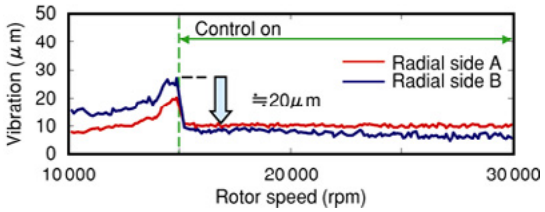


Fig. 13 Effect of automatic balancing control

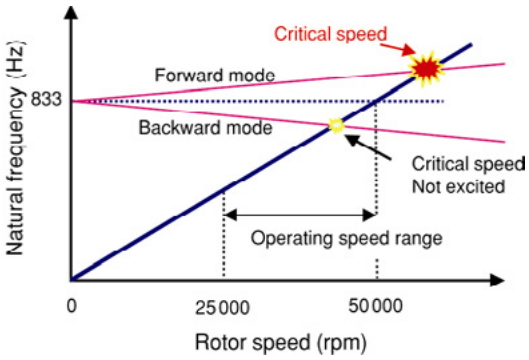


Fig. 14 Gyroscopic effect

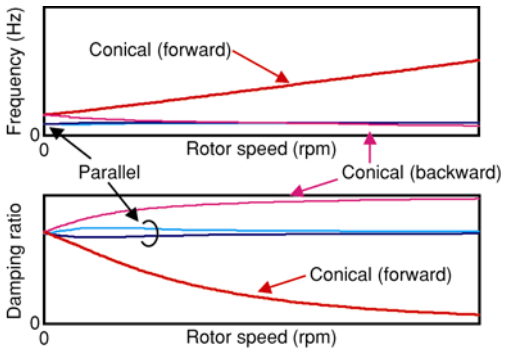


Fig. 15 Rigid mode natural frequencies and damping ratios as a function of rotor speed (closed loop simulation)

critical speed indicates the rotor speed at which resonance is excited by the aforementioned rotor unbalance force, that is to say the rotor speed at which the rotational frequency matches the resonance frequency. The gyroscopic effect is a phenomenon unique to rotors. As shown in equation (1), an interference term due to the gyroscopic effect is present in the first term on the right hand side of the two rotational equations. Due to this effect, each resonance frequency when the rotor is stopped ($\omega = 0$), branches into two high and low frequencies as the rotor speed increases. Figure 14 shows a typical representation of this phenomenon. The modes that change into the high and low frequencies are called the forward and backward modes, respectively. The influence of this gyroscopic effect increases for high speed flywheels which also have a large moment of inertia J_p, resulting in a system where the dynamic characteristics vary relative to the rotor speed.

The critical speed of rigid body mode resonance can basically be traversed by applying damping characteristics through magnetic bearing control. The feedback gain was calculated for a model with a gyroscopic term of zero (non rotating) in equation (7), and the eigenvalue of a closed loop system when controlled by this feedback gain was calculated to evaluate the probability for instability as the rotor speed increases. Figure 15 shows the results, which revealed that the damping ratio for the conical forward mode decreases as the rotor speed increases. In actual control, the effects of the phase lag characteristics of the sensors and filter are also added, so this mode has probability for instability. Therefore, a means for adjusting the feedback gain according to the rotor speed was provided to improve the damping characteristics of conical forward mode (avoidance of instability).

The relationship between the bending resonance and gyroscopic effect of rotors suspended by mechanical bearings and other high stiffness bearings are described in detail in reference (4). Research to traverse the critical speed of bending mode resonance by magnetic bearing control is also being performed, but generally the rotor is stiffened so that the critical speed is not within the operating speed range. This research set the flywheel rotor bending mode frequencies of 833 Hz or more to avoid both the critical speed and instability.

3.2.4. Control system

The controller hardware employs a commercially available rapid prototyping environment based on a digital signal processor (DSP) as shown in Fig. 16, and performs digital magnetic bearing control.

Figure 17 shows the block diagram of a magnetic bearing controller. The controller performs the appropriate filter processing, state vector calculations and feedback gain processing for each sampling signal (displacement, current), and calculates the control commands. The controller based on the optimum regulator provides aforementioned means for adjusting each filter and feedback gain parameter according to the rotor speed.

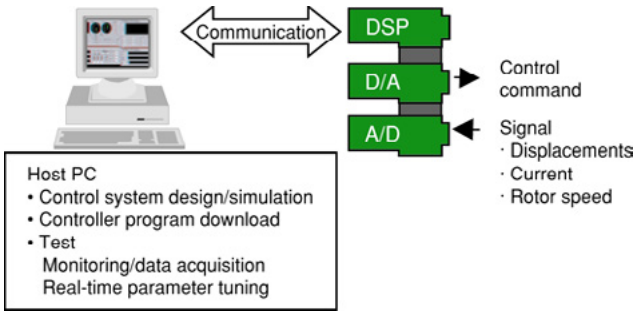


Fig. 16 Rapid prototyping system

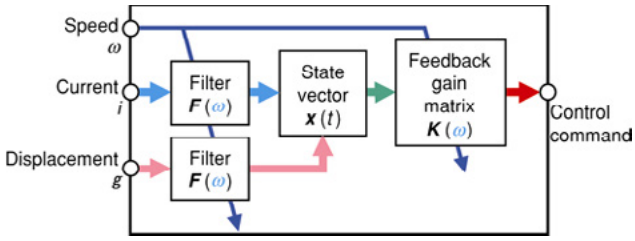


Fig. 17 Block diagram of a magnetic bearing controller

4. Research on a Flywheel Battery System

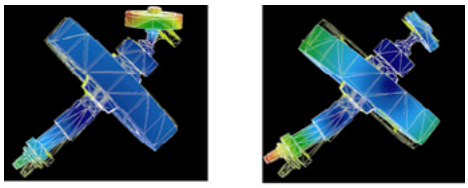
4.1. 100 Wh Model

This section describes research on a flywheel battery system that applies the aforementioned rotor and bearing technologies. A 100 Wh model was fabricated as the first step towards realizing the 250 Wh flywheel battery system. Table 4 lists the main specifications of the 100 Wh model. Compared to the final 250 Wh system that will have a five CFRP ring construction, the 100 Wh model used two CFRP rings.

Figure 18 shows the analysis of eigenvalue problems for the designed flywheel rotor. These results show that the designed flywheel satisfied the bending mode frequencies of 833 Hz or more. Figure 19 shows the 100 Wh model rotor assembly (weight 7.6 kg) and an external view of the entire model.

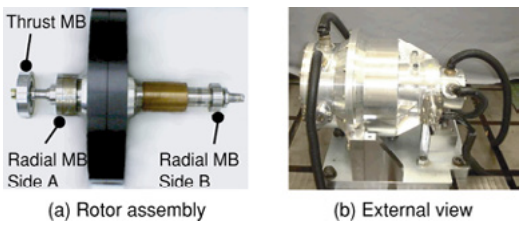
Table 4 Specifications of 100 Wh model

Max. operating speed (rpm)	50 000
Operating speed range (rpm)	25 000 ~ 50 000
Max. power (kW)	15 (@25 000 ~ 50 000 rpm)
Usable energy (Wh)	100 (CFRP ring × 2)
Natural freq. (Hz)	> 833
Bearing type	5 DOF Active magnetic bearing
Mot/Gen type	Brushless DC



(a) 1st mode 872 Hz (b) 2nd mode 1 083 Hz

Fig. 18 Bending mode shapes and frequencies



(a) Rotor assembly (b) External view

Fig. 19 100 Wh model

4.2. Rotational Test

Figures 20, 21 and 22 show the results of rotational tests conducted after setting and adjusting the magnetic bearing control parameters. Figure 20 shows the vibrational amplitude of each part during rotation. The vibration in both the radial and thrust directions has a low amplitude (maximum approximately 20 µm) at all speeds, and stable rotation was achieved up to the full speed of 50 000 rpm. Figure 21 shows the whirling orbit (Sides A and B) of the rotor at 50 000 rpm, and stable rotation could be confirmed here as well. Figure 22 is the FFT analysis results of the rotor vibration during rotation, and shows that there are no resonance or other abnormal vibrations other than the rotor synchronous vibration. There is no instability in the conical forward mode, and appropriate control is performed up to full speed. These rotational test results confirmed the validity of the adopted magnetic bearing control.

Thus, the maximum operating speed of 50 000 rpm was achieved, and storage of usable energy of 100 Wh was verified.

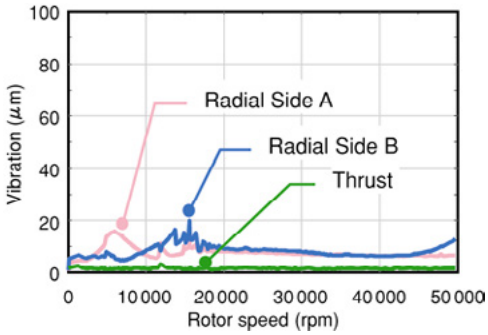


Fig. 20 Synchronous displacement up to full speed

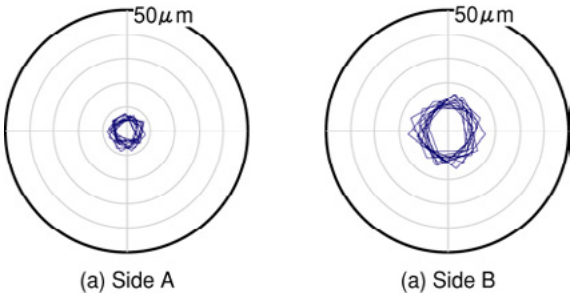


Fig. 21 Whirling orbit @ 50 000 rpm

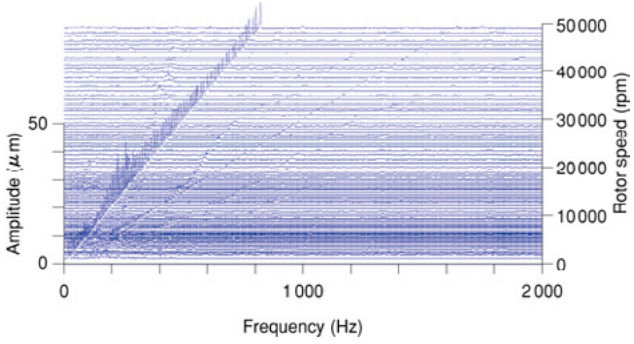


Fig. 22 Waterfall plot

4.3. Charge/Discharge Test

A test was conducted to confirm the charge/discharge performance of the flywheel battery system. Charging and discharging were performed with the drive and regenerative power command for the internal motor/generator control held constant at 7.5 kW. Figure 23 shows the results. Here, charging and discharging were performed for a total of two cycles, with one cycle consisting of charging and discharging from 25 000 rpm to 50 000 rpm. The results confirmed that the basic battery functions of charging and discharging can be performed, and that stable charging and discharging can be repeated, thus verifying compatibility as a battery. The charge/discharge efficiency for a single cycle was 86.3%.

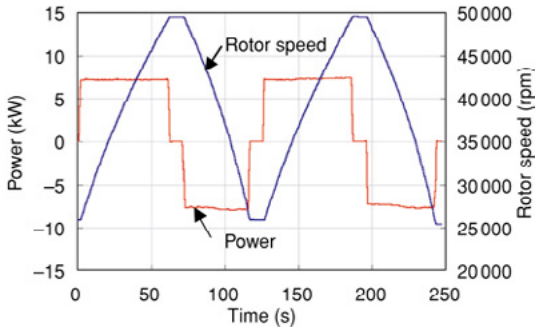


Fig. 23 Results of charge/discharge test

5. Conclusion

Research on carbon fiber composite material rotors and magnetic bearings that are the technical elements of flywheel batteries, and research on a flywheel battery system that applies these results, were carried out with the aim of realizing a 250 Wh flywheel battery system. Burst tests were conducted to evaluate the strength of a designed and fabricated CFRP rotor, and confirmed that the stress limit was 80% or more of the theoretical strength. Cyclic tests were conducted for 30 000 cycles at ordinary temperature within the operating speed range to evaluate the CFRP rotor durability, and confirmed that fiber cutting and delamination did not occur, and that the rotor had sufficient durability. For the magnetic bearings, a rotational speed tracking type digital filter was constructed for automatic balancing control. In addition, the deterioration of conical resonance stability due to the gyroscopic effect was clarified, and a corrective control method was established. A 100 Wh flywheel battery that employs the results of the rotor and magnetic bearings research was fabricated and used to achieve the maximum operating speed of 50 000 rpm, and to verify the charge/discharge functions, thus realizing a 100 Wh flywheel battery system.

The results of this research are thought to indicate the feasibility of high specific energy and low loss flywheel battery systems.

6. Afterword

In the future the authors plan to fabricate a 250 Wh flywheel battery system that applies these research results, and verify the target performance.

Note that part of this research is being conducted in conjunction with the “Research and Development of Advanced Clean Energy Vehicle (ACE)” project led by the Ministry of Economy, Trade and Industry. This project aims to develop vehicles with CO_2 emissions of half or less than existing vehicles by combining petroleum substitute clean energy fuels with hybrid systems, and has been commissioned by the New Energy and Industrial Technology Development Organization (NEDO). A part of this research is the results of research conducted during fiscal years 1999 through 2002[(5), (6), (7), (8)].

Acknowledgements

The authors would like to take this opportunity to express their deepest thanks to all related parties both in-house and at other companies for their generous guidance and cooperation with this research.

References

(1) Kobayashi, H.: Development of CFRP rotor for Flywheel Battery, HONDA R&D Technical Review, Vol. 12, No. 1, p. 85-92 (2000)

(2) Shimamura, S.: Carbon Fibers, Ohmsha, p. 217 (1984)

(3) The Magnetic Levitation Technical Committee of The Institute of Electrical Engineers of Japan: Control System Design Combined with an Observer, Magnetic Suspension Technology - Magnetic Levitation Systems and Magnetic Bearings -, Corona Publishing, p.203-210 (1993)

(4) The Japan Society of Mechanical Engineers: JSME Mechanical Engineers’ Handbook, New Edition, A3, p. 153-173 (1987)

(5) New Energy and Industrial Technology Development Organization (NEDO): Koukouritsu Clean Energy Jidousha no Kenkyu Kaihatsu Seika Houkokusho (2000) (in Japanese)

(6) New Energy and Industrial Technology Development Organization (NEDO): Koukouritsu Clean Energy Jidousha no Kenkyu Kaihatsu Seika Houkokusho (2001) (in Japanese)

(7) New Energy and Industrial Technology Development Organization (NEDO): Koukouritsu Clean Energy Jidousha no Kenkyu Kaihatsu Seika Houkokusho (2002) (in Japanese)

(8) New Energy and Industrial Technology Development Organization (NEDO): Koukouritsu Clean Energy Jidousha no Kenkyu Kaihatsu Seika Houkokusho (2003) (in Japanese)

■ Authors ■


Yoshihiro SUNAGA


Shoei ABE


Yukihiko ITAI

Theoretical Consideration to Improve Engine Cooling and Application of Coupling 3D Combustion Simulations with Heat Transfer in Water Jacket and Components

Jun XIN* Stephen SHIH* Edwin ITANO*
Yoshio MAEDA** Michio KAWAMOTO** Yoshio YAMAMOTO*

ABSTRACT

Improving engine cycle thermal efficiency is an effective way to increase engine torque and to reduce fuel consumption simultaneously. However, the extent of the improvement is limited by engine knock, which is more evident at low engine speeds when combustion flame propagation is relatively slow. In this paper, computational fluid dynamics (CFD) tools were applied to evaluate the potential for improvement of a V6 engine, and the effectiveness of various engine water jacket design concepts by judging surface heat transfer coefficient under isothermal conditions. Theoretical considerations were given to optimize the cooling efficiency. Subsequently, engine performance tests were carried out on a base engine and a prototype engine, and an improvement of engine output and fuel economy was confirmed. Furthermore, a new CFD methodology was developed in which an iterative coupling approach was taken to include the combustion chamber, water jacket, and solid components. Component temperatures were predicted explicitly and compared with measurement results.

1. Introduction

As the US light duty truck market (SUV, SUT, etc.) continues to grow, it is important to increase low engine speed torque for better vehicle dynamic performance. Improving the engine gas exchange process is a critical area to accomplish this goal. Higher volumetric efficiency usually demands anti-knock measures to take full advantage of the improved gas exchange. At the same time, it is imperative to reduce vehicle fuel consumption to help curb global warming. Improving engine cycle thermal efficiency is an effective way to achieve higher engine output and lower fuel consumption simultaneously. However, the extent of the improvement is limited by engine knock. Improving the overall level of knock resistance and uniformity of all cylinders of a multi-cylinder engine is necessary to increase thermal efficiency.

In the next section, theoretical considerations to provide uniform and effective cooling for multi-cylinder engines are explained. In this study, several design concepts were proposed, their effects on cooling performance were analyzed, and design parameters were assessed and optimized by means of CFD simulations. After design concepts were optimized with respect to heat transfer coefficient from isothermal CFD simulations, one design was tested, and the most significant test results are presented in this paper.

Then, in order to quantitatively evaluate effects of design

* Honda R&D Americas, Inc.
** Tochigi R&D Center

concepts on combustion chamber wall temperature, and subsequently on volumetric efficiency and combustion, a newly developed methodology is described that couples in-cylinder flow and combustion with convection and conduction in the water jacket and solid components such as the cylinder head and block. Procedures and calculation results from the applications are depicted. The major advantage over the isothermal water jacket analysis is that interactions among combustion, component temperatures, and the coolant flow pattern in the water jacket can be simulated directly.

2. Basic Considerations and Design Concepts of Engine Water Jacket

To address the constant increase of engine output density and environmental concerns, the water jacket of a multi-cylinder spark ignition engine needs to meet four functional requirements. First of all, the water jacket must provide adequate cooling capability to engine components in order to keep component temperatures below maximum levels. Secondly, it helps to reduce the temperature difference among cylinders so that all cylinders operate at optimal conditions. Thirdly, it is desired to arrange flow pattern so that the temperature gradient in both circumferential and cylinder axial directions is reduced. Lastly, the water jacket should have low thermal capacity so that engine warm-up can be shortened.

Nowadays, three-dimensional CFD calculations have been routinely applied in engine water jacket design and optimization[1), 2)]. The addition of conjugate heat transfer capability in most commercial CFD packages enables designers to evaluate water jacket and component temperature together. For the purpose of analyzing cooling efficiency and uniformity of the water jacket among individual cylinders, isothermal coolant flow analysis is adequate to provide a reliable indication with respect to relative cooling differences among cylinders as well as among water jacket designs. Therefore, in this paper, isothermal calculations were applied to quickly evaluate coolant flow patterns and optimize design parameters. After an optimized design was identified, coupling analysis followed so that wall temperatures and component temperatures could be determined to judge the benefit on knock toughness and durability concerns.

In the coupling analysis, in-cylinder flow and combustion calculations were coupled with flow and heat transfer calculations in the water jacket, as well as heat conduction in components, which is described in detail in the next section.

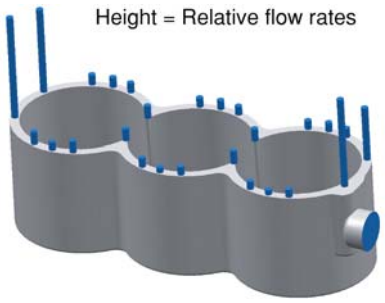


Fig. 1 Flow rate distribution through the gasket holes of the base design

A general CFD package, STAR-CD, was used in isothermal fluid calculations. For isothermal flow analysis, only the governing equations of continuity, momentum and k-ε turbulence model were solved. For simplicity, only one bank of a V6 engine water jacket was modeled. A flow rate imposed on the inlet boundary corresponded to an engine operating condition of 3 000 rpm. Figure 1 illustrates coolant mass flow rates through each gasket hole of a baseline V6 engine. The height of bars represents normalized flow rate through individual gasket holes. In the baseline, coolant flows through the engine block and cylinder head in a parallel fashion. Due to that design concept, it is necessary to have two large gasket holes on the opposite end from the water pump inlet to maintain a certain level of coolant velocity in the top portion of liners. It is apparent that most coolant enters the head from the front and rear end holes. In the base engine design, about 35% coolant flow enters the cylinder head from the two rear gasket holes. This 35% flow is for block cooling only, and not utilized for cylinder head cooling. The combustion chamber of the first cylinder gets about 30% coolant flow rate.

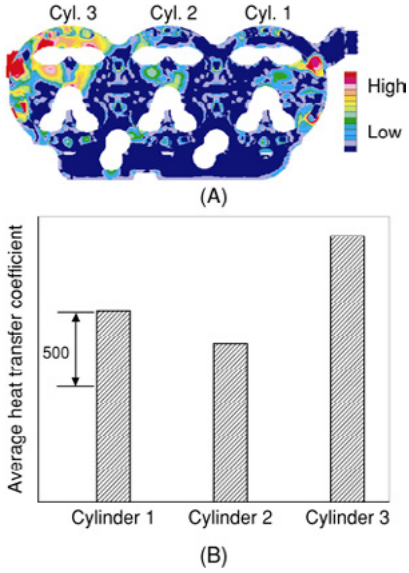


Fig. 2 Distribution of heat transfer coefficient

Heat transfer coefficient (HTC) distribution on the water jacket surface is shown in Fig. 2A. Heat transfer coefficient is a good indicator to evaluate local heat removal capability. Ideally, each cylinder in a multi-cylinder engine will have similar cooling capability, and the heat removal capability will match the thermal loading on the combustion chamber from the burnt gas. Figure 2A indicates that the base design does not achieve a relatively uniform spatial HTC distribution; the middle cylinder has the lowest cooling, and the third cylinder has the highest HTC. This is due to the high coolant flow rate in the area around the third cylinder, where the coolant flow through the gasket holes merges. These CFD results indicate that there is some room for even better performance, and such improvement will be necessary whenever there is substantial increase of engine volumetric efficiency and/or compression ratio.

Figure 2B presents the area-averaged HTC value for the head water jacket surface of each cylinder. The HTC of the middle cylinder is 25% lower than that of cylinder 3. From the CFD simulation results of the baseline V6 engine, it is evident that both fuel economy and low speed torque increase can be achieved simultaneously by improving uniformity of engine cooling capability among individual cylinders and increasing overall cooling capability to meet the demand for higher low speed torque density. It should be mentioned that the baseline V6 engine's water jacket was adequately designed to provide necessary cooling capacity to maintain component temperatures and knock toughness according to the strict design standard, and was confirmed by engine and vehicle tests. Also, the number of parts and the manufacturability and commonality of parts should be considered to provide the best value to the customer. For instance, in the baseline engine design, the head gaskets for the front and rear banks are the same.

In the new design, a serial cooling concept was proposed[3]. The first measure taken was to apply a block partition so that most of the coolant flows through the entire cylinder block from the exhaust side to the intake side before entering the water jacket in the cylinder head, as shown in Fig. 3A. To accommodate this design idea, the hole pattern of the head gasket changed, as illustrated in Fig. 3B. Two holes at the rear end in the base V6 engine gasket were eliminated. Coolant flow rate in the engine block and head was expected to increase significantly, and top liner regions were expected to be properly cooled. The total area of gasket holes on the intake side was reduced to ensure that more coolant flowed through all combustion domes in the cylinder head. To further increase HTC level on the combustion domes, ribs were added to the top surface of the water jacket in the new cylinder head as illustrated in Fig. 3C.

Figure 4 illustrates the coolant flow path in the water jacket after adopting the features described in Fig. 3. The comparison of HTC distribution of the base and new cylinder head water jackets is given in Fig. 5A, with the shown surface viewed from the combustion chamber. It is obvious that the HTC of the new design is much higher everywhere. In comparison to the base engine design, the spatial HTC distribution is more uniform. Area-averaged HTC values for individual cylinders are shown in Fig. 5B. The HTC of the middle cylinder increases by almost 75%. With respect to the trend, the HTC values gradually increase from the upstream to the down stream cylinders as coolant temperature rises. The HTC distribution of the engine block is compared in Fig. 5C between the base V6 engine and a new V6 engine.

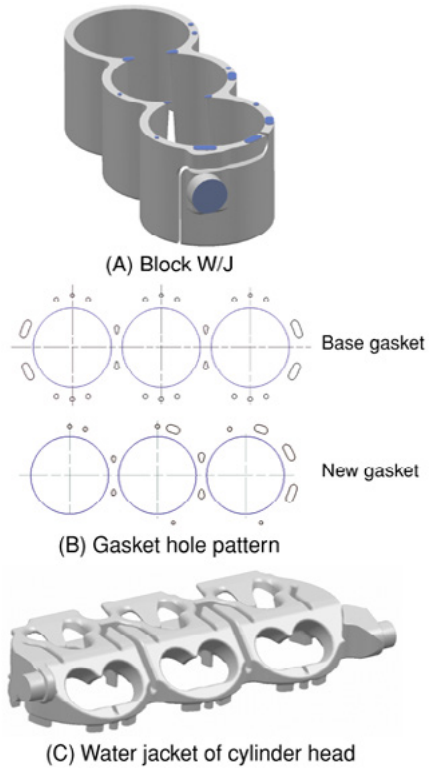


Fig. 3 Modifications to engine components for an optimized water jacket design

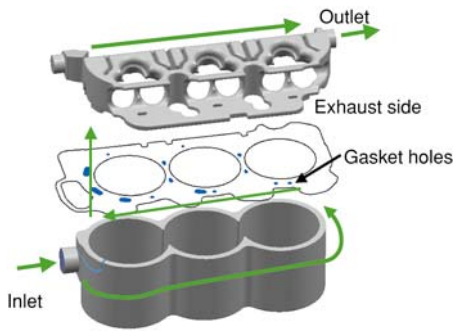


Fig. 4 Overall coolant flow path in the new water jacket

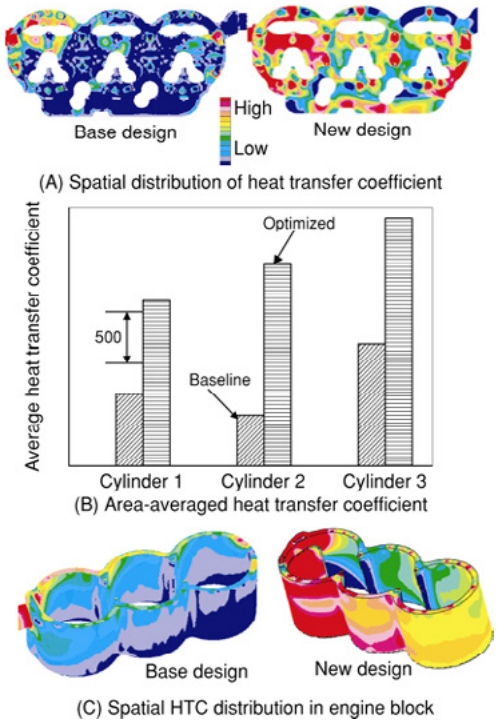


Fig. 5 Comparison of spatial HTC between the baseline and an optimized design

Due to the high coolant flow rate flowing through the entire block portion of the new water jacket, HTC values on the top liner region are also increased considerably, as shown in Fig. 5C.

The base and new V6 engines were then tested with regular octane (approximately 87 (R+M)/2) gasoline to evaluate the effects of the design changes on engine power and fuel economy. The knock limited ignition timing vs. volumetric efficiency is shown in Fig. 6. Each line represents the knock characteristic of one cylinder. It is apparent that there is a wide variation of knock limited ignition timings among the 6 cylinders. For 4 000 rpm, it is almost 6.5 degrees of crank angle. With the new water jacket design, the scatter of knock limited ignition timings becomes narrower in an engine speed range from 3 000 rpm to 5 000 rpm, as shown in Fig. 6, due to improved cooling efficiency uniformity of the individual cylinders. Furthermore, it is also evident that the lower limit of ignition timing of the 6 cylinders is raised within this speed range, and is advanced by 2.5, 3.5, and 3.5 degrees, for 3 000 rpm, 4 000 rpm and 5 000 rpm respectively. However, the upper limit of ignition timing is not advanced as much as the lower limit. Other test results are presented in a separate paper[3].

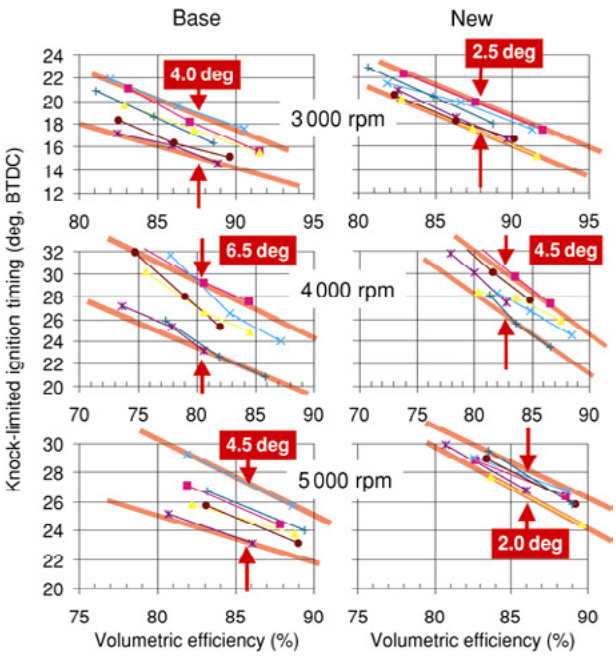


Fig. 6 Effects of water jacket design on knock limited ignition timings of individual cylinders

3. Coupling of Combustion Simulations with Water Jacket

In the preceding section, isothermal CFD simulations were performed to optimize water jacket design with respect to cooling efficiency and uniformity of heat transfer coefficient on surfaces. However, isothermal fluid CFD simulations predict neither the effects of the water jacket on component temperature nor its effects on in-cylinder flow and combustion. Such quantitative information is crucial to predict component durability and knock toughness. Therefore, a simulation methodology was developed to couple in-cylinder flow and combustion with coolant flow and heat conduction in components.

3.1. Description of In-cylinder Flow and Combustion Modeling

The modified KIVA-3V code[4] was used to simulate the full cycle of 720 crank angle degrees of a 4-stroke engine, which includes intake, compression, ignition and combustion, and exhaust processes. In order to obtain a certain level of prediction accuracy of component temperatures, a realistic heat flux boundary condition is essential. Whether flame propagation and combustion rate can be predicted reasonably is a fundamental requirement. Enormous efforts to develop more accurate sub-models for physical and chemical phenomena have been made to make 3D simulations predictive. Comprehensive reviews can be found in the literature[5]. To be complete, some critical models are described here.

3.1.1. Ignition model

The implemented ignition model was similar to the DPIK (Discrete Particle Ignition Kernel) model proposed by Fan and Reitz[6] with some small modifications to accommodate applications to the sequential ignition process[7]. In the DPIK ignition model, the flame kernel is represented by mass-less particles. The locations of these particles define the outer surface of flame kernels, and the number of particles within a computational grid cell represents the flame surface area, which is related to reaction rates. The particle velocity components are calculated as:

$$u_{p,i} = \left[\frac{T_{ad,i}}{T_{l,i}} S_{L,i} + \sqrt{\frac{2k_i}{3}}\right]\cos(\theta)\cos(\phi) \quad (1)$$

$$v_{p,i} = \left[\frac{T_{ad,i}}{T_{l,i}} S_{L,i} + \sqrt{\frac{2k_i}{3}}\right]\cos(\theta)\sin(\phi) \quad (2)$$

$$w_{p,i} = \left[\frac{T_{ad,i}}{T_{l,i}} S_{L,i} + \sqrt{\frac{2k_i}{3}}\right]\sin(\theta) \quad (3)$$

where, $T_{ad,i}$ is the adiabatic flame temperature, and subscript 'i' means the ith spark plug. For instance, $T_{l,i}$ is the local gas temperature at ignition timing corresponding to spark plug 'i' for multiple spark plug applications.

$$T_{l,i} = T_{k1,i}\left(\frac{P_{k2,i}}{P_{k1,i}}\right)^{1-1/\gamma} \quad (4)$$

where $T_{k1,i}$ and $P_{k1,i}$ are the temperature and pressure of associated ignition cell at corresponding ignition timing, $P_{k2,i}$ is instantaneous pressure inside a kernel region.

The parameter k is the turbulence kinetic energy, and S_L is the laminar flame speed, which is calculated as follows

$$S_{L,i} = [s_1 - s_2(\Phi_i - s_3)^2]\cdot\left(\frac{T_{l,i}}{298}\right)^{\alpha_1-\alpha_2(\Phi_i-1)} \times \left(\frac{P_{k2,i}}{1.013\times10^5}\right)^{-\beta_1+\beta_2(\Phi_i-1)} (1-2.1R_i) \quad (5)$$

The instantaneous flame kernel diameter is calculated as:

$$D_{\ker nel,i} = \frac{2}{N_i}\sum_{n=1}^{N_i}\left|\vec{r}_{n,i} - \vec{r}_{p,i}\right| \quad (6)$$

where N_i is the number of active flame kernel particles (particles that collide with walls are eliminated from the count), $\vec{r}_{p,i}$ is the center location of an initial ignition kernel, and $\vec{r}_{n,i}$ is the location of a discrete kernel particle. If a kernel diameter reaches the order of integral length scale, chemical reactions in cells swept by kernel particles from the corresponding spark plug are modeled with the characteristic time scale combustion model, while other kernels are still growing, and kernel growth and reaction rates in the volume under the influence of that spark plug are still modeled with the DPIK model.

The criterion to switch from the DPIK ignition model to a normal combustion model is kernel diameter, based on

$$D_{\ker nel,i} \geq C_k \bar{l}_i \quad (7)$$

the parameter $\bar{l}_i$ is averaged turbulence length scale, which is defined as

$$\bar{l}_i = 0.16\left[\sum_{j=1}^{ncell} k_j / ncell\right]^{1.5} / \left(\sum_{j}^{ncell} \varepsilon_j / ncell\right) \quad (8)$$

3.1.2. Combustion model

The characteristic-time scale combustion model[8] is used, and reaction rates are calculated by

$$\frac{\partial \rho_s}{\partial t} = -\frac{\rho_s - \rho_s^*}{\tau_c} \quad (9)$$

where p_s is the density of species s, and p_s^* is the local and instantaneous thermodynamic equilibrium value of the density of species s. The characteristic conversion time is considered to be a combination of a turbulent-mixing time and local laminar-kinetics time, that is:

$$\tau_c = \tau_t + \tau_l \quad (10)$$

Here it is assumed that time scale for all species is identical. The effect of different time scales on species is reported in another publication[9]. The turbulent mixing time scale is determined as follows:

If

$$\frac{c_{m2}(Y_p - Y_p^*)}{c_{m3}(Y_F - Y_F^* + Y_{O2} - Y_{O2}^*)} \geq 1 \qquad \tau_t = c_{m2} k / \varepsilon \quad (11)$$

or if

$$\frac{c_{m2}(Y_p - Y_p^*)}{c_{m3}(Y_F - Y_F^* + Y_{O2} - Y_{O2}^*)} < 1 \qquad \tau_t = c_{m3}\frac{k}{\varepsilon}\cdot\frac{(Y_F - Y_F^* + Y_{O2} - Y_{O2}^*)}{(Y_p - Y_p^*)} \quad (12)$$

where $c_{m3} = 0.09$, and $c_{m2} = 0.6c_{m3}$

Laminar flame time scale is determined by the following[10]:

$$\tau_l = 1.916\times10^{-12}\cdot T\cdot\left(\frac{P_0}{P}\right)^{[1+2(-0.16+0.22(\phi-1))]} \cdot e^{(1-0.08|\phi-1.15|)\times3\times10^4/(1.987T)}/(1-2.1R)^2 \quad (13)$$

where R is residual gas fraction, and P_0 = 1atm.

3.1.3. Model of wall function

To resolve near-wall transport, improved wall function in KIVA-3V is used[4]. The wall heat flux is determined by,

$$\dot{q} = \frac{\rho v_l c_p F(T - T_w)}{\mathrm{Pr}_l y} \quad (14)$$

where

$$F = \frac{R'\cdot \mathrm{Pr}_l/\mathrm{Pr}_t}{1/\kappa \ln R' + B + 11.05(\mathrm{Pr}_l/\mathrm{Pr}_t - 1)} \quad (15)$$

if R'>11.05, or F = 1 if R'≤11.05.

And

$$R' = \frac{c_\mu^{1/4} K^{1/2} y}{v_l} \quad (16)$$

where v_l is laminar kinematic viscosity, y is distance from the wall, and κ is Karmann's constant. Pr_l and Pr_t are laminar Prandtl and turbulent Prandtl numbers, respectively. K is turbulence kinetic energy.

3.2. Cycle-Averaged Heat Flux Calculations

Although in-cylinder phenomena and heat transfer within components are of different time scales, it has been shown that component temperature distribution is not affected by transient processes in a combustion chamber except within an extremely thin layer. It is therefore reasonable to couple in-cylinder analysis with component and water jacket calculations on a cycle-averaged basis. The schematic of the coupling process[7] is shown in Fig. 7.

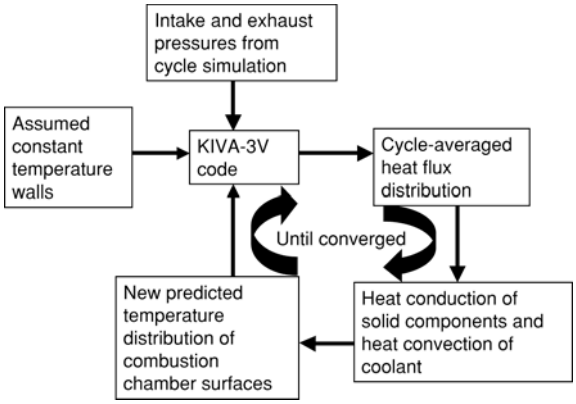


Fig. 7 Illustration of iterative coupling procedures

Cycle-averaged local heat flux is calculated as:

$$\dot{q}_{i,j} = \sum_{n=1}^{n_{720}} \frac{\dot{q}_{i,j}^n \cdot \Delta t^n}{\frac{120}{N_e}} \quad (17)$$

where N_e is engine speed in rev/min, and the subscripts i and j are indexes of cells on 3D surface domain. Heat flux on the liner can be attributed to three sources. One is directly from in-cylinder gas on the portion of liner surface that is exposed to gas at any instant. The second is heat transfer from the piston to the liner via the rings. The last is from friction between the rings and skirt and liner converted to heat. In the current investigation, the last source was omitted. At the very bottom portion, the liner could either receive heat from or dissipate heat to crankcase flow. In this study, the interest is on the top liner portion, and it is believed that the bottom portion does not have meaningful impact on the top portion with respect to temperature distribution. Therefore, a guessed value is used for that region. As for the heat flux on the portion of the cylinder liner swept by the piston ring, it is calculated by the following formulae:

$$\dot{q}_{i,j,liner} = (\dot{q}_{i,j,liner})_{gas}\ ,\ z \le h \qquad (18)$$

$$\dot{q}_{i,j,liner} = (\dot{q}_{i,j,liner})_{gas} + \zeta\, \dot{Q}_P /(\pi DS)\ ,\ z > h \qquad (19)$$

where $\dot{Q}_F$ is the total heat flux of the piston top surface from gas, and ζ is the percentage of piston heat flux transferred to the liner through the piston rings. In this study it is assumed that 70% of the heat received by the piston is transferred to the liner. The meanings of other symbols are explained in Fig. 8.

Heat flux on the valve seats is calculated based on the heat balance of the valves. Cycle-averaged heat flux on the valve heads is distributed into three parts: through the valve seats, through the valve stems, and from gas. The computational domain for the in-cylinder flow and combustion calculations is shown in Fig. 9. Time-dependent pressure conditions from one dimensional simulations are applied to the inlet and outlet.

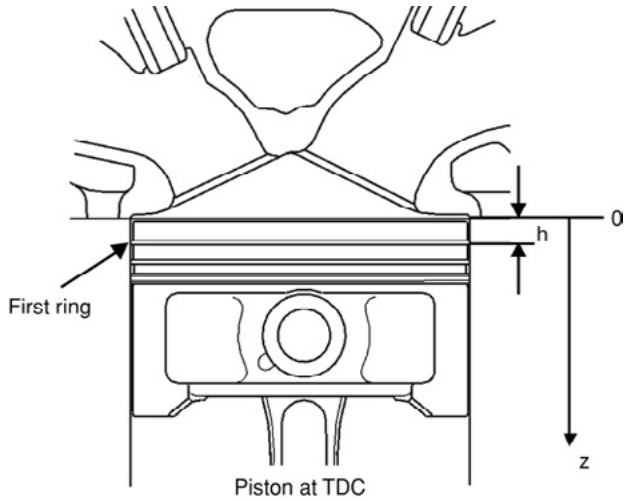


Fig. 8 Zone definitions on the cylinder liner surface to calculate heat flux

3.3. Solid Components and the Cooling Jacket

The computational domain for heat conduction analysis consists of the cylinder head, head gasket, cylinder block, and cylinder liners. For the applications in this work, only one bank of a V6 engine is considered, assuming symmetry of the two banks. The CFD domain for heat convection in the cooling passages is also a one-bank water jacket. The solid and water jacket domains are shown in Fig. 9. A general computational fluid dynamics code, VECTIS, was used for solid components and the water jacket. Time-step resolved coupling for both liquid/solid and solid/solid interfaces is available in this package. A standard k-e turbulence model is employed for water jacket flow calculation, and phase change in water jacket is not considered, which could result in higher predicted temperatures than actual in some regions where phase change is expected to be important.

Valve seats are not directly modeled in this investigation; instead, the heat flux from the valve heads is imposed on the head surfaces which valve seats are exposed to.

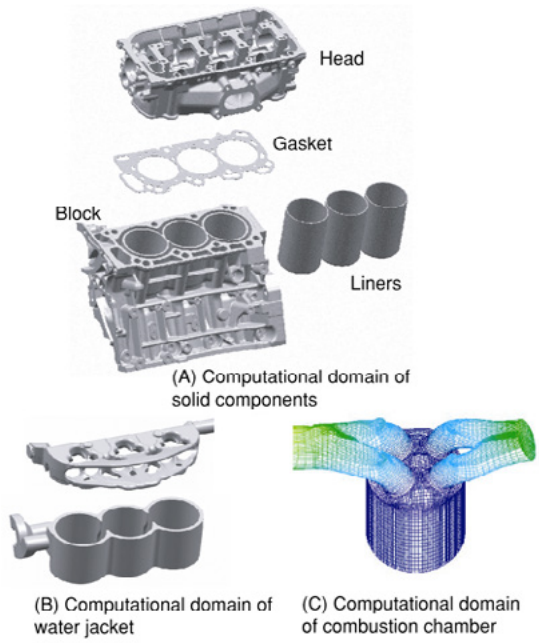


Fig. 9 Computations domain for conjugate heat transfer analysis

3.4. Applications of the Methodology

A critical engine operating condition (6 000 rpm, equivalent A/F ratio 0.759) was chosen to illustrate the methodology and its applications. To begin with, constant wall temperatures of 410 K, 460 K, 470 K, 415 K, and 580 K were applied to the cylinder liner, head, piston, intake valves, and exhaust valves, respectively. A full cycle of 720 crank angle degrees was simulated with the KIVA code. Cycle-averaged heat flux distribution on cylinder head and liner surfaces is shown in Fig. 10. It is apparent that surface heat flux is highly non-uniform even though the initial surface temperatures were assumed to be uniform. The area between exhaust valves has the highest heat flux.

Consequentially, the predicted spatial heat flux results from 3D combustion simulations were applied to conjugate heat transfer analysis with VECTIS as illustrated in Fig. 7. Figure 11 shows calculated surface temperature distributions on the combustion chamber and liner surfaces. It should be

emphasized that spatial temperature distributions are not uniform due to spatially varied heat flux from the combustion chamber, non-uniform wall thickness, accessibility of coolant flow, and cooling efficiency. Furthermore, the results also demonstrated large wall temperature variation among cylinders.

It is known that local heat flux on the combustion chamber surface depends on the instantaneous heat transfer coefficient, local gas temperature, and local wall temperature. As indicated in Fig. 11, wall temperature varies both along cylinder axis and along the tangential direction, which is expected to have significant effect on the magnitude and direction of instantaneous local heat flux. Furthermore, wall temperature changes will affect thermodynamic properties of gaseous media and trapped mass. These variations will change heat transfer coefficient and gas temperature. Therefore, a uniform wall temperature assumption in 3D combustion calculations cannot produce satisfactory heat flux information necessary to predict overall engine component temperature levels. With this consideration, it is necessary to iterate between combustion calculations and conjugate heat transfer analysis until wall temperatures on combustion chamber surfaces converge. Therefore, the calculated wall temperature distribution is mapped to the KIVA combustion chamber model. Figure 12 shows the temperature distribution on the chamber surface for one cylinder. New temperature conditions for KIVA combustion calculations were correctly mapped. Then, the new in-cylinder flow calculation with the new wall temperature distribution was performed, and new heat flux results on the combustion chamber surface were obtained. Typically, the results converged after 3 iterations[7].

To validate the robustness of the tool and the accuracy, the developed tool was applied to a new V6 engine. Two different water jacket design concepts, named D1 and D2, were evaluated with the proposed CAE tool. The design D1 is the baseline design. In the design D2, a vertical insert is placed in the water jacket of the engine block, and the head gasket is modified accordingly to achieve a desired coolant flow pattern. The overall flow path of these two design concepts is illustrated in Fig. 13.

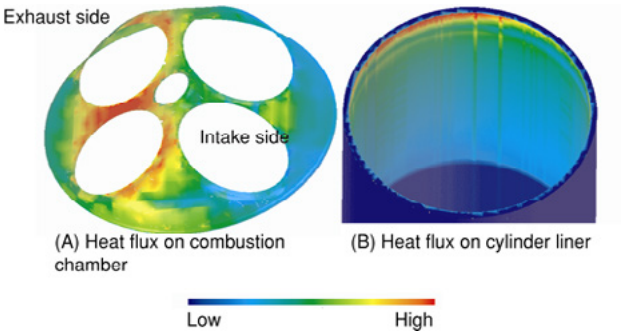


Fig. 10 Calculated spatial heat flux mapped on corresponding component surfaces

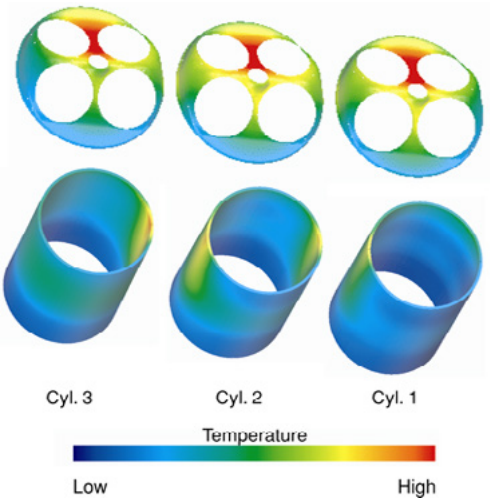


Fig. 11 Calculated spatial temperature distribution

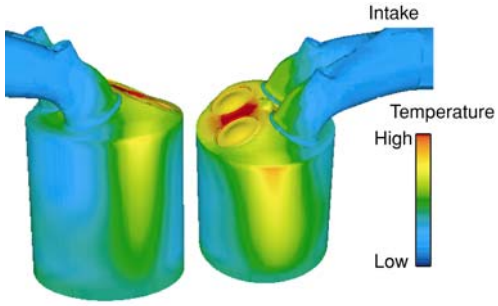


Fig. 12 Mapped temperature distribution on combustion chamber

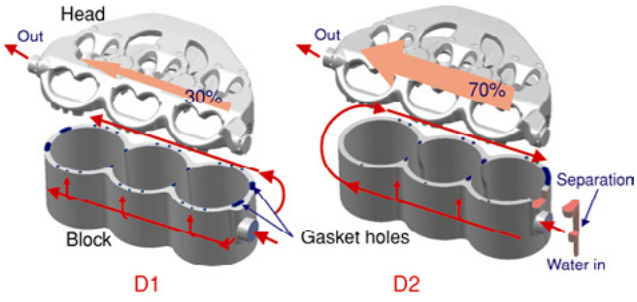


Fig. 13 Coolant flow path of water jacket designs

The comparison of measured and calculated component temperature difference between the D1 and D2 designs is shown in Fig. 14 at an engine speed of 6 000 rpm. The results show reasonable agreement between experimental and numerical results, and good correlation is confirmed even

though there is discrepancy in the magnitude of temperature reduction. Unlike the other three locations, the calculated temperature reduction at L3 is lower than the measured value. It is not clear what specific factors result in this discrepancy. Even though no experimental data was used to set up the model, such reasonable agreement can be achieved with the methodology, and critical information can be obtained. It makes the methodology a valuable tool for new engine development. Figure 15 shows the measured temperature at location L1 across the entire engine operating speed range. Again, as predicted, the design concept D2 has lower temperature values than the design concept D1.

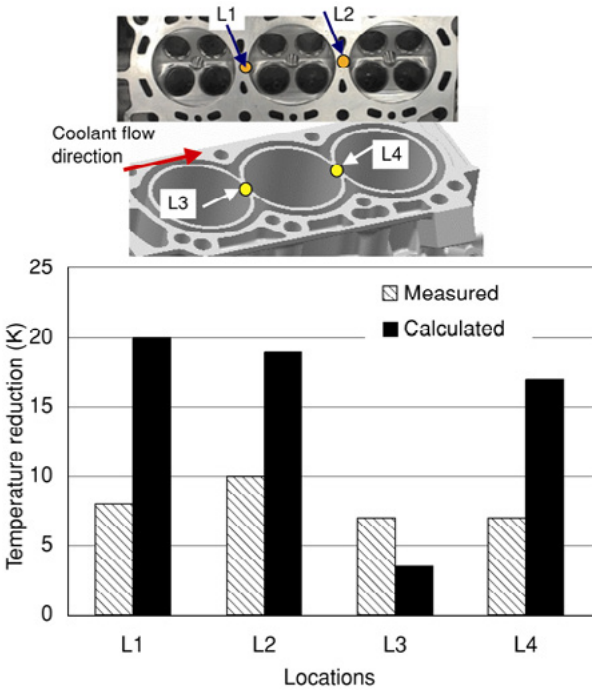


Fig. 14 Comparison of measured and calculated temperature difference

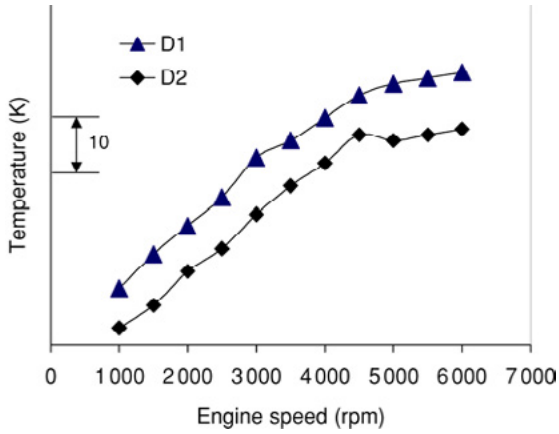


Fig. 15 Measured temperatures at the location L4 for D1 and D2 designs

4. Conclusions

In this paper, a Honda V6 engine was analyzed by using three-dimensional CFD calculations to evaluate the potential for improvement without significantly altering the current mass production process in order to improve engine power and fuel economy simultaneously. In the first part, isothermal CFD simulations were performed to effectively evaluate and optimize design parameters of the engine water jacket with respect to heat transfer coefficient on the water jacket surface. In the second part, the methodology of coupling in-cylinder flow and combustion simulations with heat transfer calculations in solid components and cooling passages was developed to account for interactions among them, and therefore, to provide more complete information to evaluate design concepts in the early stage of engine development. The conclusions can be summarized as follows:

(1) For the purpose of evaluating effects of design changes of engine water jackets on cooling efficiency and uniformity, isothermal 3D flow analysis is effective and adequate. Design optimization can be achieved within a relatively short period.

(2) In the new optimized design, the cooling uniformity of the water jacket among the 6 cylinders was significantly improved, and the overall level of cooling efficiency in both the cylinder head and block was increased.

(3) To quantify improvement of knock toughness and to address durability concerns, a coupling methodology was developed to predict combustion chamber temperatures.

(4) The predictions from the coupling methodology were validated by the measurement results. There is good correlation between predicted temperature reduction and measured temperature reduction.

Acknowledgment

The authors would like to thank Prof. Rolf Reitz at the University of Wisconsin-Madison for productive research collaboration and his insights.

References

(1) Norris, P., Wepfer, W., Hoag, K., Courtine-White, D.: Experimental and Analytical Studies of Cylinder Head Cooling, SAE 931122

(2) Moeckel, M.: Computational Fluid Dynamic (CFD) Analysis of a Six Cylinder Diesel Engine Cooling System with Experimental Correlation, SAE 941081

(3) Shih, S., Itano, E., Kawamoto, M., Y. Maeda, Xin, J.: Engine Knock Toughness Improvement Through Water Jacket Optimization, SAE 2003-01-3259

(4) Amsden, A.: KIVA-3V, A Block-Structured KIVA Program for Engines with Vertical or Canted Valves, Los Alamos Report LA-13313-MS, July (1997)

(5) Reitz, R. D., Rutland, C. J.: Development and Testing of Diesel Engine CFD Models, *Prog. Energy Combust. Sci.* Vol. 21 (1995)

(6) Fan, L., Reitz, R. D.: 2000 Spray and Combustion Modeling in Gasoline Direct Injection Engines, ICLASS 2000 issue of *Atomization and Spray*

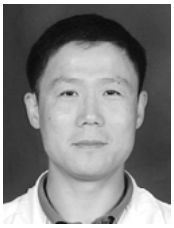
(7) Xin, J., Shih, S., Itano, E., Maeda, Y.: Integration of 3D Combustion Simulations and Conjugate Heat Transfer Analysis to Quantitatively Evaluate Component Temperatures, SAE 2003-01-3128

(8) Abraham, J., Bracco, F. V., Reitz, R.: Comparisons of Computed and Measured Premixed Charge Engine Combustion, *Combustion and Flame*, Vol. 60, pp. 309-322 (1985)

(9) Xin, J., Montgomery, D., Han, Z., Reitz, R.: Multidimensional Modeling of Combustion for a Six-Mode Emissions Test Cycle on a DI Diesel Engine, *J. Engineering for Gas Turbines and Power*, Vol. 119, pp. 683-691 (1997)

(10) Kuo, T., Reitz, R.: Three Dimensional Computations of Combustion in Premixed-Charge and Direct Injected Two-Stroke Engines, SAE 920425

■ Authors ■


Jun XIN


Stephen SHIH


Edwin ITANO


Yoshio MAEDA


Michio KAWAMOTO


Yoshio YAMAMOTO

Development of LEV-II Compliant Low Precious Metal Perovskite Catalytic System

Yoshiaki MATSUZONO* Masahiro SAKANUSHI*
Hiroshi KITAGAWA*

ABSTRACT

A LEV-II compliant catalytic system employing a low precious metal perovskite catalyst has been developed as part of research efforts to contribute to the preservation of the global environment and the conservation of natural resources. Conventional catalyst systems are effective in purifying exhaust gases, but the reduction of the large amounts of precious metals they employ (Pt, Rh, Pd, etc.) is desirable in order to conserve resources.

However, perovskite catalysts containing no precious metals have lower durability and purify exhaust emissions less effectively during warm-up than catalysts with high precious metal content.

The research described in this paper combined a perovskite catalyst with Honda's original high-accuracy A/F control and quick warm-up systems, enabling the LEV-II regulations to be cleared and achieving a level of performance with 2 g of precious metal catalyst equivalent to that previously requiring 4 g or more.

1. Introduction

Exhaust gas regulations are becoming increasingly stringent around the world. In California, the LEV-I (Low Emission Vehicle Phase I) regulations will be replaced by the LEV-II (Phase II) regulations in 2004. In addition, Tier II regulations have already been decided on for the entire US. These regulations require that NOx emissions be reduced to approximately one-quarter of currently stipulated levels, and extend the useful life to 120 kmiles. Figure 1 shows an outline of the emissions levels stipulated by these regulations.

Catalytic systems are the major after treatment systems for exhaust gas. The increased amounts of precious metals that must be used in these systems to meet the requirements of these enhanced regulations has sparked concerns over the worldwide exhaustion of these resources. The development of high-performance, low precious metal exhaust gas after treatment systems is therefore an urgent research agenda. However, if the precious metal content of conventional catalysts is reduced, their after treatment performance during warm-up and after long-term aging declines. Perovskite-type mixed metal oxides are widely used in semi-conductors, etc., but their use in catalytic systems produces the same set of issues generated by reducing the amount of precious metals, and they have therefore to date received little use as a catalyst material.

In the research discussed in this paper, a new low precious metal catalyst employing a perovskite mixed metal oxide[(1)] jointly developed with Catalyst Solution Inc. is combined with Honda's original high-accuracy A/F control and quick warm-up systems. This combination enabled the standard of the LEV-II regulations to be met, including the newly extended useful life, and has reduced the formerly required 4 g or more of precious metals per unit to 2 g.

* Tochigi R&D Center

2. Test Conditions

2.1. Test Vehicle

This project used the '01 Accord EX 2.3L in-line four-cylinder VTEC SULEV as the base test vehicle. Tests are conducted without alteration of the under-floor catalytic system or exhaust system layout. The volume of catalyst used remained the same at 1.7 L, and the control system was also unchanged. Figure 2 shows an outline of the test system.

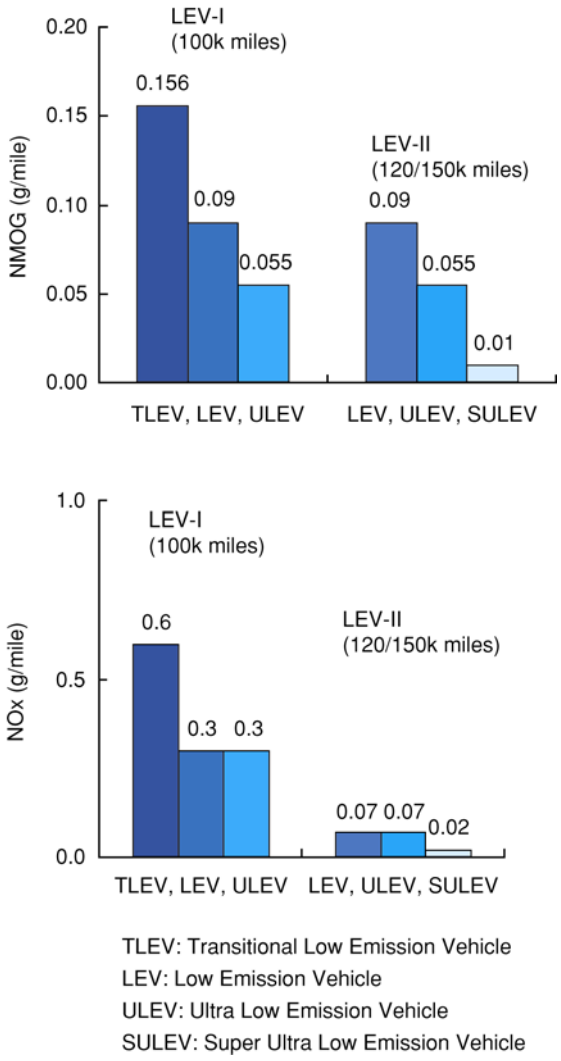


Fig. 1 Relationship between LEV-II and LEV-II regulations

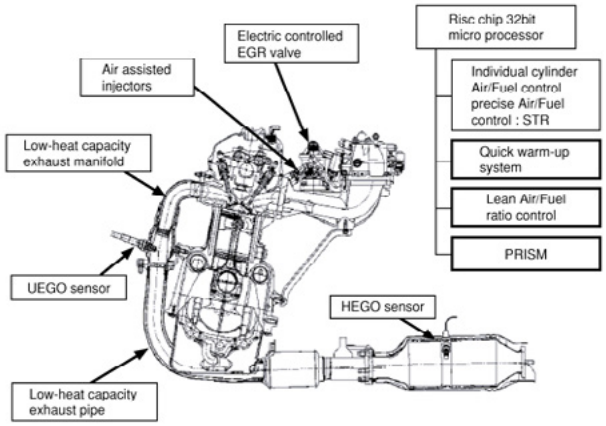


Fig. 2 Overview of test vehicle system

2.2. Control System

The control system employed in the test vehicle is high-accuracy A/F control, PRISM (Prediction and Identification Sliding Mode control[2, 3]). The PRISM system is employed to provide rapid activation of the catalyst at start-up, reduce feed gases by the use of lean burn after start-up, and reduce exhaust gases after activation of the catalyst.

2.3. Rapid Catalyst Warm-up System

Engine exhaust energy increases the temperature of three-way catalysts, raising their level of activation. To maximize this effect, a Quick Warm-up System (QWS[4]) was developed which uses a rotary air control valve (RACV) to control the volume of intake air at a cold start (before activation of the three-way catalyst), and simultaneously controls ignition timing.

The concept behind the control used in QWS is illustrated in Fig. 3. From top to bottom, the graphs show changes over time in the degree of opening of the RACV, the engine speed, and ignition timing. QWS uses feed forward control when the engine is idling after start-up to provide a high volume of intake air. Proportional and integral (PI) feedback control is used to control the ignition timing in order to maintain the target engine speed.

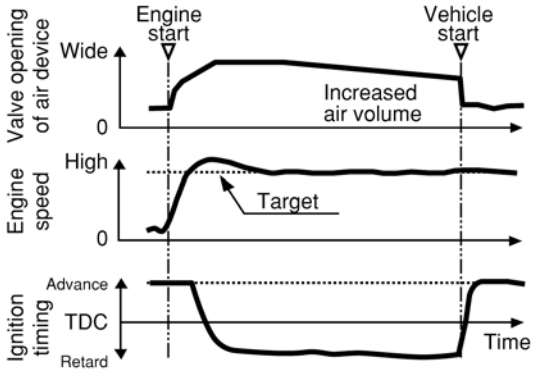


Fig. 3 Ignition feedback control for QWS

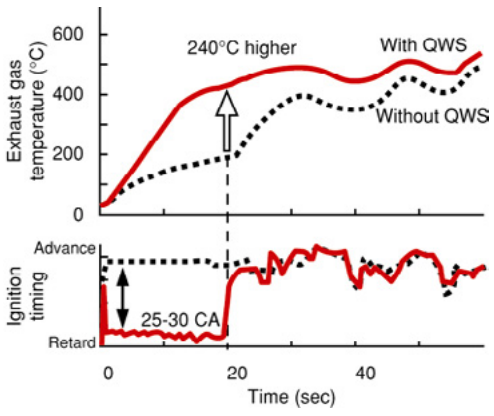


Fig. 4 Effect of QWS at start-up period of FTP

Figure 4 shows the ignition timing control provided by QWS and its effect in increasing exhaust gas temperature at start-up. The use of QWS increases the temperature of the exhaust gas by 240 °C in 20 seconds after start-up against a conventional control system. This enables rapid activation of the catalyst.

2.4. Reduction of Exhaust Gas after Activation of Catalyst

Figure 5 shows a conceptual diagram of the feedback-system. The aim of this system is to precisely control the exhaust gas A/F ratio to a value suitable for the catalyst. There is an extended period of time in which no effect is produced until the fuel from the injector is detected by the post-catalyst Heated Exhaust Gas Oxygen sensor (HEGO), and the control application takes this period into consideration. It is also now possible to obtain an understanding of how the properties of the catalyst change with the vehicle mileage. The section in which calculations are performed is made up of three modules, the real-time identifier, the predictor and the sliding mode controller.

The real-time identifier contains a model of the catalyst, and identifies the dynamic characteristics of the model in real time on the basis of output from the pre- and post-catalyst sensor.

The predictor uses θ (a_1, a_2, b_1), the parameters of the catalyst model calculated by the real time identifier, and output from the pre- and post-catalyst HEGO sensors to make a predictive calculation of the future value of the output of the post-catalyst HEGO sensor.

The controller is highly robust, and employs adaptive sliding mode control[5].

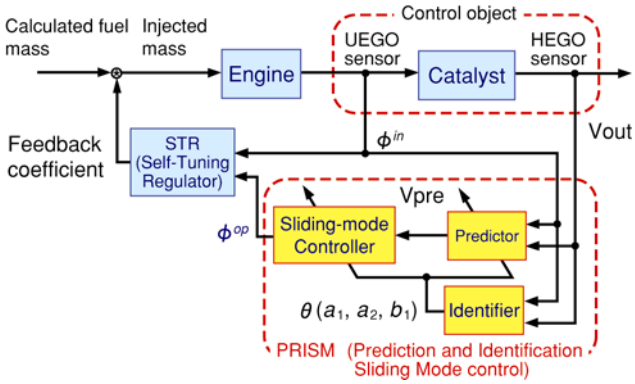


Fig. 5 Overview of feedback-system

Figure 6 shows the dynamic principle of sliding mode. The sliding mode controller in PRISM functions to restrict the output, VO_2, from the HEGO sensor to the switching line in a phase plane with axis representing the deviation from target values for sensor output and allows VO_2 to slide back to the zero point. To determine the target value for VO_2, the controller calculates the target A/F ratio for the self-tuning regulator (STR)[6], which feeds back the pre-catalyst A/F ratio.

Figure 7 shows the effect of PRISM control during an FTP cycle. The post-catalyst HEGO sensor output is

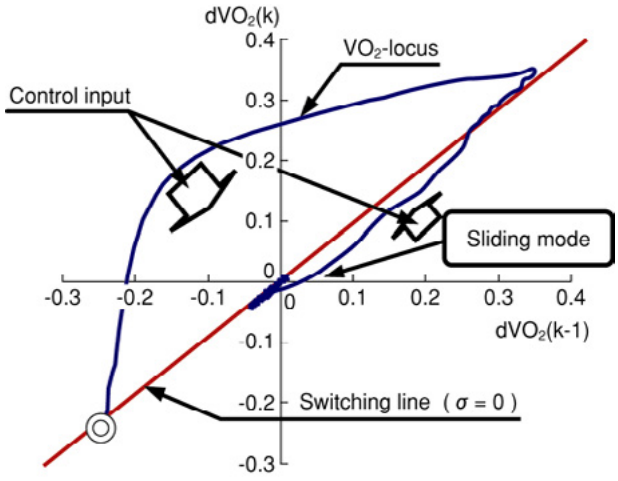


Fig. 6 VO_2 locus in phase plane

accurately controlled to the target value with no bias towards either 0 V (lean environment) or 1 V (rich environment). This indicates that the environment in the three-way catalyst is always close to the theoretical A/F ratio, and verifies the fact that PRISM provides high-accuracy control to produce the optimum A/F ratio for a three-way catalyst.

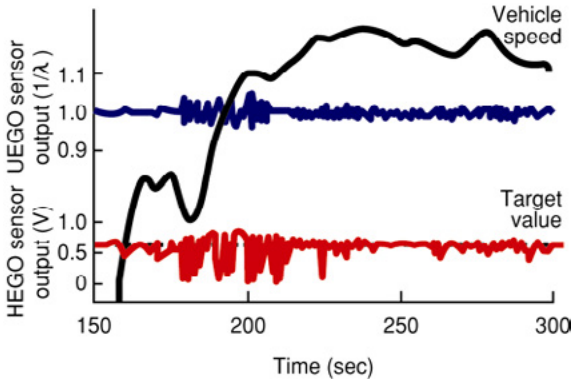


Fig. 7 Improved controllability of secondary HEGO sensor output

2.5. Catalyst

The catalyst substrate is a 600 cell per square inch model with a wall thickness of 4.3 mil manufactured by NGK Co., Ltd., and is made up of two ceramic beds of 0.7 and 1.0 L. For the tests, two types of catalyst coatings, perovskite-type mixed metal oxides and precious metals, were prepared. One was termed catalyst A, and is presently used in vehicles for the Japanese market, and the other was catalyst B, newly developed in this project to comply with the US LEV-II regulations. The amount of precious metals employed in both A and B was 33 g/ft^3 (Pt:Pd:Rh = 4:25:4). These catalysts were tested in the vehicle after aging to the equivalent of 120 kmiles.

2.6. A/F Sweep Test

The A/F sweep test was conducted using a 2.3 L in-line

four-cylinder engine on an engine dynamo. The engine runs at 2 000 rpm and manifold vacuum is maintained at –350 mmHg. A/F ratio is controlled with an external control unit. The pre- and post-catalyst exhaust gas concentrations are measured, and the catalyst reduction ratio is measured within a fixed range of A/F ratios. The value at which the CO and NOx reduction ratios are the same is used for the catalyst reduction ratio.

2.7. Light-off Temperature Test

The light-off temperature test is conducted using the same equipment as the A/F sweep test. The catalyst temperature is kept constant using a heat exchanger. The pre- and post-catalyst exhaust gas concentration is measured and the catalyst reduction ratio is measured within a fixed range of catalyst temperatures and evaluated. As in the A/F sweep test, a value at which the reduction ratio of CO and NOx is the same is used as the catalyst reduction rate.

3. Test Results

3.1. Light-off Temperature Test

Figure 8 shows results obtained for catalysts A and B. Catalyst C is also included for the purpose of comparison. Catalyst C is utilized in the '98M Accord ULEV, which is fitted with an in-line four-cylinder 2.3 L engine. In the light-off temperature tests, catalyst A achieved a 99% reduction ratio at 430 °C, and catalyst B at 380 °C. In other words, catalyst B demonstrated a 50 °C improvement in light-off temperature against catalyst A. Catalyst C achieved a 99% reduction ratio at 340 °C.

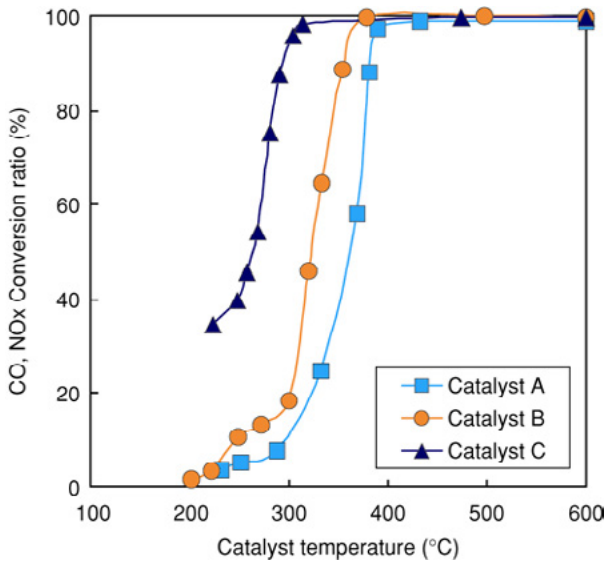


Fig. 8 Reduction ratios vs. catalyst temperature

3.2. A/F Sweep Test

Figures 9 and 10 show results for catalysts B and C in A/F sweep tests. Catalysts B and C display very similar reduction ratio characteristics in the 43 000/hr area of space velocity (SV), but there are clear differences in the SV = 72 900/hr area. Here, catalyst B shows a narrower range of A/F ratio in which a target or higher reduction ratio can be obtained compared to catalyst C.

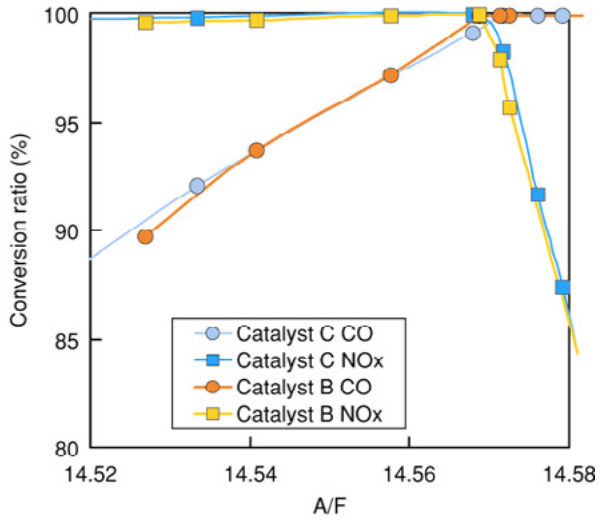


Fig. 9 Reduction ratio properties vs. air fuel ratio (SV = 43 000/hr)

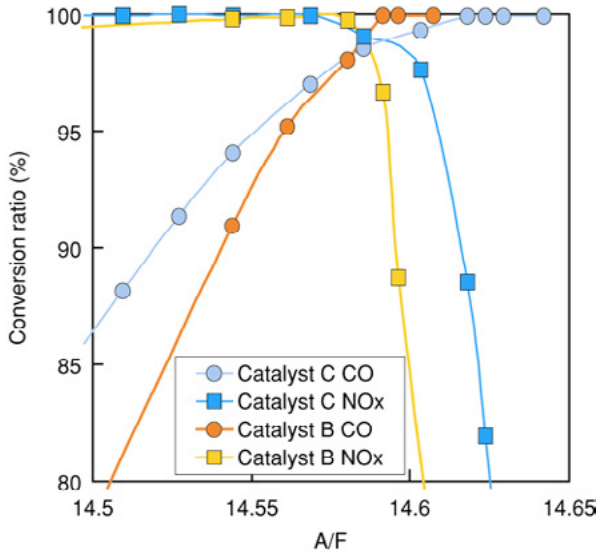


Fig. 10 Reduction ratio properties vs. air fuel ratio (SV = 72 900/hr)

3.3. Effect of QWS

Figures 11 and 12 show the effect of QWS in increasing catalyst temperature and reducing exhaust gases during an FTP cycle. As Fig. 11 shows, when QWS is not employed, the catalyst temperature only reaches 250 °C 20 seconds after start-up. However, when QWS is employed, the temperature reaches 400 °C. This indicates that the reduction ratio 20 seconds after start-up increases from 10% to 99%. As Fig. 12 shows, this enables a significant reduction in exhaust gases at start-up in an FTP cycle.

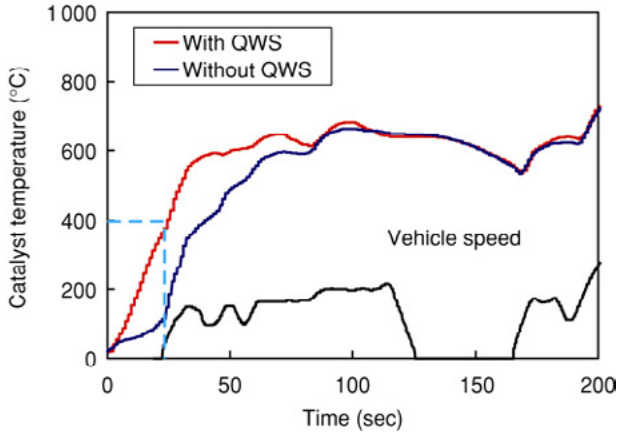


Fig. 11 Catalyst temperature during the start of FTP

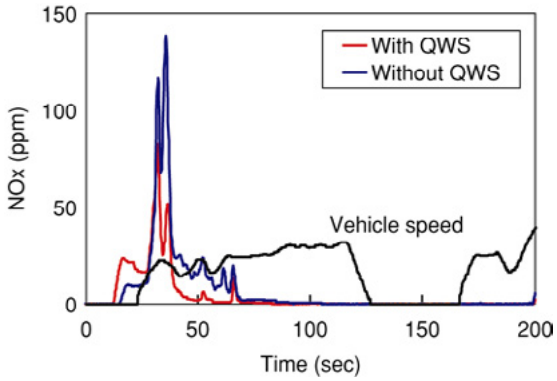


Fig. 12 NOx emission during the start of FTP

3.4. Effect of High-accuracy A/F Control

Figures 13 and 14 show exhaust gas emissions and the behavior of the post-catalyst HEGO sensor output in an FTP cycle when the PRISM high-accuracy A/F control system is employed. When PRISM control is not utilized, the output of the post-catalyst HEGO sensor diverges significantly from the target values. Employment of PRISM control increases the level of convergence with target values, and makes the sensor output more stable. As the results shown in Fig. 14 demonstrate, this leads to a significant reduction of exhaust gas emissions in the high-SV area of the FTP cycle.

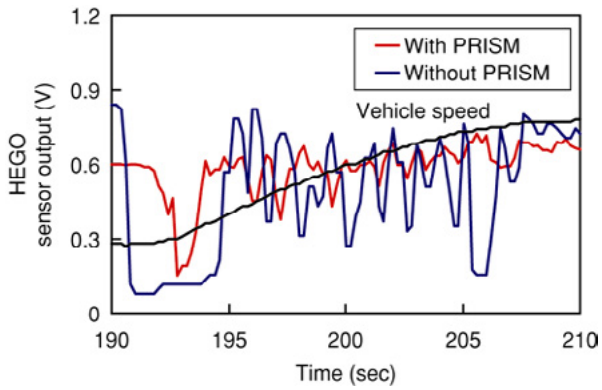


Fig. 13 Post-catalyst HEGO sensor output during FTP

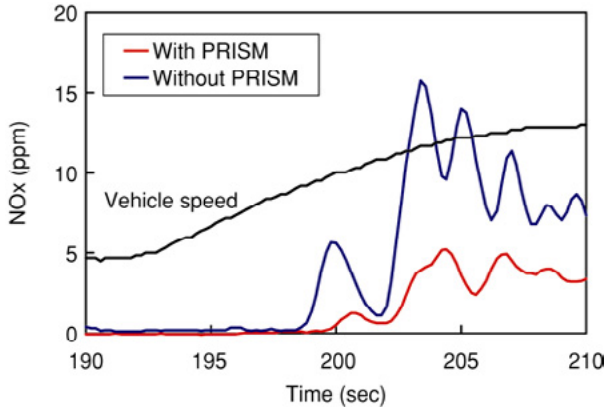


Fig. 14 NOx emission during FTP (with PRISM)

3.5. Effect of Extended Mileage

Figure 15 shows results for exhaust gas emissions obtained from vehicles fitted with rapid aging catalysts A and B and run in an FTP cycle. No significant differences in performance between catalysts A and B with respect to CO and HC components were observed during aging to 120 kmiles. With respect to NOx components, despite the fact that no major difference is observable in aging up to 50 kmiles, there is a significant difference in performance at 120 kmiles, with catalyst B reducing emissions to 1/4 the level of catalyst A. These results demonstrate that catalyst B is superior to conventional catalyst A in exhaust gas reduction performance even after extended mileage.

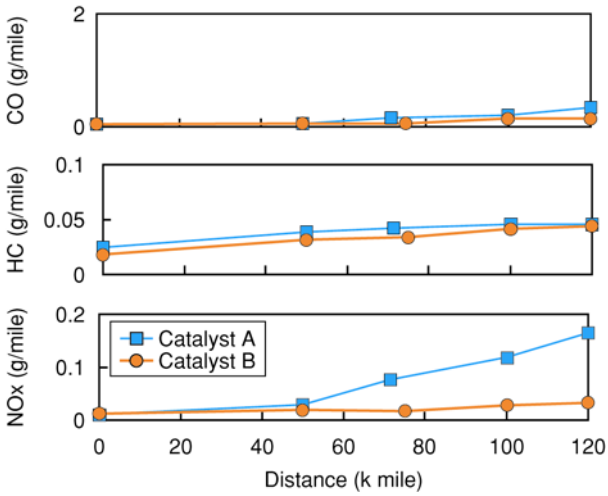


Fig. 15 FTP emission shift at extended mileage

3.6. Results of Exhaust Gas Measurements in FTP Mode

Figure 16 shows the results of measurements of exhaust gas emissions in FTP mode using newly developed catalyst B. A catalyst aged to the equivalent of 120 kmiles is used for measurements. The results show that the new catalyst meets the LEV-II standard for CO, HC and NOx.

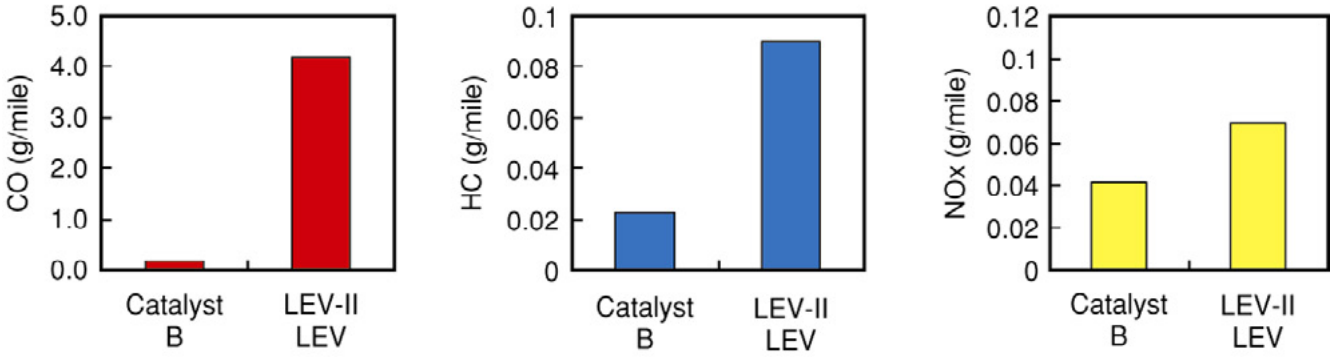


Fig.16 FTP emission results for development catalyst after begin aged to the equivalent of 120 kmiles

4. Conclusion

A perovskite catalyst was developed which possesses superior light-off performance and durability to conventional perovskite catalysts. However, while the new catalyst shows equivalent performance to that of catalysts with a high precious metal content at low SV in the A/F sweep test, it cannot match the performance at high SV or in the light-off test.

Combining the new catalyst with Honda's original PRISM (high-accuracy A/F control) and QWS (quick catalyst warm-up system) supplemented its light-off performance and reduced A/F window width at high SV, and enabled the achievement of an equivalent level of exhaust gas reduction performance to conventional high precious metal catalysts.

The adoption of this catalyst technology for use in a 2.3 L in-line four-cylinder engine enabled conformity to the requirements of the LEV-II regulations.

In addition, it is possible to reduce the conventionally required 4 g or more of precious metals by more than 50% to 2 g. The future broader application of this system will be very effective in preserving the world's limited reserves of precious metals, and represents one of Honda's solutions to the issue of the potential exhaustion of these resources.

References

(1) Golden, S.J., Polli, A.D., Hawthorne, R., Hatfield, R., Cotton, M.G., Flynn, K., Truex, T.: Advanced Low PGM Three-Way Catalysts for LEV-II and ULEV-II Compliance, SAE Paper 2002-01-0344

(2) Nonami, K., Den, H.: Sliding Mode Control, Tokyo, Coronasha, p. 263 (1994)

(3) Yasui, Y., Akazaki, S., Ueno, M., Iwaki, Y.: Adaptive Sliding Mode Control for Secondary O2 Feedback, A Second Report, HONDA R&D Technical Review, Vol. 11, No. 2, p. 65-71 (1999)

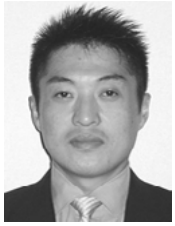
(4) Ueno, M., Akazaki, S., Yasui, Y., Iwaki, Y.: A Quick Warm-up System during Engine Start-up Period Using Adaptive Control of Intake Air and Ignition Timing, HONDA R&D Technical Review, Vol. 11, No. 1, p. 73-78 (1999)

(5) Maki, H., Hasegawa, Y., Akazaki, S., Komoriya, I., Nishimura, Y. Hirota, T.: Real Time Control Using STR in Feedback System, SAE Paper 950007

(6) Kitagawa, H., Urata, Y., Yasui, Y., Mibe, T.: Development of Super Ultra Low Emission System, HONDA R&D Technical Review, Vol. 12, No. 2, p. 37-44 (2000)

■ Authors ■


Yoshiaki MATSUZONO


Masahiro SAKANUSHI


Hiroshi KITAGAWA

Research on Reduction of Unusual Noise in Wet Multiple Disk Clutch for 4WD

Masaki INOUE* Yasunori ARAI*
Toshiaki AZEGAMI* Yasuo HIRAO*

ABSTRACT

When AT clutches are utilized in torque-on-demand 4WD systems, in which rear wheel traction is controlled by pushing force from a wet multiple disc clutch, an unusual noise is generated during turning or takeoff by the continuous input of differences in speed. The status of lubrication in a clutch unit in isolation was analyzed to find the cause, and results showed that the lubrication flow rate to the clutch was low, and that the lubricant was not being uniformly supplied to every section. A test vehicle was set up to reproduce the conditions of the unit analysis, and the unusual noise occurring in the unit was effectively reproduced. It was determined that the noise is related to the ratio of porosity and the amount of deflection in friction materials. These results enabled the specifications of the lubricant to be improved. In addition, friction materials with increased porosity and deflection were developed to improve the oil retention characteristic in the clutch. Vehicle tests were repeated employing these measures, and no unusual noise was generated.

1. Introduction

Recently, wet multiple disc clutches have come into increasing use in FFD vehicle-based torque-on-demand type 4-wheel drive systems. Sometimes, automatic transmission clutches are used as wet multiple disc clutches, but there are considerable differences between the use conditions in AT and 4-wheel drive transmissions, so these components actually require quite different types of performance. Differences in speed in AT occur in a short period of shifting, while differences in speed constantly occur in torque-on-demand 4-wheel drive systems, due to slipping of the front wheels, so the engaging time of the clutch is long and the engaging frequency is high. Consequently, an unusual noise is sometimes emitted from the clutch during turning, when differences in speed occur continuously, and during takeoff.

This project consisted of three stages: The factors in the unusual noise from the clutch during turning and takeoff were analyzed; a reproducing mode was constructed in an actual vehicle; and specifications were proposed to counter the issue.

2. Issues in Adoption of Automatic Transmission Clutches

2.1. Configuration of 4-Wheel Drive Systems

The dual-pump system (DPS) used by Honda is an example of the torque-on-demand 4-wheel drive systems.

As shown in Fig. 1, in this system, oil pressure generated by a rotation speed difference between the front and rear wheels is applied to a piston, which moves a multiple disc clutch through a mechanism.

* Tochigi R&D Center

This is composed of the pump body which generates the oil pressure, the clutch which converts the piston thrust into torque, and the rear differential which distributes the torque to the right and left wheels.

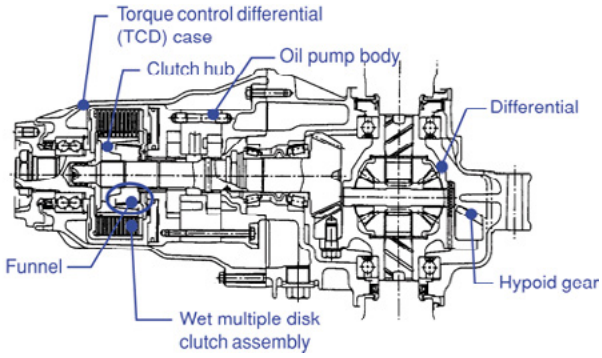


Fig. 1 Structure of DPS

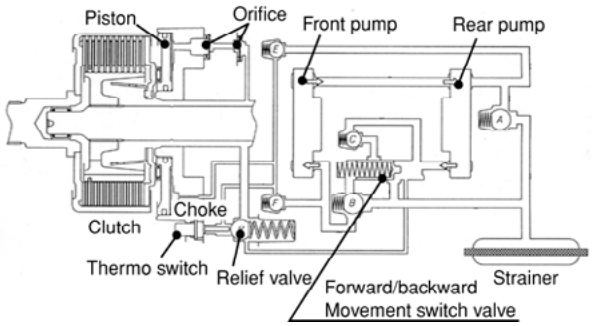


Fig. 2 Hydraulic circuit of DPS

2.2. Issues in Use Conditions of 4-Wheel Drive

A vehicle containing a DPS with an automatic transmission clutch was test-driven in continuous turns on pavement. Figure 3 shows the rear propeller shaft torque, difference of speed at the DPS clutch, and rear differential case vibration data. The unusual noise generated during clutch engagement was a metallic sound; as Fig. 4 shows, it had a frequency of about 500 Hz.

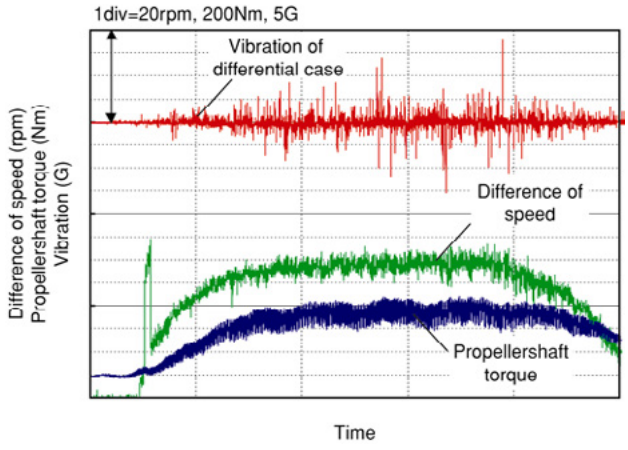


Fig. 3 Example of unusual noise

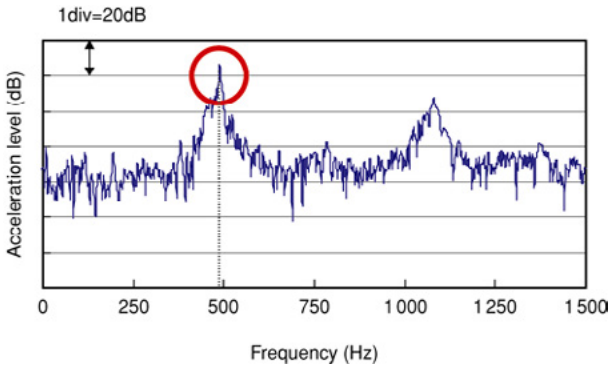


Fig. 4 Frequency characteristic of unusual noise

Visual confirmation of the clutch generating the unusual noise indicated, as shown in Fig. 5, that the plate had been polished to a mirror finished surface in contrast to the appearance of a normal (quiet) plate, and blemishes had been produced by local contacts. The surface roughness of the quiet plate and the plate producing the unusual noise are compared in Table 1. The arithmetical mean deviation of the profile on the quiet plate ranged 0.126 μm – 0.252 μm, while that of the plate producing unusual noise was 0.088 μm – 0.167 μm.

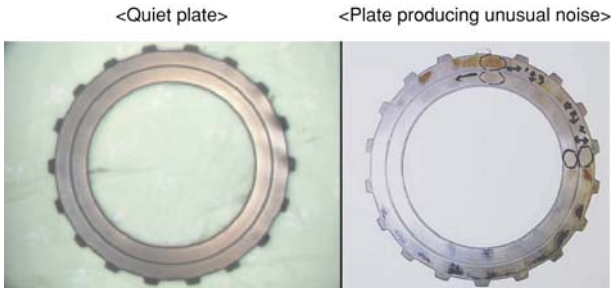


Fig. 5 Condition of clutch plate surface

Table 1 Comparison of surface roughness of clutch plates

Ra (μm)	Quiet plate	Plate producing unusual noise
Minimum value	0.126	0.088
Maximum value	0.252	0.167

3. Analysis of Factors

3.1. Measuring Lubricant Flow Rate

The flow rate of lubricant was checked as part of the analysis of factors in the polishing of the clutch plate surface. In the DPS, lubrication is done by supplying oil from the pump body, as shown in Fig. 6. It had been assumed that all the oil emitted by the pump body was supplied to the clutch, so the flow rate at the clutch had always been measured from pump body only. In this project, however, the flow actually passing through the clutch was measured to determine lubricant supply flow rate. Figure 7 diagrams the new method of measurement, and Fig. 8 furnishes a comparison of the calculated flow rate with the amounts actually measured at the pump body and at the clutch.

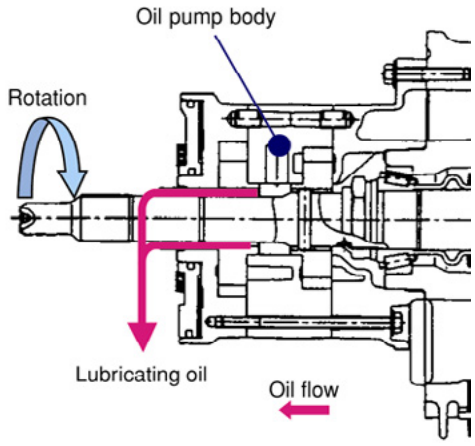


Fig. 6 Conventional lubrication measurement method

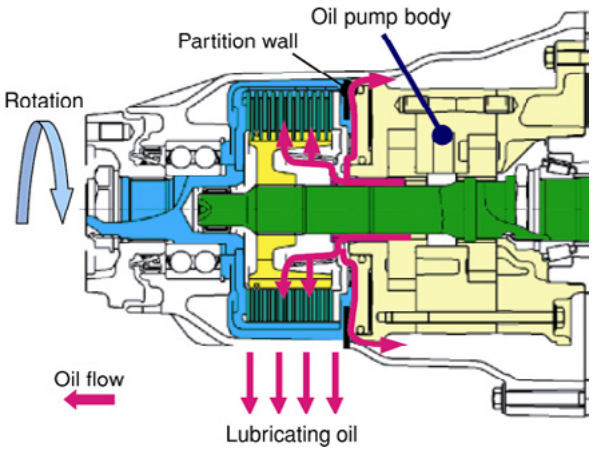


Fig. 7 Modified lubrication measurement method

In the conventional method, the flow rate reached its maximum value at vehicle speeds of 30 km/h or higher, and was close to the theoretical levels when the vehicle was moving at under 10 km/h, speeds normal during parking or takeoff from a junction. The new measuring method showed, however, that only about 70% of the theoretical flow rate of lubricant was supplied to the clutch at low vehicle speeds.

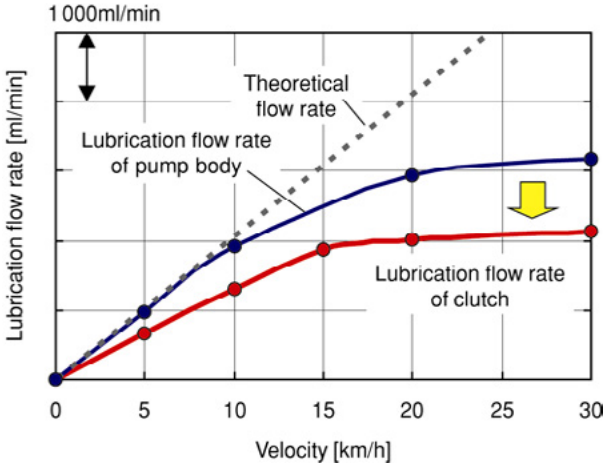


Fig. 8 Comparison of lubrication flow rate

3.2. Setting Reproducing Mode in Actual Vehicle

The results of the measurements of lubricant flow rate predicted that supply is low during parking and takeoff on snow-covered roads. This is expected, since the vehicle speed is low, and in turn, the oil pump runs at low RPM. The input torque is high in these running modes, however, as is clutch engagement frequency. Accordingly, it was attempted to create modes which would reproduce unusual noise and mirror-polishing of the clutch plate surfaces by combining the parking condition and takeoff from low-μ surfaces (see Fig. 9).

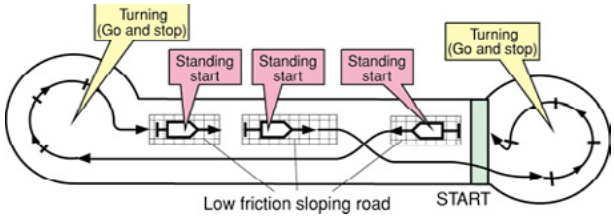


Fig. 9 Modified vehicle confirmation mode

3.3. Verification of Reproducing Mode in Actual Vehicle

On examining the vehicle after carrying out the reproducing mode, the unusual noise was noted during turning and takeoff on the low-μ surfaces. Also, as visible in Fig. 10, the clutch plate exposed to the reproduction mode showed the same mirror finished surface as the plate which had produced the unusual noise.

The results of roughness measurements of these plates shown in Table 2, indicate levels below 0.1 μm. This indicates that the conditions creating the plate which had produced the unusual noise had been reproduced.

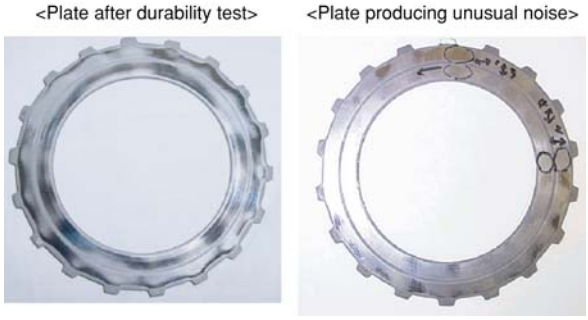


Fig. 10 Comparison of clutch plate condition

Table 2 Comparison of surface roughness of clutch plates

Ra (μm)	Plate after durability test	Plate producing unusual noise
Minimum value	0.017	0.088
Maximum value	0.106	0.167

4. Specifications for Measures against Unusual Noise

4.1. Improving Lubricant Specifications

4.1.1. Lubricant flow rate

The causes for the ineffective supply of lubrication at the

clutch were confirmed visually. When the pump is isolated, ordinarily, lubricant is only ejected in the direction of the clutch; with the clutch installed in place, however, lubricant was seen to be leaking in the opposite direction, as shown in Fig. 11.

This turned out to be due to blockage of the lubricant when the clutch was attached; oil was found to be leaking through the key slot for driving the rear pump. A collar was attached over the key slot, as in Fig. 12, to prevent the leak. This increased the flow in the low-speed region by about 20% as shown in Fig. 13.

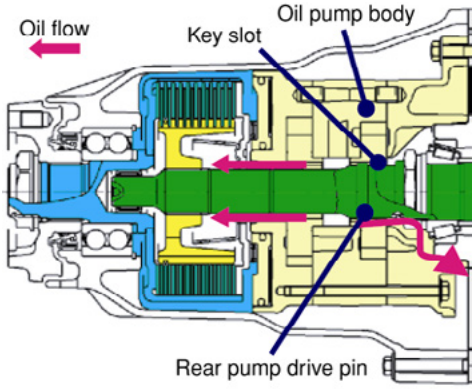


Fig. 11 Lubricating oil flow in DPS assembly

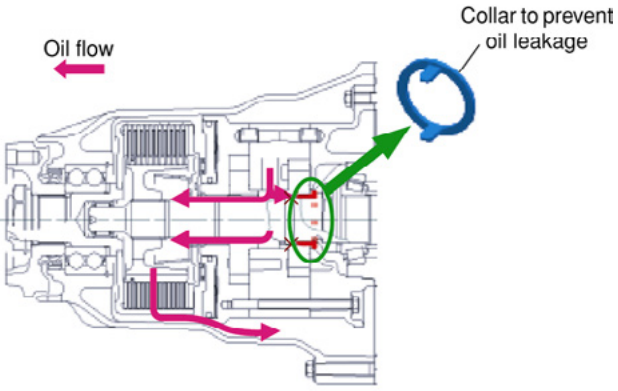


Fig. 12 Modified lubricating oil flow

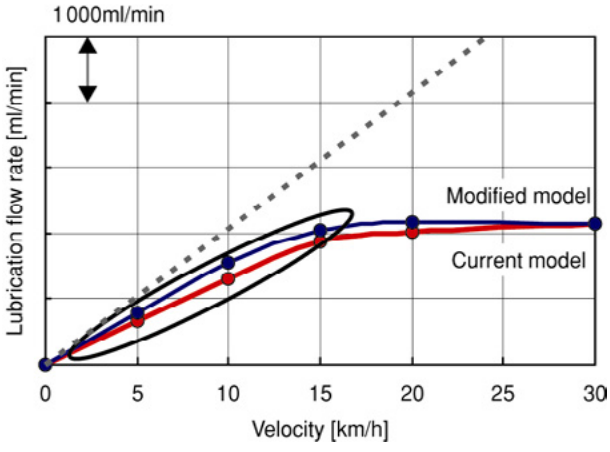


Fig. 13 Comparison of lubrication flow rate

4.1.2. Distribution of clutch lubricant

Next, a visual confirmation of lubricant distribution in the clutch showed that there was a large flow emitted from the clutch guide from the side close to the oil pump to the vicinity of the center, but lower volumes were seen farther from the pump.

This can probably be attributed to the oil flying off under centrifugal force when passing through the funnel, whose purpose is to distribute the oil (see Fig. 14).

A wall was added to partially obstruct the slit of the hub in the clutch, as shown in Fig. 15, to catch flying oil and maintain a better supply of oil in the locations distant from the oil pump.

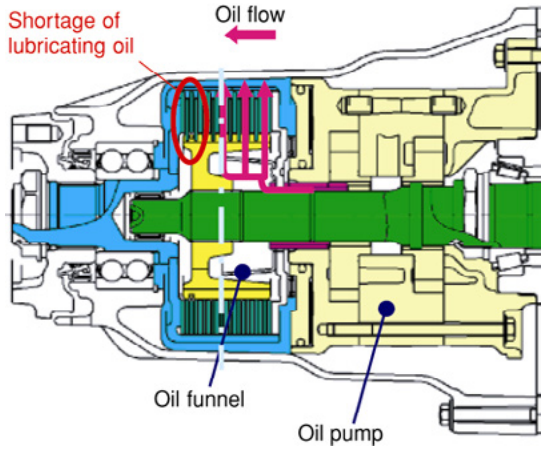


Fig. 14 Lubricating oil flow of DPS

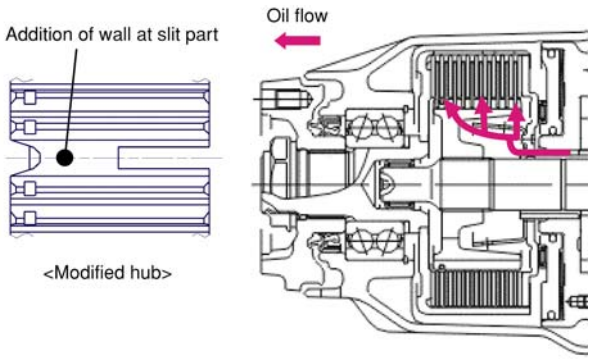


Fig. 15 Configuration of modified clutch hub and lubricating oil flow in DPS clutch

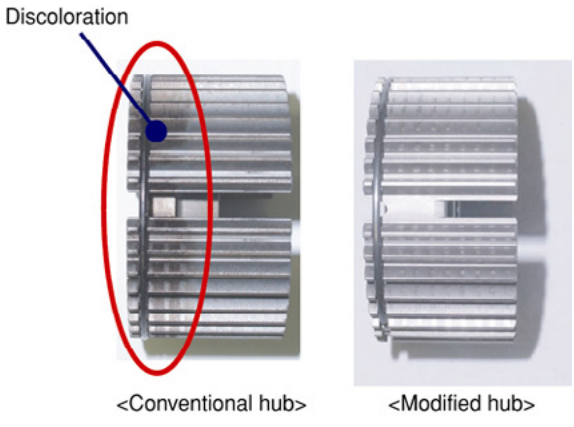


Fig. 16 Result of clutch continuously sliding test

When the results of the specifications revised to promote lubrication were confirmed visually, the lubricant was found to be evenly distributed. A vehicle test was carried out in which abrupt rotation speed differences were continuously induced to heat the clutch on purpose. As the results show in Fig. 16, the rear portion of the clutch in the vehicle with standard specifications became discolored, while the same location in the improved clutch showed no particular discoloration. This measure was concluded to be effective.

4.2. Development of New Clutch Friction Material

4.2.1. Relation between unusual noise and friction material characteristics

Next, the porosity and deflection of the clutch friction material were analyzed as a factor of the unusual noise.

The porosity was measured with a mercury porosimeter. The method for measuring deflection is shown in Fig. 17. The deflection was defined as the displacement occurring when the same load is applied on the clutch assembly as in an actual vehicle.

The analysis showed that, as shown in Fig. 18, the higher the porosity, or the greater the deflection, the less tendency there was for unusual noise generation.

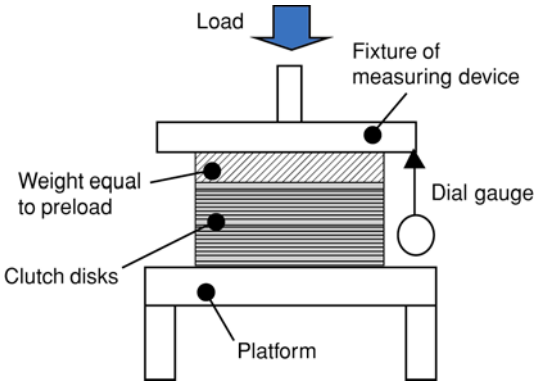


Fig. 17 Measurement method

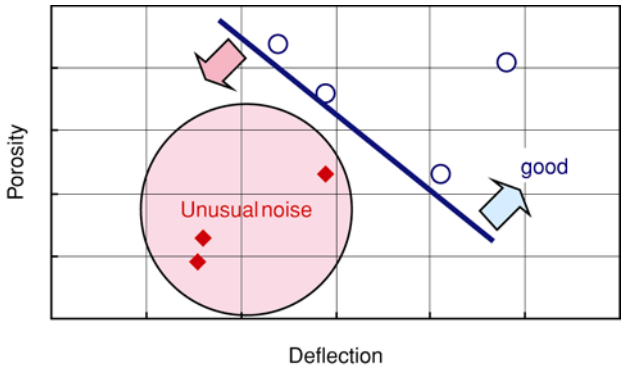


Fig. 18 Relation of porosity and deflection to unusual noise

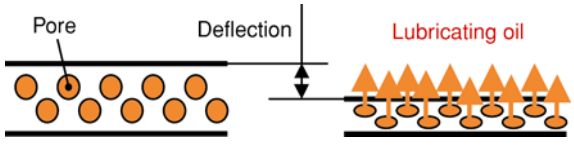


Fig. 19 Model of clutch lubrication

Figure 19 explains this; when the clutches engage, pores filled with lubricant are compressed, which tends to squeeze out the lubricant. Even when there is little lubricant supply, the material then self-lubricates, reducing the occurrence of the unusual noise.

4.2.2. Friction material characteristics

A friction material was developed with four times the porosity of the conventional material. Figure 20 indicates that this has 2.5 times the deflection of the conventional material.

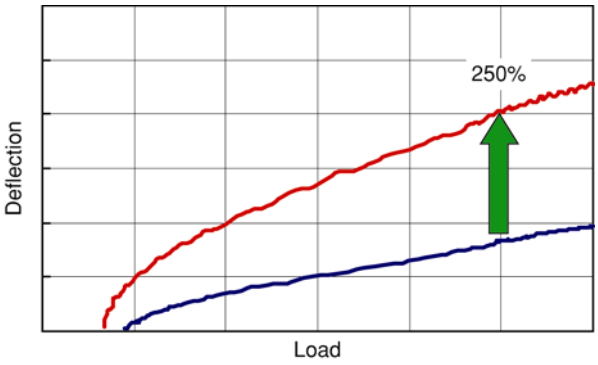


Fig. 20 Comparison of deflection characteristic

4.3. Verifying Effect of Countermeasures

No unusual noise was noted in reproducing mode when the newly developed friction material with improved lubrication specifications was tested in an actual vehicle.

Also, as shown in Fig. 21, no mirror finished surface was found in the clutch plate used in reproducing mode. The surface roughness was measured and found to equal that in quiet plates, as shown in Table 3.

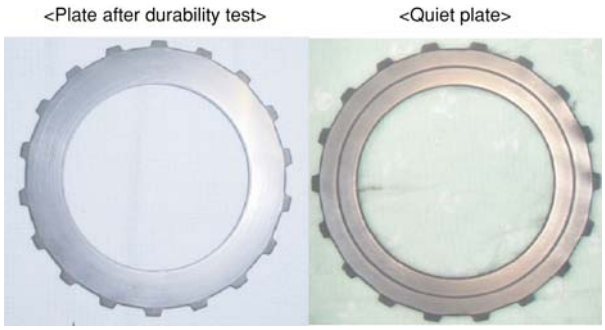


Fig. 21 Comparison of clutch plate condition

Table 3 Comparison of surface roughness of clutch plates

Ra (μ m)	Plate after durability test	Quiet plate
Minimum value	0.114	0.126
Maximum value	0.187	0.252

5. Conclusion

Research was carried out to find ways to reduce the unusual noise occurring on turning and takeoff when an automatic transmission clutch is used in a torque-on-demand

type 4-wheel drive system. The following results were obtained:

(1) It was found that the clutch plate in a product emitting the unusual noise had been polished to a mirror finished surface, and that this was due to insufficient flow rate of the lubricant used at the clutch.

(2) A reproducing mode of an actual vehicle in which the clutch lubricant is low and the load is high was constructed by combining parking and takeoff on low-μ surface conditions; this enabled verification of the unusual noise and the mirror surface finish on the clutch plate.

(3) As a measure against unusual noise and mirror surface finish of the clutch plate, an oil leak to the parts other than the clutch was stopped, which increased the lubricant flow rate, and steps were taken to ensure a uniform distribution of lubricant inside the clutch.
Also, a friction material with greater porosity and deflection was developed to improve its capacity to hold lubricant.
A vehicle was installed with these improvements and tested in the reproducing mode; the unusual noise and mirror surface finish of the clutch plate were eliminated.

Acknowledgements

The authors extend their deep appreciation to F.C.C. Co., Ltd. and the many other personnel inside and outside Honda for their cooperation in this project.

References

(1) Society of Automotive Engineers of Japan, Inc.: Automatic transmission, Tribology in Automobile, Tokyo, Yokendo Ltd., p. 151-155 (1994)

(2) Kobayashi et al.: Development of Dual Pump 4WD System, HONDA R&D Technical Review, Vol. 8, p. 77-82 (1996)

(3) Hamada et al.: Weight Saving of 4WD Vehicles by Optimizing Distribution of Torque between Front and Rear Wheels, Journal of Society of Automotive Engineers of Japan, Inc., Vol. 46, p. 99-103 (1992)

(4) Hamada et al.: Realtime 4wd Dual Pump System, Automotive Engineering, Vol. 43, No. 7, p. 16-25 (1994)

■ Authors ■



Masaki INOUE



Yasunori ARAI



Toshiaki AZEGAMI



Yasuo HIRAO

Research on Longitudinal Vibration of MT Vehicle during Acceleration

Yoshihiro KATAGIRI* Hiroshi YATANI* Hajime IGAMI*
Hiroyuki SAITOU* Tatsuya SHIRAKI* Ikuo OOMORI*

ABSTRACT

Waveforms of longitudinal vibration during acceleration in MT vehicles have been used to develop five evaluation indices corresponding to sensory evaluations. The mechanism of longitudinal vibration during acceleration was clarified in each part of the system through which it is transmitted: engine, drive train, tires, engine mounts and suspension. A simulation model was constructed employing design values as the main elements, enabling specifications to be tested in the initial development phase, before the construction of an actual vehicle. This method was utilized in the development of the new model Accord, enabling suspension characteristics and engine torque control, among other design elements, to be optimized at an early stage, and resulting in the reduction of development time by half.

1. Introduction

Recently, performance areas evaluated by human sensitivity, such as the comfort and responsiveness of the driver, became as important as dynamic performance, noise, fuel economy and other performance areas that are evaluated numerically. However, it is difficult to accurately quantify these types of performance areas, so vehicle development must rely on sensory evaluation using actual vehicle tests, which means that vast amounts of manpower are used through trial and error testing.

Body longitudinal vibration that occurs when the accelerator pedal is depressed is a source of discomfort for the driver, and is an important area that must be improved for MT vehicles. Cases of improving this phenomenon by methods such as optimization of the engine mount stiffness[1] have been reported in the past.

This type of vibration concern is rooted in various properties of large numbers of components, and at the same time often has a trade-off relationship with other areas. This means that the related items are complexly intertwined and there are few cases where the issue can be solved simply by improving the characteristics of a single part. In addition, it is extremely difficult to clarify the generation mechanism and degree of effect through actual vehicle tests, so accurate analysis technology is needed.

This paper reports the results of constructing and applying evaluation indices and a simulation model to the development of mass production vehicles.

2. Development Goals

In order to shorten the development time for MT vehicles, it is important to improve the specifications as much as possible in the initial development phase and reduce trial and error in actual vehicle tests.

The accumulation of vehicle behavior simulation know-how has made it possible to accurately analyze transient behavior. However, actual vehicle measurement data concerning element characteristics is needed to accurately reproduce behavior, which makes this difficult to use in the initial development phase. In addition, thus far evaluation has been determined by sensory evaluation

* Tochigi R&D Center

through actual vehicle test rides, so there are no substitute evaluation indices, and it would be difficult to make a grade judgment even if vehicle behavior could be simulated.

Therefore, the three main goals of this study were as follows.

(1) Constructing evaluation indices capable of substituting for sensory evaluation
(2) Constructing a simulation that can be utilized from the initial development phase
(3) Applying these indices and simulation to the development of mass production vehicles to shorten the development time

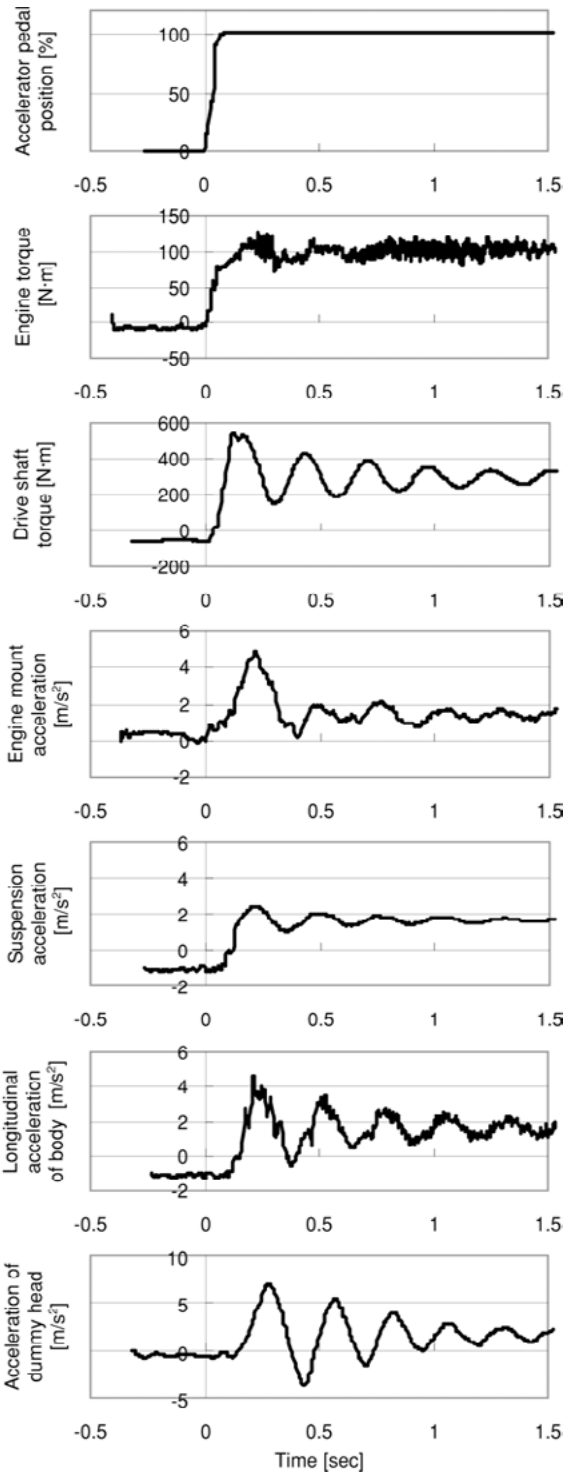


Fig. 1 Time history of body vibration by acceleration shock WOT acceleration, 2nd gear, 1 500rpm

3. Construction of Evaluation Indices

To investigate evaluation indices, test ride comparisons of market vehicles were performed with multiple drivers, and sensory evaluation was conducted using the ten-point method. These results and measurement values were then compared and analyzed, and evaluation indices were constructed.

3.1. Test Method

The body longitudinal vibration frequency during acceleration differs according to the gear ratio, and the frequency increases at higher speed gear steps. In addition, the vibration when accelerating again from the state after deceleration fuel cut is larger than when accelerating from the steady cruising state.

The feeling is particularly worsened by the 3 to 8 Hz vibration that occurs when cruising at the low speed of 20 to 40 km/h in 1st through 3rd gears. Figure 1 shows some measurement examples. The body longitudinal vibration process during acceleration was confirmed through actual vehicle tests in which the accelerator pedal was pressed from the fully closed position to the fully open position to accelerate at the prescribed engine speed, and the torque and vibrations were measured. These measurements were taken for over ten types of vehicles with different shift steps, engine speeds and accelerator pedal openings. The engine torque during actual cruising used the net torque obtained by measuring and processing the internal pressure of all four cylinders in consideration of the combustion variance of each cylinder. Also, body longitudinal vibration during acceleration is felt as rocking of the head relative to the seat and neck, so a sensor was attached to the head of a dummy to measure the longitudinal acceleration. When the accelerator pedal is pressed to the fully open position, the engine generates sudden torque which produces torque fluctuations on the drive shaft. A short time thereafter, fluctuations occur almost simultaneously in the engine mount and the suspension, followed by overshoot and low cycle fluctuations in the body longitudinal direction. Then, after another short delay, fluctuations occur as measured by the instrumented dummy.

Figure 2 shows the frequency analysis of the dummy head acceleration and the body longitudinal vibration. The dummy head acceleration is amplified around 4 Hz, and attenuated at 11 Hz and higher.

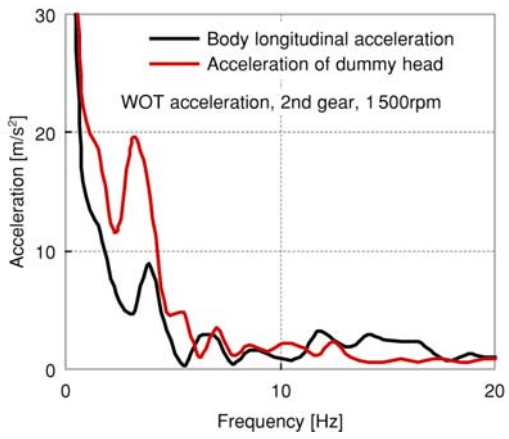


Fig. 2 Results of frequency analysis of dummy head acceleration

3.2. Creation of Indices

On the other hand, it was assumed from the questionnaire results that drivers feel the overshoot of the first peak as shock, and the subsequent vibrations as jerking. At the same time they feel the response speed (response) of the first peak, that is to say, a quick acceleration rise as comfort and acceleration that does not drop as smoothness. These subjective driving sensations were expressed as numerical values and compared with the results of sensory evaluation to construct five evaluation indices. Figure 3 shows the approach to each index, and the formulas used to calculate each numerical index are defined as follows.

(A) Shock: Non-dimensional value of the overshoot relative to the acceleration expected by the driver

$$\text{Overshoot} = \ddot{X}_A / \ddot{X}_{AVE} \quad (1)$$

(B) Jerking: Fluctuation energy amount obtained by integrating the low frequency fluctuation relative to the acceleration expected by the driver

$$\text{Swing energy} = 1/2 \cdot m \cdot \{ \int | \ddot{X}_B - \ddot{X}_{AVE} | dt \}^2 \quad (2)$$

(C) Response: Response speed relative to the driver's acceleration pedal operation

$$\text{Delay time} = t_P + t_N \quad (3)$$

(D) Quickness: Comfortable acceleration rise linked with the driver's acceleration pedal operation

$$\text{Torque increase} = (\ddot{X}_A - \ddot{X}_B) / t_P \quad (4)$$

(E) Smoothness: Minimum acceleration produced by the fluctuations during acceleration

$$\text{Minimum acceleration} = \ddot{X}_C \quad (5)$$

Nomenclature :

$\ddot{X}_A$: Peak of acceleration [m/s^2]
$\ddot{X}_{AVE}$: Average acceleration [m/s^2]
$\ddot{X}_B$: Real acceleration [m/s^2]
$\ddot{X}_C$: Bottom of acceleration [m/s^2]
t_P : Time until peak [sec]
t_N : No reactive time [m/s^2]

Figures 4 to 8 show the results of confirming the correlation of the five evaluation indices obtained by the above formulas with sensory evaluation by actual vehicle test rides, and show a high correlation in each case.

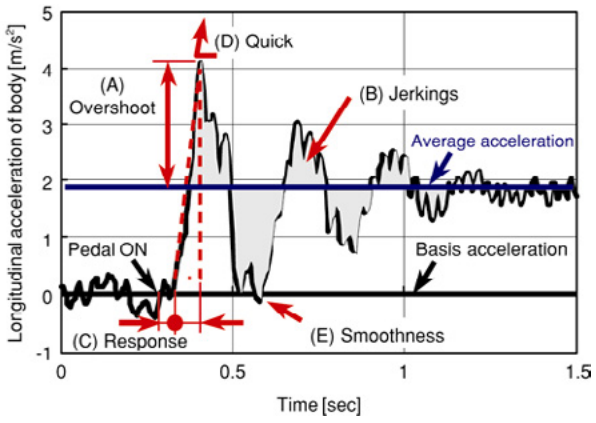


Fig. 3 Definition of index

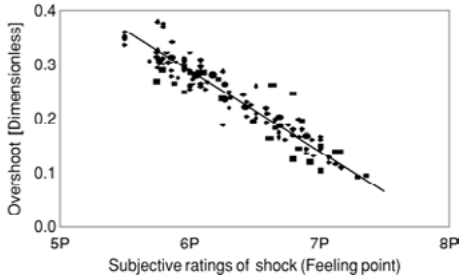


Fig. 4 Subjective ratings of shock characteristic against objective parameter

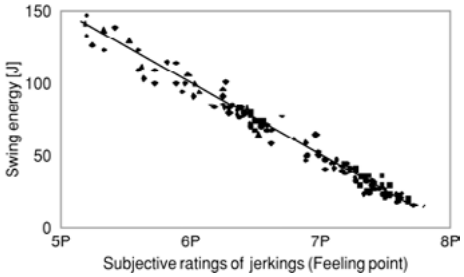


Fig. 5 Subjective ratings of jerkings characteristic against objective parameter

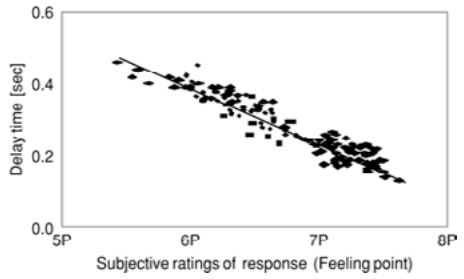


Fig. 6 Subjective ratings of response characteristic against objective parameter

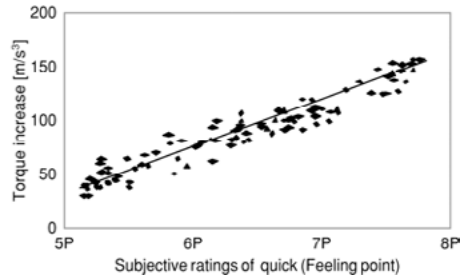


Fig. 7 Subjective ratings of quickness characteristic against objective parameter

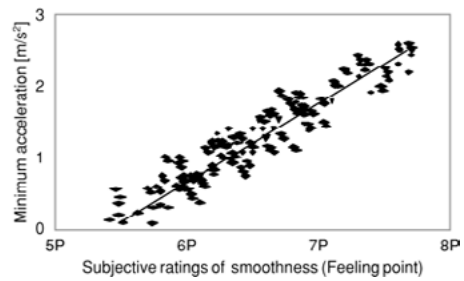


Fig. 8 Subjective ratings of smoothness characteristic against objective parameter

4. Creation of a Simulation Model

A simulation model was constructed with the body longitudinal vibration during acceleration as the coupled vibration from the engine to the transmission, drive shaft, tires, engine mount, suspension and body. The calculation formulas are shown below.

$$T_E - I_{FW}\ddot{\theta}_{FW} - T_{CL} = 0 \quad (6)$$

$$T_{CL} - C_{CL}(\dot{\theta}_{FW} - \dot{\theta}_{GB}) - K_{CL}(\theta_{FW} - \theta_{GB}) = 0 \quad (7)$$

$$T_{CL} - I_{GB}\ddot{\theta}_{GB} - T_{GB}/i = 0 \quad (8)$$

$$T_{GB} - K_{GB}(\theta_{GB}/i - \theta_{DS}) = 0 \quad (9)$$

$$T_{GB} - I_{DS}\ddot{\theta}_{DS} - T_{DS} = 0 \quad (10)$$

$$T_{DS} - C_{DS}(\dot{\theta}_{DS} - \dot{\theta}_{WH}) - K_{DS}(\theta_{DS} - \theta_{WH}) = 0 \quad (11)$$

$$T_{DS} - I_{WH}\ddot{\theta}_{WH} - T_{WH} = 0 \quad (12)$$

$$T_{DS} - I_E\ddot{\theta}_E - T_{EM} = 0 \quad (13)$$

$$F_{WH} - T_{WH}\theta_{SUS}/X_{SUS} = 0 \quad (14)$$

$$F_{WH} - M_{WH}\ddot{X}_{SUS} - F_V = 0 \quad (15)$$

$$F_V - C_{SUS}(\dot{X}_{SUS} - \dot{X}_V) - K_{SUS}(X_{SUS} - X_V) = 0 \quad (16)$$

$$F_V - M_V\ddot{X}_V - M_{PP}\ddot{X}_{EM} = 0 \quad (17)$$

Nomenclature :

T : Torque [N·m]

I : Inertia [N·m·s^2]

θ : Torsional angle [rad]

C : Damping property [N m·s/rad]

K : Torsional stiffness [N m/rad]

F : Force [N]

M : Mass [kg]

X : Displacement [m]

Subscripts :

E : Engine

F : Flywheel

CL : Clutch

GB : Gear box

i : Gear ratio

EM : Engine mount

DS : Drive shaft

WH : Tire wheel

V : Vehicle

SUS : Suspension

PP : Power plant

The characteristic data of each element used in the simulation all used the design values. The body elastic vibration frequency range is lower than 20 Hz, so the power plant and the body were treated as rigid bodies. The frequency for this phenomenon is relatively low and the dynamic magnification of rubber is close to 1, so it was thought that the load-displacement dynamic characteristics of the engine mount, suspension, tires and other elements could be replaced with static characteristics in the same manner as the clutch torsion and the drive shaft torsional stiffness. Non-linearity of these load-displacement dynamic characteristics was taken into account by applying a table function. Also, the engine torque input values used the values obtained by bench tests.

Figure 9 shows an example comparing the simulation results of body longitudinal vibration during full acceleration with actual vehicle measurement data.

This figure shows that in addition to the 3 Hz low frequency vibration which is the main fluctuation, the 15 Hz frequency component occurring on the first peak can also be calculated.

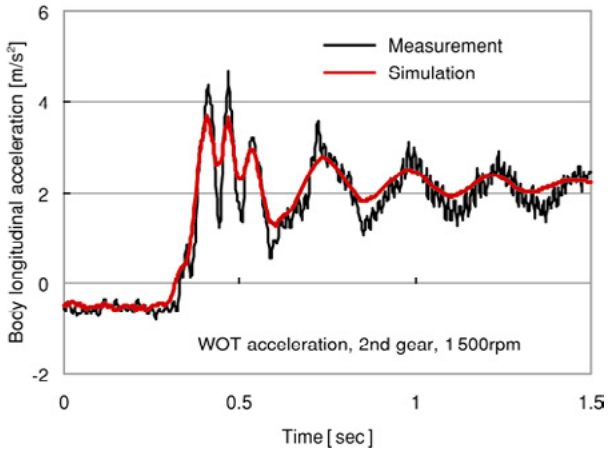


Fig. 9 Results of verification of simulation

5. Application to Development

5.1. Analysis of Contribution

The above simulation was conducted in the initial development phase of the new model Accord, and the results of analyzing the contribution of each evaluated part to body longitudinal vibration are shown in Fig. 10. This shows that the drive shaft stiffness, suspension stiffness, engine torque control, engine rotation inertia and body inertia have a significant effect. Therefore, suspension stiffness and torque control measures were investigated.

5.2. Countermeasure Effects

5.2.1. Suspension characteristics

Of the various suspension characteristics, the front and rear compliance characteristics are determined to simultaneously achieve the conflicting required performances of riding comfort and handling and stability. These characteristics are necessary when backward force acts on the vehicle, and it was found that changing the forward characteristics, which are a cause of shock during acceleration, had no effect on these performances. Therefore, the characteristics were changed to asymmetrical characteristics in the forward and backward directions as shown in Fig. 11 to reduce the shock during acceleration while maintaining riding comfort.

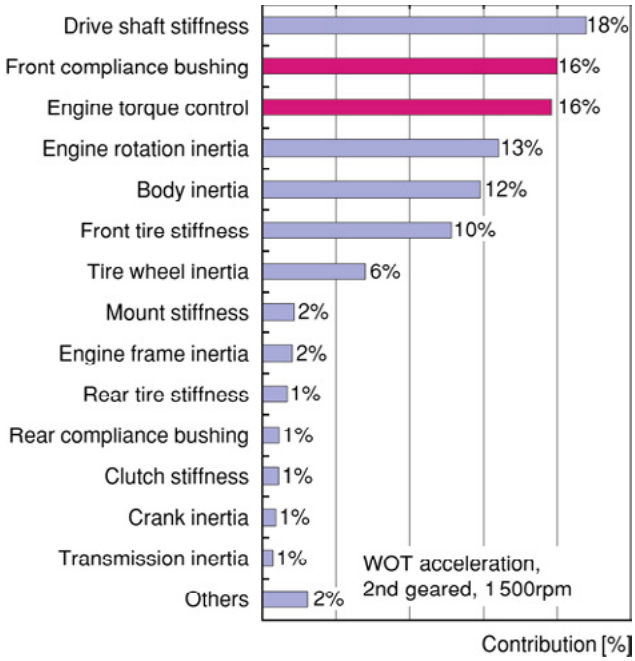


Fig. 10 Analysis of contribution of each part

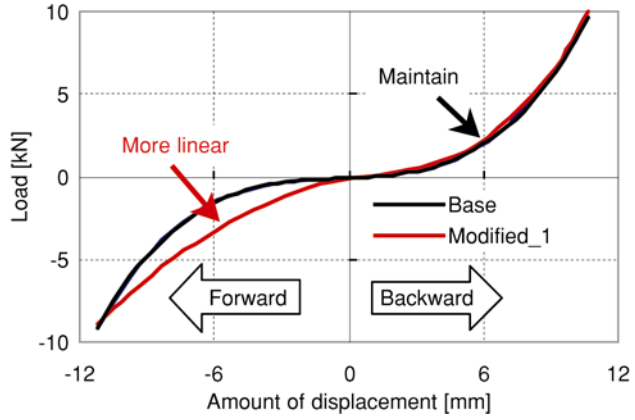


Fig. 11 Compliance bushing characteristic

Figures 12 and 13 compare the results before and after changing the compliance bush characteristics of the suspension. These figures show that the first suspension displacement peak during acceleration has been reduced, and at the same time the 15 Hz overshoot seen on the first peak has also been improved.

5.2.2. Engine torque control

Analysis of contribution showed that shock and jerking are the most affected by engine torque control, so improvement of these two items was investigated.

Conventional engine torque control methods include delaying the ignition timing angle or reducing the intake air volume and fuel injection amount to limit the engine torque rise speed, thus reducing overshoot and low frequency fluctuations.

First the optimum engine torque rise for improving shock was investigated. Figure 14 shows the changes in the evaluation index scores. Increasing the engine torque rise speed was found to improve response and quickness, but to worsen shock, jerking and smoothness, with shock in particular changing significantly. The optimum scores were achieved by reducing the speed by approximately 20% relative to the initial setting data.

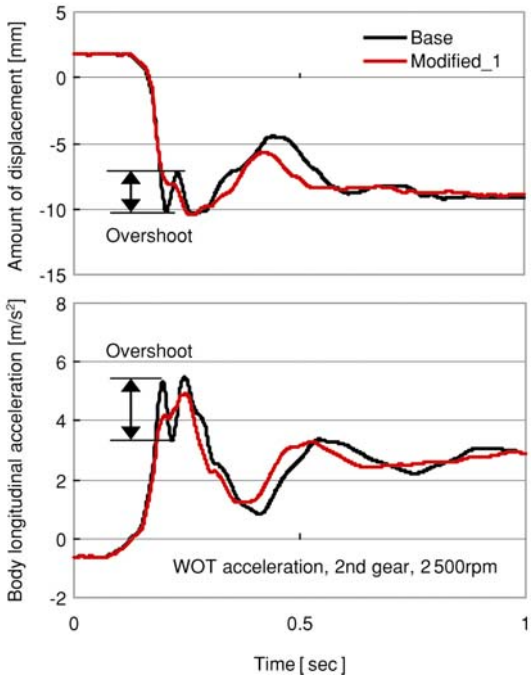


Fig 12 Influence of compliance bushing (Simulation)

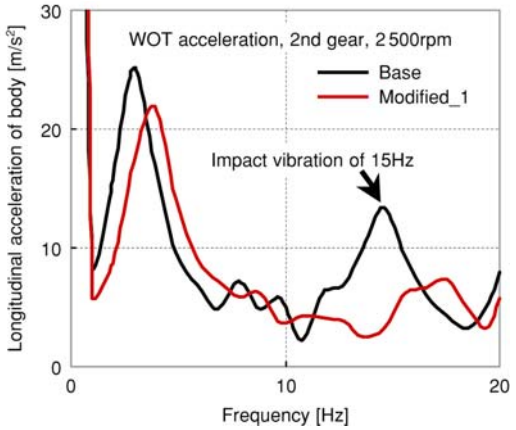


Fig. 13 Result of frequency analysis of body longitudinal acceleration of body (Simulation)

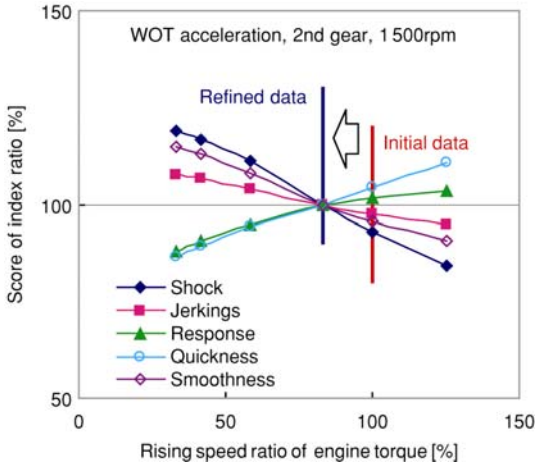


Fig. 14 Comparisons of speed of increase of engine torque (Simulation)

Next the optimum engine torque control timing for improving jerking was investigated. The control timing delay at various engine speeds was measured. The allowable timing delay was the value obtained using the aforementioned indices. As the engine speed decreased, the control delay became more pronounced and jerking worsened. The cause of this control delay was the longer arithmetic processing interval for engine rotation sync control. Changing the program reduced this control timing delay in the low speed range as shown in Fig. 15.

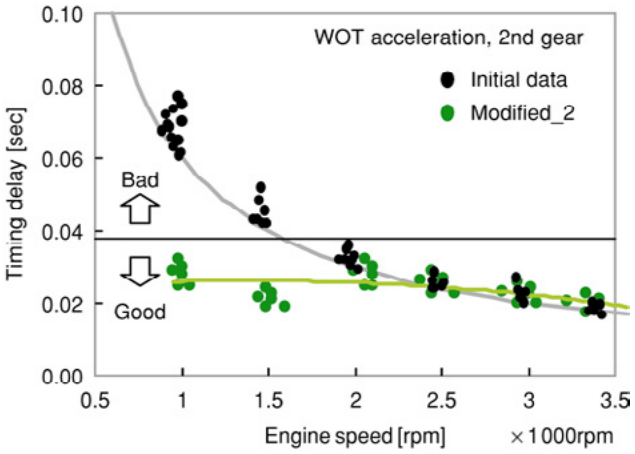


Fig. 15 Engine timing delay characteristics (Simulation)

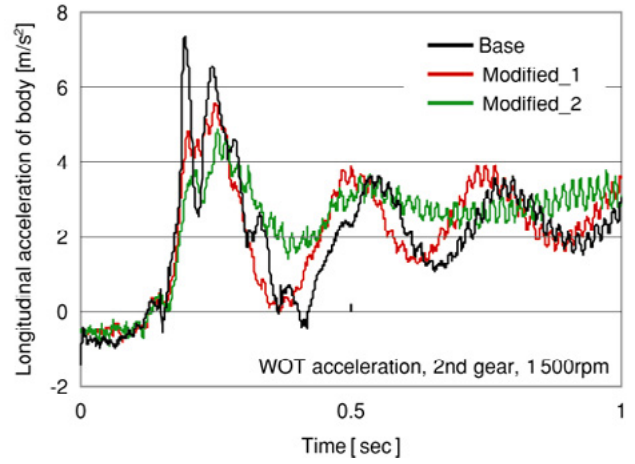


Fig. 6 Test results

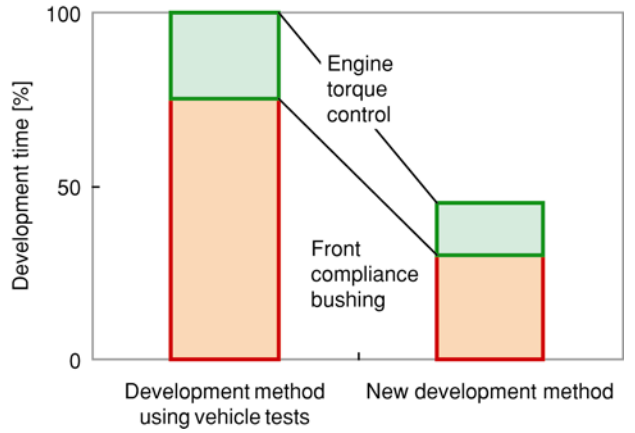


Fig. 17 Development time for acceleration feeling

Figure 16 shows the measurement results for body longitudinal vibration that reflects these countermeasures. Modified_1 with improved suspension characteristics and Modified_2 with engine torque control added show vast improvements to shock and jerking.

5.3. Effects of Application to Development

The newly developed method reduced trial and error in actual vehicle tests, and halved the development time as shown in Fig. 17.

6. Conclusion

Body longitudinal vibration of MT vehicles during acceleration was studied, and the following results were obtained.

(1) Five evaluation indices for shock, jerking, response, quickness and smoothness were constructed to take the place of sensory evaluation of body longitudinal vibration during acceleration.
(2) Using the design values for all the characteristics data of each element used in the simulation made it possible to investigate specifications in the initial development phase before an actual vehicle exists.
(3) The development time of mass production vehicles was cut in half.

Reference

(1) Inoue, M.: Analysis on Acceleration/Deceleration Shock and Vibration in FF Vehicle, Proceedings Journal of Society of Automotive Engineers of Japan 921087 (1992)

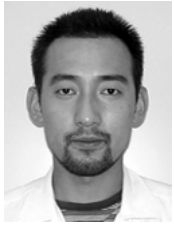
■ Authors ■


Yoshihiro KATAGIRI


Hiroshi YATANI


Hajime IGAMI


Hiroyuki SAITOU


Tatsuya SHIRAKI


Ikuo OOMORI

Study of Coaxial Counter Rotating Rotary Tilling System at Front Rotary Type Compact Walking Tractor

Yoshitaka OHTA* Susumu OHKUBO* Keiji IINO*
Masatoshi NAGAOKA* Keiji NAGANO* Nobuchika KATAGIRI*

ABSTRACT

A computer simulation of tilling force has been conducted for a compact walking tractor equipped with rear driving wheels and a front rotary shaft to estimate the effect of tilling force on behavior and tilling depth for a down cut rotary and a coaxial counter rotating rotary. The tractor uses a down cut rotating tine that rotates in the same direction of the driving wheels, and a coaxial counter rotating tine that rotates on the same shaft simultaneously. Further, an actual machine test was conducted to examine the correlation between the simulation and test results. It was demonstrated that by using the coaxial counter rotating rotary, the effect not only stabilized the behavior of the tractor but also accomplished twice the tilling depth of a conventional down cut rotary.

1. Introduction

Compact walking tractors with rotary tilling systems comprised of tines that rotate about a rotary shaft to till the soil are configured with a rotary shaft in two different formats; with and without separate driving wheels.

Of those tractors configured with separate driving wheels, there are rear rotary types, which are configured with a rotary shaft behind the driving wheels as shown in Fig. 1, and front rotary types which are configured with a rotary shaft in front of the driving wheels as shown in Fig. 2.

In the rear rotary type, the direction of the tilling reaction passes close to the unit's center of gravity. Therefore, fluctuations in the tilling reaction do not cause unstable tractor behavior. For similar reasons, the rotary shaft is prevented from lifting up off the earth's surface due to the tilling reaction, which facilitates a more desirable level of deep tilling.

However, fitting the motor in a forward position that will help reduce the handle operating load as the rotary shaft is lifted from the soil's surface during turning makes the tractor larger. Fitting it in a higher position that allows the rotary shaft to be lifted up as required, makes the center of gravity higher, which causes an unbalance. As a result, the usual positioning for the motor is low and in close proximity to the driving wheels and an iron balance weight is then needed to be attached to the forward underside of the tractor to adjust the center of gravity. The weight of a tractor increases by that of the balance weight (Fig. 3).

Additionally, because the wheels and motor are located in front of the rotary shaft and the handles are set behind the rotary shaft, it inevitably becomes difficult to perform tilling in narrow field areas surrounded by walled boundaries.

In front rotary type tractors, the rotary shaft is mounted on the front of the unit enabling tilling right up to the barrier edge. Moreover, the handles are located behind the driving wheels and the motor is mounted at the front, which provides an optimal center of gravity without having to add a balance weight. This reduces the overall weight of the tractor unit and contributes to its compact design since the motor is not mounted in an overhanging position.

Contrary to the rear rotary type tractors, the direction of

* Asaka R&D Center

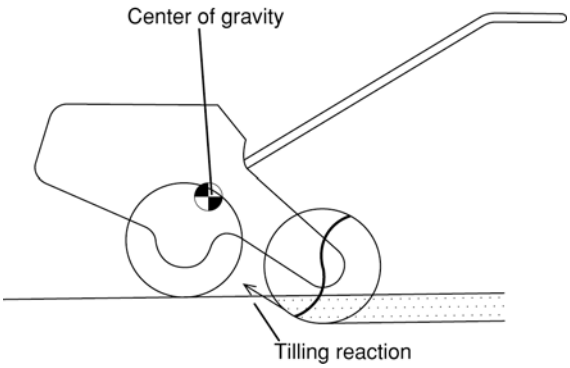


Fig. 1 Rear rotary walking tractor

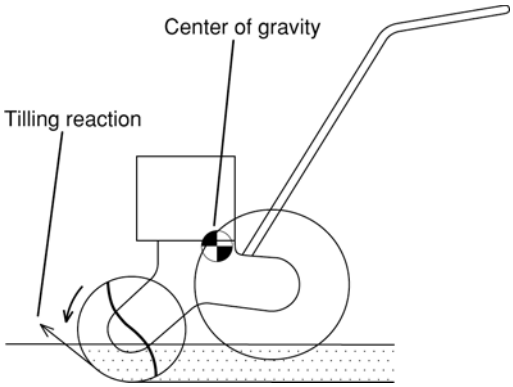


Fig. 2 Front rotary walking tractor

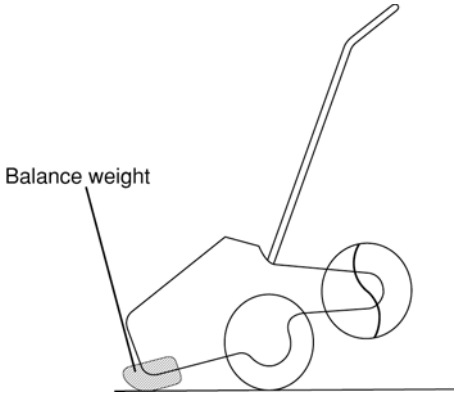


Fig. 3 Turning position of rear rotary walking tractor

the tilling reaction of the front rotary type is offset from the center of gravity. The resultant fluctuation in the tilling reaction causes imbalanced tractor behavior.

Also, in adopting a down cut rotary in which the driving wheel direction and the rotational direction of the rotary shaft are the same, the tilling reaction causes the rotary shaft to lift up, which does not promote tilling depth.

Whereas in adopting an up cut rotary configuration as shown in Fig. 4, in which the rotary shaft rotates in the opposite direction of the driving wheels, the tine bites the soil more forcefully and the tractor tends to lift upward in the back direction leading to what is commonly known as dashing. Regardless, neither of these configurations provide a satisfactory level of performance.

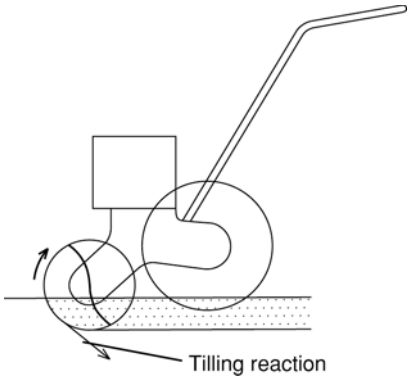


Fig. 4 Front rotary walking tractor with up cut tilling

The coaxial counter rotating rotary, which is configured with a rear rotary, is highly praised for its stable deep tilling performance without giving rise to any dashing action. It offsets the reactive tilling force by tilling as the down cut tine and up cut tine rotate along a shared axis. As shown in Fig. 5, combining the coaxial counter rotating rotary with the front rotary configuration would diminish the fluctuating tilling reaction, stabilize tractor behavior, and also serve to suppress any dashing and lifting up of the rotary shaft. This gave impetus to the idea of creating a new tractor that would be lightweight and compact but capable of stable tilling, deep tilling, and tilling up to the barrier edge.

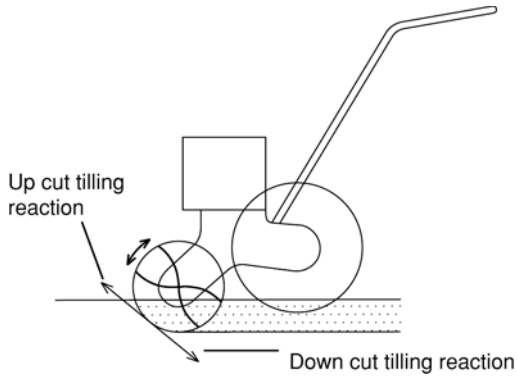


Fig. 5 Front rotary walking tractor with coaxial counter rotating tines

This report describes that the above stated effects were verified by estimating the tractor behavior from its simulated tilling reaction and then correlating the estimation with actual test results.

2. Estimating Tilling Performance

2.1. Calculating Tilling Reaction

A computer simulation[(1)] of the tilling force was conducted respectively for compact walking tractors with a down cut rotary and a coaxial counter rotating rotary. A newly designed tine for the FF300, Honda's front mount coaxial counter rotating rotary tractor, was used in the testing. The tine layout was designed to provide a constant tilling pitch to minimize the fluctuation in vertical tilling reaction movement. Furthermore, a right and left alternating tine configuration was employed to minimize fluctuation in

the yawing and rolling momentum. These settings provided a tilling width of 450 mm, a tine diameter of ϕ 280 mm, a tilling depth of 120 mm, a machine speed of 0.15 m/sec and a rotary speed of 130 rpm. The soil hardness was set to an approximate value of 20 with a Yamanaka soil hardness tester assuming typical untilled soil.

Figures 6 and 7 show the tine layout configuration and Figs. 8 and 9 show the simulated results of the two tilling reactions. Figure 10 shows the definitions of the six components of the tilling reaction.

2.2. Estimating Tractor Behavior

The six tilling reaction components shown in Fig. 10 were considered for the influences they exert on the tractor behavior during operation.

The yawing momentum, Mz, and the side force, Fx, cause yawing to the tractor and the deterioration of the tractor's straight line stability.

The longitudinal load, Fy, influences the tractor's propelling force causing the tires to slip which in turn causes the actual machine speed to fluctuate during tilling.

The vertical load, Fz, and the pitching momentum, Mx, act to cause the rotary shaft to lift up (+) or sink (–) at the ground contact tire center. If a momentum were exerted to cause the rotary shaft to lift upward (+) and this momentum was greater than the momentum created by the weight of the tractor unit itself, the rotary shaft would tend to lift up off the ground surface and decrease the tilling depth.

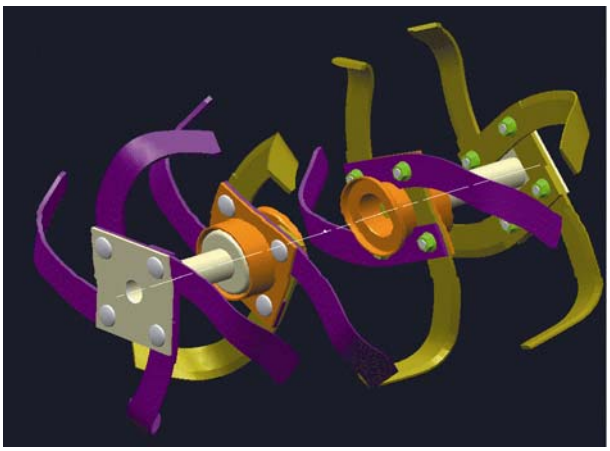


Fig. 6 Tine layout of down cut tines

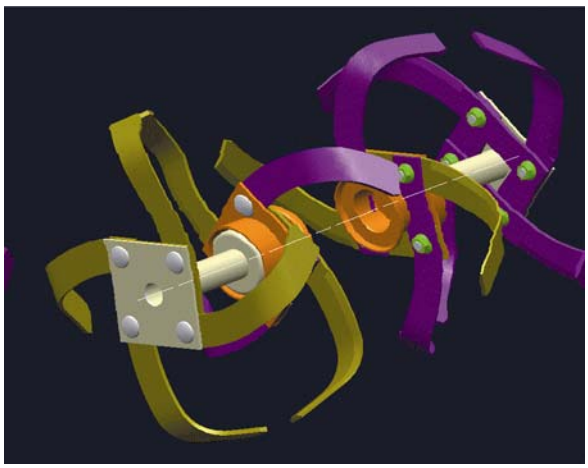


Fig. 7 Tine layout of coaxial counter rotating tines

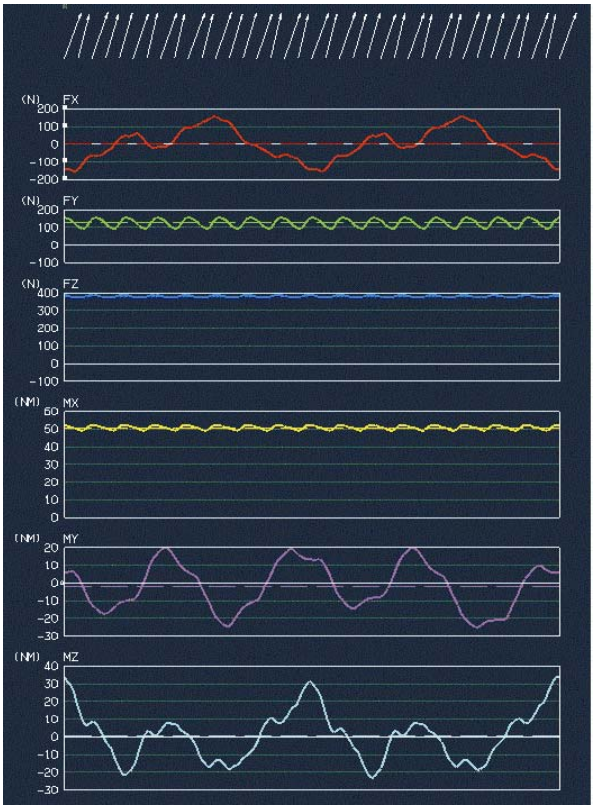


Fig. 8 Simulated result of down cut tilling reaction

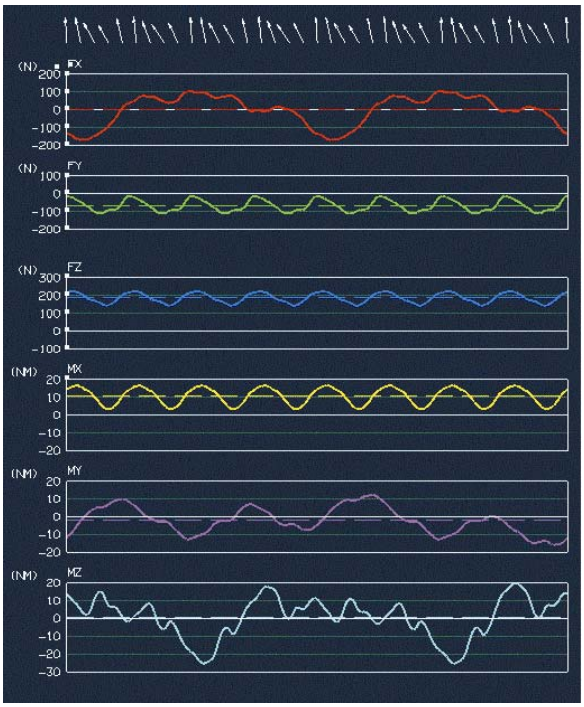


Fig. 9 Simulated result of coaxial counter rotate tilling reaction

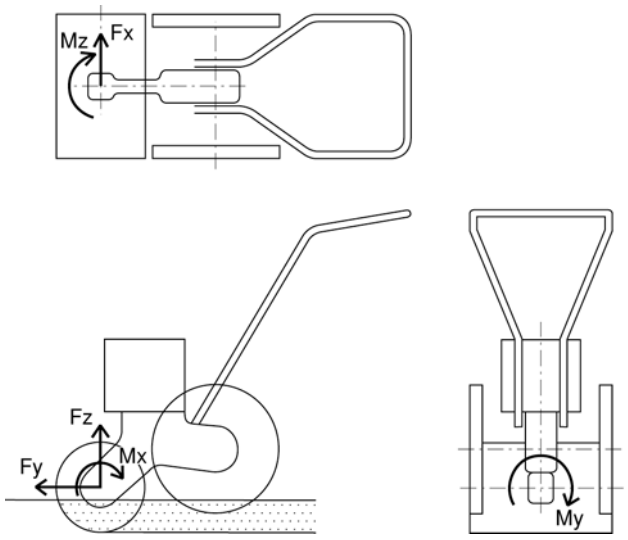


Fig. 10 Six components of tilling reaction

The sinking momentum has been addressed by attaching a tilling depth adjustment wheel in front of the rotary shaft to help prevent sinking. The rolling momentum, My, causes the tractor to roll, which prevents even tilling.

Based on actual machine specifications and the calculated results, an analysis was conducted into the performance differences between the down cut rotary (hereafter abbreviated to down cut) and the coaxial counter rotating rotary (hereafter abbreviated to counter rotating) to evaluate the lifting action of the rotary shaft and its effect on tilling depth.

Actual measured values on the FF300 were used to set the tire sinking depth to 20 mm from the soil's surface before tilling.

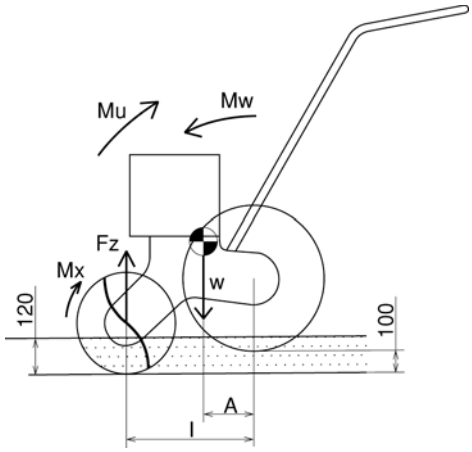


Fig. 11 Moment of tilling reaction and gravity moment on the ground contact center of tires

The average lift momentum value around the ground contact tire center is represented by $\overline{Mu}$ and expressed as follows:

$$\overline{Mu} = \overline{Mx} + l \cdot \overline{Fz} \quad (1)$$

The rotary shaft push momentum exerted by the tractor weight is represented by Mw and expressed as follows:

$$Mw = W \times A \quad (2)$$

Here, in order to help prevent the rotary shaft lift momentum caused by the tilling reaction, the following formula must be satisfied:

$$Mw > \overline{Mu} \quad (3)$$

The FF300 tractor specifications and the average values from the calculated results for Fz and Mx as shown in Fig. 8 and Fig. 9 were used to verify whether this relationship could be satisfied.

Table 1 Comparison of moment of tilling reaction and gravity moment

l(m)	A(m)	W	Mw(Nm)	Rotating direction	$\overline{Mx}$	$\overline{Fz}$	$\overline{Mu}$	Judgment
0.347	0.18	480N	86	Down cut	51	380	183	Mw<$\overline{Mu}$
				Coaxial counter rotating	11	180	73	Mw>$\overline{Mu}$

The calculated results showed Mw <$\overline{Mu}$ for the down cut for which the rotary shaft tended to lift up, and Mw >$\overline{Mu}$ for the counter rotating for which the rotary shaft did not lift up.

2.3. Estimating Tilling Depth

The point at which Mw and $\overline{Mu}$ balance each other out is considered to be an ideal tilling depth. If it is assumed that $\overline{Mu}$ is relative to tilling depth d, then the tilling depth d can be estimated from the ratio of Mw to $\overline{Mu}$, as shown in Table 1.

With Mu being the estimated value when the tilling depth is 120 mm, then the following formula can be used to calculate the value d.

$$d = 120mm \times \frac{Mw}{\overline{Mu}} \quad (4)$$

Table 2 shows the calculated results.

Table 2 Estimation of tilling depth

	Mw (Nm)	$\overline{Mu}$ (Nm)	d (mm)
Down cut	86.4	183	56.7
Coaxial counter rotating	86.4	73	142

The difference between the down cut and the counter rotating is 2.5 times.

3. Correlation with Actual Machine Test

The correlation between the above calculated results and the actual machine test result was examined. Table 3 shows the specifications of the test machine used.

3.1. Straight Line Stability

Straight line stability is thought to be influenced by the fluctuation in Mz and Fx. The fluctuation ranges Mz and Fx taken from Fig. 8 and Fig. 9 are listed in Table 4.

All the Mz and Fx values associated with the down cut are larger indicating that the straight line stability is less than that of the counter rotating.

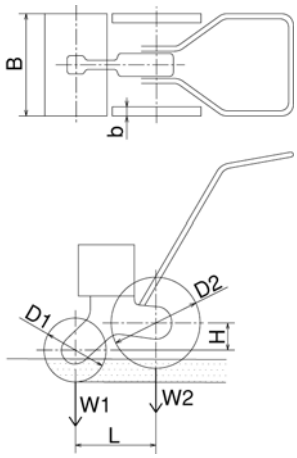


Fig. 12 Explanation of Table 3

Table 3 Specifications of test machine

W1	249N
W2	231N
D1	280mm
D2	400mm
L	0.347m
H	0.160m
b	40mm
B	450mm
Vehicle speed	0.15m/sec
Tine rotating speed	130rpm

Table 4 Fluctuate ranges of yawing moment and side force

		Max	Min	Fluctuate range
Mz	Down cut	35Nm	-24Nm	59Nm
	Coaxial counter rotating	20Nm	-25Nm	45Nm
Fx	Down cut	150N	-150N	300Nm
	Coaxial counter rotating	100N	-160N	260Nm

Table 5 shows the actual test machine results taken from soil hardness tests measured with a Yamanaka soil hardness tester.

As the soil became harder, the down cut configuration showed an irregularity in the forward movement component of the tilling reaction due to lateral differences in soil hardness. This resulted in a deterioration of the tractor's straight line stability. However, no particular differences were detected in the high frequency vibration inferred from the tilling reaction graph waves.

Table 5 Test result of yawing stability

Soil hardness	12	17	22
Down cut	○	△	×
Coaxial counter rotating	○	○	○

3.2. Actual Machine Speed

Fluctuation in the actual machine speed is thought to be influenced by $\overline{Fy}$. Table 6 shows the respective $\overline{Fy}$ values. From this, speed increases for the down cut and speed decreases for the counter rotating can be estimated.

Figure 13 shows the evaluation results of the actual testing machine.

Table 6 Forward element of tilling reaction (average)

	$\overline{Fy}$
Down cut	120N
Coaxial counter rotating	-65N

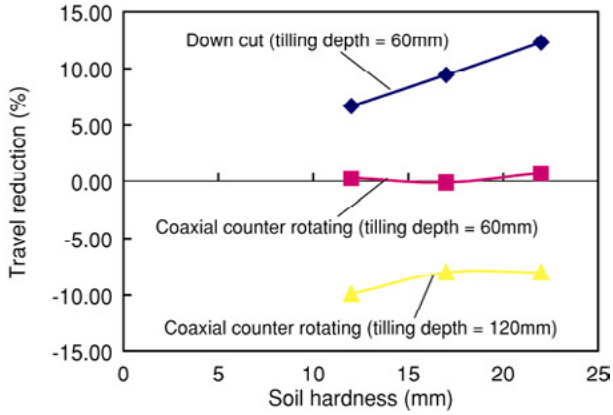


Fig. 13 Travel reduction versus Soil hardness

Test results indicated down cut speed increases and counter rotating decreases, which matches the calculated results. This was due to the tilling reaction directed in the backward direction on the up cut tine being greater than the forward directed tilling reaction on the down cut tine. Therefore, even if the down cut / up cut ratio is greater on the down cut rotary, the tilling reaction on the up cut rotary is superior in the longitudinal direction. Consequentially, since the tilling reaction increases as the soil becomes harder, fluctuation of machine speed also tends to increase.

3.3. Tilling Depth

Table 7 shows the estimated values for tilling depth for a soil hardness of 20.

Figure 14 shows a comparison of estimated values and the results of the actual testing machine.

The comparison was conducted on a soil hardness of 20 for which the counter rotating showed a tilling depth approximately twice that of the down cut. Also, this difference tends to increase as the soil becomes harder.

The counter rotating tilling depth closely approximated the estimated value; however, the down cut tilling depth was 1.5 times greater than the estimated value. This large discrepancy with the estimated value has been left as an issue that will need to be investigated in the future.

Table 7 Estimated tilling depth

	Tilling Depth
Down cut	56.7mm
Coaxial counter rotating	142mm

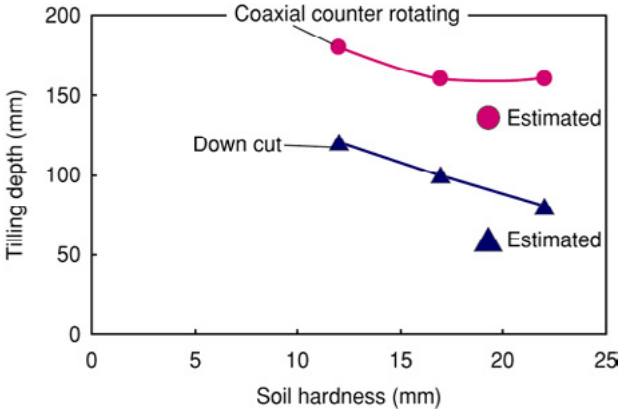


Fig. 14 Tilling depth versus Soil hardness

3.4. Rolling

Rolling is thought to be influenced by the fluctuation range of My. Table 8 shows the respective My fluctuation ranges.

Table 9 shows the results of the actual testing machine.

Almost no difference was detected between the down cut and counter rotating construction. Since the down cut tilling depth becomes shallower as the soil becomes harder, the absolute value for the tilling reaction decreases. This has led to the belief that because the rolling momentum fluctuation range also decreases, there is little difference between the two formats.

Table 8 Fluctuate ranges of rolling moment

	My		
	Max	Min	Fluctuate range
Down cut	20	-25	45
Coaxial counter rotating	12	-16	28

Table 9 Test result of rolling stability

Soil hardness	12	17	22
Down cut	○	△	△
Coaxial counter rotating	○	△	△

4. Conclusion

A comparison of the front rotary type walking tractors was conducted on a down cut rotary configuration and a coaxial counter rotating rotary configuration. The testing yielded the following results.

(1) When tilling untilled soil with a hardness approximating 20, the coaxial counter rotating rotary showed significant performance improvement over the down cut rotary with respect to straight line stability.
This is due to minimized variation in the forward movement component of the tilling reaction due to random variation in soil hardness engaged by the right and left tines.

(2) The down cut rotary showed an increase in the actual machine speed caused by the tilling reaction. Conversely, the coaxial counter rotating rotary showed a decrease in speed.
Furthermore, the fluctuation of machine speed tended to increase as the soil became harder.

(3) In tilling soil with a hardness approximating 20, the coaxial counter rotating rotary achieved a tilling depth twice that of the down cut rotary. Also, the difference in tilling depth tended to increase as the soil became harder.

(4) No particular difference was detected between the down cut rotary and the coaxial counter rotating rotary with respect to rolling.



Fig. 15 External view of FF300

Table 10 Major specifications of FF300

Items	Specifications
Engine model name	GXV57
Engine type	Air cooled 4-stroke OHV single cylinder
Engine displacement (cm^3)	57
Maximum power (kW)	1.8
Rated power (kW/rpm)	1.0/4 000
Maximum torque (Nm/rpm)	3.0/4 000
Compression ratio	8.0
Minimum specific fuel consumption (g/kWh)	354
Fuel tank capacity (cm^3)	1 100
Overall length (mm)	1 465
Overall width (mm)	465
Overall height (mm)	1 010
Dry weight (kg)	50
Tine speed (rpm)	131
Tilling width (mm)	450
Tine diameter (mm)	ϕ 280
Starting system	Recoil starter
Main clutch type	Shoe clutch
Transmission speeds	3Forward, 1Reverse

5. Afterword

This research has led to the development of the FF300, a front mounted coaxial counter rotating rotary walking tractor, released for sale in the Japan domestic market in March 2003. The unit is a lightweight, compact walking tractor that is easy to turn and provides increased tilling depth and straight line stability. The FF300 has received high praise and is popular among users.

Figure 15 shows an external view of the FF300 and Table 10 lists the unit's main specifications.

In carrying out this research, the authors would like to extend their deepest appreciation to the cooperating research team, and individuals, both internal and external, for their invaluable support.

Reference

(1) Kokuryo, T. et al.: Development of Coaxial Counter Rotating Rotary Tilling System, HONDA R&D Technical Review, Vol. 6, p. 110-118 (1994)

■ Authors ■


Yoshitaka OHTA


Susumu OHKUBO


Keiji IINO


Masatoshi NAGAOKA


Keiji NAGANO


Nobuchika KATAGIRI

Development of Adsorbent for Natural Gas Storage

Hiroshi OGASA* Yoshiyuki MORITA*
Masaru OKU* Nagatsugu MUKAIBOU*

ABSTRACT

Carbon adsorbent was selected as a means of efficiently storing methane, the main component of natural gas. Simulations were first employed to determine an ideal adsorptive pore structure. The results of the simulations were applied to establish a target in the development of activated carbon, with coconut shell, coal and carbon nano-materials (Buckminsterfullerene, carbon nano-tubes) as starting materials. TEM analysis confirmed that the activated carbon produced in this research possessed the ideal pore structure targeted. This activated carbon is capable of storing 0.155 NL/cm^3 of natural gas at low pressure (3.5 MPa). This represents 77.5% of the capacity of high-pressure (20 MPa) compressed natural gas (CNG) storage. The material's storage capacity for adsorbed methane gas is one of the highest among reported figures.

1. Introduction

Recently, the demand to reduce automotive exhaust gas emissions and develop alternative fuels has increased from the viewpoint of global environmental issues and exhaustion of energy resources. Against this background, automobiles fueled by natural gas are cleaner vehicles that can greatly reduce exhaust gas emissions. This is accomplished simply by making minimum modifications to a gasoline based vehicle. Three methods have been devised for storing natural gas in automobiles as shown in Fig. 1. The first of these, compressed natural gas (CNG) fuel is stored at high pressure (20 MPa or 25 MPa), so a cylindrical pressure vessel is needed which reduces the degree of freedom for the vehicle body package. Liquefied natural gas (LNG) fuel is stored at the low temperature of –162 °C, so a fuel container with a special dual structure is needed. This research concerned adsorbed natural gas (ANG) which can be efficiently adsorbed and stored at relatively low pressure as a method for easily storing natural gas, and this paper describes adsorption which is the core technology for ANG.

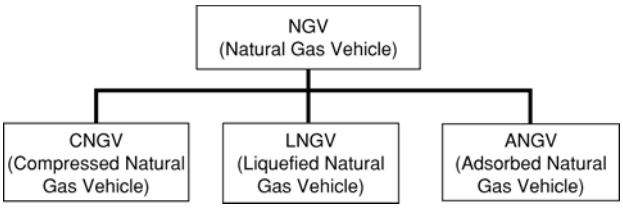


Fig. 1 Fuel storage methods for natural gas vehicles

First, the target natural gas storage capacity for the adsorption was set at 20 Nm^3 (0.2 NL/cm^3) for a 100 L container equivalent to the gas storage of the CNG CIVIC GX that Honda has marketed since 1998, and the storage pressure was set at 3.5 MPa.

* Tochigi R&D Center

2. Development of Adsorption

The adsorption was developed by selecting the base materials and handling process (carbonization and activation methods), and improving the preparation conditions.

2.1. Selection of Materials

2.1.1. Activated carbon

Activated carbon raw materials that are currently used for industrial applications can be broadly classified into plant based and fossil fuel based materials[1]. Typical plant based raw materials include coconut shell (CCS), wood and pulp. However, of these, coconut shell in particular accounts for approximately 30% of the activated carbon in the marketplace, and most of this is used for steam activated applications. Next, fossil fuel based materials can be divided into raw materials such as coal that can be converted into activated carbon without processing, and raw materials such as petroleum pitch, coal tar and synthetic polymers that undergo primary processing and are then converted into activated carbon. This research selected coconut shell, which is cheap and allows easy improvement of performance, and coal with a low impurity content as the starting raw materials.

2.1.2. Carbon nano-materials

The discovery of BuckminsterFullerene (C_{60}) in 1985 and carbon nanotubes in 1991 have stimulated efforts to research technology for synthesizing large amounts of carbon nano-materials and to develop applied technologies in recent years. Amidst this trend, numerous studies have been presented on using carbon nanotubes for hydrogen storage[2]. The authors thought that sufficient adsorption levels could be expected for methane molecules, which have greater adsorption energy than hydrogen molecules, so this research selected carbon nanotubes and BuckminsterFullerene as the raw materials.

2.2. Adsorption Manufacturing Method

2.2.1. Carbonization and activation methods

The process for converting the raw materials into adsorption materials requires carbonization and activation. The carbonization process carbonizes the raw materials, and the activation process grows pores in the carbonized materials. Activated carbon is normally made using the above two processes, but carbon nano-materials are already carbonized in the raw material stage, so they can be converted into adsorption type using only activation. Activation processes can be grouped into physical activation and chemical activation processes[1]. Physical activation uses steam, carbon dioxide gas or other gases as the activation agent, and the pore growth mechanism uses the method of gas erosion from the raw material surface. Steam activation is more economical, so this process is most widely used for industrial applications.

On the other hand, chemical activation uses KOH, phosphoric acid or other chemicals, and the pore growth mechanism uses the methods of chemical erosion and intercalation from the surface and inside of the raw materials. Chemical activation uses more expensive chemicals as the activation agency and requires a handling process after activation, so it is not used widely for industrial applications[1]. This research fabricated adsorption substrates using the two representative methods of steam activation and KOH activation as the activation methods. Figure 2 shows the steam and KOH activation mechanisms.

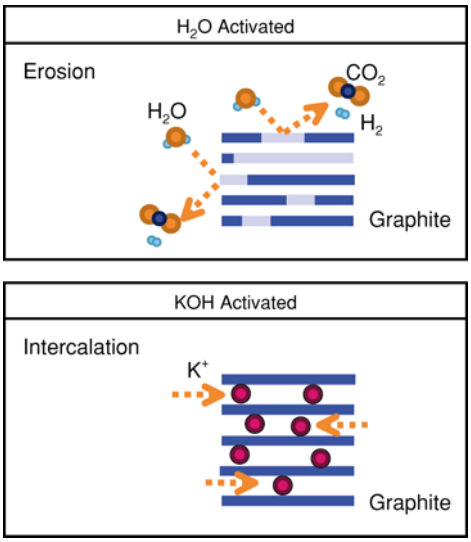


Fig. 2 Activation mechanism

2.2.2. Monolith manufacturing method

After the carbonization and activation process, the adsorbent is in powder or granulated powder form. When packaging this into a fuel container, the format must prevent damage when charging. In addition, this is an automobile mounted part, and the format must be unaffected by vibrations when cruising and changes in temperature and humidity. Furthermore, like a gasoline canister, the structure must prevent the adsorbent from breaking down into particles during repeated adsorption/desorption cycles. Therefore, the powder and granulated powder adsorbent was molded into a monolith to meet these performance requirements. Figure 3 shows the molding process.

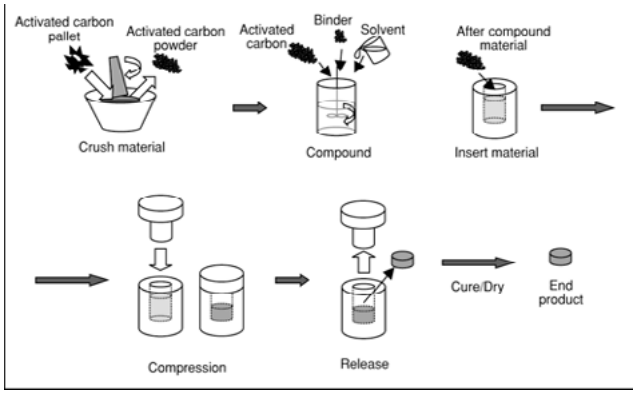


Fig. 3 Molding process of monolith

3. Adsorption Simulation

The adsorption simulation was used to predict adsorption pore structures that would be effective for methane gas storage, and to provide direction for the research. The simulation used the Cerius[2] made by Accelrys Inc. (USA), and adsorption performance was calculated by the monte-carlo method.

3.1. Activated Carbon

Figure 4 shows the basic simulation model. The simulation calculated the methane adsorption capacity for different pore sizes using this model[3]. Figure 5 shows the adsorbed status for each pore size. The calculation results showed that a graphite layer distance (distance between graphite layer centers) of approximately 11 Å provided the ideal adsorption for methane molecules. Figure 6 shows these results in terms of pore size and gas storage capacity. These calculation results showed that the ideal pore structure for methane storage was a peak pore size of 7.8 Å, and the specific surface area at that time is 2 630 m^2/g.

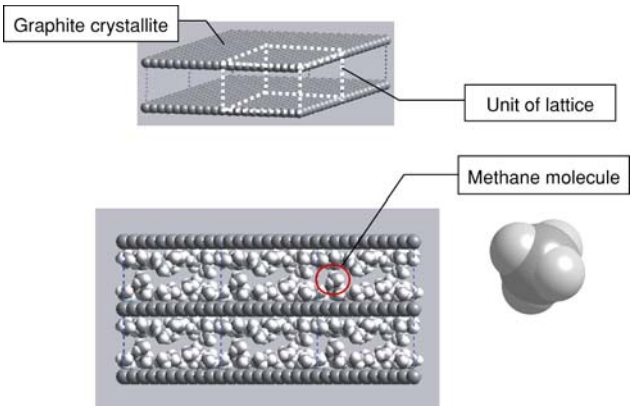


Fig. 4 Basic model of adsorption

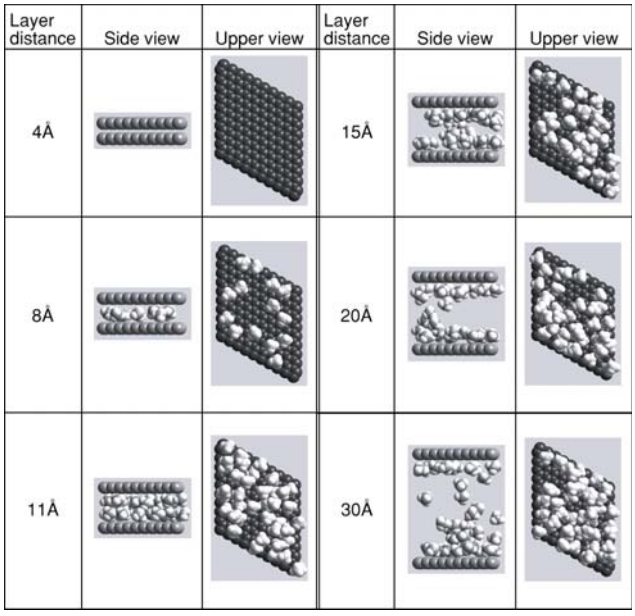


Fig. 5 Status of adsorption with change in layer distance

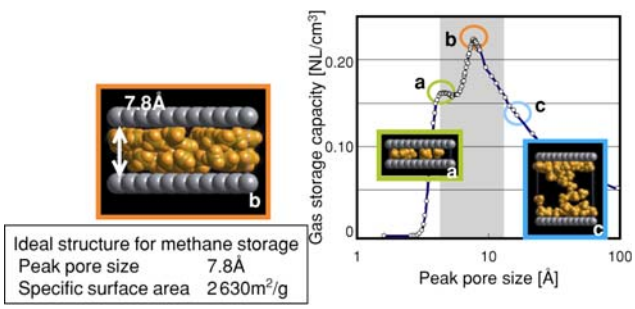


Fig. 6 Pore size and storage capacity

3.2. Carbon Nano-materials

An adsorption model was constructed and simulations were performed for carbon nano-materials in the same manner as activated carbon. Figure 7 shows the simulation model. There are still many unknowns in terms of model creation and simulation methods for BuckminsterFullerene and carbon nanotubes, so the simulation was conducted using the same setting conditions for activated carbon[4] [5].

Figure 8 shows the simulation results for activated carbon and carbon nano-materials. At a pressure of 3.5 MPa, the gas storage capacity was 0.205 NL/cm^3 for the carbon nano-tube(CNT), and 0.216 NL/cm^3 for activated carbon. This indicated that the adsorption with the most ideal pore structure was activated carbon.

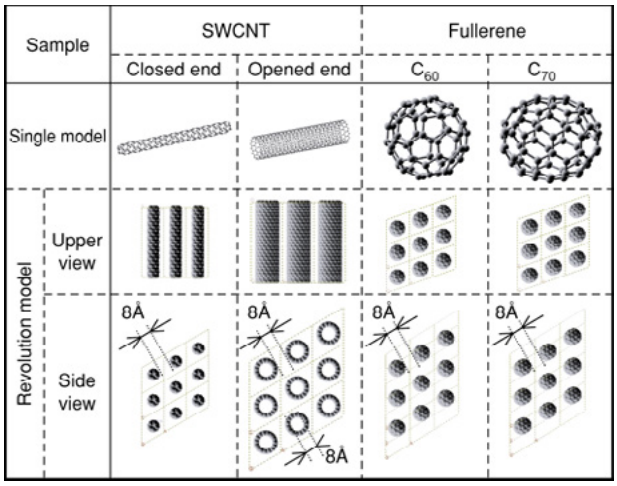


Fig. 7 Adsorption model for nano-carbon materials

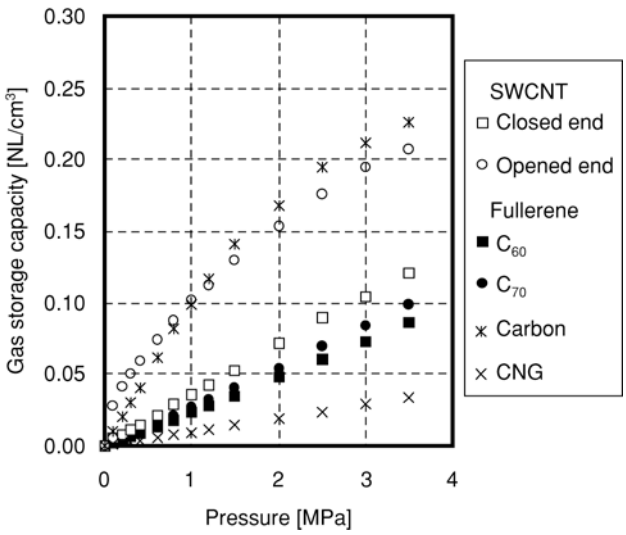


Fig. 8 Results of simulation

4. TEM Surface Observation

The purpose of TEM surface observation was to obtain a relative comparison of the internal structures of the adsorbents used in the tests. In addition, the pore status can also be understood by performing image analysis on the TEM images.

4.1. Activated Carbon

TEM surface analysis was performed for the two types of activated carbon (coconut shell/steam activation, coal/KOH activation) evaluated by this research. Figure 9 shows the analysis results. These results confirmed that the activated carbon made using coal and KOH activation could be fabricated to values near the peak pore size of 7.8 Å and specific surface area of 2 630 m^2/g which were the ideal pore structure obtained by the adsorption simulation. In contrast to this, coconut shell and steam activation resulted in a smaller specific surface area (obtained using the BET method) at the ideal peak pore size, and conversely a larger than ideal peak pore size at the ideal specific surface area. This indicated that the combination of coconut shell and steam activation is not suitable for methane adsorption.

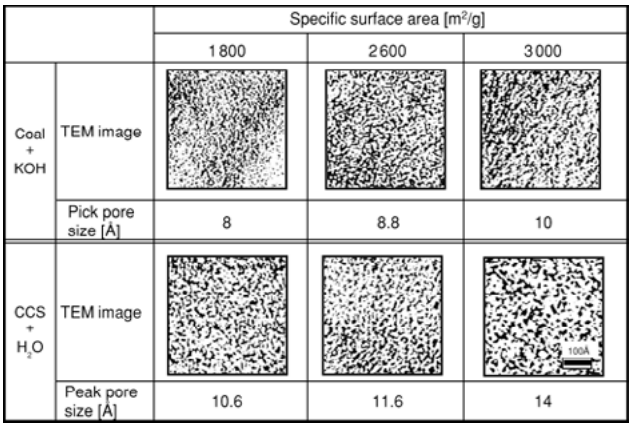


Fig. 9 TEM image of activated carbon

4.2. Carbon Nano-materials

In its synthesized state, C_{60} has an extremely stable structure comprised of hexagonal and pentagonal faces[5]. It has been reported that effective methane adsorption sites can be obtained by applying activation to this stable structure[6]. This research compared the surface status before and after activation to confirm the changes produced by activation. Figure 10 shows the TEM analysis results for C_{60}.

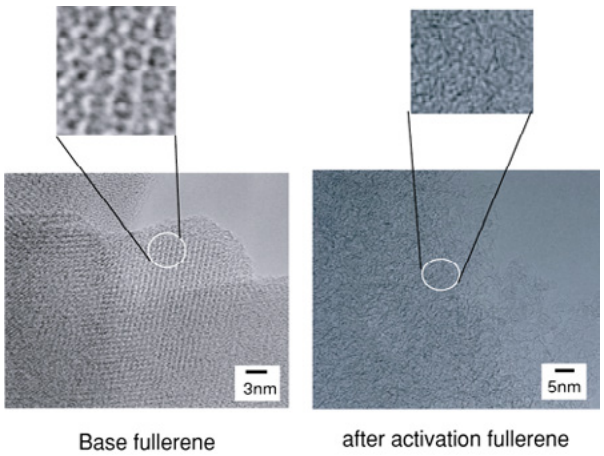


Fig. 10 TEM image of fullerene

While a neat and orderly graphite crystal lattice can be confirmed before activation, this cannot be confirmed at all after activation. These results are thought to indicate that C_{60} does not maintain a neat soccer ball structure after activation, and instead the carbon atoms decompose into an amorphous form. Why this amorphous structure is effective for methane adsorption has not yet been theoretically solved at present, but a clear structural change can be confirmed. Figure 11 shows the BuckminsterFullerene measurement results for different activation conditions.

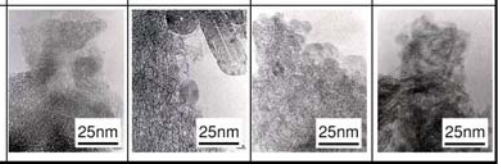
Specific surface area (m^2/g)	1122	1363	2346	2594
Storage capacity (NL/cm^3)	0.115	0.105	0.111	0.113
Adsorption ability (NL/g)	0.13	0.14	0.20	0.25
Bulk density (g/cm^3)	0.699	0.565	0.413	0.335
TEM image				

Fig. 11 Analysis of pore structure for activated fullerene

Next, Fig. 12 shows the TEM analysis results for carbon nanotubes. Carbon nanotubes are classified into single wall (SWCNT), double wall (DWCNT) and multi wall (MCNT) according to the number of tube layers[2]. However, simulation results showed that SWCNT are the most effective in terms of methane adsorption capacity relative to carbon density. However, it is extremely difficult to synthesize only SWCNT, and it is not uncommon for MWCNT and C_{60} to also be present. Therefore, TEM analysis was performed to confirm the quality of the test materials evaluated by this research (Fig. 12). The results confirmed a small amount of catalytic residue, but the material was synthesized with an even tube size of 15 Å, and the test material quality was confirmed to be extremely high, with almost no MWCNT or other types present.

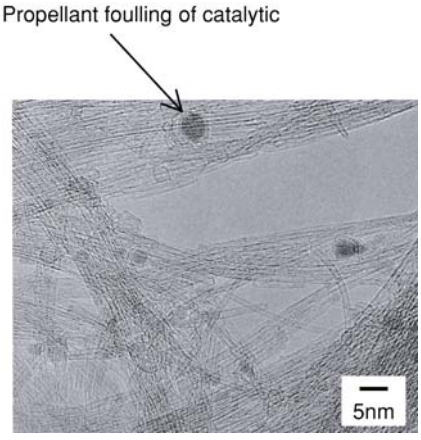


Fig. 12 TEM image of CNT

5. Pore Analysis

Image processing was performed on the TEM images, and Fig. 13 shows the activated carbon pore distribution calculated from the image processing results. The calculation results show that the ideal case in the simulation is an even peak pore size of 7.8 Å, but the pore size for actual activated carbon has a distribution, and this distribution must be taken into account when predicting the gas storage capacity. The analysis results confirmed that the peak pore size for activated carbon made using coal and KOH activation is the same 7.8 Å as the ideal peak pore size, and that a sharper pore size distribution can also be achieved than that for coconut shell and steam activation. This is thought to indicate that activated carbon made using coal and KOH activation is closer to the ideal.

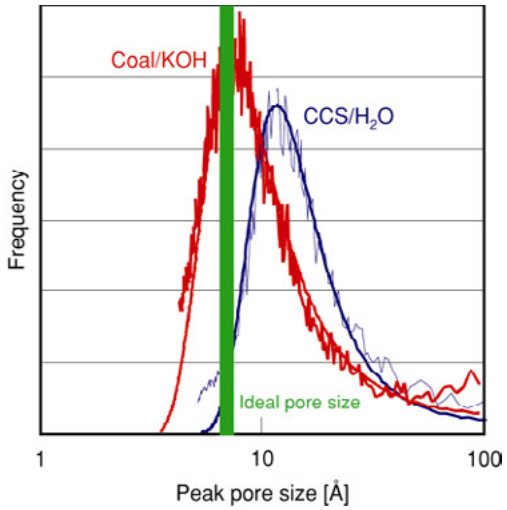


Fig. 13 Pore size distribution

6. Evaluation of Adsorption Ability

6.1. Activated Carbon

Figure 14 shows the methane adsorption test results for activated carbon molded into a monolith. Improvement of the activated carbon is broadly divided into three steps, and the conditions (temperature, time, etc.) for activation, which is the core technology, are expressed as the degree of activation. This degree of activation has an extremely high correlation with the bulk density of the activated carbon. First, in step 1 the degree of activation was improved using coconut shell and steam activation. The results clearly show the coconut shell tendency, and make it possible to ascertain the adsorption ability.

Next, in step 2 the raw materials and activation method for the activated carbon were changed, and a vast improvement in ability was confirmed compared to step 1. Therefore, in step 3 the coal raw materials and degree of activation were further reviewed compared to step 2. As a result, the activated carbon achieved a methane storage capacity of 0.155 NL/cm^3, which is 77.5% of the target gas storage capacity.

6.2. Carbon Nano-materials

Figure 15 shows the adsorption test results for carbon

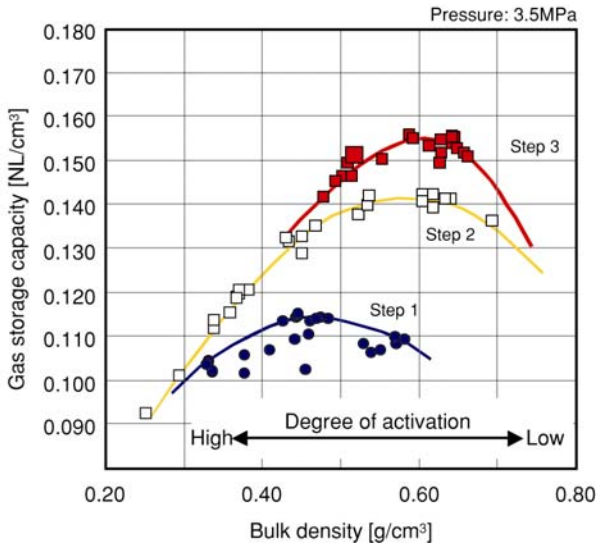


Fig. 14 Adsorption performance of activated1 carbon

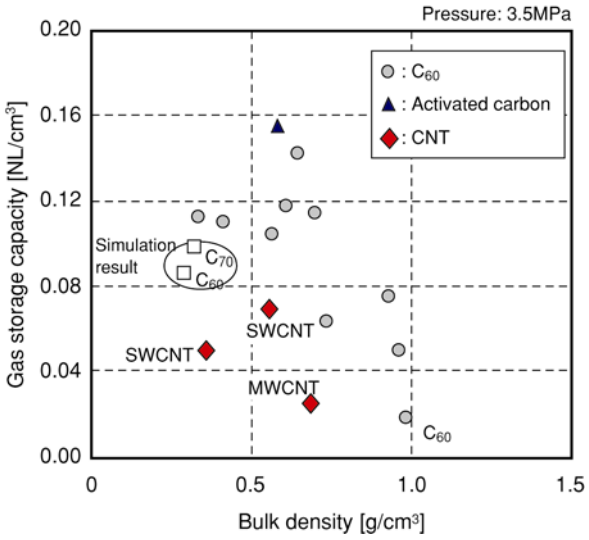


Fig. 15 Adsorption performance of nano-carbon

nano-materials. Carbon nano-materials are carbonized by the synthesizing process in the raw material stage, so the adsorption was fabricated using only activation. The adsorption test results for carbon nano-materials showed that SWCNT and MWCNT could only obtain gas storage capacities approximately 50% that of activated carbon, but C_{60} achieved roughly the same value as activated carbon.

7. Adsorption Performance Achievement Level

Figure 16 shows a comparison of storage capacity for various methane adsorption systems[7] - [10]. Like hydrogen storage, there is no global evaluation standard for methane adsorption, so there may be some deviation based on the measurement method. However, comparison with values reported in research thus far confirmed that the results achieved by this research are among the world's highest.

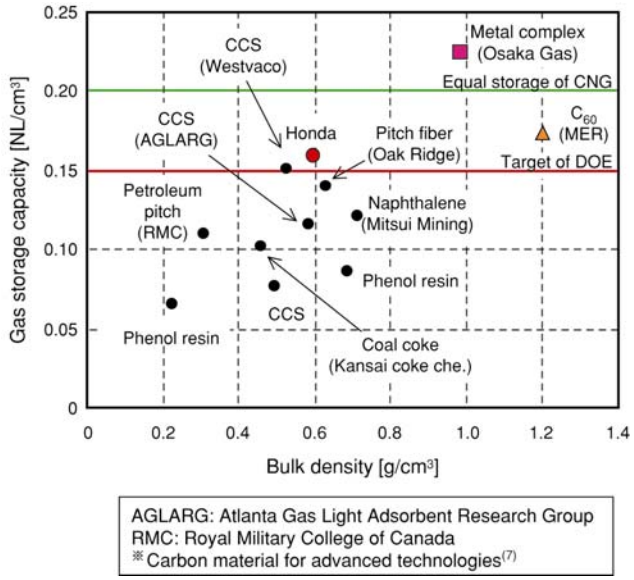


Fig. 16 Comparison of methane storage capacity

8. Conclusion

The results achieved by this research are as follows.

(1) The methane storage capacity using activated carbon was 0.155 NL/cm^3 at a pressure of 3.5 MPa. This represents 77.5% of the gas storage capacity for CNG for a 100 L container at a pressure of 20 MPa and which is the target for this research.

(2) Research to apply carbon nano-materials as the adsorption obtained C_{60} performance roughly equivalent to activated carbon.

(3) Adsorption simulation calculation results showed that the methane storage capacity of the ideal graphite structure is 0.216 NL/cm^3, and that the pore structure at that time has a peak pore size of 7.8 Å and a specific surface area of 2 630 m^2/g.

This project is a compilation of the research results from fiscal year 1997 through fiscal year 2002 within the Advanced Clean Energy Vehicle Project, which is being researched through a grant from the New Energy and Industrial Technology Development Organization (NEDO) via the Japan Automobile Research Institute (JARI).

Acknowledgements

The authors wish to express their thanks to JARI and the NEDO committee for their advice in pursuing this research. The authors would also like to thank Professor Sakata of Faculty of Engineering of Okayama University for his valuable advice, and the many people at various research organizations for their cooperation with this research.

References

(1) Sanada Y., Suzuki M., Fujimoto K.: Activated Carbon, Kodansya

(2) Tanaka K.: Carbon Nanotube, Kagakudojin

(3) Kimberly R Matranga, Alan L. Myers and Eduardo D. Glandt: Storage of Natural Gas by Adsorption on Activated Carbon, Chemical Engineering Science, Vol. No. 7, p. 1569-1579

(4) Shinohara H., Saitou Y.: Chemistry and Physics of Fullerenes, Publishing of Nagoya University

(5) Tanigaki K., Kikuchi K., et al.: Fullerenes, Sangyoutosyo

(6) Workshop on High Functionality Material of Carbon Family Nanotechnology, 25 April, 2001, NEDO

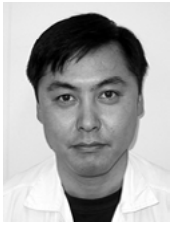
(7) Timothy D. Burchell: Carbon Materials for Advanced Technologies

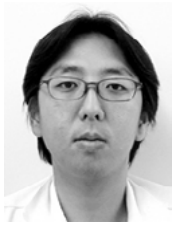
(8) Gas Storage Workshop, Royal Military College of Canada, July, 2001

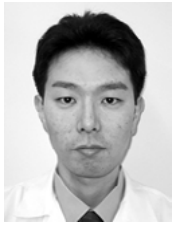
(9) Tim Burchell and Mike Rogers: Low Pressure Storage of Natural Gas Vehicular Applications, SAE Paper 2000-01-2205

(10) Advanced Clean Energy Vehicle Project, Report from 1997 to 2002, NEDO

■ Authors ■


Hiroshi OGAWA


Yoshiyuki MORITA


Masaru OKU


Nagatsugu MUKAIBOU

Development of Lightweight Valve Spring Retainer Made from Aluminum Powder Metal for Motorcycle Races

Kosuke DOI* Hiroyuki HORIMURA* Kyo TAKAHASHI*

ABSTRACT

In order to enhance the engine performance of racing motorcycles, by aiming to increase critical engine speed, a valve spring retainer made of lightweight powder aluminum alloy has been developed. The high strength abrasion resistance aluminum, “NCP 400” (Nano Crystal Powder metal with crystal grain size of 400 nm), was created through blending optimum amounts of hard grains to provide abrasion resistance to the Nano Crystal Powder aluminum alloy consisting of Nano-sized crystal grains. Optimum temperature control and a forging method for the material property established the warm-precision-closed-forging technology where post-machining is unnecessary in parts manufacturing. The safety factor (the ratio of the margin of a part to the maximum stress when in use) verification method was set up, where the retainer load could be evaluated quantitatively based on the movement of the valve train during operation.

1. Introduction

Recently even factory machines in the MotoGP class, which is the pinnacle of motorcycle racing, are shifting from conventional 2-stroke engines to 4-stroke engines with valve systems. This has created an extremely high need for lightweight valve systems that allow high engine speeds. In response to this need, valve spring retainers made from titanium alloy have been adopted in place of the steel retainers used in mass production vehicle engines in order to reduce the inertia force of reciprocating motion parts. However, in consideration of the ratio of fatigue strength to weight, there are limits as to how far the weight with titanium alloy can be reduced. As a means of further reducing the weight, the authors have manufactured aluminum valve spring retainers since the mid-1990s for application to factory “works” racers and as kit parts. (Fig. 1) This paper presents the design of aluminum powder metal materials developed for retainers, and describes the manufacturing technology and a method for verifying the safety factor in parts manufacturing.

2. Development Targets

The development targets for the lightweight valve spring retainer were set as follows.

(1) A weight reduction of 20% or more compared to the conventional titanium alloy retainer.
(2) Abrasion resistance should be assured without surface treatment (hard anodizing coating, etc.).

3. Materials Technology

Conventional aluminum valve spring retainers were manufactured using a composite material made of hard particles mixed into rapidly solidified powder. Honda introduced retainers with Al-14.5%Si powder metal + ceramic powder composite material specifications to mass production vehicle engines in 1989. In addition, retainers with 2000 type aluminum powder metal + alumina + hard alumite specifications are currently used in other companies’ motorcycles.

* Asaka R&D Center

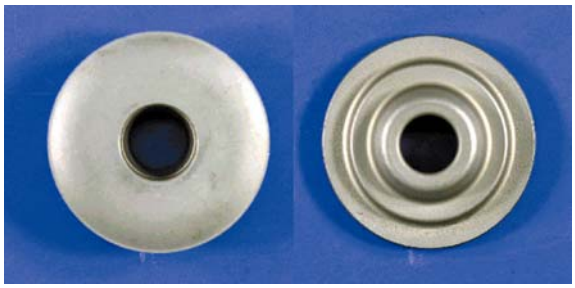


Fig.1 Valve spring retainer made from aluminum powder metal

Similar specifications were also considered in this development, but the conclusion was reached that they were not better for racing, mainly due to strength issues. Therefore, the decision was made to use Nano Crystal Powder aluminum metal developed by Honda's Basic Research Division as a metal with characteristics surpassing those of conventional rapidly solidified powder metals.

3.1. Ensuring Strength by Controlling the Structure of Rapidly Solidified Powder

In contrast to the conventional approach of expanding the limit of solid solution and grain refining by rapid cooling, Al base amorphous metals have been discovered in addition to La base, Zr base and other amorphous metals. Research on super-cooled metals that allow the manufacture of bulk amorphous metals is currently the focus of attention around the world, and various research institutions are continuing studies with the aim of practical application. Nano crystal aluminum metal has a structure comprised of nano-size crystal particles obtained by controlling the structure utilizing the crystallization from the amorphous phase and an intermetallic compound. The newly developed Nano Crystal Powder aluminum metal is already in the crystal phase in its powder state, but the structure is obtained through homogeneous nucleation from the super-cooled liquid state, so it is homogeneous. The metal composition was selected from the following viewpoints.

(1) Manufacture should be possible using existing air atomizing facilities.
(2) The metal should be comprised of low-cost elements.
(3) Increases in the specific weight of the metal should be kept to a minimum.

Particularly in terms of (1) above, a combination of elements with a high amorphous forming ability was required due to limitations on the cooling speed and melting temperature. Figure 2 shows groups of elements with high amorphous forming abilities with aluminum as the main element. It has already been found that high amorphous forming ability can be obtained by adding one element from each of groups A and B shown in Fig. 2 to aluminum to create a three or more element system, so the addition elements were selected from these groups. Figure 3 shows a comparison of crystallizing temperature and material cost for three-element alloys that include a group A element. Fe was selected from group A due to its high crystallizing temperature and low cost. In addition, Fig. 4 shows a graph of the alloy density and the alloy cost for three-element metals including each representative element in group B. Ti was selected from group B because it has the lowest specific weight and is low cost. In order to enhance the amorphous forming ability, Si was added as the fourth element to the

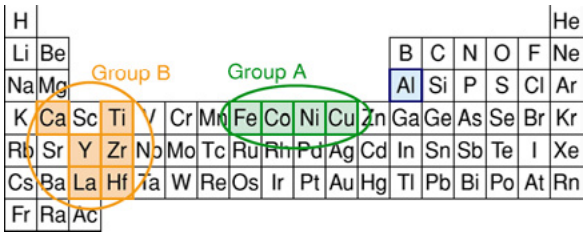


Fig.2 Combination of elements which form amorphous

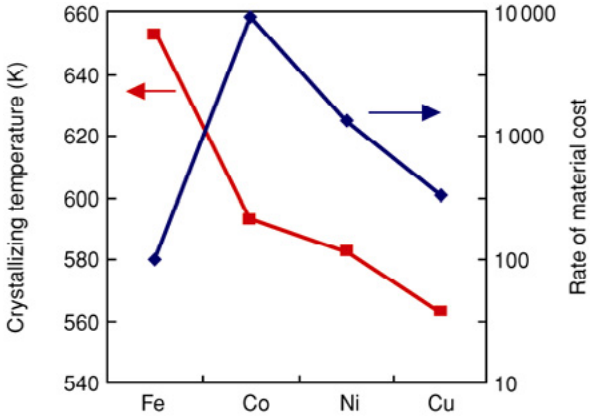


Fig.3 Crystallizing temperature of Al-(Gr. A element)-(Rare earth element) alloy and rate of material cost of Gr. A element

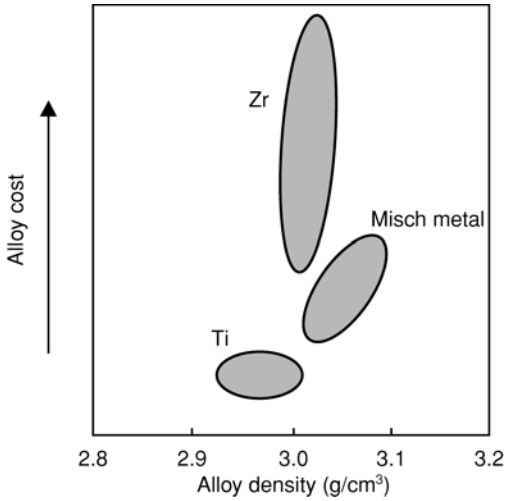


Fig.4 Relationship between alloy density and alloy cost (Al-Fe- Gr. B element alloy)

base of the Al-Fe-Ti alloy to create a four-element Al-Fe-Ti-Si alloy. Note that the interaction between Si and Ti worked to increase the amorphous forming ability, and had the effect of spheroidizing the Al-Fe compound which suppressed the drop in toughness.

Figure 5 shows the relationship between the Fe, Ti and Si addition amounts and the mechanical properties. The tensile strength increased together with the Fe addition amount, but at 6 atomic percent (hereafter, at%) or more the melting point became too high, making atomization difficult with existing mass production facilities. Ti also worked to increase the tensile strength in the same manner, but at 1at%

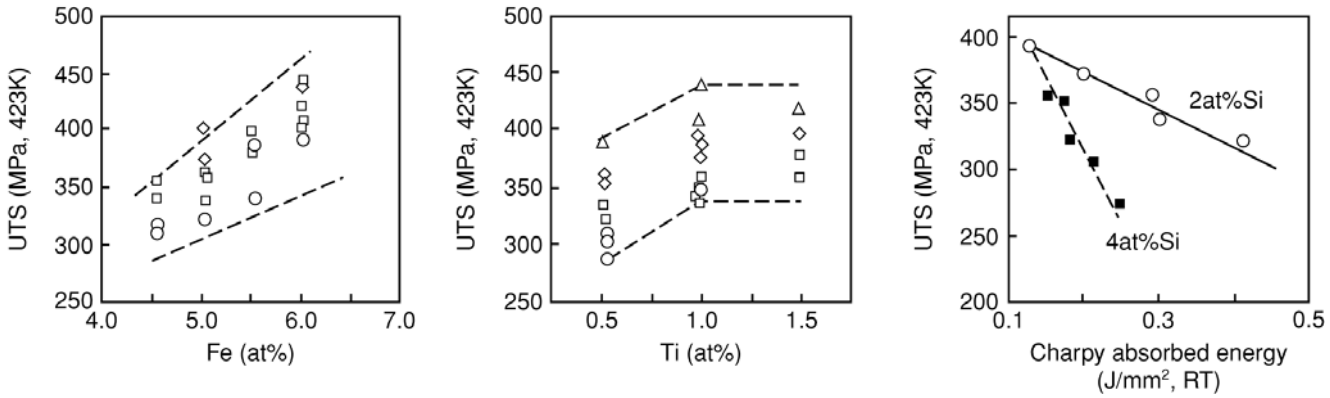


Fig.5 Relationship between amount of addition element and mechanical properties

or more there was no further increase in the tensile strength. Si shows a high impact value ratio with respect to tensile strength at 2at%. In consideration of these results, Al-6at%Fe-1at%Ti-2at%Si was determined as the optimum alloy composition.

3.2. Ensuring Abrasion Resistance with the Optimum Hard Particle Mixture

Possible methods for improving abrasion resistance are as follows.

(1) Surface treatment such as hard alumite or hard plating
(2) Creating a composite material by dispersion compounding of hard particles

The authors selected method (2) which endows the material itself with abrasion resistance. This is because method (1) increases the cost of parts manufacturing, and the advantage of powder materials is that hard particles can be dispersion compounded afterwards to the base powder metal. When creating a composite material, it is necessary to select the hard particle size and amount, and to confirm the effects on the mechanical properties. In addition, if dispersion compounding is uneven, this may result in uneven mechanical properties or create a starting point for fatigue fracture. Figure 6 shows concept drawings of the effects of the alumina addition amount and particle size on abrasion resistance and strength. In general, larger addition material particle sizes and amounts tend to cause the strength to drop but the abrasion resistance to rise. Figure 7 shows the mechanical properties of actual composite materials. Based on these test results, an addition amount of 5% (average particle size of 3 μm) was selected to achieve a balance between strength and abrasion resistance. Abrasion tests were conducted using a pinion disk shaped friction abrasion tester as shown in Fig. 8. In addition, the mixing conditions for mixing alumina were set using a rotation and revolution type rotary mixer. Figure 9 shows the composite material structure. This shows that the alumina is evenly dispersion compounded. Table 1 shows the mechanical properties of the final composite material. This metal has a high fatigue strength and tensile strength even in the temperature range at which this metal is used as retainers (423 K). The authors named this high strength abrasion resistant aluminum material “NCP400” (Nano Crystal Powder metal). The “400” indicates a crystal size of 400 nm. The crystal particle size of this metal can be controlled from 20 nm to 1 μm by varying the heat history, but the balance between strength and toughness is best at around 400 nm.

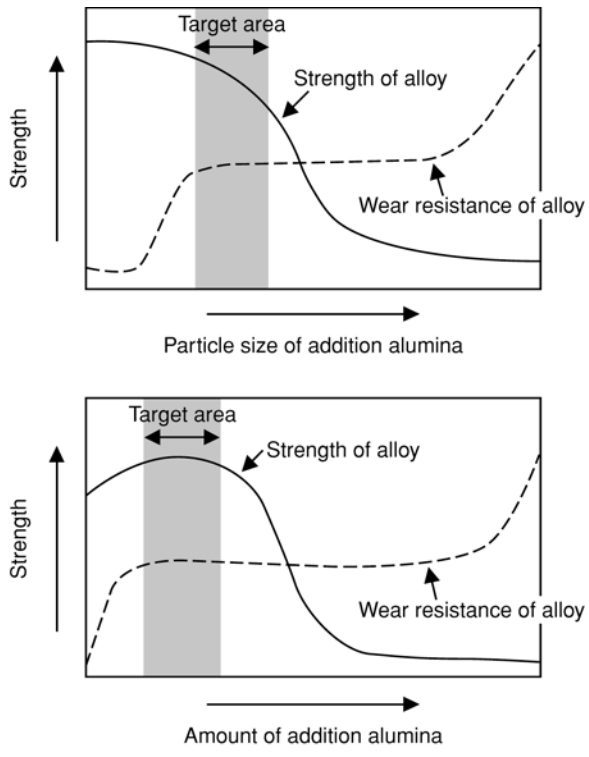


Fig.6 Amount and particle size of alumina

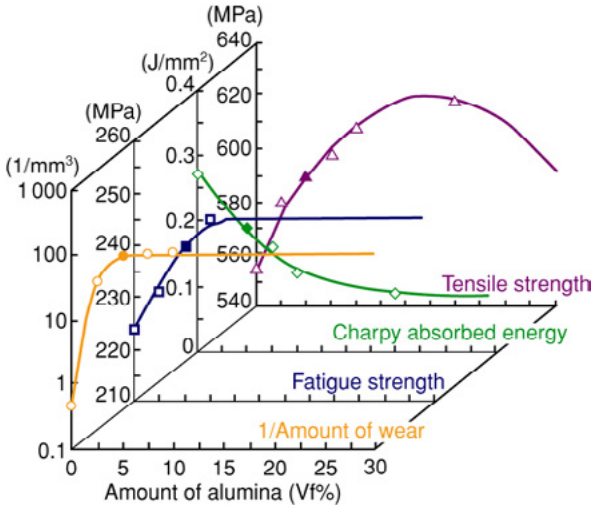


Fig.7 Mechanical properties of composite metal

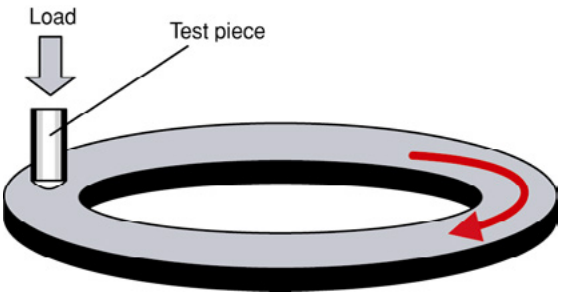


Fig.8 Abrasion test

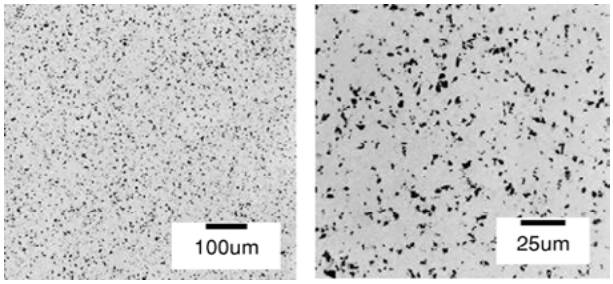


Fig.9 Microstructure

Table 1 Mechanical properties of NCP400

		RT	423K	473K
Tensile strength	(MPa)	590	485	445
Yield strength	(MPa)	484	412	374
Elongation	(%)	3.0	3.7	4.3
Fatigue strength	(MPa)	220	210	–
Charpy absorbed energy	(J/mm^2)	0.14	–	–
Young's modulus	(GPa)	97	94	89
Density	(g/cm^3)	3.04	–	–

4. Parts Manufacturing Technology

4.1. Precision Closed Die Forging

Precision closed die forging which does not require post-machining was attempted in order to enhance the strength and reduce the machining cost of the developed retainer. The nano crystal structure of NCP400 makes it easier to work than conventional aluminum powder metals, but compared to normal wrought products it has high strength at elevated temperatures, which gives it high deformation resistance when hot. In addition, it is also characteristic in that it experiences almost no work hardening. Therefore, special consideration must be given to the forging design, lubricant selection, work temperature, die temperature and other conditions. Of these, temperature control is a particularly important element.

4.1.1. Work temperature

The work temperature was determined from the relationship between the material properties of high temperature elongation and the recrystallizing temperature. Figure 10 shows the relationship between temperature and elongation for NCP400. In contrast to elongation of only a few percent at normal temperature, elongation begins to increase noticeably when 573 K is exceeded. Figure 11 shows the relationship between the work retention temperature and hardness. Here, structure growth starts and the product strength drops when 773 K is exceeded. Therefore, forging tests were conducted with the work heating temperature in the range from 573 K to 773 K, and as a result 623 K was selected as the optimum work temperature. There is no change in the hardness even after holding the work at 623 K for 100 hours, and there is sufficient heat resistance. Note that the work was heated using a mesh belt type continuous oven, and the belt speed and ambient temperature were set to stabilize the work at 623 K at the belt exit.

4.1.2. Die temperature

If the die temperature is too high, the product dimension accuracy deteriorates and concerns such as seizing, adhesion and a shortened die life occur. Conversely, if the temperature is too low, the temperature of the heated work drops, causing cracking and making it not viable to mold sound products. Figure 12 shows the positions where forging cracks occur, and Fig. 13 shows the relationship between the die temperature in molding and the occurrence rate of forging cracks. Periphery cracks and crown cracks both show a high correlation with die temperature, with the occurrence rate rising sharply at 473 K or lower. Therefore, 523 K was selected as the optimum die temperature. In addition, both the upper and lower dies were controlled using imbedded heaters to maintain a stable die temperature during forging.

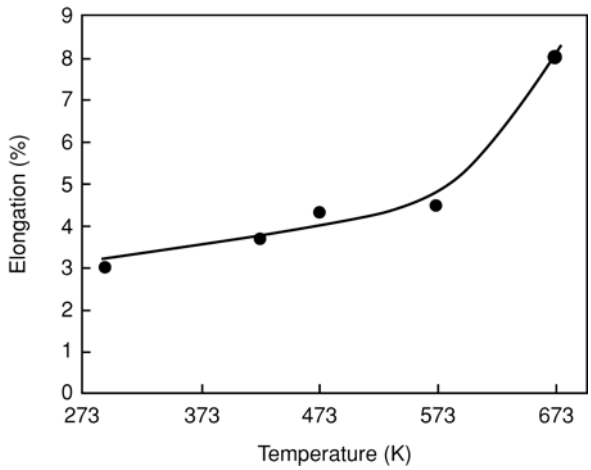


Fig.10 Relationship between temperature and elongation

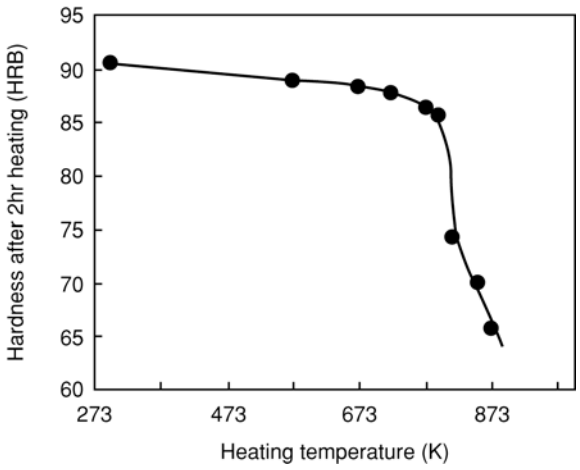


Fig.11 Tempering curve

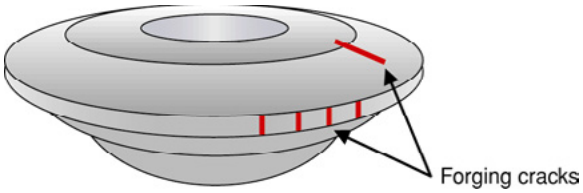


Fig.12 Position of forging cracks

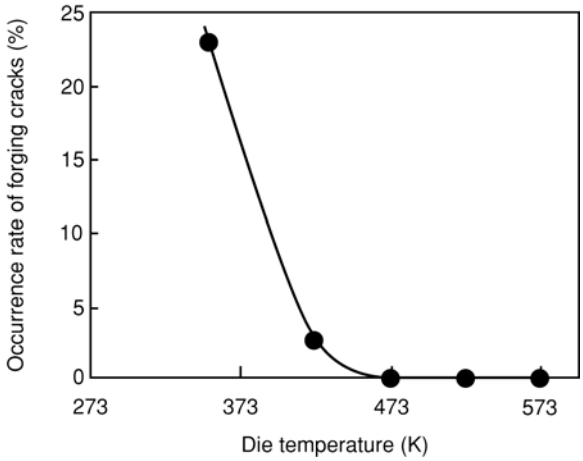


Fig.13 Relationship between die temperature and occurrence rate of cracks

4.1.3. Forging design

The nano crystal aluminum metal has superior plastic working characteristics compared to conventional aluminum powder metal. However, the structure is nanometer size so the working hardness is small and deformation easily concentrates in a single area. Therefore, the metal must be worked evenly and gently in each part during the molding process. For this reason, a holed billet was fabricated and closed die forging was performed by two-step molding. Figure 14 shows this design. The results of unit fatigue tests on the flange of forged parts showed a fatigue strength improvement of 20% compared to machined parts. This is thought to be due to the flow molding effects of forging.

4.2. Verification of Safety Factor

4.2.1. Loads received by the retainer

Most valve systems used in racing motorcycles are DOHC lifter types in which the cam drives the valves directly via a valve lifter. Figure 15 shows a model drawing of the portion around the lifter. The loads received by the retainer are as follows.

(1) Flange bending load produced by the lift load from the spring and the dynamic inertia load
(2) Longitudinal splitting impact load received from the cotter during valve bounce due to over-revolution, etc.
(3) Bearing surface friction load produced by sliding with the valve spring

Unit motoring tests and engine evaluation verified that sufficient durability with respect to (3) was achieved by optimizing the hard particle mixture as described in section 3.2 above. Therefore, (1) and (2) are discussed below.

4.2.2. Measurement of valve system motion

In order to quantitatively measure the loads received by the retainer during operation, it is important to understand the valve system motion. In the static state, the only load received by the retainer is the lift load from the valve spring. However, when engine rotation causes the spring to reciprocate between the installed condition and the lift condition, the inertia force of the mass of the spring moving parts (approximately 1/3 of the spring mass for a variable pitch spring) also applies in addition to the static lift load. When this inertia force of the reciprocating motion parts exceeds the valve spring load at high revolutions, the valve is no longer driven along the designed cam profile and instead exhibits motion such as bounce and jumping. As a result, the inertia force of this acceleration is also applied to the retainer, making it difficult to predict the load simply with calculations. Mass production vehicles are not used at revolutions in this range, but assuring durability in this range is important for racing vehicles.

Thus far there have been a number of reports concerning the measurement of valve system motion[(1)], but none which converted this motion to the load received by the retainer and performed quantitative evaluation. Therefore, the authors attempted quantitative evaluation using the valve gauge method which does not use laser measurement or other large scale facilities, and also does not require special machining of the cylinder heads. This is an extremely simple method in which two strain gauges are affixed in the axial direction of the valve stem as shown in Fig. 16, and measurement is performed on the cylinder head unit by a motoring device as shown in Fig. 17. Measurement is performed at two opposing points on the valve stem to eliminate strain in the valve bending direction. The average value of the two measurement values was taken as the axial strain, and this strain was converted into a load. Figures 18 to 21 show the waveforms obtained by this method. At extremely low speed (crank revolutions of 60 r/min or less), there is no inertia force and the waveform is straight as shown in Fig. 18.

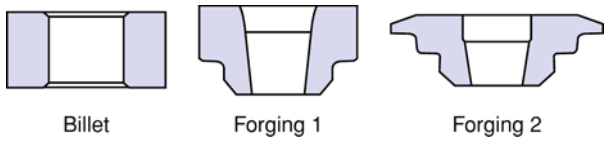


Fig.14 Forging design

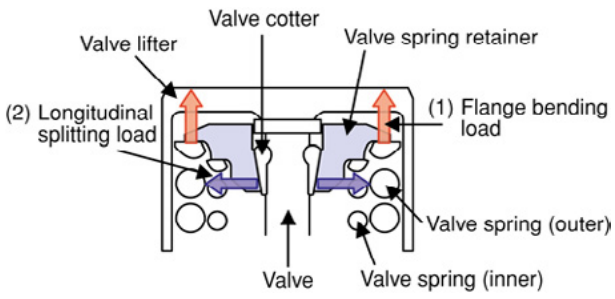


Fig.15 Valve system

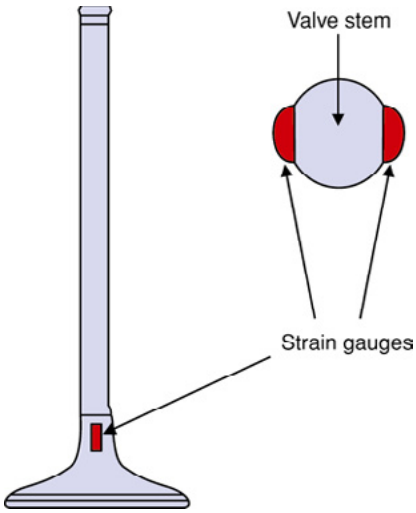


Fig.16 Sticking location of strain gauge

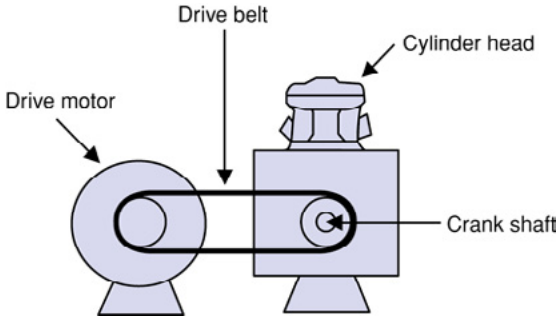


Fig.17 Motoring test

However, in the medium speed range (about 3 000 r/min), the inertia force caused a change in the waveform as shown in Fig. 19. Progressively increasing the speed resulted in a compressed waveform with a projection around the end of the lift as shown in Fig. 20, and then a tensile waveform as shown in Fig. 21. Figure 20 shows the compressed waveform produced when the parts from the valve to the valve lifer, which jump around the middle of the cam up-slope, land on the cam down-slope. Figure 21 shows the tensile waveform produced when the jump extends past the cam down-slope and the valve lands directly on the valve seat. The authors read the peak load at this time and obtained the acceleration of the reciprocating motion parts using the equation of motion shown in equation (1) below.

$$a = Fv/M \quad (1)$$

a : Acceleration of the reciprocating motion parts
Fv : Measured load produced on the valve
M : Inertia mass received at the strain gauge attachment positions (valve stem)

The retainer flange bending load ((1) in Fig. 15) can be expressed as follows.

$$Ftuba = Fol + Fok \quad (2)$$

$$Fok = Mo \times a \quad (3)$$

$Ftuba$: Load applied to the retainer flange
Fol : Lift load of the outer valve spring
Fok : Inertia load of the outer valve spring
Mo : 1/3 of the outer valve spring mass

(Strictly speaking the lift load is not constant with respect to the time axis and there is a phase difference between Fol and Fok, but the load is expressed simply here as the sum of the two.)

Substituting equation (3) into equation (2) yields the following.

$$Ftuba = Fol + Mo \times a \quad (4)$$

In addition, the retainer longitudinal splitting load ((2) in Fig. 15) can be expressed as follows.

$$Ftate = Ftl + (Mr + Mo + Mi) \times a \quad (5)$$

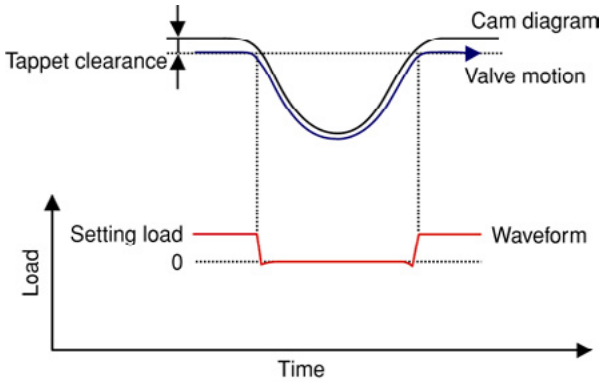


Fig.18 Waveform of load (under 60 r/min)

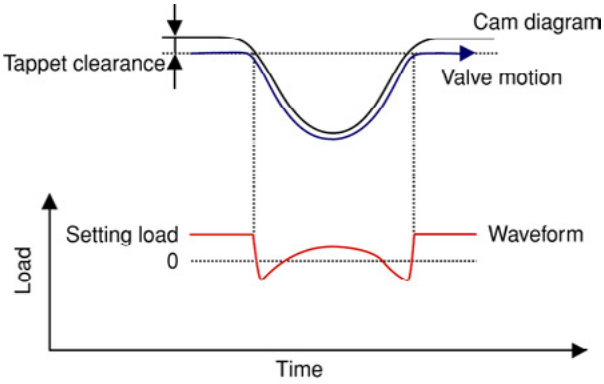


Fig.19 Waveform of load (about 3 000 r/min)

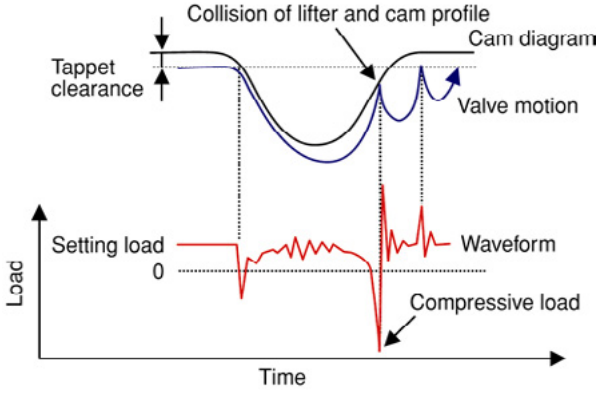


Fig.20 Waveform of load (high engine speed)

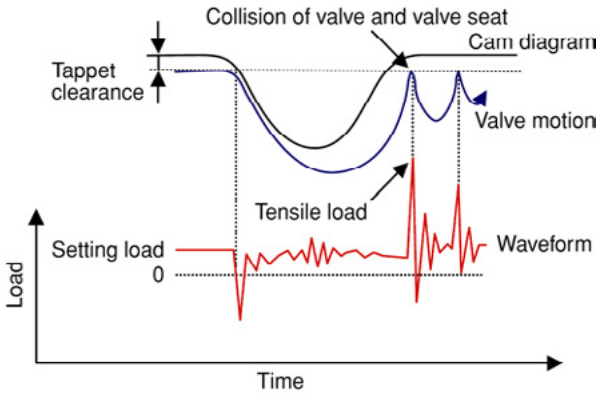


Fig.21 Waveform of load (high engine speed)

Ftate : Retainer longitudinal splitting load
Ftl : Total lift load of the outer and inner valve springs
Mr : Retainer mass
Mi : 1/3 of the inner valve spring mass

Figure 22 shows a graph plotting the loads obtained by equations (4) and (5) against the engine speed on the horizontal axis.

4.2.3. Unit fatigue test and static destruction test

Since it became possible to measure the loads in an actual engine as described in section 4.2.2, unit tests were conducted to understand the actual forces acting on the retainer with respect to those loads. Two types of unit tests were performed in accordance with the destruction modes in an actual engine. These were a fatigue test with respect to the flange bending load, and a static destruction test with respect to longitudinal splitting. Figure 23 shows an example jig shape. Note that the valve spring seat does not evenly contact the entire surface of the retainer, and instead has a large surface pressure distribution at the spring end and directly opposite (180°) the spring end. Therefore, the jig was shaped to receive the retainer at two points to match these conditions. Based on these test results and the results shown in Fig. 22, the better retainer shape was set to provide a safety factor of 1.2 or more in an actual engine.

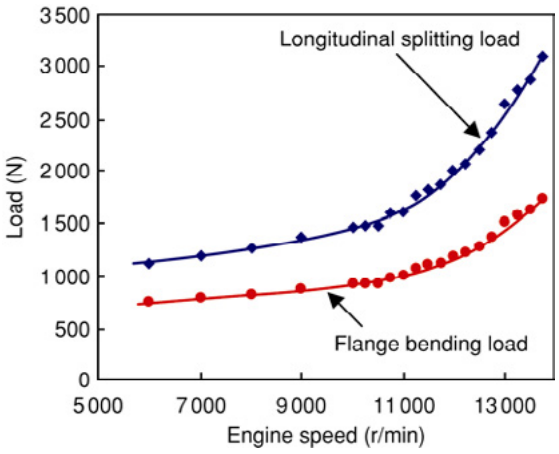


Fig.22 Relationship between engine speed and load which retainer receives

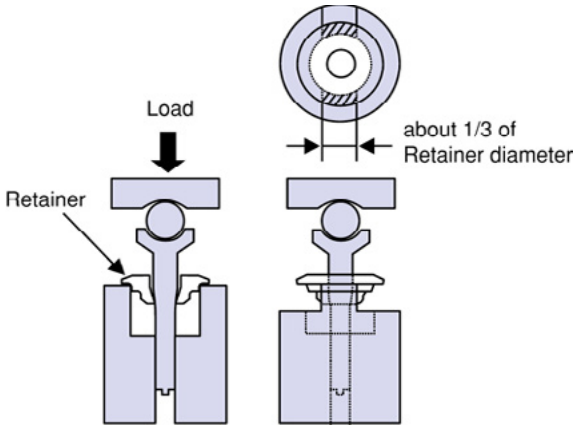


Fig.23 Component jig test

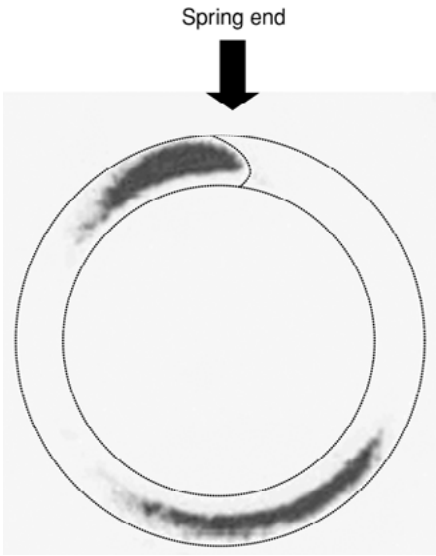


Fig.24 Pressure distribution of valve spring seating surface (by No carbon paper)

4.2.4. Analysis by computer-aided engineering

An attempt was made to clarify the correlation between the fatigue limit obtained by the unit fatigue test and the maximum stress obtained through analysis by computer-aided engineering for this retainer. The computer-aided engineering model used a 1/2 model, the unit fatigue test jig was used as is, and the contact conditions were set to accurately simulate the fatigue test. This improved the development efficiency by reducing the test man hours. Figure 25 shows an example simulation.

5. Effects in an Actual Engine

Weight reduction of 23% was achieved compared to conventional titanium alloy retainers. This stabilized the valve system motion, reduced the load on other valve system parts, and made it possible to increase the limit revolution speed of valve bounce by 220 r/min. As a result, the engine limit revolution speed increased, and the improved output led to greater competitive strength. This retainer had been applied to factory “works” racers in the super-bike class since the mid-1990s, and has contributed to six consecutive

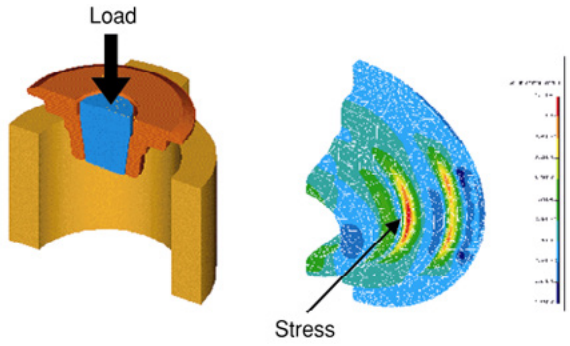


Fig.25 FEM simulation of component jig test

victories in the Suzuka 8-hour Endurance Road Race. In addition, it is also sold as a kit part.

6. Conclusions

(1) Weight reduction of 23% was achieved compared to conventional titanium alloy retainers.
(2) Nano Crystal Powder aluminum metal with high strength and high toughness was developed.
(3) Technology for realizing the optimum hard particle mixture was established to provide abrasion resistance.
(4) Precision closed die forging technology was established to reduce the parts supply cost.
(5) A safety factor verification method was established which allows quantitative evaluation of the retainer load from the valve system motion.

Acknowledgements

The authors wish to express their deep thanks to all related parties at Toyo Aluminium Co., Ltd. and Sumitomo Electric Industries, Ltd. for performing joint material development, and Tanaka Seimitsu Kogyo Co., Ltd. for parts manufacturing.

Reference

(1) Kanda, H., Tanaka, M.: Establishment of Valve Displacement Measurement by Laser Equipment, HONDA R&D Technical Review, Vol. 12, No. 2, p. 141-146 (2000)

■ Authors ■


Kosuke DOI


Hiroyuki HORIMURA


Kyo TAKAHASHI

Development of High-heat-resistant High-nitrogen Containing Austenitic Stainless Steel for Exhaust Gasket

Takashi KATSURAI* Tadao NISHIYAMA* Shuji HAMANO**

ABSTRACT

SUS301-EH is widely used as a material for exhaust system gaskets, but a decline in the material's ability to seal gases due to its reduced hardness at temperatures in excess of 400 °C makes it impossible to use it in high-temperature applications. The research described in this paper determined that the following methods were effective in controlling the softening of stainless steel at high temperatures: (1) The addition of a nitrogen component; (2) Stabilization of the austenite structure; (3) The addition of a molybdenum component. The application of this material to exhaust gaskets has enabled the achievement of excellent seal performance even in tightened sections in high-temperature environments of 400 °C and above, which was problematic for conventional gasket materials.

1. Introduction

Improvements to combustion and exhaust systems are being made in recent years to balance the requirements of better exhaust emission control performance and reduction in CO_2 emissions through enhanced fuel consumption. The effect of cutting down the catalytic temperature rise time for activating the catalyst quickly has become significant, and engines with a shortened exhaust system passageway up to the catalyst and reduced exhaust system heat capacity are currently in operation. In view of such developments, the temperature of exhaust system components is becoming higher, and the usage environment of gaskets used for sealing the exhaust is becoming more severe.

* Tochigi R&D Center
** Daido Steel Co., Ltd.

2. Development Goals

SUS301-EH stainless steel with high strength and excellent spring characteristics has been used until now as the material for metallic gaskets used for sealing exhaust at the connections of components in the exhaust system and cylinder head. This gasket is made of a thin sheet of 0.2 mm thickness as shown in Fig. 1, has a bead formed on it and has a shape that envelopes the exhaust port. This bead acts as a spring. Its function is to seal the exhaust that passes through the clearance between the cylinder head and the flanges of exhaust system components, which deform during operation due to heat from high temperature combustion gases. However, the deformation of flanges of tightened parts has tended to be excessive in recent years because of the high temperatures of the exhaust system components[(1)]. Since gaskets are also subjected to high temperature usage environments, the gasket material is required to possess high spring characteristics in high temperature environments.

When the temperature exceeds 400 °C, SUS301-EH, which is conventionally used as the gasket material, suddenly becomes soft and loses its spring characteristics. Consequently, the gasket needs to be used in environments where the temperature is below 400 °C. However, for the newly developed three-cylinder engine shown in Fig. 1, a structure in which the turbocharger is directly fitted to the cylinder head is adopted in order to shorten the exhaust system passageway up to the catalyst and to reduce the heat capacity. The temperature of flanges at the connections exceeded 500 °C, and SUS301-EH could no longer be used. Thus, a high–heat-resistant gasket material that could retain its sealability characteristics adequately, without softening at temperatures of 500 to 600 °C, was required.

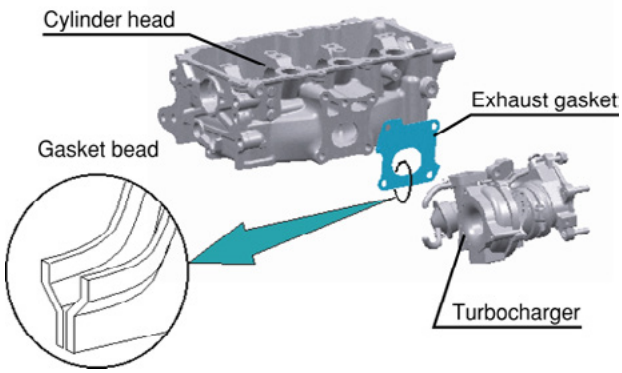


Fig. 1 Illustration of exhaust gasket

3. Study of Methods to Retain Hardness at High Temperatures

3.1. Required Properties of Gasket Material

The gasket was tightened between the flanges, held at various temperature ranges for 400 hours, and then taken out. The height of the bead remaining (residual bead height) and the hardness were measured. Figure 2 shows the relationship between the residual bead height and the hardness. According to this figure, when the hardness drops below HV400, the bead undergoes plastic deformation due to the flange tightening force and the residual bead height becomes practically zero. In this way, the hardness of the material is an important factor that governs the sealability of the gasket.

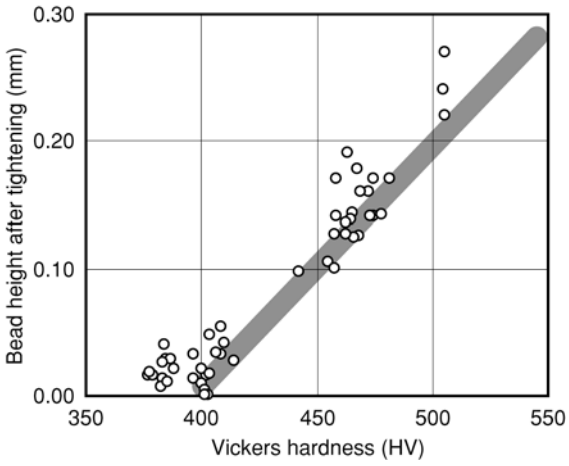


Fig. 2 Relationship between hardness and bead height after hot tightening

The higher the hardness is, the greater the spring restoring force becomes and the more superior its sealability is.

As demonstrated above, the gasket material should possess hardness greater than HV400 and should enable the bead to be formed. SUS301, the material conventionally used in gaskets, is a metastable austenitic stainless steel. Strain energy is given to this material in the final cold rolling stage of the steel manufacturing process. As a result, a high strength strain-induced martensitic structure is obtained, which gives high hardness to the material. During final cold rolling, a large dislocation can be introduced in the strain-induced martensitic structure, giving rise to work hardening. Thanks to the transformation of martensite and the synergistic effect, a tempered rank of EH (Extra Hard) with hardness greater than HV500 can be obtained.

3.2. Causes of Hardness Reduction of SUS301-EH

If SUS301-EH is held for a long period at a high temperature, it becomes soft because the large dislocation introduced during the final cold rolling is released and recovered to its original state, and the strain-induced martensite returns to austenitic structure due to inverse transformation.

Figure 3 shows the results of hardness measured after holding SUS301-EH at a high temperature for 400 hours. It can be observed from the figure that at temperatures greater than 400 ºC, the softening of the material progresses rapidly. It is well known that the inverse transformation of structure of strain-induced martensite occurs at temperatures near 800 ºC[(2)]. The cause of the rapid reduction in hardness at temperatures near 400 ºC is attributed to the recovery. Accordingly, it is important to inhibit the release of dislocation introduced by the strain so as to control softening in the temperature range of 500 to 600 ºC.

SUH660 and SUS631 are well known as stainless steel materials for high temperature use. Ni-based Inconel-625 is also widely used as a heat-resistant material. Figure 3 shows the hardness characteristics at high temperatures of SUS301-EH and Inconel-625. According to this figure, Inconel-625 can retain its hardness at room temperature even up to a temperature of 800 ºC. However, the initial hardness at room temperature is about HV350 to HV400, and therefore, it is unsuitable for use as gasket material. Thus, the existing heat-resistant materials could not retain high hardness in a stable condition over the range of temperatures

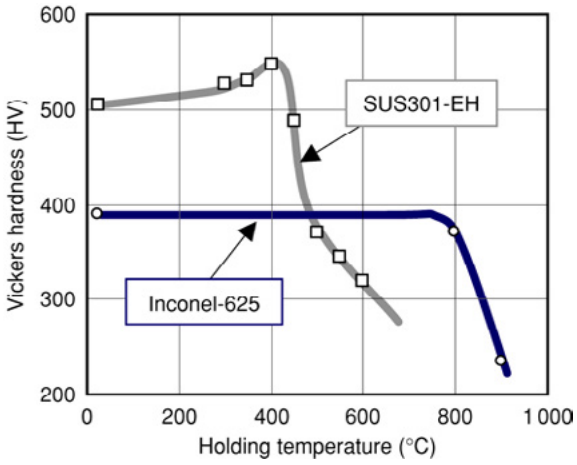


Fig. 3 Relationship between hardness and bead holding temperature after 400 Hr

from room to high temperatures, and high sealability required of a gasket material could not be attained when they were used.

3.3. Concept of Material Design

The material for gaskets used at high temperatures should satisfy the balancing requirements of: (1) high hardness to ensure spring characteristics, and (2) stable structure that inhibits softening at high temperatures. For this purpose, the dislocation introduced in the structure for high strength by work hardening should be made to adhere fast so that it is not released at high temperatures and softening does not occur. Two methods are effective for adherence of the dislocation: the method of dissolving C and N, which are interstitial solid solutions, in the crystal lattice and the method of precipitating C and N as carbides and nitrides[3]. In this development work, attempts were made to prevent as far as possible, the motion of the dislocation by the synergistic effects of both methods. Particularly, since N has a higher solubility in solid than C, it is not likely to form coarse precipitates such as $Cr_{23}C_6$ even if held for a long period in high temperature and is unlikely to become brittle. Thus it was decided that dissolving a large amount of N was an effective method[4, 5]. Moreover, steel with high N-content has been reported[6 - 8] to have high strength and excellent workability. It is also considered to be ideal for bead forming[2] of gaskets to which strain has been applied locally.

The solubility in liquid of N in molten steel follows the Sieverts' Law $[N\%] = A\,[P_{N2}]^{1/2}$. Therefore, the partial N_2 pressure (P_{N2}) cannot be increased in the conventional Vacuum Oxygen Decarburization (VOD) process, and the general practice is to use solubility in liquid of high N containing steel at about 0.2%. Only the high Cr, high Ni, Mo-based seawater-resistant 0.5%N Super Stainless (Avesta Sheffield 654SMo)[10] and 1.0%N steel experimentally tried out by pressurized ESR (Electro Slag Re-melting) apparatus have been reported as other high N-added steels[11, 12]. It was considered that increasing the amount of additives Cr and Mn, which are elements that enhance the solubility of N in molten steel, would increase the amount of N added under similar conditions of partial N_2 pressure without changing the refining method[13, 14].

Moreover, the method of forming austenitic structure, which has a face centered cubic lattice (fcc) structure with high solubility in solid, is effective in dissolving the solid N even at room temperature. Furthermore, the fcc structure enhances hardness at high temperature since its self-diffusion coefficient is small because of the high packing density of atoms. Therefore, the effect of forming austenitic structure is considered to be significant.

N, an interstitial element being dissolved in the austenitic structure, forms an Interstitial-Substitutional (I-S) bond with Cr, Mn, and Mo, which are substitutional solid elements, and is known to possess characteristics that enhance strength further[15]. Its combination with Cr, Mn, and Mo as an additive is considered to be very effective[16]. The addition of Mo to a newly developed material was studied in particular because of its effect in improving strength at high temperatures by solid solution hardening.

Based on the results of the study mentioned above, component design was carried out with the following as the basis: (1) addition of N; (2) stabilization of austenitic structure; and (3) addition of Mo. The development target values for the material were set as retention of initial hardness greater than HV450 and retention of residual hardness greater than HV450 even after 400 hours at 600 ºC.

3.4. Results of Validity Verification of Component Design

The material of each component was held for 400 hours at 600 ºC, and the effects of various parameters for residual hardness were analyzed. Figure 4 shows the effects of the addition of N. It was confirmed from this figure that the residual hardness increases almost directly in proportion to the amount of N added up to an addition of 0.3%N. Next, Fig. 5 shows the results that confirm the effects of material structure. To express the state of material structure here, the Ni equivalent (*Nieq*) according to Delong's equation[17] (1) is used.

$$Nieq(\%) = Ni\% + 0.5 \times Mn\% + 30 \times (C\% + N\%) \quad (1)$$

The results showed that when Ni-equivalent is high and the austenitic structure is stable, the residual hardness after retention at high temperatures is high, confirming that the stable austenitic structure is effective as the parent phase. Finally, Fig. 6 shows the effects of the addition of Mo. From these results, it was confirmed that the addition of Mo is also effective in the retention of hardness at high temperatures.

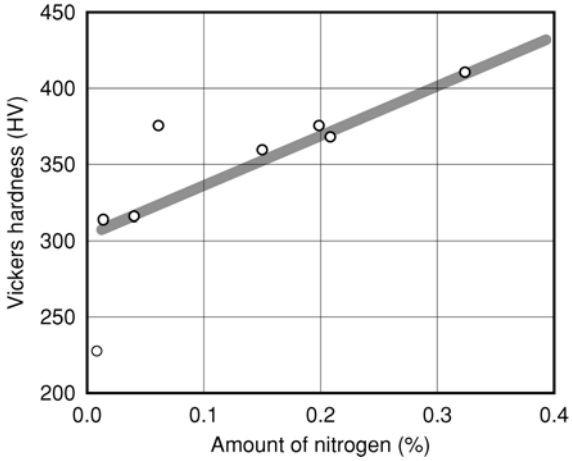


Fig. 4 Effect of amount of nitrogen on hardness after 600 °C × 400 Hr holding

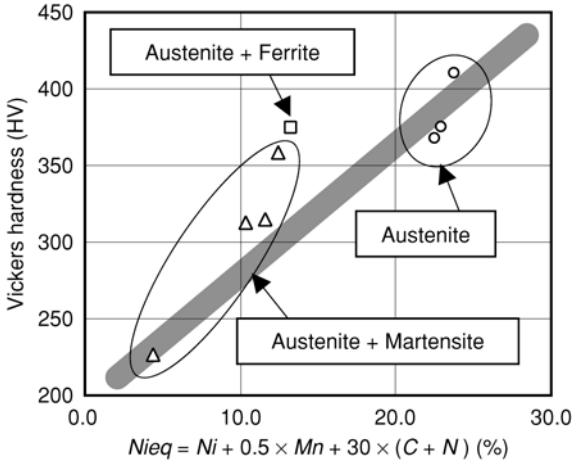


Fig. 5 Relationship between Ni equivalent and hardness after 600 °C × 400 Hr holding

The validity of component design was verified from the results above, therefore, optimum specifications that maintain an appropriate balance were studied. Since the effects of the addition of N are particularly large, it was considered that the emphasis should be placed on having N as the maximum solid solution in the component specifications[18].

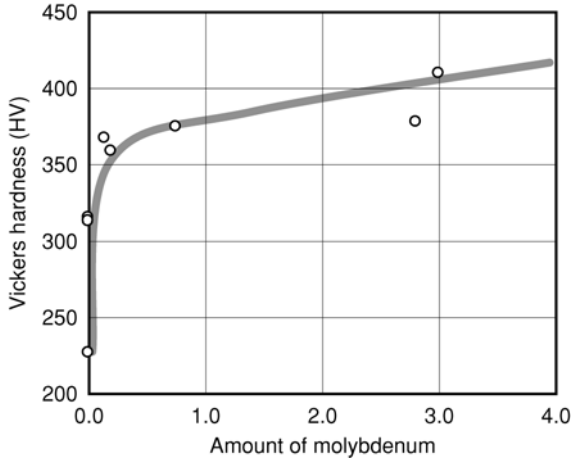


Fig. 6 Effect of amount of molybdenum on hardness after 600 °C × 400 Hr holding

3.5. Setting Material Component Specifications

Table 1 shows the approach to component design based on: (1) N as the maximum solid solution; (2) Stabilization of austenitic structure, and (3) The addition of Mo. The settings are explained in a simple manner below.

N : Addition to molten steel until the saturated soluble amount

C : Added as the minimum limit required for reducing other interstitial solid solutions for obtaining N as the maximum solid solution

Ni : Element for stabilizing austenite; appropriate amount is to be added since it reduces the solubility in solid of N

Mn : Element for stabilizing austenite; appropriate amount is to be added since it enhances the solubility in solid of N for compensating stabilization of austenite which declines due to inadequate Ni

Cr : Greatest element for N solid solution; added as 23% so that maximum solid solution is obtained at the solution temperature

Si : Added as the minimum limit since it is an element generating ferrite

Mo : Appropriate amount is to be added to enhance heat resistance

V : Added so that minute amount of C adheres as carbide and also to prevent increase in size of coarse grains

Table 1 Alloy design concept

N	High	Solid-solution hardening
C	Low	Increase solubility of nitrogen
Ni	Proper	Stabilize austenite
Mn	Proper	Increase solubility of nitrogen
Cr	High	Increase solubility of nitrogen
Si	Low	Stabilize austenite
Mo	Proper	Increase heat resistance
V	Proper	Prevent increase in grain size

Table 2 shows the components of the newly developed material with 0.5% N solid solution, designed based on the results of the study above. It was also confirmed that a hardness level of HV470 could be attained, which is adequate for gasket material by implementing final cold rolling at a reduction of 60% for the said material.

Table 2 Chemical composition of newly developed steel

(wt%)

C	Si	Mn	Ni	Cr	Mo	V	N
0.02	0.2	6.0	10.0	23.0	2.0	0.1	0.5

4. Verification of Effects

4.1. Hardness Characteristics during High Temperatures

Figure 7 shows the results of the measurements of change in hardness after holding the newly developed material for 400 hours at high temperatures. The figure shows that the hardness value is maximum at 400 to 450 ºC. Subsequently, a softening trend that is proportional to the temperature was verified. It can also be observed that the initial hardness is retained even at 600 ºC. Compared to the softening of SUS301-EH at temperatures above 400 ºC, the temperature at which softening starts has been raised by more than 200 ºC. Softening that occurred near 400 ºC due to the release of dislocation was also completely inhibited.

Figure 8 shows the results that confirm the effects of retention time corresponding to softening at high temperatures. According to this figure, the hardness at 600 ºC has increased from the initial hardness in 10 hours but subsequently there is no change. At temperatures above 700 ºC, the softening has practically ended in about 100 hours. Subsequently, the onset of softening is extremely small, with dependence more on temperature than on time.

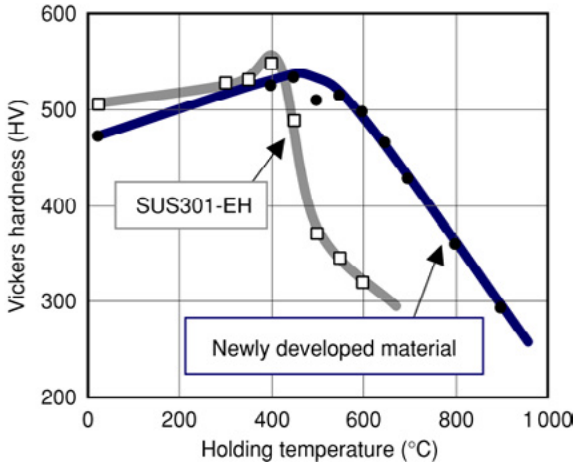


Fig. 7 Relationship between hardness and holding temperature after 400 Hr

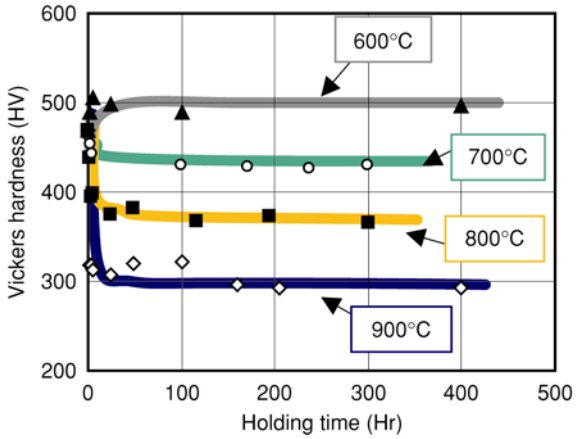


Fig. 8 Relationship between hardness and holding time

4.2. Hardening Mechanism at Temperatures below 600 °C

The hardening mechanism was analyzed since the hardness increases at temperatures of 600 ºC and below compared to the initial hardness. Figure 9 shows the results of observations made on the material held at 600 to 900 ºC for 400 hours using the optical microscope. These observations show the processed structure in grains caused by strain and grains elongated due to rolling at 600 ºC. Elongated grains remained at 700 ºC similar to the condition at 600 ºC, but it was also observed that microstructures of recrystallized fine-grains or precipitates near the grain boundary were formed. Furthermore, at temperatures of 800 ºC and 900 ºC, these microstructures grew and became coarse.

To verify whether the hardening mechanism at 400 to 600 ºC was due to precipitates or not, an attempt was made to identify the precipitates in samples held for 400 hours at 600 ºC by the melting extraction method, but precipitates could not be detected. Moreover, no change in hardness was observed and precipitates could not be detected even when solution treated materials without strain were held for a long period at the same temperatures. From these results, the hardening mechanism at 400 to 600 ºC is considered to be strain aging with enhanced adhering capacity of dislocation, as a result of accumulation of solid N around the dislocation introduced at final cold rolling at a reduction of 60%, which forms a Cottrell atmosphere. The mutual interaction due to the I-S bond is also predicted to have a considerably large effect [15), (16), (18)].

4.3. Hardening Mechanism at Temperatures above 600 °C

It was confirmed from the results of observation with an optical microscope that the microstructure generated in the vicinity of the grain boundary has a large effect on the change in hardness of the newly developed material at high temperatures. Figure 10 shows the results of analysis by the scanning electron microscope for material held at 400 hours at 900 ºC. It was verified from the results that two kinds of precipitate — black-colored high Cr, N-based precipitate less than 2 µm and white-colored high Cr, Mo-based precipitate of about 3 µm — existed in these microstructures. Figure 11 shows the results of the analysis of these precipitates by an electron beam diffraction pattern. It was confirmed from these results that the black-colored high Cr, N-based precipitate was Cr_2N but similar identification of the white-colored high Cr, Mo-based precipitate could not be made.

It is well known that in the case of high nitrogen containing steel, Cr_2N precipitates at temperatures above 600 ºC [19), (20)]. In the case of the newly developed material too, precipitation hardening is considered to occur due to precipitation of Cr_2N

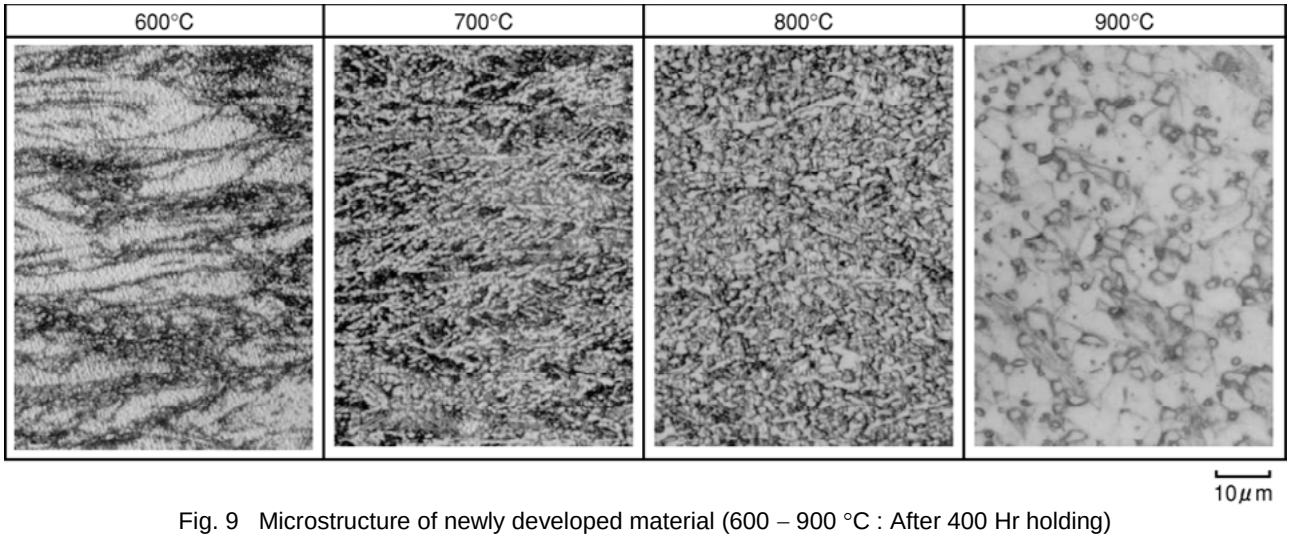


Fig. 9 Microstructure of newly developed material (600 – 900 °C : After 400 Hr holding)

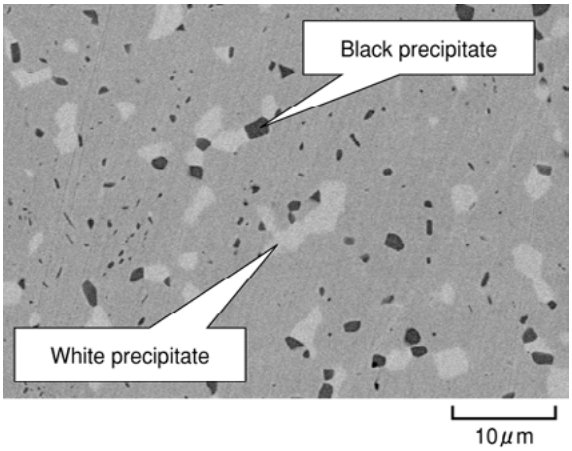


Fig. 10 Scanning electron micrograph after annealing (900 °C × 400 Hr)

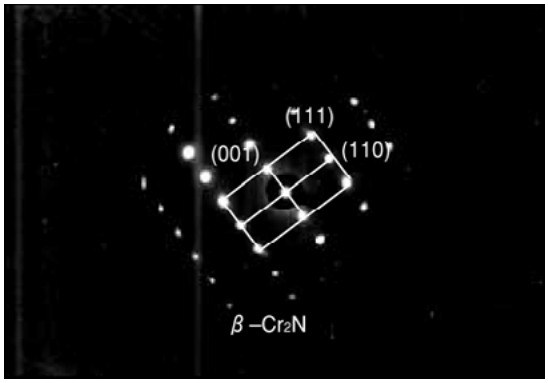


Fig. 11 Result of analysis by electron beam diffraction pattern

at temperatures above 600 ºC. Cr_2N is said to precipitate preferentially over grain boundary and dislocation [21]. It has been confirmed also from Fig. 9 that it precipitates near the recrystallized grain boundary in the structure at 900 ºC.

Figure 12 shows the change in structure corresponding to holding time at temperatures of 700 ºC and 800 ºC at which hardness reduction occurs. It is observed from the figure that precipitates are formed in the structure after a holding time of 100 hours at both temperatures, but practically no change in the structure occurs even if held up to 400 hours. Comparing the condition of such a structure with the softening characteristics shown in Fig. 8, it is seen that practically no change in hardness occurs in the range where no change in the structure occurs.

Based on these results, it can be concluded that Cr_2N precipitates preferentially on the grain boundary or on the dislocation at temperatures above 600 ºC and inhibits softening due to the release of the dislocation. Furthermore, softening progresses because recrystallized structure is formed in addition to the release of dislocation at high temperatures of 800 to 900 ºC. However, the precipitated Cr_2N generates pinning effects, therefore, growth of the recrystallized grains is probably inhibited. That is probably why the change in structure and hardness at high temperatures above 700 ºC became extremely slow. However, as the temperature increases, Cr_2N, which possesses pinning effects, flocculates and becomes coarser. These pinning effects reduce and the grain growth inhibiting effect at the grain boundary decreases, therefore, the softening is considered to have increased.

It is presumed that the same factors have participated in the growth inhibiting effect of precipitates and secondary recrystallized grains in case of white-colored high Cr, Mo phase, but it could not be confirmed.

4.4. Conclusion Related to Hardening Mechanism

It was confirmed that the newly developed material possesses two levels of hardening mechanisms when N is added. The first is the strain aging due to solid N in the temperature range below 600 ºC, while the second is the precipitation hardening of Cr_2N in the temperature range above 600 ºC. The dislocation introduced during final cold rolling is considered to act effectively in both levels.

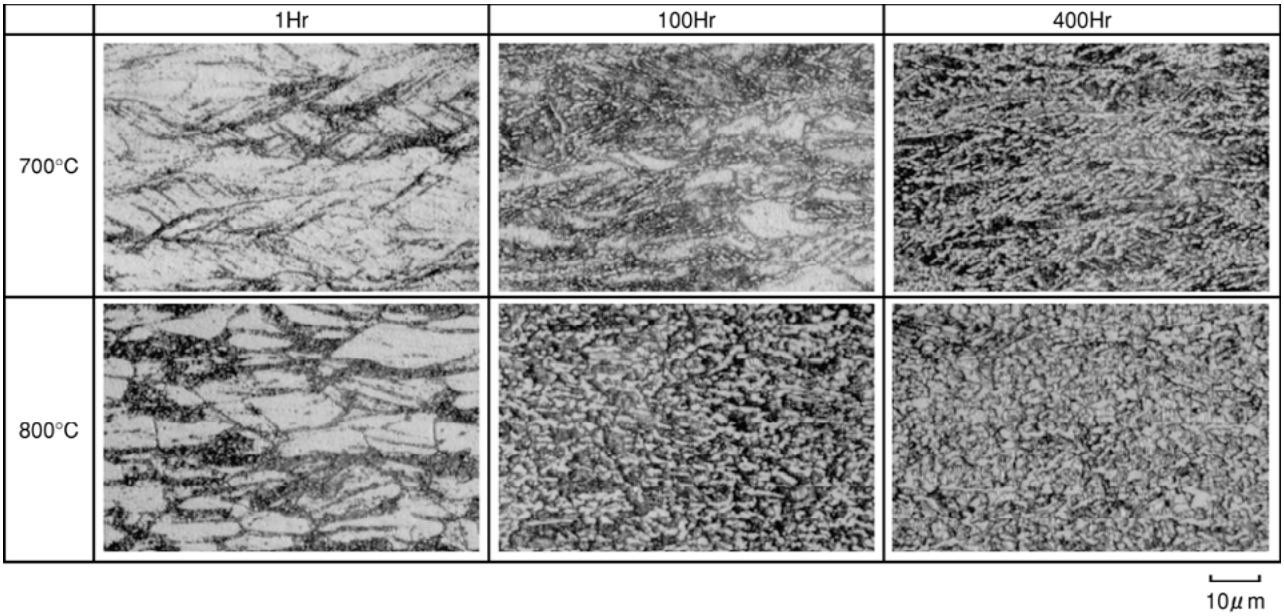


Fig. 12 Microstructure of newly developed material (700, 800 °C : After 1 – 400 Hr holding)

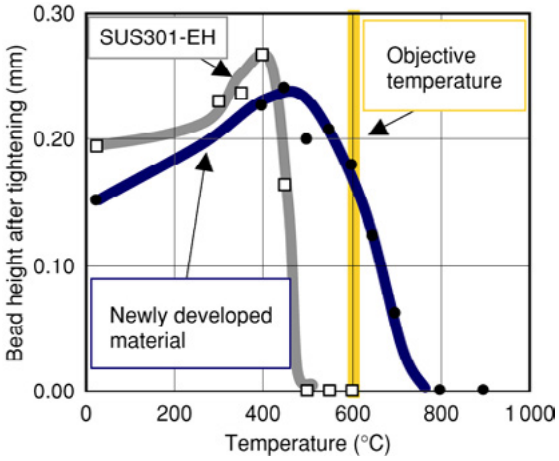


Fig. 13 Relationship between temperature and bead height after tightening test

In conclusion, when material with alloy components in which (1) solid N has been increased, (2) stable austenitic structure has been formed, and (3) Mo has been added, is subjected to final cold rolling at a reduction of 60%, inhibition of growth of recrystallized grains due to micro-precipitates of Cr_2N and strain aging due to solid N could be achieved. Thus, softening at high temperatures that had occurred in SUS301-EH conventionally was inhibited, and the temperature at which softening starts could be improved by more than 200 ºC.

5. Results of evaluation of engine compatibility

A gasket was manufactured using the newly developed material. It was fitted to an actual engine, the engine was operated and the height of the residual bead was measured. From the results and the hardness reduction characteristics at high temperatures shown in Fig. 7, the relationship between the change in height of the residual bead and temperature was determined. This relationship is shown in Fig. 13. From the figure, it was observed that while the residual bead height reduced rapidly and sealability degraded at temperatures above 400 ºC when SUS301-EH was used, the residual bead height above initial values was retained at temperatures up to 600 ºC and no degradation in sealability occurred in the case of the newly developed material.

The temperature of the gasket of the newly developed engine using the newly developed gasket material was about 500 ºC, indicating that the residual bead height had adequate sealability against heat deformation of the flange. Furthermore, it was also confirmed that the gasket had excellent sealability in the engine endurance tests.

6. Conclusion

To inhibit softening at high temperatures, efforts were made to develop a new material focusing on strain aging by using N and inhibition of growth of recrystallized grains by using nitrides. The result was the development of a spring material for use at high temperatures up to 600 ºC wherein no hardness degradation occurred. This temperature was more than 200 ºC higher than the temperature of conventional materials at which hardness degradation occurred. This newly developed material was used as the material in exhaust gaskets, and it was confirmed that it possessed excellent sealability when used in tightened parts at temperatures higher than 400 ºC at which sealing was difficult in conventional gasket materials such as SUS301-EH. The results of the development are summarized below.

(1) The sealability of the gasket was evaluated by the hardness of the material. For attaining stable sealability, hardness greater than HV400 is necessary.
(2) At temperatures below 600 ºC, the dislocation introduced in final cold rolling adheres due to strain aging of solid N, and the initial hardness can be retained.
(3) At temperatures above 600 ºC, softening occurs because of the release of the dislocation. However, micro-precipitates of Cr_2N occur in the grain boundary, which causes precipitation hardening and inhibits the growth of recrystallized grains. Therefore, softening almost stops even if held for a long period.
(4) By using the gasket with the newly developed material, the initial sealability can be retained up to about 600 ºC.

Acknowledgments

The authors acknowledge with gratitude all the staff of Nippon Leakless Corporation who manufactured the gasket.

References

(1) Ishii, K., Katsurai, T., Nakata, M., Wakamatsu, H., Nakasone, H.: Analysis of Sealing Behavior of Exhaust Manifold Gasket during Running the Actual Engine, HONDA R&D Technical Review, Vol. 8, p. 152-159 (1996)

(2) Katsurai, T.: Development of High Fatigue Strength Ultra-Fine Grained Stainless Steel for Cylinder Head Gasket, Honda R&D Technical Review, Vol. 12, No. 1, p. 151-158 (2000)

(3) Kubota, S., Tomoda, Y.: Characteristic Features of Work Hardening in Nitrogen Bearing Austenitic Steels, CAMP-ISIJ, Vol. 10, p. 538 (1997)

(4) Koga, T., Shimizu, T., Okabe, M.: The mechanical Properties at Elevated Temperatures of High Nitrogen Stainless Steel, CAMP-ISIJ, Vol. 13, p. 638 (2000)

(5) Wada, S., Ohta, Y.: Effect of Alloying Elements on Properties for Ultra High Nitrogen Containing Stainless Steel, Nippon Stainless Technical Report, No. 24, p. 13-30 (1989)

(6) Katada, Y., Sagara, M., Kobayashi, Y., Kodama, T.: Creation of High Nitrogen-bearing Stainless Steel and Its Mechanical Properties, CAMP-ISIJ, Vol. 15, p. 438-441 (2002)

(7) Speidel, Markus O.: Corrosion Science of Stainless Steels, Proceedings of International Conference on Stainless Steels, ISIJ, p. 25-35 (1991)

(8) Koga. T., Shimizu, T., Okabe, M.: Warm Workability and Tensile Property of High Nitrogen Austenitic Stainless Steel, Electric Furnace Steel, 67-2, p. 81-86 (1996)

(9) Takahashi, I., Yoshida, T., Mineura, K., Ohta, Y.: Study of Ultra High Nitrogen Containing Stainless Steel,

Nippon Stainless Technical Report, No. 22, p. 1-27 (1987)

(10) Azuma, S.: Characteristics of Constitution of High Nitrogen Containing Stainless Steel, Fushoku-Boshoku Symposium, No. 119, p. 7-12 (1998)

(11) Uno, H., Katada, Y.: The State and the Point at Issue of the Development of Corrosion Resistant High Nitrogen-bearing Stainless Steels in NRIM, Function of Alloy and Development of New Material by Nitrogen on Stainless Steel, ISIJ-Forum, p. 38-45 (1999)

(12) Katada, Y., Uno, H., Kodama, T.: Creation of High Nitrogen-bearing Stainless Steel by Pressurized ESR Method, CAMP-ISIJ, Vol. 13, p. 356 (2000)

(13) Kikuchi, M., Kajihara, M., Frisk, K.: Solubility of nitrogen in austenitic stainless steels, Proc, Intl. Conf. High Nitrogen Steels, p. 63-74 (1989)

(14) Kowanda, C., Speidel, Markus O.: Solubility of nitrogen in liquid iron base and nickel base alloys with Co, Fe, Mn, Mo and Cr under elevated nitrogen partial pressure, CAMP-ISIJ, Vol. 13, p. 355 (2000)

(15) Murayama, M., Hono, K., Hirukawa, H., Ohmura, T., Matsuoka, S.: The Microstructural Evolution of Nitrogen Doped Austenitic Stainless Steel after Fatigue Testing, CAMP-ISIJ, Vol. 12, p. 458 (1999)

(16) Ito, H., Nakamura, N., Takagi, S.: Effect of Chromium and Manganese Content on Equilibrium Soluble Nitrogen Content in High Nitrogen Austenitic Stainless Steels, CAMP-ISIJ, Vol. 11, p. 1151 (1998)

(17) Long, C. J. et al: The ferrite content of austenitic stainless steel weld metal, The Welding Journal, Vol. 7, p. 281-297 (1973)

(18) Isobe, S., Okabe, M.: Aging Behavior of Cold Worked Austenitic Stainless Steels with Nitrogen, Electric Furnace Steel, 56-2, p. 122-132 (1985)

(19) Ogawa, M., Hiraoka, K., Shiga, C., Katada, Y., Uno, H.: Nitride Precipitation Behavior at HAZ of High Nitrogen Bearing Stainless Steel, CAMP-ISIJ, Vol. 13, p. 636 (2000)

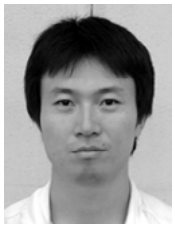
(20) Ogawa, M., Hiraoka, K., Katada, Y., Sagara, M.: Study on Nitride Precipitation Behavior at HAZ of High Nitrogen Stainless Steels and of it, CAMP-ISIJ, Vol. 15, p. 446-449 (2002)

(21) Woo, I., Horinouchi, T., Kikuchi, Y.: Influence of Nitride Precipitation on the HAZ Toughness of High Nitrogen Containing Ni-Free Austenitic Stainless Steel, Tetsu-to-Hagane, Vol. 88, p. 29-35 (2002)

■ Authors ■



Takashi KATSURAI



Tadao NISHIYAMA



Shuji HAMANO

Development of High-strength Induction Hardened Crankshaft

Hayato ONDA* Tetsuya ASAI* Kenji FUJIKI*
Hirotsugu KUDO* Kazumasa MUROFUSHI*

ABSTRACT

A high fatigue strength and wear resistant induction hardened crankshaft has been developed for diesel engines. Crankshafts for use in diesel engines must be engineered to tolerate the high loads generated by high in-cylinder pressures, and be capable of resisting wear caused by the carbon, which collects in the lubricating oil as a combustion by-product. Simultaneous hardening of the shaft and the fillet has been adopted in the newly developed crankshaft to achieve even higher strength while reducing the number of production processes, resulting in the development of a crankshaft with excellent fatigue strength, resistance to wear, and mass producibility. A special material was developed for the crankshaft to enable the curvature occurring during induction hardening of the fillet to be easily corrected. In addition, control of inclusions in materials has enabled the lead component, conventionally added to increase machinability, to be removed without sacrificing workability.

1. Introduction

The demand continues to grow for automobiles to place lower loads on the environment than ever before. There are high expectations placed on the diesel engine from the viewpoint of regulations on CO_2 emissions.

The diesel engine operates at higher cylinder pressures than the gasoline engine, causing high loads, particularly bending loads, on the crankshaft. Furthermore, the inclusion of combustion by-products (carbon) into the lubricating oil, a problem which does not occur in gasoline engines, requires high wear resistance in the reciprocating parts of the journal. This has necessitated development of materials and heat-treating technologies for more wear and stress resistant crankshafts.

* Tochigi R&D Center

2. Development Aims

Both selection of constituents and heat-treating processes are essential means for strengthening crankshafts against the high loads in diesel engines. Many methods for strengthening are in use[(1)].

Figure 1 shows an example of a conventional, mass-produced induction hardened crankshaft for passenger vehicles. Most induction hardened crankshafts receive induction hardening at the journals in order to improve wear resistance, and the fillets are roller-burnished in order to maintain high fatigue strength[(1)]. Roller-burnishing processes are effective at strengthening fillets, but since fatigue strength is increased by residual compressive stresses, unless the material is quite hard, the residual stresses are low and the

fatigue strength is not expected to be enhanced. This obliges the use of materials with poor workability. Another concern is that two production steps must be performed, heat treatment of the journal and roller-burnishing of the fillet, requiring more processing equipment. Therefore, a specification was created for induction hardening of the fillet shown in Fig. 1 with the double goals of establishing high fatigue strength while simplifying the sequence of operations on the production line, in the general process outlined in Fig. 2. Although further improved fatigue strength is obtained by applying induction hardening to the fillet in addition to the journals, there is another issue: the shaft is bent by the distortion induced by heat treatment during hardening. This distortion can be controlled by increasing the rigidity of the crankshaft, but this approach results in a weight increase. A light crankshaft can be made if it is possible to correct the shaft distortion during induction hardening. In order to accomplish this, it was therefore determined to develop a new crankshaft material, with due consideration to workability and induction hardenability, in addition to correction of shaft distortion, which is the major issue in induction hardening of the fillet. Simultaneously, a technology, which improves machinability, was employed instead of adding lead, in order to decrease the use of hazardous materials, which are harmful to the environment.

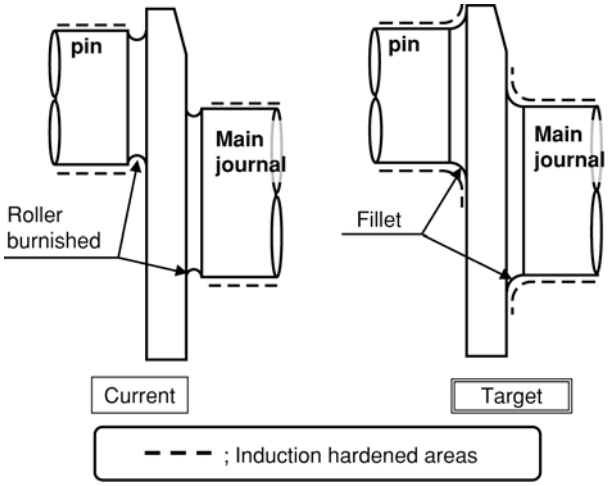


Fig. 1 Feature of the target crankshaft

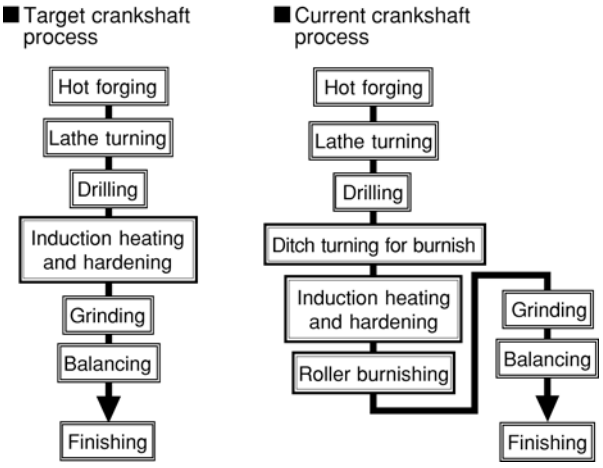


Fig. 2 Production process for induction hardened crankshaft

3. Material Specifications

Vanadium-containing micro alloyed steel is one example of a crankshaft material suitable for induction hardening in mass production for diesel engines[2]. This material has a high degree of hardness after hot forging. It cannot be made on current crankshaft production lines, because tooling and processes would need to be optimized for its adoption. Therefore, the new material was developed with an eye to the considerations described in the following section.

3.1. Wear Resistance of Reciprocating Parts of the Shaft

Induction hardened test pieces were subjected to a wear test at the reciprocating parts with oil seals, using carbon-contaminated oil. The results of the test are shown in Fig. 3. The allowance of wear volume was determined to be 50 μm or less from the axial tracking characteristics of the oil seals. The trend in the minimum results in Fig. 3 was used to define a lower limit of HMV 580 for surface hardness. Also, as shown in Fig. 4, a correlation has been shown between surface hardness and the amount of C in the crankshaft material during induction hardening of the actual crankshaft. By this relation, a C content of 0.37 Wt% was set in order to reach the target surface hardness.

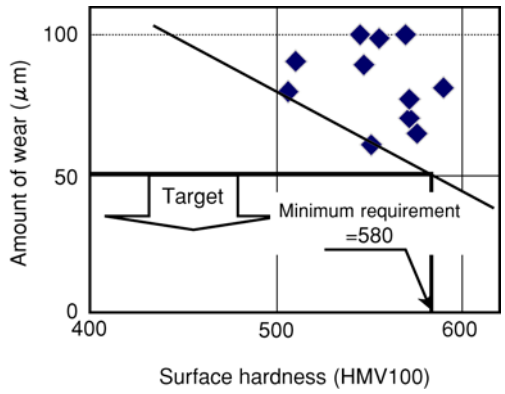


Fig. 3 Relation between surface hardness and amount of water

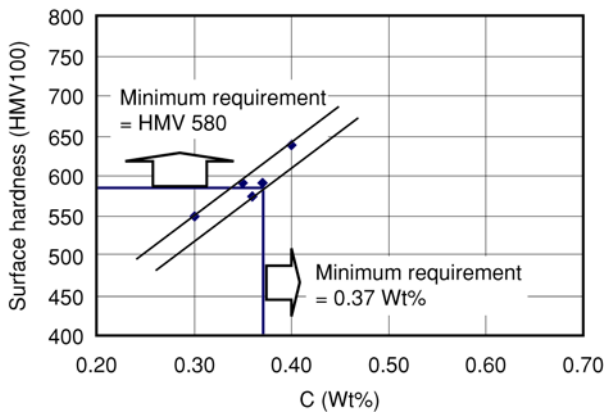


Fig. 4 Relation between amount of C and surface hardness

3.2. Producibility, Workability, Machinability

It has been reported that there is a correlation between carbon equivalents (*Ceq*) and material hardness after hot forging[3].

$$Ceq = C + \frac{1}{10}Si + \frac{1}{5}Mn + \frac{5}{22}Cr + 1.65V - \frac{5}{7}S$$

Figure 5 shows the relation found in an actual crankshaft between the material Ceq and material hardness. An upper hardness limit of HRB 98 was set in deference to the processing conditions on the existing crankshaft production line, and a lower limit of HRB 85 was selected in order to maintain sufficient fatigue strength in the actual crankshaft; thus, a Ceq of 0.54 – 0.60 wt% was specified. Si, Mn and Cr are generally known to improve induction hardenability, so these were investigated for their abilities to improve fatigue strength while not raising material hardness. Si raises fatigue strength by raising the strength of ferrite in the ferrite-pearlite structure, though the material internal hardness is reported to be small[4]. In this development effort, the Si amount was set at 0.50 Wt% in consideration of Ceq range, and Mn was set at 0.60 Wt% to strike a balance.

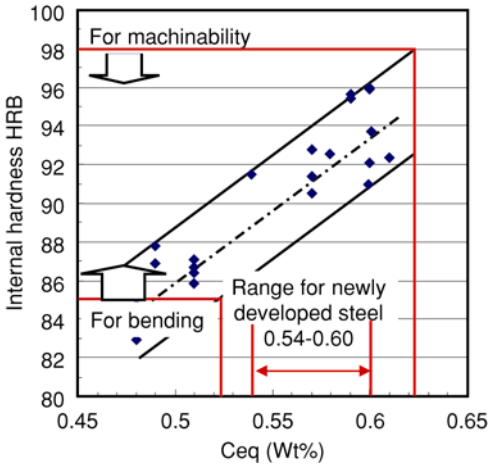


Fig. 5 Relation between Ceq and internal Hardness

3.3. Improvement of Induction Hardenability

Boron was added in order to improve and stabilize the induction hardenability. Addition of small quantities of B has been reported to raise induction hardenability without raising post-forged material hardness[5]. If N is present in the steel, BN is generated, reducing the solid-solution B; sufficient B was therefore ensured by adding Ti and pinning N in order to reduce solid-solution N.

3.4. Eliminating Lead

Finely dispersed sulfide inclusions are an effective replacement for lead in free-cutting steel[6]. They provide locations for crack onset in the material during machining, improving chip frangibility, thereby improving machinability.

The material constituents, determined by the considerations expressed so far, are listed in Table 1, and Fig. 6 provides microstructure of the material.

Table 1 Chemical composition of developed steel

C	Si	Mn	P	S	Cr	Ti	B	Pb	Ceq
0.39	**0.50**	**0.60**	**<0.030**	**0.050**	**0.18**	**<0.08**	**Add.**	**–**	**0.57**

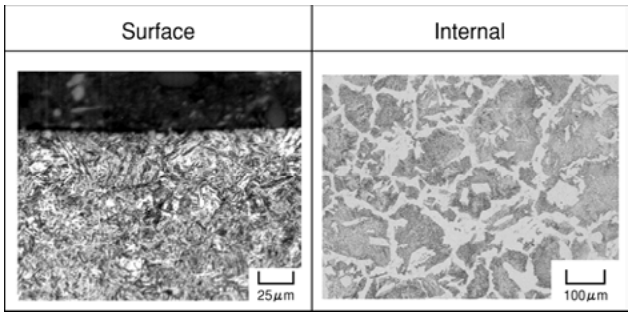


Fig. 6 Microstructure of crankshaft

4. Crankshaft Specifications

4.1. Approach to Crankshaft Strength

As shown in Fig. 7, crankshafts contain pins, journal fillets and lubrication supply openings (oil holes), which are important locations for considerations of strength. Fillets require extra strength to support the bending loads during operation, and oil holes require extra strength during support

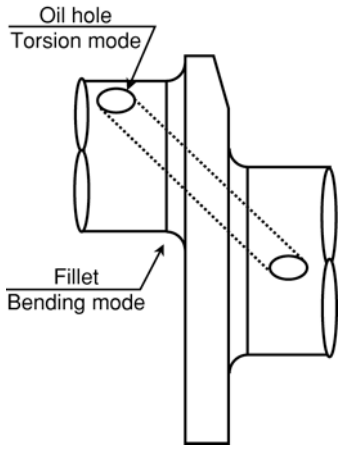


Fig. 7 Stress concentration point of crankshaft

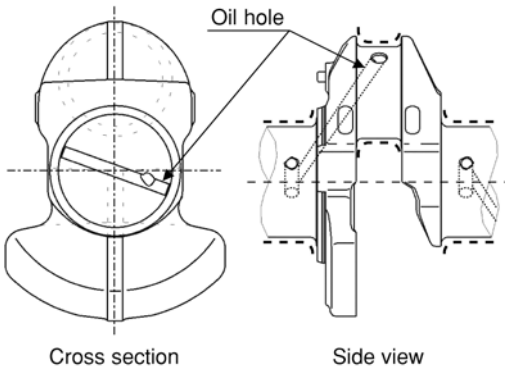


Fig. 8 Oil hole layout

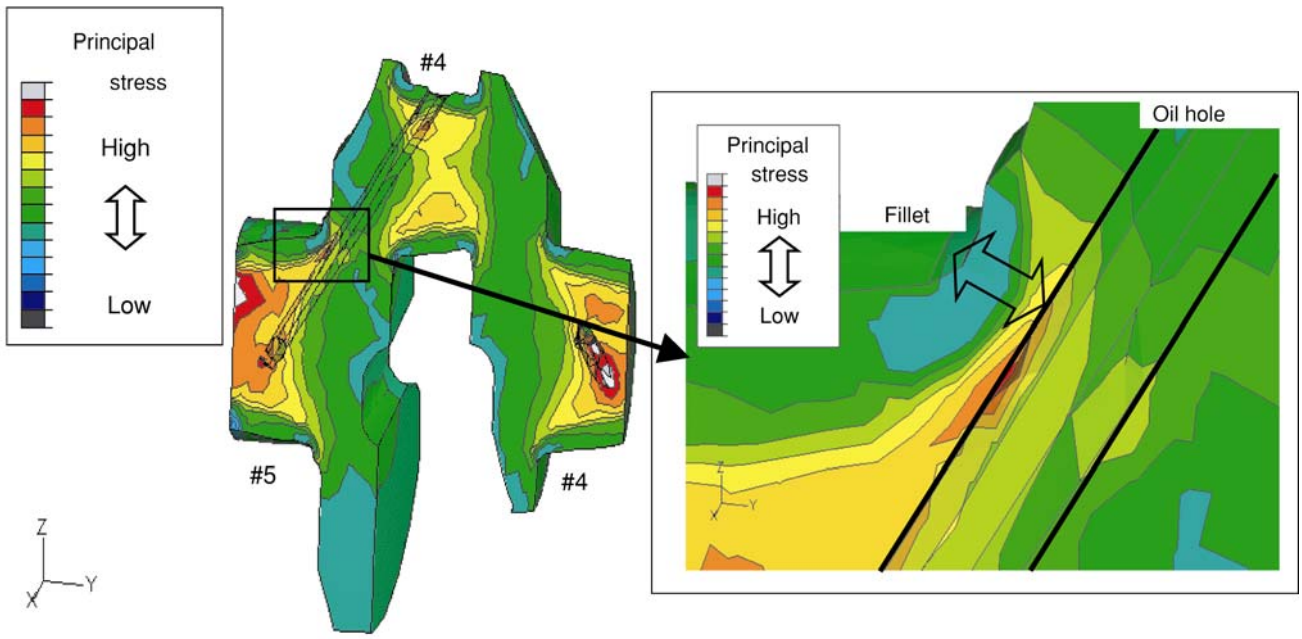


Fig. 9 Residual stress analysis around oil hole

of torsional loads.

It is known that high fatigue strength of a fillet can be obtained by increasing the effective depth of the hardened layer. Excessive depth means that excessive thermal energy is imparted to the crankshaft, however, which can cause it to bend or stretch. Therefore, an optimal depth of induction hardening was specified as appropriate for actual loads, in order to obtain an effective depth of the hardened layer with suitable fatigue strength. Residual stresses are also a key parameter for achieving fatigue strength. As shown in Fig. 2, the crankshaft under development is ground after the induction hardening in order to finish the shaft surfaces of reciprocating parts. Release of the residual stresses which evolved during induction hardening may occur due to the effect of the heat generated during the grinding process. Thus, the residual stress level was specified in order to meet a target fatigue strength after experimentally determining the relationship between fatigue strength and residual stresses.

The oil holes are close to the fillets, as shown in Fig. 8, so there is not much material thickness between them. Martensitic structures are created near the surface during induction hardening of the fillets, giving rise to residual compressive stresses. But the volume ratio accounted for by martensite drops with depth beneath the fillet, and the residual compressive stresses turn to tension. Voids like oil holes must be designed with caution, since they can become locations for initiation of cracking in a tensile stress field. Therefore it was determined to obtain the CAE-recommended optimal material thickness here. Figure 9 shows a contour diagram of the residual stress field from the oil hole design. Figure 10 presents a composite of these results and the relation between distance from the fillet, residual stress (σ_1) and the volumetric fraction of martensite (Ψ_M). It is visible that the further from the fillet, the lower the residual stress; the material thickness between the fillet and the oil hole was therefore set at 6.3 mm in order to keep the

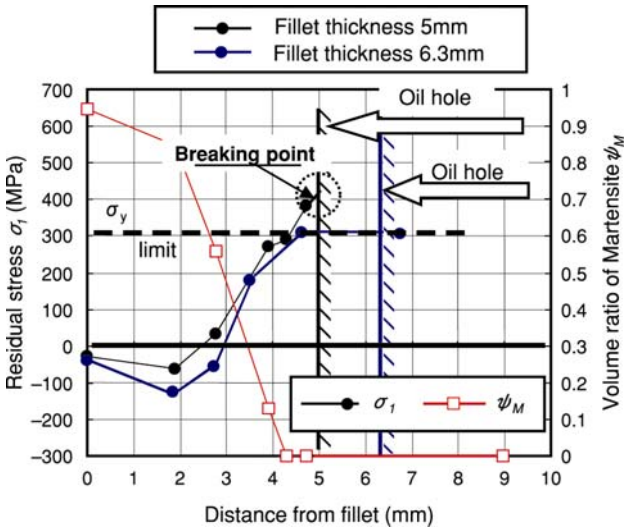


Fig. 10 Residual stress distribution around oil hole

stress lower than the material yield stress (σ_y). A test was also carried out in an actual crankshaft in order to verify that this had adequate fatigue strength.

4.2. Component Strength Characteristics

The specifications were set on the basis of the approach described above and the strength test results of components. Figure 11 displays a diagram of a crankshaft fillet fatigue test. The test employed actual crankshafts with altered effective depths of the hardened layer and residual stresses, and correlations between these parameters and fatigue strength were investigated. The relation between effective

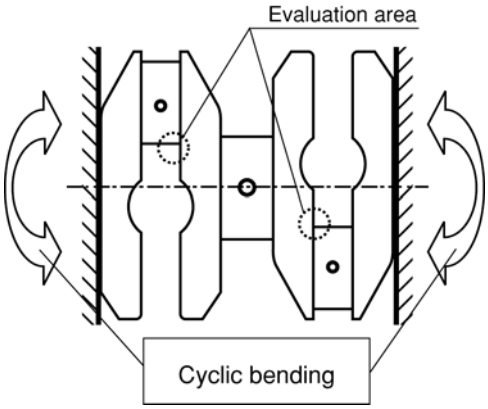


Fig. 11 Bending fatigue test for crankshaft

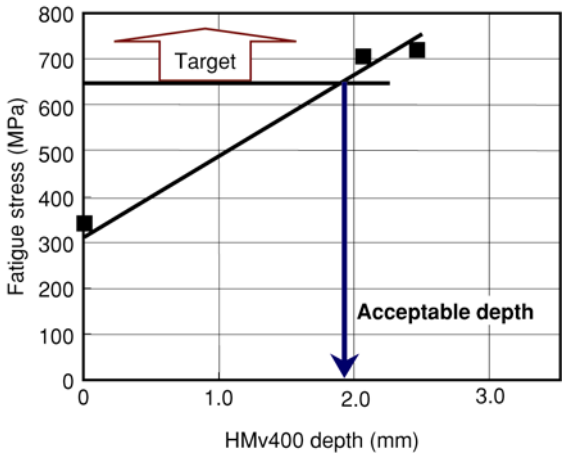


Fig. 12 Relation between depth of hardening and fatigue strength

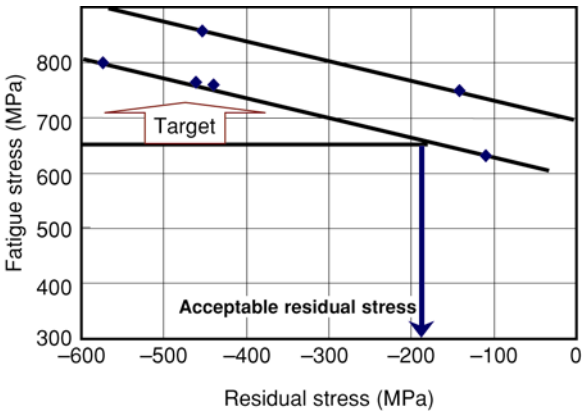


Fig. 13 Relation between residual stress and fatigue strength

depth of the hardened layer and 10^7 cycle fatigue limit is shown in Fig. 12 and that between residual stress and 10^7 cycle fatigue limit is shown in Fig. 13. This allowed setting of the effective depth of the hardened layer and residual stress level to obtain the target strength.

Figure 14 shows a diagram of a fatigue test for oil holes. Figure 15 provides the results from a torsional test of a crankshaft with the CAE-recommended thickness over fillets. The results presented here show that sufficient strengths were

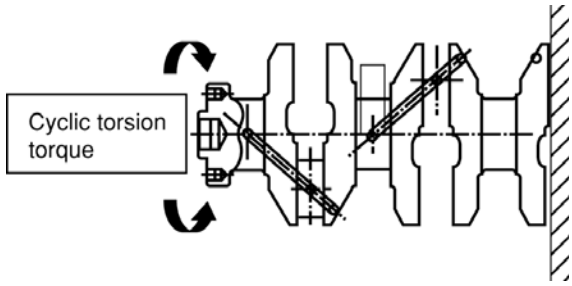


Fig. 14 Torsion fatigue test for crankshaft

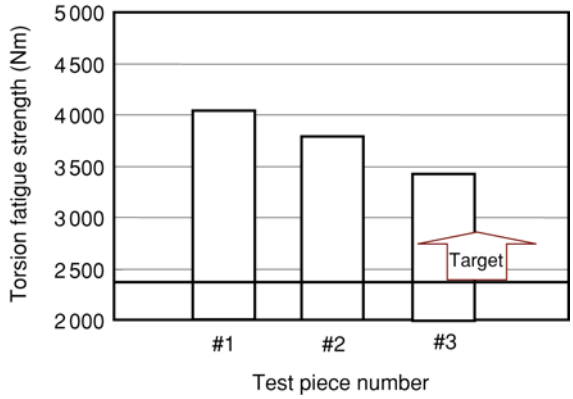


Fig. 15 Torsion fatigue test

obtained against the required strength.

4.3. Wear Resistance at Shaft-Metal Reciprocating Parts

Until the present, researchers have always relied on tests in actual engines to assess wear resistance at shaft-metal reciprocating parts, but this was a concern because it was not possible to make precise assessments of relations between material characteristics and wear. One of the goals of this development was to investigate unit testing methods allowing quantitative assessments. Figure 16 shows a schematic of a unit test apparatus. This apparatus would allow control of the lubricant temperature and sample cycle number. The lubricant contaminated by simulation equivalent to real diesel engine oil was used for the test. Figure 17 is a graph of the relation between test time at a given C concentration and

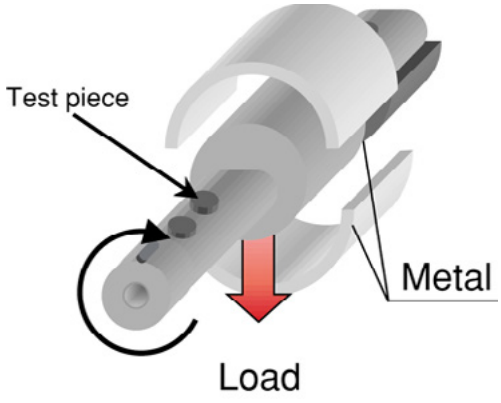


Fig. 16 Wear test of the shaft

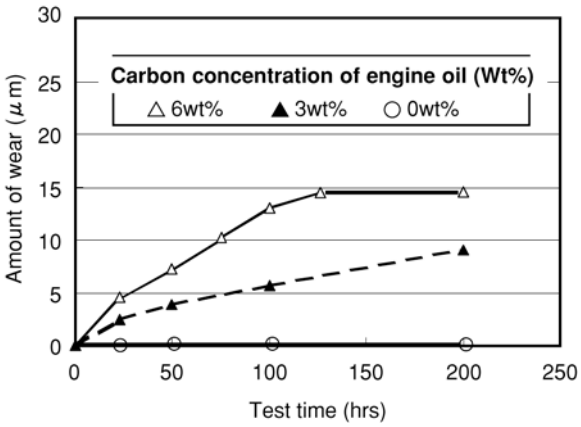


Fig. 17 Relation between test time and wear amount

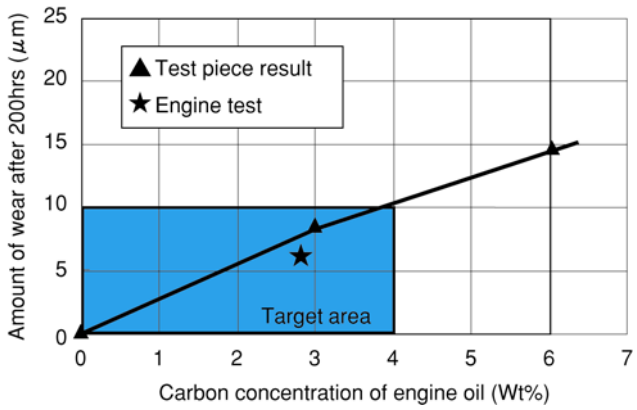


Fig. 18 Wear resistance test

amount of wear. Figure 18 summarizes some of the information in Fig. 17, the relation between carbon concentration in the oil and amount of wear after the 200-hour test. The result shows the amount of shaft wear in an actual engine is almost the same under the identical C concentration. This confirms that this unit evaluation method is valid for estimating the shaft wear in an actual engine in a very short time. This method allowed for the setting of the specifications for materials with superior wear resistance and for induction hardening.

5. Production Technologies

5.1. Correction of Shaft Distortion

The developed crankshaft is induction hardened at the fillets, so hardening-induced distortion was an issue. The following items were investigated as solutions:

1) Reducing bending distortion during induction hardening
2) Correction of bending distortion after induction hardening

For the first item, tests were carried out on control of hardening patterns on both sides of the fillet, the effect of the order of hardening of the pins and journals, and the characteristics of the distortion, using actual crankshafts. The conditions that resulted in the minimum distortion were selected. Next, the post-treatment correction of bending was investigated for the purpose of reducing axial runout. Generally, excessive correction applied to shafts after surface hardening processes like induction hardening can lower fatigue strength. Attempts at bending correction of components with too-high interior hardness will also fail to elicit adequate revision of the shape, because the high yield strength is not exceeded. The authors anticipated that this component would respond to correction, however, since the hardness of the developed material had been specified with the need for correction in mind. Bending correction was carried out on crankshafts and they were then tested for fatigue strength. Fig. 19 shows the observed relation between plastic strain and ratio to maintain fatigue strength. This allowed estimation of the limiting plastic strain for obtaining fatigue strength; the maximum allowed correction for the crankshaft was specified on this basis.

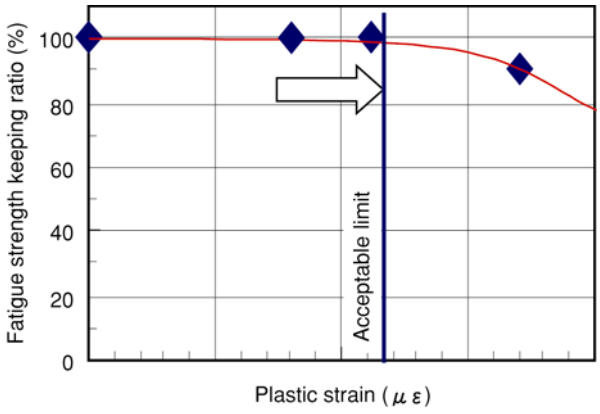


Fig. 19 Relation between plastic strain and fatigue strength

5.2. Machine Workability

As mentioned above, one of the goals of this development effort was to eliminate lead, a conventional additive to improve machinability. Because the crankshaft in this development represented the first application of lead-free material, the following issues were confirmed on the actual production line, and technical improvements were made to the processing conditions.

1) Tool slide parameters and RPM settings
2) Scrutiny of the tools used
3) Cutting oil parameters

Figure 20 shows the final results for miller tool life with relation to life in production of the current crankshaft. The lead-free crankshaft was adopted without sacrifice of current tool efficiency.

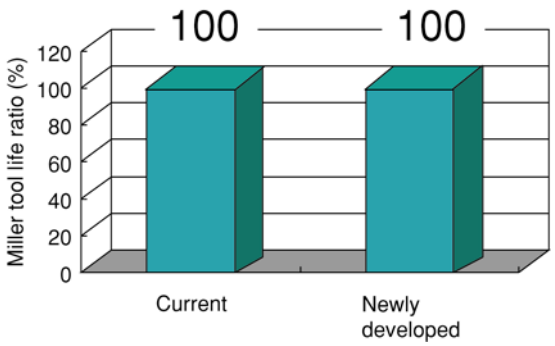


Fig. 20 Machinability result

6. Conclusion

As described above, an induction hardened crankshaft has been developed with superior strength and producibility.

(1) A material was developed which offers satisfactory workability, hardenability and correctability in shaft components.
(2) A lead-free steel was made possible by control of sulfide inclusions in the material.
(3) Optimized oil hole design specifications were established using CAE.
(4) By setting fillet hardening specifications, the roller burnishing process, which has been adopted for an induction hardened crankshaft in conventional passenger vehicles, was eliminated and the manufacturing process was simplified, while obtaining even higher strength.

This crankshaft is incorporated in the Accord with the Honda-developed diesel engine bound for sale in the European market this autumn.

Acknowledgements

The authors extend their deep appreciation to all the parties inside and outside Honda involved with this development project, especially those at Sumitomo Metals Kokura Ltd. and Sumitomo Metals Ltd.

References

(1) Iwama, N.: Trend of Special Steel for Automotive Parts, Journal of Society of Automotive Engineers of Japan, Vol. 55, No. 10, p. 64 (2001)

(2) Hamazaki, A., Kobayashi, Y.: Current State of SMI's Die Forged Products for Automobiles, SUMITOMO METALS, Vol. 48, No. 4, p. 49 (1996)

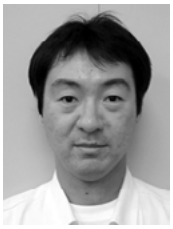
(3) Sato, T.: Micro-alloyed High-strength Steel, SUMITOMO METALS, Vol. 45, No. 4, p. 121 (1993)

(4) Kurita, M., Toyama, K.: Effects of Strengthening Mechanisms on Fatigue Properties of Ferrite Pearlite Hot-Rolled Sheet Steel, TETSU-TO-HAGANE, Vol. 80, No. 1, p. 66 (1994)

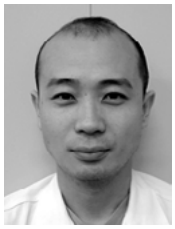
(5) Kurebayashi, Y., Nakamura, S.: A Case Hardening Steel, “ALFA Steel”, for Cold Forging, DENKI-SEIKO, Vol. 69, No.1, p. 57 (1998)

(6) Amataka, A., Suwa, S.: Development of Pb-free Free-cutting Steel Enabled to Omit Normalizing for Crankshafts, Honda R&D Technical Review, Vol. 14, No. 1, p. 141 (2002)

■ Authors ■


Hayato ONDA


Tetsuya ASAI


Kenji FUJIKI


Hirotsugu KUDO


Kazumasa MUROFUSHI

Development of 1 600 N/mm^2 Class High Strength Bolts

Mitsuo TAKASHIMA* Zenji IIDA*
Kentaro TAKADA* Seiji MORI*

ABSTRACT

Many different types of bolts are employed in automotive applications for a variety of different purposes and uses, and their strength generally ranges from 700 N/mm^2 to 1 200 N/mm^2. The current focus on increasing fuel economy to help reduce global warming has led to the idea to increase the strength of bolts and reduce their size in order to lower weight. However, increasing the tensile strength of conventional bolts increases the incidence of delayed fractures, and is therefore not suitable for mass-market vehicles. This project studied the use of high carbon steel rods, which are less susceptible to delayed fracture than conventional bolt materials, as a solution to this issue. The difficulty of heading when employing high carbon steel rods was solved by improving the material through the addition of the optimum amount of Cr, utilizing a new forming method in which the spindle is hardened during heading, and adopting a hexalobular shape with excellent formability. The application of these techniques made it possible to form bolts from high carbon steel rods, and has enabled the development of a 1 600 N/mm^2 class high-strength bolt. The new material and techniques have been used in the manufacture of the conrod bolts used in 2003 models, and have enabled the size of the bolts to be reduced from conventionally used M12 to M9, and the weight of an individual bolt to be reduced by 80 g.

1. Introduction

Nearly one thousand bolts are used in each automobile. In some parts such as the engine and the transmission, high strength bolts of material strength 1 200 N/mm^2 class are extensively used with the aim of achieving lightness/weight reduction in the automobile, and connecting rod bolts of 1 400 N/mm^2 class are also used. On the one hand, while automobile weight reduction has become an increasingly important issue, changing over to high strength bolts increases the probability of delayed fracture. Thus, the use of expensive materials like maraging steel, which is only applicable to special applications such as aerospace and racing, became a necessity, and their use in mass production vehicles such as automobiles was difficult. To resolve these issues, and considering the aspects of economy and quality, research was carried out for selecting the optimum material and manufacturing process, thus the development of 1 600 N/mm^2 class bolts began.

* Tochigi R&D Center

2. Raw-Material Settings

2.1 Lower-Priced Raw Material without Delayed Fracture

The authors investigated optimum materials without delayed fracture that can be deployed in mass production vehicles. Figure 1 shows the relationship between delayed fracture and strength of various kinds of iron and steel materials[(1)]. When the tensile strength of steel exceeds 1 200 N/mm^2, there is a tendency of reduction in the characteristics of delayed fractures. This tendency is particularly noticeable as the strength increases. There are broadly two kinds of material that satisfy the delayed fracture characteristics at this high strength level. The first kind is maraging steel, but this material is expensive and difficult to use considering the cost in mass production vehicles. The second kind is non-quenched and non-tempered high tensile strength steel wire. This non-quenched and non-tempered steel wire is less expensive and compared to quenched and tempered high strength steel of similar strength, the delayed fracture characteristics are better. Delayed fracture is caused by a crack that occurs when hydrogen in steel accumulates in the stress concentration part. It is reported[(2)] that the main reasons why high tensile strength steel wire is superior are the ability of the microstructure of the drawn wire due to cold drawing and the high-density dislocation to inhibit hydrogen diffusion and crack propagation. The use of 1 800 N/mm^2 class tensile strength steel wire in the main cable of Akashi Strait Bridge is a recent example of the application of high tensile strength steel wire. The authors focused their attention on developing a totally new non-quenched and non-tempered work hardened type material for bolts.

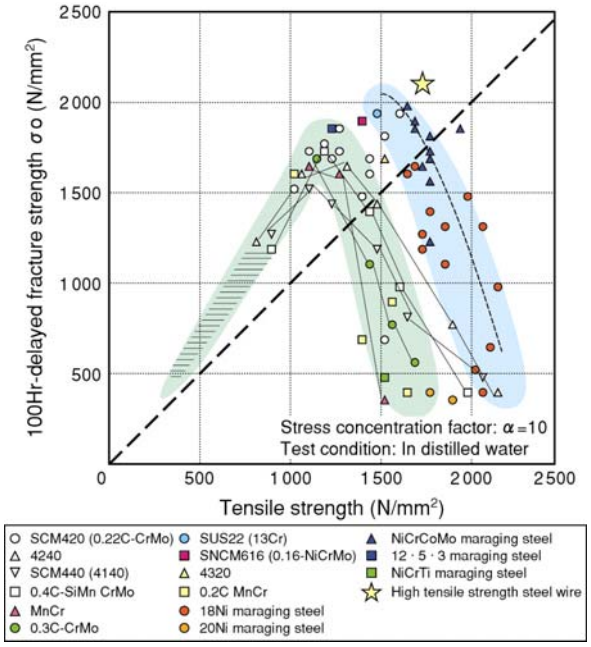


Fig. 1 Delayed fracture characteristics of various materials

2.2. Raw Materials – Issues

The high tensile strength steel wire is a high strength material that is less expensive and possesses excellent delayed fracture characteristics. However, since the strengthening method involves work hardening by drawing, as shown in Fig. 2, applications were limited to wires only. However, when forming the bolt using high tensile strength steel wire, a head section is required, and forming a head was considered to be extremely difficult. Head sections of bolts made of conventional materials were formed by reducing the hardness, such as by spheroidizing and annealing. Subsequently, the bolt was strengthened by quench and temper so that formability did not pose any concerns.

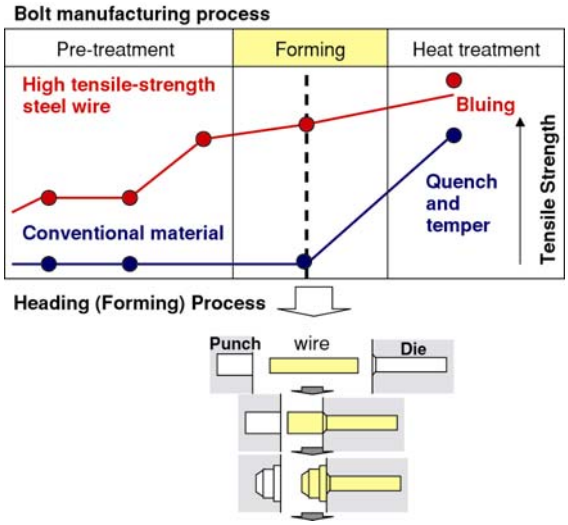


Fig. 2 Bolt manufacturing process

2.3. Material Improvement

Improvements were made at the raw material stage to strike a balance between high strength and formability of high tensile strength steel wires.

Normal high tensile strength steel wires consist of the C-Si-Mn composition, where Si and Mn are generally added to enhance strength. However, the value of reduction of area decreased in conventional strength improvement methods, resulting in degrading the formability of the head. Therefore, the focus was laid on Cr, which can balance strength and value of reduction in area, and a study of the components was carried out. While strength improvement by the addition of Si and Mn causes solid-solution hardening of ferrite in pearlite, the addition of Cr brings about reinforcement by grain refinement of the microstructure, thus enabling a balance to be achieved with formability improvement.

In order to determine the optimum Cr amount, Cr was added to normal high tensile strength steel wire (JIS-SWRS82B), as shown in Table 1, and the results were verified. Figures 3 and 4 show the amount of Cr added, the reduction of area, and the material structure. If Cr is added, the value of reduction of area improves up to 0.2% of the Cr amount and the strength is maintained, but when an amount exceeding this value is added, the effect is mitigated. As can be understood from the structure, Cr assists in the formation of the structure at low temperature by delaying the transformation from austenite to pearlite and also in the formation of a grain-refined structure. However, if an excessive amount is added, the transformation completion time is prolonged and the initially transformed cementite parts and spheroidizes as time elapses. Based on these results, the optimum amount of Cr to be added was fixed at 0.2%.

Table 1 Chemical composition

C	Si	Mn	P	S	Cr
0.80 ~ 0.85	0.12 ~ 0.32	0.60 ~ 0.90	≦0.025	≦0.025	0.20

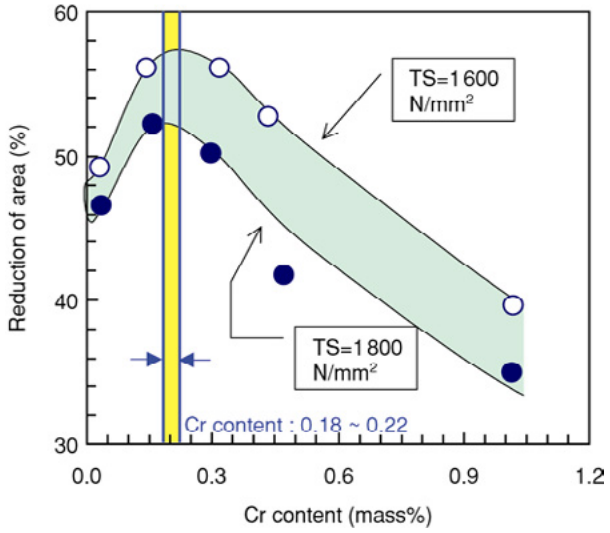


Fig. 3 Relationship between Cr content and reduction of area

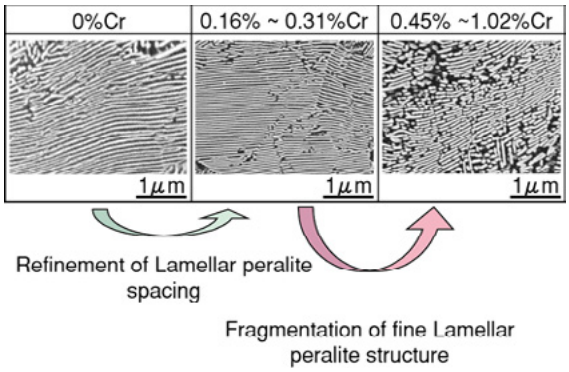


Fig. 4 Change of microstructure with changing Cr content

3. Applicability of New Formation Method

A study was conducted on the new formation method utilizing material characteristics.

3.1. Characteristics of Wire Drawn Material

Figure 5 shows the characteristics of the material when drawn to a wire. If this material is made to undergo plastic deformation in the tensile direction, the tensile strength improves and the compression yield point is lowered. This phenomenon is called the Bauschinger effect. Utilizing this effect, a new formation method for improving the bolt formability was established.

3.2. New Formation Method

An appropriately drawn wire beforehand was used for utilizing the Bauschinger effect. Figure 6 shows the newly developed formation method. The diameter of the wire loaded in the existing method and the shank diameter of the finished material are the same. When high tensile strength steel wire is used in this method, heading is difficult because the wire is very hard at the loading stage. Accordingly, the authors adopted a heading method in which a thick wire of low hardness level was used and the head was formed in the forming stage while work hardening the shank portion. Not only is the loaded wire of low hardness, but it is also close to

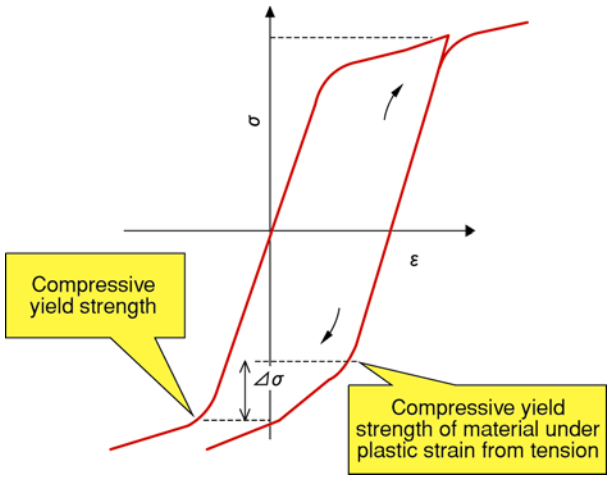


Fig. 5 Bauschinger effect

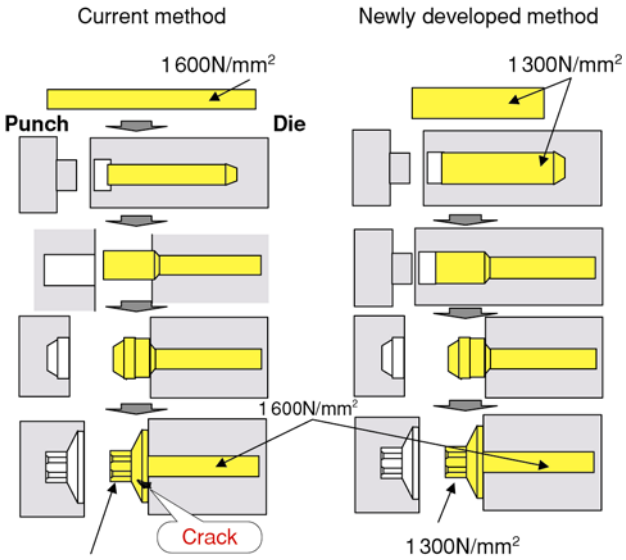


Fig. 6 Current method and newly developed method

the diameter of the completed head, therefore, the formation of the head by this method is easy. However, the strength guarantee of the head section needs to be considered when using this method. This is because the head section and the shank section have the same hardness in the conventional quenched and tempered materials, and in this case, a low hardness portion exists in a part of the head section.

3.3. Strength Guarantee for Head Section

Figure 7 shows the FEM analysis results for a tightened bolt for analyzing the strength of the head section. They are bolt stress distribution and bolt hardness distribution after heading, and its ratio. Hardness is directly proportional to strength; therefore, the value obtained by dividing the hardness distribution by stress distribution represents the strength margin of every section. Values of each section are shown assuming the value of the shank section as 1. As observed above, the value of the head section is greater than 1 over the entire range, and the minimum value occurs in the shank section. This indicates that the weakest part is the shank section and not the head section. It was confirmed from actual tensile tests that the fractured location is in the shank section (threaded part), similar to that of conventional bolts.

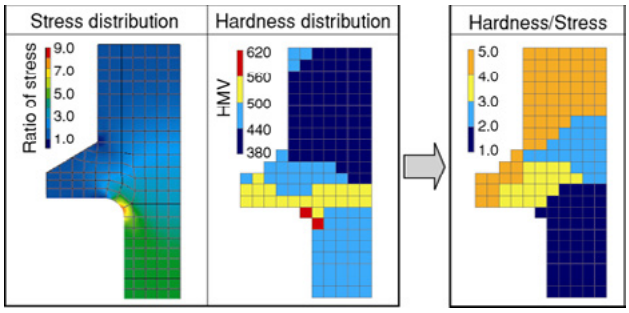


Fig. 7 Stress and hardness distribution in bolt

3.4. Reduction Rate

If the new formation method is used by making use of the Bauschinger effect, reduction in area occurs as the wire is drawn from the initial stage. However, the reduction in thickness of the solid lubricant coating used for improving the formability may become a concern, and it must be studied. Figure 8 shows the relationship between the residual amount of solid lubricant coating and the reduction rate of drawn wire. This solid lubricant coating is used with the aim of improving the formability in the heading process after lead patenting, and its thickness decreases with the reduction in area. Accordingly, a reduction rate of 20-25% was set after drawing, as the optimum value that strikes a good balance between the reduction in coating thickness due to the reduction in area during the drawing and heading processes, and the Bauschinger effect.

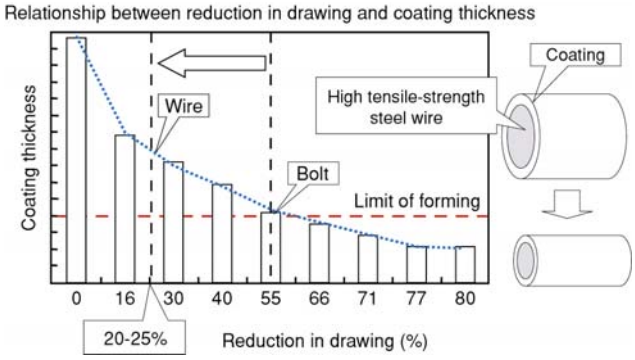


Fig. 8 Relationship and reduction of area in drawing and amount of lubricant adhering

4. Improvement of Formability in Shape

4.1. Shape of the Head

Normally the bolt head shape is hexagonal, as shown in Fig. 9. However, packing the raw material in the six corners for forming a hexagonal shape from a round bar requires a large reduction ratio, and in the case of high tensile strength steel wire, the header properties degrade excessively. Therefore, as shown in Fig. 10, the hexalobular shape was used that can be formed from a round bar with little processing. Since the completed hexalobular shape is comparatively closer to the round shape, the reduction ratio of the raw material is small, and forming is simpler. We have made improvements to further enhance the formability of the hexalobular shape. As shown in Fig. 11, a part of the convex portion of the hexalobular shape was ground off and the

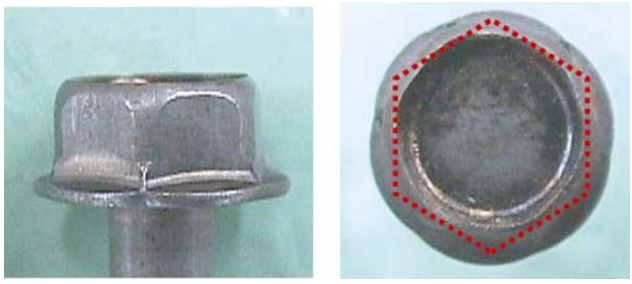


Fig. 9 Hexagon

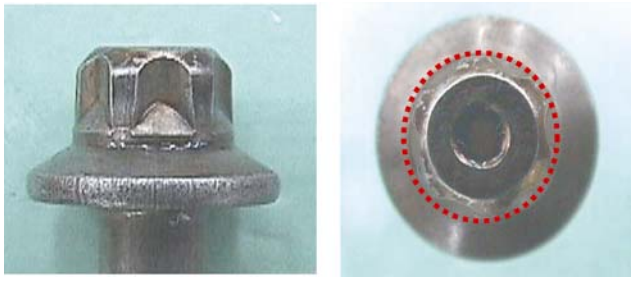


Fig. 10 Hexalobe

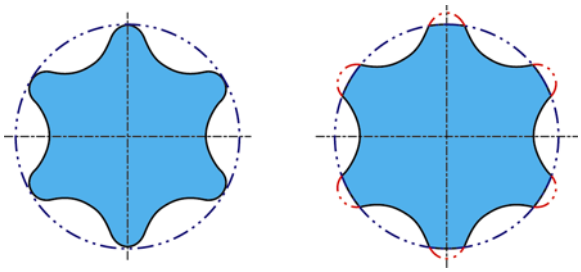


Fig. 11 Improved hexalobe

difference in height between the concave and convex portions was reduced. This resulted in the completed shape coming closer to the rounded shape, which resulted in a smaller reduction ratio, and contributed to improving the formability. However, grinding off a part of the convex portion is likely to reduce the limiting value of the tightening torque. To avoid this, a part of the convex portion was ground off from a hexalobular shape that was one size larger. Even though the contact area is less, the radius is large and therefore, it is likely that a large torque equivalent to that of the conventional shape can be applied. Moreover, by using a tool that is one size larger, off-the-shelf products can be used.

Figure 12 shows the torque values that can be transmitted by the improved hexalobular shape and hexagonal shape with the same outer shape. Compared to the hexagonal shape, the hexalobular shape can transmit larger torques with smaller dimensions. Based on these observations, it can be said that the hexalobular shape does not only improve the header properties but also has superior properties from the point of view of torque transmission and weight savings in the head section. This is a very satisfactory situation that contributes to weight savings and size reduction, and fulfils the aim of this study. The shank section of the bolt could be reduced in size by providing higher strength material, and furthermore, the head shape could also be set to have the minimum weight for the required tightening torque.

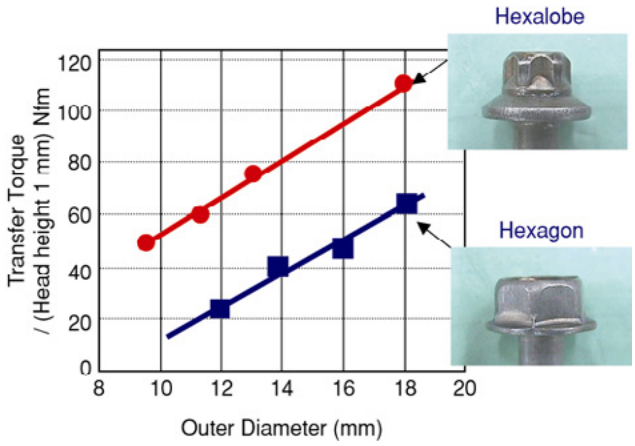


Fig. 12 Impact of hexalobular heads on weight reduction

4.2. Improvement in Rollability

After the heading threading may also be performed by roll forming, in which cold forging is used, but an improvement in formability was necessary for this process also. As shown in Figure 13, formability was improved by increasing R, the radius at the thread root, and reducing the thread height. Increasing R, the radius of the root, helps to improve the fatigue strength of the thread, and this specification is therefore used for threads of bolts used in the fields of aeronautics and space aviation. The improvement in fatigue strength of the 1 600 N/mm^2 bolt was verified, as shown in Fig. 14. There was a 9% improvement in the fatigue strength under the condition of 80% of average stress (tension in case of bolts) at 0.2% yield.

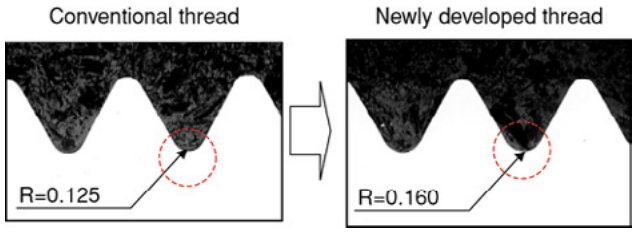


Fig. 13 Increasing the radius at the thread

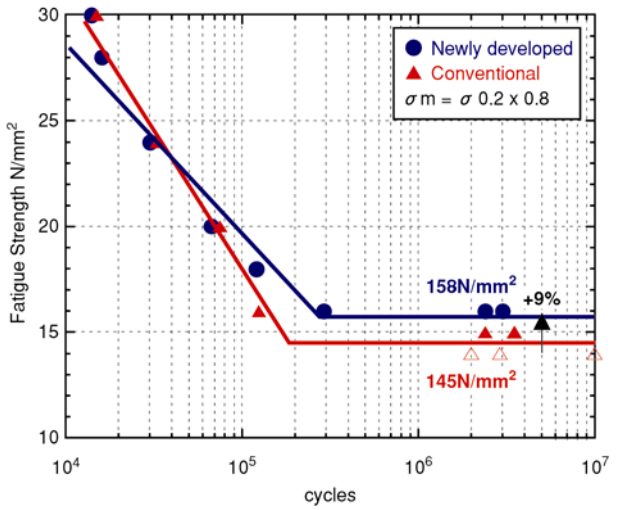


Fig. 14 Fatigue strength of newly developed bolt

Moreover, when this technology is used, the contact areas of the male and female threads become a little bit smaller. As in the connecting rod, there is no buckling in the contact area of the female thread of the steel bolt. However, when aluminum is used, it does affect the buckling of the surface but it is possible to cope with this by extending the engaging length.

5. Coping with Stress Relaxation

It is well known that stress relaxation occurs when non-quenched and non-tempered material like high tensile strength steel wire is used in a high temperature environment, and in the case of automobiles, it is applicable to the engine or the transmission. Figure 15 shows the relationship between initial bolt tension and residual bolt tension when the temperature is maintained at 140 °C, equivalent to that of the engine environment. From this, we can understand that high tensile strength steel wire if used near the material strength limit has large stress relaxation due to heat compared to quenched and tempered material. If used as is, then the concern of reduction in tension occurs. Moreover, as mentioned earlier, the quenched and tempered material being compared, may be subjected to delayed fracture in the high stress region. Therefore, the results of these tests only reflect stress relaxation and ignore the delayed fracture of quenched and tempered material.

The dislocation introduced during the wire drawing process is activated by the rise in temperature, shifts under the influence of the stress field, and as a result, deforms. This is the cause of the stress relaxation in the high tensile strength steel wire. Accordingly, we studied how to introduce the Cottrell atmosphere, which is formed by giving thermal energy to the mobile dislocations and thus activating light elements like C, N, to penetrate the unstable parts of the dislocation and make it a sessile dislocation. By maintaining the temperature at 200-300 °C so that C, N are sufficiently diffused in order to introduce the Cottrell atmosphere, characteristics equivalent to quenched and tempered material were obtained, as shown in Fig. 15.

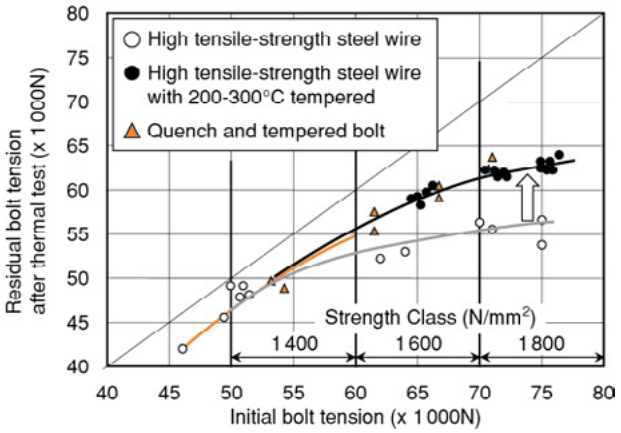


Fig. 15 Relationship between initial bolt tension and residual bolt tension

6. Application Results

Figure 16 shows the comparison of bolts manufactured using this technology and actual examples of bolts manufactured using the existing materials. The thread size of

the connecting rod bolts was reduced from M12, when using the existing materials, to M9. As a result, the weight of an individual bolt in each connecting rod was reduced by 80 g, and when the connecting rod was included, the weight was reduced by 240 g per unit. The outer dimensions of the big end could also be reduced from 88 mm to 81 mm.

This reduction in weight also extended to the complete engine, and the results are shown in Fig. 17. The layout shown in red lines is the design using conventional technology, while the layout in blue lines show the design using the newly developed technology. The specifications of the dimensions shown by the blue lines are the same as those of the mass production engine. The results obtained using the new technology show a significant improvement in the output even though the basic framework of a conventional engine has remained unchanged.

The weight reduction effect when all the vehicle's bolts were substituted by bolts using the new technology was investigated. When the bolt size was reduced to achieve tension equivalent to the strength and size of the conventional bolt, a reduction in weight in the bolts alone of about 7-8 kg/vehicle was achieved. Furthermore, if the reduction in weight of peripheral parts such as connecting rods is also considered, then further savings in weight can be anticipated.

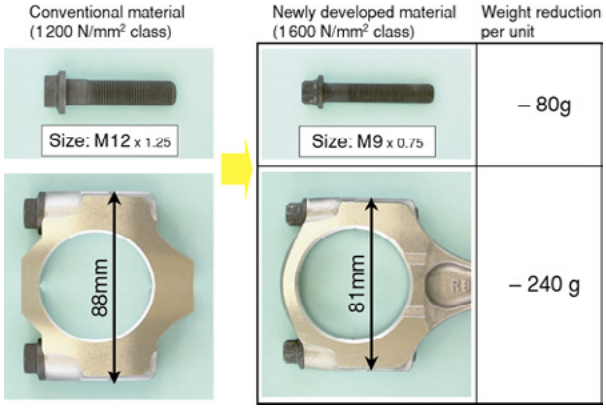


Fig. 16 Application for connecting rod bolt

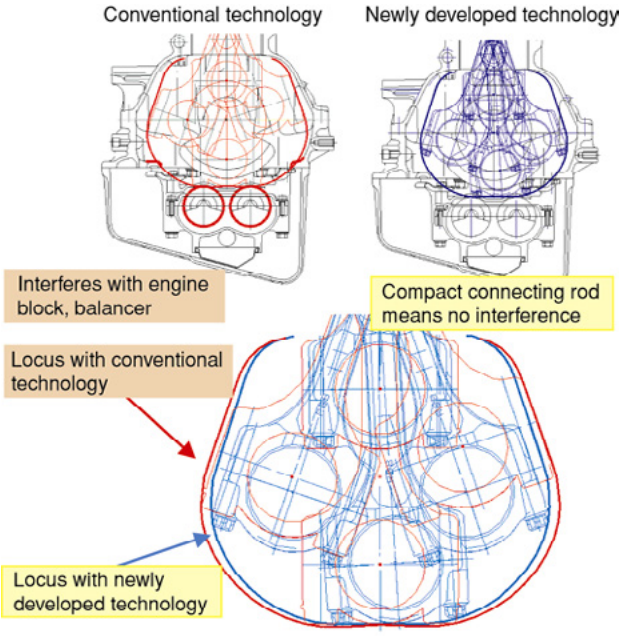


Fig. 17 New engine with newly developed connecting rod bolt

7. Conclusion

High tensile strength steel wire, considered to be unsuitable for formation of bolts by conventional methods was studied, and formability of the bolts was improved as given below, with the aim of developing bolts of the 1 600 N/mm^2 class.

(1) The optimum Cr addition amount for the high tensile strength steel wire was set at 0.2% to improve the value of reduction in area.
(2) A method to form the head section from low hardness, large-diameter wire while work hardening it, was used.
(3) The optimum reduction rate was taken as 20-25% for balancing the Bauschinger effect and residual solid lubricant amount.
(4) The hexalobular shape was used in the head section considering the ease in formability and weight savings this shape offers.

Finally, the optimum bluing conditions were set as measures against relaxation specific to non-quenched and non-hardened materials.

In view of the above-mentioned points, it was possible to mass-produce 1 600 N/mm^2 class bolts with superior delayed fracture characteristics for the first time in the world.

Acknowledgements

We are deeply grateful to the staff of Saga Tekkosho, who worked tirelessly to manufacture the bolts, and to the staff of Kobe Steel, Ltd., who studied improvements to the materials and assisted us in our development work.

References

(1) Matsuyama, S.: Okurehakai, Nikkan Kogyo Shinbun

(2) Takai, K.: Hydrogen Trapping Behavior and Delayed Fracture of Cold -Drawn Pearlite Steel, Materia Japan, Vol. 39, No. 3, p. 239-242 (2000)

■ Authors ■


Mitsuo TAKASHIMA


Zenji IIDA


Kentaro TAKADA


Seiji MORI

Development of Plastic Organ-type Accelerator Pedal Assembly

Tomohiro SAKURABA* Hideto NEBUYA*
Teruo KATOH** Tomoaki ABE**

ABSTRACT

An organ-type pedal attached to the floor by a pivot has been developed to increase the comfort of accelerator pedals. The trace of the new pedal is in the same phase as the motion of the sole of the human foot.

A plastic hinge structure has been adopted for the pivot. Tests on a plastic hinge structure were conducted. Results showed that polyester elastomer possessed superior fatigue resistance, therefore, this was selected as the hinge material. The newly developed thin hinge has enabled the new pedal to equal conventional pedal structures in strength and durability. The hinge section was immersed in oil, grease and other chemical agents to test durability, and results showed no change in physical properties.

The connection of the pedal to the floor was also altered. The flexibility of the material has enabled snap-fit assembly, and the connection is strong enough to resist an extraction load of over 900 N.

1. Introduction

The overhung accelerator pedal shown in Fig. 1 is the conventional design among accelerator pedals for passenger vehicles.

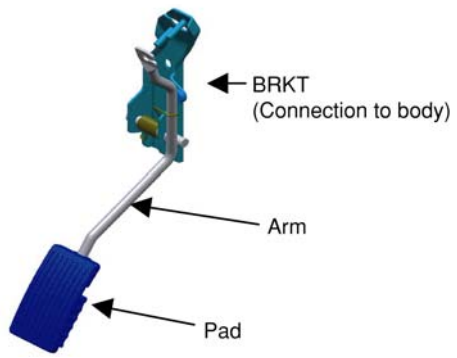


Fig. 1 Conventional accelerator pedal assembly

The overhung accelerator pedal consists of a bracket attached to the vehicle body above the pedal, a metal arm, and a pad. This structure is widely used because it is simple, requires few parts, and is cost efficient.

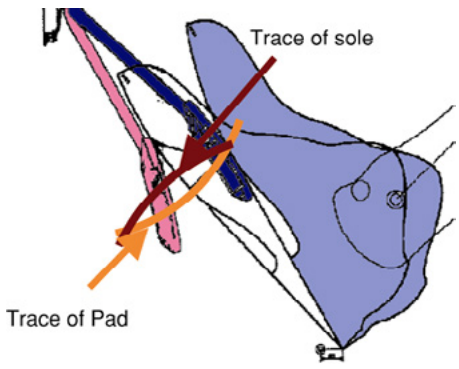


Fig. 2 Trace of conventional accelerator panel

* Tochigi R&D Center
** F. tech Co., Ltd.

The issue with this pedal is that the arc, which the pad follows (Fig. 2, Trace of Pad), is different from the arc of the sole of the driver's foot (Fig. 2, Trace of Sole). This makes it more difficult to provide a good feel to the pedal during operation.

Matching the trace of the pad to the trace of the sole is essential for improving the feel of the overhung accelerator pedal. For example, a comfortable feel is possible with an organ-type pedal because the pedal is fixed on the floor while the bottom of the pad is pivoted so as to move. If the pad on an overhung accelerator pedal were simply extended and attached to the floor, this would interfere with the operation of the pedal. Therefore, we investigated an organ-type pedal structure, using as many of the existing components of the conventional overhung-type as possible for component reliability. As shown in Fig. 3, the new structure was proposed in which the pad of the overhung-type was extended downward and connected to the floor with a pivot, and a hinge was provided with the pivot to make it movable. This paper describes a newly developed plastic accelerator pedal that has a mounting structure integral with the floor.

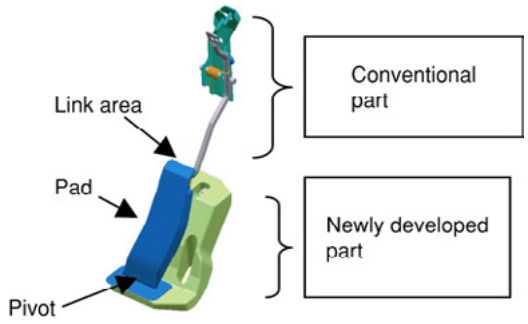


Fig. 3 Accelerator pedal assembly

2. Technical Elements of Development

Figure 4 shows details of each component of the pedal displayed in Fig. 3. The plastic pad was fixed to the floor and the hinge area was designed so that the entire pad is movable, enabling the traces of the sole and pad to be identical. There is still divergence between the trace of the arm of the conventional structure and the trace of the pad; this is accommodated by the link mechanism. In addition, the mounting structure of the hinge area must be firmly attached to the floor in order to support the movement of the entire pad.

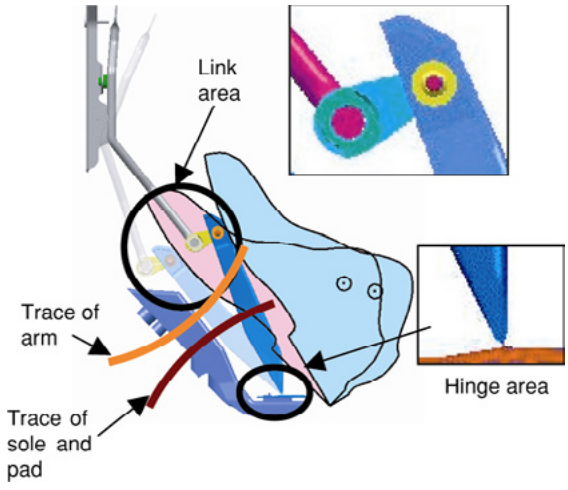


Fig. 4 View of hinge pivot and link area

The following technical elements were developed in order to realize this structure:

(1) Specifications and durability of the plastic hinge
(2) Vehicle mounting structure
- Establishment of the mounting structure on the floor
- Establishment of the link structure to absorb discrepancy with arm motion

3. Specifications and Durability of the Plastic Hinge

The plastic hinge structure for the new accelerator pad requires both tolerance of fatigue due to the repeated motion and adequate strength against operating forces.

Optimal materials and component shapes to satisfy these requirements were investigated. For material selection, it was decided to use test pieces as shown in Fig. 5. The test piece was flat and featured a hinge section in the center, as shown in Detail C. The basic thickness of the piece was 1.0 mm, but the hinge section was 0.5 mm thick.

Two types of polypropylene (PP-B and PP-C) were selected for the plastic material because these are reported to offer superior qualities for hinge function[1]. Two types of polyester elastomer were also selected because these

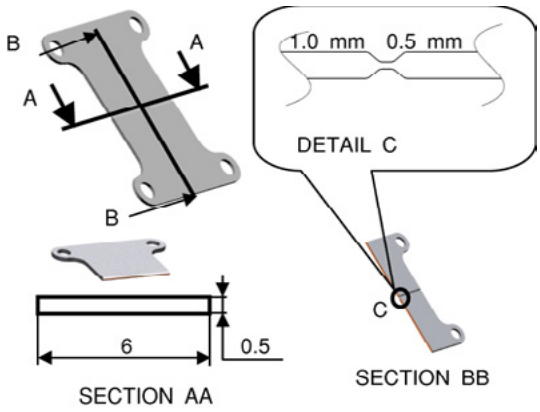


Fig. 5 Test piece

Table 1 Material property

Item	Unit	Material				
		PP			Polyester	
		A	B	C	D	E
Tensile strength	MPa	19	20	21.5	7.8	14.2
Elongation	%	150	350	>500	610	390
Flexural modulus	MPa	1 370	1 320	1 080	70.6	210
Izod Impact	J/m	88	98	196	NB	NB
MI	–	15	9	3	8	8

possessed elongations above the target value of 300%. Finally for comparison, PP-A, a material with an elongation of 150% was also selected for a total of 5 materials tested. Table 1 presents the representative properties for each of these.

3.1. Fatigue Test

The durability test was carried out as follows. A test apparatus was built that subjected only the hinge section of each test piece to motion in order to evaluate the durability under conditions matching actual use. Figure 6 shows the principle of operation of the apparatus. The upper edge of the hinge test piece was fixed, and the lower edge was connected to an arm that moved so as to flex the hinge. The structure allowed adjustments of various rotation angles. Figure 7 shows the entire test equipment. The gate-shaped upper fixture and the mobile arm of the lower section are plainly visible. Specimens shaped as shown in Fig. 5 were tested in cold and hot environments, at temperatures from –30 °C to +80 °C. The superiority of the material was assessed by the percentage of retained tensile strength after testing. The retained tensile strength was measured after 3 million cycles at each rotation angle and at different cycle numbers up to 3 million cycles under a constant rotation angle of 45°.

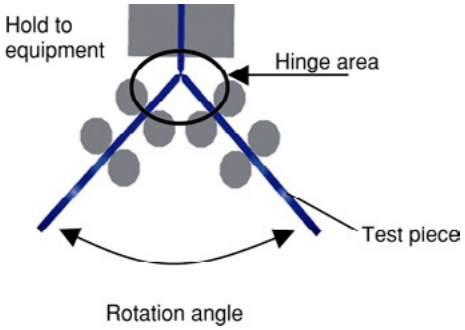


Fig. 6 Schematic of durability test



Fig. 7 Test equipment

Figures 8 and 9 show the retention rate of tensile strength after a 3 million cycles durability. Figure 10 shows the retention rate of tensile strength after the various cycle numbers at the rotation angle of 45°.

The results in Figs. 8 and 9 indicate a dependence of the decrease in retained tensile strength on rotation angle in both PP and polyester elastomers. The greater the rotation angle, the greater the degradation in strength. Comparison of the A, B and C types of PP in Fig. 8 showed that hinge performance in durability was affected by material elongation; the type with elongation below 300% showed a sharp degradation in the 45° rotation region. The polyester elastomers had superior

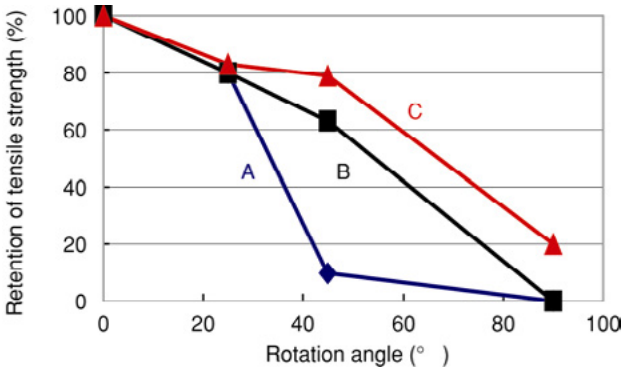


Fig. 8 Retention of tensile strength after durability test (PP)

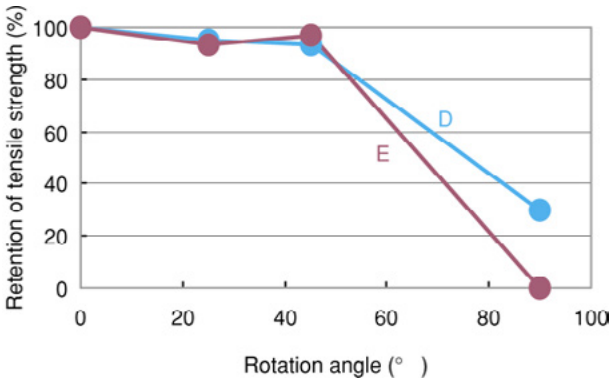


Fig. 9 Retention of tensile strength after durability test (Polyester)

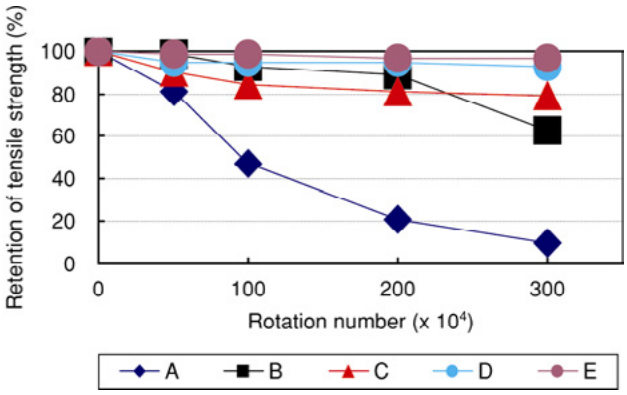


Fig. 10 Retention of tensile strength after durability test (for each rotation number)

fatigue properties; both materials D and E showed almost no degradation in tensile strength after the durability test at angles of 45° or below. The results in Fig. 10 for each rotation number show that the PP demonstrated gradual reductions in retained tensile strength after 500,000 cycles, while polyester elastomers demonstrated almost no such reductions through 3 million cycles.

According to the layout, the operating rotation angle in the actual pedal hinge will be less than 45°; therefore, it was decided to use the polyester elastomers, which demonstrated no strength degradation after a durability test at this operation rotation angle.

3.2. Strength Tests

The superiority of polyester elastomers was verified by the fatigue tests. Test pieces shaped as shown in Fig. 5 were subjected to three further strength tests in order to identify the best hinge shapes and materials. Two types of hinge shape were tested: Type 1, a piece with a straight part at a thin hinge section in order to reduce the stress concentration; Type 2, a piece with a thin hinge section.

(1) Tensile strength test
Input load is applied to the entire hinge
(2) Shear load test
Input load is applied at the tip of the hinge
(3) Torsion torque test
Input torsion load is applied about the axis at the center of the hinge.

The test methods and results are shown in Figs. 11, 12 and 13. The results of the strength tests for shape showed that the initial strength of Type 1 was higher for all three tests within the same material.

Within the same shape, there was a dependence of strength on material tensile strength; polyester elastomer E proved superior.

From the above results, polyester elastomer E was chosen as the hinge material, and Type 1 was chosen as the hinge shape. For good hinge function, the thin section was designed at 0.5 mm thickness, and the length of the straight part was set at 1.0 mm in order to prevent stress from concentrating on the hinge section.

3.3. Chemical Resistance

The following tests for chemical resistance were carried out on polyester elastomer E, which had shown superior fatigue durability and strength performance.

The elastomer was soaked for 72 hours in six chemicals including oil, grease and gasoline to which it could commonly be exposed to in everyday use, and the physical property change was re-checked.

The fraction of retained strength in tensile loading was used as the parameter for physical property change. The results are shown in Fig. 14.

Retained strength was over 90% for all chemicals. It was verified that polyester elastomer E had nearly no degradation in physical properties.

4. Structure for Mounting on Body

4.1. Establishment of Mounting Structure on Floor

The pad in the organ pedal must be connected to the floor mount, in contrast to the requirements of the conventional structure.

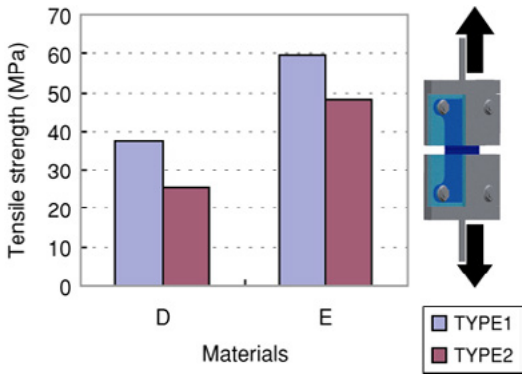


Fig. 11 Results of tensile strength test

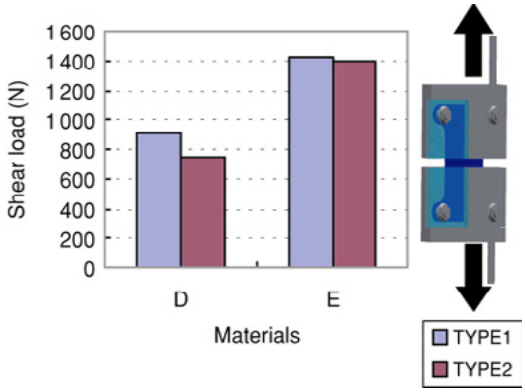


Fig. 12 Results of shear load test

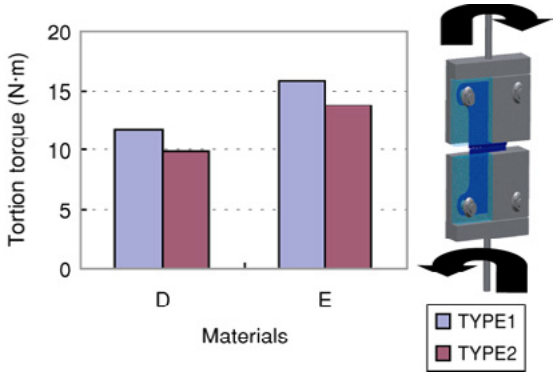


Fig. 13 Results of torsion torque test

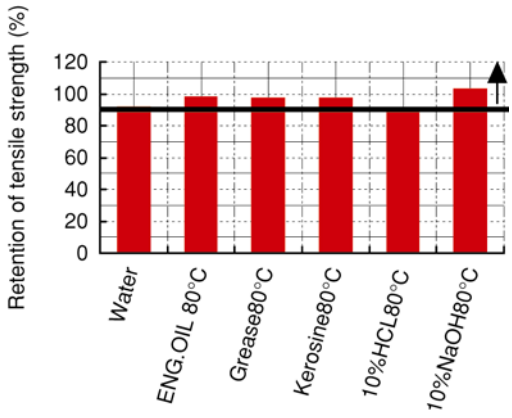


Fig. 14 Results of chemical resistance test

Figure 15 shows each part of the connecting section of push-in snap-fit construction that was considered to be convenient to use between the pad and the stopper on the floor mount.

The snap-fit construction satisfies several requirements: ease of assembly (assembly with a single hand motion), strength (difficulty of accidental disassembly) and ease of maintenance (easy removal). An integral back-plate was designed on the stopper to fix the pawls on the pad. The back-plate is shown in Fig. 16(a).

During attachment, the back-plate is pushed down, while the pawls of the pad are inserted into the stopper, as shown in Fig. 16(b). The back-plate flexes to allow the pawls to enter the inside of the stopper, as shown in Fig. 16(c).

Once the pawls have been pushed in all the way and opened, the back-plate springs back upward, as shown in Fig.16 (d), being clipped by the pawls. If an extraction load is exerted on the pad, the pawls would have to flex inward so as to exit, but the back-plate inside the pawls prevents them from flexing inward. This provided toughness to the mechanism against disassembly; it resisted a load of over 900 N. On the other hand, it is easy to disassemble the mechanism for maintenance by inserting a tool or other object to depress the back-plate. This eases maintenance tasks. The extraction load on the pads and stopper was measured after 100 repetitions of assembly and disassembly; it was at a level similar to that during initial assembly.

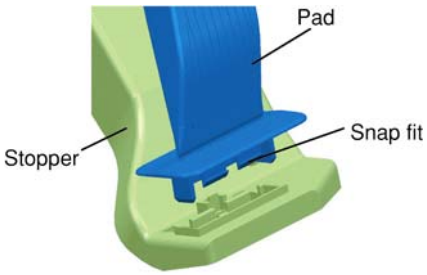


Fig. 15 Snap fit connection

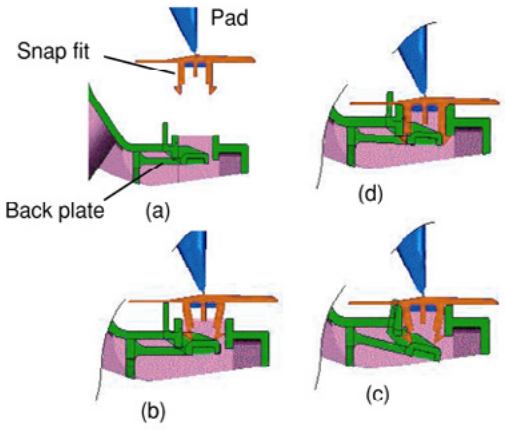


Fig. 16 Snap fit mechanism

4.2. Establishment of Link Structure to Absorb Discrepancy with Arm Motion

Figure 17 shows a detailed drawing of the link installed between the upper structural components from the previous structure and the organ-type pad. The link-arm is allowed to pivot about the shaft and is held in place with the push-nut. Figure 18 shows operating positions of the link-arm and the pad when the pad moves by being pushed with the foot. The cross angle of the link arm and pad changes due to the differences in traces of the arm and the pad, but the link-arm operates smoothly, as it is supported via two points, the pivot of the pad and the pivot of the arm.

Section A-A from Fig. 17 is shown in Fig.19. Spherical shape bearings were selected in order to absorb variations in parallelism, and a sliding link structure was used to absorb scatter in components and assembly.

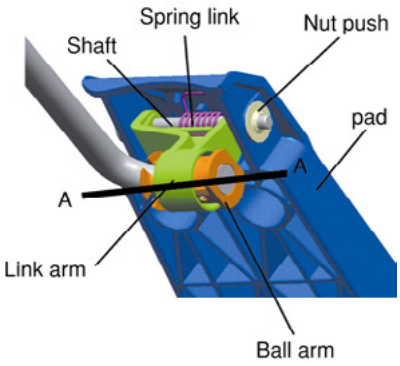


Fig. 17 Link area

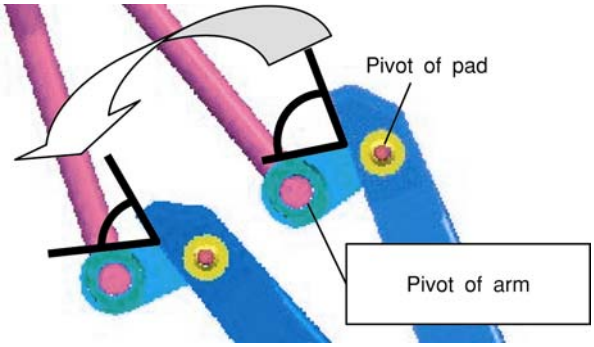


Fig. 18 Mechanism of link section

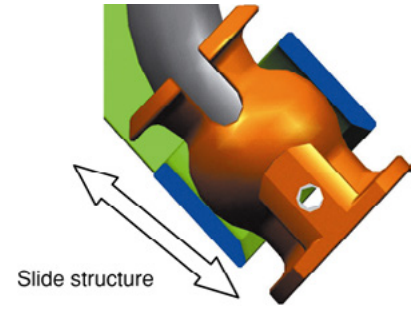


Fig. 19 Linkage of link arm and ball arm

5. Results for Operating Feel in Actual Vehicle

The operating feel in an actual vehicle of the plastic organ-type accelerator pedal developed in this project was investigated.

Figure 20 shows the relation between pedal stroke and operating load. In the overhung pedal, there is a non-linear increase in operating load with pedal stroke; as a result, there tends to be a heavy feeling against the sole of the foot in the latter part of the stroke. In the organ-type pad, however, the increase of operating load is linear with pedal stroke.

There was also an improved, firm feel to the organ-type pedal. This is attributed to the greater width at the bottom of the tapered organ-type pedal, as shown in Fig.21. The fact that the pad is connected to the floor at the bottom also may contribute to this because this structure restrains the movement of the lower part of the pad.

Tests in actual vehicles confirmed that the organ-type accelerator pedal provides an improved operating feel.

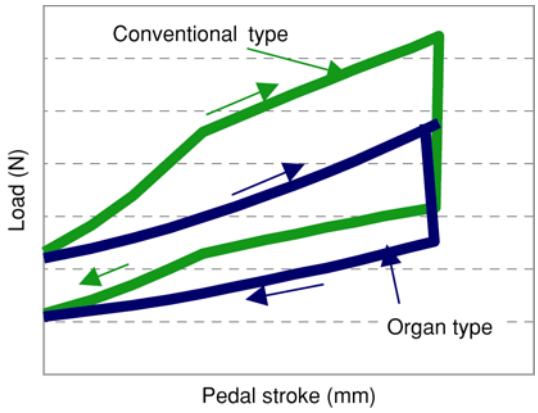


Fig. 20 Comparison of feel of load



Fig. 21 Pad shape

6. Conclusion

We developed the organ-type accelerator pedal which offers durability and reliability at a level equal to that in accelerator pedals of conventional construction and provides a good operating feel because its arc matches the arc of the sole of the foot. The technical elements of this development are mentioned as follows.

(1) Methods for evaluating the materials and structures of the plastic hinge mechanism were conceived and showed that both polypropylene and polyester elastomers demonstrated degradations in durability at rotation angles of over 45°. These were particularly marked in PP.
(2) Materials with elongations of over 300% are suited for hinge mechanisms operating at angles of 45° or lower. Polyester elastomers have superior fatigue properties.
(3) A durable and high-strength organ-type pedal was developed by combining the hinge structure of the polyester elastomer. The structure is provided with a straight part at the hinge to avoid stress concentrations.
(4) A strength of over 900 N was obtained in the structure of the joint where the pedal is attached to the floor by designing a snap-fit, which exploited the potential of soft material, resulting in a structure offering easy assembly and easy handling during maintenance.
(5) The design and acceptance of the link structure, which allowed use of components of the conventional accelerator pedal, enabled mounting of the organ-type pedal on a car body.

Acknowledgements

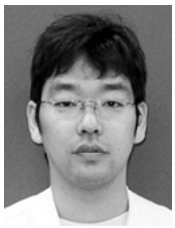
The authors extend their deepest thanks to the personnel of F. tech and all related parties who cooperated in this project.

Reference

(1) Plastic Processing Technology Handbook Committee: Forming Unitary Hinges, Plastic Processing Technology Handbook, Tokyo, Nikkan Kogyo Shimbun, Ltd., p. 196-197 (1984)

■ Authors ■


Tomohiro SAKURABA


Hideto NEBUYA


Teruo KATOH


Tomoaki ABE

Development of Soft-feeling In-mold Paint for Urethane Steering Wheel Grip

Tatsuya ITAKURA*

ABSTRACT

The steering wheel is the interior component that is touched with the highest frequency. To improve the feel of the steering wheel, this project developed a soft feeling in-mold coating that can be used in existing in-mold processes. The target was to achieve the feel of aniline leather, which is the most pleasant leather to touch. Equipment measuring the sense of friction was utilized to obtain values to which a standard deviation was applied, enabling measurement of softness and the sense of grip necessary for steering. The combination of a soft polyester resin and urethane resin beads in the paint formula, in combination with a soft-type polyester-denatured hexamethylene diisocyanate (HMDI) hardener gives the paint a very soft feel.

1. Introduction

When a driver sits in an automobile, the first thing they touch to operate the vehicle is the steering wheel. The function of the steering wheel is to transmit the driver's intention to control the vehicle in the desired direction. However, in addition to its function as a steering device, the steering wheel has functions such as an air bag mount to help protect the driver as well as containing various switches for operating electrical components. The gripped portion (hereafter referred to as "grip") was formerly made of materials such as wood or PVC resin, but currently most steering wheels are molded from semi-hard polyurethane. In addition, other commercialized options combine functionality, a high margin of safety (MOS) and design properties, such as leather wrapping to improve the feel, or printing a wood grain onto a hard resin to improve the visual aesthetic properties for higher class vehicles as shown in Fig. 1. Amidst this background, the recent trend particularly among European vehicles is to simply produce a soft feeling part by coating plastic products with a pleasant feeling paint, and to also create a luxurious appearance by suppressing the gloss.

This project developed new technology to provide a soft feel with paint technology that could formerly be achieved only by leather wrapping. The content of this paper reports the development of these materials and describes a method for quantitatively measuring softness.

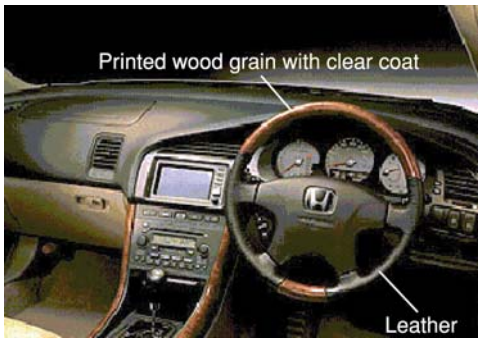


Fig.1 Honda INSPIRE steering wheel

* Tochigi R&D Center

2. Development Goals

The fabrication method for the steering wheel grip consists of molding polyurethane over steel, magnesium alloy, or other metal core by an in-mold process, and simultaneously applying an in-mold paint to the surface. The function of the paint is to match color and gloss with other interior components and also to improve durability. These processes are shown in Table 1.

Table 1 RIM-Urethane steering wheel grip manufacturing processes

No.	Manufacturing processes	Purpose / Content
1	Applying mold release paint	To release the urethane steering wheel grip
2	Applying in mold paint	· A barrier of void occurring from formed urethane · Match other interior low gloss parts
3	Armature set to dies	Hardness, impact resistance
4	Mold closed	Preparation for urethane injection
5	Injection of RIM urethane	Urethane injection of a fixed quantity
6	Mold opened	Release product
7	Safekeeping calmly	Room temperature turn of a product

The theme of this project was to develop a new paint with the aim of proposing a desirable grip that allows comfortable operation by providing a softer feel than the current in-mold paint used.

3. Targets

3.1. Target Feel

The ideal feel desired for the grip is currently thought to be that of leather, which not only has a pleasant appearance and smell, but also has a soft texture and provides functionality. Of the various types, aniline leather, which is used for high grade furniture, is considered to have a particularly good feel. Therefore, the target feel was set as equivalent or better than aniline leather.

3.2. Processability

The target was a coating which does not require changes or modifications to existing production facilities. The material should have spray properties (atomization), a batch process viscosity stability (pot life) and demold properties (die demold properties) equivalent to the current in-mold paint.

4. Quantification of Surface Feel and Target Values

Surface feel was quantified by using the KES-SE friction tester (KATO TECH CO., LTD) shown in Fig. 2. Property values obtained using a piano string jig that simulates a human fingerprint have a high correlation with sensory evaluation[1]. This project also applied this measurement method to set quantitative values for softness which were used as the target values. Figure 3 shows an example KES-SE measurement chart.



Fig.2 Friction tester KES-SE (KATO TECH CO.,LTD)

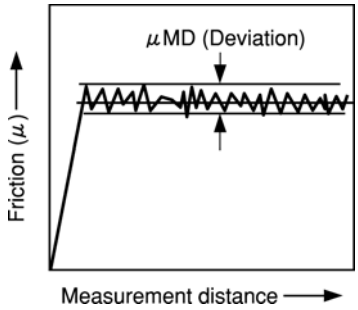


Fig.3 Fixed quantity test

As the friction grip force μ increases, the surface becomes less slippery and the grip force increases. Also, a small standard deviation μMD indicates a smooth and even surface. When dividing the friction force (μ) by the standard deviation (μMD) results in a high value, this indicates high friction and a smooth surface, which represents a soft feel. When applying this to the steering wheel grip, the operational function of grasping must be taken into account, so the surface feel must be improved without lowering the friction force (μ), which is the grip force. Therefore, evaluation criteria was based on softness feel (μ/μMD) and friction force (μ).

Using aniline leather as the goal, grip force and softness feel target values were set as follows:

- Grip force (μ): 0.0927
- Softness feel (μ/μMD): 30.3

5. Development of Soft Touch Paint

5.1. Investigation of Soft Touch Paint Composition

Table 2 shows the general components of the 2K curing soft touch paint that is applied to provide a pleasant feel to products such as automotive interiors and household appliances.

This soft touch paint is comprised of main resins consisting of acrylic and polyester polyol resins which make up the binder, filler materials, additives to maintain the

Table 2 Components of soft-feeling paint

	Components
Main resin	Polymer
	Pigment
	Filling
	Additive (Activator, UVA, etc)
	Solvent
Hardener	HMDI (Hexamethylene diisocyanate)
	Solvent

stability (accelerator, UV absorber, etc.), solvents, and the hardener which consists of HMDI, which is the subject activator for the polyol curing reaction, and a solvent. Based on these materials, a new soft feel in-mold paint was developed.

5.2. Selection of the Main Resin and Filler Material

Acrylic and polyester were selected as the main resins used in the soft touch paint based on feel and durability. Hard acrylic, soft polyester and a blend of these two resins were investigated to confirm the difference in the feel. In addition, the paints shown in Table 3 were prepared by mixing three types of filler materials with the main resins. The filler materials used were silica which is generally used as a flattening agent, polyurethane beads that are a texturing agent, and a mixture of collagen and soft wax that is thought to improve the texture by providing a feel of absorbed moisture. Test pieces were fabricated using the in-mold method, and the friction feel of each paint was measured. Figure 4 shows these results.

The results showed that the paints containing polyurethane beads as the filler material provided the most pleasant feel. In addition, soft polyester was found to be the best main resin. Paints containing silica or collagen/soft wax had a lower grip feel compared to polyurethane beads or silica. The surface conditions of paints No. 6, 7 and 8 were photographed to analyze this phenomenon. Figure 5 shows these photographs.

Minute bumps occurred in paint containing polyurethane beads, which are thought to have contributed to the soft feel.

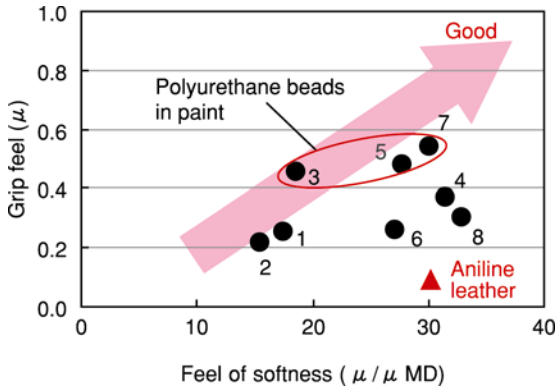


Fig.4 Friction of base polymer and variant filling in in-mold paint

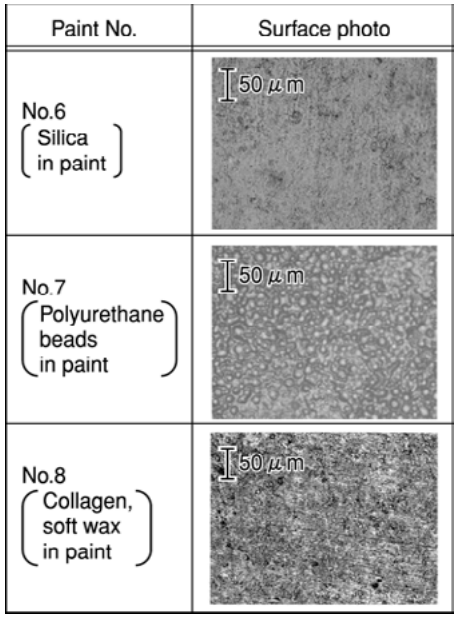


Fig.5 Surface of in-mold paint

Table 3 Components of base polymer and variant fillings

Paint No.	Base polymer	Hardener	Filling
1	Hard acrylic	HMDI (Hexa methylene diisocyanate)	Silica
2			Acrylic beads
3			Polyurethane beads
4	Hard acrylic + polyester		Silica
5			Polyurethane beads
6	Soft Polyester		Silica
7			Polyurethane beads
8			Collagen/Soft wax

In contrast, the paint films that used silica or the collagen and soft wax had smooth surfaces. This indicated that the silica and collagen/soft wax mixtures were not present in the surface layer after in-mold processing. This phenomenon is thought to occur because the silica and collagen/soft wax are oriented on the inner mold exposed surface or dispersed in the film, so they do not contribute to the outer side of the actual molded product. In other words, these fillers are oriented on the inner die face during the in-mold painting process, so they are not present on the outermost surface of the actual molded product. Figure 6 shows pattern diagrams of these conditions.

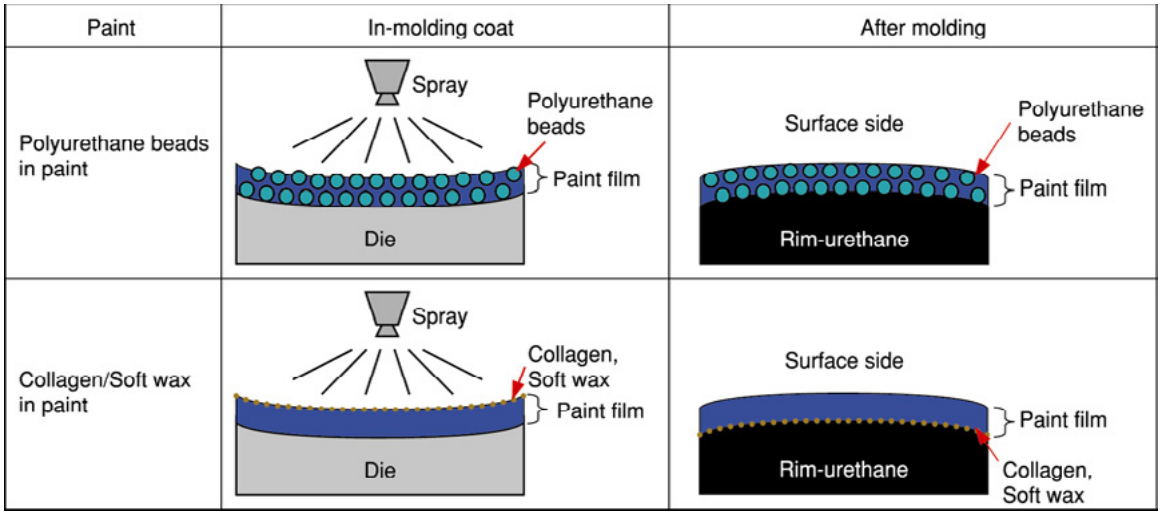


Fig.6 Image of soft filling effect at paint method

5.3. Selection of Hardener

The effects of the hardener were investigated using the base mixture of soft polyester as the base resin and polyurethane beads as the filler material. The paint hardness can be varied by modifying the hardener. The paint mixtures shown in Table 4 were made with three types of hardeners consisting of normal HMDI and two modified HMDIs. Modifications were based on adding polyester to the HMDI frame. Test pieces were fabricated using the in-mold method, and the friction of each paint was measured. Figure 7 shows the results.

These results confirmed that hardeners with a higher degree of modified polyester provide a more pleasant feel. There are two theoretical reasons behind this phenomenon. First, the hardener itself was modified by the polyester to become softer. Secondly, the clearance between the base resin in the hardener and reaction components (functional groups) increased, thus expanding the cross linking structure of the cured paint film and causing the stiffness to drop. Figure 8 shows a schematic diagram of this condition.

Table 4 Variation in hardener components

Paint No.	Base polymer	Hardener (HMDI)	Filling
7-1	Soft polyester	Normal	Polyurethane beads
7-2		Polyester-low graft	
7-3		Polyester-high graft	

· HMDI softness : Polyester-high graft >Polyester-low graft >Normal

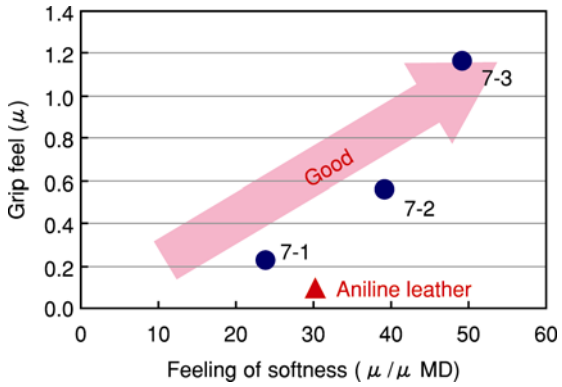


Fig. 7 Friction of in-molding paint with different hardness

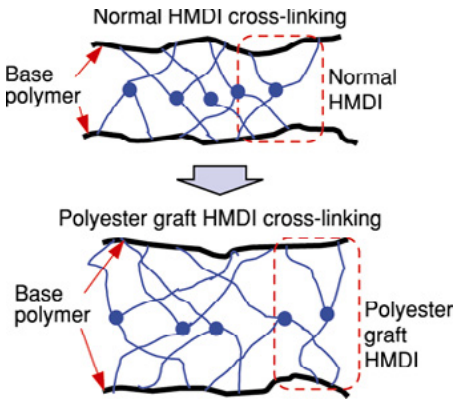


Fig.8 Image of paint bridge formation

6. Processability

Investigating various mixtures enabled development of an in-mold paint with a very soft feel by using a polyester polyol as the base resin, polyurethane beads as the filler material, and isocyanate with a polyester modified hardener. Therefore, the paint properties were confirmed on an actual steering wheel fabrication line. At this time the paint viscosity was found to increase faster than the current paint during the application window. When the paint viscosity rises quickly, the time that the paint can be used after mixing is limited, causing an increase in waste. This has a large impact on paint line workability and cost.

Therefore to counter measure, the addition of a solvent inhibitor was investigated to block the organic tin catalyst effects at normal temperature when mixing the paint. Figure 9 shows the results confirming the effects of mixing this solvent inhibitor on the friction feel.

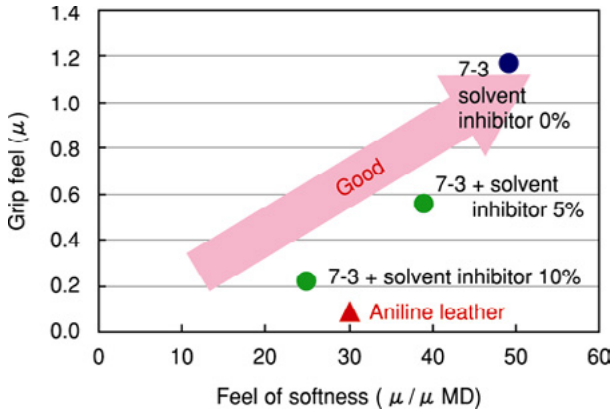


Fig.9 Friction of paint containing solvent inhibitor

Adding 5% and 10% solvent inhibitor for blocking the catalyst to prototype paint 7-3 caused the friction feel to drop. This phenomenon is presumed to occur because the solvent inhibitor limited the catalyst effect during the curing step of the in-mold painting process. Therefore, the reaction format between the base resin and the hardener differed depending on the presence of the solvent inhibitor.

Table 5 shows results for the performance of paint containing 5% solvent inhibitor.

Table 5 Performance of in-mold paint containing 5% solvent inhibitor

Item	Result
Pot life	Same as current
Storage stability	Same as current
Paint atomization	Same as current
Painting machinery conformity	Same as current
Mold-release stability	Same as current

These results confirmed that there were no problems with pot life and storage stability, which affect the paint properties, or with the atomization properties using the same application equipment as the current material. In addition, compatibility was also confirmed with existing production facilities, painting equipment, and die demold properties showed to be equivalent to the current paint. Therefore, paint containing 5% solvent inhibitor was determined as the final paint formulation.

7. Coating Performance

Table 6 compares the coating performance of the newly developed and the current in-mold paint.

The newly developed in-mold paint exhibited performance equal to or better than the current mass production paint in areas such as chemical resistance and long-term durability. In addition, the low-gloss appearance matches with other interior components and the friction property was also superior to the current in-mold paint. This is thought to be a result of the flat appearance produced by the minute texture of the polyurethane beads. Also polyurethane beads maintain a degree of high durability compared to the flattening agents used in the current in-mold paint, which suppresses the rise in gloss due to wear.

Table.6 Coating performance

Test item	Soft in-mold paint	Current in-mold paint
Light resistance	Pass (Grade 4)	Pass (Grade 4)
Heat resistance	Pass (Grade 4)	Pass (Grade 4)
Humidity resistance	Pass (Grade 4)	Pass (Grade 4)
Chemical resistance	Pass (Grade 4)	Pass (Grade 4)
Wear resistance	Pass (Grade 5)	Pass (Grade 4)
Gloss (60°)	2.0	3.2

· Grade 5 : No defect
· Grade 4 : Some inferior, but almost unnoticeable

8. Surface Feel Survey

As described above, surface feel was quantified by measuring the friction, and a soft paint mixture was developed. Then, sensory evaluation using steering wheel grips was conducted to determine whether a soft feeling was actually obtained.

Three grips were fabricated using the newly developed paint, the aniline leather target and the current paint. A survey was conducted with 12 male and female subjects. The survey was based on Sheffe's pair comparison method, which is suitable for touch sensation where other samples for which quantitative numeric expression is difficult. In addition, of the various Sheffe's pair comparison methods, the Nakaya modified method which allows individual repetition was used[(2)]. Figure 10 shows the survey results.

The responses were divided relatively with "like" to the right and "dislike" to the left of the center 0. The order of preference was found to be the newly developed paint, aniline leather and then the current mass production product. As in the friction feel measurement results the newly developed paint was rated more favorably than aniline leather.

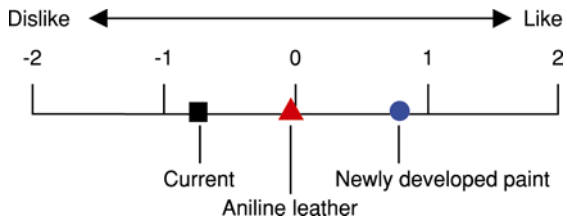


Fig.10 Result of paired comparisons survey

9. Conclusion

A soft feel in-mold paint was newly developed for steering wheel grips, and the obtained surface feel is softer than aniline leather. The knowledge acquired through the

development of this new paint is as follows:

(1) Soft polyester resin provides the most pleasant feel results as the main component for the in-mold paint.
(2) Adding polyurethane beads as the filler material produces bumps on the paint film surface after molding and provides a pleasant texture.
(3) Softer hardeners are effective for improving the feel by increasing the degree of modification to the polyester in HMDI.
(4) Polyurethane beads give the newly developed soft in-mold paint a surface pattern that reduces surface gloss and improves friction property compared to the current paint.
(5) Adding a solvent inhibitor to block the effects of the curing catalyst reduces the appeal of the surface feel.
(6) Grip feel [μ] and Softness [μ/μMD] measurements obtained using the KES-SE friction tester are effective for quantifying the feel, and match closely to the results of the sensory survey.

This newly developed soft in-mold paint was adopted for the new 2003 model ACCORD (Japan, U.S., Asia, China).

Acknowledgements

The author wishes to express his deep thanks to OHASHI CHEMICAL INDUSTRIES LTD., TS tech Co., ltd., NIHON PLAST CO., LTD. and all other related parties for their immense cooperation in the development of this soft-feeling in-mold paint.

References

(1) Yasuda, K.: S0982A (0286-6943) Kogyo Tosou No. 147, p. 87-92 (1997)

(2) Satou, S.: Statistical sensory inspection test method, Nikkagiren p. 263-270 (1995, 2nd Edition)

■ Author ■



Tatsuya ITAKURA

Development of Active Noise Control System for Engine Booming Noise

Toshio INOUE* Akira TAKAHASHI*
Satoru MINOWA* Hisashi SANO*

ABSTRACT

The critical issue with active noise control technology is the balance between cost and performance, due to the need of expensive high-performance DSP processors for the many convolution operations required. As a result, there are few applications of this type of technology to reduce booming noise.

The purpose of this paper is to propose a new algorithm significantly reducing the amount of arithmetic operations by focusing on the fact that booming noise is a narrow band noise. This algorithm enables us to employ an inexpensive controller even though adaptive signal processing is utilized. The integration of this system with an audio system further improves the balance of cost and performance.

The system developed in this study was applied to a new vehicle model in combination with an active control engine mount system to reduce booming noise generated in three-cylinder operation by a new V6 engine provided with cylinder on demand. The result is the achievement of excellent fuel economy and NV performance.

1. Introduction

The demand for fuel economy of automobiles is increasing, and as a consequence, new technology for achieving better fuel economy for the power plant as well as reducing the weight of the vehicle is being actively studied. The demand for improving the noise and vibration performance so as to improve the marketability of the vehicle has also become strident. However, the conventional passive measures for noise and vibration were found to increase the weight of the vehicle in most cases, and this was in conflict with the demand for fuel economy. Active Noise Control (hereafter ANC) technology achieves a high-level balance of these demands[1]. This technology attains noise reduction to a level that cannot be achieved by passive measures. A speaker is used to create cancellation sound that interferes with the noise, thus making it possible to build a system that keeps the increase in weight to a bare minimum.

In a previous study, the authors implemented a system that reduces fixed frequency, low frequency road noise by using analog circuits, which are cost effective, integrated it with the audio system and used it in mass production vehicles[2]. The target of this study is engine booming noise, the frequency of which varies with changes in engine rpm. The conventional booming noise control technology[3] required a large number of signal processes as it used convolution operations, and also required high-performance and expensive signal processors like Digital Signal Processors (DSP). Thus, cost related to performance became a challenge.

* Tochigi R&D Center

The objective of this study is to construct a control algorithm that will significantly reduce the number of arithmetic processes by focusing on the fact that the engine booming noise is a narrow band noise. The objective is also to improve the balance between cost and performance by promoting integration of the proposed system with the audio system.

The audio integrated ANC system developed based on this study, was used as a standard feature in new vehicles fitted with the V6 cylinder-on-demand engine to improve the engine booming noise that occurs when the vehicle is running in three-cylinder operation thereby enabling a high-level balance between the fuel consumption and NV performance.

2. Overview

2.1. Characteristics of Engine Booming Noise

Figure 1 shows the noise in the cabin during gradual acceleration. The horizontal axis in the figure is time and the vertical axis is frequency. The peak at the center of the figure is the booming noise. It is confirmed that the frequency of booming noise during acceleration increases synchronizing with the engine rpm and that the booming noise is restricted to a narrow frequency band. As shown in Fig. 2, being a narrow band noise means that the noise waveform is very close to that of a sine wave, and the waveform of the cancellation sound used for noise reduction is also close to that of the sine wave.

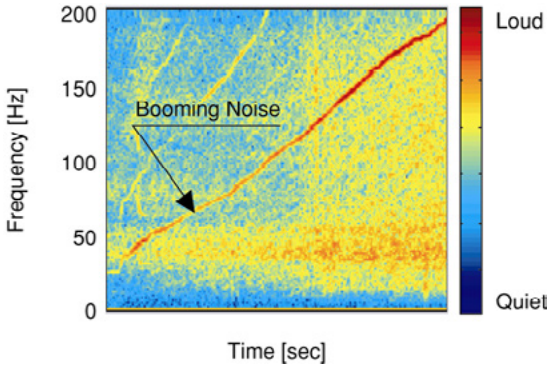


Fig.1 Contour map of noise inside cabin

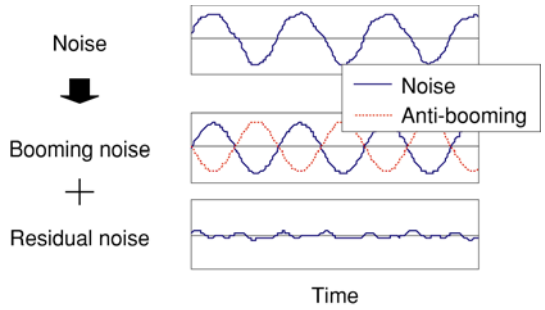


Fig.2 Time domain signal of noise inside cabin

2.2. System Overview

Figure 3 shows the system configuration. As shown in the figure, the system consists of the ANC Control Unit (Electronic Control Unit; hereafter ANC-ECU), located within the instrument panel, a microphone unit fitted in the rear tray, an audio head unit fitted with the input terminal of the cancellation signal, and speakers that are shared with the audio system. This system has two microphones since the ANC-ECU has a built-in microphone. The input signals to the ANC-ECU consist not only of the power supply, but also the rpm pulse signal (NeP) to detect the engine rpm, and the noise signal from the rear microphone unit around the rear seat. The outputs are signals for driving the speakers located in both the front doors, and the speakers fitted in the rear tray. This system employs an adaptive feed forward control[4), 5)] that operates such that the squared value of the noise signal from the two microphones is minimized. That is, it calculates the control frequency based on the engine rpm signal, creates a synchronized reference signal internally, and uses the adaptive digital filter to create the cancellation sound.

The integration of this system with the audio system was designed such that the main amplifier and the speakers were shared. Since this system is to be used in the new V6 engine with the cylinder-on-demand system, the function to communicate with the audio system for operational checks and the input circuit of Stop Cylinder Pulse (hereafter SCP) were added.

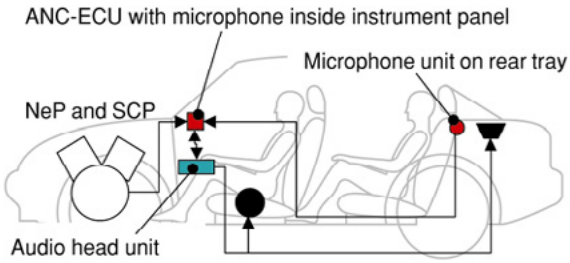
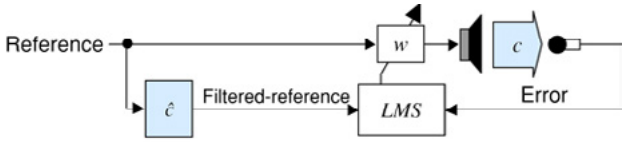


Fig.3 On-board system configuration

3. Control Technology

3.1. Issues in the Conventional Control Algorithm

Figure 4 shows the block diagram for controlling booming noise using the Filtered-Reference LMS (hereafter F-R LMS)[4), 5)], which has been widely used in past work[3)]. This control algorithm generates sine waves synchronized with the engine rpm as reference signals, converts the phase and amplitudes of the signal using the adaptive FIR (Finite Impulse Response) filter w, and then outputs the signals. The adaptive FIR filter w is updated recursively so that the



w : Adaptive FIR filter
c : Characteristic of acoustic cavity
$\hat{c}$: FIR filter estimating characteristic of acoustic cavity

Fig.4 Block diagram of filtered-reference LMS

squared value of e becomes minimal. It uses the error signal e detected by the microphone provided in the cabin and the FIR filter $\hat{c}$ modeled by the acoustic characteristics in the cabin, which is obtained as a parameter beforehand. Given below are the issues with this algorithm.

(1) Expensive signal processors are necessary

The control method uses many convolution operations (FIR filter calculation) equivalent to multiplication of vectors, which increases the number of arithmetic processes and necessitates a high performance processor. For instance, if the acoustic characteristic $\hat{c}$ is modeled by 128 filter length, multiplication needs to be performed 128 times and addition needs to be performed 127 times in each sample interval. Moreover, the convolution operations of the adaptive filter are also necessary. Furthermore, if a system with multiple speakers and microphones is to be built, then the number of arithmetic processes in the control algorithm would become abnormally high. In addition, to track the engine rpm at high speeds, the sampling frequency must be as high as possible, which necessitates high performance, high cost signal processors such as DSP.

(2) Issues related to modeling precision in the low frequency region

Since the acoustic characteristic $\hat{c}$ is modeled using the FIR filter, if the filter length is short for the actual impulse response, the precision of modeling in the low frequency region becomes poor. For instance, in a system that operates at the sampling frequency of 3 kHz, if the acoustic characteristics are modeled at 128 filter length, the frequency resolution Δf of the model becomes 23.4 Hz, the precision of the sound model for low frequencies such as 40-50 Hz decreases, and the control effect diminishes. Consequently, it is necessary to reduce the sampling frequency or to increase the number of filter length for modeling when controlling the low frequency noise. However, the problem with the former method is that it reduces the ability to track the engine rpm, and the problem with the latter is that the calculation load increases.

3.2. Reduction in the Number of Arithmetic Processes

3.2.1. Fundamental logic for reduction in the number of arithmetic processes

Figure 5 shows the booming noise shown on the complex plane. As mentioned in section 2.2, since the booming noise is a sine wave event, the cancellation sound of the booming noise is expressed as two values, *A* and *B*, on the complex plane. This is equivalent to saying that if the *RX* signal and the *RY* signal, which are reference signals perpendicular to each other and corresponding to the real axis and the imaginary axis respectively, are used, the cancellation sound is generated by taking the amplitude of the *RX* signal as *A* and the amplitude of the *RY* signal as *B*. Considering that the *RY* signal progresses at a phase of 90° with respect to the *RX* signal, the *RX* signal is shown as the real axis and the *RY* signal as the imaginary axis in the figure. This method allows the adaptive notch filters *A* and *B* that correspond to the amplitude of the perpendicular signals to track the changes in the engine rpm by using the digital signal processing. This method is known as SAN (Single-Frequency Adaptive Notch) filter[5), 6)].

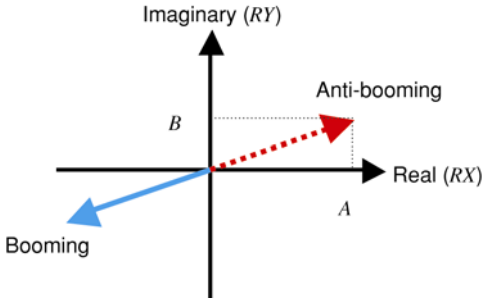


Fig.5 Polar coordinates of booming noise

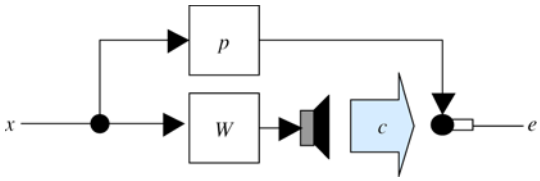


Fig.6 Block diagram of control system

3.2.2. Deployment in the control algorithm

The signal processing method to track changes in the engine rpm is given here. Figure 6 shows the block diagram of the adaptive signal process. Here, the reference signal is taken as x, adaptive filter as w, the acoustic characteristic as c, and its model as $\hat{c}$. Moreover, if p is taken as the unknown part, then the booming noise is assumed to be reference signal which reaches the microphone following the unknown part p. If it is currently presumed that there are no modeling errors, then $c = \hat{c}$ and the microphone signal e is expressed by the equation shown below.

$$e = p \cdot x + w \cdot \hat{c} \cdot x \tag{1}$$

The gradient Δ is found as shown in Fig. 7 to update the adaptive filter w so that the squared value of the microphone signal becomes a minimum. Thus, the gradient Δ is given by the equation below.

$$\Delta = \frac{\partial(e^2)}{\partial w} = 2 \cdot e \cdot \hat{c} \cdot x \tag{2}$$

Therefore, as shown in Fig. 7, the control system to track the changes in the engine rpm is built by updating the adaptive filter w recursively so as to attain the optimum value by the equation below.

$$w_{n+1} = w_n - \mu \cdot \Delta \tag{3}$$

Here, μ expresses the step size parameter.

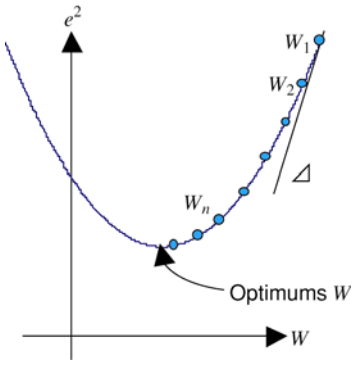


Fig.7 Optimization of evaluation function by LMS method

Next, equation (2) shows the method to reduce the number of convolution processes of the $\hat{c} \cdot x$ calculation as much as possible. For this, the frequencies of the acoustic characteristic $\hat{c}$ are analyzed and saved as a table for the control frequencies as shown in Table 1. The values corresponding to the frequencies to be controlled are read from the table and used in the calculations. The acoustic characteristic $\hat{C}$ in the frequency f is expressed using the complex expression (take j as an imaginary unit) shown below.

$$\hat{C}(f) = C_R(f) + j \cdot C_I(f) \tag{4}$$

Here, the method for realizing $\hat{c} \cdot x$ is shown, based on the acoustic characteristics in equation (4). It shows the calculation method using the *RX* signal in x for $\hat{C} \cdot x$

$$\begin{aligned} \hat{C}(f) \cdot RX &= C_R(f) \cdot RX + j \cdot C_I(f) \cdot RX \\ &= C_R(f) \cdot RX + C_I(f) \cdot RY \end{aligned} \tag{5}$$

Equation (5) uses the fact that *RY* is a signal that progresses at a phase of 90° with respect to *RX*, $j \cdot RX = RY$. In the same way, the calculation method when the *RY* signal is used in x, is given below.

$$\begin{aligned} \hat{C}(f) \cdot RY &= C_R(f) \cdot RY + j \cdot C_I(f) \cdot RY \\ &= C_R(f) \cdot RY - C_I(f) \cdot RX \end{aligned} \tag{6}$$

Table 1 Control parameter of acoustic characteristic

f [Hz]	C_R	C_I
30	30	−20
.....	.....	.....
40	15	−10
41	13	0
42	40	25
43	62	47
.	.	.
.	.	.
.....	.....	.....
100	−12	−49

Equation (6) uses $j \cdot RY = -RX$. Figure 8 shows the block diagram for engine booming noise control using equations (5) and (6). A feature of this control method is that the Frequency Domain Filtered-Reference (hereafter Freq, F-R SAN) does not make use of any convolution operation, as compared to the use of many convolution operations equivalent to the multiplication of vectors by the F-R LMS method, which is a common control method. That is, the main feature is that all the calculations involve multiplication and addition of singular values. Shown below are the updated equations of the adaptive notch filters *A* and *B*

$$\begin{aligned} A_{n+1} &= A_n - \mu \cdot e \cdot \{C_R(f) \cdot RX + C_I(f) \cdot RY\} \\ B_{n+1} &= B_n - \mu \cdot e \cdot \{C_R(f) \cdot RY + C_I(f) \cdot RX\} \end{aligned} \tag{7}$$

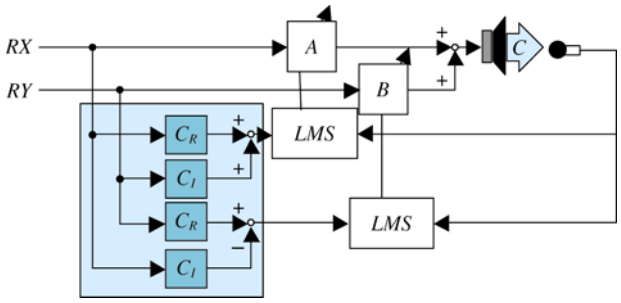


Fig.8 Block diagram of Freq. F-R SAN algorithm

3.3. Effect of Reduction in Arithmetic Processes

The number of arithmetic processes for one sample of Freq. F-R SAN and F-R LMS algorithms were compared. Table 2 shows a comparison of the number of arithmetic processes carried out by the Freq. F-R SAN algorithm and F-R LMS algorithm in one sampling period when the acoustic characteristics were modeled by 128 filter length and adaptive filter modeled by 64 filter length. This table represents the case of one output and one control point. The number of arithmetic processes of filter for the sound model, adaptive filter, the number of updated arithmetic processes of the adaptive filter and their sums were also compared. It is clear from this table that the booming noise is controlled by the Freq. F-R SAN algorithm with approximately 1/25th the number of arithmetic processes of the F-R LMS algorithm. The difference in the number of arithmetic processes becomes larger when the multi-output multi-point control system is constructed in which the number of microphones or output increases.

Table 2 Comparison of arithmetic operations carried out by Freq. F-R SAN algorithm and F-R LMS algorithm in one sampling period

	Freq. F-R SAN	F-R LMS
Acoustic characteristic convolution	6	255
Adaptive filter convolution	3	127
Adaptive signal processing	12	129
SUM	21	511

In addition to the reduction of the number of arithmetic processes, if the acoustic characteristics are maintained as a table at a resolution of 0.5 or 1 Hz, Freq. F-R SAN enables precise modeling restricted to the frequency range, where the control is implemented. Hence, this can resolve the issue of reduction in sampling frequency or increase in the volume of arithmetic processes in F-R LMS.

3.4 Stability Compensation for Control System

Parameters for stable operation of the Freq. F-R SAN system were introduced. The following two cases of unstable operations of the control system may be considered.

(1) When the noise components other than control frequency components included in the microphone signals are large.
(2) When frequency difference arises between that of the booming noise included in the microphone signal and the control frequency.

For both (1) and (2), the operation of the control system may become unstable. This is because the adaptive filter operates to reduce the frequencies other than those it should control, in regard to control frequencies predicted from the engine rpm, when the signals of control frequency components included in the microphone signal are relatively smaller compared to other frequency components. To inhibit this, mixing of signals of the control frequency component according to the size of adaptive filter in the microphone signal may be considered. Figure 9 shows the block diagram for this process.

A large α is effective in improving the stability. However, increasing α inhibits the control output and reduces the control effect.

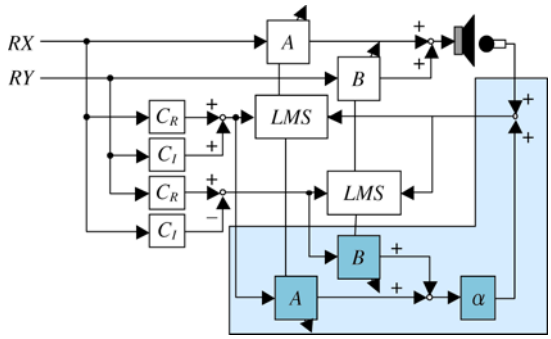
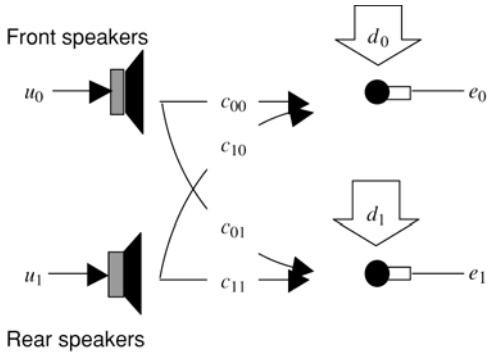


Fig.9 Block diagram of frequency domain filtered-reference SAN with stable parameter

3.5. Simplification of System Configuration

The number of microphones is reduced to simplify the system configuration. Reduction in the number of microphone units has a large effect not only on unit cost reduction, but also on overall cost reduction since items such as harness and garnish become unnecessary. Therefore, we considered a technique to control the front and rear seat booming noise by using a single microphone unit. A single microphone system was developed from the two microphone systems shown in Fig. 10. This single microphone system generates the output signal for the rear seat by compensating the front seat output signal using the rear seat compensation filter F as seen in Fig. 11.



d_0 : Booming noise in front passenger seat

d_1 : Booming noise in rear passenger seat

Fig.10 Two microphone system

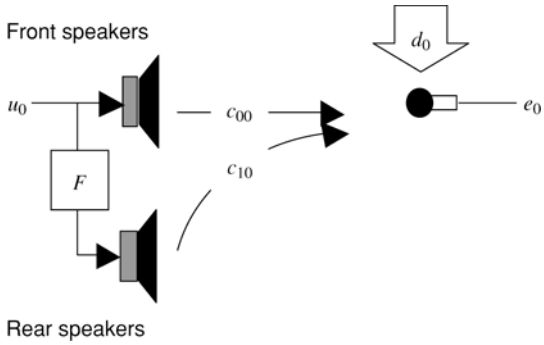


Fig.11 One microphone system

3.5.1. Identification method for rear seat compensation filter *F*

(1) Identification method that uses the booming noise distribution at the front and rear seats.

Using this method, the booming noise at the front and rear seats is reduced. The acoustic characteristics up to each of the front and rear microphones from each of the front and rear speakers are distinguished by subscripts from 00 to 11 as seen in Fig 10. The microphone signals e_0, e_1 are expressed in equations (8) and (9). The two equations are assumed to be zero for operations under ideal conditions. Further, when the front and rear seat booming noise distribution is fixed, this condition is expressed by equation (10).

$$e_0 = c_{00} \cdot u_0 + c_{10} \cdot u_1 + d_0 = 0 \quad (8)$$

$$e_1 = c_{01} \cdot u_0 + c_{11} \cdot u_1 + d_1 = 0 \quad (9)$$

$$q = \frac{d_1}{d_0} \quad (10)$$

From equations (8), (9), and (10) the front and rear output ratio F is obtained. c_{00} - c_{11} and q here, are taken as C_{00} - C_{11} and Q in the frequency range. From the above, the equation below is obtained.

$$F(f) = \frac{U_1(f)}{U_0(f)} = \frac{C_{01}(f) - Q(f) \cdot C_{00}(f)}{Q(f) \cdot C_{10}(f) - C_{11}(f)} \quad (11)$$

(2) Identification method that uses acoustic characteristics of the cabin only.
By applying this method, the amplified sound generated at the rear seat is controlled when reducing the booming noise at the front seat. The output signal for control of the front seat arrives at the rear seat according to the transmission characteristic c_{01}. The rear seat output signal is used to cancel the amplified sound generated at the rear seat. The rear seat compensation filter F used here is given in the equation below.

$$F(f) = -\frac{C_{01}(f)}{C_{11}(f)} \quad (12)$$

3.5.2. Use of rear seat compensation filter *F*

Since the identified rear seat compensation filter F in the frequency range is a complex number, it is expressed by the equation below together with equations (11) and (12).

$$F(f) = F_R(f) + j \cdot F_I(f) \quad (13)$$

The rear seat compensation filter F is retained as a table for frequency f similar to the table for acoustic characteristics $\hat{C}$ shown in Table 1, and it is used in calculations after reading the values corresponding to the control frequencies. Figure 12 shows the corresponding control block diagram. This control system requires an extremely low number of arithmetic processes for the rear seat output similar to acoustic characteristics $\hat{C}$. It enables a single microphone system with a cost effective microprocessor to be realized, and is therefore, an effective method. While using this method, it is necessary to use the equation below in acoustic characteristics $\hat{C}$.

$$\hat{C}(f) = \hat{C}_{00}(f) + F(f) \cdot \hat{C}_{10}(f) \quad (14)$$

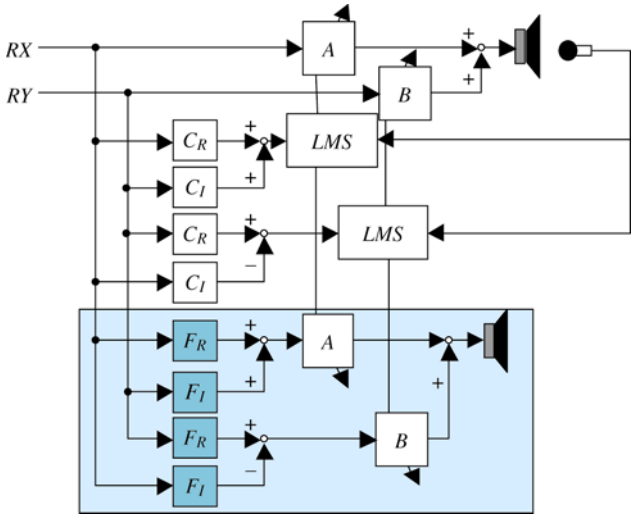


Fig.12 Block diagram of frequency domain filtered-reference SAN with rear area compensation

The front and rear seat booming noise reduction system shown in (1) requires prior studies because of the premise that the booming noise ratio q of the front and rear seat, including the phase in equation (10), is constant during acceleration / deceleration or when the difference of body weight in mass production vehicles is confirmed. The system for inhibiting increase in noise at the rear seat of (2) uses a parameter that can be identified only from the acoustic characteristics of the cabin. Therefore, when compared to (1), its operation is stable, but it cannot effectively reduce the booming noise at the rear seat. Consequently, it is important to select and use the appropriate method according to the vehicle characteristics.

4. Integration with the Audio System

To integrate this system with the audio system, a method was applied in which the control output signal was incorporated in the audio unit, as shown in Fig. 13, the power amplifier in the audio head unit was shared, and the speakers were driven. Consequently, the following two specifications were added to the audio head unit:
(1) A mixer circuit was fitted just in front of the power amplifier in the audio head unit
(2) The power amplifier was set to operate even when the user has turned off the main switch

In addition to the above two additional specifications, a function for communicating between the ANC-ECU and audio head unit was added as a checking function for the assembly process at the plant or support services for malfunction occurrences.

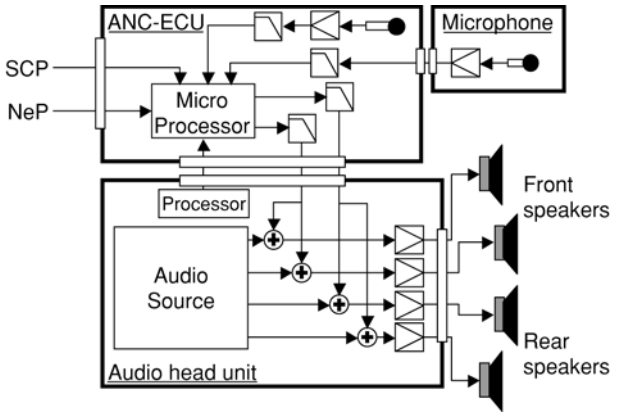


Fig.13 System configuration

5. Application Results

This system was used in vehicles fitted with V6 cylinder-on-demand-engines. During three-cylinder operation, besides the engine vibration, the intake sound and exhaust sound also deteriorate, and the booming sound in the cabin deteriorates due to torque converter lock-up. This system was set so that it could demonstrate maximum noise reduction by incorporating the SCP signal that shows three-cylinder operation for good efficiency in the reduction of booming noise. Figures 14 and 15 show the reduction effect attained by this system. It is confirmed from the figure

that the reduction effect is approximately 10 dB for 1.5th order component of the engine booming noise that deteriorates due to torque converter lock up in the vicinity of 1 800 rpm. Further, this system uses a Fujitsu semiconductor device, which is a 16-bit micro controller F2MC-16LX/MB90562/A.

This system enables the user to drive without being aware of three-cylinder operation.

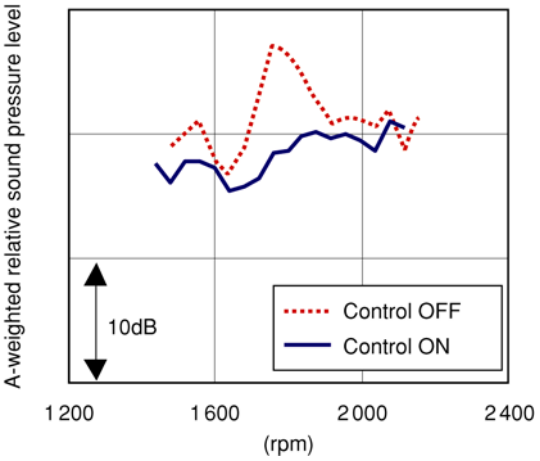


Fig.14 1.5th order sound pressure level at front seat

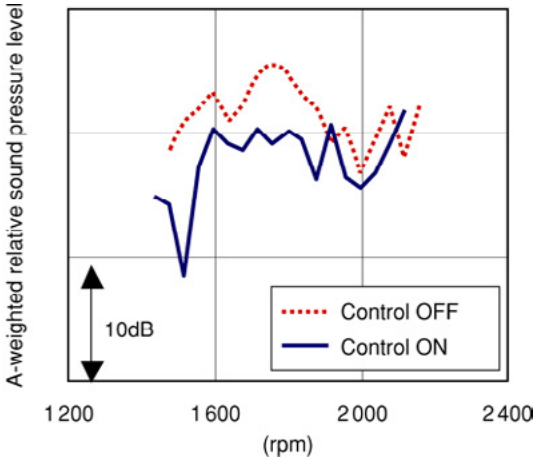


Fig.15 1.5th order sound pressure level at rear seat

6. Conclusion

The Active Noise Control System was developed aiming at reducing the engine booming noise, integrated with the audio system, and was mass produced. This system enabled a balance to be obtained between fuel economy and NV performance by using measures against the booming noise during three-cylinder operation for a V6 cylinder–on-demand system. Henceforth, this active control technology for noise and vibration is anticipated to be given a prominent position because of the good balance between weight reduction/ fuel economy and noise vibration performance.

Acknowledgments

We are deeply grateful to Matsushita Electronic Components Co., Ltd. for their wholehearted cooperation in this development.

References

(1) Nelson, P.A., Elliott, S.J.: Active Control of Sound, Academic Press, London (1993)

(2) Sano, H., Inoue, T., Takahashi, A., Ishihara, D., Yamashita, D.: Active Control System for Low Frequency Road Noise Combined with an Audio System, HONDA R&D Technical Review, Vol. 12, No. 2, (2000)

(3) Hasegawa, S., Tabata, T., Kinoshita, A., Hyodo, H.: The development of an active noise control system for automobiles, Society of Automotive Engineers Technical Paper, No. 922086 (1992)

(4) Haykin, S.: Adaptive filter theory Second Edition, Prentice-Hall (1991)

(5) Widrow, B., Stearns, S.D.: Adaptive Signal Processing, Prentice-Hall (1984)

(6) Ito, K., Miyasaka, I., Uto, S., Hamada, H.: Implementation of Active Control System using Single-frequency Adaptive Notch Filter, Proc. Spring Meet. Acoustic Society of Japan, 1-9-12 (1994)

■ Authors ■


Toshio INOUE


Akira TAKAHASHI


Satoru MINOWA


Hisashi SANO

Development of Active Control Engine Mount

Hideki MATSUOKA* Tetsuo MIKASA* Hirotomi NEMOTO*

ABSTRACT

An active control engine mount system has been developed to control noise and vibration in a completed vehicle employing a 3-liter V6 cylinder-on-demand engine. The research described in this paper focused on the fact that engine vibrations caused by fluctuations in torque can be estimated from fluctuations in crank revolution, and developed a new fixed feed forward control algorithm which does not employ sensors such as a load cell or an accelerometer. A higher responsive low-heat linear solenoid actuator has been developed for use in the system, and its unique coupling structure with an excitation plate inside the hydraulic engine mount makes it extremely reliable. The results show that noise and vibration performance during three-cylinder drive is equivalent to that obtained at full-cylinder drive.

1. Introduction

Active Control Engine Mount (ACM) technology is to control engine mounts actively by taking pulses synchronized with engine rpm as reference signals. Active Control Engine Mounts have been studied since the 1980s[(1)]. Various adaptive feedforward control methods have been investigated, such as one to monitor and cancel the input load of engine vibrations using a load sensor, and one to monitor directly and cancel the evaluation points of noise and vibrations (NV) of the car body using microphone or accelerometer. In the late 90s, two types of ACMs were developed and practically used. One is a method to operate the vacuum actuator by using mapping control [(2)]. Another one is to operate the electromagnetic actuator by using adaptive control [(3)]. The functions of the former are limited to the idling range, so that the system is extremely simple. The latter method controls a wider range up to 130 Hz, however it employs an electromagnetic actuator with a permanent magnet or an exclusive load sensor, and this results in higher system costs and heavier weight. The target of this research is an engine equipped with the cylinder-on-demand system. From the point of view of cost reduction, this study focuses on ACM that ensures reliability and adequate vibration isolation over the rpm range in three-cylinder drive, and the control method that does not require exclusive sensors.

The cylinder-on-demand system reduces pumping loss and improves mileage by keeping the valves of the three cylinders on one bank closed when the load during operation is light, such as, when the engine is running at constant speed or decelerating. However, the vibration amplitude in three-cylinder operation increases due to the halved basic order caused by less cylinders in operation and the higher combustion pressure due to the increase in the workload per cylinder. Therefore, the isolation capacity of conventional engine mounts is insufficient, and the deterioration of NV performance in the completed vehicle is one of the biggest concerns. The aim of the ACM development is to minimize the costs and to achieve NV performance that does not make a driver feel like a vehicle is under three-cylinder operation.

* Tochigi R&D Center

2. Overview

2.1. Vibrations of the V6 Cylinder-On-Demand Engine

Generally, engine vibration is classified into two categories. One is generated due to the inertia force caused by the motion of components, and another one is generated due to engine combustion. The vibration under three-cylinder operation of the 60-degree V6 cylinder-on-demand engine is mainly due to the 1.5th order of the engine rpm. However, vibration caused by engine combustion becomes the main contributor since the inertia force that accompanies the motion of the piston-crank is balanced regardless of the number of cylinders in operation. Thus, if the combustion pressure or the fluctuation in crank rotation that occurs due to the combustion pressure is determined, the engine vibration is estimated and applied in ACM control.

2.2. System Overview

Figure 1 shows the system configuration. The V6 power plant is mounted on ACMs at the front and rear parts of the sub-frame, under the transmission, and on both sides of the side frame. The most efficient ACM locations are at the front and rear since the engine rotational vibrations due to combustion occur in vertical direction at these locations, and the vibration highly contributes to NV phenomena in a completed vehicle. The ACM control unit (Electronic Control Unit, ECU) is located in the cabin, and is connected to the engine ECU. The harness for driving the ACM is connected to the two ACMs in the engine room.

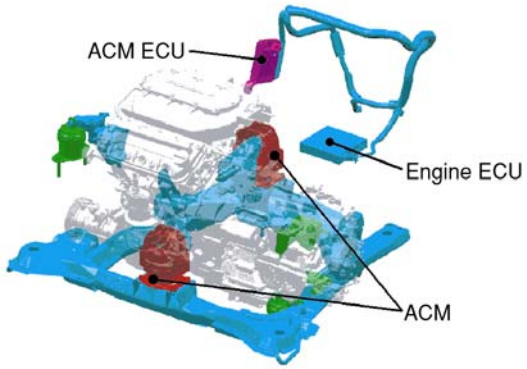


Fig. 1 ACM system configuration

Figure 2 shows the block diagram. The ACM ECU receives the crank and the cylinder pulse signals for the existing engine control from the engine ECU. The deviations in the crank rotation caused by engine combustion are detected from the crank pulse, while the cylinder pulse is applied as the phase reference for control. Thus, this system estimates the magnitude and phase of the engine vibrations, determines the duty signal for operating the ACM and vibrates the excitation plate inside of the ACM using the actuator.

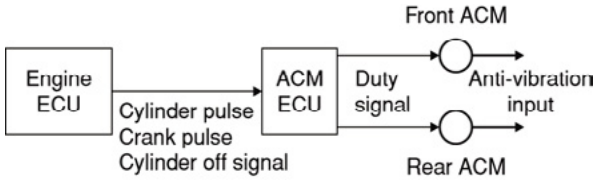


Fig. 2 Block diagram of ACM system

3. Control System

3.1. Engine Excitation Force and Crank Rotation Torque

Figure 3 shows a general piston-crank model. Because of the angle of connecting rod β, the force F due to combustion is separated into the force Fs, which pushes the cylinder walls, and the force Fc, which pushes the connecting rod.

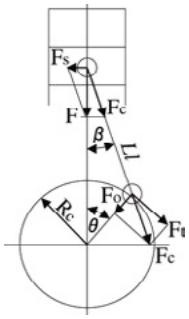


Fig. 3 Piston-crank model

The force that pushes the cylinder walls, *Fs*, and turns the crank, *Tq* during combustion are expressed as below.

$$Fs = F \tan \beta$$
$$Fc = \frac{F}{\cos \beta} \quad (1)$$

$$\begin{aligned} T_q &= FcRc \sin(\theta+\beta) \\ &= F\,Rc \sin(\theta+\beta)/\cos\beta \\ &= F\,Rc\left(\sin\theta + \frac{1}{2\lambda_c}\sin 2\theta\right) \end{aligned} \quad (2)$$
$$\lambda_c = Ll / Rc$$

As calculating the effect of phase θ of the crank with the equation above, Fs and Tq are considered to have an almost proportional relationship at the ignition timing ($\theta = 0 \sim 20°$) in the three-cylinder operating condition. Therefore, the magnitude of the engine vibrations is estimated by detecting the fluctuations in the crank rotation from the crank pulse and calculating the P-P value. The phase is also calculated by comparing the timing at the maximum P-P value and the cylinder pulse (TDC reference pulse).

3.2. Control Algorithm

Figure 4 shows the details of the control algorithm. This system determines the current waveform that drives the actuator based on the estimated engine vibration values mentioned in 3.1. The vibration calculation part calculates

the P-P value of the crank rotation, compares the peak timing and the TDC timing, and calculates the phase. Next, the duty control part inputs a waveform to the front and rear ACM to cancel the engine vibration in every cycle. Concretely, the aggregates of duty signals are outputted in the drive cycle. The phase is obtained from the reference pulse of each TDC.

Compared to the method to control the replacement of fixed maps as an engine is in operation, this one is superior because it is capable to follow up even if operating conditions such as engine rpm and load fluctuate or deteriorate.

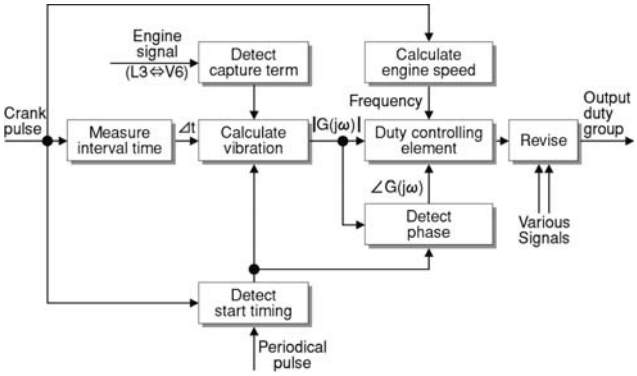


Fig. 4 Detailed block diagram of ACM

4. Actuator

The characteristics required for the ACM actuator are high response / force, small size, low weight, minimum heat buildup in coil, reliability, and low cost. Various types of electromagnetic actuators are compared based on these requirements. As a result, a linear solenoid system with well-balanced performance in those requirements was adopted and developed exclusively.

4.1. Characteristics of the Electromagnetic Circuit

For the shape of the air gap that generates force, a tapered configuration is used (Fig. 6) to stabilize the force–lift characteristics. For the electromagnetic circuit, a configuration

$$d\phi / dU = Pg \qquad (3)$$

is established to minimize the iron loss and the coil copper loss. Concretely, as shown in Fig. 5, $\alpha 1$ and $\alpha 2$ are set so as to be approximated at point P, the intersection of the iron core magnetization curve and a line from constant electromagnetic energy U1 (impressed current*the number of coil winding) at $\theta \fallingdotseq \tan^{-1}$Pg (Pg is air gap permeance).

4.2. Magnetic Flux Density Distribution

Figure 6 shows the calculation results of the magnetic flux density distribution in the electromagnetic circuit that consists of the coil, core, and armature. The equation (3) holds well since the magnetic flux density in the circuit does not use the area that exceeds the permissible value (flux saturation area) but the area close to the permissible value.

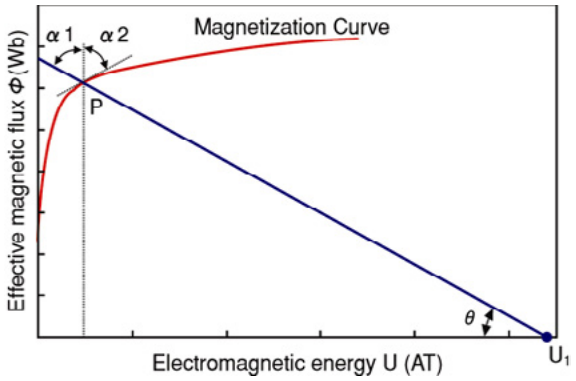


Fig. 5 Magnetic circuit characteristic of linear solenoid

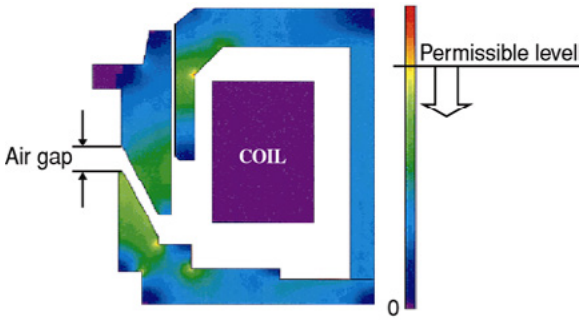


Fig. 6 Magnetic flux density of magnetic circuit

4.3. Heat Build-up Characteristics

An engine mount is generally exposed to high temperatures like radiant heat from the exhaust system. If the electromagnetic actuator is employed in the ACM drive, special attention must be paid to the heat build-up characteristics to ensure reliability. The applied linear solenoid actuator in this study has superior energy conversion efficiency. Furthermore, this actuator includes a driving circuit capable to impress the current waveform, in which unnecessary current components that generate heat internally have been removed. Thus, a very low heat buildup that does not affect the reliability is achieved. As seen in Fig. 7, even in continuous conductive operations, the rise in temperature of the coil surface is below 30 °C, and the rise in temperature

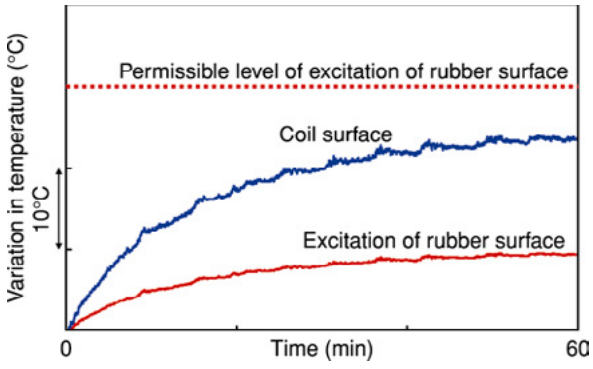


Fig. 7 Temperature characteristics

of the rubber surface (See Fig. 9) of the excitation plate closest to the actuator is about 10 °C. These values are sufficiently lower than the permissible temperatures.

4.4. ACM Control Unit

In order to drive an actuator that has high response and force, an ACM ECU is developed which includes a function to amplify high electric current in variable frequency and a driving circuit durable to the generated heat during these fluctuations. Also a diagnosis function is provided that includes a monitoring function for the actuator control unit Fig. 8.

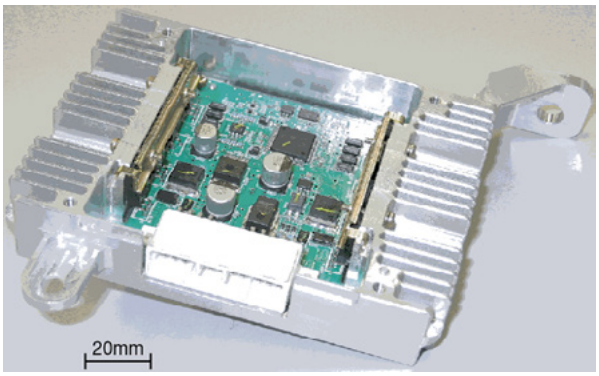


Fig. 8 ECM ECU

5. Structure of ACM

5.1. Structure Overview

Figure 9 shows a cutaway view of the ACM. The structure of the upper part of the ACM is similar to the conventional hydraulic engine mount. A linear solenoid type actuator is fitted in the lower part. The main feature of the hydraulic engine mount is the air-release diaphragm, located above the mounting rubber. Accordingly, overall height of the mount is shortened. This helped in achieving the compactness of the actuator mentioned earlier and overall height similar to that of the conventional hydraulic engine mount. Furthermore, as the rubber body that holds load is enveloped in mount liquid, hardening of rubber due to ozone aging and heat aging is reduced. This contributes to the stabilization of aging deterioration performance in the active control system. The actuator is coupled to the excitation plate on the mount side, and it is constructed to convert the actuator driving force to liquid pressure. Generally, the engine mount is equipped to the part which is exposed to water. Therefore, the direct coupler structure with double-molded coils is adopted to ensure reliability of the electrical circuit.

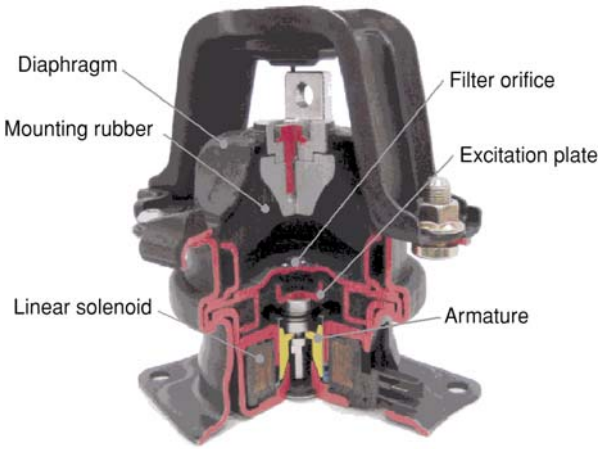


Fig. 9 Cutaway view of ACM

5.2. Coupling of Actuator and Excitation Plate

The coupling structure of the linear solenoid and the liquid hydraulic engine mount has two features as mentioned below to work both functions properly.

(1) Use of a mechanism for adjusting the armature (mover) setting position.
(2) Use of a mechanism that enables to couple the armature and shaft of the excitation plate, allowing coaxial misalignment and deflection.

Accordingly, the linear solenoid and hydraulic engine mount are coupled with the precise control of conventional construction, and a balance between the force stabilization and bearing reliability is established.

6. Characteristics of ACM

6.1. Determination of Hydraulic Engine Mount Characteristics

Characteristics required for the hydraulic engine mount in an ACM are mentioned below:

(1) It ensures damping force equivalent to a hydraulic engine mount having equivalent static spring constant.
(2) The ratio of mount generating amplitude / actuator force is high.
(3) It lowers the dynamic spring constant in the driving frequency range.
(4) It satisfies the durability requirements of the actuator drive.

Appropriate selection of the excitation plate specification is particularly important to optimize a balance of the four characteristics above. In this study, the specification of the excitation plate is selected based on tests on several types of samples and parameter studies on rubber hardness and the outer diameter of the excitation plate using a dynamics calculation model of the hydraulic engine mount and the characteristics of the dynamic spring constant is determined.

6.2. Reduction of Harmonics

The generation of harmonics becomes an issue in the base order of driving in ACM development. Harmonics is generated due to free vibrations of the excitation plate when electric current is cut-off by the duty drive. Thus, countermeasures are provided for the excitation plate and current control respectively. Figure 9 shows one of the measures that utilizes a filter orifice above the excitation plate. The filter orifice function includes assisting generative force characteristics by controlling the dynamic spring constant in addition to free vibration control of the excitation plate. Figure 10 shows the dynamic spring characteristics. Since the characteristics are stabilized in the control zone, the bottom frequency of the filter orifice is set up at 90 Hz. As a result, the reduction of harmonics generative force during actuator drive is possible as shown in Fig. 11.

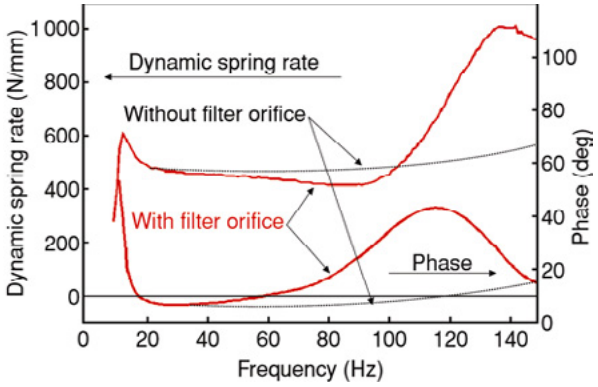


Fig. 10 Passive characteristics of ACM

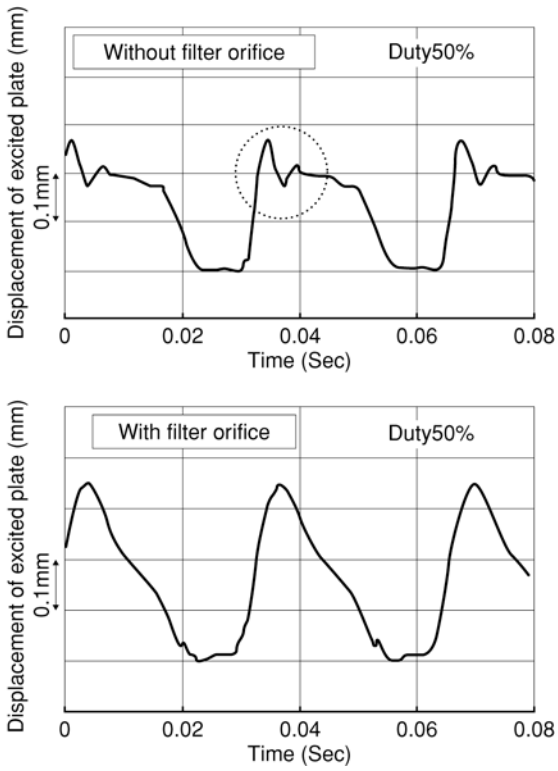


Fig. 11 Effect of filter orifice

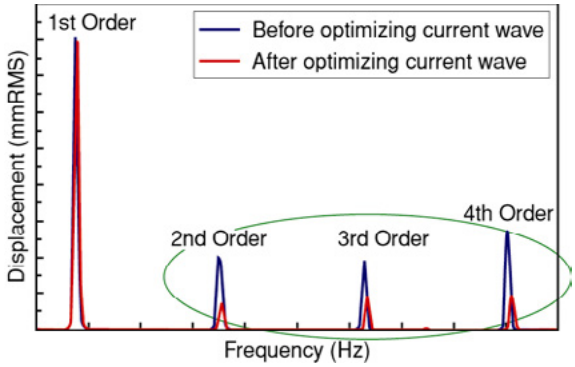


Fig. 12 Effect of harmonics of optimizing current wave

Another measure for control of harmonics is to improve the drive current. By gradually cutting off the electric current generated by the duty drive, the improvement in amplitude of the harmonics is confirmed (as shown in Fig. 12) in wide frequency ranges for components greater than the second order components of the drive.

7. Achievements

7.1. Generating Displacement of ACM Unit

Figure 13 shows the unit displacement generation. As shown in the figure, the current system achieves a better displacement performance in the entire range compared to the engine displacement in the three-cylinder drive condition.

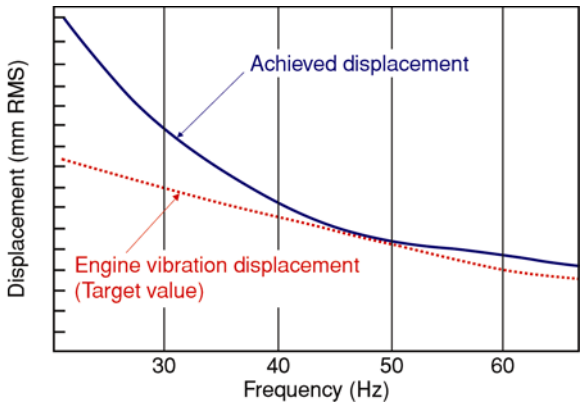


Fig. 13 Characteristics of ACM

7.2. Completed Vehicle Noise and Vibration Performance

This ACM system is applied to a vehicle equipped with V6 cylinder-on-demand engine, and the noise and vibration level in the three-cylinder drive is checked. As shown in Fig. 14, the result shows that the ACM load transfer is reduced by approximately 10 dB in the entire operating range compared to the no controlled condition. And the booming noise in the cabin and steering vibrations, shown in Figs. 15 and 16, are drastically reduced as well. Moreover, further booming noise reduction is achieved by applying active noise control with the ACM system together, and noise and vibration performance is realized equivalent to that experienced during full-cylinder operation, even in three cylinders operation.

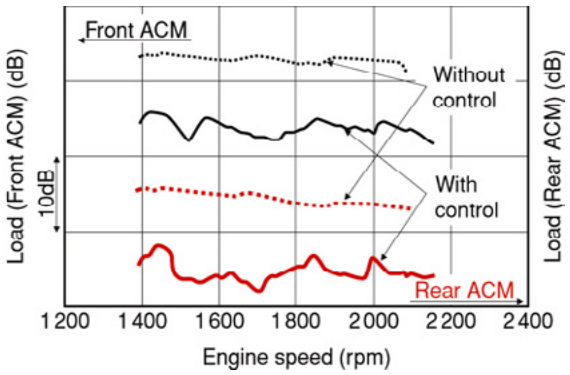


Fig. 14 Reduction of transfer load at three-cylinder drive

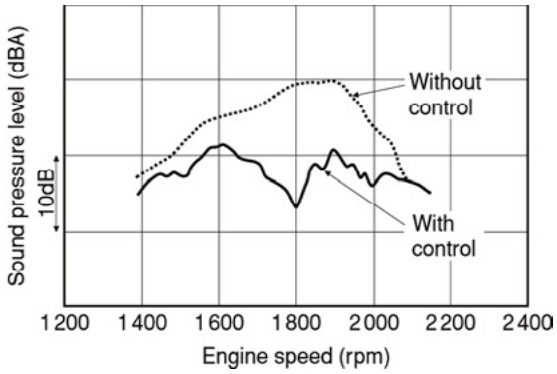


Fig. 15 Reduction of sound pressure in completed vehicle at three-cylinder drive

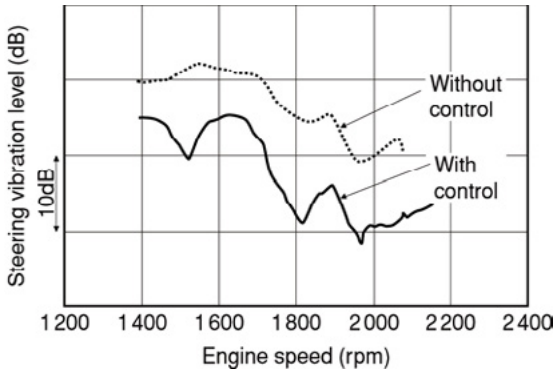


Fig. 16 Reduction of steering vibration in completed vehicle at three-cylinder drive

8. Conclusion

The following is the summary of this active control engine mount development:

(1) An ACM system equipped with an exclusive linear solenoid type actuator with high efficiency and low heat generation, and a vibration estimating type feed forward control system by crank rotation pulse signal, which is the existing signal, was developed.

(2) Amplitude characteristics that exceed the engine vibrations in the active driving condition were satisfied; adequate isolated vibration value was obtained, thereby enhancing the marketability of V6 cylinder-on-demand engine in noise and vibration performance.

(3) A packaging similar to that of the conventional hydraulic engine mount was realized by shortening the overall height of the hydraulic engine mount and the exclusive compact actuator.

(4) For reliability for low heat generation in the actuator, a coupling structure between armature and the excitation plate that allowed coaxial misalignment and deflection in the coupling was established, which ensures a sufficient durability.

Acknowledgment

We are deeply grateful to all concerned staff of Tokai Rubber Industries, Ltd., and Keihin Corporation for their wholehearted cooperation in this development.

References

(1) Fuller, C. R., et al.: Active Control of Vibration, ACADEMIC PRESS, (1996)

(2) Ozaki, H.: Development of Active Engine Mount, JSAE, Annual Congress 983, p. 141-144 (1998-5)

(3) Aoki, K., et al.: Noise and Vibration Reduction of Diesel Engine Vehicle Making Use of the Active Control Engine Mount (ACM) System, JSAE, Annual Congress 983, p. 133-136, (1998-5)

■ Authors ■


Hideki MATSUOKA


Tetsuo MIKASA


Hirotomi NEMOTO

Study of Hydro Bush for Reduction of Harshness and Road Noise

Yasuo MIYAMOTO* Sou NAKAMURA*

ABSTRACT

Isolation rubber bushes with hydro structures have low dynamic stiffness and high damping, and also allow high degrees of freedom in setting the required characteristics. The project discussed in this paper studied the methods of utilizing these advantages in suspension bushes in order to improve ride comfort and reduce road noise.

With regard to the harshness experienced when driving on a stepped road, the inputs are in phase for the left and right tires in the majority of cases, and this phenomenon formed the focus of this study. Hydro bushes with different characteristics for the right and left sides were used to generate phase differences in the force transmission to the chassis, enabling the development of a method of countering the force transmission on the left and right sides. This method has enabled the force transmission in the chassis on a stepped road to be reduced.

Tire vibration when driving on a rough paved road is transmitted to the cabin through the suspension. It was discovered that considerations of the rubber bush in the suspension system as a spring element and a damping element, and of the arm as a rigid body element and an elastic element, were important factors in the reduction of road noise. Optimization of the hydro bushes on this basis enabled the level of road noise experienced in the cabin to be reduced.

1. Introduction

Harshness when passing over stepped road joints and road noise on rough paved roads are sources of discomfort for passengers, and have a large influence on product appeal. Reducing this vibration and noise is an important issue for vehicle development, and research has been conducted on many areas including the body system and suspension system[(1), (2)].

However, the countermeasures for road noise in the body system often lead to worse fuel economy or handling performance due to an increase in the body mass, and the countermeasures for harshness and road noise in the suspension system are often a trade-off with handling and stability due to lower tire and bush stiffness. For these reasons, such countermeasures could not be implemented.

On the other hand, isolation rubber parts with hydro structures realize both the required dynamic stiffness and damping, and also allow a higher degree of freedom in setting the required characteristics. As such these parts are widely used mainly in the engine mount system, and have dramatically improved ride comfort, noise and vibration performance. Thus, it was thought that applying this technology to the suspension might hold the same potential for dramatically improving product appeal as for the engine mount system.

* Tochigi R&D Center

We analyzed the behavior of the suspension and the body over road surfaces that produced harshness and road noise using a sedan body style vehicle with double wishbone type suspension (Fig. 1) in both the front and rear. These results were then used to study how the characteristics of hydro bushes should be set to effectively reduce harshness and road noise in a vehicle.

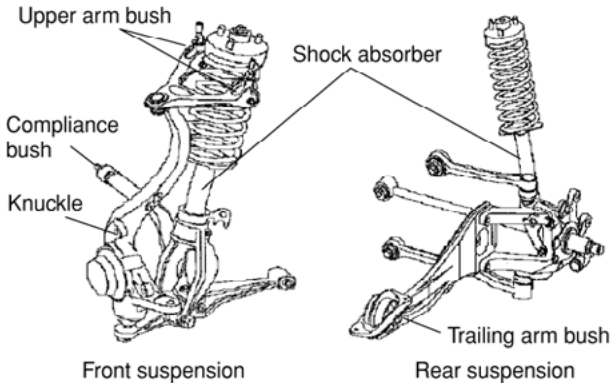


Fig. 1 Double wishbone type suspension

2. Investigation of Methods for the Reduction of Harshness

2.1. Selection of Road Surface and Vehicle Speed

Road surfaces that produce a feeling of harshness have various profiles, and these can be broadly classified as follows.

(1) Road surface with random shape (such as unpaved roads, etc.)
(2) Road surfaces with a regular period (such as choppy pavement on U.S. freeways[3], etc.)
(3) Road surfaces with a single stepped joint or multiple stepped joints with a sufficiently long period (such as bridge and overpass joints or repaired sections in paved roads, etc.)

Road surfaces with a random shape or a regular period are suitable for power spectrum analysis, but the next input will excite the suspension before the suspension vibrations stemming from the first input have subsided, so time series analysis is difficult. Road surfaces that are suitable for time series analysis are those with a single stepped joint or multiple stepped joints with a sufficiently long period. Therefore, we analyzed the suspension and body behavior over a road surface with only a single stepped joint established on a test ground.

Figure 2 shows the relationship between the speed and the peak value of the longitudinal body acceleration over this stepped road joint. The maximum acceleration occurred at 50 km/h, so this speed was used for analysis.

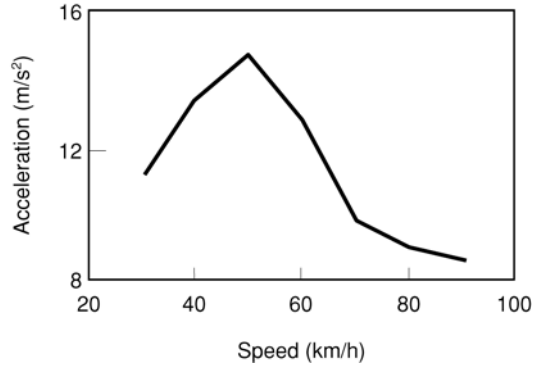


Fig. 2 Relation of speed and longitudinal body acceleration

2.2. Analysis Results

Figure 3 shows the time series wave form of acceleration for the body when passing over the stepped road joint at 50 km/h. This waveform is comprised of an acceleration component due to the tire enveloping and a periodic acceleration component.

The interval up to 0.2 sec is the effect of transmission from the front suspension, and the effect of transmission from the rear suspension is included from 0.2 sec onward. Therefore, Fig. 3 shows only the effects of the front suspension.

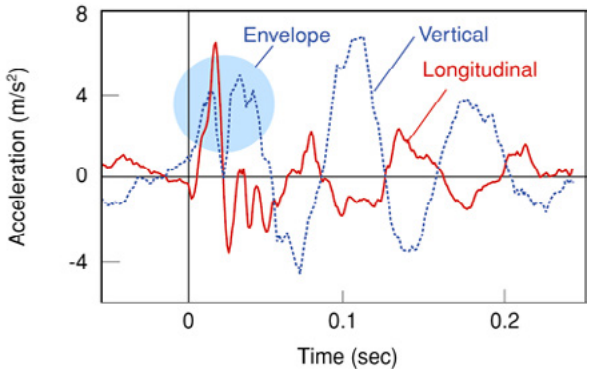


Fig. 3 Acceleration on body on stepped road (time series)

Figure 4 shows the results of analyzing the power spectrum density of this wave form from 0 sec to 0.2 sec.

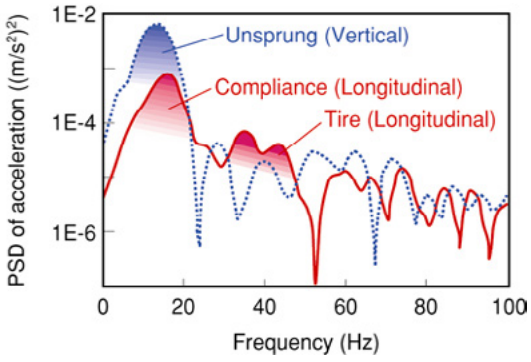


Fig. 4 Acceleration of body between 0sec and 0.2 sec

Looking at the power spectrum density of this acceleration, there are several peaks in the longitudinal direction at 16 Hz, 35 Hz and 43 Hz, and in the vertical direction at 13 Hz. Based on a comparison of the results of vehicle bench tests and tire unit tests, the longitudinal 16 Hz

component is thought to be the unsprung mass compliance resonance, the longitudinal 43 Hz component is thought to be the tire longitudinal resonance, and the vertical 13 Hz component is thought to be the unsprung mass vertical resonance.

The first cycle after contact impulse has a period of 0.028 sec, which corresponds to 35 Hz. The time from contact impulse to the acceleration peak is 0.013 sec, which is longer than 1/4 the cycle period (0.006 sec) of the tire longitudinal resonance. This period is thought to be the stage when the compliance bushes displace in the compliance direction, and is thought to be affected by both the tire and bush characteristics. The length of this period is thought to produce a lower frequency component (35 Hz) than the tire longitudinal resonance (43 Hz).

These vibrations are generated irrespective of the suspension type, so they are universally important. Methods for reducing vibration transmission in the vertical body direction include reducing the radial dynamic stiffness and increasing the damping of the tires, reducing the damping force of the shock absorbers, reducing the dynamic stiffness of the shock absorber mounts, and so on. However, these methods affect product appeal over a wide range from handling and stability to fuel economy. Therefore, the target was set for reducing vibration transmission in the longitudinal body direction.

2.3. Investigation of Hydro Compliance Bush Characteristics

Methods for reducing the longitudinal input to the body include reducing the tire stiffness and reducing the static stiffness of the bush. However, these methods also reduce the handling and stability. A realistic method that does not involve a trade-off with product appeal items other than harshness is to adjust the dynamic characteristics of the compliance bush without changing the static stiffness by using a hydro structure. The subject frequencies are the components of 16 Hz (compliance resonance), 35 Hz and 43 Hz (tire longitudinal resonance). Thus, damping these vibrational components with the compliance bush and reducing the vibration transmitted via the compliance bush were thought to be important.

First, an investigation was conducted to determine which of the frequency components deserved the most attention. The compliance bushes of the front suspension were changed to hydro bushes (loss tangent peak value of approximately 0.6), four different damping peak frequencies were set, and the relationship between the damping peak frequency of the bushes and the results of subjective evaluation on vehicle test at 50 km/h over a stepped road joint was investigated. (Fig. 5)

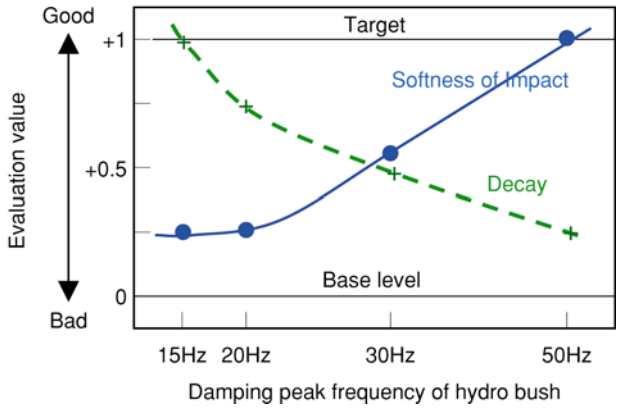


Fig. 5 Subjective analysis of harshness

The results showed that softness of impact was better when the damping peak frequency of the bush was set near the tire longitudinal resonance frequency, and decay was better when the damping peak frequency of the bushes were set near the compliance resonance frequency. This indicated that the relationship between softness of impact and decay is a trade-off, and a good balance between the two was confirmed when the damping peak was set near 30 Hz.

Figure 6 shows the longitudinal body acceleration for a conventional bush that does not have a hydro structure, and Fig. 7 shows the longitudinal body acceleration for a hydro bush with the damping peak set at 30 Hz.

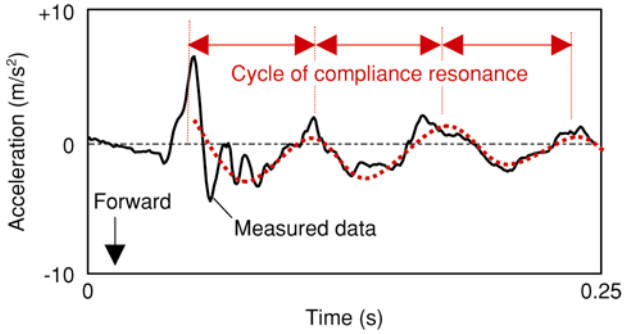


Fig. 6 Longitudinal body acceleration at conventional bush

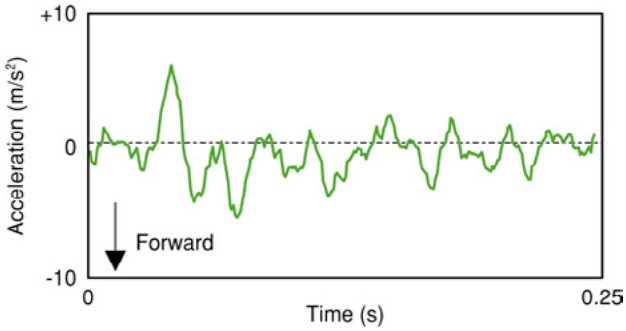


Fig. 7 Longitudinal body acceleration at hydro compliance bush (same phase)

The conventional bush shows poor decay of the compliance resonance, and this overlaps with the high frequency component to form a pointed time series waveform of longitudinal body acceleration. In contrast to this, when using the hydro bush with the damping peak frequency set at 30 Hz, the peak value of longitudinal body acceleration was reduced, and decay of the compliance resonance also improved.

However, in terms of the absolute softness and decay levels, the effects were insufficient and new methods had to be investigated.

2.4. Investigation of Phase Control

Most stepped road joints in the world are joints that stretch perpendicular to the direction of travel (for example, bridge joints, choppy pavement on U.S. freeways, etc.). When passing over these stepped road joints, the right and left tires contact the stepped joint at the same time, and the forces generated on the right and left tires are also transmitted at the same time to the body via the suspension. The phenomenon is thought to increase the body acceleration.

Therefore, a method was devised for canceling the vibrations transmitted from the right and left compliance bushes to the body by giving these vibrations a phase difference so that they interfered with each other. This mechanism is shown in Fig. 8. In order to realize this mechanism, the initial peak (35 Hz component) of the acceleration transmitted from the suspension to the body had to be given a different phase for the right and left bushes. The hydro bush characteristics for performing this phase control were set as follows.

(1) One bush was given high damping in the 35 Hz range, and the transmission phase angle advance was increased.
(2) The other bush was given low damping in the 35 Hz range, and the transmission phase angle advance was reduced.

We realized this asymmetry of the right and left bushes by changing the orifice design parameters (section area and length). In addition, we also considered the characteristics of the right and left bushes in the compliance resonance range and tire longitudinal resonance range for reducing the suspension longitudinal vibration. For this reason, the loss tangent peak frequency and peak value were set to ensure damping of 0.15 or more at the loss tangent. Figures 9 and 10 show the characteristics of the hydro bush using this phase control.

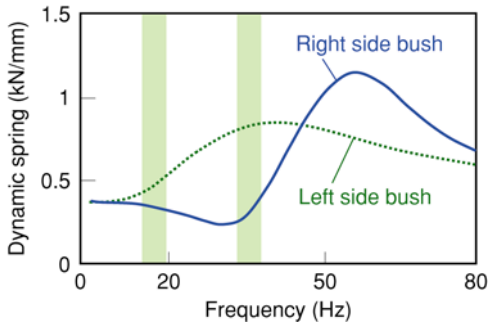


Fig. 9 Dynamic spring of hydro compliance bush

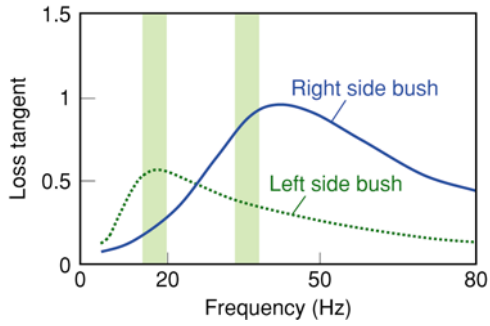


Fig. 10 Damping characteristic of hydro compliance bush

2.5. Effect on Vehicle Test

The effect was confirmed at 50 km/h over a stepped road joint. When the damping peaks were set at 30 Hz for both the right and left compliance bushes, the forces were transmitted

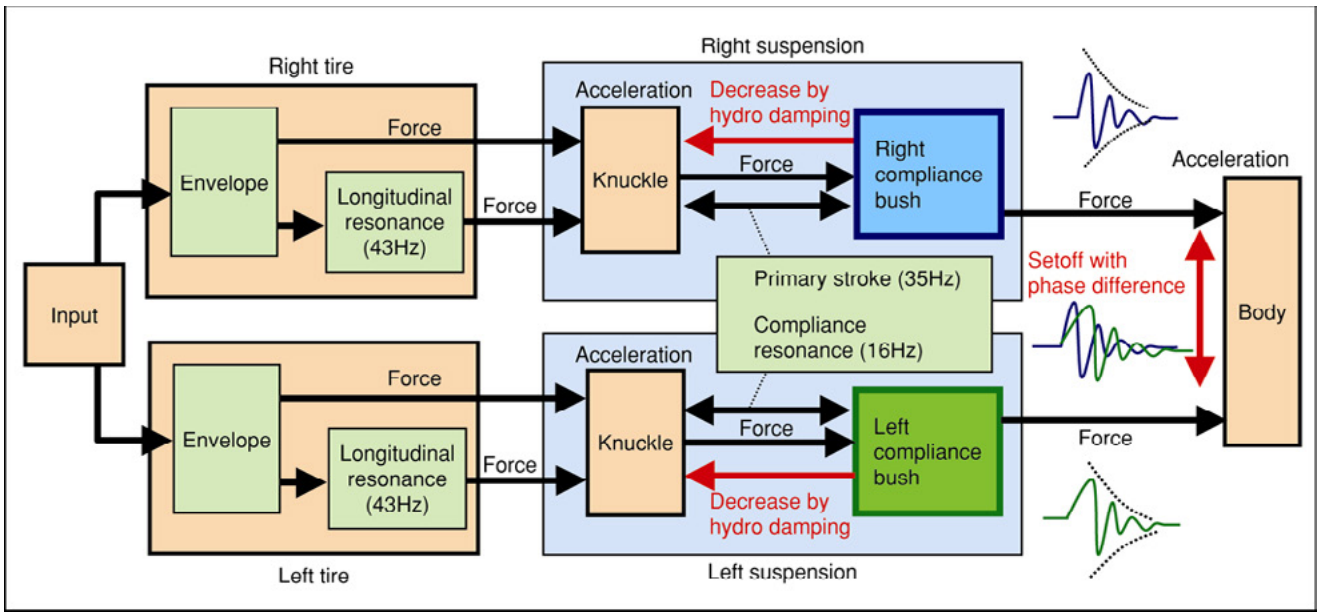


Fig. 8 Mechanism of phase control

in phase from the right and left bushes to the body, so the first peak on the positive side had a pointed shape. In addition, the decay was also poor (Fig. 7). In contrast, Fig. 11 shows the longitudinal body acceleration when phase control is performed using bushes with the characteristics shown in Fig. 9 and Fig. 10. Here, the longitudinal body acceleration peak on the positive side is divided into two peaks, and the peak height has dropped by 30%. In addition, from the second peak onward the force transmitted from the right and left bushes counter each other, and the decay has also improved. Handling and stability were also unaffected which had been a concern with the asymmetrical bush dynamic characteristics. This is thought to be because the bush static characteristics contribute greatly to handling and stability, and this symmetry was maintained.

This mechanism was confirmed to be effective not just for stepped road joints, but also for other harsh road surfaces. Figure 12 shows the body acceleration on choppy pavement on a U.S. freeway.

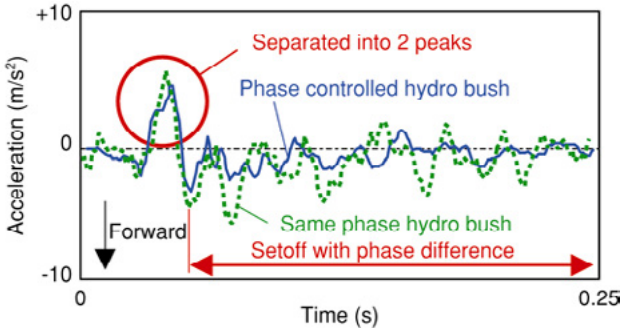


Fig. 11 Longitudinal body acceleration at hydro compliance bush (phase control)

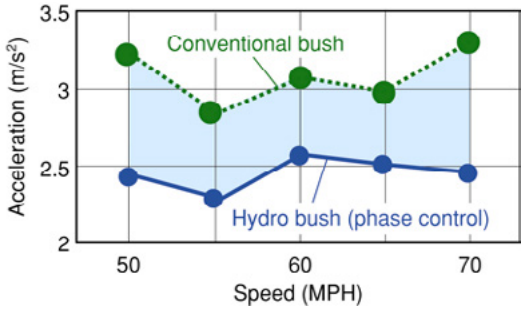


Fig. 12 Maximum longitudinal acceleration of body on choppy road

3. Investigation of Methods for Reduction of Road Noise

3.1. Analysis of Cabin Sound Pressure

Figure 13 shows the power spectrum density (1/3 octave band) for the cabin sound pressure over the road noise evaluation road. The sound pressure is high in the 250 Hz and 500 Hz ranges, so lowering the sound pressure in these ranges is thought to be important.

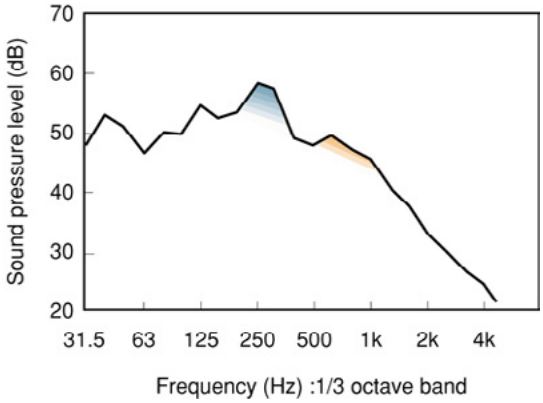


Fig. 13 Sound pressure in a cabin

3.2. Analysis of 250 Hz Range

The 250 Hz range in the 1/3 octave band is known to be caused by transmission of the tire cavity resonance. Narrow band analysis revealed the tire cavity resonance peaks at 230 Hz and 240 Hz. The transfer path of the suspension was analyzed, and the results showed that vertical vibration of the trailing arm bush had a high contribution rate in the tire cavity resonance range, accounting for 22% of the overall suspension. Therefore, it was thought that reducing the vertical dynamic stiffness of the trailing arm bush at 230 Hz and 240 Hz would improve road noise in the 250 Hz range.

3.3. Analysis of 500 Hz Range

A hypothesis was formed that the 500 Hz range in the 1/3 octave band is caused by a rigid-body mode of the suspension arm. Theoretical calculations based on the inertia mass of the arm and the stiffness of the bush led to the presumption that the rigid-body mode of the front upper arm contributes to this range. Therefore, the ball joint side of upper arm was excited using a tester for measuring the dynamic stiffness, the force at the body side of the bush mounting point was measured, and the transmission characteristics were measured. The results confirmed a transmission peak at 480 Hz. (Fig. 14)

Next, the front suspension spindle was excited randomly in three directions, and an acoustic sensitivity peak was

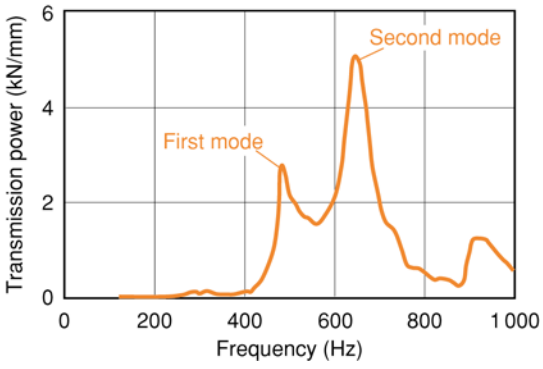


Fig. 14 Frequency response characteristics of arm assembly

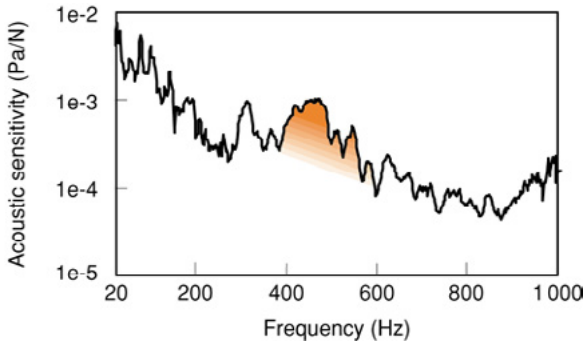


Fig. 15 Acoustic sensitivity of front wheel (random vertical excitation)

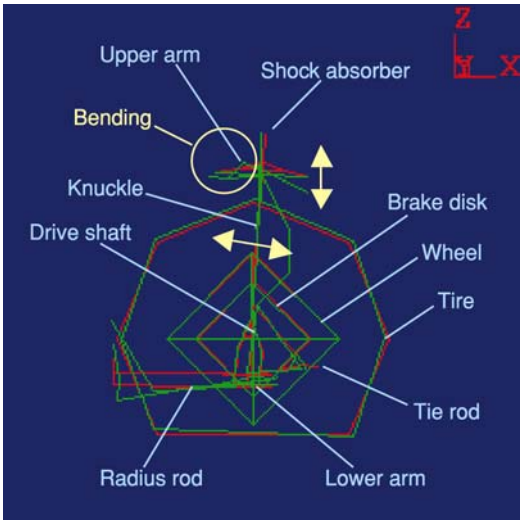


Fig. 16 Modal animation of front suspension at 464 Hz (side view)

confirmed at 464 Hz as shown in Fig. 15. Modal analysis of the suspension at this frequency confirmed the vibration mode shown in Fig. 16. This mode is comprised of a mode in which the knuckle undergoes longitudinal elastic deformation, a rigid-body mode in which the upper arm uses the ball joint as a fulcrum and the bush as a spring element, and the elastic mode of the arm itself.

Based on the above analysis, it is thought that road noise in the 500 Hz range can be improved by giving the bush high damping to suppress the rigid-body mode and elastic mode of the upper arm, and giving the bush a low dynamic stiffness to suppress transmission of these vibrations to the body.

3.4. Reduction by the Trailing Arm Bush

The vertical dynamic characteristics of the trailing arm bush contribute greatly to tire cavity resonance (230 Hz, 240 Hz), so the target was set at reducing the vertical dynamic stiffness at these frequencies.

The dynamic characteristics of the hydro bush are such that as the phase angle approaches 90°, the pumping action of the fluid in the orifice becomes stronger, allowing the dynamic stiffness to be reduced. Conventional hydro bushes use the gap between the inner tube and the stopper as the orifice, and a resonance system is formed by the mass of the fluid in that orifice and the expansion elasticity of the main rubber. In this case advancing the phase angle reduces the dynamic stiffness in the tire cavity resonance range.

The improved method uses a double orifice type in which a new orifice is added to the stopper portion of the conventional structure. Figure 17 shows this structure model. Resonance of the fluid in one orifice is created at 190 Hz by the resonance system comprised of the mass M1 and spring elements K2 and K4 in Fig. 17, and resonance of the fluid in the other orifice is created at 240 Hz by the resonance system comprised of the mass M2 and spring elements K3 and K4. The presence of these two resonance systems expands the frequency range over which a phase angle near 90° can be obtained, thus expanding the frequency range over which the dynamic stiffness can be reduced by the pumping action of the fluid in the orifices.

This made it possible to further reduce the dynamic stiffness in the tire cavity resonance range, and at the same time to suppress the aggravation of the dynamic stiffness peak value near 300 Hz. The improved hydro bush structure is shown in Fig. 18, and the characteristics are shown in Fig. 19 and Fig. 20.

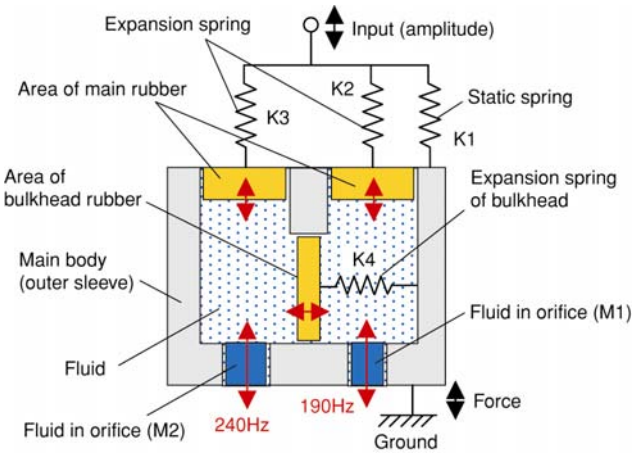


Fig. 17 Structure model of hydro trailing arm bush (double orifice type)

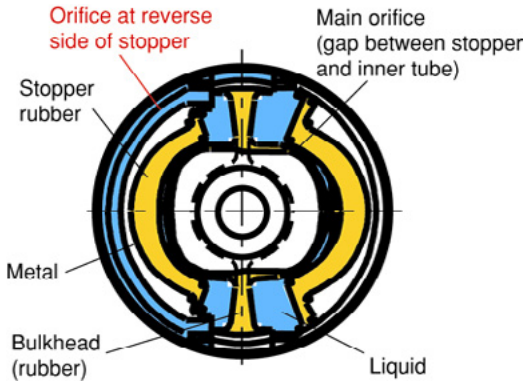


Fig. 18 Structure of hydro bush (trailing arm)

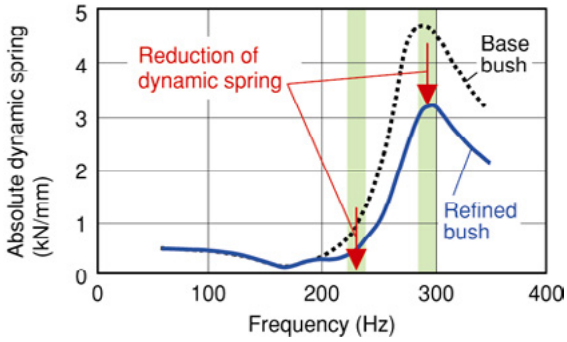


Fig. 19 Dynamic spring of hydro bush (trailing arm)

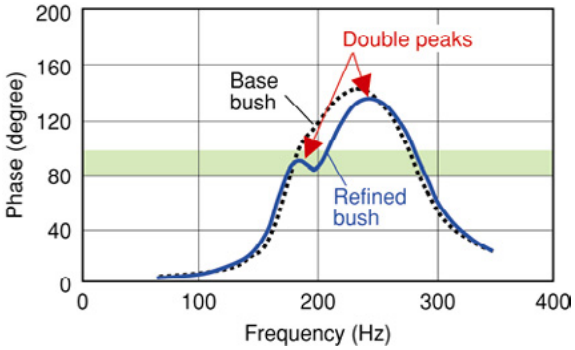


Fig. 20 Damping of hydro bush (trailing arm)

3.5. Reduction by the Front Upper Arm Bush

Giving the bush high damping to suppress arm resonance in the 500 Hz range and low dynamic stiffness to suppress transmission were thought to be effective measures.

A good method for achieving these characteristics was thought to be to set the resonance of the fluid in the orifices at 600 Hz, and to utilize the pumping action of the fluid in the orifices at lower frequencies. However, the resonance of the fluid in the orifices could not be raised to 600 Hz using a structure with a fluid chamber and orifices like a normal hydro bush.

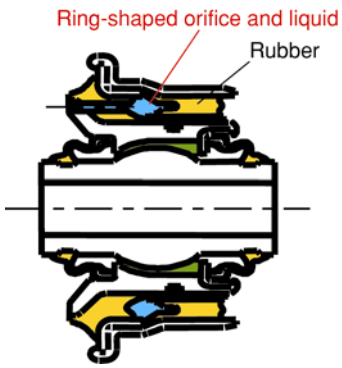


Fig. 21 Structure of hydro bush (front upper arm)

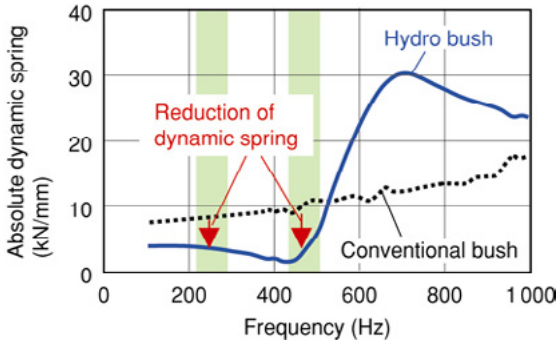


Fig. 22 Dynamic spring of front upper arm bush

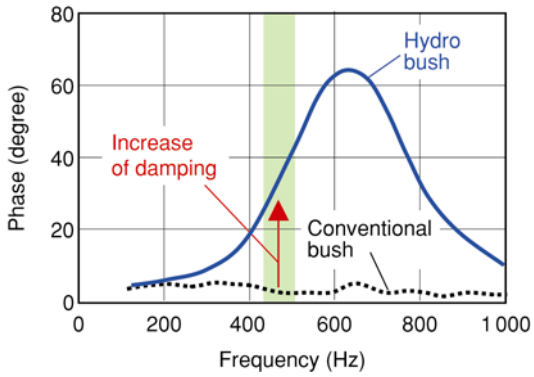


Fig. 23 Damping of front upper arm bush

Therefore, a ring-shaped orifice was used as shown in Fig. 21, and this was given both piston functions for pressurizing the fluid and orifice functions. This made it possible to set the resonance of the fluid in the orifice at 600 Hz, and to achieve the ideal characteristics of low dynamic stiffness and high damping in the 500 Hz range. In addition, the dynamic stiffness could also be reduced in the tire cavity resonance range. (Fig. 22, Fig. 23)

3.6. Effects on Vehicle Test

The newly developed hydro bushes were assembled into a vehicle, and the effects were confirmed. As shown in Fig. 24, a reduction of the sound pressure in the 250 Hz and 500 Hz ranges was confirmed.

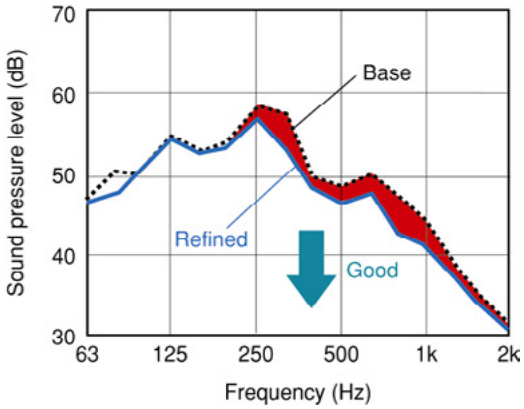


Fig. 24 Effect of road noise refine

4. Conclusion

The suspension behavior was analyzed in detail regarding harshness and road noise, and hydro bushes with new structures were developed based on these results. Through this development, the following knowledge was obtained.

(1) Body vibration when passing over stepped road joints is affected in the vertical direction by the unsprung vertical resonance and the tire enveloping characteristics, and in the longitudinal direction by the compliance resonance and the tire longitudinal resonance. Reducing the transmission of these resonance phenomena is an effective countermeasure for reducing harshness.

(2) Factors contributing to road noise include suspension vibration caused by tire cavity resonance, and the rigid-body and elastic modes of the arms. Reducing the dynamic stiffness of the bush is an effective countermeasure for the former, and increasing the damping and reducing the dynamic stiffness of the bush in the rigid-body and elastic modes of the arms is an effective countermeasure for the latter.

(3) Longitudinal body vibration over stepped road joints can be reduced and harshness can be improved (reduction of maximum longitudinal body acceleration and improvement of decay) by giving the right and left hydro compliance bushes different dynamic characteristics and controlling the phase of the transmission.

(4) The force transmission and the arm resonance phenomenon could be reduced and road noise could be improved by introducing new hydro structures (double orifice, ring-shaped orifice) for the trailing arm and front upper arm bushes.

This project was able to provide a glimpse of the potential for improving NVH product appeal by applying hydro bush technology to the suspension system.

On the other hand, the suspension system has many limitations such as endurance reliability, production technology and space layout, and there are currently few cases of hydro bushes being applied to mass production vehicles.

In addition to research on methods for utilizing the features of hydro bushes, research to resolve these hardware issues is also considered necessary as a future theme. Hydro bushes have great potential for improving NVH product appeal, and research in this area is expected to expand in the future in order to create even more attractive products (vehicles).

Acknowledgments

The authors wish to express their deep thanks to Hokushin Corporation, Tokai Rubber Industries Ltd., Yamashita Rubber Co., Ltd. and all related parties for their cooperation with this project.

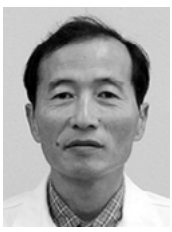
References

(1) Minakawa, M. et al.: A vibration transfer reduction technique by use of method of measuring force transmitted from road surface to tire, JSAE, Vol. 54, No. 11, p. 21-26 (2000)

(2) Sano, H. et al.: Low order modeling of an acoustic path for active noise control and design method of feedback control, HONDA R&D Technical Review, Vol. 12, No. 1. P. 129-136 (2000)

(3) Miyagishima, Y.: Introduction to a proving center in North America, JSAE, Vol. 54, No. 6, p. 13-17 (2000)

■ Authors ■



Yasuo MIYAMOTO



Sou NAKAMURA

Improvement of Dynamic Spring Characteristics of Engine Mounts with Non-combination Type Dynamic Damper

Hitoshi NAITOH*

ABSTRACT

Cabin noise originating in the power plant has been reduced by utilizing non-combination type dynamic dampers to reduce the absolute value of the complex spring constant (K*) of the engine mounts in the high-frequency range.

Development first employed simulations, which demonstrated the superiority of the non-combination type to the combination type dynamic dampers. Next, the study focused on how best to exploit the structural characteristics of non-combination type dynamic dampers to enable them to be applied to the rubber parts of the engine mount. Single non-combination type dynamic damper units have been shown to control increases in K* caused by rubber surging and mount bracket resonance. Cabin noise in a completed vehicle has been also reduced. Finally, it has been confirmed that the targeted durability can be kept even with the use of the dynamic dampers on the rubber parts of the engine mount.

1. Introduction

Customer requirements with respect to the comfort of automotive cabins are continually increasing, and the targets for in-cabin quietness are consequently being raised. At the same time, there are demands for vehicles to be made lighter as a means of responding to environmental issues, and to achieve this the thickness of component panels is being reduced and aluminum and other lightweight materials are beginning to replace steel. Lower weight generally means lower rigidity, and this tends to lead to increases in-cabin noise and vibration. Lightweight damping and soundproofing materials have been developed to prevent this, but preventive measures which concentrate on automotive panels having a large area are rather inefficient from a weight efficiency perspective, and other preventive measures which focus on the sources of noise and vibration can be considered more fundamental.

Of the various forms of in-cabin noise and vibration, the research discussed in this paper targeted those generated by vibration in the power plant, and tested the effectiveness of a lightweight engine mount structure in ensuring the quietness of the cabin by reducing the vibration transmitted to the chassis by the power plant. The results of this research are presented below.

2. Research Goals

One of the factors present in the transfer paths of vibration originating in the power plant to the body panels that causes the amount of vibration to increase is rubber surging in the engine mounts. Rubber surging is resonance generated in the rubber sections themselves. The absolute value of the complex spring constant (K*), increases in the frequency range of this resonance, increasing the vibration transmissibility from the power plant to the chassis. As a

* Tochigi R&D Center

result, the level of noise and vibration in the cabin increases. The aim of the research discussed here was to reduce the increase in vibration input caused by rubber surging in the engine mounts with a lighter-weight countermeasure than conventionally used.

To date, when rubber surging has become an issue, various countermeasures have been available, such as positioning plate-shaped objects called intermediate plates in the center of the rubber sections. However, these conventional measures simply shift the frequency of the surging. After this shift in frequency, noise and vibration in the cabin increases correspondingly in the new frequency range. The use of combination type dynamic dampers is also possible, but these have the same effect, causing K* to peak at frequencies higher and lower than the initial surging frequency[1]. Rather than conventional combination type dynamic dampers, this research project therefore utilized improved non-combination type dynamic dampers to attempt to control the increase in K* caused by rubber surging in the target frequency range.

3. Overview of Non-combination Type Dynamic Dampers

Figure 1 shows the structures of the non-combination type dynamic damper used in this research project and the conventionally used combination type dynamic damper. The non-combination type dynamic damper is a two-part structure, consisting of an added mass covered by an elastic material and a surrounding housing. The added mass of the conventional dynamic damper is connected to the target of vibration reduction by rubber or some other elastic substance. In the non-combination type, the added mass is covered in an elastic material, but this is not connected to the target of vibration reduction. This added mass can move freely in the housing which covers it to prevent it flying off.

In addition to producing the same damping effect by combination type dynamic dampers, this structure enables the vibration response peaks generated as a result of the use of dynamic dampers to be reduced. Figure 2 shows a two degree of freedom spring-mass model with a non-combination type dynamic damper, and Fig. 3 shows the results of a simulation employed to confirm its vibration reduction effect[2]. Here, the target of vibration control is M1; the base section is excited at a constant amplitude of acceleration and the amplitude of response acceleration in M1 is compared without a damper, with a combination type dynamic damper and with a non-combination type dynamic damper. The specifications of the dynamic dampers were established to reduce the peak occurring at around 1 000 Hz when no damper was used. As Fig. 3 shows, in comparison with the effect of the combination type damper in reducing the peak at 1 000 Hz, the use of the non-combination type dynamic damper reduced the peak occurring at around 650 Hz due to the use of the combination type damper, and as a result there is a virtually flat response, without the two peaks occurring when dynamic dampers are not utilized.

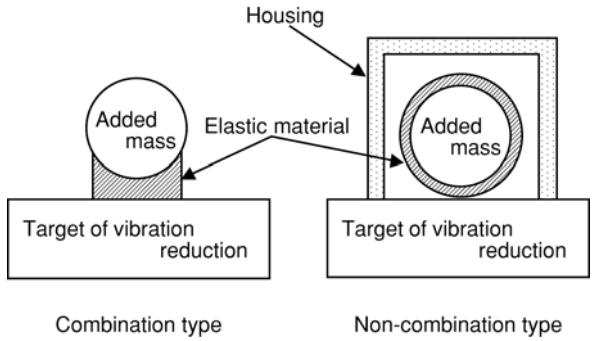


Fig. 1 Examples of dynamic damper structures

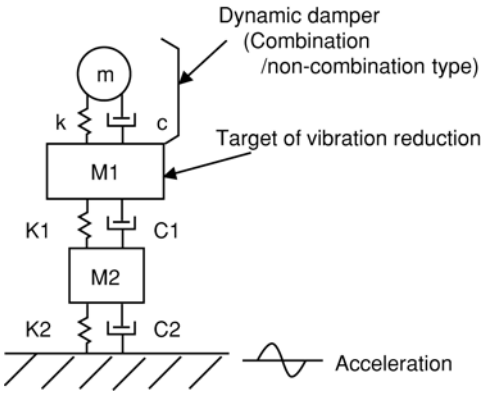


Fig. 2 Analytical spring-mass model of two degrees of freedom

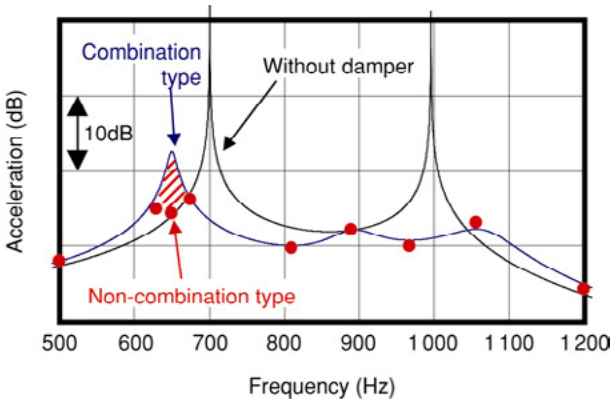


Fig. 3 Comparison of vibration reduction effect

4. Application to Engine Mounts

While continuing to investigate the characteristics of non-combination type dynamic dampers, in which the added mass is contained within a housing, research focused on a type of engine mount in current use, and tested the effectiveness of the damper when applied to it. To exclude the effect of the natural vibration of the bracket attached to the chassis, a bush type engine mount with a circular bracket was produced. Tests were conducted with this as the base component. Figure 4 shows a schematic view of this engine mount, and Fig. 5 shows its dynamic spring characteristics. This shape is very commonly used in engine mounts. Measuring K* in a vertical direction when the engine mount is excited at a constant amplitude of acceleration enables evaluation of the dynamic spring characteristic.

As can be seen in Fig. 5, this engine mount demonstrates rubber surging at around 740 Hz, and K* peaks in that

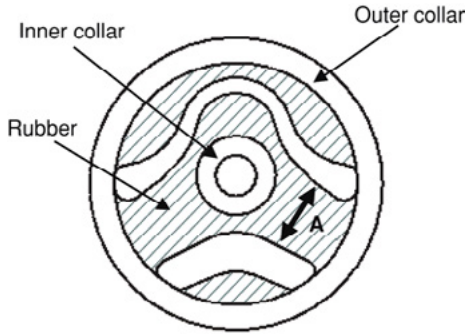


Fig. 4 Schematic view of engine mount

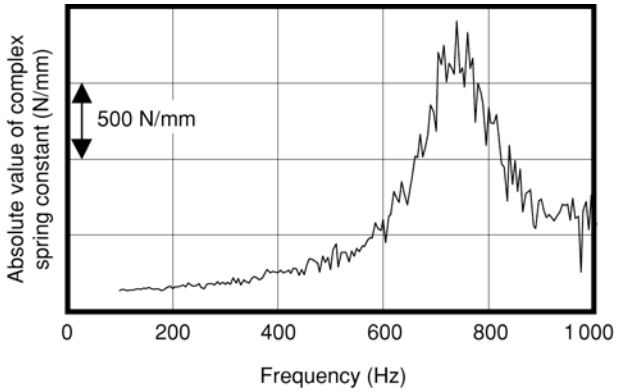


Fig. 5 Absolute value of complex spring constant

frequency range. This rubber surging is thought to be a first—order resonance generated when the inner and outer collars at the ends of the rubber section are fixed. Positioning a non-combination type dynamic damper at the center of the rubber section was judged to be effective in reducing this resonance response. Considerations of ensuring durability in the rubber sections towards displacement generated by the power plant led to the selection of a round pipe housing in which stress would not concentrate, which was vulcanized into the center of the rubber section. The added mass was made cylindrical to match the shape of the space inside the housing, and both ends of the housing were plugged to prevent it from flying out. Because the direction of displacement of the first-order resonance mode of the target rubber section is basically the direction shown as A in the cross-section in Fig. 4, the outer circumference of the added mass was covered in an elastic material. Figure 6 shows a cross-section of the structure of this non-combination type dynamic damper, and Fig. 7 shows the engine mount after application of the damper.

This structure is effective because the added mass is covered in an elastic material and fitted inside a housing rather than being connected to the target of vibration reduction by an elastic material. For example, when rubber is used as the elastic material, a thickness of 3 mm is required in the rubber section to ensure the strength of the metal mold forming the section, and it is not possible to fit a combination type dynamic damper in the same space. The possibility of size reduction is another characteristic of non-combination type dynamic dampers, which is not shared by combination type dynamic dampers.

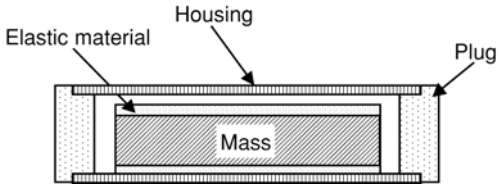


Fig. 6 Section of non-combination type dynamic damper structure

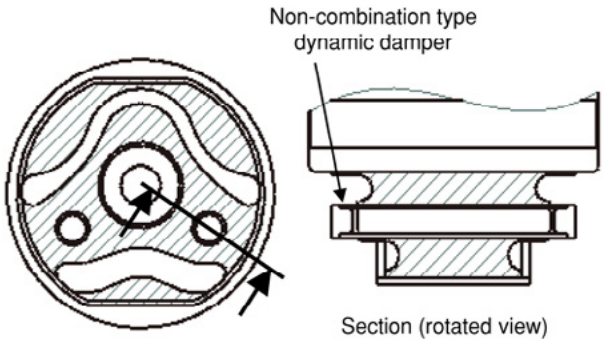


Fig. 7 Non-combination type dynamic damper applied to engine mount

5. Results of Confirmation of Unit Characteristics

5.1. Characteristics of the Bush Type Engine Mount

Unit characteristics were measured using the bush type mount employed to neutralize the effect of the natural vibration of the bracket. Measurements were taken using the mount as shown in Fig. 4 (in isolation) and Fig. 7 (with attached non-combination type dynamic damper). The range of frequencies for evaluation of the dynamic spring characteristics was 100 Hz to 1 000 Hz, the range which is particularly problematic for cabin noise originating in the power plant when the vehicle accelerates. The static spring constant was equivalent in both mounts.

5.1.1. Dynamic spring characteristics

In addition to testing with and without the non-combination type dynamic damper, the type of a damper shown in Fig. 7 without the added mass was used in order to

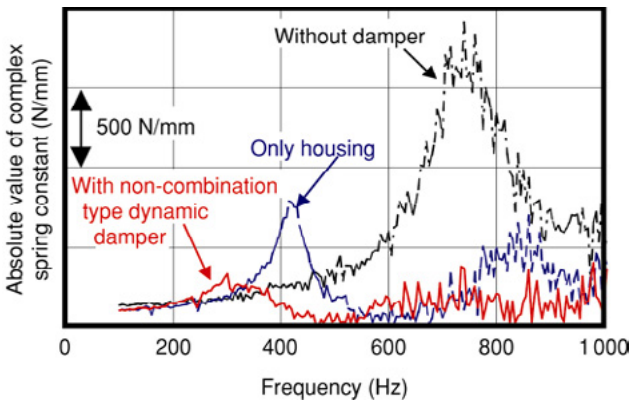


Fig. 8 Comparison of effect of reduction of absolute value of complex spring constant

test the characteristics when a mass is added as when employing an intermediate plate. K* was measured in a vertical direction. The fixed amplitude of acceleration utilized in the measurement of K* was the same as used in the previous measurements. Measurement results are shown in Fig. 8. As this graph shows, the peak around 740 Hz is reduced when the housing only is used, but this generates two new peaks, around 420 Hz and 860 Hz. By contrast, the damper with the built-in mass does not generate a noticeable peak and shows a virtually flat characteristic in the target frequency range.

5.1.2. Comparison with hydraulic engine mounts

A comparison was done of the absolute value of complex spring constants in a currently used (bush type) hydraulic engine mount and of the engine mount employing a non-combination type dynamic damper described above. Hydraulic engine mounts are utilized to reduce K*. A schematic of the hydraulic engine mount used in the comparisons is shown in Fig. 9. When the comparison tests were conducted, the hardness of the rubber in the engine mount employing the dynamic damper was altered to make its static spring constant in a vertical direction to match that of the hydraulic engine mount.

The results of measurements of K* are shown in Fig. 10. A constant amplitude of acceleration was utilized for excitation when measurements were taken. As can be seen in the graph, the hydraulic engine mount shows peaks at around 460 Hz and 750 Hz, while the engine mount employing the non-combination type dynamic damper demonstrates a flat response with no conspicuous peaks. The engine mount with the dynamic damper reduces K* to a lower level than the hydraulic mount across virtually the entire frequency range.

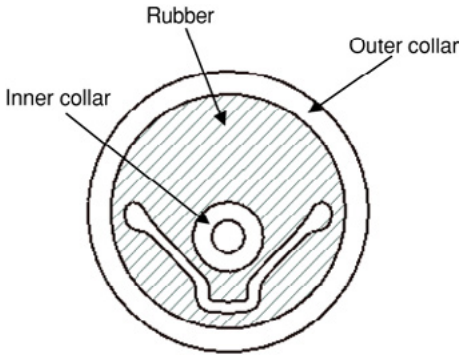


Fig. 9 Hydraulic engine mount

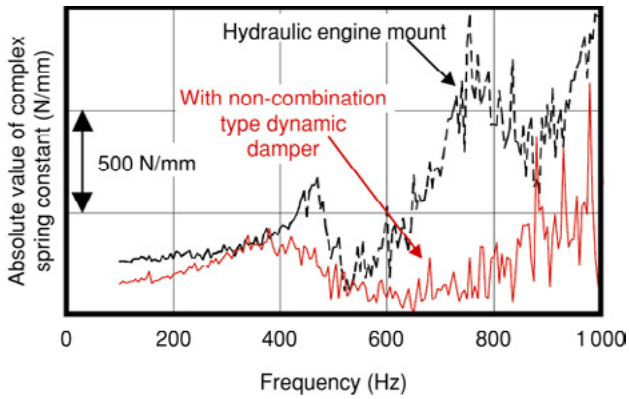


Fig. 10 Effect of reduction of absolute value of complex spring constant

5.2. Dynamic Spring Characteristics of Completed Product

K* of the bush type engine mount described above was measured in the mount when pressed into the bracket connecting to the chassis, as when used in a vehicle. A comparison was conducted of performance with and without the non-combination type dynamic damper. Figure 11 shows the engine mount with the damper applied. The same type of mount was used in tests without the dynamic damper. The results of measurements of K* are shown in Fig. 12. The test piece was excited with a constant amplitude of acceleration during these measurements.

The graph shows that when the non-combination type dynamic damper was not used, K* peaked at around 700 Hz due to rubber surging and at around 1 000 Hz due to resonance in the connecting bracket. However, when the dynamic damper was utilized, the level of both these peaks was reduced, and a virtually flat characteristic was obtained in the target frequency range.

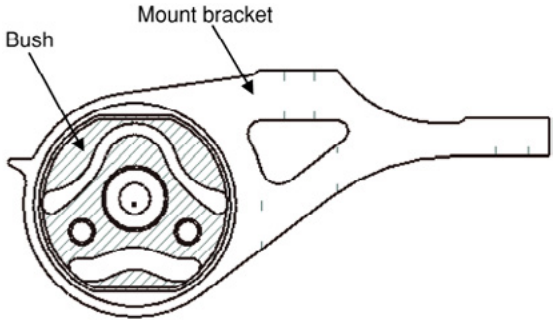


Fig. 11 Engine mount with non-combination type dynamic damper

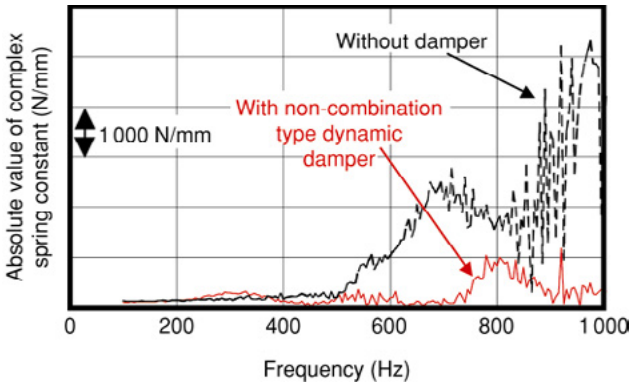


Fig.12 Effect of reduction of absolute value of complex spring constant

6. Results of Vehicle Performance Tests

The engine mounts described above were fitted in a vehicle, and the level of quietness in the cabin was compared with and without the non-combination type dynamic damper. Evaluation criteria were the vibrational acceleration at the engine mount points and sound pressure level in the center of the cabin while the engine was idling. The respective measurement results are shown in Figs. 13 and 14. The horizontal axes of the graphs show the central frequencies in the 1/3 octave band. Figures 12 to 14 show that the

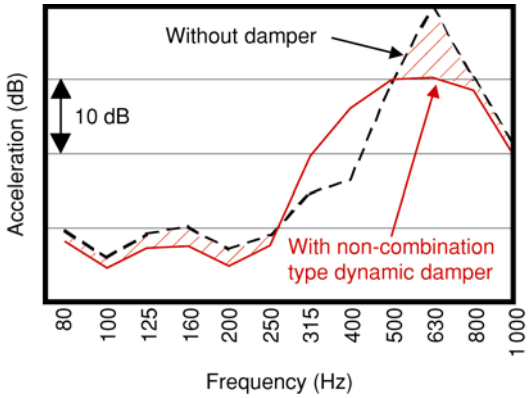


Fig. 13 Effect of reduction of vibration of engine mount point of body side

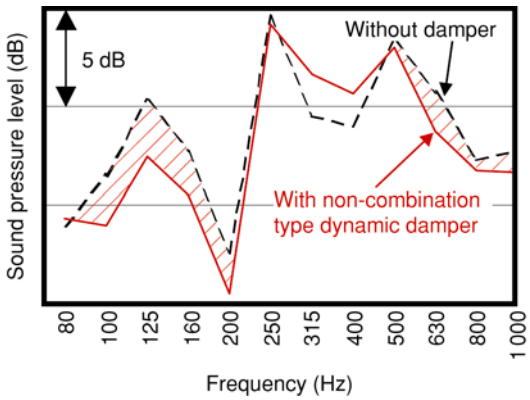


Fig. 14 Effect of reduction of sound pressure of interior noise

vibrational acceleration of the engine mount points has been reduced in the frequency range in which K* has been reduced, and the sound pressure level in the center of the cabin has consequently been reduced.

7. Results of Unit Durability Tests

To evaluate the durability of the rubber section due to displacement from the power plant when a non-combination type dynamic damper unit is fitted, unit durability tests were conducted using identical excitation conditions to those utilized in current tests of mass production units. Figure 15 shows the appearance of the engine mount after the completion of tests. The tests confirmed that no cracks or similar deviations occurred in the rubber section.



Fig. 15 Engine mount after endurance test

8. Conclusion

Research was conducted on the use of non-combination type dynamic dampers to reduce the level of increase of K* caused by rubber surging in the engine mounts, in order to reduce noise and vibration in vehicle cabins. Unit tests and vehicle tests were conducted to verify the effectiveness of the dynamic damper. The following outcomes were generated by the research:

(1) In comparison with a combination type dynamic damper, it was shown that the non-combination type dynamic damper reduced response peaks without increasing vibration in other frequency ranges.

(2) A structure employing a non-combination type dynamic damper was proposed as a measure to control rubber surging in the engine mount.

(3) The application of a non-combination type dynamic damper to the rubber section of an engine mount significantly reduced K* in the target frequency range and produced a virtually flat response characteristic compared to the base product. The non-combination type dynamic damper also achieved superior results to a hydraulic engine mount employing a structure designed to reduce K* in the target frequency range.

(4) When the engine mounts fitted with non-combination type dynamic dampers were employed in a vehicle, the vibrational acceleration at the engine mount points was reduced in the frequency range in which K* was reduced. Consequently, the sound pressure level in the center of the cabin was reduced.

(5) It was confirmed that unit durability requirements due to displacement originating in the power plant were satisfied even when a non-combination type dynamic damper was fitted to the rubber sections of the engine mount.

Acknowledgments

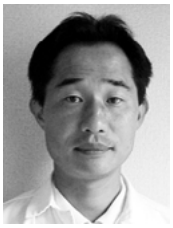
The authors wish to take this opportunity to offer their sincere thanks to the many individuals who assisted them in this project, in particular to all concerned at Tokai Rubber Industries, Ltd.

References

(1) Taniguchi, O., et al.: Forced Vibrations in Systems with Two Degrees of Freedom, Vibrational Engineering Handbook, Yokendo, p. 132 - 136 (1991)

(2) Aida, S., et al.: Vibration in Systems with Multiple Degrees of Freedom, Mechanical Engineering Handbook, Tokyo, The Japan Society of Mechanical Engineers, p. 43 - 47 (1987)

■ Author ■



Hitoshi NAITOH

Study of Sound Isolation Structure for Engine Generators

Toru FUKUDA* Katsumi MARUYAMA*
Kazuhito TAKEMURA* Shinichi SUZUKI*

ABSTRACT

In the development of sound isolation type generators, a three-division case structure divided into two cool zones and one hot zone was studied. This study was aimed at achieving compatibility between sound isolation and cooling capabilities that are in a trade-off relationship. Sound isolation of 12.1 dB(A) was achieved by this structure, while obtaining equivalent cooling capabilities to that of open frame type generators. As a result of adopting this new generator structure for India domestic consumption, the Indian noise regulation phase II was achieved for the first time by a mass produced generator.

1. Introduction

As generators are used at any time of the day or night — in the fields of leisure and construction, for business use in worksites, etc., or for emergency backup power — there has long been a strong demand for sound isolation. In recent years there has been an increasing demand for inverter generators that control engine speed according to electrical load, and for sound isolation type generators with an engine and alternator covered by a case. Moreover, reflecting the market demand for sound isolation, many countries and regions have enacted strict sound isolation regulations regarding generators. For instance, the EU has issued 2002/2006 regulations, and India has issued 2002/2003 regulations.

Generally, the following two types of sound isolation methods are employed with generators.

1) Methods to reduce the noise created by the source — engine, alternator, air cleaner, and muffler.
2) Methods to reduce the noise emitted from the source — engine, alternator, air cleaner, and muffler — by covering them with a case.

Of these two, the sound isolation type generator (2) shows a tradeoff relationship between sound isolation and cooling capability. For instance, if there are openings in a casing to introduce cooling air, the area of the openings must be as large as possible to improve cooling capability, but at the same time noise can be emitted through those openings.

Therefore, a case structure for the sound isolation type generator was adopted that achieves both an advanced sound isolation effect and sufficient cooling capability. This paper gives an overview of a case structure and examines its sound isolation effect and cooling capability by using the example of an open frame cylindrical alternator generator's sound isolation.

2. Development Goals

Representative generators are shown in Fig. 1.

1) Open Frame Type (Pipe Frame Structure)
   The engine and a cylindrical or integrated winding alternator are mounted to a pipe frame.
2) Inverter and Sound Isolation Type

* Asakahigashi R&D Center

The engine and multi-polar alternator are placed inside a case[1].

3) Sound Isolation Type
The engine and a cylindrical or integrated winding alternator are placed inside a case.



Fig. 1 Typical structure of engine generators

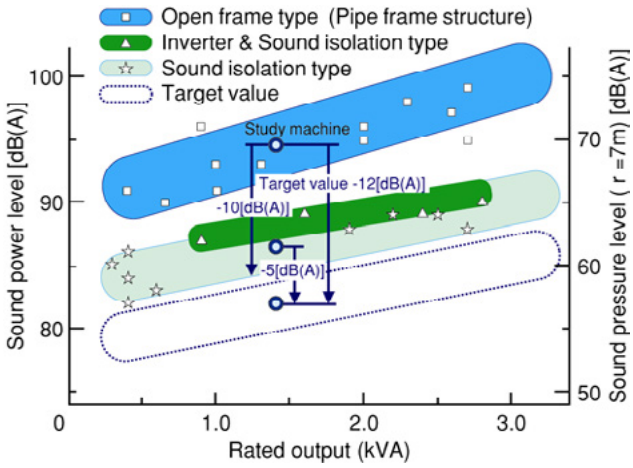


Fig. 2 Noise value according to type

The noise values at a rated power of 3 kVA or less (when rated power is 3/4) are shown in Fig. 2 according to type. The left vertical axis is the sound power level (Lw), which expresses the sound output from the generator (source of noise). The right vertical axis is the sound pressure level (Lp) at a point 7 m from the generator. The relationship between Lw and Lp is shown in Equation 1, with the generator placed on the ground in an ideal half-free sound field, therefore, Lp = Lw – 25 [dB(A)].

$$Lp = Lw - 20 \log_{10} r - 8 \quad (1)$$

For reference, sound pressure levels[2] in ordinary living environments are shown in Table 1.

Table 1 Sound pressure level in a living environment

80 dB(A)	Subway in the car
70 dB(A)	Bell of a telephone, Loud street
60 dB(A)	Quiet passenger car, Ordinary conversation
50 dB(A)	Quiet office

The target when applying sound insulation to the open frame type has been set as –12 dB(A)[3] based on the following points.

1) In comparison with the open frame type, there must be a reduction of –10 dB(A) or more, at which level, the average human being feels the noise reduced by 1/2.
2) In comparison with conventional sound isolation types, there must be a reduction of –5 dB(A) or more, at which the average human being clearly recognizes sound isolation.

The target value positioning is shown in Fig. 2, in the same manner.

Figures 3, 4, and 5 show the flow of cooling air and engine exhaust for each representative type generator. The cooling capability is evaluated according to temperatures of various parts of the generator including: oil temperature, spark plug seat temperature, and fuel temperature inside the carburetor. The target temperature for each part was set at the level of the existing generator.

The issues of sound isolation and cooling capability with the existing sound isolation type generator arise from the fact that the structure is essentially an open frame type (Fig. 3) enclosed in a case. As for noise, the major source of noise is the direct exhaust of the engine's combustion gases, which is also true of the inverter and sound insulation type shown in Fig. 4. As for cooling capability, there is a rise in temperature inside the case due to the retention of cooling air duct surface heat and air leaking from gaps in the duct joints. At the same time, heat is recirculated to cooling air inlets, resulting in a drop in cooling efficiency. Furthermore, after operation has stopped, because the height difference between the cooling air outlet and inlet is relatively small, cooling through natural convection inside the cooling air ducts does not occur, and the temperature inside the case rises due to residual heat.

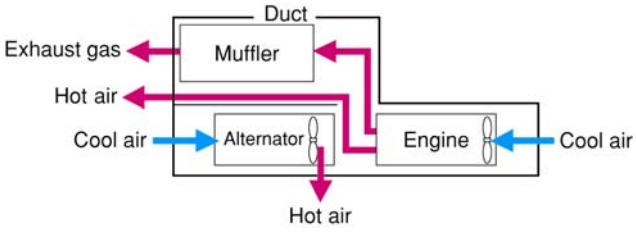


Fig. 3 Open frame type (Pipe frame structure)

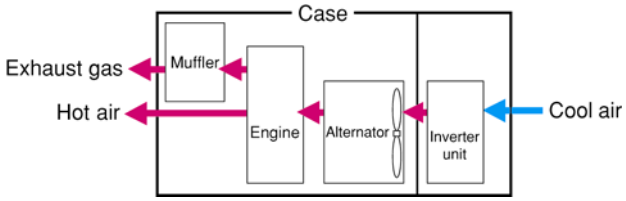


Fig. 4 Inverter & Sound isolation type

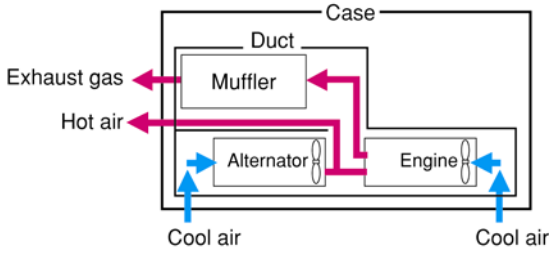


Fig. 5 Sound isolation type

In order to resolve these issues with the conventional sound isolation type, a new structure was studied, considering the following points in terms of sound isolation and cooling capability.

The main sound isolation points were as follows.

1) Engine exhaust gases are emitted through indirect exhaust, reducing exhaust noise.
2) Cooling air ducts are made long, and noise absorption material is placed inside the ducts, to attenuate noise.
3) The opening area of the cooling air inlet is made as small as possible to minimize noise leakage.

The main cooling capability points were as follows.

1) A simple divided structure with a seal effect was used to completely separate cool zones and hot zones inside the case. This prevents retention and recirculation of heat due to thermal transmission.
2) The height difference of cooling air outlets and inlets is maximized, creating sufficient cooling through natural convection, thereby minimizing a temperature rise when stopped.
3) Cooling air flow path obstructions are reduced, maintaining sufficient cooling air volumes.

3. Sound Isolation Technologies

3. 1.Case Structure

A new case structure was proposed based on the main points in sound isolation and cooling capability noted above. Figure 6 shows the flow of cooling air and engine exhaust inside the case. An overview is given below.

1) The case is divided into 3 sections internally by vertical dividers. The dividers completely separate the central hot zone from the cool zones on either side. The hot zone contains the engine, alternator, and muffler, while the cool zones contain the air cleaner, carburetor, fuel tank, battery, and electrical parts.
2) On top of the central hot zone is a silencing chamber, and the muffler's exhaust gas is exhausted indirectly through this.
3) The cooling air inlets are in the bottom plate, and the exhaust outlet is on the top of the case.

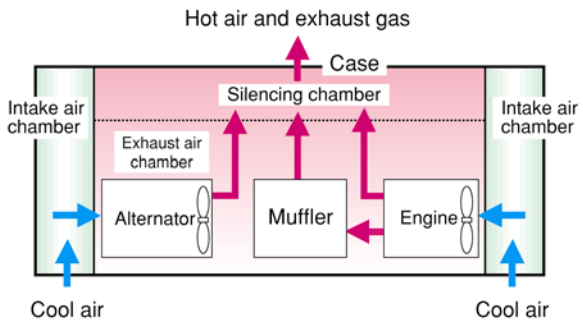


Fig. 6 New sound isolation type

3.2. Confirmation of Sound Isolation Effect

The sound isolation effect was confirmed using a prototype with a 3-section case structure.

Figure 7 shows the level of sound isolation effect in each chamber, using the 3-section structure. In total, the sound reduction effect was 12.1 dB(A).

The spec is explained from the left (the numerical values are the sound power level).

1) Engine and alternator only (same level as the open frame type). [94.1 dB(A)]
   This shows the state before being enclosed by the case.
2) Addition of hot zone exhaust chamber. [–5.6 dB(A)]
   This shows the noise source sound insulation effect.
3) Addition of a separated silencer chamber above the exhaust chamber. [–0.9 dB(A)]
   This shows the further sound absorbing effect of the indirect exhaust and the longer exhaust path.
4) Addition of an intake air chamber on the engine side. [–4.8 dB(A)]
   This shows the effect of isolation from the air intake noise of the air cleaner and recoil starter, and from noise in the hot zone leaked from the divider walls.
5) Addition of an intake air chamber on the alternator side. [–0.6 dB(A)]
   This shows the effect of isolation from the alternator air intake noise, and from noise in the hot zone leaked from the divider walls.

Moreover, a sound absorbing and heat insulating material is attached to the hot zone within the case, and sound-absorbing material is also placed in the cool zones. In order to determine the contribution rate of a case without the heat-insulating and sound-absorbing material for sound isolation, noise measurements were taken both with and without the heat-insulating, noise-absorbing material. As shown in Fig. 8, the results show a reduction of 6.3 dB (A) with the case structure, which is equivalent to 52% of the total sound isolation effect of 12.1dB (A). This shows that even without the heat-insulating noise-absorbing material, it is possible to achieve a noise level that is on a par with the conventional sound isolation type.

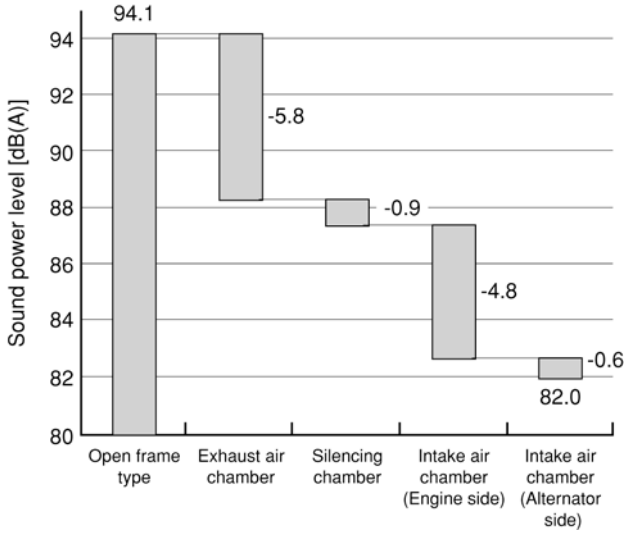


Fig. 7 Effect according chamber

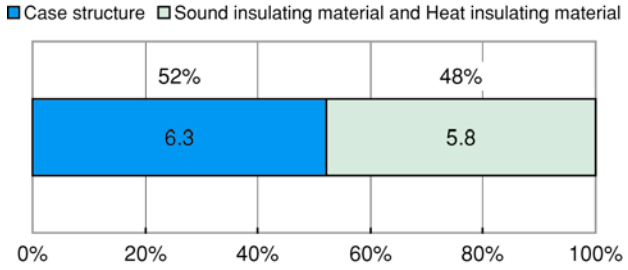


Fig. 8 Effect according chamber

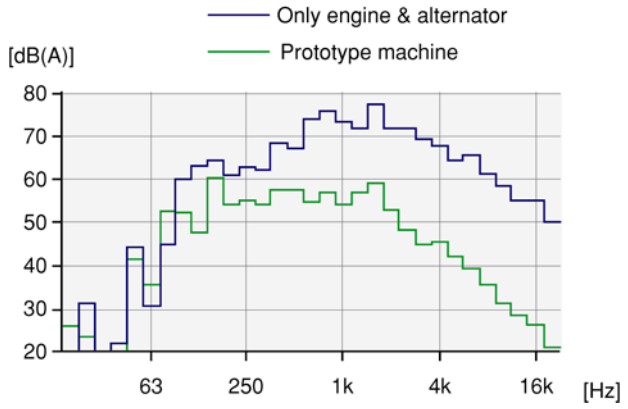


Fig. 9 Frequency analysis result

In addition, Fig. 9 shows the results of frequency analysis during rated load operation. (The location of the measurement microphone is 2 m from the generator.) In comparison with the engine and alternator only, the prototype unit demonstrates a sound isolation of 250 Hz or more at all frequencies.

3.3. Cooling Air Volume

3.3.1. Estimating the required cooling air volume

In order to make cooling capability feasible, the cooling fan air volume required for the 3-section structure to maintain output equivalent to the open frame type was estimated.

Taking the amount of heat of the fuel as Qk,

$$Qk = Qp + Qg + Qc + Qw^{(4)} \quad (2)$$

Qp : Generator power
Qg : Amount of exhaust gas heat
Qw : Amount of heat by which the cooling air is warmed
Qc : Heat generated from the hot zone

Here,

$$Qk = H \times Fc \quad (3)$$
$$Qg = \Delta Tg \times \rho(T) \times C(T) \times V \times N \times \eta_v \quad (4)$$
$$Qw = W \times \rho(T) \times C(T) \times \Delta T1 \quad (5)$$

H : Fuel lower calorific value
Fc : Prototype engine's fuel consumption rate
ΔTg : Exhaust temperature rise from the temperature of the prototype muffler's cool zone
ρ : Air density
C : Specific heat of air
V : Prototype engine's displacement
N : Engine speed
W : Cooling fan air volume
ΔT1 : Temperature rise from the temperature of the cooling air's cool zone
η_v : Charging efficiency

The temperature of the cooling air discharged from the engine must be 80 °C or less, as determined by the heat resistance temperature of the wire harness in the hot zone, and the outside temperature is assumed to be 40 °C.

Qc consists of the amount of heat exhausted to the outside of the engine immediately from the hot zone, and of heat exhausted into the cool zone through the barrier wall.

$$Qc = Q1 + Q2 \quad (6)$$

Q1 : Amount of heat exhausted outside immediately from the hot zone
Q2 : Amount of heat exhausted into the cool zone through the separator

In order to prevent a rise in temperature of the case surface and thermal transmission to the cool zone, heat-insulating material is applied to each of the hot zone surfaces, as noted in Table 2.

Table 2 Heat insulating material

Front / Top / Rear face	With heat insulating material
Bottom surface	With no heat insulating material
Separator	With heat insulating material to one half

Here, with a steel plate thermal conductivity of 80 (W/mK) and an insulation material thermal conductivity of 0.04 (W/mK), and considering the insulation material's area ratio, it can be assumed that almost all the heat transmitted from the hot zone to the cool zone is transferred to the cooling air. Therefore,

$$Q2 = \rho(T) \times C(T) \times W \times \Delta T2 \fallingdotseq 0.50 \times Qc \quad (7)$$

ΔT2: Temperature rise in inlet cooling air

Figure 10 shows the relationship between cooling air volume and ΔT2. According to the open frame type data, when the target is ΔT2 = 5 °C, air volume W is approximately 5.5 (m^3/min).

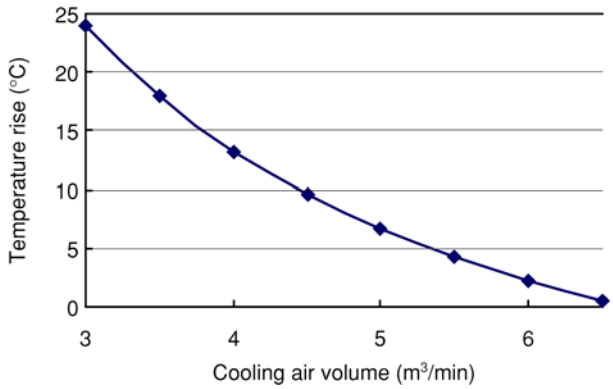


Fig. 10 Relation between temperature rises and cooling air volume

3.3.2. Confirmation of cooling air volume

Table 3 shows the results of the intake air temperature measured by the prototype unit at an air volume of 5.5 (m^3/min). The alternator intake air temperature near the muffler was high, but other values were close to those of the open frame type. In addition, in order to evaluate the cooling capability, the results of the temperature measurements for the main parts must be considered. Table 4 identifies the results. Although slightly higher than with an open frame type, all are within the requirement limits.

Table 3 Intake air temperature

Intake air temperature	Open frame type (°C)	Prototype machine (°C)
Air cleaner	43	43
Recoil	43	46
Alternator	42	49

<ambient temperature : 40°C>

Table 4 Main parts temperature

Main parts temperature	Open frame type (°C)	Prototype machine (°C)
Oil	112	115
Plug seat	222	235
Carburetor gas	52	45
Main winding	90	100

<ambient temperature : 40°C>

4. Application on Generators for the Domestic Market in India

4.1. Background to Indian Noise Regulations

Most of the generator use in India is for emergency use during frequent power outages. The electrical power supply in India has not kept pace with economic growth. Per capita capacity of electrical generation facilities in India is 1/20th that of Japan, and comparing cities, Delhi has a capacity of approximately 1/40th that of Tokyo. In addition, due to poor transmission power networks and facilities, there is a transmission loss of approximately 45%. Therefore, power outages are chronic throughout the country. Generators used by individuals, shops, and small-scale offices, which account for 80% of generator users, begin operating simultaneously when power outages occur, so particularly in cities, generator noise and exhaust are large social concerns.

Therefore, the India government has enacted laws restricting the noise and exhaust gas emission from gasoline and kerosene powered generators.

Table 5 gives the specifics of timing and noise levels in the noise regulations.

Table 5 Noise limit for generator

	Phase Ⅰ	Phase Ⅱ
Application date	September, 2002	September, 2003
Sound power level (L_{WA})	90 dB(A)	86 dB(A)

4.2. Application to the EXK2000 (new sound isolation type generator)

The EXK2000 was developed, adopting the new 3-section structure. In addition to maintaining a cooling capability on a par with the open frame type, the new structure gives a noise value of 82.5 dB(A), which is an 11.6 dB(A) noise reduction in comparison with the open frame type EBK2000's 94.1 dB(A). The structure of the EXK2000 is given in Fig. 11, the external appearance is shown in Fig. 12, and the major specifications are given in Table 6.

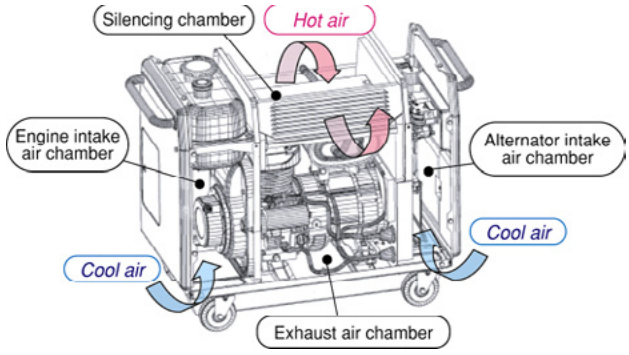


Fig. 11 Configuration of EXK2000



Fig. 12 EXK2000

Table 6 Major specifications

Model		EXK2000
Engine	Type	4-stroke SV
	Displacement (cm^3)	197
	Speed (rpm)	3 000
Alternator	Type	Cylindrical type
	AC frequency (Hz)	50
	Max AC output (VA)	1 600
	Rated AC output (VA)	1 400
	DC output	12V-8.3A
Dimensions	Dimensions L × W × H(mm)	890 × 430 × 685
	Dry weight (kg)	76
	Sound power level [dB (A)]	82.5

5. Conclusion

The following results were achieved through research into sound isolation technologies for engine generators.

1) It was verified that by adopting a new 3-section structure for a sound isolation type generator, cooling capability equal to that of the open frame type is maintained while achieving sound isolation that is equal to or better than that of the conventional sound isolation type generator.
2) Applied to the EXK2000, it was possible to obtain approval for Phase II of India's noise restrictions, considered the world's strictest. This was the first generator in the world to meet India's Phase II requirements.
   In addition, by adopting the 3-section structure to models with different output, both EXK1200 and EXK2800 were also able to obtain approval for Phase II of the noise restrictions.
3) By adopting the same structure, output equivalent to the open frame type generator can be maintained, and it is possible to change to the sound isolating spec.

Acknowledgements

The authors would like to take this opportunity to express their gratitude to the many people, both within their company and beyond, for their support and cooperation in this research and development project.

References

(1) Tanaka, Y., Kawauchi, T., Ito, K., Nakamura, M.: Development of the Light-weight and Compact Portable Generator - GENE21 Series, HONDA R&D Technical Review, Vol. 11, No. 2, p. 15-22 (1999)

(2) Department of Environment and Disaster Services, Environmental Policy Division, Saitama Prefectural Government: 1999 White Paper on the Environment in Saitama, Saitama, p. 103-114 (1999)

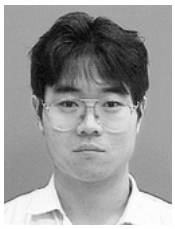
(3) The Japan Society of Mechanical Engineers: Mechanical Noise Handbook, Tokyo, Sangyo Tosho, p. 29-30 (1991)

(4) Kitamura, K., Otake, K.: Fundamental Heat Transfer Engineering, Tokyo, Kyoritsu Shuppan, p. 12-29 (1991)

■ Authors ■



Toru FUKUDA



Katsumi MARUYAMA



Kazuhito TAKEMURA



Shinichi SUZUKI

Heat Radiation Analysis Based on Internal Flows of Radiator

Takashi WATANABE* Masayuki IWATA*

ABSTRACT

Rectangular-shaped radiators for motorcycles have been used previously in many cases. With the latest high-powered engines, the use of any shaped radiators is increasing to get high heat radiation within a limited space. This type of radiator has different cooling tube lengths. It is more difficult to predict the heat radiation amount for this type as compared to rectangular types, as velocity distribution is uneven. Moreover, a sufficient analysis regarding heat radiation characteristics has not been done and dependency of flow amount on heat radiation has been unclear. By combining calculations of a three-dimensional flow field and one-dimensional heat radiation, a method has been constructed that can predict the heat radiation amount for any shaped radiators easily and precisely.

1. Introduction

The ordinary construction of motorcycle radiators contain a large number of flattened cross section cooling tubes running vertically within a rectangular radiator frame, with all the tubes of the same length. Recently, it has become necessary to design radiators capable of large amounts of heat radiation, as engines are producing increasing power. Meanwhile, more and more radiators are now designed with any shapes due to layout space restrictions. Many such any shaped radiators show considerable deviations from their predicted heat radiation characteristics when these are calculated with the methods developed for rectangular radiators.

There have been limited analysis of the heat radiation value from radiators, mainly because most of the radiators have been rectangular, lending themselves to empirical formulas developed from previous models. With the increasing need to use any shaped radiators, however, there has come an increasing need to develop new analytical techniques for quantitative heat radiation characteristics of radiators and for accurate predictions of heat radiation performance in radiators of any shapes. Oshima reported on one method for predicting the radiator heat radiation value[(1)], but there have been few discussions of specific methods for the influence of coolant flow rate or the characteristics of heat transfer from the cooling tubes to the air. Furthermore, there has not necessarily been enough research into the influence of flow rate and radiator specifications on heat radiation characteristics even for the rectangular radiators conventionally used.

The authors have developed a system capable of predicting the heat radiation characteristics of a radiator of any shapes quickly and with high accuracy, by combining a three-dimensional flow field calculation with one-dimensional heat transfer calculation.

2. Investigation of Analysis Methods

The basis of the cooling performed by a radiator is typically a forced convection heat transfer. Analysis can be divided into treatment of the flow field and treatment of the heat transfer, i.e., first, the flow field alone is analyzed, and

* Asaka R&D Center

then, those results are used to examine the heat transfer. Actual analyses are carried out in one of the following three methods.

Method A: The flow of radiator coolant in the tubes is considered as a one-dimensional flow with a uniform profile across the cross section. The flow field and heat transfer analyses are both done in one dimension.

Method B: Three-dimensional analyses are performed for both the flow field and the heat transfer.

Method C: The flow field is solved in three dimensions and after that, the heat analysis is done in one dimension.

Since the fundamental theory of Method A is simplified, it is easy to write in-house code; since the calculation time is short, it is easy to observe the effects of many parameters. On the other hand, the speed distribution of the coolant flow in the tubes is strongly influenced by the geometry of the radiator tank and other components, so this has the drawback of limited accuracy because of the one-dimensional assumption for speed distribution.

Heat transfer analysis in Method B is based on the speed distribution with full consideration of system geometry. Figure 1 shows the predicted temperature distribution on the radiator surface, according to this method. Figure 2 is the image of the actual radiator from a thermo-viewer. The results of temperature distribution in these two analyses match qualitatively. However, the calculation time for a single case is long in this method, and extremely long if the coolant flow rate is a parameter of the calculation.

In Method C, a three-dimensional analysis is carried out only for one case in any single shape for the time-consuming flow field calculation; all heat transfer parameters are analyzed in one dimension. This method offers the advantages of speedy results and practical accuracy levels when flow rate is a parameter. Procedure C was used in this study due to these advantages. A comparison of all three methods is shown in Table 1.

3. Formulation of One-Dimensional Analysis of Cooling Tube

3.1. Modeling of Cooling Phenomena

The first task in the analysis of heat transfer in cooling tubes is the creation of the model. Figure 3 shows the state of heat flow in a tube used in a radiator. As water passes through the tube, it loses heat through the tube walls and its temperature drops. In order to analyze heat exchange, the overall heat resistance R between the heat exchange medium (water), and the destination of the heat flow, (air), must be found. This value is the sum of the three resistances given below[(2), (3)].

$$R = 1 / H = 1 / hw + t / \lambda + 1 / ha \qquad (1)$$

R : Overall heat resistance
H : Overall heat-transfer coefficient
hw : Coefficient of heat transfer from water to cooling tube wall
ha : Coefficient of heat transfer from cooling tube wall to air
t : Cooling tube thickness
λ : Thermal conductivity of cooling tube

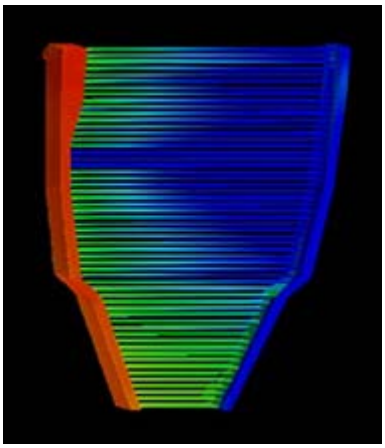


Fig. 1 Temperature distribution by simulation

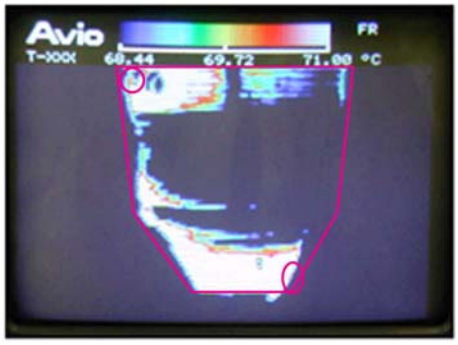


Fig. 2 Temperature distribution by thermo-viewer

Table 1 Comparison among three methods for heat radiation of radiators

Methods	Flow field calculation	Heat radiation calculation	Calculation time	Calculation accuracy
A	One dimension	One dimension	Accept-able	Un accept-able
B	Three dimension	Three dimension	Un accept-able	Accept-able
C	Three dimension	One dimension	Accept-able	Accept-able

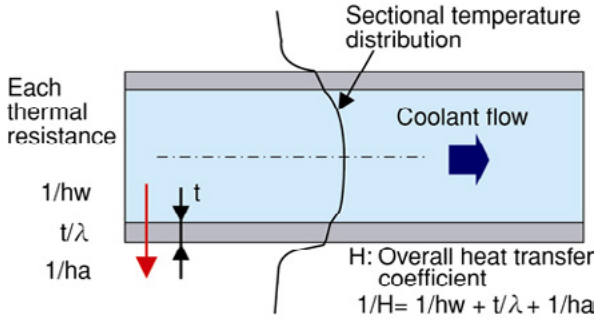


Fig. 3 Cooling model of radiator tube

Both *hw* and *ha* represent heat transfer coefficients between fluids and solids, but they are deeply influenced by the flow conditions at the wall. In other words, they are influenced not only by the flow velocity but also by whether the flow is laminar or turbulent. Therefore, it is necessary to pre-determine, in the usual flow zone used for practical uses, whether the flow is laminar or turbulent in order to select the experimental formula and the theoretical values for heat transfer. The formulas for Reynolds' number and coefficient of heat conduction given below were borrowed from References (2) and (3).

(1) Water flow in cooling tube

$$Re_d = ud / v \quad (2)$$

$$d = 4A / s \quad (3)$$

Re_d : Reynolds number

u : Flow velocity

v : Kinematic viscosity

d : Hydraulic diameter

A : Cross sectional area of tube

s : Cross section circumferential length of tube

When Re_d < 2 300, flow is laminar, and the Nusselt number Nu_d is determined as follows:

$$Nu_d = 3.66 + 0.063\,(Gz + 0.039Gz^{0.33}) \quad (4)$$

$$Gz = (x / d) / (Re_d\, Pr) \quad (5)$$

Pr: Prandtl number

The flow is turbulent at Re_d > 2 300; Nu_d is then defined by this equation:

$$Nu_d = 0.023\, Re_d^{0.8} Pr^{0.3} \quad (6)$$

From the definition of the Nusselt number, the coefficient of heat transfer *hw* is:

$$hw = \frac{Nu_d \lambda}{x} \quad (7)$$

(2) Air flow over cooling tube surface

When the flat plate boundary layer theory is applied, the laminar flow condition is:

$$Re_x = Ux / v < 3.2E5 \quad (8)$$

U : Flow velocity

x : Distance from leading edge of flat plate

In laminar flow, the mean Nusselt number Nu_m and mean coefficient of heat transfer *ha* are given by the following equations:

$$Nu_m = (0.458 Pr^{0.33} Re_x^{0.5}) \times 2.0 \quad (9)$$

$$ha = \frac{Nu_m \lambda}{x} \quad (10)$$

The results of the investigations using Eq. (2) indicated that both laminar and turbulent flows would be found in the cooling tubes under ordinary operating conditions of the motorcycle. On the other hand, when the cooling tube surface contacts air, the flow can be judged as laminar using Eq. (8) with actual operating conditions considered. Therefore, it was found that Eq. (9) is applicable.

3.2. Formulation of Numerical Procedure for One-Dimensional Heat Radiation Value

Heat balance in a single cooling tube is considered (see Fig. 4). If the temperature changes by the amount dT as the coolant passes through an infinitesimally thin zone of thickness dx, Eq. (11) can be obtained. Heat conduction in the direction of coolant flow is negligible in the cooling tube because its influence is very small.

$$Cp\, \rho\, uA\, dT = -Hs(T - To)dx - s\varepsilon\sigma(T^4 - To^4)dx \quad (11)$$

C_p : Coolant specific heat

ρ : Coolant density

A : Cross-sectional area of tube

s : Cross section circumferential length of tube

u : Mean velocity on cross section of tube

H : Overall heat-transfer coefficient from cooling water to air

T_o : Ambient air temperature

T : Coolant temperature at distance x from inlet

ε : Thermal emissivity

σ : Stefan-Boltzmann constant

Equation (11) is an ordinary differential equation showing temperature $T(x)$ in coordinate x. The first term on the right side indicates heat radiation due to heat transfer, and the second term, heat radiation due to thermal radiation. The temperature distribution can be found by solving this equation. Mathematical solution of this equation is difficult due to the second term, but it is easily solved by numerical integration. Figure 5 shows an example of results for Eq. (11) solved with the fourth-order Runge-Kutta method. The figure shows water temperature distribution in the cooling tube assuming an inlet temperature of 353 K and ambient temperature of 283 K. It indicates the temperature gradually drops as it flows through the tube from the inlet to the outlet. The three lines represent flow velocities of 0.5 m/s, 1.75 m/s and 3.0 m/s in the tube; the higher the flow velocity, the higher the exit temperature.

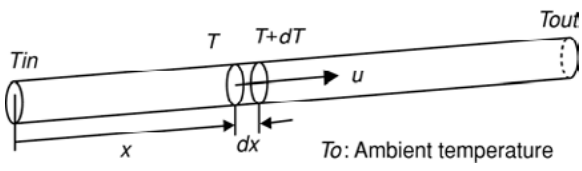


Fig. 4 Cooling tube model to introduce one dimensional heat radiation theory

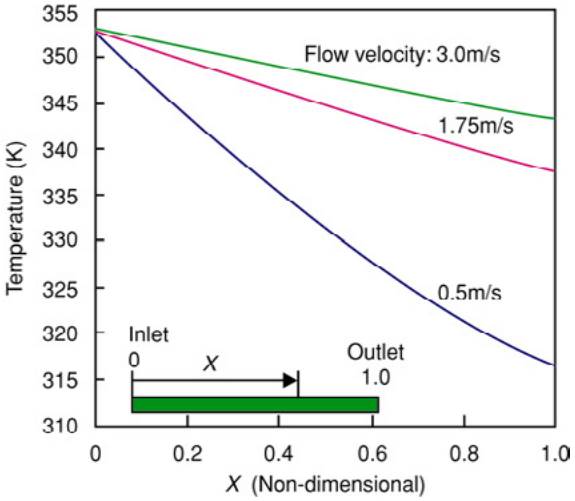


Fig. 5 Temperature distribution on cooling tube obtained from one dimension theory

If the inlet temperature is T_{in} and the outlet is T_{out}, the heat radiation value in a single tube Q_i is given by Eq. (12).

$$Qi = Cp\rho u\, A(Tin - Tout) \quad (12)$$

T_{in} : Inlet temperature

T_{out} : Outlet temperature

4. Correlation between Measured Values and Theoretical Predictions

4.1. Overview of Experiment

Equation (11) showed that the cooling tube outlet temperature and the heat radiation value could be calculated if the geometrical specifications of the tube, tube inlet temperature and ambient air temperature were known. In order to confirm the validity of this equation, a heat radiation test was carried out with a single tube to obtain the heat radiation value for comparison with the results of Eq. (11). Figures 6 and 7 show a schematic and a photograph of the test apparatus.

Single aluminum tubes of the type installed in a complete radiator were used in the following specifications:

Specification A: Cross-section 24 mm × 2.0 mm, length L = 600 mm, with fins

Specification B: Cross-section 24 mm × 2.0 mm, length L = 800 mm, with fins

Specification C: Cross-section 24 mm × 2.0 mm, length L = 800 mm, no fins

The fins were attached to the top and bottom of each tube; the heat radiation area with fins attached was 15.6 times the area with no fins. The test conditions were the following:

(1) Wind velocity was constant and water velocity in the tube was adjusted to observe coolant speed-dependent changes in the heat radiation value.

(2) Water velocity was constant and cooling wind velocity was adjusted to observe wind speed-dependent changes in the heat radiation value.

The inlet temperature T_{in} and ambient temperature T_{out} were set at 353 K and 283 K, respectively. The heat radiation value for the entire tube Q was calculated by measuring the outlet temperature T_{out} in accordance with Eq. (13).

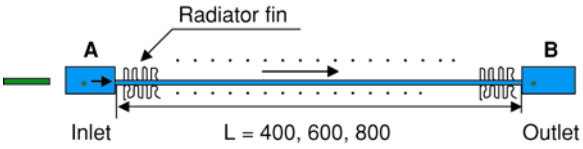


Fig. 6 Cooling tube for testing

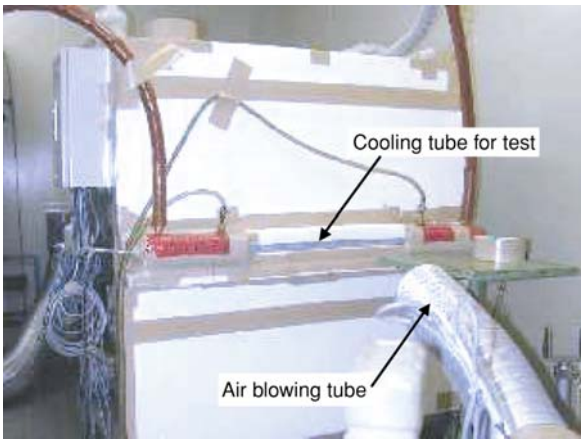


Fig. 7 Outside view of experimental device for cooling tube

$$Q = Cp\rho q(Tin - Tout) \quad (13)$$

C_p : Water specific heat

ρ : Water density

q : Volume flow rate

4.2. Comparison of Experimental Measured and Theoretical Predictions

The following discusses the results of the test and compares them with the results predicted by Eq. (11). The thermal emissivity ε, used in Eq. (11), was set at 0.08 for the aluminum surface.

(1) Without fins

Figure 8 compares the calculated values and measured values for heat radiation with a Spec. C tube under constant wind and varying water velocity in the tube. This figure shows wide disparities between the two measured values at low coolant speeds. This was probably due to measurement errors because of the low absolute values for heat radiation when fins are not attached to the tube. The theoretically predicted value was about halfway between the two measured values and represented the average of the two measurements quite well.

Figure 9 also compares calculated and measured values from a Spec. C tube, but here, the water velocity was constant while the wind velocity was varied. There was some divergence of the measured values from the predictions at the highest wind velocities, but overall, the values matched well.

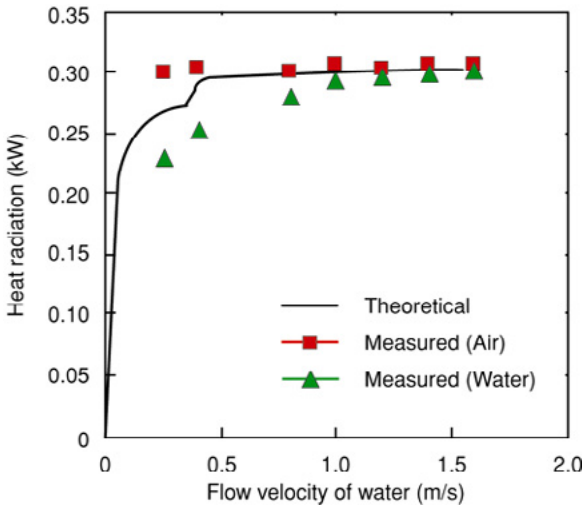


Fig. 8 Heat radiation characteristics of single tube (Wind velocity: Const. Without Fins)

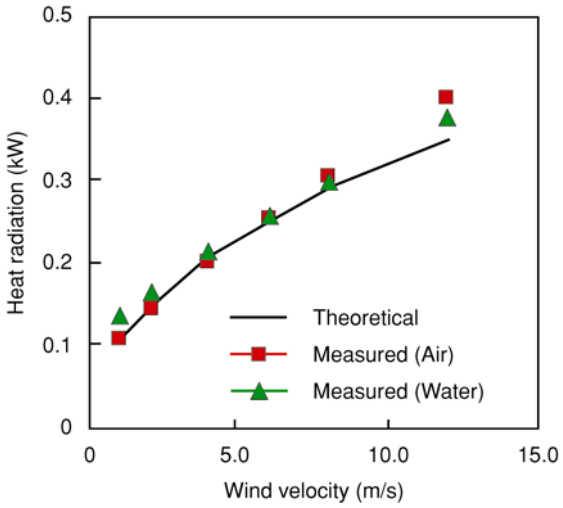


Fig. 9 Heat radiation characteristics of single tube (Water velocity: Const. Without Fins)

These results indicate that Eq. (11) accurately predicted the heat radiation value when the fins are not attached.

(2) With fins

Since the heat-radiating area was increased 15.6 times by the addition of fins, the value of *ha* in Eq. (1) was modified to show the influence of this change.

Figures 10 and 11 show the predicted and measured values for heat radiation from single tubes 600 mm and 800 mm long. In both cases, the wind velocity was constant and the results were observed while the water velocity was varied. These findings again confirmed the validity of Eq. (11).

Figures 12 and 13 show predicted and measured heat radiation values from tubes 600 and 800 mm long under constant water velocity and varying wind velocity. These indicate some deviation of the actual values from the predictions by the laminar flow theory at the low and high wind velocity range, but there is a good match in the center of the range.

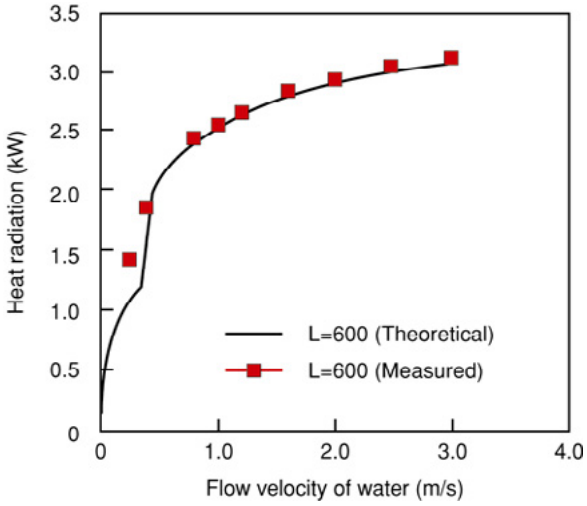


Fig. 10 Heat radiation characteristics of single tube (Wind velocity: Const. With Fins)

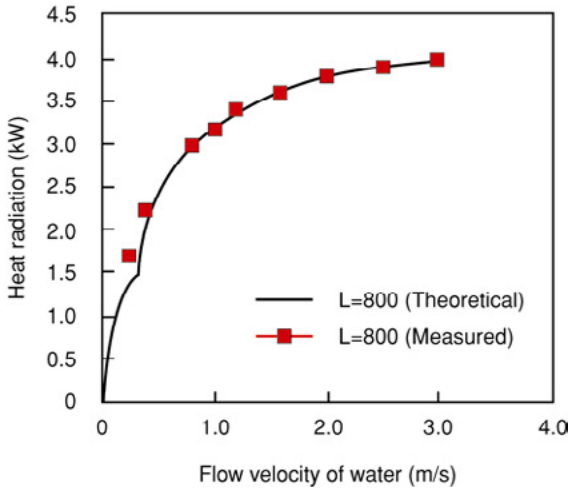


Fig. 11 Heat radiation characteristics of single tube (Water velocity: Const. With Fins)

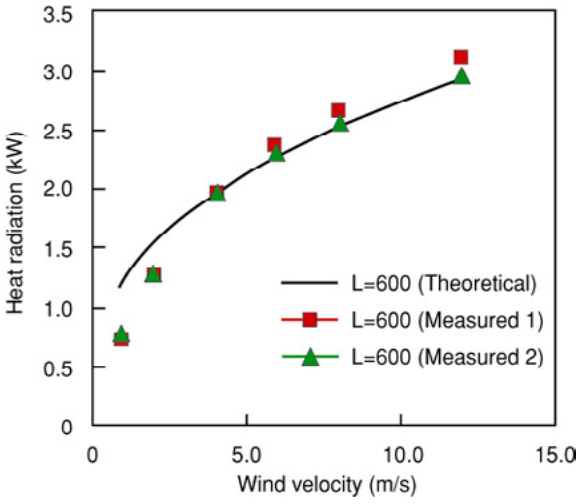


Fig. 12 Heat radiation characteristics of single tube (Water velocity: Const. With Fins)

(3) Comparison of heat radiation with and without fins

Figure 14 shows the ratio between heat radiation values when the tubes were and were not equipped with fins for both theoretical and measured values. There is a good quantitative match between the theoretical and measured values nearly everywhere. These results show that the ratio of heat radiation is not constant but dependent on the coolant flow velocity in the tube. The reason is that, according to Eq. (6), the higher the flow velocity, the higher the Nusselt number on the water side; this changes the overall heat transfer coefficient H. Since this behavior was reproduced by Eq. (11), the present theory seems to have been confirmed.

(4) Effect of thermal transfer

Since Eq. (11) allows accounting for emissivity ε, a measure of the influence of thermal radiation, the calculation was re-performed by varying ε.

Figure 15 shows the characteristics of heat radiation at emissivity of 0.08[3] for aluminum used for a cooling tube this time and at ε = 1.0, the upper limit for this parameter. Heat radiation was increased about 7% by raising ε from 0.08 to 1.

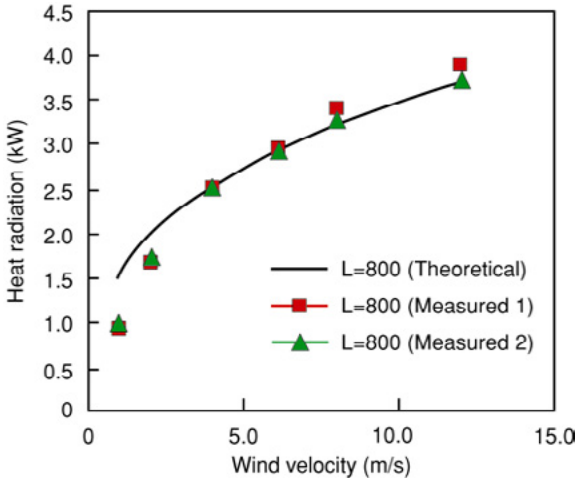


Fig. 13 Heat radiation characteristics of single tube (Water velocity: Const. With Fins)

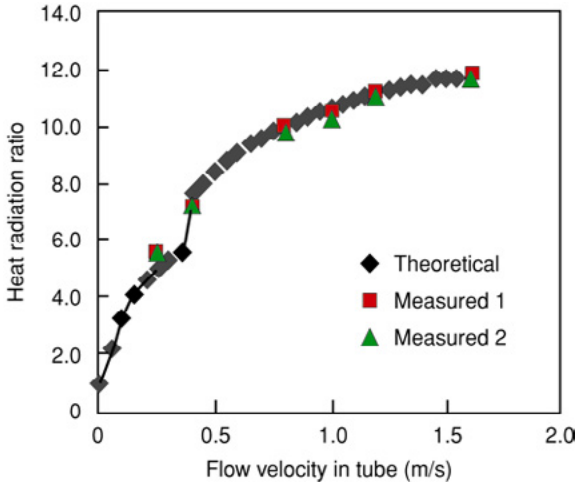


Fig. 14 Comparison between experimental results and theoretical results of heat radiation ratio (r): (heat radiation with fins)/(heat radiation without fins)

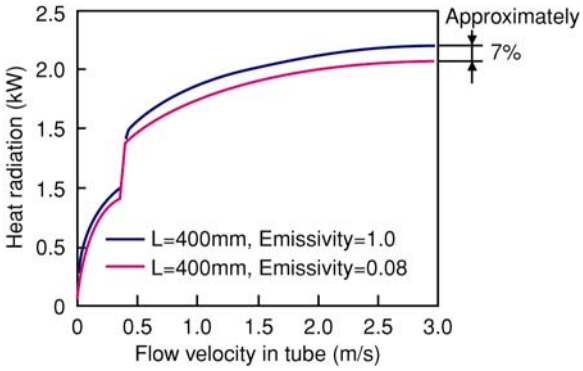


Fig. 15 Influence of emissivity in thermal radiation

Since the thermal emissivity of a real material is always less than 1, the difference due to increased ε would be less than 7%, but this result shows the necessity of thermal radiation in the performance of radiators.

5. Extension of Results to a Complete Radiator

It has been shown that the theory predicts experimental results reasonably well for single radiator tubes. An actual radiator is made up of multiple tubes; the theory for single tube can be extended to multiple tubes as follows. The heat radiation value Q_{tot} from a complex radiator consisting of n tubes with different lengths (of lengths L_1, L_2, …, L_n) is the sum of the heat radiation Q_i from each cooling tube.

From Eq. (12),

$$Qtot = \sum_{i=1}^{n} Qi \tag{14}$$

The temperature reduction of mixed coolant water flowing from different tubes, T_m, is given by:

$$Tm = \frac{\Sigma Qi}{Cp \Sigma ui Ai} \tag{15}$$

ui : Flow velocity in i^{th} tube

Ai: Cross-sectional area of i^{th} tube

However, the area ratio for heat radiation due to the addition of fins is different from that of single tubes. Since each pair of neighboring tubes shares a fin, the area ratio is one-half the value calculated for single tubes.

Thus, if ui is already established, it is possible to find the temperature reduction of the coolant due to heat radiation and cooling in a complete radiator consisting of multiple tubes. Here ui can be found from three-dimensional flow field calculations. Figures 16 and 17 show the results of the three-dimensional fluid flow calculations for the flow field of a complete radiator. They show the pressure distribution and the distribution of mean flow velocities in each cooling tube, respectively. Figure 18 presents a comparison of the predicted heat radiation characteristics using the preceding flow velocity distribution and the actual measured values. The vertical axis represents the dimensionless heat radiation value, where the value 1 represents the heat radiation attained when the flow rate is 100 l/m.

This graph indicates that the calculations showed an acceptable match with actual results in a complete radiator.

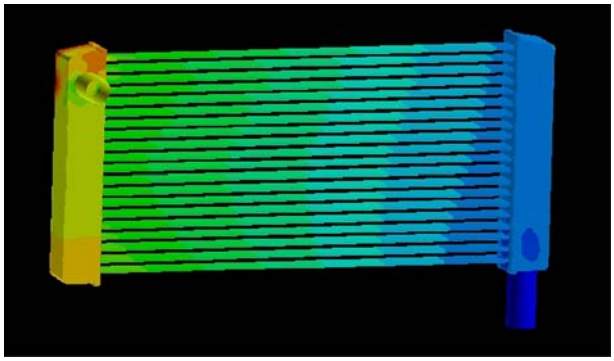


Fig. 16 Pressure distribution obtained from three-dimensional flow field simulation

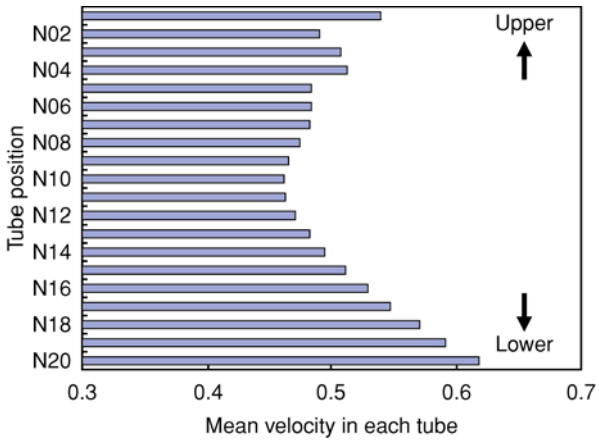


Fig. 17 Mean velocity distribution over whole tubes

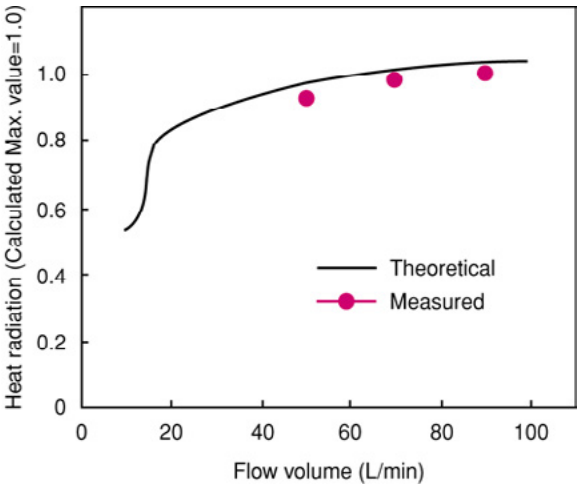


Fig. 18 Comparison of heat radiation characteristics between theoretical values and experimental values

6. Conclusion

Combining calculations for a three-dimensional flow field and a one-dimensional heat transfer model of a motorcycle radiator of any shapes enabled creation of a method for quickly and accurately predicting heat radiation characteristics under a wide variety of conditions.

This method allows rapid estimation of heat radiation characteristics for radiators of various face shapes, so it is useful for refinement of radiator specifications in early stages of development.

References

(1) Oshima, T.: Development of a Prediction Method for Engine Cooling Performance Using CFD (2nd Report), Society of Automotive Engineers of Japan, Inc. Preprint No. 109-01, 20015412, p. 13-16 (2001)

(2) Aihara, T.: Heat Transfer Engineering, Shokabo, p. 281 (1994)

(3) Katsuto, Y.: Outline of Heat Transfer, Yokendo, p. 445 (1976)

■ Authors ■




Takashi WATANABE Masayuki IWATA

Technical Papers Submitted to Out-of-company: January, 2003 to June, 2003

(English Papers only)

Date	Conference	Title	Author	Organization
2003/1/1	JSAE/JSAE Review Vol.24 No.1	Enhancements in vehicle stability and steerability with slip control	Kin Keiyuu Osamu Yano Hiroyuki Urabe	Tochigi R&D Center PSG Co., Ltd. Tochigi R&D Center
		Quantification of static seating comfort of motorcycle seats	Mitsue Koyano Takeshi Kimishima Kengo Nakayama	Asaka R&D Center
2003/1/6～9	AIAA (American Institute of Aeronautics and Astronautics/41st Aerospace Sciences Meeting and Exhibit Conference (Reno, USA)	Wave-Drag Characteristics of Over-the-Wing Nacelle Business-Jet Configuration	Michimasa Fujino Yuichi Kawamura	Honda R&D Americas Honda R&D Americas
2003/1/23	Intel Corp./Intel Research Forum and Seminar Series =Robotics Forum= (Oregon, USA)	ASIMO is working in the real world.	Yoshiaki Sakagami	Wako Research Center
2003/3/3～6	SAE/2003 SAE World Congress (Detroit/USA)	The Effect of Geometry on Stiffness and Deformation in Exhaust Manifolds for In-line 4-cylinder Engines	Masaru Enomoto	Tochigi R&D Center
		Development of 1600 N/MmU2 Class Ultra-High-Strength Bolts	Mitsuo Takashima Zenji Iida Seinosuke Tanaka Katsuhiro Tsukiyama Nobuhiko Ibaragi Yuuichi Namimura	Tochigi R&D Center Tochigi R&D Center Saga Tekkohsho Co., Ltd. Saga Tekkohsho Co., Ltd. Kobe Steel, Ltd. Kobe Steel, Ltd.
		Development of the Pre-coat Type Adhesive for All Olefin Instrument Panel	Tetsuya Oda Atsushi Kawada Corey McEnhill	Tochigi R&D Center Tochigi R&D Center Honda R&D Americas
		Development of Lead Free Cationic E- coating for Automobile Body in White	Hiroyuki Morishita Katsuyoshi Kaneko	Tochigi R&D Center Tochigi R&D Center
		Development of Metal Pushing V-Belt Stress Simulation for Continuously Variable Transmission	Toshihiro Saito	Tochigi R&D Center
		An Examination of Eps Using Cables to Connect the Steering Wheel and Gearbox	Koichi Suyama	Tochigi R&D Center
		Rear-end Collision Velocity Reduction System	Kenji Kodaka Makoto Otabe Yoshihiro Urai Hiroyuki Koike	Tochigi R&D Center Tochigi R&D Center Tochigi R&D Center Tochigi R&D Center
		New Approach to High Rigidity Body Construction Using Dynamic Analysis	Mikio Shibaoka Kaoru Kusaka Yoshiharu Itai Yasushi Nakanishi	Tochigi R&D Center Tochigi R&D Center Tochigi R&D Center Tochigi R&D Center
		A New Concept for Occupant Deceleration Control in a Crash-Part 2	Yasuki Motozawa Makoto Tsuruta Yasushi Kawamura Junya Noguchi	Tochigi R&D Center Tochigi R&D Center Tochigi R&D Center Tochigi R&D Center
		High Reliability Electronic Throttle System Design	Eiji Hashimoto Shusuke Akazaki Yuji Yausi Tetsuya Ishiguro	Tochigi R&D Center Tochigi R&D Center Tochigi R&D Center Tochigi R&D Center
		Development of Metal Pushing V-Belt for Continuously Variable Transmission - Investigation for Clearance between Elements, Strength of Element and Strength of Ring Material-	Tooru Yagasaki Shigeru Kanehara Hideaki Aoyama Kazuo Ishii Yoshinari Okada	Tochigi R&D Center Tochigi R&D Center Tochigi R&D Center Tochigi R&D Center Tochigi R&D Center
		Development of a Power Train for the Hybrid Automobile -the Civic Hybrid	Hirohisa Ogawa Masato Matsuki Takahiro Eguchi	Tochigi R&D Center Tochigi R&D Center Tochigi R&D Center
		Prediction of the SEA Input Parameters for the Sound Package	Kazuhito Misaji Hiroko Tada Tsuyoshi Yamashita M. Mantovani C. Gaudino T. Falk	Tochigi R&D Center Tochigi R&D Center Tochigi R&D Center Rieter Automotive Switzerland Rieter Automotive Switzerland Rieter Automotive Switzerland
		Development of a Hybrid SEA Modeling Scheme for a Passenger Car	Kazuhito Misaji Hiroko Tada Tsuyoshi Yamashita Mitsuo Nakamura Hidenori Tanaka Shinichi Kokabu Daisuke MORIE	Tochigi R&D Center Tochigi R&D Center Tochigi R&D Center Honda R&D Europe UK California State University California State University California State University
		Development of a Low Precious-metal Automotive Perovskite Catalytic System for LEV-II	Yoshiaki Matsuzono Masahiro Sakanushi Hiroshi Kitagawa	Tochigi R&D Center Tochigi R&D Center Tochigi R&D Center
		Development of a Lane mark Recognition System for a Lane Keeping Assist System	Kenichi Mineta Kiyozumi Unoura Tetsuo Ikeda	Tochigi R&D Center Tochigi R&D Center Tochigi R&D Center
		Improvement of thermal resistance for lean Nox Catalyst	Masato Kanaeda Hidehiro Iizuka Kazutoshi Higashiyama Osamu Kuroda Toshihumi Hiratsuka Norihiro Shinotsuka Hiroshi Ohno Toshikatsu Takanohashi Naohiro Satoh	Hitachi Research Laboratory, Hitachi, Ltd. Hitachi Research Laboratory, Hitachi, Ltd. Hitachi Research Laboratory, Hitachi, Ltd. Hitachi, Ltd. Hitachi, Ltd. Hitachi, Ltd. Tochigi R&D Center Tochigi R&D Center Tochigi R&D Center

Date	Conference	Title	Author	Organization
2003/3/3～6	SAE/2003 SAE World Congress (Detroit/USA)	Development of a Driver Assistance System	Shinnosuke Ishida Jun Tanaka Satoshi Kondo Masahito Shingyoji	Tochigi R&D Center Tochigi R&D Center Tochigi R&D Center Tochigi R&D Center
2003/4/1～3	SAE/The 12th International Pasific Conference on Automotive Engineering (Bangkok, Thailand)	Development of a 125cm3 4-stroke Engine for Motorcycle with Low Fuel Consumption and Low Emission for Thailand	Yoshinobu Sawamura Norio Saito Bunichiro Sakamoto Hideo Kobayashi Yoshihisa Hirose	Asaka R&D Center Asaka R&D Center Asaka R&D Center Asaka R&D Center Asaka R&D Center
		Development of an ECU Integrated Throttle Body System Module for Compact Fuel Injection System Used in Small Motorcycles and Scooters	Nobuhiro Shimada Shunji Akamatsu Minoru Ueda Akira Hayashi Yoshiaki Hirakata	Asaka R&D Center Asaka R&D Center Asaka R&D Center Asaka R&D Center Asaka R&D Center
2003/4/1～4	SAE-Thailand/IPC-12 (The 12th International Pacific Conference on Automotive Engineering) (Bangkok, Thailand)	Research on Aluminum Structures for Crash Energy Absorption	Toru Kawano Yuta Urushiyama	Tochigi R&D Center Tochigi R&D Center
		Development of a New Power Train for the Civic Hybrid	Asao Ukai Takashi Kamimura	Tochigi R&D Center Tochigi R&D Center
		Development of a New Lightweight Compact CVT	Hisashi Kunii Makoto Sumi	Tochigi R&D Center Tochigi R&D Center
2003/4/2～3	VDA/VDA Technical Congress 2003 (Wolfsburg, Germany)	Development of a Power Train for the Hybrid Automobile - the Civic IMA	Masato Matsuki Yuichi Hirano Atsushi Matsubara	Tochigi R&D Center Tochigi R&D Center Tochigi R&D Center
2003/4/25～26	Institute of Psychology Christian-Albrechts University/45th Meeting for Experimental Psychologists (Kiel, Germany)	Influence of simulated driving on language production	Martina Neidhart Miklos Kiss Marc Wittmann Ernest Poppel Peter Gugg Alexander Steffen Hiroyuki Kamiya	Generation Research Program Ludwig-Maximilians -University Generation Research Program Ludwig-Maximilians -University Generation Research Program Ludwig-Maximilians -University Generation Research Program Ludwig-Maximilians -University SCIENCIA GmbH SCIENCIA GmbH Tochigi R&D Center
		Warning signals in the car: how should they be constructed?	Miklos Kiss Martina Neidhart Marc Wittmann Ernest Poppel Peter Gugg Alexander Steffen Hiroyuki Kamiya	Generation Research Program Ludwig-Maximilians -University Generation Research Program Ludwig-Maximilians -University Generation Research Program Ludwig-Maximilians -University Generation Research Program Ludwig-Maximilians -University SCIENCIA GmbH SCIENCIA GmbH Tochigi R&D Center
2003/5/2	The Robotics Institute./Robo Cup 03 First American Open (Pittsburgh, USA)	New ASIMO is progressing an ability for supporting human activity.	Yoshiaki Sakagami	Wako Research Center
2003/5/5～8	SAE/2003 SAE Noise & Vibration Conference & Exhibition (Traverse City, Michigan, USA)	A Support System for Development of Sporty Sound and Its Application	Yasuo Ishii Masashi Iwai Koji Ito Tsuyoshi Yamashita	Tochigi R&D Center Tochigi R&D Center Tochigi R&D Center Tochigi R&D Center
		Improvement of Engine Noise for the 2003 Accord Using Hybrid CAE Technology	Tatsuhide Sakai Tetsuya Miyahara	Tochigi R&D Center Tochigi R&D Center
		Perception Modeling and Quantification of Sound Quality in Cabin	Kousuke Noumura Junji Yoshida	Tochigi R&D Center Tochigi R&D Center
		Testing Uniqueness of a Hybrid Sea Modelling Solution for a Passenger Car	Kazuhito Misaji Hiroko Tada Tsuyoshi Yamashita Mitsuo Nakamura Shinichi Kokabu Hidenori Tanaka Daisuke Morie	Tochigi R&D Center Tochigi R&D Center Tochigi R&D Center Honda R&D Europe UK California State University California State University California State University
		SEA Model Building of Automotive car Body-in-White Using Experiment and FEM	Kenji Nishikawa Kazuhito Misaji Minoru Kamata Toru Yamazaki	Tochigi R&D Center Tochigi R&D Center The University of Tokyo Kanagawa Univ.
		Reducing Crank Rumble Using Transfer Path Analysis to Assess Engine Modifications	Mike Croker Matthew Maunder Yoshihiro Imai Noboru Sannodo Takashi Kondo	Ricardo Consulting Engineers, Ltd. Ricardo Consulting Engineers, Ltd. Tochigi R&D Center Honda R&D Americas, Ohio Center Tochigi R&D Center
2003/5/15	Automotive Engineering, Technical University Vienna and others/24th International Vienna Motor Symposium (Wien, Germany)	The Hybrid Catalyst, a New Catalyst Concept to improve Catalyst Efficiency of Diesel Catalyst Systems by Thermal Management	Rolf Bruck Seiichi Hosogai Kazunari Komatsu Yasuaki Unno	Emitec Tochigi R&D Center GKN plc GKN plc
2003/5/19～22	NHTSA, MILT of Japan, METI of Japan/18th International Technical Conference on the Enhanced Safety of Vehicles (Nagoya, Japan)	Development of Finite Element Model for Child Pedestrian Protection	Masayoshi Okamoto Yuukou Takahashi Fumie Mori Masahito Hitosugi Jane Madeley Johan Ivarsson Jeff R. Crandall	Tochigi R&D Center Tochigi R&D Center PSG Co., Ltd. Dokkyo Univ. School of Medicine University of Virginia United States of America University of Virginia United States of America University of Virginia United States of America

Date	Conference	Title	Author	Organization
2003/5/19 ～22	NHTSA, MILT of Japan, METI of Japan/18th International Technical Conference on the Enhanced Safety of Vehicles (Nagoya, Japan)	Development of a Technology to Prevent Deviation from an Intended Lane While Turning Using Vehicle Dynamics Control	Keiyuu Kin Hiroshi Sekine Osamu Yano Hiroyuki Sugishita	Tochigi R&D Center Tochigi R&D Center PSG Co., Ltd. PSG Co., Ltd
		Rear-end Collision Avoidance Assist System	Kenji Kodaka Makoto Otabe Yoshihiro Urai Hiroyuki Koike	Tochigi R&D Center Tochigi R&D Center Tochigi R&D Center Tochigi R&D Center
		Innovative Body Structure for the Self-protection of a Small Car in a Frontal Vehicle-to-vehicle Crash	Masuhiro Saito Tetsuya Gomi Yoshinori Taguchi Takeshi Yoshimoto Tomiji Sugimoto	Tochigi R&D Center Tochigi R&D Center Tochigi R&D Center Tochigi R&D Center Tochigi R&D Center
		Advanced FE Lower Limb Model for Pedestrians	Yuukou Takahashi Yuji Kikuchi Fumie Mori Atsuhiro Konosu	Tochigi R&D Center Tochigi R&D Center PSG Co., Ltd. Japan Automobile Research Institute
		Validation of the Human Head FE Model Against Pedestrian Accident and Its Tentative Application to the Examination of the Existing Tolerance Curve	Yasuhiro Dokko Robert Anderson Jim Manavis Peter Blumburgs Jack McLean Liyn Zhang King H.Yang Albert I.King	Tochigi R&D Center The University of Adelaide Australia The University of Adelaide Australia The University of Adelaide Australia The University of Adelaide Australia Wayne State University USA Wayne State University USA Wayne State University USA
		A Study of Compatibility Test Procedure in Frontal Impact	Satoshi Takizawa Tomiji Sugimoto Hideki Suzuki	Tochigi R&D Center Tochigi R&D Center Tochigi R&D Center
		Research of an Advanced Seatbelt	Koichi Kamiji Hiroshi Akaba	Tochigi R&D Center Tochigi R&D Center
	JSAE/SAE / 2003 JSAE/SAE International Spring Fuels & Lubricants Meeting (Yokohama, Japan)	A Study of Extension of Engine Coolant Life Using Low Phosphate Organic Acid Inhibitors	Mitsuru Oosawa Yoshiyuki Morita Takashi Nagashima	Tochigi R&D Center Tochigi R&D Center Tochigi R&D Center
		Indicated Mean Effective Pressure Measuring Method Using Optical Fiber Pressure Sensor	Keiichi Nagashima Tsunemichi Kawa Kazuo Tsuchiya	Tochigi R&D Center Tsukasa Sokken Co., Ltd. Meiji Univ.
2003/5/29 ～31	The Electrochemical Society of Japan/2003 International Conference on Advanced Capacitor (Kyoto, Japan)	Application Studies of Electric Double-layer Capacitor System for Fuel Cell Vehicle	Naohiko Oki Shinji Kato Koji Tamenori Minoru Noguchi Kazuya Hiratsuka Katsuya Ikeda	Wako Research Center Wako Research Center Wako Research Center Wako Research Center Asahi Glass Co., Ltd. Asahi Glass Co., Ltd.
2003/6/1	Institution of Mechanical Engineers/International Journal of Engine Resarch Vol.4 No.2	A Calculation Method for Indicated Mean Effective Pressure Based on Harmonic Analysis of Pressure Waveform	Kazuo Tsuchiya Keiichi Nagashima	Meiji Univ. Tochigi R&D Center
2003/6/4～6	Rieter Automotive Switzerland/RIETER Automotive Conference 2003 (Luzern, Switzerland)	Optimum Design of a Sound Package Component within the Automotive VEACTOR System	Kazuhito Misaji Hiroko Tada Tsuyoshi Yamashita N.Baldanzini H.Patzold M.Mantovani	Tochigi R&D Center Tochigi R&D Center Tochigi R&D Center University of Florence Rieter Automotive Switzerland Rieter Automotive Switzerland
2003/6/8～12	MPIF (Metal Power Industries Federation)/2003 International Conference on Power Metallurgy & Particurate Materials (LasVegas, USA)	Development of High Strength & Free Machined Power Forged Connecting Rod	Masaki Amano Russell Scott Hideaki Ushio	Tochigi R&D Center Honda R&D Americas, Ohio Center Honda R&D Americas, Ohio Center
2003/6/10 ～13	AABC (Advanced Automotive Battery Conference)/2003 3rd International AABC (Nice, France)	Application Studies of The Ultracapacitor System for Honda FCV	Koji Tamenori Shinji Kato Naohiko Oki Koichi Yamamoto Akihiro Anekawa Minoru Noguchi	Wako Research Center Wako Research Center Wako Research Center Wako Research Center Wako Research Center Wako Research Center
2003/6/16 ～19	ASME-IGTI(American Society of Mechanical Engineers-International Gas Turbine Institute)/ASME TURBO EXPO 2003 (Atlanta, USA)	Advanced Micro Power Generators-micro GT	S.Kang Jim Johnston Minoru Matsunaga Toshiyuki Arima Hideaki Tsuru F.Prinz	Stanford University Stanford University Wako Research Center Wako Research Center Honda R&D Americas Stanford University
		Microturbine Researches at Honda	Koichi Shinmura	Wako Research Center

Editor’s Postscript

It has already been 15 years since our inaugural issue. For some reason people tend to recall things in blocks of five years or ten years. In much the same way, I read back in the *Technical Review* the other day, starting with the inaugural issue. Though I can hardly say that I read every issue cover to cover, so many things triggered particular memories. I realized that the *Technical Review* presents a vivid picture not only of the changes in our technology, but also of the shifts and changes in our society. Of course, I know perfectly well that the products we deal with are essentially aggregations of the achievements made in a variety of technical fields. Still, I can't help but feel that the technical fields have expanded in those 15 years, in response to the major changes that have taken place in society.

In that case, what does the present issue tell us? This time (*Honda R&D Technical Review*, Vol. 15, No. 2) we are presenting ten “Introductions of new technologies” articles and 24 “technical papers”. Together with articles dealing with evolutions in existing technology, this issue carries several submissions relating to fuel cell vehicles, continuing from our previous issue. The number of submissions from overseas R&D centers has been quite steady, and we are carrying three.

We hope that this material will make our achievements more widely known in the world, subjecting it to critique, and providing a training forum for engineers who seek further improvement. Limited though our abilities may be, we want to take an active part as we make this forum available. We are hoping to receive your further continued cooperation and support.
(Urata)

Honda is constantly addressing the question of how to contribute to environmental issues that extend into the world's future. We take the view that it is crucial to act. The R&D divisions play a significant part in corporate activities. We have also sought to operate according to Honda's fundamental principles and to acknowledge our own impact on the global environment and to address the various individual issues involved. Consequently, starting with this issue of the *Honda R&D Technical Review*, we have decided to use recycled paper and soy ink in the interest of the effectively using resources and protecting the environment.
(Godo)
(Tsuruga)

Honda R&D Technical Review English Version Vol.15 No.2
The following associates provided us with their cooperation and expertise:

Pankaj	Aeri	Honda R&D Americas, Inc. Ohio Center
Karen	Arneson	American Honda Motor Co., Inc.
Bill	Bezilla	Honda R&D Americas, Inc. Ohio Center
Jayme	Birken	Honda R&D Americas, Inc. Ohio Center
Jeff	Brown	Honda R&D Americas, Inc. Ohio Center
Bobbie	Burke	Honda R&D Americas, Inc. Ohio Center
Bryan	Cerra	Honda R&D Americas, Inc. Ohio Center
Mary	Christopherson	Honda North America Inc.
Dennis	Chung	Honda R&D Americas, Inc. Ohio Center
Marcos	DeLeon	Honda R&D Americas, Inc. Ohio Center
Jim	Dykeman	Honda R&D Americas, Inc. Ohio Center
Charles	Gagliano	Honda R&D Americas, Inc. Ohio Center
Lee	Goldring	Honda North America Inc.
Corky	Kamei	Honda R&D Americas, Inc. Ohio Center
Christopher	Kipfer	Honda R&D Americas, Inc. Ohio Center
Dan	Leibovitz	Honda R&D Americas, Inc. Ohio Center
Steve	Mathison	Honda R&D Americas, Inc. Los Angeles Center
Chris	Nichols	Honda R&D Americas, Inc. Ohio Center
Alan	Seid	Honda R&D Americas, Inc. Ohio Center
Joshua	Sigmund	Honda R&D Americas, Inc. Ohio Center
Randy	Skiles	Honda R&D Americas, Inc. Ohio Center
Randy	Wieland	Honda R&D Americas, Inc. Ohio Center
William	Willen	American Honda Motor Co., Inc.













HONDA